

**PHOTO- AND THERMALLY DRIVEN LIGATION TECHNIQUES
AND THEIR APPLICATION IN STEP-GROWTH
POLYMERIZATION OF BIOINSPIRED AND SYNTHETIC
MATERIALS**

Zur Erlangung des akademischen Grades eines

DOKTORS DER NATURWISSENSCHAFTEN

(Dr. rer. nat.)

der KIT-Fakultät für Chemie und Biowissenschaften

des Karlsruher Instituts für Technologie (KIT)

genehmigte

DISSERTATION

von

Thomas Gegenhuber

geboren in Speyer, Deutschland

KIT-Dekan:	Prof. Dr. Reinhard Fischer
1. Referent:	Prof. Dr. Christopher Barner-Kowollik
2. Referent:	Prof. Dr. Michael A. R. Meier
Tag der mündlichen Prüfung:	14. Dezember 2017

Die vorliegende Arbeit wurde im Zeitraum von Februar 2014 bis November 2017 am Institut für Technische Chemie und Polymerchemie am Karlsruher Institut für Technologie (KIT) – Universitätsbereich unter der Betreuung von Prof. Dr. Christopher Barner-Kowollik angefertigt.

This is Major Tom to Ground Control

I'm stepping through the door...

From "Space Oddity" – David Bowie

ABSTRACT

In the present work, novel avenues to step-growth (SG) polymerization processes are developed in the field of segmented copolymer design as well as polymer-peptide materials. Therefore, highly efficient thermally or photo-induced reactions, such as Diels-Alder (DA) reactions as platforms for polymerization and bioorthogonal reactions, are employed. In addition, spatially resolved surface functionalization with specific peptides is demonstrated in a reversible fashion.

First, SG polymerization is conducted by exploiting two different DA reactions using an AA/BB monomer system and subsequently employing these SG polymers as precursors for reversible addition fragmentation chain transfer (RAFT) polymerization. In case of the photo-induced DA reaction, difunctional *ortho*-methyl benzaldehydes are utilized in combination with difumarates effecting a DA based SG polymerization upon irradiation with UV-light. Having incorporated a trithiocarbonate moiety within the difumarate monomer, the SG polymer features multiple RAFT groups in the backbone. Thus, the SG precursor polymer is readily available as multi-chain transfer agent for subsequent RAFT polymerization affording segmented copolymers with high molecular weights. In an in-depth study, the SG and the RAFT polymers are investigated – in collaboration with the team of Prof. D’hooge from Ghent University – by *in silico* calculations to gain a deeper insight into the polymerization processes. Furthermore, these calculations provide access to fundamental molecular characteristics of the obtained polymers, e.g. the distribution of the RAFT group in the polymer chain after the RAFT polymerization. In addition, simulations enable the optimization of experimental parameters, since a side reaction during the photo-induced SG polymerization requires careful adjustment of the monomer stoichiometry. In a second DA based SG system – also an AA/BB monomer system – a thermally induced DA reaction of a difunctional cyclopentadienyl monomer and a difumarate, bearing RAFT groups, yields well-defined SG polymers. Here, the absence of any side reaction, the facile procedure at ambient temperature with no need of catalysts or complex reaction setup underpins the powerful reaction protocol. In a similar fashion compared to the photo-induced system, the SG polymers are employed in a subsequent RAFT polymerization obtaining segmented copolymers with high molecular weights.

In the second part of the current thesis, cysteine-rich domain (CRD) peptides are exploited as synthetic tool for SG polymerization as well as for encoding CRDs to surfaces in a spatially-resolved fashion to bring the complexity of SG polymerization to the next level. CRDs bear multiple cysteine units which are capable to form intra- or intermolecular disulfide bonds in an equilibrium between disulfides and thiols (disulfide reshuffling). Such

a disulfide reshuffling process is known in nature, where α,ω -CRD-functional proteins as end-groups of minicollagens undergo an SG polymerization triggered by an enzymatic stimulus.¹ Here, the disulfide reshuffling is adapted in a synthetic SG polymerization mimicking its archetype in nature and as encoding tool to create functional spatially-resolved surfaces by photo-induced ligation chemistry. The α,ω -functional polymers as macromonomer, decorated with CRDs at their chain termini, undergo SG polymerization by disulfide reshuffling of the terminal CRD units. To obtain such a macromonomer, the CRDs need to be coupled to a polymer: In the first step, the CRDs are folded in a mild reoxidative procedure, forming disulfides to protect the thiols. In subsequent reactions, functional anchor sites for highly efficient bioorthogonal reactions are introduced to the CRDs by active ester chemistry. To assess the applicability and reactivity of the bioorthogonal reactions, the functional CRDs are coupled to small organic compounds in DA reactions, nitrile-imine mediated tetrazole-ene cycloadditions (NITEC), and copper-catalyzed azide-alkyne cycloadditions (CuAAC). After successfully application of the CRDs in bioorthogonal reaction protocols with small molecules, the functional CRD reactions are translated to polymeric systems.

Having established the functionalization protocols of CRDs, CRDs are employed as a reversible functionalization platform in surface encoding using a combination of photo-induced chemistry (NTIEC) and a disulfide reshuffling protocol. Here, CRDs are immobilized onto tetrazole functional surfaces by NITEC in a spatially-resolved fashion. By writing CRD repellent areas onto the surface, an inverse CRD pattern is obtained in a two-step process. Furthermore, specifically modified CRD peptides are immobilized onto the surface by disulfide reshuffling. In a similar fashion, the CRDs are released from the surface under mild reoxidative conditions. The second functional CRD species is readily available to be detected in in-depth surface analysis by time-of-flight secondary ion mass spectrometry (ToF-SIMS). Here, the coded and decoded surfaces are characterized and imaged by ToF-SIMS, illustrating the successful writing and erasing of the second CRD peptide derivative on and from the surface, respectively.

ZUSAMMENFASSUNG

In der vorliegenden Arbeit werden neue Konzepte für Stufenwachstumspolymerisationen im Bereich segmentierter Copolymere und Polymer-Peptide Materialien vorgestellt. Hierfür werden effiziente thermische sowie lichtinduzierte Reaktionen, u.a. Diels-Alder (DA) Reaktionen, als Plattform für Polymerisations- und bioorthogonale Reaktionen verwendet. Zusätzlich wird eine reversible orts aufgelöste Oberflächenfunktionalisierung mit speziellen Peptiden gezeigt. Zunächst werden Stufenwachstumspolymerisationen durchgeführt, wobei zwei verschiedene DA Reaktionen mit AA/BB-Monomersystemen angewandt werden, um die daraus resultierenden Stufenwachstumspolymere als Templat für die reversible Additions-Fragmentierungs Kettenübertragungs (RAFT) Polymerisation einzusetzen. Im Falle der lichtinduzierten DA Reaktionen werden difunktionale *ortho*-Methyl Benzaldehyd Monomere in Kombination mit Difumaraten Monomeren unter UV-Lichteinstrahlung polymerisiert. Bei der Polymerisation werden multiple Trithiocarbonat Gruppen in die Wiederholeinheit und in das Rückgrat des Polymers eingebaut, welche zuvor im Difumarat Monomer vorhanden sind. Dadurch kann das Stufenpolymer ohne Postmodifikation direkt als Templat für die RAFT Polymerisation eingesetzt werden, wodurch segmentierte Copolymere generiert werden. In einer detaillierten Studie werden das Stufen- sowie das RAFT-Polymer in Kooperation mit Prof. D'hooge von der Universität Gent in *in silico* Berechnungen untersucht um einen tieferen Einblick in den Polymerisationsprozess zu gewinnen. Des Weiteren können die Berechnungen fundamentale molekulare Eigenschaften der verschiedenen Polymere bestimmen, z.B. die Verteilung der RAFT-Gruppen im Polymer nach der RAFT Polymerisation. Zusätzlich können die Simulationen die experimentellen Parameter für die Polymerisation optimieren, da durch eine Nebenreaktion während des lichtinduzierten Stufenwachstums die Stöchiometrie der Monomere angepasst werden muss. In einem zweiten Stufenwachstumsprozess, ebenfalls ein AA/BB Monomersystem, wird eine thermisch induzierte DA Reaktionen von Dicyclopentadienen und analogen Difumaraten durchgeführt um wohldefinierte Stufenwachstumspolymere zu erzeugen. Hier zeigt der Stufenwachstumsprozess keine Nebenreaktionen und die Effizienz des Systems spiegelt sich in der einfachen Prozedur wider, u.a. durch den simplen Reaktionsaufbau, redundantem Katalysator und Reaktion bei Raumtemperatur. Wie im Falle des lichtinduzierten Systems, wird das thermisch generierte Stufenpolymer als Templat für eine RAFT Polymerisation eingesetzt um wohldefinierte segmentierte Copolymere mit hochmolekularen Spezies zu erhalten.

Im zweiten Teil werden Cystein-reiche Domänen (CRDs) als funktionelle Einheit für Stufenwachstumspolymerisation und orts aufgelöste Oberflächenmodifikation verwendet. CRDs sind kurze Peptide, die multiple Cysteineinheiten tragen und in der Lage sind intra- oder intermolekulare Disulfidbindungen zu bilden. Diese Disulfidbindungen liegen in einem sensiblen Gleichgewicht vor, welches, abhängig von einem Stimulus oder von den Umgebungsbedingungen, zwischen den Thiolen und den Disulfiden schalten kann (Disulfid-Reshuffling). In der Natur tritt ein Disulfid-Reshuffling von CRDs in einem Stufenwachstumsprozess von Minikollagenen auf, welcher von einem enzymatischen Stimulus ausgelöst wird. Dieser natürliche Stufenwachstumsprozess soll adaptiert werden, indem CRDs einerseits analog für synthetische Stufenwachstumsprozesse verwendet werden, und andererseits um als Entwicklungsmotiv für orts aufgelöste funktionale Oberflächen zu fungieren. Im Falle der Stufenwachstumsprozesse sollen Polymere mit je zwei CRD-Endgruppen hergestellt werden, die durch Disulfid-Reshuffling eine Stufenwachstumspolymerisation auslösen. Im ersten Schritt werden die CRDs oxidativ intramolekular gefaltet um die Thiole vor Nebenreaktionen zu schützen. Dann werden an die gefalteten CRD-Einheiten orthogonale Ankergruppen angebracht, die für die Kopplung an das Polymer geeignet sind. Gleichzeitig werden Polymere mit dem entsprechenden Gegenstück hergestellt. Um die Ligationsmethode zwischen Polymer und Peptid zu prüfen, werden die funktionalen CRDs mit Kleinmolekülen in bioorthogonalen Reaktionen eingesetzt, u.a. DA Reaktionen, Kupfer-katalysierte Azid-Alkin Cycloadditionen (CuAAC) und Nitril-Imin medierte Tetrazol-En Cycloadditionen (NITEC). Nach der erfolgreichen Kleinmolekülstudie, werden diese auf polymere Systeme übertragen.

Nachdem die Funktionalisierung von CRDs erfolgreich durchgeführt wurde, werden CRDs als reversible Funktionalisierungseinheit für Oberflächenmodifikationen verwendet, wobei hier lichtinduzierte Reaktionen und das Disulfid-Reshuffling angewandt werden. Hierzu wird lichtinduziert im ersten Schritt eine aus Polyethylenglykol bestehende CRD abweisende Schicht auf der Oberfläche angebracht um im zweiten Schritt die CRDs kovalent und orts aufgelöst auf den nicht CRD-abweisenden Stellen zu immobilisieren. In der nächsten Stufe wird eine speziell funktionalisierte CRD durch Disulfid-Reshuffling aufgebracht, die entsprechend in einem ähnlichen reoxidativen Verfahren wieder von der Oberfläche entfernt wird. Diese speziell funktionale CRD ist mit einer Gruppe versehen, die durch Flugzeit-Sekundärionen Massenspektrometrie (ToF-SIMS) selektiv detektiert werden kann. Nach dem Schreib- bzw. Lösprozess kann die Bildgebung durch ToF-SIMS das erfolgreiche Beschreiben bzw. Entfernen der speziell funktionalen CRD erfolgreich darstellen.

ERKLÄRUNG

Hiermit erkläre ich, dass die vorliegende Arbeit im Rahmen der Betreuung durch Prof. Dr. Christopher Barner - Kowolik selbstständig von mir verfasst und keine anderen als die angegebenen Quellen und Hilfsmittel verwendet wurden. Stellen mit wörtlich oder inhaltlich übernommenen Inhalten sind durch Zitate als solche gekennzeichnet. Die Satzung des Karlsruher Instituts für Technologie (KIT) zur Sicherung guter wissenschaftlicher Praxis wurde beachtet und die Abgabe und Archivierung der Primärdaten gemäß Abs. A (6) der Regeln zur Sicherung guter wissenschaftlicher Praxis des KIT beim Institut ist gesichert. Ich garantiere, dass die elektronische Version mit der gedruckten Ausgabe übereinstimmt. Des Weiteren erkläre ich, dass ich mich weder in einem weiteren laufenden Promotionsverfahren befinde noch dass ich bereits einen anderen Promotionsversuch unternommen habe.

Karlsruhe, den 6. November 2017

Thomas Gegenhuber

PUBLICATION LIST

Publications arising from this Thesis

- (3) Gegenhuber, T.; Schenzel, A. M.; Goldmann, A. S.; Zetterlund, P. B.; Barner-Kowollik, C. *Chem. Commun.* **2017**, 53 (77), 10648–10651.
- (2) Gegenhuber, T.[§]; De Keer, L.[§]; Goldmann, A. S.; Van Steenberge, P. H. M.; Mueller, J. O.; Reyniers, M.-F.; Menzel, J. P.; D'hooge, D. R.; Barner-Kowollik, C. *Macromolecules* **2017**, 50 (17), 6451–6467.
- (1) Gegenhuber, T.; Abt, D.; Welle, A.; Özbek, S.; Goldmann, A. S.; Barner-Kowollik, C. *J. Mater. Chem. B* **2017**, 5 (25), 4993–5000.

Additional Publications

- (3) Estupiñán, D.; Gegenhuber, T.; Blinco, J. P.; Barner-Kowollik, C.; Barner, L. *ACS Macro Lett.* **2017**, 6, 229–234.
- (2) Gegenhuber, T.; Krekhova, M.; Schöbel, J.; Gröschel, A. H.; Schmalz, H. *ACS Macro Lett.* **2016**, 5, 306–310.
- (1) Gegenhuber, T.; Gröschel, A. H.; Löbbling, T. I.; Drechsler, M.; Ehlert, S.; Förster, S.; Schmalz, H. *Macromolecules* **2015**, 48, 1767–1776.

[§]: T.G. and L.d.K. contributed equally.

CONTENTS

Abstract	V
Zusammenfassung	VII
Erklärung	IX
Publication List	XI
Contents	XIII
1 Motivation	1
2 Introduction	3
3 Theoretical Background and Literature Review	5
3.1 Polymer Science: An Introduction	5
3.2 Chain-Growth Polymerization.....	6
3.3 Step-Growth Polymerization.....	32
3.4 Modern and Contemporary Ligation Reactions	40
3.5 Surface Patterning and Functional Surface Design	56
3.6 Protein and Peptide Fundamentals	58
3.7 Kinetic Modeling of Polymerization Reactions	70
4 Segmented Copolymers by Sequential Step-Growth and RAFT Polymerization	73
4.1 Introduction and Concept	73
4.2 Step-Growth by Photo-Induced DA Reactions and Subsequent RAFT Polymerization: Synthesis of Segmented Copolymers	75
4.3 Step-Growth by Thermally Induced DA Reactions and Subsequent RAFT Polymerization: Synthesis of Segmented Copolymers	98
4.4 Conclusion	108
5 Cysteine-Rich Domain Peptides for Step-Growth Polymerization and Surface Patterning	111
5.1 General Introduction and Outline.....	111
5.2 CRDs as Polymerization Tool in Macromolecular Assemblies.....	112
5.3 Exploiting CRDs for Recodable Surface Design	131
6 Concluding Remarks	139

7	Experimental Section	143
7.1	Materials	143
7.2	Instrumentation	144
7.3	Synthesis Procedures of Small Molecules	150
7.4	Polymerization Procedures.....	181
7.5	Reactions with CRD Peptides	185
7.6	Preparation and Functionalization of Surfaces	193
8	Appendix	197
8.1	Step-Growth by Photo-Induced DA Reactions and Subsequent RAFT Polymerization: Synthesis of Segmented Copolymers	197
8.2	Step-Growth by Thermally Induced DA Reactions and Subsequent RAFT Polymerization: Synthesis of Segmented Copolymers	218
8.3	Cysteine-Rich Domain Peptides for Step-Growth Polymerization and Surface Patterning	222
8.4	CRDs in Recodable Surfaces.....	224
8.5	List of Abbreviations	225
8.6	List of Figures.....	228
8.7	List of Schemes.....	241
8.8	List of Tables.....	249
9	References	251
	List of all Publications and Conference Contributions	271
	Curriculum Vitae	273
	Acknowledgements Danksagung	274

1

1 MOTIVATION

The current thesis is motivated by the need to establish highly efficient reactions to obtain complex biological and synthetic macromolecular structures. By employing photo-induced and thermally triggered orthogonal ligations, bioinspired and fully synthetic step-growth (SG) polymerizations are enabled. The first section of the thesis covers the application of Diels – Alder (DA) reactions for SG processes in combination with reversible addition fragmentation chain transfer (RAFT) polymerization. Herein, thermally as well as photo-induced DA reactions are employed in SG processes to incorporate repetitive RAFT moieties in the polymer backbone. By designing the monomer molecules accordingly, the RAFT groups are in a well-defined sequence along the polymer backbone. Finally, segmented copolymers are obtained by subsequent RAFT polymerization, exploiting the SG polymers as multi-chain-transfer agents (mCTA). Since the RAFT process is highly complex, *in silico* investigations *via* kinetic Monte Carlo simulations are employed to understand and describe the RAFT polymerization. The aim is to draw conclusions and trends regarding the incorporation of monomer units during the RAFT polymerization. The ligations exploited for the SG polymerization comprise the use of photo-induced DA reactions of photo-caged dienes, formed upon irradiation from *ortho*-methyl benzaldehydes, and thermally driven DA reactions employing cyclopentadienyls in combination with fumarates as dienophiles.

The second project area covers the usage of cysteine-rich domain (CRD) peptides in combination with state-of-the-art ligation tools for bioinspired SG polymerization as well as reversible surface encoding. CRDs show a conserved pattern of six cysteine units in an overall sequence of 18 amino acids. In their native state, the six cysteine units form intramolecular disulfide bonds generating the tertiary structure of one single peptide chain. In nature, it was found that CRD sequences in minicollagens of the fresh-water animal

Hydra are responsible for the maturation of nematocysts, a capsule released by *Hydra* in the event of defense or prey capturing. In more detail, the CRDs are located at the termini of minicollagens, a short form of collagens. By changing the environmental conditions during the maturation of the nematocyst, the CRDs at the termini start to polymerize with further CRD units, forming a membrane. The mechanical properties are dominated by the minicollagens and are found to be robust but flexible. As in the sequence of the CRD, the formation of disulfide linkages is not random but highly precise and – due to their reactivity – determined by the primary structure of the peptide itself. In the current thesis, the unique property of CRDs, *i.e.* the directed formation of disulfide bonds between CRD units, was intended as platform for biohybrid SG polymerization. In a first step, CRD need to be attached to both end-terms of an α,ω -functional polymer and subsequently polymerized by disulfide formation between the peptides termini. Based on the reversibility of disulfide formation, the depolymerization of the bioinspired SGs was envisaged. Furthermore, the disulfide linkage can be exploited for rewritable surfaces. In a first step, CRDs are written spatially resolved by photo-induced reactions to the surface and subsequently reacted with further CRD-units in solution, bearing a special marker for tracking. Finally, the marker bearing CRDs written to the CRD surface can be released from the surface, establishing a reversibly encodable surface.

2

2 INTRODUCTION

Polymer science and technology advanced within the last decades from one dimensional to multi-dimensional designs of well-defined polymer architectures.² To date, the usage of consumer plastics covers the major part of today's polymer production.³ Due to recently rising demands for green chemistry, energy saving and sustainability, novel materials were discovered, often based on transdisciplinary collaboration.⁴ By removing the boundaries between traditional fields, biochemistry, molecular polymer engineering and bioinorganic chemistry have become today's driving forces in advanced soft matter materials design.⁵⁻⁷

Polymers in general are defined and distinguished by their microstructure, topology, composition, molecular weight distribution, and as well as their functionalities. Each of these aspects need to be addressed in the polymers' synthesis and ultimately defines their unique properties. Before the Second World War, the pioneering works of Staudinger,⁸ Carothers,^{9,10} and Flory^{11,12} founded polymer science as a field. After the Second World War, these works had a dramatic impact on the development of polymer science and the society. Homopolymers and copolymers are critical for everyday applications, having termed our time the "era of plastics".¹³ In the field of polymer science, trends are focus in the fusion of both polymeric and protein/peptide based hybrids and DNA combinations with polymer materials.¹⁴ Furthermore, controlled polymerization techniques have been developed to afford not only linear but also multidimensional structures, such as stars,¹⁵ comb-shaped macromolecules,¹⁶ structured two dimensional surfaces and three dimensional objects,¹⁷ supramolecular polymers,¹⁸ branched and hyperbranched polymers,¹⁹ dendrimers,^{20,21} graft polymers, block or gradient copolymers,²²⁻²⁴ and anisotropic polymer particles,²⁵ respectively. Photo-induced and in general reactions with low activation energy pioneered the way to sustainable chemistry.²⁶ The application of

polymerization catalysts and the development of novel polymerization processes enabled modern soft matter materials.³ Moreover, several functionalities were incorporated into polymers, enabling postmodification and reprogrammable materials, such as gels, sols and networks.²⁷ In the 1990s reversible deactivation radical polymerization (RDRP) enabled to a plethora of novel polymeric structures, expanding the scope of previously established polymerization techniques.²⁸⁻³⁰

Polymer scientists play a critical role in overcoming the pollution of the planet, such as the plastic waste in the oceans, the pile of rubbish in the cities and the general pollution of our planet caused by industries all over the world. Furthermore, the rising need for energy and thus, the exploitation of the earth need to be tackled by developing processes that save power and preserve our environment.

In the following chapter, the fundamentals of the current thesis are introduced such as polymer science, modern ligation techniques, surface functionalization, and an overview about proteins regarding their function, synthesis, and application in combination with synthetic methodologies.

3

3 THEORETICAL BACKGROUND AND LITERATURE REVIEW

3.1 Polymer Science: An Introduction

Macromolecules are species from high molecular masses, commonly in the range of 100,000 or millions of Dalton.³¹ Monomers are molecules from low molecular masses and are capable to react with each other to generate a macromolecule. A polymer is a macromolecule that consists of either one or different monomers and is classified by 'similar' repeating subunits, *i.e.* a repetitive structural element in the polymer chain.³¹ The length of the monomer units covalently linked to together is referred to as degree of polymerization that plays a key role in the properties of a polymer. Commonly, polymers do not feature a precise molecular weight, yet they have a distribution of molecular weights. Exceptions are some natural monodisperse macromolecules, such as proteins. Such high molecular materials can be obtained by synthetic or by natural processes and reactions, such as enzymatic, step-growth or chain-growth methodologies. Classical examples for natural macromolecules are proteins and cellulose, whereas synthetic representatives are polyethylene and polystyrene, respectively.³¹

Polymerization reactions are divided into the categories step-growth, chain-growth, and ring-opening polymerization, each being further subdivided into different methods and classified by the mechanism of the polymerization.³²

A common method for the generation of polymers is chain-growth polymerization.³³ Chain-growth polymerizations can be started by radical and ionic initiation, or upon the utilization of organometallic coordination catalysts. In general, the monomer structure dictates the specific polymerization type. Nevertheless, many monomers are not restricted to only one

specific polymerization reaction, as will be discussed in the corresponding sections.³³ SG polymerizations cover many different reactions, e.g. condensation and addition reactions.³² These methods are more complex to classify since a plethora of functionalities are employed in SG polymerization and the reaction does not necessarily feature a typical initiator, in comparison to chain-growth polymerization. A specialty of SG polymerization is the straightforward incorporation of hetero atoms into polymer backbones, such as oxygen, sulfur, and nitrogen, in contrast to conventional chain-growth polymers. Ring-opening polymerization (ROP) entails the reaction of cyclic monomers towards linear polymers. Nevertheless, ROP is classified as a separate polymerization technique, although it comprises ionic, or metathesis polymerizations in a chain-growth manner.³² Some ROP methods are introduced in the corresponding sections with respect to their relevance. Ring-opening metathesis polymerization is a subclass of ROP, obtaining linear polymers with eventually ring-containing repeating units under the preservation of the double bond.³⁴ In the following, an introduction about polymerization techniques and reactions will highlight the characteristics of the corresponding methods.

3.2 Chain-Growth Polymerization

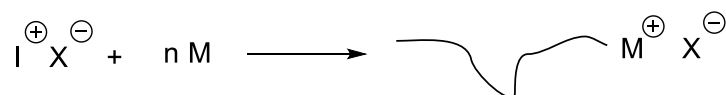
3.2.1 Ionic and Living Polymerization Methods

A classic approach in chain-growth polymerization is the use of ionic species, *i.e.* cationic and anionic polymerization.^{35,36} Here, an active chain bearing a carbocation or a carbanion is generated upon initiation available for propagation with monomer molecules, such as vinyl or cyclic monomers. Furthermore, ionic polymerizations are restricted to a limited monomer selection in order to sufficiently stabilize the active species, *i.e.* cationic requires monomers with electron pushing substituents, whereas anionic polymerization comprises monomers with electron deficient substituents.³¹ Generally, ionic polymerization of vinyl monomers demonstrate very high reaction rates and are sensitive to impurities and contamination in the reaction medium.³² Both cationic and anionic polymerization can be conducted in a controlled manner, whereas anionic polymerization represents the archetype of living polymerization.³⁶ A living polymerization requires the absence of termination and transfer reactions ($R_p \gg R_t, R_{tr}$). In addition to living polymerization, a polymerization is termed controlled if (i) the molecular weight can be adjusted, (ii) a narrow molecular weight distribution is obtained, and (iii) (near) quantitative end-group functionalization is accessible.³⁶ A controlled polymerization is not necessarily living, such as radical polymerizations due to termination, as well as a living polymerization can be uncontrolled, due to errors in reaction setup (poor stirring), retarded initiation, or

depolymerization. In the following an overview of anionic and cationic polymerization is provided.

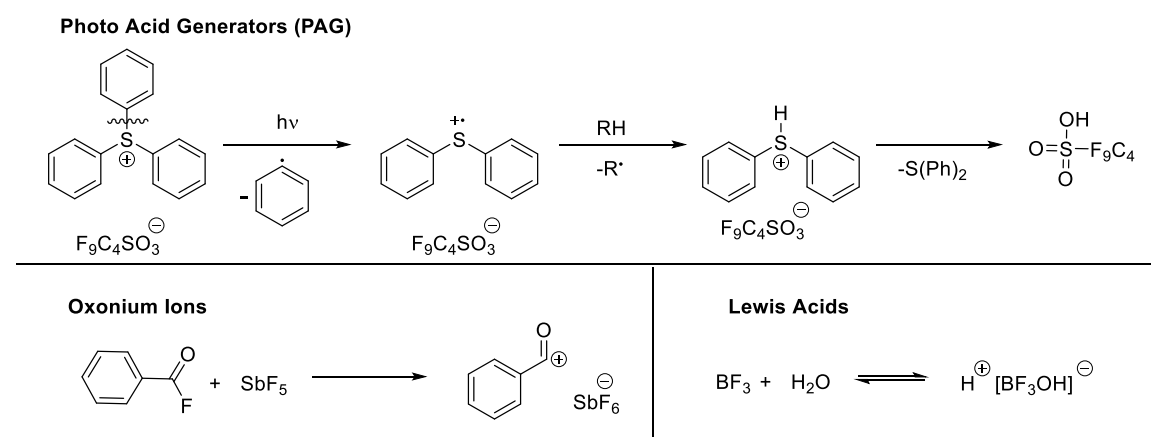
3.2.1.1 Cationic Polymerization

The mechanism of a cationic polymerization comprises a carbocation as active species for propagation (refer to Scheme 3-1).³⁵ After initiation, the active chain end consists of an ion pair that is able to undergo reaction with further monomer units.



Scheme 3-1. Cationic polymerization upon initiation with IX of the monomer M.

In order to initiate a cationic polymerization, typical initiators are Brønsted acids, such as HBr, HSO₃, or HSbF₆, Lewis acids, such as AlCl₃, BF₃ or SnCl₄, metallorganic complexes, oxonium ions, or photoinitiators, e.g. photo acid generators (refer to Scheme 3-2).^{32,33}



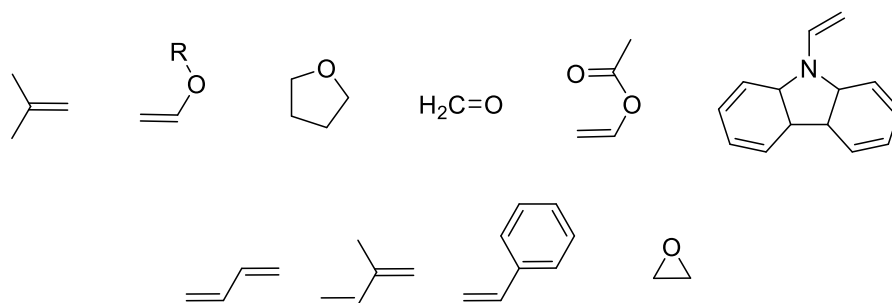
Scheme 3-2. Conventional initiators in cationic polymerization (clockwise): Photo acid generators (PAG), Lewis acids, and oxonium ions.

Cationic polymerization is a very sensitive technique and therefore, reaction protocols need to be designed carefully:

- Temperature: Due to high propagation rates in cationic polymerization, the reactions have to be conducted at very low temperatures below 0 °C. Otherwise, the polymerization struggles from termination and transfer reactions.³²
- Solvent polarity: The solvent requires sufficient stability and inertness towards acids and electrophilic groups. Feasible solvents are methylene chloride, toluene, chloroform, and nitrobenzene. Furthermore, the tacticity can be influenced by the polarity of the solvent, e.g. in case of the polymerization of vinyl ether.³¹

- Size of counterion: The size of the anion as counterpart of the active carbocation adjusts the propagation rate, e.g. anions with large size can dissociate more easily, therefore free ion pairs are formed, showing higher propagation rates.^{32,35}

Monomers applicable for cationic polymerization bear mainly electron pushing groups in order to stabilize the carbocation. Examples are isobutylene, butadiene, isoprene, styrene, vinyl ethers, vinyl acetate, *N*-vinyl carbazole, formaldehyde, as well as cyclic monomers for cationic ROP, such as tetrahydrofuran (THF), and epoxides (refer to Scheme 3-3).³³



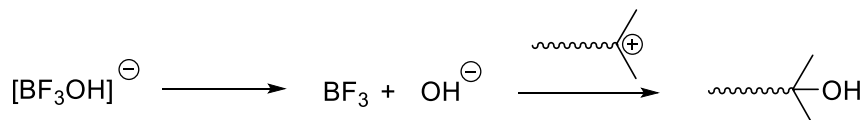
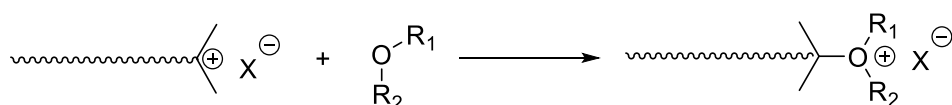
Scheme 3-3. Monomers applicable for cationic polymerization. Monomers in the top row are employed in industrial scale, whereas the monomers in the bottom row are employed in other polymerization techniques on industrial scale.

The propagation rate of the polymerization R_p can be expressed by Eq. (1):³²

$$R_p = \frac{K \cdot k_i \cdot k_p}{k_t} [I][ZY][M]^2 \quad (1)$$

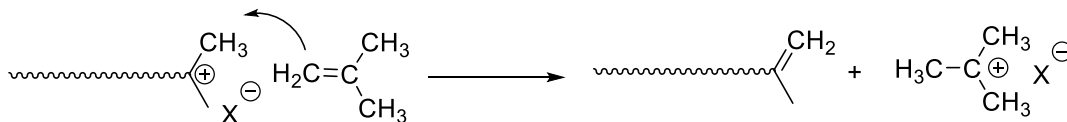
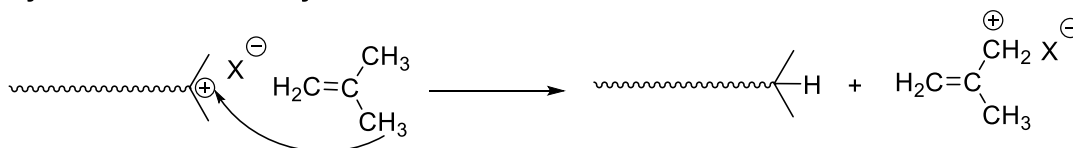
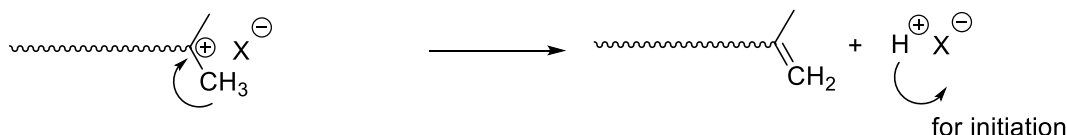
With: K : equilibrium constant of active species from initiator/coinitiator; k_x : rate coefficients for propagation (p), initiation (i), and termination (t); $[I]$: initiator concentration; $[ZY]$: coinitiator concentration; $[M]$: monomer concentration.

Nevertheless, during cationic polymerization many transfer and termination reactions are present. Termination occurs upon reactions of the active chain with the counterion, either due to recombination with the anion or due to cleavage of the anion yielding terminating species (refer to Scheme 3-4). Furthermore, depending on the monomer, unreactive chain ends can be formed e.g. during the polymerization of vinyl ethers.³³

Counterion Recombination**Counterion Cleavage****Generation of Unreactive Chain End**

Scheme 3-4. Termination reactions in cationic polymerization. Counterion recombination, counterion cleavage, and formation of unreactive chain ends.

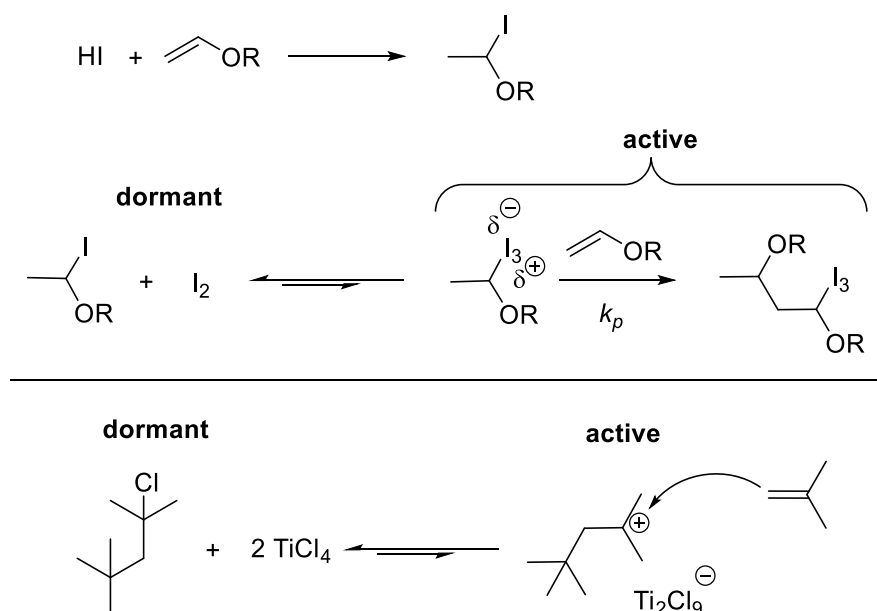
In addition, different transfer reactions are present in cationic polymerization, either reactions with the monomer, such as proton and hydride transfers, or proton elimination at the chain end (refer to Scheme 3-5). Although water is able to terminate the reaction, the usage of stoichiometric amounts as co-initiator with regard to the initiator is in general applicable without termination.³³

Proton Transfer to Monomer**Hydride Transfer to Polymer****Proton Elimination at Chain End**

Scheme 3-5. Transfer reactions in cationic polymerization. Proton transfer to the monomer, hydride transfer to the polymer, and proton elimination at the active chain end.

A controlled cationic polymerization of vinyl ethers can be achieved by employing specific initiators, e.g. a combination of iodine and hydrogen iodide.³⁵ After initiation, a

corresponding active species is formed in a reversible deactivation process between the iodide, representing a dormant chain end, and the triiodide, representing the active chain end species (refer to Scheme 3-6, top behalf). Here, the equilibrium is strongly pushed to the dormant species and thus, the reduction of the polymerization rate significantly reduces transfer and termination events.³¹ Furthermore, a controlled cationic polymerization of isobutylene is achieved by a deactivation process with alkyl and titanium halides, respectively (refer to Scheme 3-6, bottom behalf).³⁷ Here, the deactivation of the propagating chains lead to a drastically reduction of the active chains and therefore, control is gained due to reduced transfer and termination events. Generally, controlled cationic polymerization has to be carried out in exclusion of any nucleophilic contaminations. To reduce the sensitivity of the polymerization, additives can be employed, such as Lewis bases, in order to remove disruptive contaminations, to reduce transfer reactions, and to stabilize the carbocation.³⁵

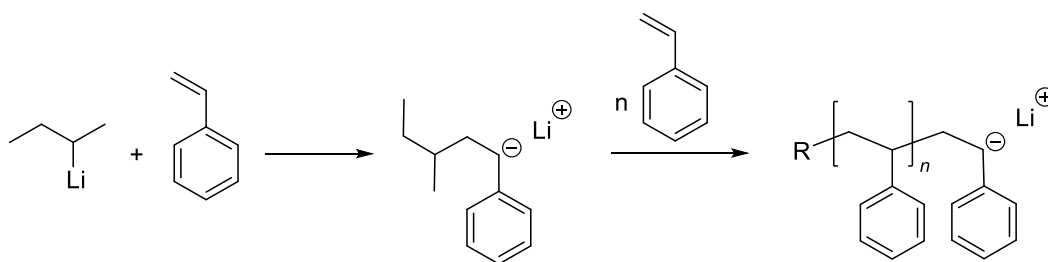


Scheme 3-6. Controlled cationic polymerization of vinyl ether (top) and isobutylene (bottom).^{35,37}

Cationic polymerization is nowadays applied on industrial scale for the synthesis of vinyl ethers and isobutylene polymers, since they cannot be obtained properly with other polymerization techniques.³⁸ Copolymers with isobutylene are employed in rubbers, since polyisobutylene serves as an excellent sealant.³⁹ Poly(vinyl ether)s are employed in dispersion latices and adhesives.³⁸

3.2.1.2 Anionic Polymerization

Anionic polymerization represents the archetype of living polymerization, since under certain conditions it can be conducted without transfer or termination reactions ($R_p \gg R_t, R_{tr}$).³⁶ The polymerization propagation proceeds *via* a carbanion that is generated by nucleophilic initiators, such as lithium organyls, as illustrated in Scheme 3-7.³³ Certainly, similar to cationic polymerization, anionic polymerization is very sensitive to contamination, in this case protic impurities. In case the polymerization reactants are from high purity and the reaction setup provides exclusion of contamination, anionic polymerization proceeds with very high propagation rates. Furthermore, after full consumption of the monomer, the propagating chain end is still active, referred to as 'livingness', and further monomer can be added for propagation. In addition to conventional anionic polymerization of vinyl monomers, anionic ROP and group transfer polymerization are subclasses of anionic polymerization.^{40,41}



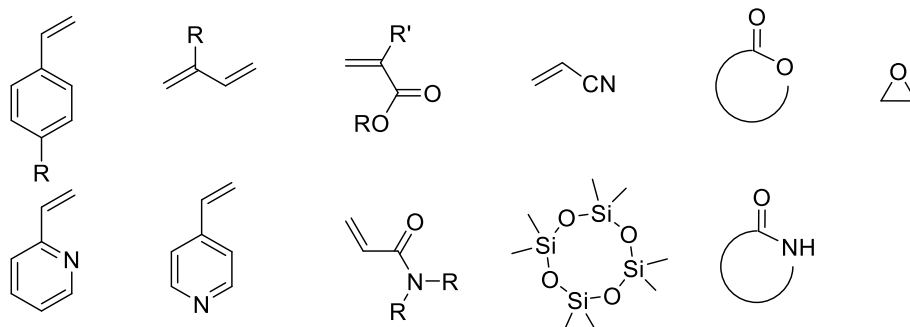
Scheme 3-7. Anionic polymerization of styrene with *sec*-butyl lithium as initiator.

Typical initiators are alkali metals, amines, alcoholates, metallorganyl bases, and electron transfer reagents.³² Prominent initiators are lithium organyls, such as *n*-butyl lithium, *sec*-butyl lithium and *tert*-butyl lithium. The reactivity is highest for *tert*-butyl lithium and lowest for *n*-butyl lithium, due to decreasing basicity of the derivatives.⁴² Since no termination and transfer is present in living anionic polymerization, the propagation rate can be calculated from the initial monomer and initiator concentration and the propagation rate coefficient k_p (refer to Eq. (2)):

$$R_p = k_p [M][I]_0 \quad (2.)$$

With $[M]_0$, $[I]_0$: initial monomer/initiator concentration; k_p : propagation rate coefficient.

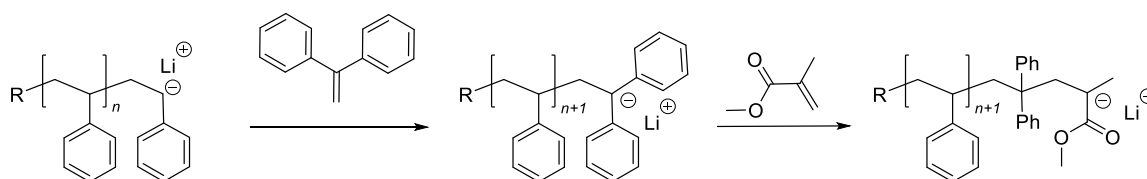
Typical monomers in anionic polymerization are styrene derivatives, vinylpyridines, butadiene, isoprene, methacrylates, acrylates, acrylonitrile, acrylamides, epoxides, cyclic siloxanes, lactames, and lactones (refer to Scheme 3-8).^{36,41}



Scheme 3-8. Typical monomers in anionic polymerization, featuring styrene derivatives, dienes, vinylpyridines, (meth)acrylates, acrylamides, acrylonitrile, or cyclic monomers such as siloxanes, lactones, lactames, and epoxides.

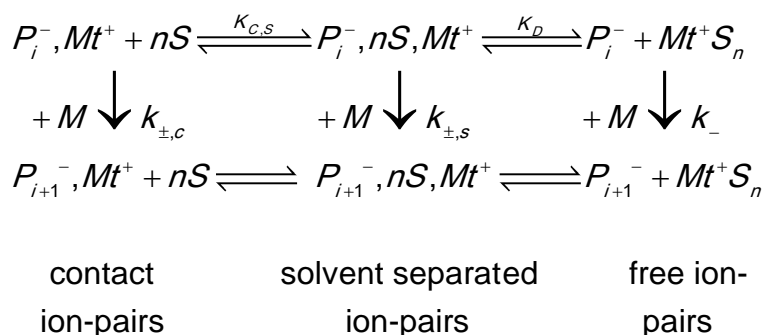
In case of unpolar monomers, the initiator requires high reactivity, otherwise no polymerization is induced. For polar monomers, the initiator selection is crucial, as strong nucleophiles are able to cleave esters and amides in (meth)acrylates or acrylamides.⁴³ In case of ester and amide containing monomers, less reactive initiators are necessary for the polymerization. Additionally, in polymerization of highly reactive monomers, such as (meth)acrylates and acrylamides, low temperatures $\ll 0\text{ }^{\circ}\text{C}$ are required in order to reduce side reactions, such as backbiting, ester cleavage, and cyclization.

Living anionic polymerization is a classical method for the synthesis of block copolymers (BCPs) with narrow dispersities.⁴⁴ Generally, the sequence of the monomer addition is essential to afford the desired block copolymer with low dispersities. The order of block synthesis has to be chosen from lowest to highest monomer reactivity or monomer sensitivity for hydrolysis. In case of a polystyrene-*block*-poly(methyl methacrylate) (PS-*b*-PMMA), the PS block needs to be synthesized first. Certainly, the active chain-end can attack the ester bond of MMA and a loss of control is the consequence. A prominent way to circumvent ester hydrolysis is the decoration of the chain ends with a less reactive group, such as 1,1-diphenylethylene (DPE), after full consumption of styrene. Upon the addition of the DPE, all active chain ends are decorated with the DPE (refer to Scheme 3-9). Here, DPE cannot propagate with itself, obtaining a less reactive active chain end.⁴⁵ In the opposite order, an active MMA chain is rather unable to reinitiate styrene.



Scheme 3-9. Sequential anionic polymerization of styrene and MMA. After consumption of styrene, the chain ends are decorated with DPE in order to reduce the chain end reactivity.⁴⁵

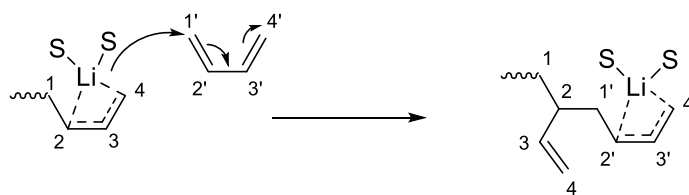
The preparation and the setup of anionic polymerization are elaborate, since all reactants require high purity and the reaction vessel has to be free of any contamination such as oxygen or water. Furthermore, anionic polymerization in polar solvents requires low temperatures of $-80\text{ }^{\circ}\text{C}$, whereas unpolar solvents can be employed in polymerizations at higher temperatures of around $40\text{ }^{\circ}\text{C}$. In addition, only few solvents are capable to be employed in anionic polymerization, such as THF, benzene, toluene, and alkanes. Halogenated solvents are unsuitable as well as any protic solvents with low pK_a values. With respect to the initiator, the carbanion is associated with a corresponding cation. Depending on the solvent, concentration and temperature, the ions are present as a contact ion-pair, solvent-separated ion-pair, or as free ion-pairs (refer to Scheme 3-10). In polar solvents, such as THF, the ions are free or solvent separated, whereas in unpolar solvents, such as cyclohexane, either solvent separated or contact ion-pairs are present. Generally, the propagation rate strongly depends on the association of the ions, showing higher propagating rates for free ions than for solvent separated ion-pairs than for contact ion-pairs. A key role influencing the reaction kinetics is the size of the counterion. In unpolar solvents, large cations are employed, providing better charge separation, whereas smaller cations are employed in polar solvents, as they dissociate easier.



Scheme 3-10. Different states of ions at active chain-end in anionic polymerization of styrene. With: $k_{\pm,c}$: propagation coefficient for contact ion-pairs; $k_{\pm,s}$: propagation coefficient for solvent separated ion-pairs; k_- : propagation coefficient for free ion-pairs. With: $k_{\pm,c} \ll k_{\pm,s} < k_-$.³⁶

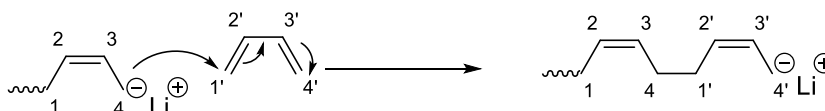
Anionic polymerization is strongly influenced by the polarity of the reaction medium, *i.e.* polar and unpolar solvents. A prominent monomer to illustrate the influence of the solvents polarity on the microstructure of a polymer is 1,3-butadiene (refer to Scheme 3-11).⁴⁶ In the case of unpolar solvents, the polymerization of 1,3-butadiene predominantly yields 1,4 polybutadiene, whereas the polymerization in polar solvents mainly yields 1,2 polybutadiene, so-called vinyl polybutadiene.

polar solvent



S = Solvents

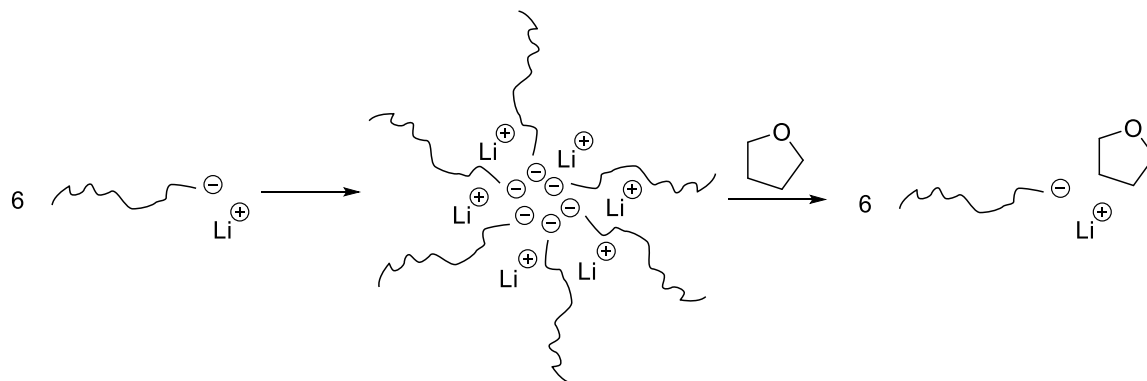
unpolar solvent



Scheme 3-11. Influence of the solvents polarity on the microstructure of polybutadiene. Anionic polymerization of 1,3-butadiene with lithium cation: Top: Polymerization in polar medium yields 1,2-polybutadiene. Bottom: Polymerization in unpolar medium yields 1,4-polybutadiene (only *cis* shown).⁴⁶

This phenomenon can be explained by the charge localization at the propagating chain. In case of polar media, a complexation of the propagating chain end with the cation and the solvent molecules leads to a delocalization of the charge, demonstrating highest charge density in position 2, favoring the addition in position 1,2 (refer to Scheme 3-11, top behalf). If an unpolar reaction medium is employed, the active chain end is closely associated to the cation with the highest charge density in position 4, namely a contact ion pair, and the next monomer is added in 1,4 position (refer to Scheme 3-11, bottom behalf). Additionally, the 1,4-polybutadiene can be formed as *cis* or *trans* isomers, where *trans* is thermodynamically and *cis* kinetically favored, respectively. During the polymerization, an equilibrium between both isomers favors the formation of the *trans* configuration. Hence, the control over *cis/trans* formation is obtained by adjusting the kinetics, *i.e.* the *cis* configuration can be triggered by increasing the polymerization rate. Furthermore, the microstructure can be influenced by additives and by the cation. By selecting large cations, the formation of the 1,2 structure is promoted. A similar result is obtained *via* the addition of complexation ligands, such as bispiperidionemethane.⁴⁷ Why is the control over the microstructure of polybutadiene important? The answer can be given by the mechanical property of the polymeric material. A pure 1,2-polybutadiene has a glass transition temperature of approx. -10°C , whereas a pure *cis* 1,4-polybutadiene shows a glass transition temperature of approx. -110°C . Apparently, the control over the microstructure during the polymerization of butadiene and derivatives, such as isoprene, enables the adjustment of the macroscopic properties.⁴⁶ Problems in anionic polymerization concern aggregation of active chains ends or initiator molecules.³⁶ Since these aggregates lower the reactivity, the control over the reaction is lost and a broadening of the molecular weight distribution is the consequence. A prominent example is the aggregation of lithium

containing chain ends, forming dimers, tetramers or hexamers in unpolar media. Such a behavior in unpolar media can be circumvented by the addition of very stoichiometric amounts of THF, as the formation of monoetherates complexes dissolves the aggregates (refer to Scheme 3-12). In case of polar solvents, low temperatures lead to the aggregation of active chain ends. Such a behavior was found for methacrylates. To dissolve aggregates, ligands or chelate reagents can be added.



Scheme 3-12. Aggregation of chain ends and dissolving aggregates by THF addition forming monoetherate complexes.

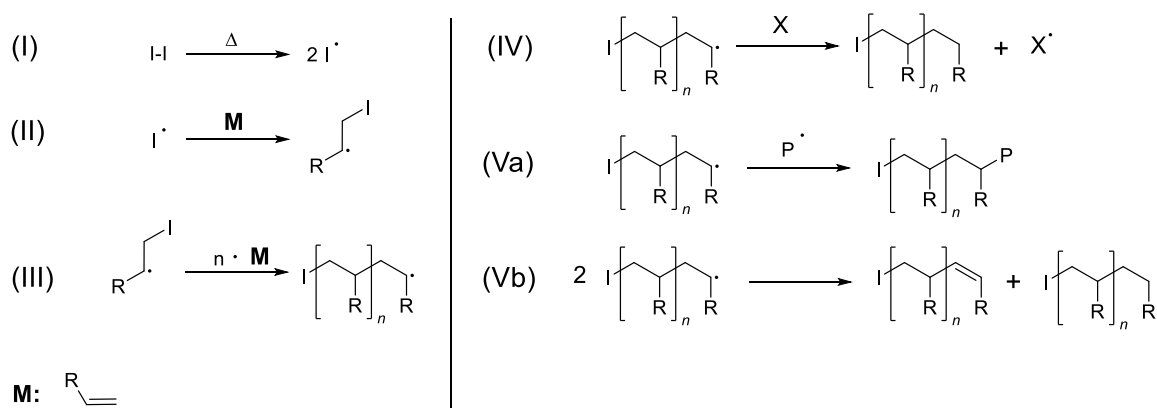
The scope of anionic polymerization can be extended by the utilization of additives.³⁶ Prominent additives are salts, Lewis-bases, and ligands. Salts, referred to as μ -ligands such as LiCl, LiBH₄, and CsBH₃CN, in general suppress dissociation of the ion pair and therefore, retard the polymerization. Lewis bases, referred to as σ -ligands, such as crown ether and tertiary amines, are capable to coordinate with the counterion or to dissolve aggregates. Anionic polymerization on industrial scale is applied in the fabrication of rubbers, e.g. for tires and sealants.³⁸ Furthermore, concepts have been developed to employ anionic polymerization as substitute for radical polymerization by a drastically retarded polymerization. Here, *via* addition of Lewis acids, the active chain end is less sensitive to terminating contaminations, enabling polymerization at elevated temperatures and in bulk.⁴⁸

3.2.2 Radical Polymerization

3.2.2.1 Free-Radical Polymerization

The generation of synthetic polymers has been carried out in a multitude of ways, yet the majority of synthetic polymers are nowadays produced by free-radical polymerization (FRP).³¹ FRP is facile to perform and can be started by various radical sources, most prominent are redox, thermal, and photo-induced initiation.³³ The mechanism of FRP is divided into four steps, namely initiation, propagation, termination, and transfer (refer to

Scheme 3-13). During the initiation, the initiator cleaves homolytically or heterolytically and forms at least one highly reactive radical able to react with a monomer, starting the polymerization (refer to Scheme 3-13, (I)). The transfer of the radical to the double bond starts a chain growth process (II), propagating (III) until a second radical terminates the reaction, termed recombination (Va). An alternative way to terminate the chain-growth process is by abstracting a radical, termed disproportionation (Vb). During propagation, only the radical of the growing chain undergoes the reaction, implying that all other monomers remain unaffected until the propagating chain or an initiator radical attack. The termination process is determined by the structure and the reactivity of the monomer. Thus, if a bulky monomer hinders recombination, disproportionation is favored. In addition, the viscosity of a polymer chain increases with conversion, thus, termination becomes a diffusion controlled process.^{49,50}



Scheme 3-13. General radical polymerization mechanism: (I) Initiator decay (here homolytic cleavage) and (II) initiation of the polymerization by addition of the radical initiator I to the double bond of the monomer **M**. (III) Propagation of the polymerization with further vinyl monomer units **M**. (IV) Transfer of the radical by transfer agent, solvent, or dead chain X. (Va) Termination *via* recombination, (Vb) termination *via* disproportionation of two active chains reacting, yielding a saturated and an unsaturated polymer chain.

3.2.2.2 Kinetics

In FRP, a combination of complex processes is present and these can be generally divided into three stages: Initiation phase, steady state and termination phase. During the initiation phase, the number of radicals increases quickly to reach a constant value and the reaction rate reaches its maximum. The reason for the constant number of radicals is the occurrence of equal initiating and terminating events, referred to as steady state. During the steady state, the reaction rates decrease slowly. At the end of the steady state, R_p increases due to rising viscosity (gel-effect or Trommsdorff-Norrish-effect),⁵¹ causing reduced diffusion and the radical concentration increases due to less termination. In the further progress of the polymerization, the viscosity increases and strongly reduces diffusion, yielding a drastically decreasing polymerization rate (glass-effect). The

consequences of the FRP mechanism is the limited control over the final molecular weight distribution and the polymer end groups. To describe the rate of the polymerization, all processes of the mechanism can be described with respect to the concentrations of participating reaction components and rate coefficients. Generally, some fundamental assumptions are defined *a priori*:³³ First, the radical concentration is chain length independent, implying a constant propagation rate coefficient k_p . Furthermore, significant consumption of monomer occurs during propagation and can be neglected during initiation. Hence, the propagation rate R_p can be expressed as the decrease of the monomer concentration $[M]$ (refer to Eq. (3)):

$$-\frac{d[M]}{dt} = R_p \quad (3.)$$

In addition, after initiation and during the steady state, the radical concentration reaches a threshold value, due to a similar rate of initiation and termination (referred to as Bodenstein'sche Quasistationaritätsbeziehung or steady state assumption, refer to Eq. (4)):³

$$R_t = R_i \quad (4.)$$

For the initiation, a radical reacts with a monomer. First, the initiator has to decompose in order to generate two radicals. Since the subsequent initiation is very fast, the initiation rate is determined by the radical generation. Here, one obtains the initiation rate R_i with the initiator concentration, the initiator decay coefficient k_d , and the initiator efficiency f ($f = 1$ denotes perfect efficiency) in Eq. (5):

$$R_i = k_i [R\cdot] [M] = 2f \cdot k_d \cdot [I] \quad (5.)$$

For the propagation (R_p) and termination (R_t) rates, the polymer radical concentration $[P\cdot]$, the monomer concentration, and the corresponding rate coefficients have to be accounted (refer to Eq. (6) and (7)):

$$R_p = k_p [P\cdot] \cdot [M] \quad (6.)$$

$$R_t = 2k_t \cdot [P\cdot]^2 \quad (7.)$$

The concentration of the radical polymer chain is rather inconvenient here. Therefore, by substituting the radical concentration with the expression of the steady state assumption (Eq. (4)), one obtains the equation for the propagation rate R_p in dependency to the monomer and the root of the initiator concentration, respectively, referred to as 'square-root' law (refer to Eq. (8)):^{32,52}

$$R_p = k_p [M] \sqrt{\frac{f k_d [I]}{k_t}} \quad (8.)$$

Furthermore, transfer reactions can be present during the polymerization, such as radical abstraction, 'backbiting' or transfer to other molecules. 'Backbiting' describes an intramolecular transfer, where the active end of the polymer chain attacks a spot in the middle of the same polymer chain and may generate a less reactive radical, available for further propagation. In the case of radical abstraction, an intermolecular transfer occurs, where the newly formed radical can terminate or initiate a further polymer chain (IV), *i.e.* transfer reactions to the solvent, initiator, monomer, or a transfer agent. Transfer agents, *e.g.* thiols, are employed in radical polymerization to decrease the degree of polymerization. The transfer rate is illustrated in Eq. (9):

$$R_{tr} = k_{tr} [P\bullet] [HX] \quad (9.)$$

With [HX]: concentration of transfer agent.

In the presence of transfer reactions, the degree of polymerization is then dependent on the propagation, termination, and transfer rate (refer to Eq. (10)):³³

$$X_n = \frac{R_p}{R_t + R_{tr}} \quad (10.)$$

The chain transfer constant C_x describes the ratio of the specific transfer rate coefficients $k_{tr,x}$, *e.g.* transfer to monomer, and the propagation rate coefficient k_p . The constant C_x assesses the ability of a component to undergo transfer reactions, *e.g.* thiols as regulator in radical polymerizations feature high values for C . Here, the chain transfer coefficients are specific for the transfer species (refer to Eq. (11)):

$$C_x = \frac{k_{tr,x}}{k_p} \quad (11.)$$

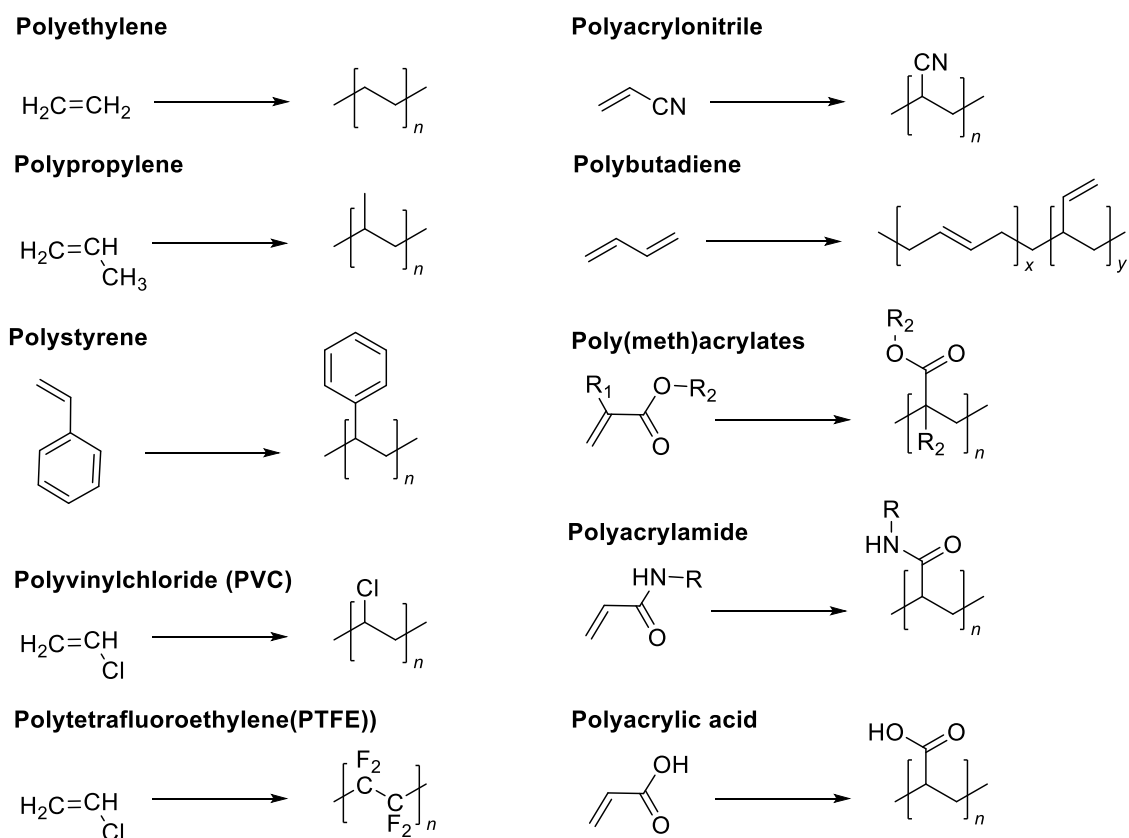
The Mayo equation (Eq. (12)) describes the effect of intermolecular transfer reactions on the degree of polymerization X_n by the degree of polymerization $X_{n,0}$ without transfer and the transfer to employed reactants, such as monomer (M), initiator (I), solvent (S) and optional transfer agent (T):³³

$$\frac{1}{X_n} = \frac{1}{X_{n,0}} + C_M + C_I \frac{[I]}{[M]} + C_S \frac{[S]}{[M]} + C_T \frac{[T]}{[M]} \quad (12.)$$

3.2.2.3 Application of Radical Polymerization

A significant amount of consumable and engineering plastics is nowadays produced by radical polymerization.³⁸ The main advantage of radical polymerization is its insensitivity to impurities and contamination in comparison to especially ionic polymerization methodologies. The general classes of monomers readily available for radical polymerization are vinyl derivatives. Examples for different polymers obtained by radical polymerization are illustrated in Scheme 3-14, such as polyethylene, polypropylene, polystyrene, polyvinylchloride (PVC), polytetrafluoroethylene (PTFE), polyacrylonitrile, polybutadiene, poly(methyl methacrylate), polyacrylates, polyacrylamide, poly(acrylic acid).³¹ Copolymers obtained from radical polymerization are also important in industry, such as polybutadiene-co-polystyrene, polystyrene-co-polyacrylonitrile (SAN), polystyrene-co-polybutadiene-co-polyacrylonitrile (ABS).³³

Processes in radical polymerization on multi-ton scale comprise bulk, precipitation, emulsion, and suspension polymerization, respectively.³⁸ Polymers, for instance from emulsion polymerization, are directly available for their application as latex and dispersion paints.⁵³ Furthermore, radical polymerization can be combined with polymer foaming, e.g. suspension polymerization of styrene, loaded with low boiling alkanes under pressure.⁵⁴



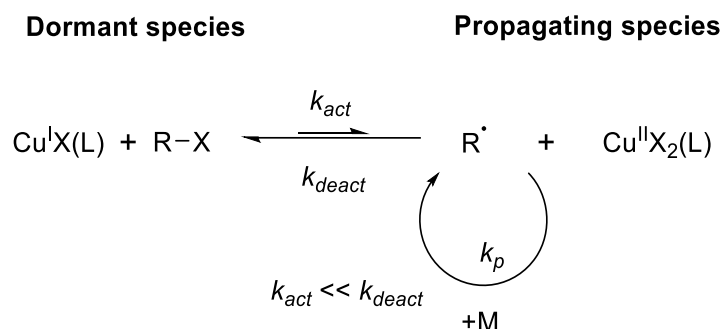
Scheme 3-14. Selection of important polymers generated from radical polymerization processes.

3.2.3 Reversible-Deactivation Radical Polymerization

Reversible-deactivation radical polymerization (RDRP), formerly referred to as ‘living’ or controlled radical polymerization,⁵⁵ is an adapted FRP. The mechanisms of RDRP are either an overlaid activation/deactivation process or a heavily retarded radical polymerization through drastic reduction of the radical concentration during the chain growth, promoting a steady growth of all propagating polymer chains. The most common RDRPs are atom transfer radical polymerization (ATRP), reversible addition-fragmentation chain transfer (RAFT) polymerization, and nitroxide-mediated polymerization (NMP).^{56–61} RDRPs cannot be described as “living” polymerizations, because of the aforementioned presence of (limited) termination and transfer processes. Therefore, the term ‘living’ radical polymerization and derivatives are officially no longer in use.⁵⁵

The RDRP methods have to be carefully differentiated according to their mechanism. In the case of ATRP and NMP, the radical polymerization is heavily retarded by drastic radical concentration, whereas an overlaid activation/deactivation mechanism leads to control during RAFT polymerization. The control over the polymerization can be confirmed by comparison of the experimentally observed polymerization degree X_n to its theoretical development and the analysis of end-group fidelity by e.g. mass spectrometry.⁶² ATRP was firstly reported in 1995 independently by Matyjaszewski²⁸ and Sawamoto⁶³, demonstrating the use of transition metal halides in combination with organic halides to gain control over a radical polymerization. Such a concept is closely associated to the controlled cationic polymerization of isobutylene by reversible deactivation with titanium halides (refer to Chapter 3.2.1.1).³⁵ The concept of ATRP entails a drastic reduction of the radical concentration by a reversible deactivation redox process, mainly with Cu^I/Cu^{II} halides, converting the propagating polymer chains R into a deactivated state (dormant species R-X, refer to Scheme 3-15). Here, a halide X, commonly bromine or chlorine, is abstracted from the polymer by copper halides, oxidizing Cu^I to Cu^{II}. A ligand is necessary in order to reach a sufficient solubility of the copper halide.

The abstraction of the halide from the polymer is strongly driven to the deactivated state; only a small amount of polymer chains is in the active state to react with a monomer unit. After the addition of the monomer unit, the active chain is ideally immediately converted to the deactivated state. Therefore, the deactivation rate coefficient k_{deact} must be larger than the activation rate coefficient k_{act} , pushing the equilibrium to the side of the dormant species.



Scheme 3-15. Fundamental mechanism of atomic transfer radical polymerization (ATRP).⁶⁴

In case of sufficient initiator efficiency, the number average degree of polymerization X_n in ATRP depends on the monomer conversion p and the ratio of monomer to initiator feed concentrations $[M]_0/[RX]_0$ (refer to Eq. (13)):⁵⁷

$$X_n = \frac{[M]_0}{[RX]_0} \cdot p \quad (13.)$$

Through this process, all chains are pseudo-growing with the same rate, which is in contrast to FRP. In FRP, terminated high molecular weight chains as well as propagating oligomeric chains are present during initiation phase already. In addition, after initiation, the number of chains in ATRP is constant and defined by the amount of the alkyl halide R-X, in contrast to FRP. Due to the retardation, the reaction rate is slower compared to FRP.⁶² As shown in Eq. (14), the concentration of the active species in the numerator is lower than the dormant species in the denominator and consequently, the propagation rate is decreased in comparison to FRP.⁶⁵

$$R_p = k_p [M] \cdot [P\bullet] = k_p [M] \cdot K_{\text{ATRP}} \frac{[P-X][Cu^{\text{I}}L]}{[X-Cu^{\text{II}}L]} \quad (14.)$$

The benefit of ATRP is its excellent control over the polymerization of several conventional monomers, and the highly useful halide end-group. The halide is subsequently available for postmodification reactions, e.g. substitution with pseudohalides, such as azides,⁶⁶ and cyclopentadienyls.⁶⁷ After its discovery, ATRP was consequently enhanced and improved based on its initial reaction design. A standard protocol nowadays is represented by the activator regenerated by electron transfer (ARGET) ATRP by adding a reducing agent into the reaction mixture and starting from a $\text{Cu}^{\text{II}}\text{X}_2$ catalyst. Here, the polymerization is less sensitive to impurities and traces of oxygen, since the Cu^{I} species can be generated *in situ*. Other variants of ATRP were developed, such as e-ATRP,^{68,69} or photo-initiated ATRP,⁷⁰ also referred to as photo-RDRP,⁷¹ or photo-induced living radical polymerization.⁷² Although the amount of copper catalyst in ATRP has been drastically

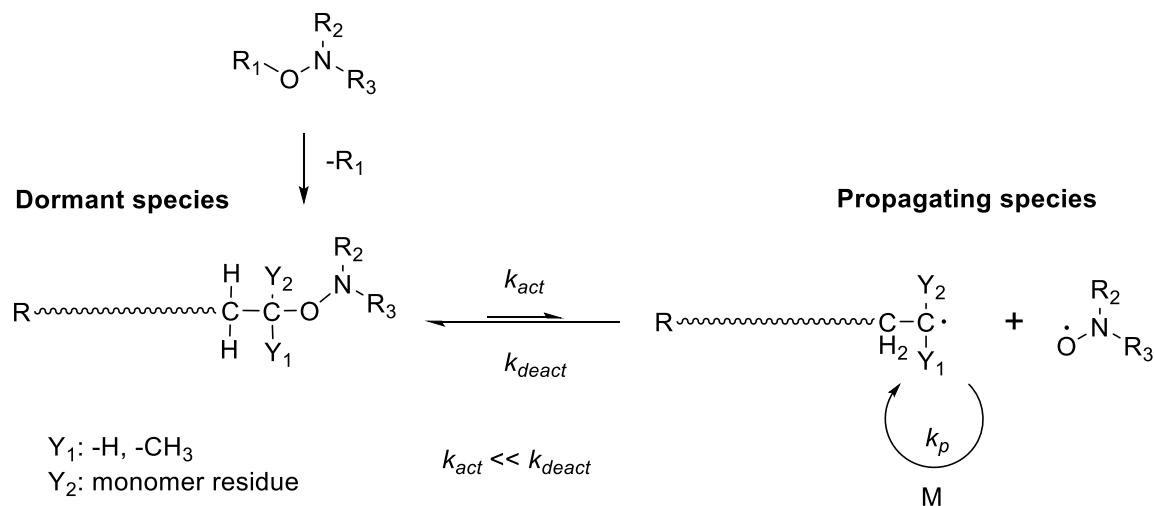
reduced from the initial approach, e.g. by ARGET,⁷³ the main drawback of all ATRP methodologies is still justified by the need for transition metals, due to their cytotoxicity and their rather high expenses.⁷⁴

In a similar fashion to ATRP, NMP utilizes an activation/deactivation process for mediation of radical polymerization that is established by the usage of persistent radicals, such as nitroxides (refer to Scheme 3-16). By employing either conventional radical initiators or initiating mediating agents, control is obtained *via* the fast deactivation of the propagating polymer chain by recombination of the polymer chain radical and the persistent nitroxide radical.

The degree of polymerization X_n is determined by the change of the monomer concentration, the initial concentration of the compound RY, generating the persistent radical, and the rate coefficients with regard to persistent radical decomposition (k_d), propagation (k_p), and recombination with persistent radical (k_c) (refer to Eq. (15)):⁶⁰

$$X_n = \frac{[M]_0 - [M]}{[RY]_0 (1 - e^{-\beta k_d t})} \quad \text{with } \beta = \frac{k_p [M]_0}{(k_p [M]_0 + k_c [Y\cdot]_0)} \quad (15.)$$

Nitroxides for their usage as persistent radicals were firstly reported by Solomon and Rizzardo in 1986,⁷⁵ and further developed to obtain control over polymerization by Georges and colleagues.²⁹ The application of NMP has widened from the early beginnings, *i.e.* using different nitroxide species for generating biohybrids, block copolymers, complex polymeric architectures, and for surface initiated NMP.⁶⁰



Scheme 3-16. Fundamental mechanism of nitroxide-mediated polymerization (NMP).⁶⁰

Disadvantages of NMP are the sometimes complex synthesis of the mediating agents⁷⁶ as well as the limited monomer selection. Nevertheless, issues in terms of high

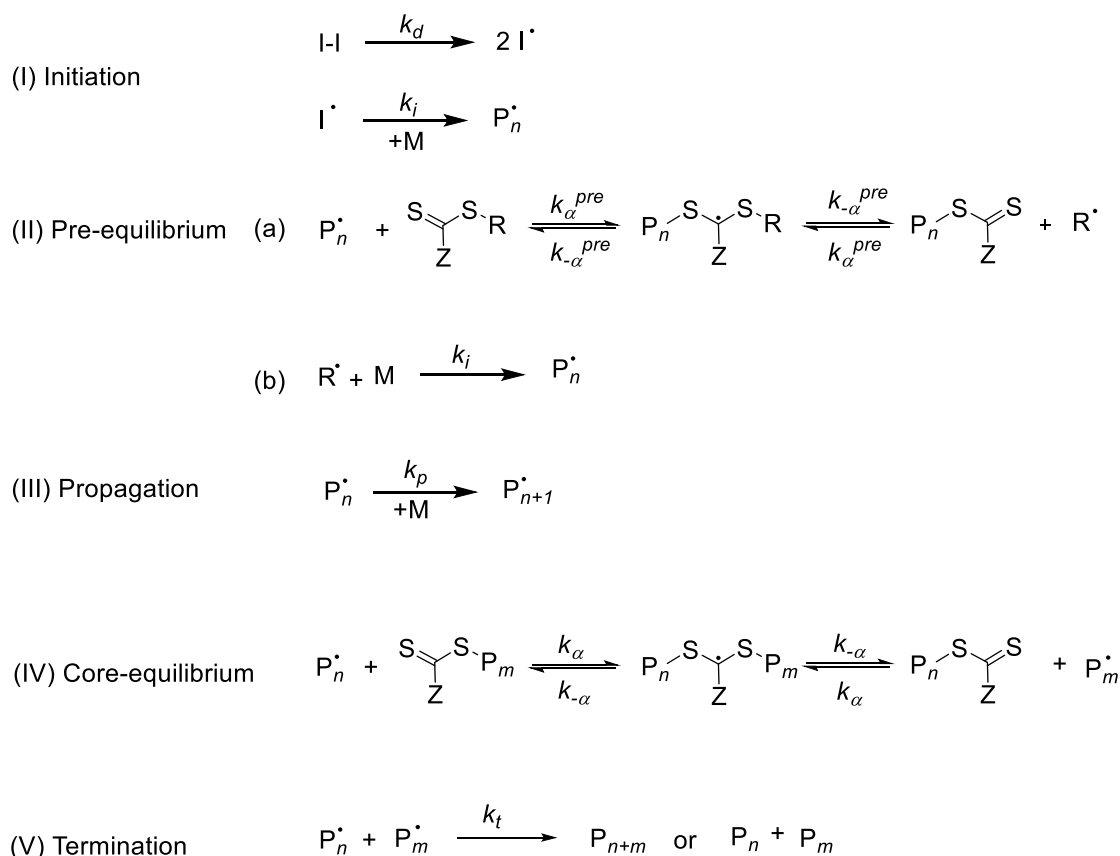
temperature demand,⁷⁷ monomer limitations,^{78,79} low yields of alkoxyamines,⁸⁰ and poor mediating activity have been addressed to extend the scope of NMP.⁶⁰ Although new mediating agents were synthesized, NMP is still more limited in terms of monomer selectivity and feasibility in comparison to other RDRP techniques.

3.2.4 Reversible Addition-Fragmentation-Chain Transfer Polymerization (RAFT)

3.2.4.1 RAFT/MADIX Polymerization Fundamentals and Mechanism

In addition to ATRP and NMP, the RAFT polymerization and the mechanistically identical process macromolecular design *via* the interchange of xanthates (MADIX), entails a degenerative FRP with a superimposed fragmentation/transfer process.^{58,81–83} By employing special dithiocarbonyl compounds, control is obtained over the radical polymerization due to a very fast addition and fragmentation process of propagating chains, leading to a steady polymer chain growth. Furthermore, the process reduces the probability to terminate in comparison to FRP, although the radical concentration is not reduced, in contrast to ATRP and NMP.⁷⁶ The RAFT process was introduced by Rizzardo, Thang, and Moad in 1998 at the Commonwealth Scientific and Industrial Research Organization (CSIRO) in Melbourne, Australia,⁸⁴ meanwhile MADIX was introduced by Charlot and colleagues in 2000 by using xanthates as a novel RAFT group.⁸⁵ Although the mechanism is identical, the term MADIX is still in use for RAFT polymerizations with xanthates. The RAFT/MADIX mechanism is depicted in Scheme 3-17:⁸⁶ The initiation step entails the decomposition of a typical radical initiator, reacting with a monomer unit to start the propagating chain. In the pre-equilibrium, the initiated polymer chains add to a RAFT group and a radical intermediate is formed. Subsequently, the R-group fragments off in order to start further chains (for more details regarding the R-group refer to Chapter 3.2.4.2). It has to be noted that the addition in the pre-equilibrium needs to be very fast in order to react with ideally all initiated chains before propagation, since further chains are started by the R-group of the RAFT agent. Therefore, the initiator is always employed in a much lower molarity than the RAFT agent, obtaining only propagating chains attached to RAFT groups. During propagation, polymer chains in their active state add monomer units, as in FRP. In the core-equilibrium, a propagating chain is added to the RAFT group and another polymer chain is eliminated for further propagation. Due to the permanently occurring addition/fragmentation, all polymer chains grow steadily and a control over the molecular weight evolution is obtained. Furthermore, termination events are still present, but due to the fast addition/fragmentation to the RAFT group, termination

events are unlikely. In contrast to NMP or ATRP, the mechanism of RAFT polymerization is more similar to FRP with the additional pre- and core-equilibria.



Scheme 3-17. Mechanism of RAFT polymerization described in five steps. (I) Decomposition of the initiator I, reacting with a monomer unit M to start the propagating chain P_n^\cdot . (II) In the pre-equilibrium (a) all initiated polymer chains are added to a RAFT group. (b) R-group is eliminated in order to start further chains. (III) During propagation, polymer chains in active state add monomer units. (IV) In the core-equilibrium the propagating chain P_n is added to the RAFT group and the polymer radical P_m is eliminated. (V) Termination by e.g. recombination.⁸⁶

The propagation rate of the RAFT polymerization is closely associated with FRP, as no further equilibrium, as in case of ATRP, is present during the process (refer to Eq. (16)):⁵⁹

$$R_p = k_p [M] \sqrt{\frac{fk_d [I]}{k_t}} \quad (16.)$$

Problems of the RAFT process are found in the intermediated state during the pre- and core-equilibrium. If the intermediate radical is too persistent, missing fragmentation leads to the loss of the control over polymerization, based on the irregular growth of polymer chains leading to high dispersities. Nevertheless, a stable intermediate with lifetimes up to seconds can improve the controlled polymerization process, due to a persistent radical effect.⁸⁷ If the persistent radical does not participate in termination, the radical concentration of active chains is virtually reduced, leading to decreased termination. A side

effect is a retarded polymerization rate. Furthermore, a so-called hybrid effect has been observed for RAFT polymerization, as explained in the following. The theoretical M_n in RAFT polymerization can be calculated with regard to the initiation process (refer to Eq. (17)):⁵⁹

$$M_n^{theo} = \frac{p \cdot [M]_0 \cdot M_{mono}}{[RAFT]_0 + 2f [I]_0 (1 - e^{-k_d t}) \left(1 - \frac{f_c}{2}\right)} + M_{RAFT} \quad (17.)$$

With p : conversion; $[X]_0$: initiator, RAFT or monomer concentration at t_0 ; M_x : Molecular weight of monomer and RAFT agent, respectively; f_c : termination type (e.g. $f_c = 1 \rightarrow 100\%$ recombination).

In case of a fast initiation, the second summand in the denominator converges to zero and the theoretical M_n of the RAFT polymerization simplifies to Eq. (18):

$$M_n^{theo} = \frac{p \cdot [M]_0 \cdot M_{mono}}{[RAFT]_0} + M_{RAFT} \quad (18.)$$

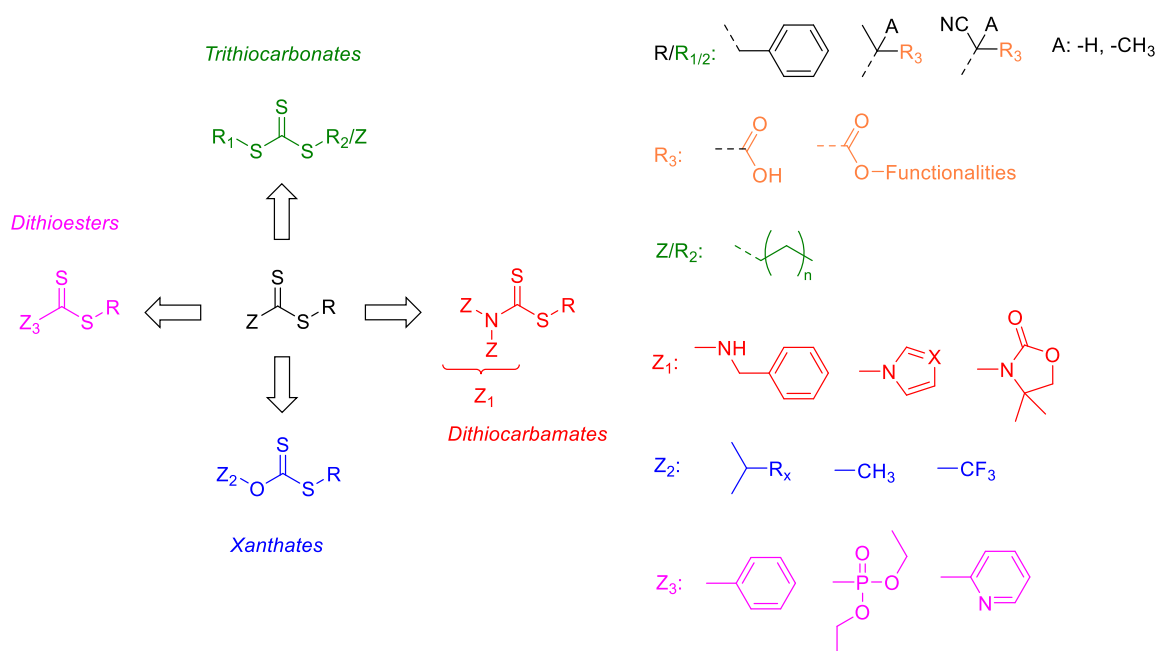
According to observations, in some cases the development of the molecular weight does not follow the relation in Eq. (18), showing the formation of high molecular weights directly after initiation. It is assumed that a large jump of the molecular weight occurs during the pre-equilibrium, followed by a subsequent linear evolution. The hybrid effect is caused by relatively low transfer constants of the RAFT agent and small addition rate coefficients of the propagating macroradicals to the C=S bond, favoring the state of the starting materials in the equilibrium and inhibiting the release of the R-group. It was mainly found in the polymerization of methyl methacrylate (MMA), a tertiary monomer, which is hard to control via the RAFT process (refer to Chapter 3.2.4.2) due to its rather stable tertiary radical during propagation.⁸⁶

3.2.4.2 The RAFT Group and Chain-Transfer Agent Design

The dithiocarbonylthio or RAFT group comprises dithioesters, trithiocarbonates, xanthates, and dithiocarbamates (refer to Scheme 3-18).⁸⁶ Each of the RAFT groups is designed according to the target monomer or monomer class, since their applicability is related to structural and stabilizing effects of the R- and the Z-group of the RAFT agent. The R-group, or leaving group, needs to provide sufficiently fast fragmentation from the dithiocarbonylthio group and to initiate a corresponding monomer with high rates after fragmentation in the pre-equilibrium. Therefore, the R-group is often designed structurally related to the propagating chain end of the specific monomer. Further, the R-group must form a sufficiently stable radical to be fragmented off the intermediate RAFT radical. Typical R-groups comprise benzyls, tertiary, or secondary hydrocarbons, as they

demonstrate sufficiently stable radical formation and high initiating propensity (refer to Scheme 3-18, top right). Problems occur in case of tertiary propagating radicals, such as MMA, since the R-group has to provide similar radical stability in order to trigger fragmentation. Therefore, the R-groups of RAFT agents for MMA have to be designed carefully, e.g. consisting of branched cyanoalkanes.⁸⁸

The Z-group, or stabilizing group, is responsible to balance the intermediate state after radical addition and has to promote the subsequent fragmentation of the R-group or a polymer chain.⁸⁶ In case the intermediate radical is too stable, a retarded fragmentation with slow polymerization are the consequences (rate retardation).^{89–92} If the stabilizing effect is too low (small addition rate coefficient), no addition of polymer chains occurs and the dithiocarbonylthio moiety remains unaffected during the radical polymerization. The Z-group is strongly dependent on the RAFT group itself, bearing aromatic units for dithioesters and dithiocarbamates, also elements with hetero atoms, such as phosphoryl or pyridyl residues for dithioesters and fluorinated hydrocarbons for xanthates (refer to Scheme 3-18).

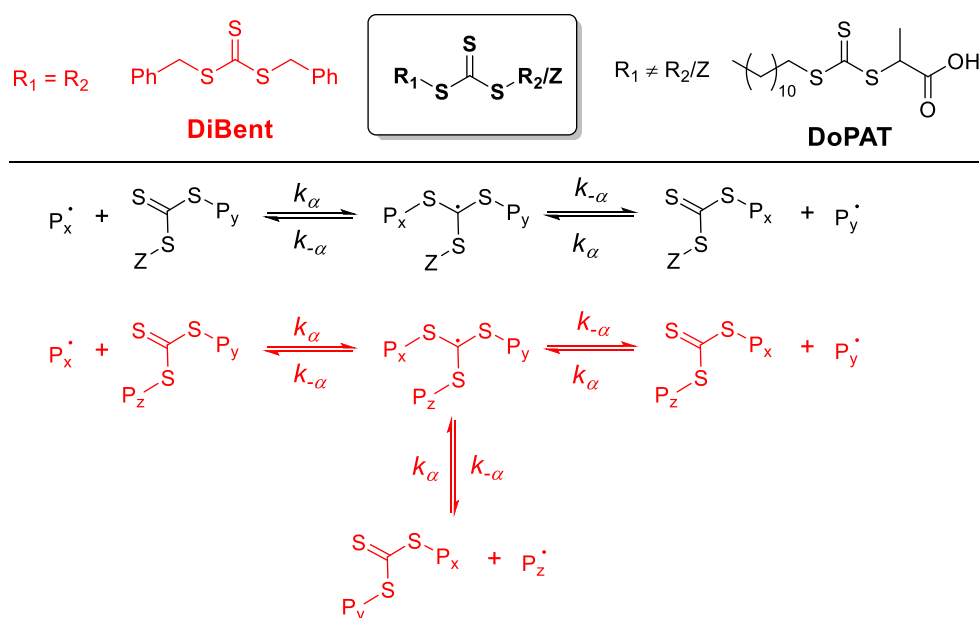


Scheme 3-18. Fundamental structural elements of RAFT agents. Different variations of R- and Z-groups are shown on the right side with respect to the according RAFT group type, indicated by the color.⁸¹

The trithiocarbonate represents a special case, due to its symmetric RAFT group structure (refer to Scheme 3-19). Here, a third sulfur atom is introduced to the thiocarbonyl and – dependent on the structure – may undergo fragmentation. In case the structure of R₁ is identical to Z, then referred to as R₂ (as shown with dibenzyltrithiocarbonate (DiBent) in Scheme 3-19), the fragmentation occurs in both directions. Thus, two steadily growing chains are formed bearing one RAFT group, affording two polymer chains linked

symmetrically by the RAFT moiety as focal point. Such a RAFT agent design allows for the facile synthesis of ABA block copolymers (BCP): Firstly, a symmetric homopolymer A is synthesized, carrying the RAFT group in the middle of the polymer chain (referred to as macro-CTA). Subsequently, a chain extension employing a monomer B directly yields the ABA diblock copolymer without any further conjugation methods.⁹³ Further, the end-groups can be decorated by identical or different functionalities, yielding α,ω -homo- or heterotelechelic polymers.

If the Z-group is differently constituted than R_1 , the fragmentation may only occur in one direction, as represented by 2-(dodecylthiocarbonylthio)-propionic acid (DoPAT, refer to Scheme 3-19). Since a dodecyl chain is unlikely to be eliminated as leaving group in comparison to the secondary hydrocarbon, an asymmetric polymer is obtained, bearing the RAFT moiety at one of the polymer end-groups, yielding an α,ω -heterotelechelic.

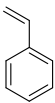
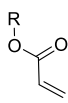
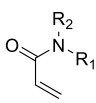
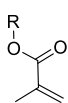
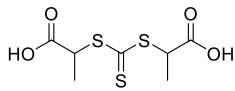
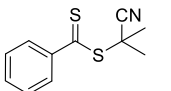
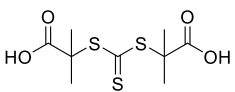
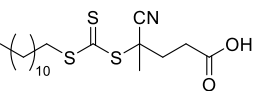


Scheme 3-19. Trithiocarbonates as symmetric RAFT groups, showing symmetric fragmentation (red) depending on the CTAs structure, e.g. for symmetric *S,S*-dibenzyl trithiocarbonate (DiBent). Regular RAFT fragmentation for asymmetric trithiocarbonate 2-(dodecylthiocarbonylthio)-propionic acid (DoPAT) in black.

In summary, RAFT agents need to be carefully designed with respect to the monomer, which is also regarded as one of the major disadvantages of RAFT polymerization. According to the target polymer or polymer structure, complex synthetic efforts are necessary because of limited variability of different RAFT agents. A short overview of suitable RAFT agents for conventional monomers is shown in Scheme 3-20.⁹⁴

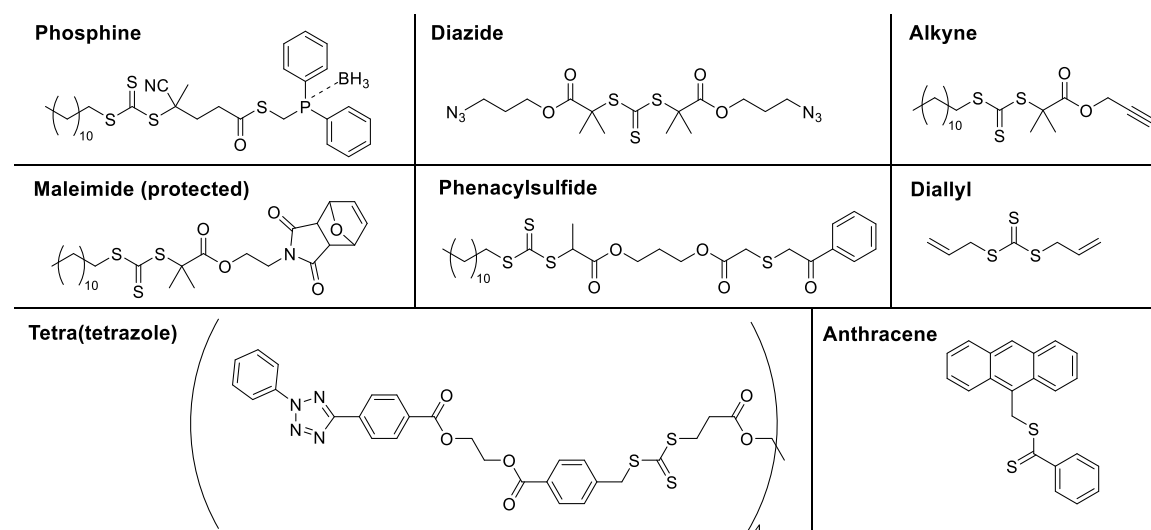
A broad range of monomer classes and end-groups are available for RAFT polymerization, since the excellent orthogonality of functional groups to the RAFT process allows their unprotected presence during the polymerization. Examples are allyls,⁹⁵ hydroxyl groups,⁹⁶ azides,⁹⁷ phenacyl sulfides,⁹⁸ tetrazoles,⁹⁹ aldehydes,¹⁰⁰ phosphines,¹⁰¹ pentafluorophenyl

active esters,¹⁰² disulfides,¹⁰³ dibromo-maleimides,¹⁰⁴ anthracenes,¹⁰⁵ cellulose,¹⁰⁶ and alkynes, respectively.¹⁰⁷

				
	◆◆◆	◆◆◆	◆◆◆	●
	◆◆	◆	●	◆◆◆
	◆◆◆	◆◆◆	◆◆◆	◆
	◆◆◆	◆◆	◆◆	◆◆◆

Scheme 3-20. Cross table of RAFT agents and suitable monomers for RAFT polymerization. ◆: suitable, ●: not suitable.

Further groups can be present in protected form, such as furan protected maleimides¹⁰⁸ or disulfides.¹⁰³ Thiols, as radical transfer agent, and amines, which can cause the loss of the RAFT group (described in Chapter 3.2.4.3), are not suitable for their presence during RAFT polymerization.



Scheme 3-21. Selection of RAFT agents with unprotected orthogonal functional groups at the R- and Z-group, as indicated.^{97,98,100,101,105,107,108}

The synthesis of RAFT agents starts from carbodithioate salts in combination with an alkylating agent.⁹⁴ Here, Grignard reagents, or simple aryl- or alkyl-halides, are preferred. The aforementioned synthesis protocols cover several primary or secondary RAFT groups, whereas tertiary RAFT groups are addressed differently.¹⁰⁹ The conditions for the RAFT group synthesis entail basic conditions, as well as radical or thermal treatment, respectively. After the RAFT group has been synthesized, further modification is possible by esterification, amidation, active-ester chemistry, click chemistry, and RAFT single unit monomer insertion,⁹⁴ achieving the functional group incorporation (refer to Scheme 3-21), as listed previously in the current chapter.

Typical monomers controllable by RAFT polymerization are styrenes (and derivatives),¹¹⁰ methacrylates, acrylates, acrylamides, (meth)acrylic acid, amino methacrylates,¹¹¹ and oligo(ethylene glycol) methacrylates.^{103,112,113} The utilization of monomers for stimuli-responsive polymers is an important domain of RAFT polymerization.^{111,114,115} With regard to initiation, RAFT polymerization can be induced by thermal, photo- or redox initiators, similar to conventional initiators in FRP and in contrast to ATRP.⁹⁴ In addition to solution and bulk polymerization, RAFT polymerization can be conducted in miniemulsions.¹¹⁶

The synthesis of BCPs can be achieved *e.g.* with sequential RAFT polymerization. In the first step, a homopolymer is synthesized by RAFT polymerization. Next, the homopolymer, still bearing the RAFT moiety, is employed as macro-CTA in a subsequent polymerization reaction in combination with additional initiator and monomer. The chain extension of the homopolymer yields *e.g.* linear BCPs.^{30,117,118} In addition, according to the design of the RAFT agent, more complex block structures can be generated, *e.g.* stars.¹¹⁹ In addition, Perrier and colleagues synthesized multi-block copolymers by RAFT polymerization to obtain complex macromolecular structures by employing trithiocarbonates.^{120,121}

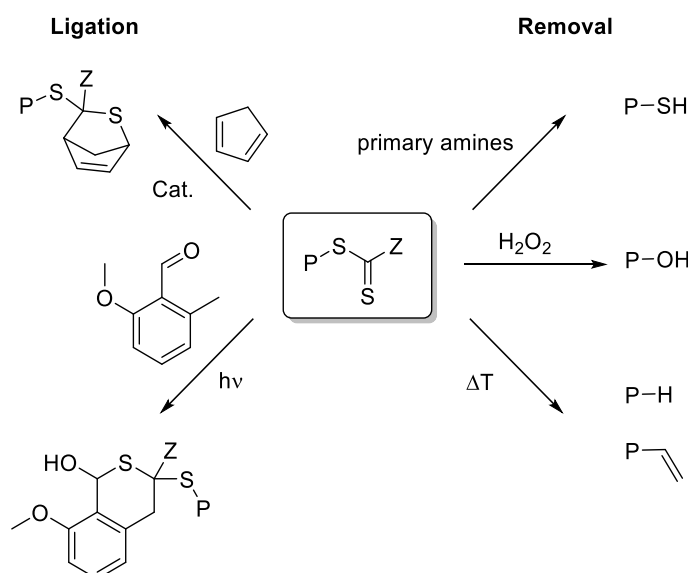
3.2.4.3 RAFT Polymerization as a Macromolecular Tool

Nevertheless, the highlights of RAFT polymerization are the very facile polymerization procedure, a broad variety of possible monomers,⁸⁶ high orthogonality to functional sites,^{97,101,122–125} absence of metal catalysts,⁸⁶ available sites for postmodification^{101,126–128} (*e.g.* RAFT group cleavage^{129–134}), the *a priori* templating of polymers (linear or star shaped polymers)^{101,135–138} and its applicability even in aqueous reaction media.^{112,139–141}

The functionalization of end-groups or side chains in RAFT polymerization is one important factor in the formation of complex macromolecular designs on the molecular level, such as graft polymers,¹⁰⁶ block copolymers,¹²⁷ star polymers,^{95,142–145} or dendrimers.¹⁴⁶ Superstructures have been formed by RAFT polymers *via* self-assembly, such as micelles,¹⁴⁷ vesicles,¹⁴⁸ membranes by a templating approach,¹⁴⁹ nanoparticles,¹⁵⁰ Janus micelles,¹⁰⁰ hydrogels,⁹³ stimuli responsive materials,¹⁵¹ and nanocontainers¹⁴⁵ for drug

delivery. Furthermore, polymerization-induced self-assembly widened the scope of RAFT.¹⁵²

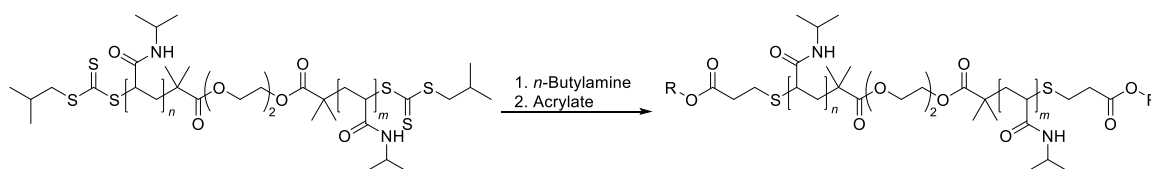
Polymers, made by RAFT polymerization, were post-modified using their end-groups as ligation tool in copper-catalyzed azide-alkyne cycloaddition (CuAAC),⁹⁷ thermally or photo-induced Diels – Alder (DA) reactions,^{127,128} or Staudinger-ligation.¹⁰¹ Here, either the dithiocarbonylthio group itself or a previously attached functionality have been addressed for ligation.



Scheme 3-22. Examples of the postmodification of RAFT groups: Ligation (left) by thermal and photo-induced DA reaction, and RAFT group removal (right) via aminolysis, oxidation or thermal treatment.^{128,134,153–156}

The RAFT group is a key factor in the postmodifications of RAFT polymers, since its availability to react with strong nucleophiles or dienes offers a wide range of opportunities for ligation (refer to Scheme 3-22). To cleave the RAFT group, treatments with primary amines (aminolysis),^{93,131,132,157} azides,¹⁵⁸ radicals (stemming from sources such as radical initiators),¹²⁹ hydrazines,¹⁵⁹ irradiation with UV-light,^{160,161} or thermal stress¹⁵⁶ have been carried out. Subsequent to the RAFT polymerization, the cleavage of the RAFT group by the aforementioned methods yields thiols,¹⁵⁷ double bonds,¹⁵⁶ hydrocarbons,¹⁶² and hydroxyl groups,¹⁵⁵ allowing further postmodification reactions, such as disulfide formation,¹⁶³ thiol-ene,¹⁶⁴ and thiol-yne reactions.¹⁶⁵

For instance, Winnik and coworkers applied a di(trithiocarbonate) for the synthesis of poly(*N*-isopropylacrylamide) and subsequent cleavage of the trithiocarbonate, obtaining an α,ω -telechelic with thiols at the chain termini.¹³¹ The dithiol telechelic polymer was then capped by a thiol-ene reaction with different acrylates (refer to Scheme 3-23).



Scheme 3-23. RAFT polymers in postmodification aminolysis and thiol-ene reaction.¹³¹

Börner et al. employed RAFT polymerization in the synthesis of graft bioconjugates, linking the *N*-terminus of the peptide *via* active ester side chains of the polymer.¹⁰² After the bioconjugation, secondary structures self-assembled by the peptides pH stimulus.

Vogt et al. employed BCPs synthesized by RAFT polymerization to induce a gelation process *via* a thermal stimulus and subsequent aminolysis of the RAFT group, in order to reverse the crosslinking (refer to Figure 3-1).⁹³ A further oxidation/reduction step above the lower critical solution temperature (LCST) offers the possibility to switch the material from micelles to crosslinked networks by disulfides/thiols.

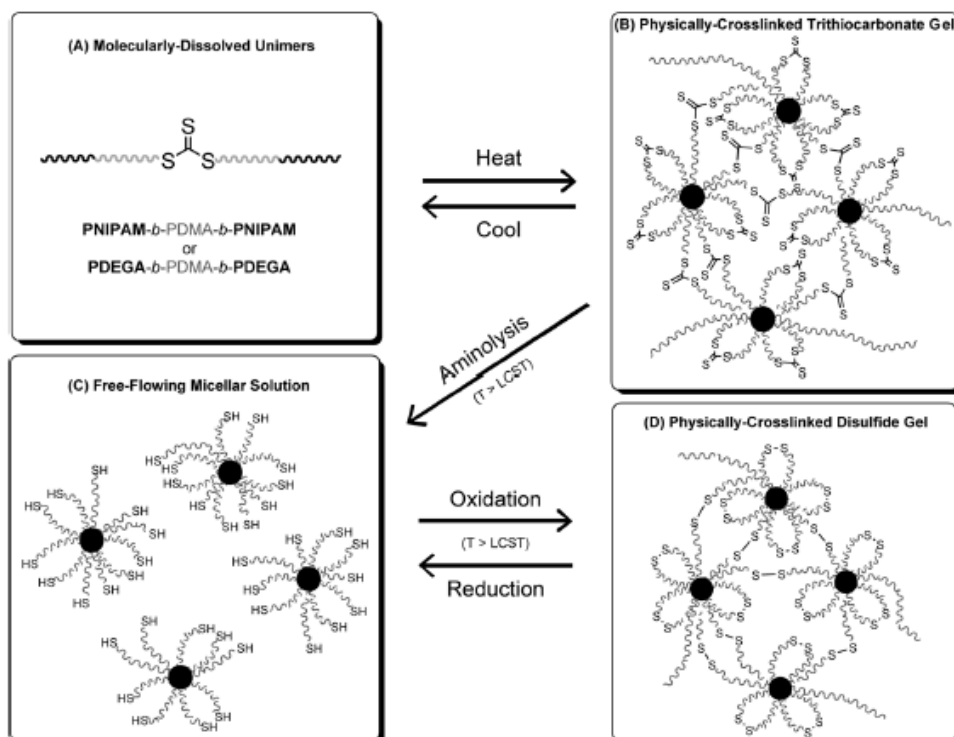


Figure 3-1. RAFT polymerization as starting point for postmodification, self-assembly, gelation and stimuli responsive materials. The figure is reproduced from A. P. Vogt and B. S. Sumerlin, *Soft Matter*, 2009, 5, 2347–2351 with permission of The Royal Society of Chemistry.⁹³

In several studies, RAFT was combined with SG polymerization in different manners, e.g. positioning a pyridyldisulfide at the R-group of an asymmetric trithiocarbonate. *Via* usage of a strong nucleophiles, the RAFT group and the disulfides are cleaved and an α,ω -telechelic polymer with thiols is generated, inducing a SG polymerization by oxidation of

the thiols to disulfides.¹³⁶ In the authors group, a SG polymerization of RAFT polymers was performed by photo-induced protocols, employing a di(trithiocarbonate) with tetrazoles in the RAFT polymerization of styrene.⁹⁹ Upon irradiation, the tetrazole end-groups of the PS form highly reactive species which undergo a nitrile-imine mediated tetrazole-ene coupling (NITEC, refer to Chapter 3.4.3.3) with a small molecule maleimide dilinker. Dan et al. realized linear BCPs by attaching RAFT groups as termini to SG polymers.¹¹⁵ A RAFT polymerization as last step yielded the BCP, obtaining a well-defined outer block of the final BCP. Members of the authors group employed a thermally triggered hetero-Diels-Alder (HDA) reaction of an AA/BB macromonomer system.¹⁶⁶ First, RAFT polymerization of isobornyl acrylate with a dithioester RAFT agent and ATRP of *n*-butylacrylate-co-isobornyl acrylate was performed, post-modifying the end-groups with two cyclopentadienyls (Cps). In a second step, a HDA SG polymerization was induced between the dithioester dienophiles and the Cp dienes upon heating to elevated temperatures in the presence of zinc chloride as catalyst.

3.3 Step-Growth Polymerization

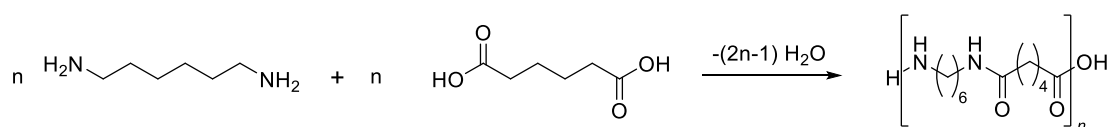
In addition to chain-growth polymerization, such as FRP, step-growth (SG) polymerization entails the formation of polymers by several types of reactions, *e.g.* condensation, addition, aromatic substitution, and radical reactions, respectively. Certainly, due to reaction equilibria, *retro* reactions, and in general slow kinetics, only a few reactions allow for their application in SG polymerization. The key difference between chain-growth and SG polymerization can be found in the active functionalities. In conventional radical polymerization, only the propagating chain – generated by a radical source – can be referred to as an active site, whereas in SG polymerization all functional groups are available to react at the same time.³² In general, SG polymerizations are divided into polycondensations and polyadditions. Polycondensation entails the polymer generation with an additional condensation product, commonly a low molecular compound (*e.g.* water or methanol). Polyaddition is defined as the growth of polymer chains by addition reactions.¹⁶⁷

3.3.1.1 Monomer Systems, Conversion and Molecular Weight

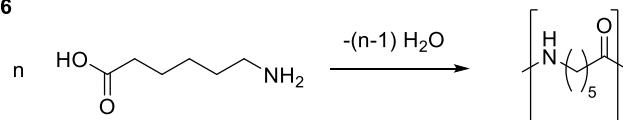
A SG monomer system can consist of either one monomer, bearing *e.g.* two reactive functionalities in one molecule, such as A and B, referred to as AB monomer system, or a multi-component system, *i.e.* two monomers bearing either only A or B functionalities, referred to as AA/BB monomer system (refer to Scheme 3-24). As illustrated in Scheme 3-24, the synthesis of polyamides (PA) is achieved by either AB or AA/BB

systems, yielding polyamide 6 (PA 6) or polyamide 6.6 (PA 6.6), respectively.³¹ More complex monomer systems are not discussed in the current chapter. The synthesis of PA 6.6 and PA 6 belongs to the polycondensation reactions, whereas PA 6 on industrial scale is synthesized *via* anionic ROP of ϵ -caprolactam.³¹ During a SG polymerization, all molecules are able to react simultaneously which significantly impacts on the length of the species formed. In the early phase of the SG, dimers, trimers and further oligomers are generated and simultaneously, the functional group concentration decreases drastically. In the later stage of the SG at high conversions, oligomers react with each other and polymers are formed with corresponding α,ω -end-groups. On the contrary, in FRP already at low conversions high molecular weight chains are generated (refer to Figure 3-2).³²

AA/BB monomer system: Polyamide 6.6



AB monomer system: Polyamide 6



Scheme 3-24. SG polymerization of an AA/BB (top) and SG or ROP of an AB (bottom) monomer system. The AB monomer system yields PA 6, whereas the AA/BB monomer system yields PA 6.6.

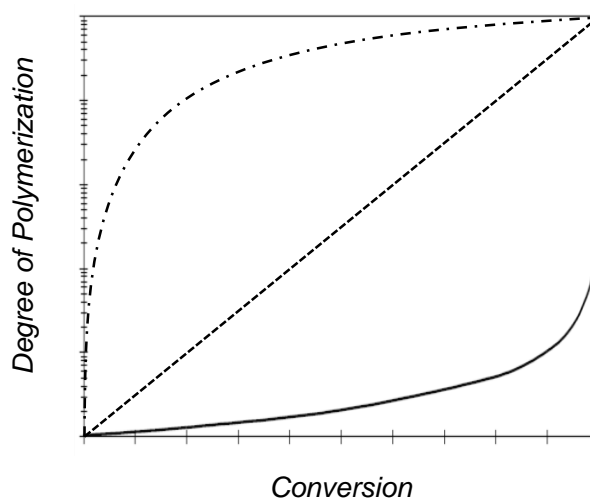
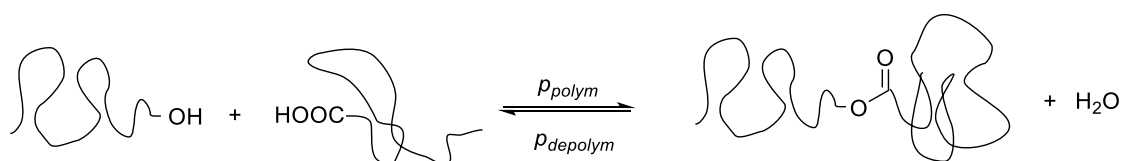


Figure 3-2. Schematic evolution of degree of polymerization with conversion for different polymerization techniques: step-growth (solid line), controlled and living methodologies (dashed line), and free-radical polymerization (dash-dotted line).³³

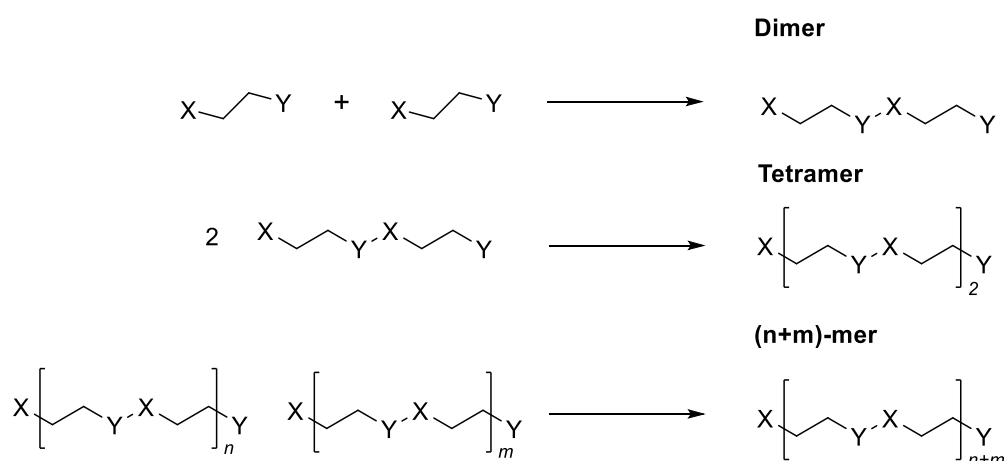
In closed systems, condensations are reversible reactions, *i.e.* the condensation products – *e.g.* water – are still available in the reaction equilibrium.³³ In case of a polymerization, both the polymerization and depolymerization occur simultaneously (refer to

Scheme 3-25). If the cleaved compound is not removed – *i.e.* no influence pushes the equilibrium to one side – the equilibrium constant K changes during the reaction until the polymerization and depolymerization rates are identical and the constant $K=1$.³² Therefore, the low molecular compound, such as water or methanol, are removed during the synthesis to push the equilibrium towards the products. The polymerization rate depends on the functional group concentration and also on their availability, as the rate decreases with increasing conversion. The generation of high molecular weights or ideally, one final cyclic polymer chain, is obtained, when all functional groups have reacted (refer to Figure 3-2). In practice, polymerization stops at a certain point, since the functional groups are not available or not accessible due to polymer chain coiling or precipitation. Furthermore, cyclization can occur that will be discussed in Chapter 3.3.1.3.



Scheme 3-25. Reversible nature of a polyesterification reaction with the equilibrium constant K .

The reason for the generation of high molecular species in the last stage of polymerization can be explained by the participating reactions. Initially, a monomer reacts with another monomer forming a dimer. By going further, the reaction of a dimer with a dimer only yields a tetramer. By summing up all reactions, the polymerization degree evolves rather slowly, as the reaction of an n -mer and an m -mer yields a $(n+m)$ -mer (refer to Scheme 3-26).³²



Scheme 3-26. Polymerization of monomers, dimers, and n , m -mers to form oligomeric species.³²

In 1936, W. H. Carothers published the first version of the so-called Carothers equation, correlating the evolution of the degree of polymerization X_n with conversion p under the assumption of perfect monomer stoichiometry (refer to Eq. (19)).¹⁶⁸ In case of off-stoichiometric conditions, *e.g.* in AA/BB monomer systems, the equation is expanded by

the stoichiometric factor r . In general, the Carothers equation allows for calculating the degree of polymerization with respect to the stoichiometric ratio r and the conversion p (refer to Eq. (20)):

$$X_n = \frac{1}{1-p} \quad (19.)$$

$$X_n = \frac{1+r}{1+r-2r \cdot p} \quad (20.)$$

With: p : conversion; r : stoichiometry of the AA/BB monomer ratio.

If the stoichiometry is ideal, *i.e.* $r = 1$, Eq. (20) is simplified to the Eq. (19), *e.g.* for an AB monomer system, since a perfect stoichiometry is given by the equimolar feed of functional groups. At the start of a SG in an AA/BB system, the AA and BB monomers form dimers and with additional monomers trimers and oligomers. Caused by the presence of two different monomers, oligomers can be formed bearing the same functional group at both ends. If the stoichiometry is ideal, such a SG proceeds in a similar fashion as in case of the AB monomer system. If the monomer feed is imbalanced, no high molecular weights are obtained due to remaining end-groups of the monomer, employed in excess. A control over the molecular weight is rather difficult, since the reaction cannot be easily terminated as in case of FRP. Therefore, a target molecular weight can be achieved by slightly off-stoichiometric conditions or by addition of chain stoppers, *i.e.* monofunctional compounds bearing either functionality A or B.³² In a similar way, the excess monomer decorates all end-groups, achieving control over the termini. Nevertheless, a SG polymerization can be regarded as controlled by converting the mechanism into a 'chain-growth condensation polymerization', which is reported elsewhere.¹⁶⁹ Here, the reactivity of the polymer chain end group has to be higher than the monomer either by specific activation or by an auxiliary catalyst.

3.3.1.2 Kinetics and Reactivity

The reaction kinetics of SG polymerizations depends on several parameters, *e.g.* reaction type, functional groups, monomer concentration, catalyst application, and solvent, respectively. In general, the kinetics can be slow due to intermediate formation or activation, such as protonation in polyesterifications. Furthermore, equilibria of reversible reactions strongly influence the net reaction speed. Hence, the removal of the small molecule condensate pushes the reaction equilibrium towards the product. In this case, the polymerization can be termed irreversible. The reaction rate of a stoichiometric self-catalyzed reaction, *e.g.* self-catalysis of carboxylic groups, depends on the monomer

concentration $[M]$, *i.e.* the kinetics can be expressed as the decreasing concentration of the functional group M (refer to Eq. (21)).³²

$$\frac{-d[M]}{dt} = k[M]^3 \quad (21.)$$

Integration of Eq. (21) yields Eq. (22):

$$2kt = \frac{1}{[M]^2} - \frac{1}{[M]_0^2} \quad (22.)$$

With: $[M]_0$: initial monomer concentration. The monomer concentration at conversion p can be expressed by Eq. (23), where the conversion p or extent of the reaction is defined by the converted functional groups at the time t .³²

$$[M] = [M]_0 - [M]_0 p = [M]_0 (1 - p) \quad (23.)$$

A combination of both Eq. (22) and Eq. (23) yields Eq. (24):

$$\frac{1}{(1-p)^2} = 2[M]_0^2 kt + 1 \quad (24.)$$

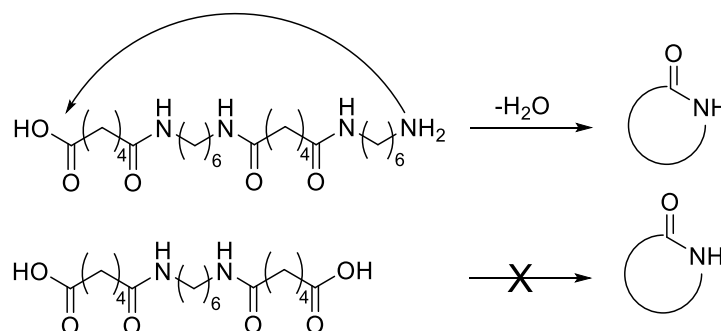
Another influence on the kinetics is given by the molecular weight of the polymer. In comparison, a polymer shows lower mobility than a small molecule. Therefore, the number of collision partners is decreased for a polymer chain, decreasing the probability of colliding with another reaction partner bearing the corresponding functionality for reaction. In this case, the reaction rate decreases at high conversions, due to less collision. Nonetheless, the reactivity of all functional group is in general independent from the polymer chain length. General considerations of the reactivity of each functional group imply that the presence of a second identical group or a counterpart group does not alter the reactivity of any groups during the polymerization.³²

Deviations from aforementioned theoretical evolution of the molecular weight with conversion can be also explained by the polarity evolution of the reaction mixture. In a polyesterification, deviations from theoretical molecular weight evolution are assumed to be caused by changes in polarity affecting the polymerization rate.¹⁷⁰ This is founded on drastic concentration decrease of carboxylic acids and alcohol functionalities that are further unavailable to stabilize intermediates, *e.g.* charged species.

3.3.1.3 Cyclization in Step-Growth Polymerization

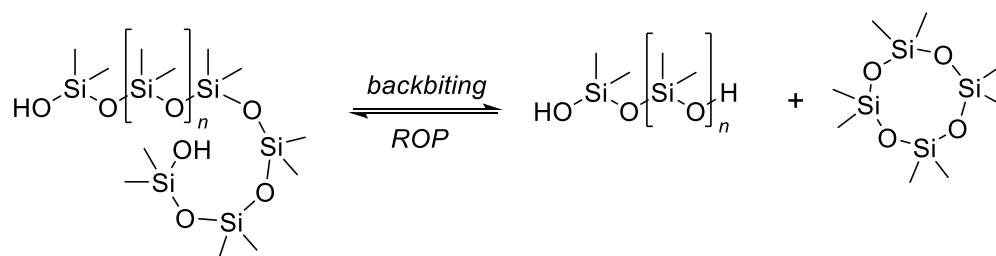
In SG polymerization, the formation of non-linear polymers can occur, in the simplest case cycles.³² Such a behavior can be found for both monomer systems, *i.e.* AB and AA/BB. Cyclization is dependent on the generated structure and reaction conditions, *e.g.* the

monomer concentration. If the concentration is too low, the intramolecular cyclization is favored, referred to as Ruggli-Ziegler dilution principle,¹⁷¹ whereas at higher concentrations the linear polymerization is promoted. An entropic effect is present in equilibria, since longer chains are depolymerizing in favor of smaller chains, increasing the number of molecules in the system. In general, a competition of cyclization vs. linear polymerization is present in all SG polymerizations,³¹ certainly, the polymerization equilibrium can be pushed to the formation of linear polymers. A control over the SG cyclization can be afforded thermodynamically or kinetically. Thermodynamic control over the SG is given in case a reversible equilibrium between the cyclic and the linear polymer is present, such as the hydrolysis of a polyester, while kinetic control is achieved if the reaction can be regarded as irreversible, e.g. polyesterification with acid chlorides, yielding an increase of cyclic chains with conversion.



Scheme 3-27. Tetra- and trimers during SG polymerization of adipic acid and 1,6-hexamethylenediamine, undergoing cyclization in case of tetramers. The trimer cannot form a cycle, due to missing functional site.

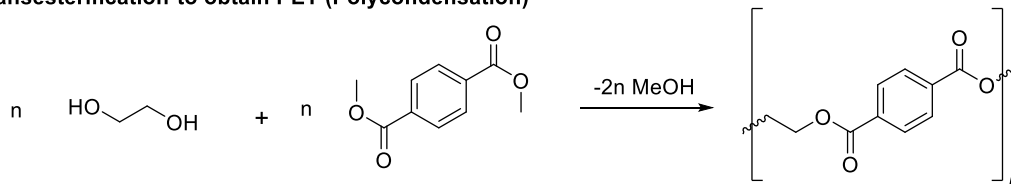
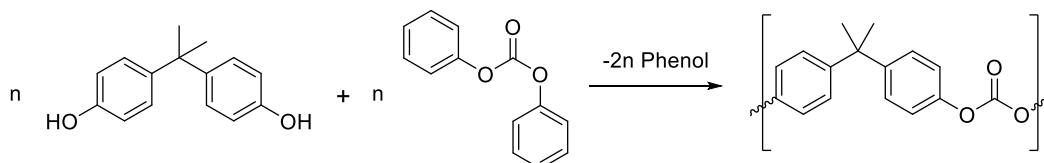
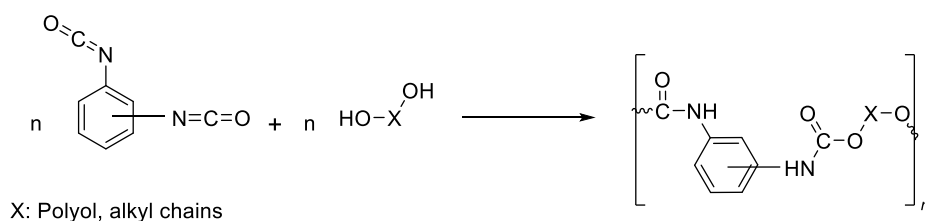
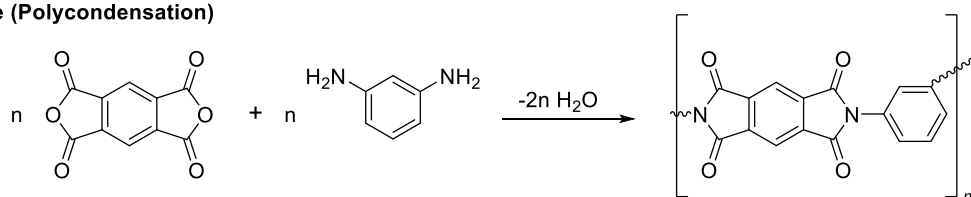
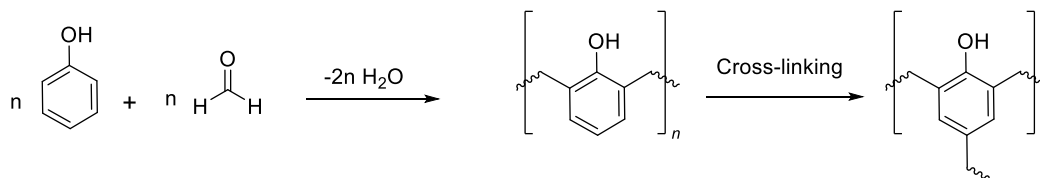
However, increased cyclization is found for AB monomer systems, already starting after the formation of dimers.³² For AA/BB systems, the absence of a self-reaction of either A or B with their selves prevents cyclization and promotes linear polymerization. Certainly, dimers or tetramers of AA/BB systems are capable to undergo cyclization since both functional groups at the termini can react with each other (refer to Scheme 3-27). If cyclization is possible, the monomer structure has to be taken in account, specifically regarding the ring strain. The formation of 6 membered rings is thermodynamically favored, whereas smaller rings of 3-4 members feature high ring strains, 5 or 7 membered ring show torsional strain and higher rings of 8-13 members show transannular repulsion.⁴² However, longer ring systems of >14 membered rings show decreasing strain of the cycle. Cyclization can also be intended, e.g. in the synthesis of cyclic siloxanes as monomers for silicon based rubbers for anionic ROP (refer to Scheme 3-28).¹⁷²



Scheme 3-28. Cyclization and depolymerization of polysiloxanes by backbiting yielding small cyclic siloxanes.

3.3.1.4 Applications of Step-Growth Polymerization

The importance of SG polymerization is evident by the wide application of polycondensation or polyaddition on multi-ton scales in industry. Examples of SG polymers as consumable and engineering plastics are PA, poly(ethylene terephthalate) (PET), polycarbonates, polyurethanes, polyimides, and phenol resins (refer to Scheme 3-29).^{3,173} PA for fiber production was developed in the 1930's by W. Carothers at DuPont, leading to PA 6.6. Meanwhile, in Germany H. Schlack at IG Farben developed an anionic ROP affording PA 6 (refer to Scheme 3-24), showing similar mechanical properties as PA 6.6. As a consequence based on early agreements between these two companies, the PA market nowadays is still divided into areas dominated by PA 6.6 such as the UK and the US, and PA 6 dominated areas e.g. Germany and Japan.³ PET is a conventional polymer for drinking bottles as well as for synthetic fibers, such as functional sport clothing.¹⁷⁴ In terms of engineering plastics, polycarbonates are utilized as highly rigid and transparent materials in housings, glasses or automotive parts.¹⁷⁵ In addition, polycarbonates have been enhanced towards applications in biomedical and biodegradable materials.¹⁷⁶ The application of polyurethanes is diverse, since the materials properties can be adjusted by the monomer design, e.g. the molecular structure of the alcohol, such as branching, multiple functionalities, or spacer lengths, changing the material's properties drastically.¹⁷⁷ Furthermore, polyurethanes are utilized in polymer foams, yielding light-weight components. Polyimides can be applied in temperature ranges up to +400 °C, which enables their usage in aerospace and astronautics applications.¹⁷⁸ Bakelite is the brand name of one of the first phenolresin materials that was invented in the beginning of the 20th century, enabling the application of polymers in electrical elements.³⁸ The scope of SG polymerization has been recently expanded to 'click' chemistry, olefin metathesis and multicomponent reactions.¹⁷⁹ Here, a key trend is the synthesis of biodegradable polymers and the utilization of sustainable preparation methods. By incorporating low fractions of biodegradable monomer units into copolymers, their degradability increases significantly.¹⁸⁰ Sustainable SG polymerizations can be carried out by enzymatic reactions.¹⁸¹

Transesterification to obtain PET (Polycondensation)**Polycarbonate (Polycondensation)****Polyurethane (Polyaddition)****Polyimide (Polycondensation)****Phenol Resins: Bakelite (Polycondensation)****Scheme 3-29.** Polymers prepared *via* SG polymerization by polycondensation or polyaddition reactions.¹⁷³

3.4 Modern and Contemporary Ligation Reactions

3.4.1 Introduction of Click Chemistry

In modern synthesis, reactions require high efficiency, atom economy, and specificity.⁴ Additionally, low activation energies, mild reaction conditions, and environmental sustainability are further requirements to synthetic chemistry today.¹⁸² In 2001, Kolb, Finn and Sharpless defined requirements for outstanding reactions, which they termed click chemistry.¹⁸³ These reactions have to fulfil several requirements:

- 1.) Very high yields
- 2.) Reliability and possibility to upscale
- 3.) No or inoffensive side product formation
- 4.) Modular approaches
- 5.) Facile or no complex purification steps (e.g. no column chromatography)
- 6.) Absence of solvents or the usage of non-toxic media such as water
- 7.) Stereospecific product formation
- 8.) Simple reaction setup and conditions (e.g. water or oxygen insensitivity)
- 9.) Starting materials and reagents from accessible sources
- 10.) Driven to one specific product

By employing reactions that follow these requirements, the tool in hand is able to be adapted not only in organic chemistry, but polymer chemistry, biochemistry, and *in vivo* applications. In polymer science, the term 'click' chemistry was further defined for the practical use in the field.¹⁸⁴ It was stated that click chemistry truly corresponds to the aforementioned criteria and not only to very successful reactions. Furthermore, some requirements of Sharpless in the original definition do not necessarily apply for polymer chemistry. Therefore, basic criteria in polymer chemistry are chemoselectivity and single reaction trajectory, whereas regioselectivity and the restriction to water as reaction medium are not of primary importance. Furthermore, polymers as reactants in combination with small molecules differ from polymer-polymer reactions. Here, equimolarity plays a key role, since routine purification of polymers *via* precipitation allows the application of excessive small molecules without entering complex purification procedures. With regard to polymer-polymer reactions, equimolarity is strictly necessary, whether the polymer starting materials cannot be separated by routine procedures. Furthermore, Sharpless did not define a confined timescale to label a reaction 'click'. Therefore, a click reaction requires a reasonable timeframe for completion.

In the following chapters, reactions are introduced, which suit at least some of these requirements.

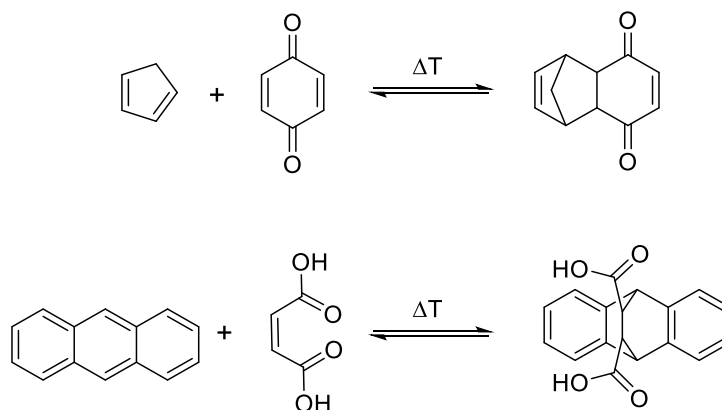
3.4.2 Diels – Alder Cycloaddition: An Introduction

An excellent example that often fulfills many of the click chemistry requirements is the Diels – Alder (DA) reaction. Here, a [4+2] cycloaddition occurs by employing a conjugated diene and a dienophile yielding a six-membered unsaturated cycloadduct (refer to Scheme 3-30).¹⁸⁵



Scheme 3-30. Most elemental case of the DA cycloaddition of a 1,3-dibutadiene as the diene and ethylene as dienophile, forming cyclohexene as the unsaturated six-membered ring.

A [4+2] cycloaddition was firstly reported by Otto Diels and his student Kurt Alder in 1928,¹⁸⁶ investigating the reaction of cyclopentadiene and *p*-quinone (refer to Scheme 3-31). These findings were expanded to further reactions, such as the synthesis of cantharidin,¹⁸⁷ reactions of anthracenes,¹⁸⁸ and early examples of hetero-Diels – Alder (HDA) reactions of nitrogen containing heterocycles.^{189,190}



Scheme 3-31. DA reactions unraveled by O. Diels and K. Alder.^{186,188}

3.4.2.1 Molecule Orbital Theory of Cycloadditions

The mechanism of the [4+2] cycloaddition can be compared to the reaction of an electrophile and a nucleophile. In contrast to electrophilic addition, the [4+2] cycloaddition proceeds in one step, in which the electrophilic and the nucleophilic carbons are situated next to each other in the dienophile (refer to Figure 3-3, right behalf).¹⁸⁵ Here, the three double bonds generate two σ -bonds and a shift of the π -bond occurs. Since the reaction proceeds in one step, it is referred to as a pericyclic reaction.

To explain the reaction in more detailed, molecular orbital (MO) theory has to be taken into account, by envisioning the MOs of the diene and the dienophile (refer to Figure 3-3). An overlap of MOs with the same color means in-phase, whereas the match between red and blue means out-of-phase. Due to the delocalization of the π -electrons in the diene, the

binding MOs are overall in-phase. The anti-binding MOs are out-of-phase and of higher energy, creating a node between the MOs, in which the probability of finding an electron is zero. The binding MO of highest energy is referred to as the highest occupied molecular orbital (HOMO), whereas the lowest non-binding MO is referred to as the lowest unoccupied molecular orbital (LUMO). LUMO and HOMO are also referred to as frontier molecular orbitals (FMO). By expressing the HOMO of 1,3-butadiene, a binding motif of two in-phase MOs is found. To describe the DA reaction, the HOMO and the LUMO of the diene and the dienophile (for instance 1,3-butadiene and ethylene in Figure 3-3) have to be inspected. In the case of ethylene, the LUMO shows the antibonding MO being out-of-phase. The two σ -bonds are then formed in the pericyclic reaction by the overlap of the in-phase MO, as shown in Figure 3-3 right handed side. The symmetry of MOs is defined by the overlap of the two MOs side by side. If the outer MOs show the same orientation (filled lobe up, empty lobe down in Figure 3-3) on both sides, the MO is called symmetric, if there is no match, they are called asymmetric.

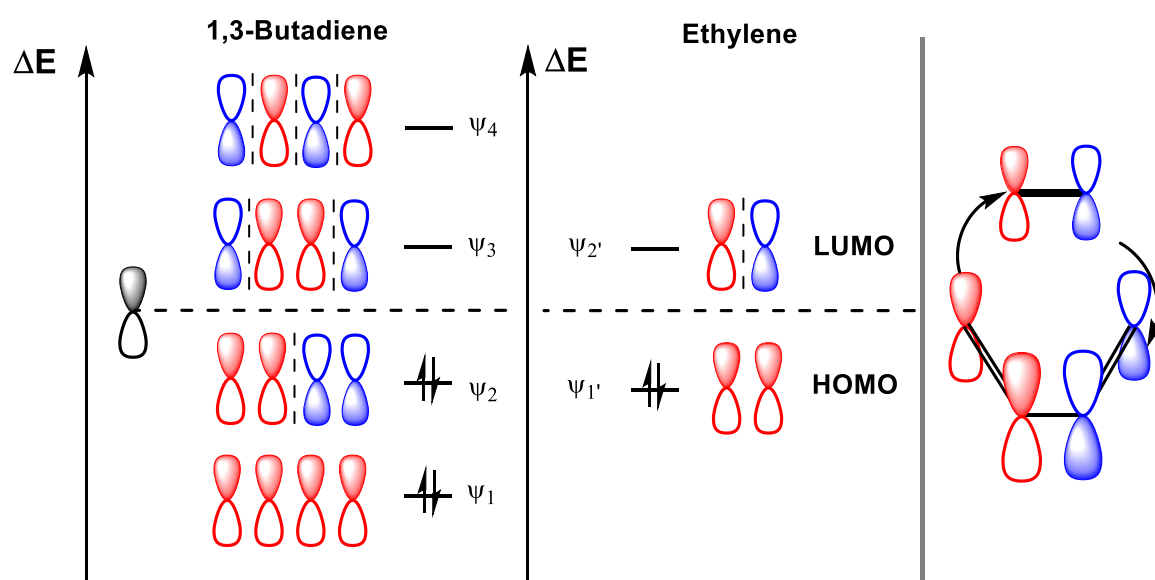
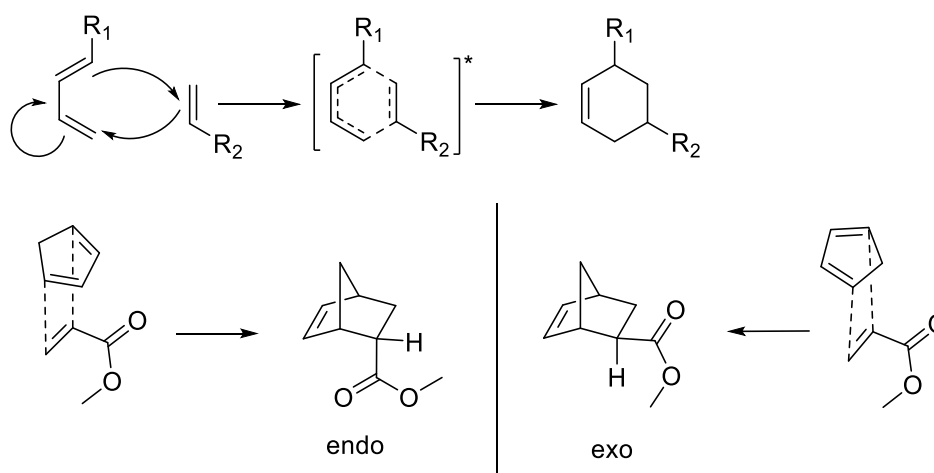


Figure 3-3. Left: MO of the diene 1,3-butadiene and of the dienophile ethylene. Right: LUMO and HOMO of the dienophile and diene undergoing a common electron demand DA reaction.¹⁸⁵ In this illustration, the size of the MOs does not represent the orbital coefficients.

In terms of adduct formation, the arrangements of the MO can occur suprafacial or antarafacial, *i.e.* suprafacial denotes the participating π -systems facing each other in order to form the σ -bond, antarafacial implies that the π -system is not facing each other for the σ -bond formation. If a six-membered ring is formed, the attack necessarily occurs suprafacially, since the antarafacial attack is hindered by geometric repulsion for smaller ring systems. MO theory also justifies why the [2+2] cycloaddition does not proceed *via* thermal stimulus, but *via* a photo-induced trigger.⁴² Common thermal DA reactions occur

from the ground state, *i.e.* the HOMO of the diene ψ_2 as shown in Figure 3-3. In the case of photo-induced reactions, one of the electrons is excited to the former LUMO ψ_3 and becomes a higher energy HOMO. The [2+2] cycloaddition proceeds from the excited state, which differs in its orbital geometry.

The DA reaction can occur between different MO combinations, *i.e.* the LUMO of the dienophile and HOMO of the diene (common electron demand DA), or the LUMO of the diene and the HOMO of the dienophile (inverse electron demand DA). Throughout the MO of the described example, it becomes obvious that decreasing the LUMO and increasing the HOMO energy level leads to lower activation energy and thus, a faster reaction occurs. Hence, by substituting one of the residuals with electron-withdrawing groups (EWG) and the counterpart with electron-donating groups (EDG), the gap between LUMO and HOMO decreases. In this context, an anticipation of suitable DA pairs is possible and has led to the development of compatible diene and dienophile species.⁴²



Scheme 3-32. Attack of double bonds in DA reaction leading to a pseudo transition state and the final formation of the product (top part). Formation of *endo/exo* adduct upon DA reaction of cyclopentadiene and methyl acrylate (bottom part).¹⁸⁵

Besides the modeling of the reaction in MOs, the attack of the diene can proceed with the residual group R pointing to or away from the dienophile. Depending on the constitution of the diene and the dienophile with regard to the substituents, a wide range of possible stereoisomers can be formed. Using cyclic dienes, the formed adduct contains a bridged bicycle. In case the diene is in a locked confirmation, *e.g.* *cis* transformation for cyclopentadienyls, the reaction proceeds in a certain orientation. Thus, if the residual groups of the diene and the dienophile are pointing in the same direction, the product is referred to as *endo*; if pointing in opposite directions, it is referred to as the *exo* product (refer to Scheme 3-32). According to the sterical repulsion, the *exo* product is thermodynamically more stable. The reason for the *endo* formation, favored kinetically, are the EWGs of the dienophile, if present, interacting with the forming double bond and

therefore lowering the energy of the transition state.⁴² Furthermore, *endo* formation can be caused by interaction of double bonds during the attack of the diene to the dienophile, e.g. the dimerization of cyclopentadiene. It is not always possible to determine which product was formed, since the *exo/endo* products can be transferred into each other by e.g. high thermal input.

If substituted dienes or dienophiles are employed, the DA reaction provides a certain regioselectivity. In case EWGs or EDGs are attached to the diene and the dienophile, the electron density coefficient of the orbitals can be increased or decreased. However, in the DA reaction the overlap of the orbitals with the highest coefficients are favored and undergo the cycloaddition. Therefore, by designing the DA pair accordingly, a highly precise regioselectivity can be achieved, as shown for the example of the unsymmetric DA reaction of methyl acrylate and (4-methyl)-1,3-pentadiene (refer to Figure 3-4, size of lobes is proportional to the electron density coefficient).

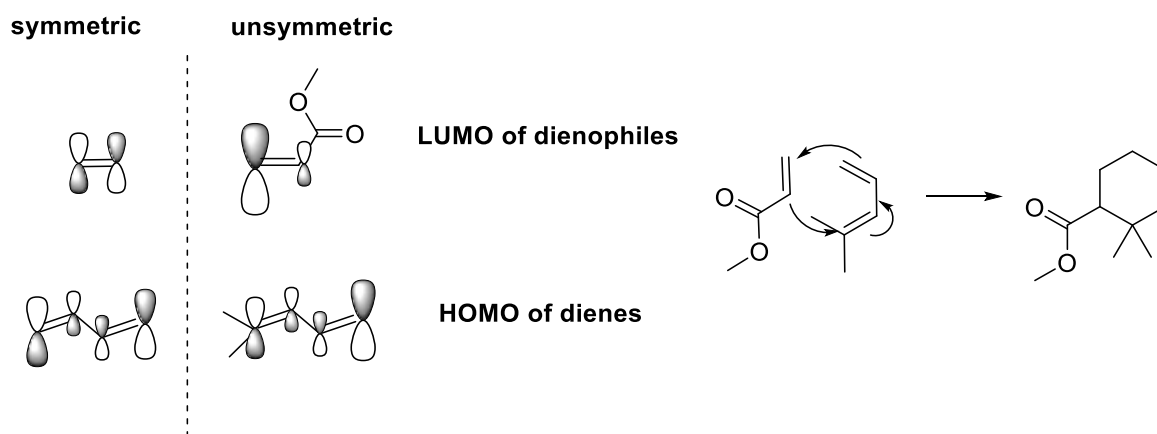
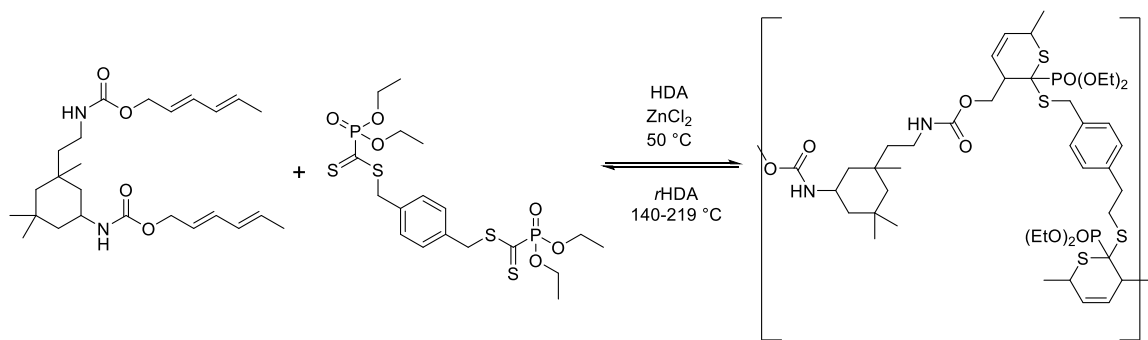


Figure 3-4. Symmetry of HOMO and LUMO of substituted and unsubstituted dienes and dienophiles, determining the regioselectivity in terms of unsymmetric DA reactants. The size of the lobe is proportional to their electron density coefficient.

3.4.2.2 Modern Usage of Thermal Cycloadditions in Polymer Science

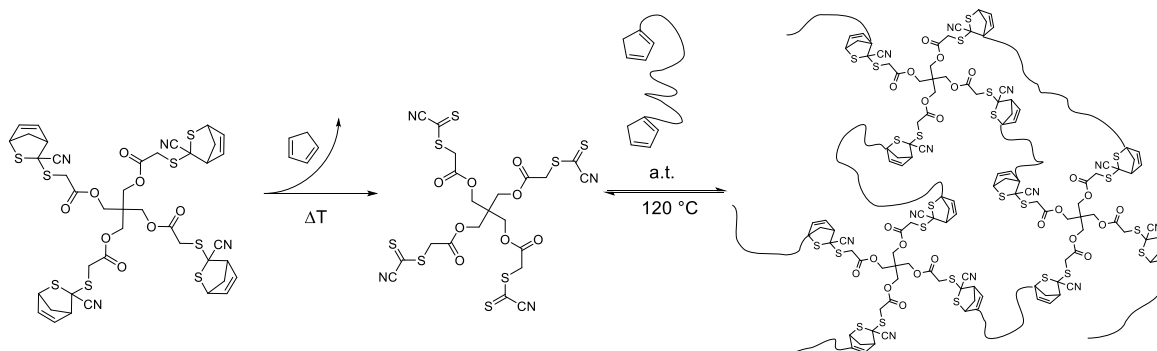
As mentioned before, the need for efficient and sustainable synthesis demands for outstanding reactions. Thermal DA reactions have been used extensively for ligations with high specificity. Since DA reactions fulfil many requirements of click chemistry and represent facile synthetic efforts, DA, HDA and their corresponding *retro* DA and HDA reactions are widely utilized in contemporary research.^{183,184,191,192} DA and HDA reactions were used for BCP formation,^{144,193,194} complex polymeric architectures,¹⁹² material science,^{153,195,196} surface chemistry,^{197–200} and SG polymerization.^{126,166} The latter represents a rarely investigated field, employing HDA reactions for the linear SG polymerization of small molecules or telechelic polymer chains.

By monitoring HDA and *retro* HDA reactions of polymer chains at different positions within polymer chains, an entropy driven bonding/debonding concept was established.^{166,201} Furthermore, the application of HDA with small molecules enabled a reversible SG polymerization by triggering the formation of the SG polymer at elevated temperature with addition of a Lewis acid, here ZnCl_2 , and subsequently depolymerizing the SG polymer *via* high thermal energy input up to 219 °C (refer to Scheme 3-33).¹²⁶



Scheme 3-33. HDA and *r*HDA of a di(sorbyl)derivative and a phosphoryl dithioesters forming the SG polymer upon addition of ZnCl_2 as catalyst at elevated temperatures and depolymerizing the polymer at high temperatures.¹²⁶

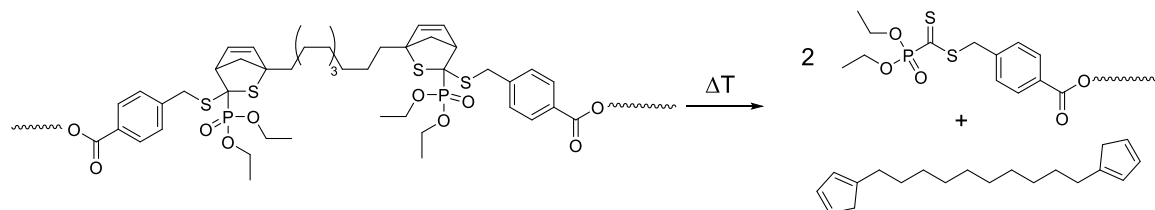
In the author's group, HDA reactions as tool in self-healing materials and bonding-debonding adhesives have been developed.^{153,196} In the case of self-healing materials, tetra-dienophile linkers were synthesized, consisting of cyanodithioester capped with Cp (refer to Scheme 3-34).¹⁵³ In order to form a network, the Cp cap is removed in a *retro* HDA reaction and subsequently a difunctional Cp linker is added, forming a covalent network by a HDA reaction at ambient temperature. Such network linkers were incorporated into a macroscopic specimen. If the specimen is destroyed, the *retro* HDA reaction can be triggered by thermal stress and shear forces to dissolve the network, obtaining a plastic material that can be reshaped into the former specimen.



Scheme 3-34. Cyclopentadienyl and dithioester as components in self-healing materials based on a HDA and *retro*-HDA reaction.¹⁵³

The usage of materials in dental applications demands for low toxicity, long-term stability and insensitivity to the exposure to heat and food residues.²⁰² Furthermore, the removal

of broken or damaged dental fillings usually requires elaborate efforts, since the strength of the adhesive cannot be reduced by any stimulus.²⁰³ Therefore, HDA chemistry represents an excellent method for dental materials, exploiting the reversibility and the insensitivity of the HDA reaction. In the author's group Cp derivatives have been employed in combination with phosphoryl dithioesters for bonding and debonding by thermal stimulus, after incorporating the HDA moieties into a polymeric network (refer to Scheme 3-35).¹⁹⁶ Upon thermal stress, the network could be reversibly degraded at temperatures of 80 – 100 °C by triggering the *retro*-HDA reaction in a very fast reaction. Furthermore, the intense color of the dithioester component visually evidences the *retro*-HDA reaction, referred to as 'self-reporting system'.



Scheme 3-35. Bonding/debonding on demand by employing a *retro* HDA reaction. Debonding is evidenced by the occurrence of a reddish color from the free phosphoryl-dithioester.¹⁹⁶

3.4.3 Photo-induced Reactions

Synthetic photo-induced chemistry is inspired by many of nature's processes, such as photosynthesis,²⁰⁴ vitamin D production²⁰⁵ or the generation of ozone.²⁰⁶ With the help of these processes, the basics of life on our planet became possible.²⁰⁷ Photochemistry was utilized without an in-depth understanding for thousands of years, when Alexander the Great already used photochromism for giving the signal for battle between his soldiers.²⁰⁸ The origin of organic photochemistry lies in the 19th century based on the works of Trommsdorff, reporting the color change of santonin from colorless to yellow upon exposure to sunlight.²⁰⁹ The physical fundamentals were then discovered by Einstein's quantum equivalence law in 1905.²¹⁰ Here, for the first time, the term light quantum was introduced and became later the basics of photochemical theory.²¹¹ In the early 20th century, fundamental reactions were conducted by Silber and Ciamician, investigating the influence of light onto the photoreactions of alcohols and carbonyl compounds,²¹² subsequently expanding their work to nitro compounds²¹³ and cinnamonic acid.²¹⁴ At a later stage, they also showed the hydrolysis of carvones upon irradiation.²¹⁵ Nowadays, photo-induced reactions have risen to a powerful method in different fields, employing photoinitiators for RDRP^{71,216} or FRP,²¹⁷ direct-laser writing (DLW),^{218,219} or photocatalysis.^{220,221}

3.4.3.1 Theoretical Background of Photochemical Processes

According to theory, light is absorbed by a molecule due to excitation of electronic energy states. In a Jablonski diagram, electronic and vibrational transitions are illustrated that occur upon and after irradiation in a simplified manner (refer to Figure 3-5).²²² With respect to the spin orientation, all different states are listed, giving an overview over possible electronic transitions. The electrons are excited from the ground state S_0 to electronic singlet states S_1 or S_2 upon irradiation according to the Franck-Condon principle. The Franck-Condon principle states that during an electronic transition, the molecule is most likely excited into the vibrational level, which has at a specific distance of the nuclei the highest value for the ψ^2 , *i.e.* probability density.^{223,224} As a consequence, the highest share of electronic transitions occurs between overlapping excited vibrational energy states.²⁰⁶ Due to a very unlikely promotion of the electrons to S_2 , the electrons are mainly excited to S_1 . After excitation, vibrational energy relaxation occurs caused by thermal energy loss, leading to the occupation of the lowest vibrational state.

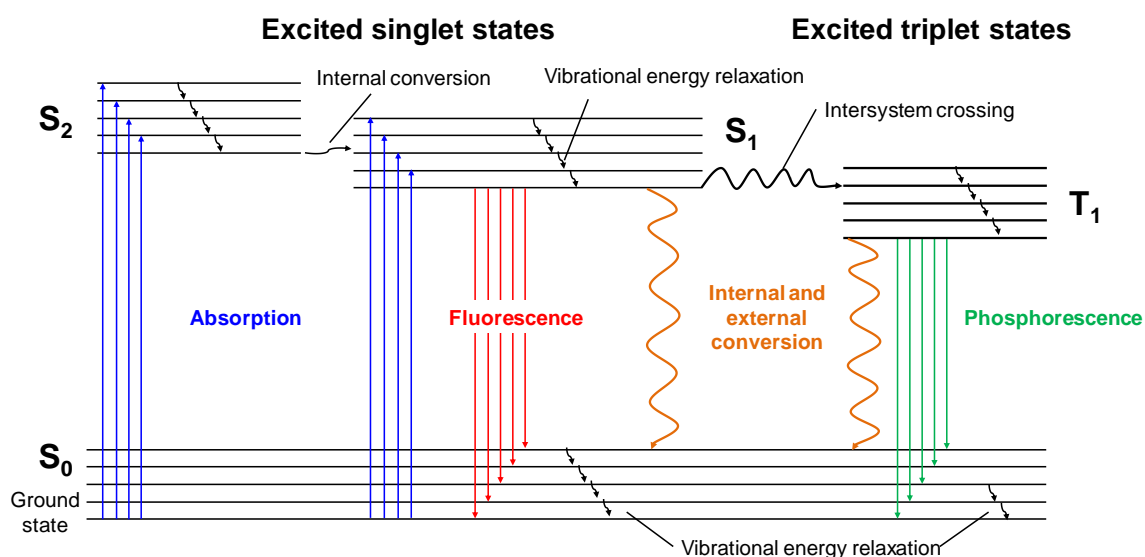


Figure 3-5. Jablonski diagram, showing the transition of electronic and vibrational states during photochemical processes upon irradiation of molecules.

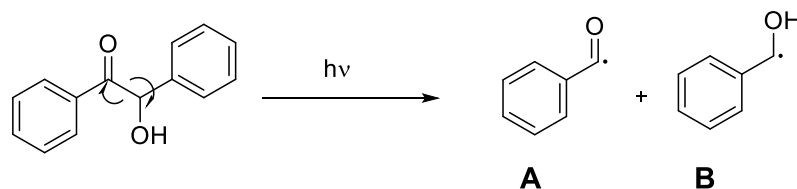
Several possible processes can occur from the lowest vibrational state in S_1 :

- Fluorescence: An emission of light occurs, showing a red-shift in the wavelength in comparison to the excitation wavelength during absorption.
- Internal conversion: A radiationless relaxation occurs from low electronic excited state to excited vibrational energy level of a lower electronic state. The spin orientation is preserved, so the transitions occur between singlet-singlet or triplet-triplet states. This intramolecular process is more likely if two electronic states are

close to each other. Most molecules show internal conversion and therefore no fluorescence.

- External conversion: A radiationless relaxation occurs due to interaction with external molecules, such as collision with solvent molecules, leading to same result as internal conversion.
- Intersystem crossing (ISC): A forbidden spin reversion leads to an elevation of the multiplicity of the molecule. More likely if vibrational energy levels are overlapping. The event competes with fluorescence.
- Phosphorescence: After intersystem crossing phosphorescence occurs as competition to internal and external conversion by emission of light. Due to unlikely and forbidden transition from T_1 to S_0 , the lifetime of phosphorescence can be in the range of seconds to minutes.

Interactions of molecules with light are based on the here presented theory and reactions have been conducted without an in-depth understanding. For practical use, the relationship between reactivity and absorption is not trivial, since photo-induced reactions are dependent on specific transitions and excitation states. The aforementioned principles have a high impact on e.g. the development and design of photoinitiators. For photoinitiators, photoluminescence *i.e.* fluorescence and phosphorescence, and internal conversion decrease the efficiency, whereas high rates of intersystem crossing and high quantum yields increase the applicability of a photoinitiator. One class of photoinitiators follows the Norrish type I reaction, *i.e.* an α -cleavage of carbonyl compounds upon irradiation (e.g. benzoin, refer to Scheme3-36).^{225,226} It could be shown that high absorbance in the UV-VIS spectrum of a photoinitiator does not correlate with its reactivity or initiation efficiency.²²⁷ Therefore, the quantum yield of such systems is of importance, *i.e.* the amount of chemical events induced per photon. It was demonstrated that photoinitiators despite very low absorption in the UV-VIS range can be excellent photoinitiators due to transitions into energy levels responsible for the chemical reaction upon irradiation.^{217,227-229}



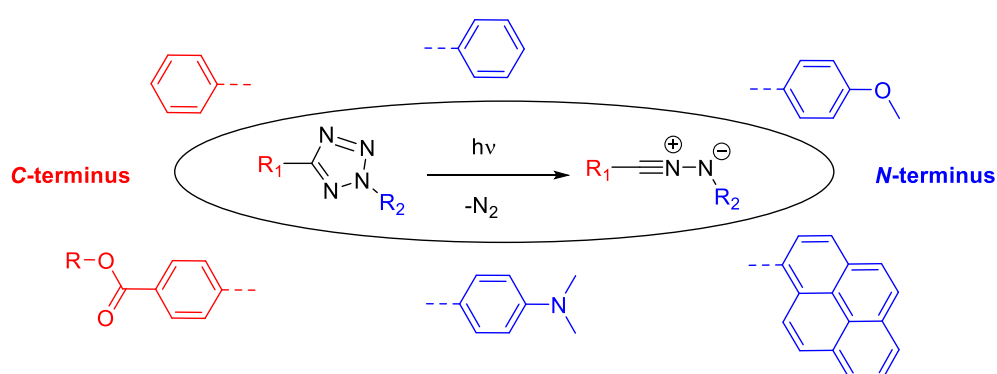
Scheme 3-36. Cleavage of benzoin upon irradiation in a Norrish type I reaction forming the highly reactive benzoyl (A) and the less reactive benzyl alcohol (B) radical.

3.4.3.2 Photo-Induced Ligation Reactions: An Introduction

In a contemporary context, light as energy input for chemical reactions became an important method for competing with thermally triggered reactions, due to the absence of high temperatures, precise spatial control ('writing') and the usage of a never draining energy source. Furthermore, photoreactions can be triggered not only by high energy light sources, such as UV light, but also with wavelengths in the visible range or in the near-infrared range of the spectrum.²⁶ Since highly efficient photo-induced reactions demand for light with certain amount of energy input, problems can be caused by irradiation damage or unintentionally cleaving of covalent bonds. In the following, photo-induced reactions are introduced that undergo different reactions, such as cycloadditions or rearrangements upon irradiation with wavelengths in the UV and visible light regime, respectively.

3.4.3.3 Nitrile-Imine Dipolar Reactions from Tetrazole Derivatives

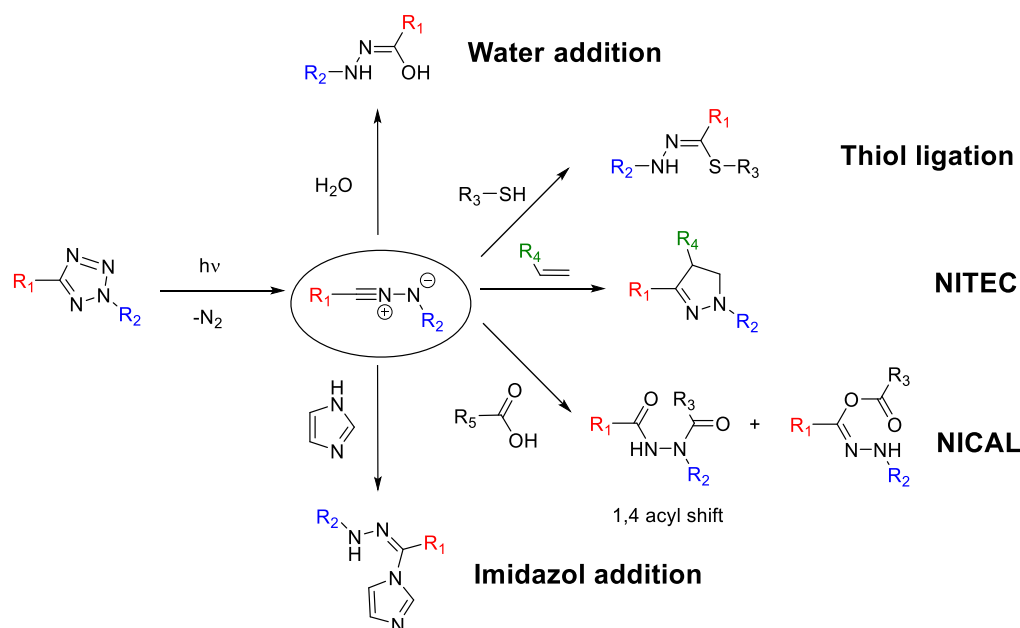
Tetrazole derivatives as photoreactive compounds were firstly reported in 1967 by Moriarty et al.,²³⁰ featuring the elimination of a nitrogen molecule upon UV irradiation of substituted tetrazoles. Although thermal dissociation of tetrazoles was already known before,²³¹ Bach showed in 1969 the first reaction of a substituted tetrazole compound in UV light under the generation of nitrogen.²³² Since then, the usage of tetrazoles in photo-reactions was rarely reported,^{233–235} until in the recent decade substantial research focused on the utilization of tetrazoles for photo-induced ligation reactions.^{236–241} Upon irradiation of the tetrazole, a nitrogen molecule is eliminated and a highly reactive nitrile-imine dipole is formed (refer to Scheme 3-37).²⁴²



Scheme 3-37. Aryl substituted tetrazole dissociation upon irradiation. Substituents at C- and N-termini influence the dissociation wavelength.

Furthermore, the wavelength regime for triggering the photo-induced reaction can be tuned by the aromatic substituent at both the C- (R_1) and the N-terminus (R_2) of the tetrazole. In Scheme 3-37 R_1 and R_2 are aromatic rings, which can be extended or

substituted. Typically, a carboxylic acid or ester functionality in *para* position is introduced at R₁. The R₂ group structure has been found to strongly influence the activating wavelength regime, triggering the photodissociation. By using a carboxylic acid substituted phenyl ring for R₁ and a unsubstituted phenyl ring for R₂, the irradiation wavelength for the dissociation of the tetrazole is in the range of 280 nm.²³⁹ By substituting R₂ with a methoxy group, the irradiation wavelength red-shifts to 320 nm for triggering the photodissociation.²⁴³ In addition, further red-shift of the tetrazole dissociation was achieved by substituting the R₂ phenyl ring with a dimethylamino group, sufficiently triggering the reaction at wavelengths in the range of 365 nm.²⁴⁴ By substituting R₂ with pyrene, even blue light in the range of 410-420 nm can be used for the dissociation of the tetrazole.^{245,246} In a study of the authors group, a tetrazole structure-reactivity correlation were addressed *via* density functional theory calculations.²⁴⁶ It could be unraveled how absorption is influenced by substituents, however, a correlation to photoreactivity could not be achieved. In the literature, the reaction of tetrazoles and dienophiles, such as maleimides and fumarates, is referred to as nitrile-imine mediated tetrazole-ene cycloaddition (NITEC).^{240,247} In addition, further reaction partners of tetrazoles were discovered such as water,²⁴⁸ thiols,²⁴⁹ carboxylic acids (nitrile-imine carboxylic acid ligation, NICAL),^{250,251} and imidazoles,²⁵² respectively, illustrated in Scheme 3-38.



Scheme 3-38. Reactions of tetrazoles after dissociation upon irradiation to the 1,3-nitrile-imine dipole intermediate reacting with water, thiols, double bonds - usually substituted with electron withdrawing groups R₄ (NITEC) - carboxylic acids (NICAL) and imidazoles (clockwise order).

A beneficial feature of NITEC and NICAL reactions are the fluorescent product, in the case of NITEC caused by pyrazoline units, which can be utilized as a self-reporting system for monitoring the conversion of the dipolar cycloaddition.⁹⁹ Tetrazole chemistry is a useful

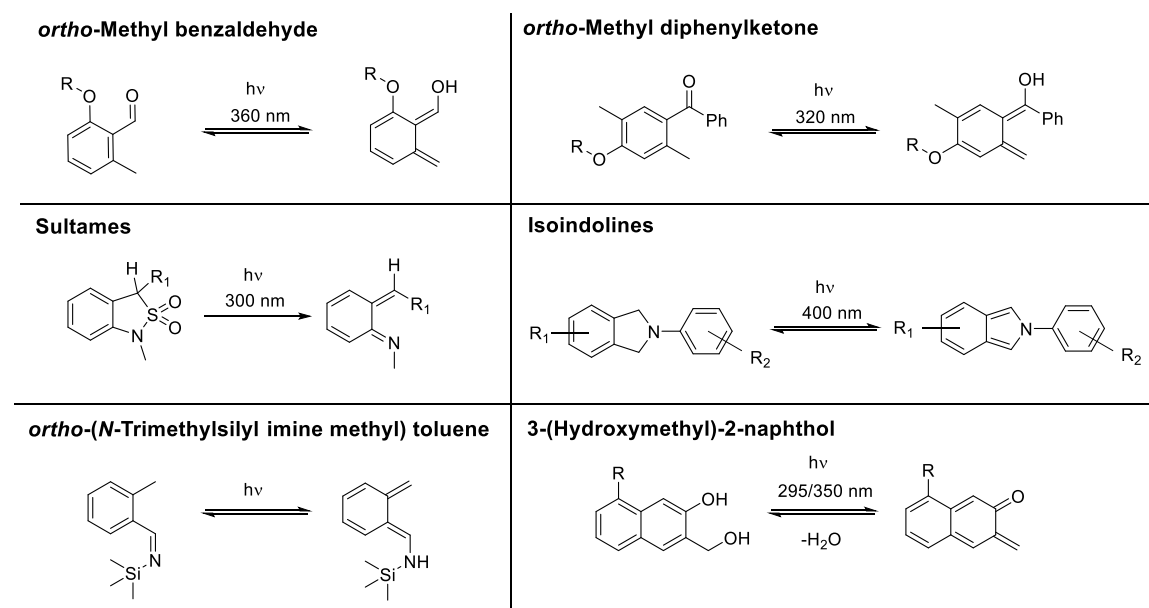
technique since it can be employed in an orthogonal fashion to e.g. RAFT polymerization.^{99,253} Furthermore, the NITEC reaction can be conducted in aqueous media.²⁵⁰ Beyond that, tetrazole derivatives can be synthesized by addressing the carboxylic group in several organic chemistry procedures, allowing further modification.²⁴⁰ Since its renaissance, tetrazole chemistry was utilized in the author's group for copolymer²³⁹ and star polymer synthesis,²⁵⁴ step-growth polymerization,²⁴⁰ self-reporting polymer systems,⁹⁹ surface patterning,^{255–258} single-chain nanoparticle fabrication,^{251,259,260} decoration of microparticles,²⁶¹ λ -orthogonal chemistry,²⁶² bioconjugation,^{263,264} and network formation,²⁵³ respectively. In addition, a study was undertaken using tetrazoles as an AA monomer in a photo-induced SG polymerization.²⁴⁰ Here, AB monomer systems bearing an acrylate or a fumarate and a tetrazole moiety yielded pyrazoline fluorescent polymers from non-fluorescent monomers. By tuning the reaction parameters and conditions of the fumarate-tetrazole monomer system, a fast SG process could be obtained showing good agreement to Carothers theory. The utilization of tetrazoles in the photopatterning of surfaces will be highlighted in Chapter 3.5.

3.4.3.4 Photocaged Dienes and Photo-Induced Diels-Alder Reactions

Another important class of photo-activated compounds in polymer science are photocaged dienes, which are formed upon irradiation (sometimes with catalysts) of corresponding aromatic compounds, such as *ortho*-methyl benzophenone,²⁶⁵ *ortho*-methyl benzaldehyde,²⁶⁶ *ortho*-(*N*-trimethylsilyl iminomethyl)toluene,²⁶⁷ isoindolines,²⁶⁸ *N*-arylimines²⁶⁹ and 3-(hydroxy-methyl)-2-naphthol derivatives²⁷⁰ (refer to Scheme 3-39). The corresponding active species are *ortho*-quinodimethanes, *ortho*-quinodimethane imines, and 2-naphthoquinone-3-methide, respectively. Examples for further photo-induced DA reactions forming highly reactive dienophiles are phenacyl- and pyrenacyl sulfides (refer to Chapter 3.4.3.5),^{271,272} forming thioaldehydes for trapping of 1,3-dienes, amines, hydroxyamines, or thiols, and phenanthrene-based methylene cyclopropanes,²⁷³ forming cyclopentyne for trapping of 1,3-diphenyl isobenzofuran.

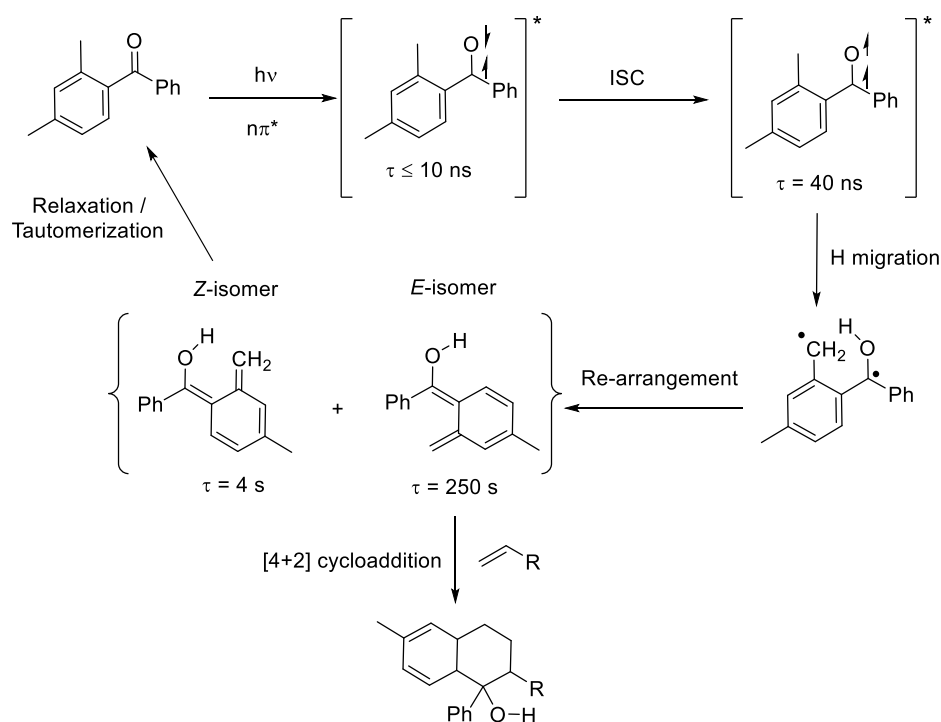
In the following, the research activities into *ortho*-methyl benzaldehydes and *ortho*-methyl benzophenones / *ortho*-quinodimethanes will be further described, and are referred to as 'photoenols'. The first report of photoenols in 1961 by Yang and later in polymer science by the author's team in 2011 demonstrated the utilization of the first generation of photoenols, namely *ortho*-methyl benzophenone.^{265,274} Yang introduced the photoenolization of benzophenone towards *ortho*-quinodimethanes upon irradiation and the subsequent trapping of the photogenerated species with dimethylfumarate.²⁶⁵ Decades later, polymer scientists used *ortho*-methyl benzophenone, as end-group of polyethylene glycol (PEG), yielding – upon UV light irradiation ($\lambda_{\text{max}} = 320 \text{ nm}$) – the highly

reactive *ortho*-quinodimethane in a DA reaction with a maleimide, as terminus of a poly(methyl methacrylate) (PMMA).



Scheme 3-39. Photo-induced diene formation of different photoreactive compounds. A subsequent trapping of the formed species usually comprises electron deficient dienophiles, such as maleimides, fumarates or acrylates.

Despite its good reactivity, drawbacks were found in the terms of reaction rate and versatility, therefore, the more reactive photoenol structure, *ortho*-methyl benzaldehyde,²⁷⁵ was used in a surface related polymer context by the author's team in 2012.²⁶⁶ Here, a faster and more versatile photo-induced DA reaction was demonstrated. A possible mechanism of the photoenol activation was published already in the 1970 by Porter, showing an excited intermediate to form the *ortho*-quinodimethanes (refer to Scheme 3-40). Upon irradiation, a fast singlet $n \rightarrow \pi^*$ transition occurs and due to a subsequent ISC the lowest triplet state is reached. From the triplet state, a tautomerism yields a biradical intermediate by hydrogen migration, which undergoes a re-arrangement to finally form the enol as an *E*- and a *Z*-isomer. The steric repulsion of the *Z*-isomer hinders the reaction and promotes its relaxation to the ground state, whereas the *E*-isomer can undergo the cycloaddition with a corresponding reaction partner. According to the aforementioned reactivity issues, the second unsubstituted phenyl ring – not participating in the activation – causes steric hindrance and therefore leads to less reactivity. Furthermore, by applying aprotic solvents, the lifetime of the *E*-isomer can be readily increased and concomitantly the reactivity.²⁶⁶



Scheme 3-40. Mechanism suggested by Porter of photoenol activation and relaxation upon irradiation and corresponding lifetimes τ valid given for reactions in cyclohexane.²⁷⁶

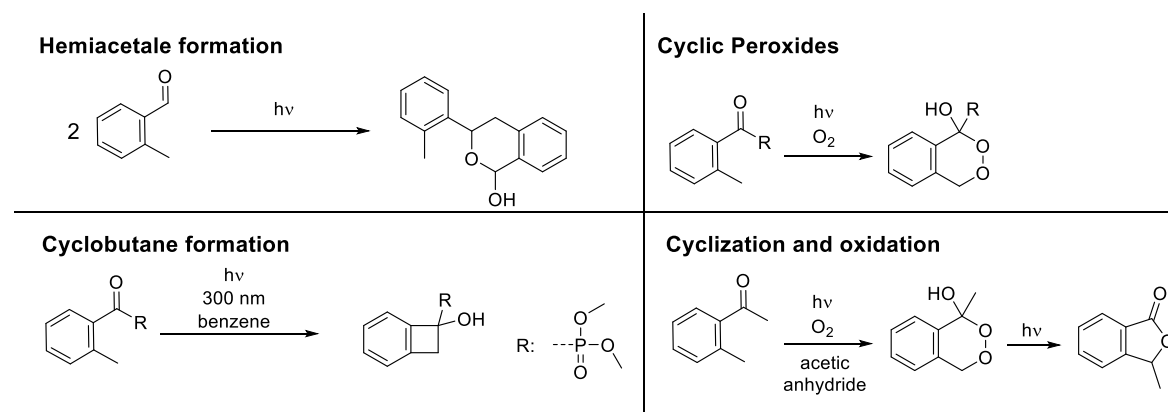
The reaction of photoenols with corresponding partners is referred to as click-chemistry,²⁶⁶ although side reactions or processes are known in literature with electron deficient dienophiles. Thereby, the design of the experiment has to be carried out carefully, since side reactions of the *ortho*-quinodimethane with present functionalities or compounds can occur (refer to Scheme 3-41):

- Cyclization to form cyclobutane dependent on substitution as competing reaction to the recovering of the starting material.²⁷⁷
- Reaction with carbonyls, such as acetic anhydride to form lactones. With further irradiation also the formation of cyclic peroxides and ring rearrangements are proposed.²⁷⁸
- Reaction with itself to form hemicacetals without exposure to oxygen and in presence of oxygen either formation of lactones or cyclic peroxides.^{275,279}

However, side reactions are mentioned in the literature and can be partially avoided by designing the experiments properly, *i.e.* adjusting low concentrations of the functional unit.²⁷⁹

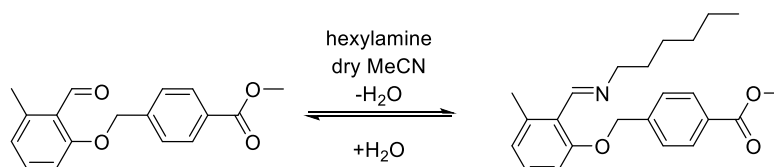
The utilization of photoenols has been intensively applied by the author's group in small molecule reactions,^{262,280} surface patterning,²⁸¹⁻²⁸⁴ BCP ligation,^{124,274,285-287} polyionic liquids,²⁸⁸ particle functionalization,^{100,289,290} orthogonal reactions with DNA,^{291,292} cellulose

decoration,¹⁰⁶ DLW,^{219,293–295} sequence controlled polymerization,^{296,297} and in combination with nano-diamonds,^{108,298} respectively.



Scheme 3-41. Possible side reactions known for *ortho*-methyl benzaldehydes, benzo/acetophenones and derivatives.

The versatility of photoenol chemistry offers potential in many fields, although possible side reactions of photoenols may make them less suitable for small molecule chemistry. A recent study in the authors group introduced a gated photochromism to the chemistry of photoenols.^{280,299} Here, by employing an amine as strong nucleophile, an imine exchange at the aldehyde group caused the loss of photoreactive properties (refer to Scheme 3-42). Since the imine formation is reversible, the photoreactivity could be restored.



Scheme 3-42. Deactivation of the photoreactivity of photoenols based on *ortho*-methyl benzaldehyde derivatives with amines.²⁸⁰

Furthermore, the usage of photoenols in the development of DLW applications enhanced the technology beyond conventional radical polymerization concepts since it allows spatially resolved modification subsequent to the DLW process.²¹⁹ Moreover, subdiffraction coding exploiting stimulated emission depletion (STED) in DLW could be successfully established with photoenols.²⁹⁵ In addition, the functionalization of deoxyribonucleic acid (DNA) by photoenol chemistry and its subsequent application in DLW demonstrates its excellent compatibility also in biological systems.²⁹¹

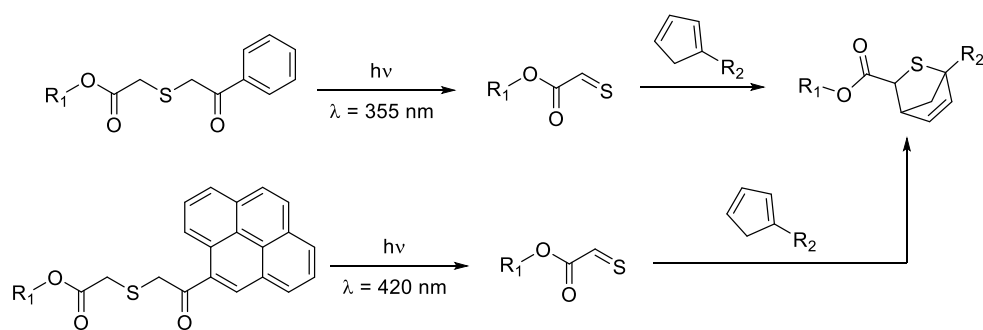
3.4.3.5 Further Photo-Induced Reactions in Polymer Science

In addition to the aforementioned examples, photoreactive organic compounds are in use for ligation in polymer science (refer to Scheme 3-43), such as oximes,³⁰⁰ azirines,³⁰¹ pyreneacyl²⁷² and phenacyl sulfides,²⁷¹ coumarins,³⁰² phencyclones,³⁰³ anthracenes,^{105,304}

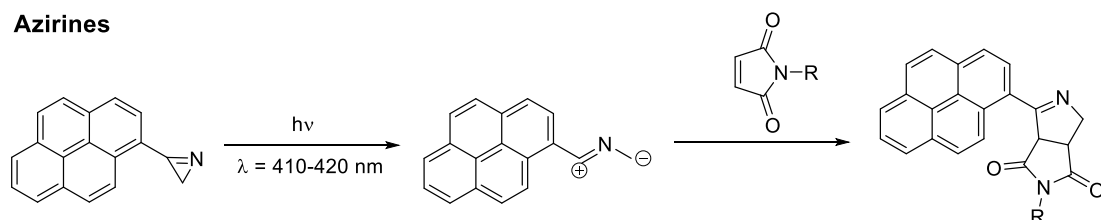
and thymines,³⁰⁵ respectively. As illustrated in Scheme 3-43, photo-induced reactions in the visible range of light are possible, e.g. by extending π -systems, which red-shifts the wavelength regime to induce the reaction.

In the case of the pyreneacyl and phenacyl sulfides, the photoreactive compounds yield thioaldehydes that represent excellent dienophiles.^{271,272,301} Beyond dienes, counterparts for thioaldehydes are amines, hydroxyamines, and thiols.³⁰⁶ In case of azirines highly-reactive nitrile-ylides are formed upon irradiation. The azirines, similar to NITEC and photoenol chemistry, react with electron deficient enes in cycloaddition reactions upon irradiation with visible light. Furthermore, coumarins, anthracenes and thymines represent a class of reversible photoreactions.³⁰⁷ By triggering the dimerization of these moieties at one wavelength regime, the *retro* reaction can be induced at another wavelength regime. Here, the *retro* reaction requires higher energy, i.e. shorter wavelengths.³⁰⁷

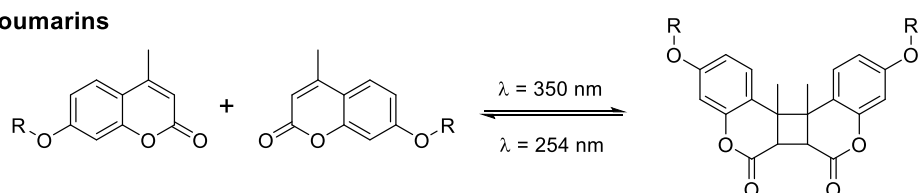
Phenacyl sulfide and Pyreneacyl sulfide



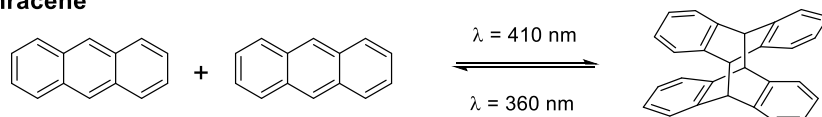
Azirines



Coumarins



Anthracene



Scheme 3-43. Photo-induced ligation techniques: Phenacyl and pyreneacyl sulfides yield thioaldehydes and subsequent reaction with cyclopentadiene. Azirines yield nitrile-ylides upon irradiation and are trapped with electron deficient enes. Coumarin and anthracene dimerization upon irradiation with corresponding wavelength regime and *retro* reaction at shorter wavelengths (from top to bottom).^{271,272,301,302,304}

3.5 Surface Patterning and Functional Surface Design

Surface chemistry is of strong interest in the scientific community since the demand of functional surfaces in terms of material conservation, sustainability and applicability is steadily increasing. These demands increased dramatically as they are important in building fabric, marine vessels, industry and gear development.^{308,309} In polymer science anti-fouling materials are of major interest, as the prominent material poly(ethylene glycol) (PEG) represents a simple but highly efficient repellent material for biological contaminations.³⁰⁸

Reversible covalent surface immobilization is challenging due to the precise cleavage and linkage of particular bonds. In addition, the non-covalent functionalization is mainly achieved by adsorption,³¹⁰ hydrogen bonding,³¹¹ or host-guest interactions.²⁵⁵ Certainly, the design of such systems is restricted by specific factors, e.g. hydrogen bonding motifs have to be designed in accordance to the corresponding counterpart.³¹² Additionally, in host/guest systems, such as cyclodextrines/adamantyls, a guest has to be identified and match the host.²⁰ Nevertheless, only rare examples are known for covalently rewritable surfaces, e.g. the authors workgroup achieved spatially resolved reversible photo-induced cycloaddition with the use of anthracene dimerization.¹⁰⁵ It was demonstrated that specifically functionalized anthracene molecules and polymers were reversibly attached to anthracene modified surfaces by irradiation at two different wavelengths consecutively. One wavelength in the visible range of light was employed for triggering the dimerization of anthracenes, the second wavelength in the UV regime for inducing the *retro*-reaction, releasing the anthracene polymer or molecule from the surface, respectively. The implementation of visible light herein underpins the value of mild methods for the reversible covalent encoding of surfaces. Further research was carried out by the author's group, demonstrating the application of thermal DA reactions on dopamine-based surfaces, writing and erasing the pattern by DA or *retro*-DA reaction, respectively.³¹³ Furthermore, the NITEC reaction based on tetrazoles was employed for the general pre-patterning of surfaces (refer to Figure 3-6).^{255,257} In one approach, azobenzenes were attached *via* NITEC for triggering *cis-trans* isomerization of azobenzene upon irradiation.²⁵⁷ In a second study NITEC was employed for the attachment of a host-guest system based on cyclodextrines and adamantyl moieties.²⁵⁵ One example for covalently spatially-resolved surface functionalization was carried out employing photo-induced ligations by Popik and co-workers, using 2-napthoquinone-3-methides in an irreversible patterning of vinyl ether functionalized surfaces.^{270,314} Here, the pattern was visualized *via* fluorescence microscopy, after successfully attaching fluorescence markers,²⁷⁰ and polymer brushes,³¹⁴ respectively. Furthermore, Popik and co-workers developed a reversible surface

functionalization with thiols and 2-naphthoquinone-3-methide in a photo-induced reaction, in which fluorophore markers were replaced by triggering the *retro*-reaction *via* light.³¹⁵

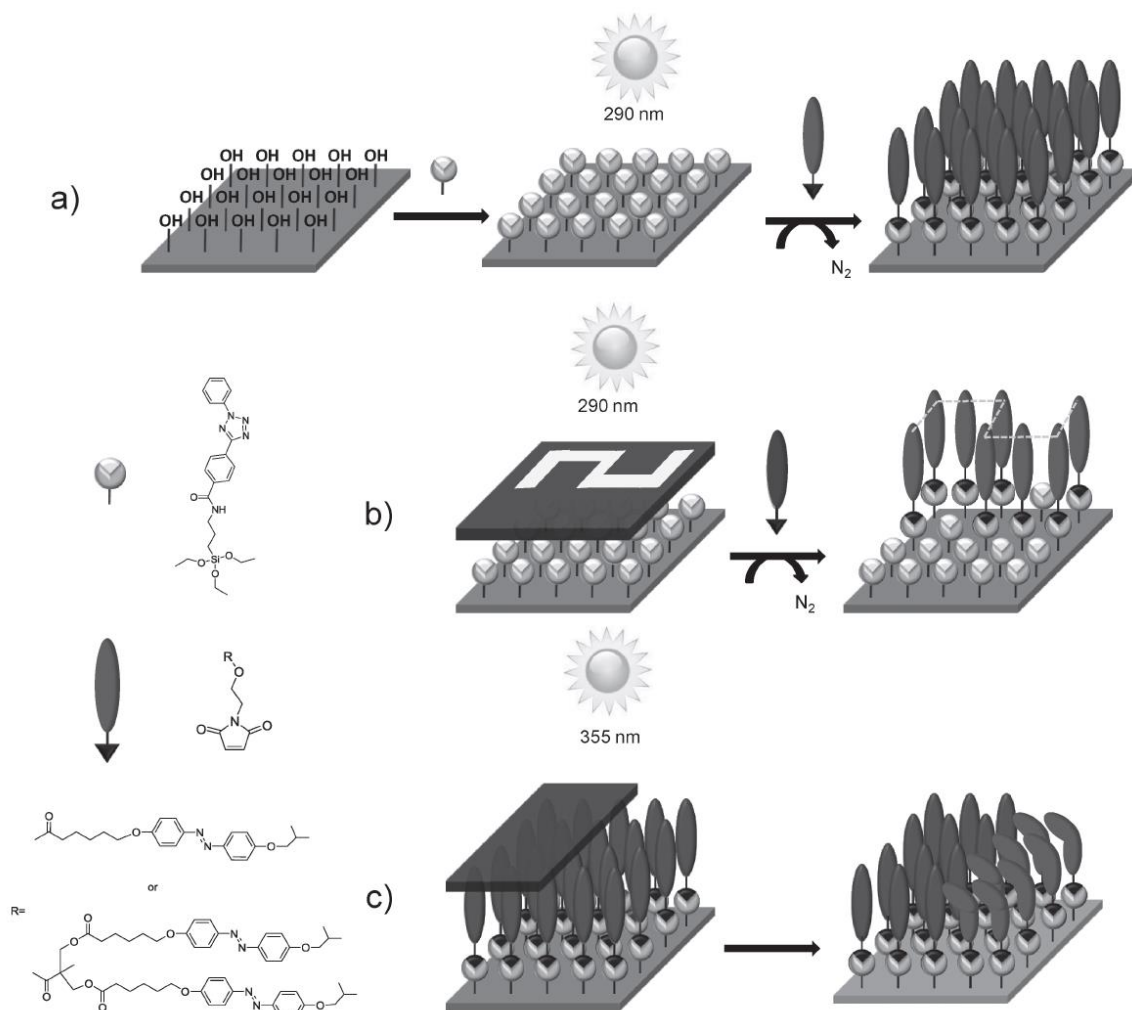
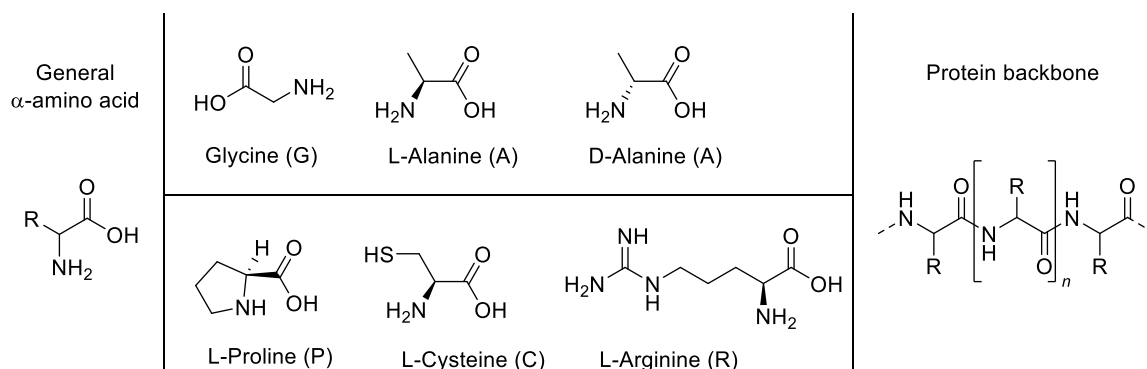


Figure 3-6. a) Functionalization of Si wafer with tetrazoles and subsequent attachment of maleimide-functional azobenzenes on the entire surface upon irradiation *via* NITEC. b) Spatial resolved attachment of azobenzenes *via* NITEC applying a meander shaped photomask. c) *Cis-trans* isomerization of azobenzenes on the surface upon irradiation in a spatial resolved fashion employing a half-covering photomask. The figure was reprinted from E. Blasco, M. Piñol, L. Oriol, B. V. K. J. Schmidt, A. Welle, V. Trouillet, M. Bruns and C. Barner-Kowollik, *Adv. Funct. Mater.*, 2013, 23, 4011–4019. with permission of John Wiley and Sons.²⁵⁷

3.6 Protein and Peptide Fundamentals

Proteins are natural copolymers with both structural and catalytic function in biological organisms. They consist of amino acids as monomer units and form long peptide chains *via* amide bonds (refer to Scheme 3-44).³¹⁶ Amino acids are chiral compounds, bearing a carboxylic acid and a primary or secondary amine, featuring substitution at α -position of the carboxylic acid, as shown in Scheme 3-44 (center). In nature, all proteins predominantly consist of L- α -amino acids, as the chirality conserves the structural information responsible for their function. So far, 21 proteinogenic amino acids have been described for the synthesis of proteins.³¹⁷ Further, they are subdivided into essential and non-essential amino acids. The former have to be ingested in human diet, in order to readily provide them for protein synthesis since they cannot be produced by the human organism. Besides canonical amino acids, proteins can be constructed from non-canonical amino acids.³¹⁸ These are incorporated in non-ribosomal pathways or by substituting certain canonical amino acids in the diet of cell cultures.³¹⁹ Furthermore, the terms proteins and peptides commonly refer to the amino acid sequence length: chains of less than 50 amino acids are called peptides, whereas longer chains, especially the ones formed in protein biosynthesis, are referred to as proteins. Proteinogenic amino acids follow a standardized nomenclature of a three- or one-letter code, to abbreviate the peptide sequence. Generally, the peptide sequence is written from the amino terminus (*N*-terminus) to the carboxylic acid terminus (*C*-terminus).



Scheme 3-44. General constitution of α -amino acids (left behalf). Glycine as simplest example of an α -amino acid, L- and D-alanine as example for enantiomers of α -amino acids (center, top row). L-proline, a cyclic amino acid with a secondary amine, L-cysteine with a thiol- and L-arginine with a guanidine group (center, bottom row). General protein backbone with the peptide bond and residual R (right behalf).

Proteins as macromolecular constructs play an important role in biological system, as they are part of many important processes in the body due to their highly complexity.³¹⁶ Therefore, they have to be generated in a precise and reproducible manner with little or no tolerance for errors. In comparison to fully synthetic macromolecules, proteins are

strictly monodisperse.³¹ In macromolecules, single bonds are capable to rotate freely and two or three-dimensional superstructures are formed by self-assembly of readily participating bonds by polar or non-polar interactions. In proteins, interactions between the amino acids side chains and the peptide bonds are responsible to form superstructures. Hydrogen bonds between the peptide bond of short sequences can form secondary structures, such as α -helices or β -sheets, as illustrated in Figure 3-7.³¹⁶

A single protein chain consists of several secondary structural elements and the combination of all substructures either of a covalent or non-covalent nature lead to the overall shape of the protein, referred to as tertiary structure of a protein chain. In addition to the robust secondary structures generated *via* hydrogen bonds, disulfide linkages, or metal complexes such as zinc, copper, or magnesium contribute to the tertiary structural complexity.^{1,320} Such an assembly of amino acid sequences in proteins occurs in a precise and well-defined process and is ultimately crucial for the later task of the protein.³²¹ Furthermore, multiple proteins chains can assemble, referred to as quaternary structures. Here, the single proteins chains can be generated separately and, therefore, their independent synthesis provides less risk of sequential or structural faults.³¹⁶

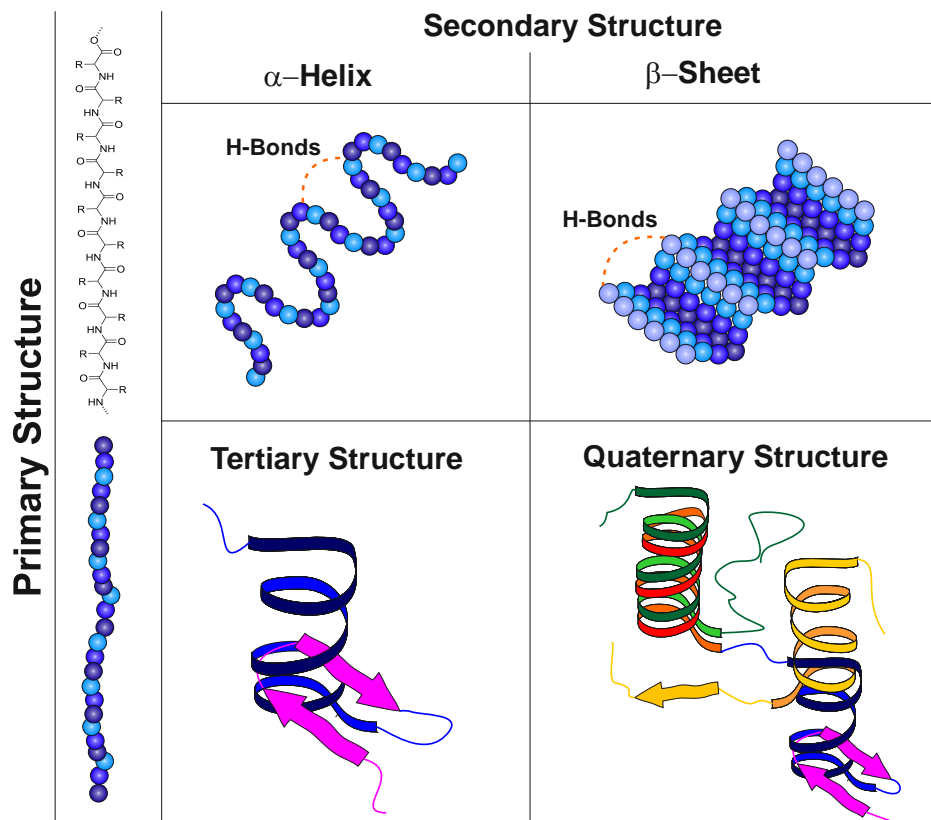


Figure 3-7. Schematic view of primary, secondary, tertiary and quaternary structures of proteins.

3.6.1 Synthesis and Design of Peptides

3.6.1.1 Solid Phase Peptide Synthesis (SPPS)

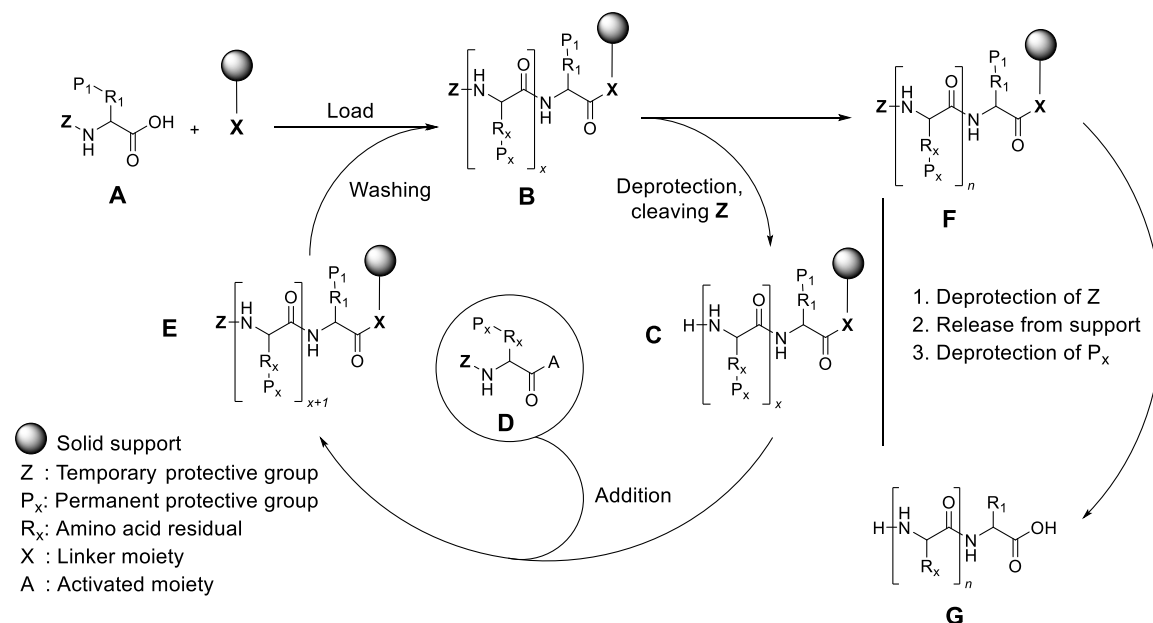
Synthesis protocols have been established to mimic the *in vivo* production of peptides without employing complex and vulnerable organisms. A milestone in preparative peptide synthesis was published by Merrifield in 1963, introducing solid phase peptide synthesis (SPPS). The utilization of solid phase substrates bearing amino acids pioneered the generation of peptide sequences on large scales.³²² By covalently linking the growing peptide chain to a solid support, such as polystyrene particles, complex purification is circumvented by performing simple washing and filtration steps in the same vessel.

Typical solid supports or 'resins' for the SPPS routine are cross-linked PS beads.³²³ Other materials are for instance polyamides and copolymers, such as PS-PEG. The loading of the solid support strongly depends on the sequence length, the swelling behaviour of the support and the complexity of the final peptide sequence.

In order to achieve maximum regioselectivity, the utilization of well selected protecting groups is crucial.³²⁴ Deprotection of the *N*-terminus has to be orthogonal to the deprotection of side chain protecting groups. Examples of protecting group pairs of amino acids commonly comprise fluorenylmethyloxycarbonyl (Fmoc) for the amine in combination with *tert*-butyloxycarbonyls (Boc), allyloxycarbonyls (Alloc), or benzyls (Z) to protect the side chain.³²⁵ A key requirement of protecting groups is their orthogonality to each other.³²⁶ In the case of the aforementioned groups, the Fmoc is cleaved under basic conditions, Boc under acidic conditions, benzyls under harsh acidic conditions such as anhydrous hydrogen fluoride, and the Alloc group by metallorganyls, *e.g.* tetrakis (triphenylphosphine) palladium (0). Hence, an orthogonal deprotection is readily provided during the peptide synthesis. Furthermore, the fluorene as cleaved compound features fluorescent properties, allowing to trace the deprotection *via* the fluorescence intensity.³²⁷

A typical procedure of the SPPS is introduced in the following (refer to Scheme 3-45):³²⁶ An *N*-protected amino acid is loaded to an inert polymer bead *via* its carboxylic acid group. In general, protecting groups are introduced prior to peptide synthesis to prevent amino acids from undesired polymerization and side reactions in solution. Subsequently, the beads are washed to remove free amino acids and coupling reagents, leaving the first amino acid covalently linked to the support. In the next step, the deprotection of the first amino acid is performed to regenerate the amine readily available for coupling with the next *N*- and side-chain protected amino acid. To address the presence of unreacted amines after the coupling, a capping by *e.g.* acylation must be carried out to avoid the formation of faulty sequences. Capped sequences cannot participate in the next coupling stages and can be readily separated chromatographically after the synthesis. These steps

of deprotection, coupling, capping, and washing are conducted multiple times to ultimately obtain the desired peptide sequence. Now, the peptide is cleaved from the support and purified by high performance liquid chromatography (HPLC).³²⁸ Ideally, the faulty, capped peptide sequences interact differently with the column material in HPLC, and the target peptide can be obtained in high purity.



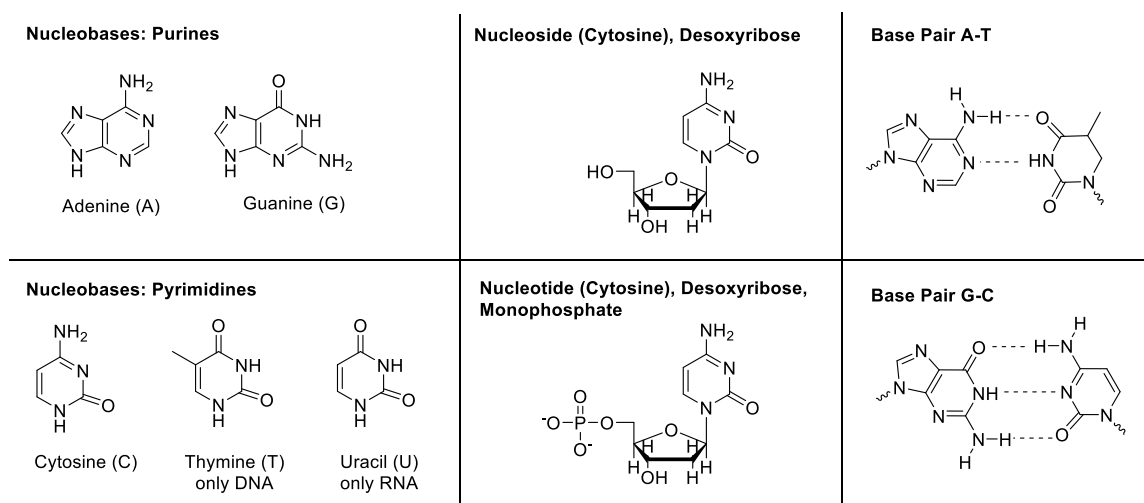
Scheme 3-45. Fundamental reaction scheme of the solid phase peptide synthesis (SPPS) referred to as Merrifield peptide synthesis.³²³ An *N*-protected amino acid (**A**) is attached to a solid support *via* the C-terminus, (**B**), and deprotected from **Z** to obtain the free amine, (**C**). **Z** represents a protecting group that can be cleaved under gentle conditions, e.g. urethanes, in contrast to **P_x** that entails a permanent specific protection of the side residual and has to be stable under the amidation coupling conditions. Then, a second activated *N*-protected amino acid (**D**) is added in high concentrations and coupled *via* amide formation to yield the dimer or *n*-mer (**E**) attached to solid support. Capping as part of the procedure is not included in the scheme, as the capping concerns faulty sequences only. After washing, the cycle starts again to finally yield the protected peptide (**F**) with the corresponding sequence with a length *n*+1. After deprotection of **Z**, the peptide is released from the solid support and all permanent protecting groups are cleaved to obtain the final protein/peptide (**G**). Here, the deprotection of **Z** can also cause deprotection of labile **P_x** groups.³²⁶

Limitations of the SPPS are found in sequence length and secondary structure formation. The length of the sequences in SPPS is usually restricted up to 50 units.³²⁹ Furthermore, due to the formation of secondary structures by hydrogen bonding, the routine SPPS cannot be generally employed for any peptide sequence. To circumvent secondary structure formation, special strategies employ further synthetic tools, such as addition of chaotropic salts,³³⁰ or introduction of amide group protecting groups, such as 2-hydroxy-4-methoxybenzyl derivatives of glycine.³³¹

3.6.1.2 Proteins and the Genetic Code

Proteins and peptides play a key role in organisms. They are responsible for enzymatic, transport, and scaffold tasks, respectively. The generation of proteins and peptides in

eukaryotes commences within the cell nucleus, where deoxyribonucleic acid (DNA) constitutes up the genetic material of a cell.³³² It contains most relevant information for the cell's life. DNA and ribonucleic acid (RNA) consist of multiple nucleotides, which are composed from nucleosides and phosphates. Nucleosides again are constructed from nucleobases and sugars, namely ribose (for RNA) and deoxyribose (for DNA, refer to Scheme 3-46, left and center).³³² DNA is distinguished from RNA with regard to one nucleobase, as thymine is exclusive to DNA and uracil to RNA. Interactions of nucleobases in DNA or RNA play an important role during protein biosynthesis in the formation of base pairs, which are generated by hydrogen bonds. These base pairs are strictly formed in a complementary fashion of purines with pyrimidines, *i.e.* adenine with thymine (DNA) or uracil (RNA), and guanine with cytosine (refer to Scheme 3-46, right behalf).³³² During biosynthesis of proteins, base pairs are responsible for interaction of RNA molecules, as will be discussed later in the chapter.



Scheme 3-46. List of nucleobases (left behalf), nucleoside of deoxyribose and cytosine (middle, center) and nucleotide of deoxyribose and cytosine monophosphate (bottom, center). Right-hand side: Base pairs of nucleobases of adenine (A) and thymine (T) in DNA and guanine (G) and cytosine (C) by hydrogen bonds (dotted lines).

A gene, a DNA fragment consisting of a nucleotide sequence, acts as a precursor of the protein's blueprint in its biosynthesis. First, a RNA copy of the DNA is generated (translation) as the blueprint that is ultimately read and rendered in the ribosomes to build a protein (transcription). In general, the biosynthesis of a protein can be divided into three steps: Transcription, maturation and translation. The transcription and translation proceed in three stages, namely initiation, elongation and termination.³¹⁶

In the following, the stages of protein synthesis are explained.³³² In the beginning of the protein synthesis, the RNA polymerase is attached to DNA in the cell's nucleus (initiation) and transcribes the DNA to a messenger RNA (mRNA), so-called elongation. During the elongation, thymine in the DNA is replaced by uracil in RNA. After the transcription is

finished, the mRNA is released from the DNA strand (termination). At this stage, the mRNA strand contains introns, code fragments of irrelevant or nonsensical information. The mRNA migrates in the so-called spliceosome, a multimer protein complex, where introns are removed. The now matured RNA consists of only information-bearing fragments, so-called exons. In the next stage, the matured mRNA migrates to the ribosomes and binds to a ribosomal subunit. At the ribosome, mRNA interacts with transfer RNA (tRNA). tRNA consists of regular and modified nucleobases, forming cloverleaf shaped secondary structures and a complex tertiary structure.³³³ In mRNA, nucleotide triplets, so-called codons, can be specifically assigned to one amino acid. In total, 64 codon combinations are possible and several amino acids can be described by different codons, e.g. arginine by six codons. In addition, 'start' and 'stop' codons exist. In one loop of the cloverleaf of the tRNA, complementary codons to the mRNA strand are present, so-called anticodons that are able to couple with the mRNA by base pairs. At another cloverleaf loop, a site, bearing one activated amino acid, exists. The start of the protein generation requires a special initiator tRNA that is usually loaded with methionine and located in the P-site, a slot in the ribosomal subunit (refer to Figure 3-8A). In this slot, the initiator tRNA binds to the codon AUG of the mRNA. After the initiation was successful, the next codon is read and a suitable tRNA binds at the A-site, an adjacent slot in the ribosome subunit. Now, the activated amino acid from the tRNA in the A-site is coupled to the initiated peptide chain, attached to the tRNA in the P-site. After the coupling, the tRNA in the P-site is unloaded and released from the ribosomal subunit in the E-site. Subsequently, the tRNA in the A-site migrates to the P-site to open the spot for another tRNA, loaded with the next amino acid. During the growth of the protein chain, this procedure is repeated multiple times until a stop-codon in the mRNA is reached, e.g. UAA (refer to Figure 3-8B). In this case, the protein is then cleaved from the tRNA and subsequently released from the ribosome. After the release, the protein obtains its final tertiary structure by self-assembly and folding processes, eventually supported by enzymes, so-called chaperons. Proteins that encounter misfolding can be transported to the proteasome, where they are digested and recycled in the metabolism.

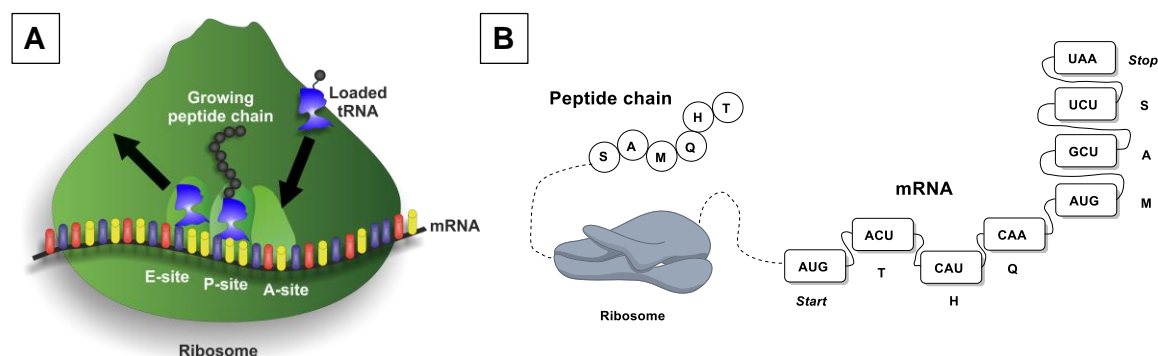


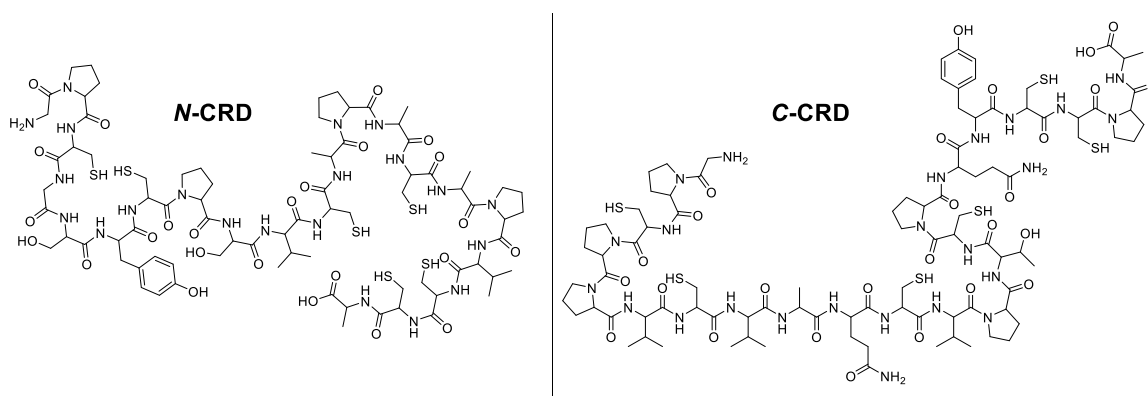
Figure 3-8. Simplified illustration of translation of mRNA to obtain the peptide chain. A: Process in the ribosome showing tRNA participating in the decoding of the mRNA. P-site: tRNA attached to the growing peptide. A-site: next loaded tRNA arrives. E-site: unloaded tRNA leaves the ribosome. B: mRNA code is translated to a peptide chain.

The synthesis of proteins and peptides in pharmacy, e.g. of insulin, requires highly efficient and affordable techniques. Since SPSS is not capable producing long and extensive peptides and proteins, recombinant methods can be harnessed to obtain more complex proteins or peptides.³³⁴ Here, a genetic template needs to be incorporated into a cell's genome and the cell has to be triggered to express the desired protein. For the expression of proteins, bacteria are more popular than eukaryotic cells, since the transfection in eukaryotic cells is a more challenging procedure.³³⁵ In bacteria, plasmids, cyclic DNA double strands, are employed for transfection, representing genes on a lower evolutionary complexity. Cells with the plasmid can be grown and forced to primarily express the desired target protein.³³⁵ Drawbacks of these methods are incompatibilities such as cytotoxicity of the generated product, protein aggregation or lack of a suitable cellular toolkit for the postsynthetic modification.^{336,337}

3.6.2 Cysteine-Rich Domains from Hydra

Hydra are members of the large family of the fresh water phylum Cnidaria.³³⁸ Nematocysts are stinging organelles from Hydra. The nematocyst or cnidocyst are capsules loaded with an arrow-like harpoon and primarily employed for predation or defence. As part of the ejection mechanism of the sting, the capsules are capable to withstand high internal pressures up to 150 bar.^{339–341} Cysteine-rich domains (CRDs) have been identified to be essential during the maturation of the nematocyst's capsule wall. During maturation, particular minicollagens participate in the capsule wall formation by undergoing a polymerization. Such minicollagens are symmetrically aligned proteins consisting of a middle block of multiple glycine-X-Y repeating units, two outer polyproline sequences of 5-25 units and two terminal CRDs. The CRDs possess a highly conserved cysteine pattern, showing a defined primary structure of six cysteines in a sequence of 18 amino

acids (CXXXCXXXCXXXCXXCC). During the capsule wall formation, the CRDs polymerize to a firm scaffold in an intricate equilibrium between intra- to intermolecular disulfide bonds, referred to as disulfide reshuffling.^{1,342} Due to the soft properties of the minicollagen middle blocks, the capsule walls are tough yet flexible. In minicollagens, different CRDs were identified. All of them follow the same scheme of cysteine incorporation. They differ in the way they undergo disulfide formation and generate folding arrangements.³³⁸ Molecular dynamic simulations and mutational approaches have successfully shown that deviations in the CRD sequence cause different polymerization behaviours.³⁴² In docking experiments, the C-CRD, named after its position in the minicollagen peptide sequence, displayed an elevated frequency for disulfide exchange reactions in comparison to N-CRDs. These differences are caused by shorter intermolecular S-S distances in symmetrically aligned dimers (refer to Scheme 3-47), allowing C-CRDs to participate in cross-linking reactions *via* two intramolecular disulfide bonds while the N-CRD motif only forms one disulfide bond.³⁴² Differences have also been described in reaction rates, suggesting faster polymerization kinetics of the C-CRD during the minicollagen cross-linking both *in vitro* and *in vivo*.



Scheme 3-47. Exemplary structural motifs of CRDs: Left: N-CRD in reduced state (GPCGSYCPSVCAPACAPVCCA). Right: C-CRD in reduced state (GPCPPVCVAQCVPQYCCPA).

For an N-CRD derivative, the thermodynamically promoted disulfide linkage of C₃-C₁₅, C₇-C₂₀ and C₁₁-C₁₉ has been determined by NMR and HPLC studies (refer to Scheme 3-47).³⁴³ Here, the C₁₁-C₁₉ disulfide bond of the N-CRD peptide shows pronounced cleavage tendency, responsible for coupling with further CRD units.³⁴² Outside the cysteine containing block, other amino acids do not affect the folding towards the tertiary structure.³³⁹ Within the cysteine motif, one proline has been identified to cause structural differences between the N-CRD and the C-CRD, depending on the proline's *trans* or *cis* configuration (refer to Scheme 3-47).³⁴²

CRD proteins can be obtained by either recombinant protein synthesis or by SPPS. Differences between the two methods manifest themselves in the intramolecular disulfide

folding of each CRD occurring during recombinant synthesis methods, as in SPPS no disulfide formation is induced during the synthesis.³⁴⁴

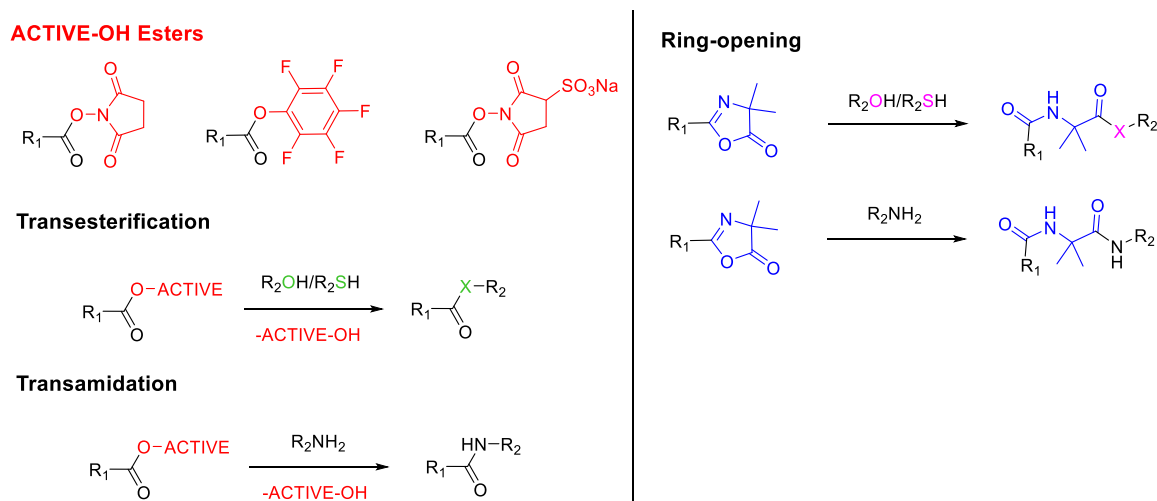
3.6.3 Active Ester Chemistry and Selected Bioorthogonal Reactions

The combination of synthetic and biological materials to yield biohybrids is one major goal of research in several disciplines such as biochemistry.³⁴⁵ It starts from simple approaches such as linking proteins to polyethylene glycol (PEG) to increase their solubility and stability.³⁴⁶ Peptides and proteins, in contrast to polymers, show monodispersity, are precise in their self-assembly and hence are able to bear encoded information.³¹ Due to their high level of complexity, DNA, peptides, and proteins are inherently sensitive to chemical exposure and need to be treated carefully when exposing them to common chemical reaction conditions.³⁴⁷ By fusing the potential of polymers and biological materials, bioconjugation accesses advantages in terms of scalability and applicability of the material, while maintaining the high level of specificity, encoded in the nature of biomacromolecules. An important role of bioconjugation is found in labelling proteins with fluorescent dyes by fusion proteins, regular enzymes, self-labelling enzymes, or small cell-permeable biarsenical dyes.³⁴⁸

Biohybrid materials have been pioneered utilizing peptides, proteins, or DNA in combination with a variety of polymers.^{349,350} Chemical conditions for reactions with complex biological materials, such as proteins, are dictated by their functional groups and the interactions of *e.g.* secondary or tertiary structural elements. Hence, reaction conditions in bioconjugation have to be adapted to prevent denaturation and harming of the biological material. In reactions with unmodified proteins, commonly addressed functional groups are thiols, carboxylic acids, hydroxyl, or amino groups in esterification, thioesterification, and amidation reactions, respectively.³⁵¹ The main disadvantage of reactions with unmodified proteins is specificity, since esterification/amidation cause by-products and cannot address only one functionality without affecting others.³⁵¹ The second issue of reactions with unmodified proteins manifests in stability. Hydroxy groups as inferior nucleophile in comparison to amines, and hydrolysable esters are not of primary interest. Amides are superior to esters, since an amide is a stable bond and employed in many biological systems, as in proteins.³⁴⁷

Active ester chemistry represents a classic ligation methodology for reactions with alcohols and amines.³⁵² The key feature of active ester chemistry in biological applications is the formation of an amide bond in combination with amines, since the reaction of the active ester moiety and the amine proceeds in a fast manner.³⁴⁷ A major advantage of active ester chemistry is the facile handling and the straight-forward synthesis of corresponding

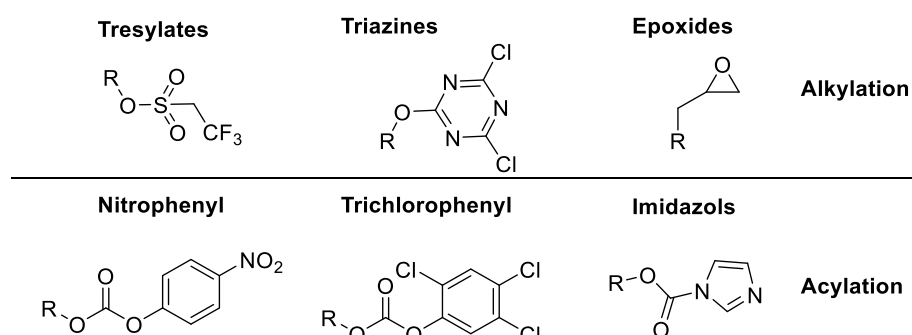
compounds.³⁵³ These can be employed in transesterification and transamidation reactions, although drawbacks include their tendency to hydrolyse and a rather low specificity. Well established procedures have been reported in the literature for *N*-hydroxysuccinimide³⁵⁴ (NHS) or hydroxysulfonylsuccinimide³⁵⁵ esters, pentafluorophenol (PFP) esters,³⁵³ and azlactone esters,³⁵⁶ as illustrated in Scheme 3-48. NHS active esters and derivatives represent a central tool in biochemistry, due to good solubility, good yet mild reactivity and commercial availability. Nevertheless, hydrolysis and storage issues can be problematic and alternatives need to be sought in cases where the extremely high reactivity of NHS is not absolutely critical.³⁵⁴ PFP active esters as hydrophobic species feature less sensitivity towards hydrolysis under conventional reaction conditions³⁵³ at the cost of slightly decreased reactivity in comparison to NHS.³⁵⁷ Furthermore, PFP esters can be readily analyzed by ¹⁹F-NMR spectroscopy, which allows the quantitative monitoring of their kinetics. Azlactones perform a ring-opening reaction in reactions with alcohols, amines and thiols forming the corresponding diamides, amidoesters or amido-thioesters.³⁵⁸



Scheme 3-48. Active ester chemistry in trans(thio)esterification and transamidation reactions by condensation of NHS-derivatives and PFP active esters (left behalf). Ring-opening reactions for azlactones forming diamides and amido-(thio)esters (right behalf).^{102,358–360}

An example for successful bioconjugation with PFP active esters, has been shown by Börner and colleagues, employing PFP esters as active site for the formation of comb-shaped bioconjugates consisting of a polymer backbone and protein side chains.¹⁰² In their study, the excellent stability of the PFP esters enables the incorporation of the coupling moiety within the monomer side chain for their unprotected use in RAFT polymerization. In a second step, a moiety of the protein is addressed in a transesterification to obtain the final bioconjugate.

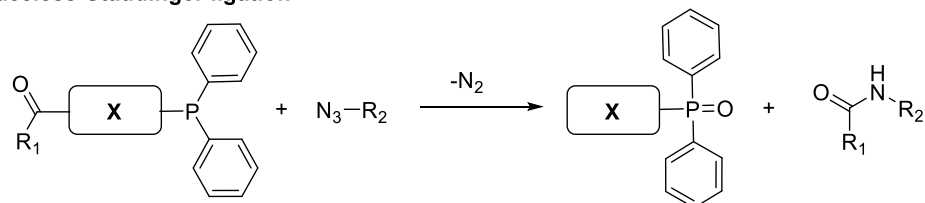
In bioconjugation alkylation and acylation reactions in combination with amines as strong nucleophiles are employed (refer to Scheme 3-49).³⁴⁷ For alkylation dichlorotriazines, tresylates as well as epoxides are utilized. Besides active ester chemistry, acylation reactions span nitrophenyl carbonates, trichlorophenyl carbonates and imidazole carbamates. General drawbacks of alkylation and acylation are their poor selectivity and orthogonality, reactivity issues and the possibility of multiple attachments. The ligation of acylation and alkylation methodologies can be enhanced by utilization of active site blocking agents in order to shield sensitive groups of *e.g.* enzymes in the area of the bond formation. It has been demonstrated that after bioconjugation in presence of blocking agents, such as benzamidine³⁶¹ and biotin-PEG, the target enzymes showed higher activity.³⁶²



Scheme 3-49. Alkylation (top) and further acylation compounds (bottom), besides active esters addressing amine moieties of peptides.³⁴⁷

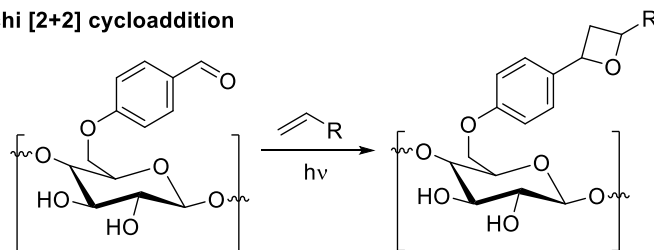
Another class of bioconjugation reactions addresses thiols from *e.g.* cysteine. These comprise thio-ene, thio-yne, thio-Michael, or disulfide reactions that have been successfully applied in polymer-protein coupling.³⁵¹ Reactants towards cysteines are alkenes, alkynes, maleimides, fumarates, disulfides, isocyanates, alkyl halides, oxiranes, thiosulfons, and sulfons.^{351,363,364} By addressing cysteines, polymer-peptide hybrids have been generated, introducing fluorescent markers or polymerizing glycosylated polypeptides.³⁶⁴ The aforementioned ligation strategies address conventional functional groups present in amino acids or in proteins and peptides. In contrast, click chemistry or reactions that can be labelled bioorthogonal have been introduced to bioconjugation. Such bioorthogonal reaction sites comprise *e.g.* azides, aldehydes, cyclopentadienes, or alkynes, leaving conventional functionalities, such as hydroxyl groups, unaffected. A selection of the aforementioned methodologies are Staudinger ligation,³⁶⁵ Paternò-Büchi reaction,³⁶⁶ inverse electron demand DA reaction on basis of tetrazines and cyclopropenes (refer to Scheme 3-50),³⁷⁰ 1,3-dipolar copper-catalyzed azide-alkyne cycloaddition (CuAAC),³⁶⁷ specific DA reactions,³⁶⁸ and strain promoted azide-alkyne cycloaddition.³⁶⁹

Traceless Staudinger ligation

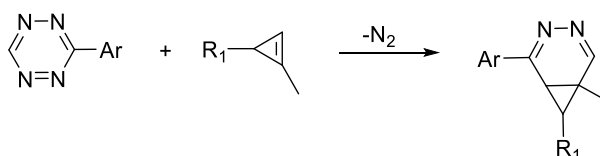


X: cleavable group

Paternò-Büchi [2+2] cycloaddition

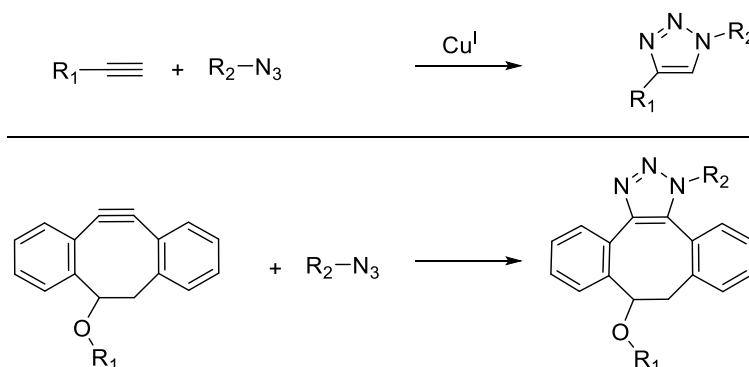


Inverse electron demand Diels-Alder reaction



Scheme 3-50. Exemplary reactions for bioconjugation, such as traceless Staudinger ligation (top), Paternò-Büchi [2+2] cycloaddition of modified cellulose (center), and tetrazine/cyclopropene based inverse electron demand DA reaction (bottom).^{366,371,370}

A common method not only in organic or polymer chemistry is the CuAAC, pioneered and named after its discoverer Huisgen (refer to Scheme 3-51).³⁶⁷ Here, azides are reacted in a 1,3-dipolar cycloaddition with alkynes by using an auxiliary metal copper catalyst. The formation of a triazole moiety represents a highly bioorthogonal approach, obtaining a stable and dense linkage. However, the application of copper in terms of cytotoxicity and redox sensitivity limits the applicability of the Huisgen reaction. To circumvent the usage of metal catalysts, azide-alkyne cycloadditions can be carried out without the need of a catalyst by employing *e.g.* cyclooctins.³⁴⁷ Strained alkynes such as substituted cyclooctynes readily react with azides to form stable conjugates.³⁶⁹



Scheme 3-51. 1,3-dipolar cycloadditions, either Cu^I catalyzed (top) or strain-promoted (bottom).^{347,367}

3.7 Kinetic Modeling of Polymerization Reactions

The prediction of polymerization reactions is highly complex, since – in contrast to single molecule reactions – a distribution of differently sized chains is present.³⁷² In addition, the viscosity of a polymerization mixture changes and, therefore, diffusion processes become essential during the polymerization.⁴⁹ Simulations and theoretical calculations to describe and predict chemical reactions have been established in order to understand, investigate and emulate reaction mechanisms. Due to increasing computational power and the development of new methods in the field, modeling enabled in-depth calculations of polyatomic systems.³⁷³ Since many-body systems feature highly complex wave functions, simulations use algorithms involving simplifications, approximations, random walk methods, and assumptions. Simulations for the modeling of polymerization kinetics comprise modular dynamics³⁷⁴ and Monte Carlo simulations,³⁷⁵ employing deterministic and stochastic methods. Monte Carlo (MC) simulations are a common method to describe complex processes by numerical and iterative approximations by a large numbers of random experiments.³⁷⁶ These stochastic approaches are in contrast to deterministic modeling techniques, which arrive at their results based on the complex numerical integration of differential equations.³⁷⁷ In polymer reaction engineering, MC simulations are nowadays able to model the degree of polymerization, sequence length distributions, cross-linking densities, end-group fidelities, and others.³⁷⁸ Furthermore, the so-called kinetic MC (*k*MC) simulations are employed to describe the evolution of chemical reactions with time. Generally, the resolution of these simulations requires a sufficient number of initial molecules. Below, the application of the Gillespie algorithm, as closely related to the *k*MC algorithm, for the description of a chemical process is discussed:³⁷⁷

In a stochastic approach, a reaction can be described by random events, each of them occurring with a certain probability dependent on the reaction rate coefficients and number of molecules. Here, we evaluate the equilibrium of A and B with the reaction coefficients k_x for each reaction pathway (refer to Eq. (25)):



In contrast to deterministic approaches, stochastic approaches can achieve more than just one trajectory. Each reaction occurs with a specific probability, calculating it from the product of the reaction rate constant with the combination of molecules participating in the reaction. Next, the time interval dt for calculation is chosen infinitesimally small in order to either have the occurrence of only one or no reaction event. The probabilities, W , to describe the number of molecules at time t after dt , is defined for both species with respect to the reaction rate coefficients k_x (refer to Eq. (26)):

$$\begin{aligned} W_+ [N_A(t)] &= k_2 N_B(t) \\ W_- [N_A(t)] &= k_1 N_A(t) \end{aligned} \quad (26.)$$

With: $N_A(t)$ and $N_B(t)$: number of molecules.

After the starting conditions are defined, a random number of time steps with varying length is generated by the algorithm, depending on the random nature of the process and the reactions' probabilities. For the A, B reaction, a second random number determines which of both reactions occurs with respect to the reaction probability. After the time interval dt , the probability of changing the number of A molecules is defined by the sum of the probability of the positively or negatively developing number of A molecules (refer to Eq. (27)):

$$a(N(t)) = W_+ [N_A(t)] + W_- [N_A(t)] \quad (27.)$$

The outcome of such a stochastic simulation shows fluctuations, referred to as stochastic noise, as the number of molecules $N_A(t)$ cannot be determined for any time.³⁷⁷ Stochastic noise is of course an effect that does not occur in deterministic approaches. Nevertheless, the stochastic noise can be addressed by increasing the number of initial molecules, showing that for real-life reactions the requirement of a sufficient number of molecules is implied. On the other hand, for systems with a low number of molecules, such as cells in living organisms,³⁷⁹ fluctuations in stochastic approaches play a key role, whereas deterministic approaches are not suitable to describe such process properly.

The development of powerful simulation techniques enabled the emulation and calculation of polymerization process, leading to an in-depth understanding of the processes and allowing the simulation of molecular weight distributions.³⁸⁰ Here, simulation software, such as PREDICI[®], has been employed to improve the duration and the precision of simulations for polymerizations.³⁷²

Based on the aforementioned techniques, the utilization of photo- and thermally induced reactions for SG and RAFT polymerization in combination with simulations as well as in surface and peptide chemistry will be highlighted in the following chapters.

4

4 SEGMENTED COPOLYMERS BY SEQUENTIAL STEP-GROWTH AND RAFT POLYMERIZATION

4.1 Introduction and Concept

The combination of SG and RAFT polymerization is rather rare and such a concept usually entails the functionalization of RAFT polymers *via* postmodification or implementation of the RAFT group in a consecutive SG process, e.g. aminolysis of the RAFT group and subsequent disulfide formation for SG polymerization.¹³¹ In the current chapter, RAFT groups are incorporated into the repeating unit of a polymer, in particular into the backbone and not into the lateral chain (refer to Figure 4-1). Herein, the direct introduction of multiple RAFT moieties into the backbone during a SG polymerization is pioneered with no need for further postmodifications. Attractive reactions for SG are DA reactions that can be triggered thermally or upon irradiation and are orthogonal to the presence of pendant RAFT groups. Contemporary efforts towards sustainable chemistry and high atom economy calls for precise chemical methods with low activation energies^{4,26} – a paradigm that is fulfilled by many DA reactions. Furthermore, DA processes can – in certain instances – proceed with high reaction rates and afford quantitative yields,^{144,196} which was demonstrated for block copolymer generation,^{124,127} surface functionalization,³¹³ and self-healing materials.¹⁵³ Here, the photo-induced DA cycloaddition of photoenols derived from *ortho*-methyl benzaldehydes (**AA**) and the thermally induced DA cycloaddition of cyclopentadiene (**CC**) in combination with fumarate monomers (**BB**) are employed as

powerful reactions for SG polymerization (refer to Figure 4-1). In this context, a trithiocarbonate is selected as the RAFT group type since it enables symmetric fragmentation during the RAFT process. Subsequently, utilization of the SG polymer as a multi-CTA in RAFT polymerization generates segmented polymer blocks, each separated by half of the SG polymer repeating unit.

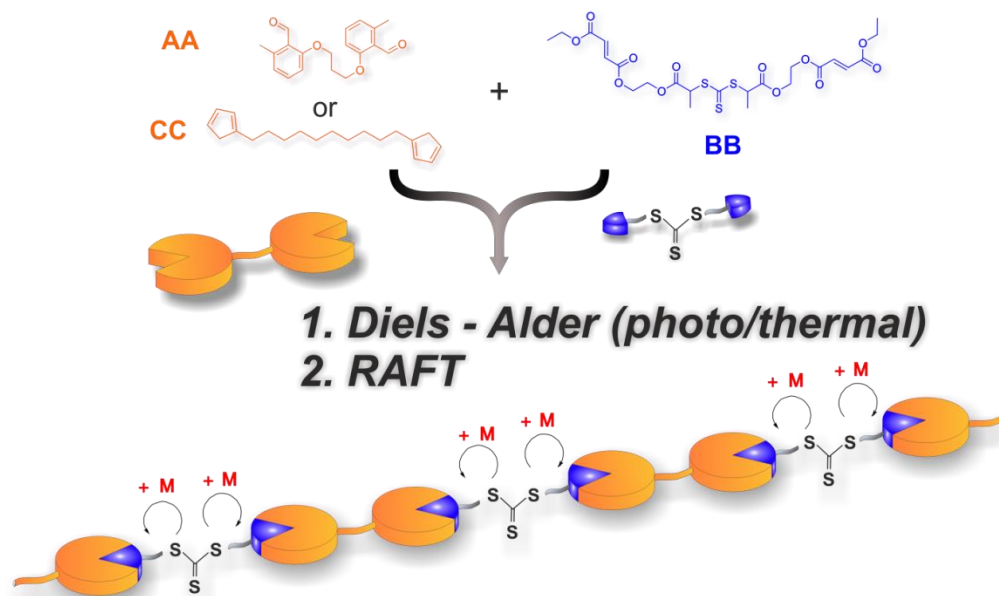


Figure 4-1. General concept of photo- (AA) or thermally induced (CC) Diels-Alder SG polymerization of corresponding monomers and subsequent RAFT polymerization.

The concept has not been described in the literature yet: It addresses the complex question of the RAFT polymerization mechanism in the presence of multiple linearly attached RAFT moieties. A polymeric system with multiple RAFT groups, covalently linked to each other in a linear fashion, might feature different reactivity of the single RAFT groups and the high number of RAFT moieties within one chain might influence the overall process. Furthermore, such multi-CTA SG polymers extend the scope of RDRP to new dimensions. Since the processes during RAFT polymerization are highly complex, the application of *in silico* investigations is required for understanding and identification of the underlying reaction mechanisms.

The following chapter is divided in two sections: (i) photo-induced DA driven synthesis of SG and their subsequent RAFT polymerization and (ii) thermally induced DA reactions for SG polymer formation and their subsequent corresponding RAFT polymerization.

4.2 Step-Growth by Photo-Induced DA Reactions and Subsequent RAFT Polymerization: Synthesis of Segmented Copolymers

In this section, a combination of photoenols and fumarates as monomers in a SG and precursors in RAFT polymerization is introduced. Here, the photoenol and fumarate monomers – representing an **AA/BB** monomer system – polymerize in a photo-induced DA reaction. Subsequently, the SG polymer is employed as multi-CTA precursor in a RAFT polymerization of styrene, obtaining segmented copolymers. In order to better understand the SG and RAFT polymerization processes, *in silico* investigations were conducted with kinetic Monte Carlo (*kMC*) simulations. By fusing the experimental and calculated data, an in-depth understanding of the processes present in both polymerization stages is achieved and access to fundamental characteristics of the polymers is granted.^A

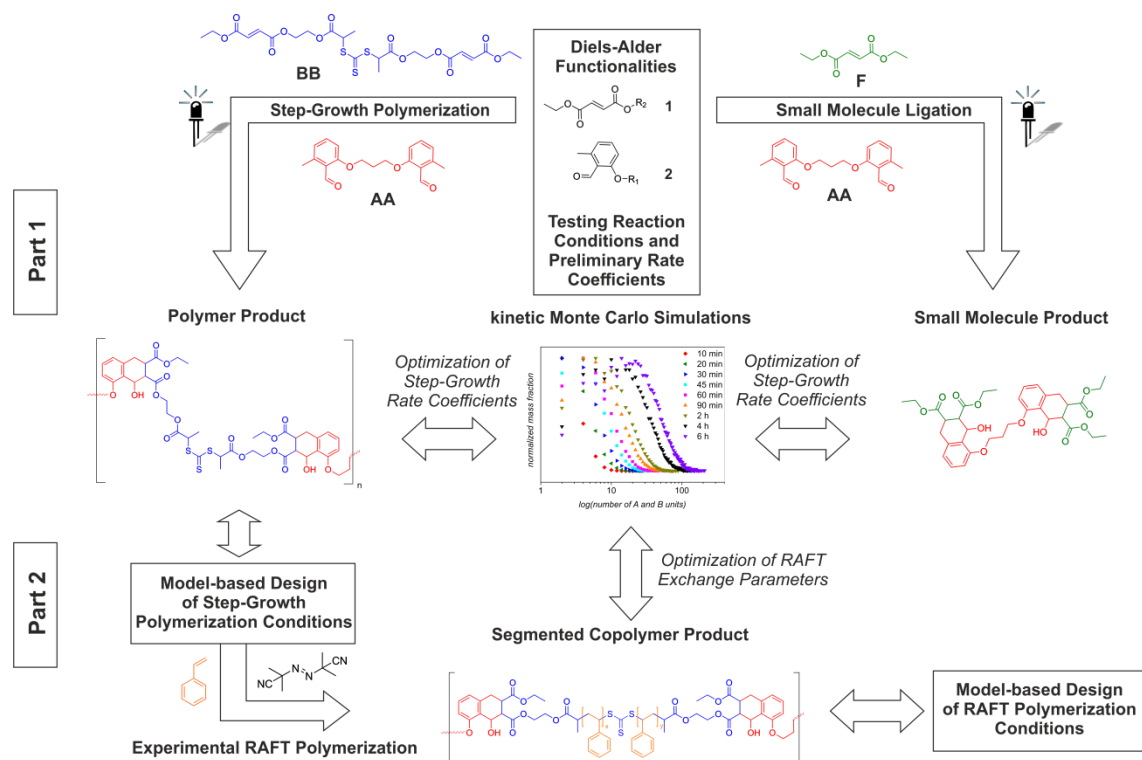


Figure 4-2. Research concept of both experimental and *in silico* investigations for designing the reaction conditions of the SG as well as the RAFT polymerization. The figure is adapted from ref.³⁸¹ with permission of the American Chemical Society.

^A Parts of this chapter are reproduced or adapted from Gegenhuber, T.; De Keer, L.; Goldmann, A. S.; Van Steenberge, P. H. M.; Mueller, J. O.; Reyniers, M.-F.; Menzel, J. P.; D'hooge, D. R.; Barner-Kowollik, C. *Macromolecules* **2017**, *50* (17), 6451–6467 with permission of the American Chemical Society. L. De Keer conducted the *in silico* calculations and contributed equally to the project. P. H. M. Van Steenberge, M.-F. Reyniers and D. R. D'hooge supervised the *in silico* investigations and participated in the scientific discussions. J. O. Mueller participated in the scientific discussions and J.P. Menzel contributed with the concentration profile of photo-induced reactions. A. S. Goldmann, and C. Barner-Kowollik motivated and supervised the experimental part as well as the entire project.

As depicted in Figure 4-2, the step- and chain-growth polymerization of *ortho*-methyl benzaldehydes in combination with fumarates were studied both experimentally and *via* *k*MC modeling investigating the reaction kinetics and monomer incorporation. The central idea of the research strategy was to combine simulations with experimentally determined molecular characteristics of the polymers to identify rate coefficients that adequately describe the polymerization processes. As proof of concept of the SG polymerization, small molecule studies with a monofunctional ene (**F**, refer to Figure 4-2) were performed to underpin the consistency of kinetic interpretation and to simplify the determination of rate coefficients. This enabled a reliable model-based optimization in terms of reaction parameters and product quality, *i.e.* high molar masses and precisely incorporated styrene blocks. To create a well-founded basis for the modeling the RAFT polymerization (refer to Figure 4-2, part 2), in the first part the parameters for the SG polymerization were optimized by exploiting small molecule reactions (refer to Figure 4-2, part 1).

4.2.1 Kinetic Modeling

A bivariate kinetic Monte Carlo (*k*MC) modeling strategy is employed for the simulation of the SG polymerization of the **AA** and **BB** monomer and the subsequent usage of the SG polymer as multi-CTA in a RAFT polymerization with styrene.^{372,382,383} These simulations enable the access to the chain length of every macrospecies as well as the number of RAFT groups in the chain. This is the first time the latter have been taken into consideration in a modeling approach of this type. By addressing simulations, a differentiation between dormant and dead chains with different numbers of RAFT groups is possible. Such information cannot be accessed by experimental data and characterization tools, yet. Thus, modeling is essential to provide additional information for the complete characterization of the segmented copolymer.³⁸⁴

4.2.1.1 Step-Growth Reactions

In the SG polymerization, the *k*MC model identified 54 relevant reactions to include them as basis in the simulations (refer to Appendix 8.1.2, Table 8-1): A discrimination is performed between functionalities at the polymers termini: **AA**, **BB**, **AA***, and **A*A***, with **A***, (* refers to the photo-activated state), as highlighted in Figure 4-3A. For simplification, only oligomers are illustrated instead of polymers. In addition, the homopolymerization of monomer **AA** is taken into account. The kinetic parameters for adapting the simulated to the experimental data of the SG are listed in Table 8-1 (refer to Appendix 8.1.1). The activation rate coefficient of **AA** is adjusted with respect to the initial conditions, *i.e.* a concentration influence on the activation from **A** to **A*** (refer to Appendix 8.1.2). Here, the

activation rate has been found to be decreased with increasing concentration. The lowered activation rate is confirmed by the calculations in the *k*MC modeling as well as by the Beer-Lambert's law, showing a decrease by a factor of three when the concentration of **AA** is increased from 0.02 mol·L⁻¹ to 0.08 mol·L⁻¹. The conversion of p_A of the benzaldehyde moiety is defined as (refer to Eq. (28)):

$$p_A = 1 - \frac{N_A + N_A^*}{N_{A,0}} \quad (28.)$$

With: $N_{A,0}$ and N_A : (initial) number of functional **A** groups; $N_{A,}^*$: number of activated **A**^{*} moieties.

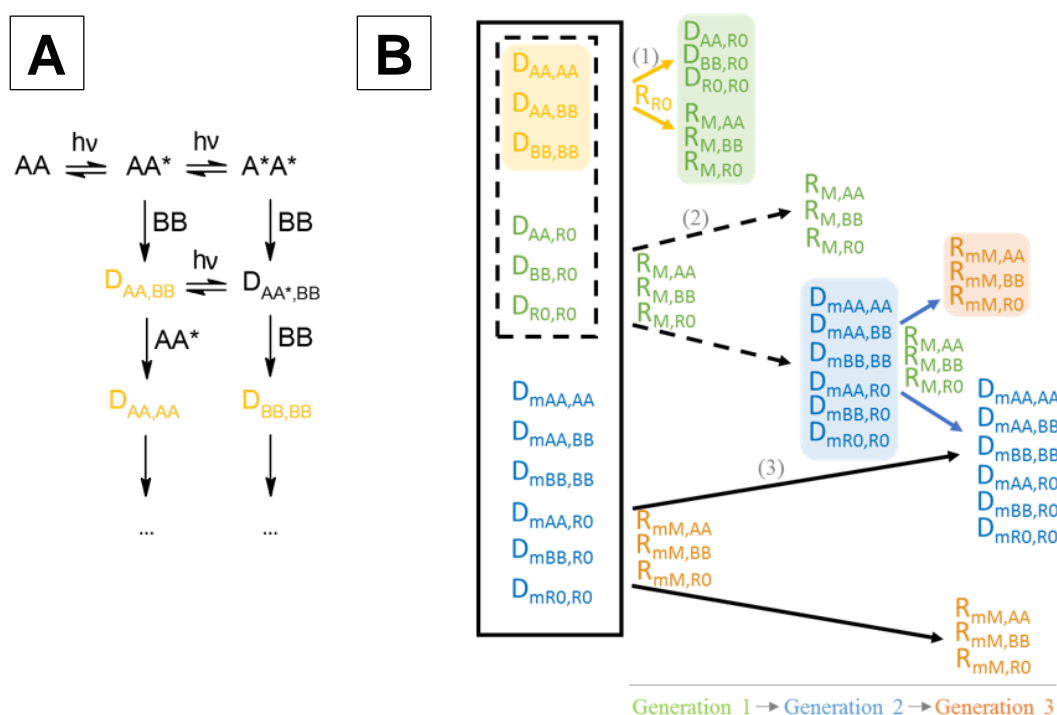


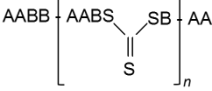
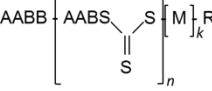
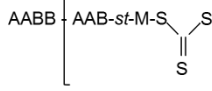
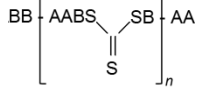
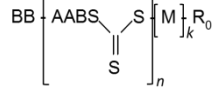
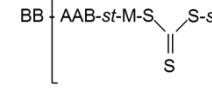
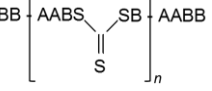
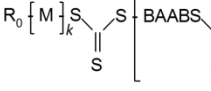
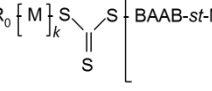
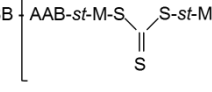
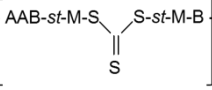
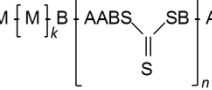
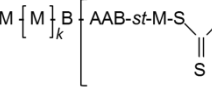
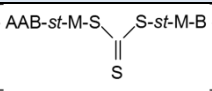
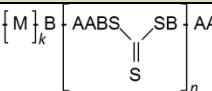
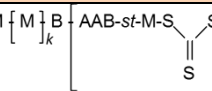
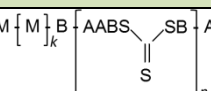
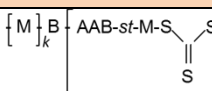
Figure 4-3. (A) Oligomerization of **AA** and **BB** in photo-induced SG polymerization into multifunctional RAFT CTA ($D_{X,Y}$; X,Y are end-groups); Full list of all 54 reactions in Table 8-1 in the Appendix 8.1.1; (B) Exchange reactions in the RAFT process (monomer **M**: styrene) and chronologically ordered divisions of the macrospecies formed. Definition of macrospecies: Table 4-1 (definition based on end-groups; R_0 : AIBN fragment); full list of all 205 reactions in Table 8-2. The figure was reprinted from ref.³⁸¹ with permission of the American Chemical Society.

4.2.1.2 Chain-Growth Reactions

For the multifunctional RAFT polymerization, a degenerative RAFT mechanism is assumed.^{86,385–387} This assumption allows for a first approximation in order to illustrate the processes presented in the current chapter. In order to do so, 205 independent reactions need to be considered in the *k*MC model (refer to Appendix 8.1.2, Table 8-2). The associated kinetic parameters are shown in Table 8-4 (refer to Appendix 8.1.5) by tuning to the experimental data of the RAFT polymerization. The RAFT exchange reactions are schematically shown in Figure 4-3B. The notation of macrospecies is outlined in Table 4-1, the homopolymer segments of **AA** are omitted in terms of simplification. Styrene units are denoted **M**, the prefix ‘-st’ implies a statistical distribution of the units in between the RAFT groups. The total chain length *i* is defined by the sum of all **A**, **B**, and **M** units (excluding the end-groups), e.g. **AABB** equals *i* = 4. In addition, *X* represents all RAFT moieties in the chain, *k* the number of styrene monomers, and *n* the number of ‘repeating units’ including one RAFT group.

The colors in Figure 4-3B represent the different generations: The first RAFT exchange describes the reaction between the SG polymer as macro precursor, *i.e.* SG polymers with either **AA**, **BB**, or **AB** end-groups, and the styrene radicals *R*₀ after initiation with AIBN. An exchange with the initiator as in the RAFT pre-equilibrium is neglected here. In the first generation, dormant macrospecies *D* as well as macroradicals *R* are formed (refer to Table 4-1, green box). The dormant macrospecies are now able to undergo exchange with the recently formed macroradicals and styrene is inserted during the propagation, here labelled as second generation of RAFT exchange (refer to Table 4-1, blue box). In the third generation macrospecies undergo exchange with further macrospecies, both bearing styrene units (refer to Table 4-1, orange box). The chains formed during the third generation of RAFT exchange do not represent a new class of macrospecies and therefore, a consistent set of exchange reactions and species is listed in Table 4-1. In the next stage, the reaction probability is enunciated with regard to the number of RAFT groups, in order to accurately reflect the kinetics of the RAFT exchange. This means, a dormant chain, bearing a high number of RAFT groups, has logically a higher probability to participate in RAFT exchange reactions than a chain with a low number of RAFT groups. Hernandez-Ortiz *et al.* reported the modeling of hydrogen abstraction of polyethylene in a post-polymer modification.³⁸⁸ Here, the viscosity strongly influences the termination, and therefore, diffusion is considered in the presented simulations.^{389,390}

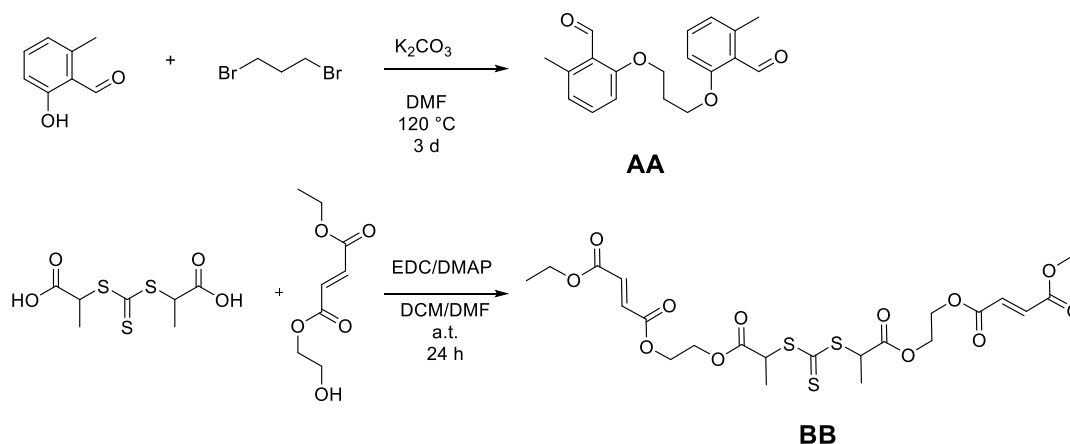
Table 4-1. Overview of the macrospecies for the kinetic modeling of the RAFT polymerization after the SG polymerization (AA homopolymer segments are omitted). Species exchange as shown in Figure 4-3. Full list of reactions refer to Table 8-2 in the Appendix 8.1.1. The table was reprinted from ref.³⁸¹ with permission of the American Chemical Society.

DORMANT CHAINS		
Precursor polymer	After chain growth	
$D_{AA,AA}$ ($i=4n; X=n$)	D_{AA,R_0} ($i=3n+k; X=n$)	D_{mAA,R_0} ($i=3n+j+k; X=n$)
		
$D_{AA,BB}$ ($i=4n; X=n$)	D_{BB,R_0} ($i=3n+k; X=n$)	D_{mBB,R_0} ($i=3n+j+k; X=n$)
		
$D_{BB,BB}$ ($i=4n; X=n$)	D_{R_0,R_0} ($i=4n+k+l; X=n+1$)	D_{mR_0,R_0} ($i=4n+j+k+l; X=n+1$)
		
$D_{mAA,AA}$ ($i=4n+j; X=n$)	MACRORADICALS	
	$R_{R_0}^{(*)}$	
	$R_0 [M]_i M^\bullet$	
$D_{mAA,BB}$ ($i=4n+j; X=n$)	$R_{M,AA}^{(*)}$ ($i=4n+k+1; X=n$)	$R_{mM,AA}^{(*)}$ ($i=4n+j+k; X=n$)
		
$D_{mBB,BB}$ ($i=4n+j; X=n$)	$R_{M,BB}^{(*)}$ ($i=4n+k+1; X=n$)	$R_{mM,BB}^{(*)}$ ($i=4n+j+k+1; X=n$)
		
	$R_{M,R_0}^{(*)}$ ($i=4n+k+l+4; X=n+1$)	$R_{mM,R_0}^{(*)}$ ($i=4n+j+k+l+4; X=n+1$)
		

(*) Assumption: macroradicals propagate at least once before they undergo transfer reactions; R_0 is an AIBN derived cyanoisopropyl fragment.

4.2.2 Monomer Design, Synthesis and Stability

The design of the participating monomers comprised the synthesis of two molecules bearing either two *ortho*-methyl benzaldehyde **AA** or two fumarate moieties **BB** (refer to Scheme 4-1). The RAFT group was incorporated in the **BB** monomer in order to obtain one RAFT group per repeating unit of the SG polymer.

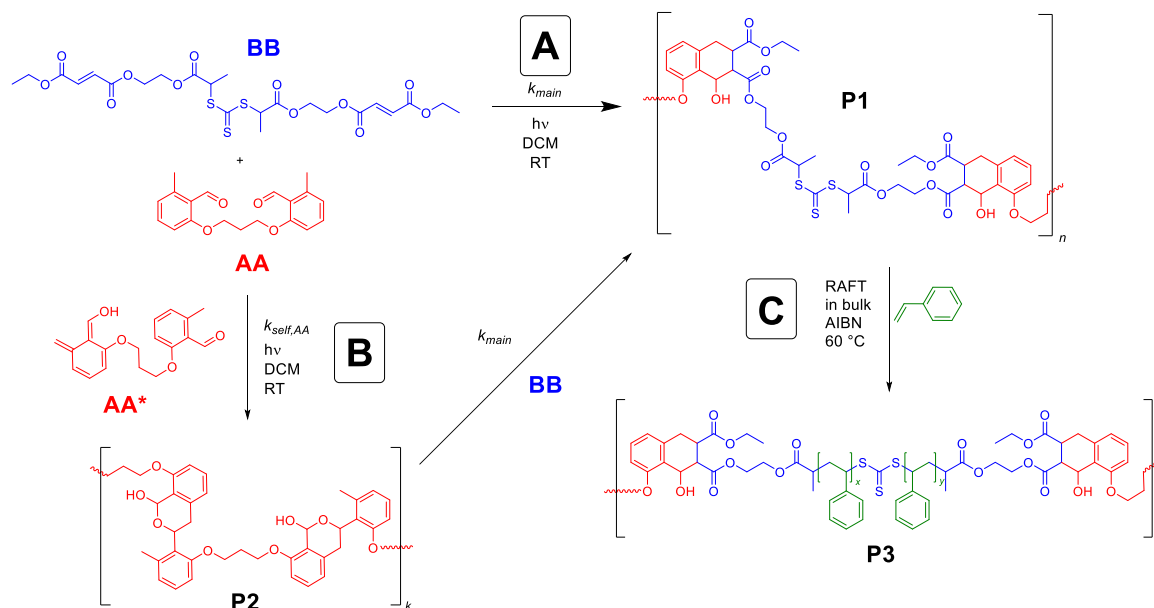


Scheme 4-1. Synthesis and introduction of **AA** and **BB** monomers.

The synthesis of both monomers **AA** and **BB** was conducted in a non-challenging and routine manner. Finally, the monomers were obtained in high purity after purification by column chromatography and recrystallization (for experimental procedures and characterization, refer to Chapter 7.3).

4.2.2.1 Reaction Concept and Monomer Stability

The photo-induced SG polymerization was achieved by the reaction of di(*ortho*-methyl benzaldehyde)s in combination with a specifically designed trithiocarbonate RAFT agent featuring two terminal fumarate groups (refer to Scheme 4-2, monomers **AA** and **BB**, respectively) in DCM. Upon irradiation of the *ortho*-methyl benzaldehyde, the SG is driven by the active *ortho*-quinodimethane intermediates, as described in Chapter 3.4.3.4. Here, irradiation in the UV range with wavelengths close to 360 nm is required to trigger the photoenolization. The photoenols as dienes subsequently react with the fumarate dienophiles in a DA reaction forming a six-membered ring (governed by the rate coefficient k_{main} in Scheme 4-2A). Depending on the *endo* or *exo* attack of the photoenol diene, different constitutional isomers of the six-membered ring are formed, yielding the SG polymer **P1**.²⁷⁴



Scheme 4-2. (A) Main reaction pathway for photo-induced SG polymerization employing di(*ortho*-methyl benzaldehyde) monomer **AA** in combination with the difumarate-RAFT monomer **BB** yielding **P1**. Isomers are omitted for simplicity. (B) Photo-induced dimerization of monomer **AA**, undergoing **AA** homopolymerization yielding **P2**; the DA self-reaction occurs after activation to the intermediate state **A(*)A***; **P2** or **AA** oligomer species can also follow the main reaction (k_{main}) pathway, leading to random copolymer with undefined sequences of $((AA)_k AABBB)$. (C) RAFT polymerization employing SG polymer **P1** as multi-CTA for segmented copolymer synthesis. For simplicity, only one example of the constitutional isomers of the different polymers is illustrated.

Before proceeding to the SG polymerization, a stability test was performed employing the monomers in DCM without a reaction partner, *i.e.* at a concentration of $0.04 \text{ mol}\cdot\text{L}^{-1}$ and with UV irradiation (emission maxima at $\lambda_{max} = 360 \text{ nm}$, refer to Chapter 7.2.7). For the RAFT agent **BB**, no molecular damage or instability was observed as confirmed both by SEC analysis (refer to Figure 4-4A, red and blue traces) and $^1\text{H-NMR}$ (refer to Figure 4-4C). In contrast, the benzaldehyde monomer **AA** surprisingly underwent a self-reaction due to the absence of an appropriate reaction partner ($k_{self,AA}$, refer to Scheme 4-2), yielding a hemiacetal as the main unit in an **AA** SG homopolymer, as suggested from the SEC traces and the NMR spectra (refer to Figure 4-4A, black and green traces, Figure 4-4B). The carbonyl group of the non-activated aldehyde hence serves as dienophile and reacts in a HDA reaction with the *ortho*-quinodimethane active intermediate. Due to the bifunctional character of **AA**, a SG is initiated, evidenced by high resolution ESI-MS (refer to Appendix 8.1.3.1, Figure 8-1). Thereby, it became apparent that homopolymerization of **AA** may occur to a certain extent in the **AA/BB** SG polymerization. In addition, the **AA** oligomers may react with $(AABB)_k$ oligomers leading to the formation of random sequences, namely $((AA)_k AABBB)$; $k \geq 0$, refer to Scheme 4-2A). To determine the extent of the homopolymerization, the formation of the

by-product as competitive reaction is initially assumed to proceed with a similar rate coefficient, setting as initial point $k_{self,AA} = k_{main}$.

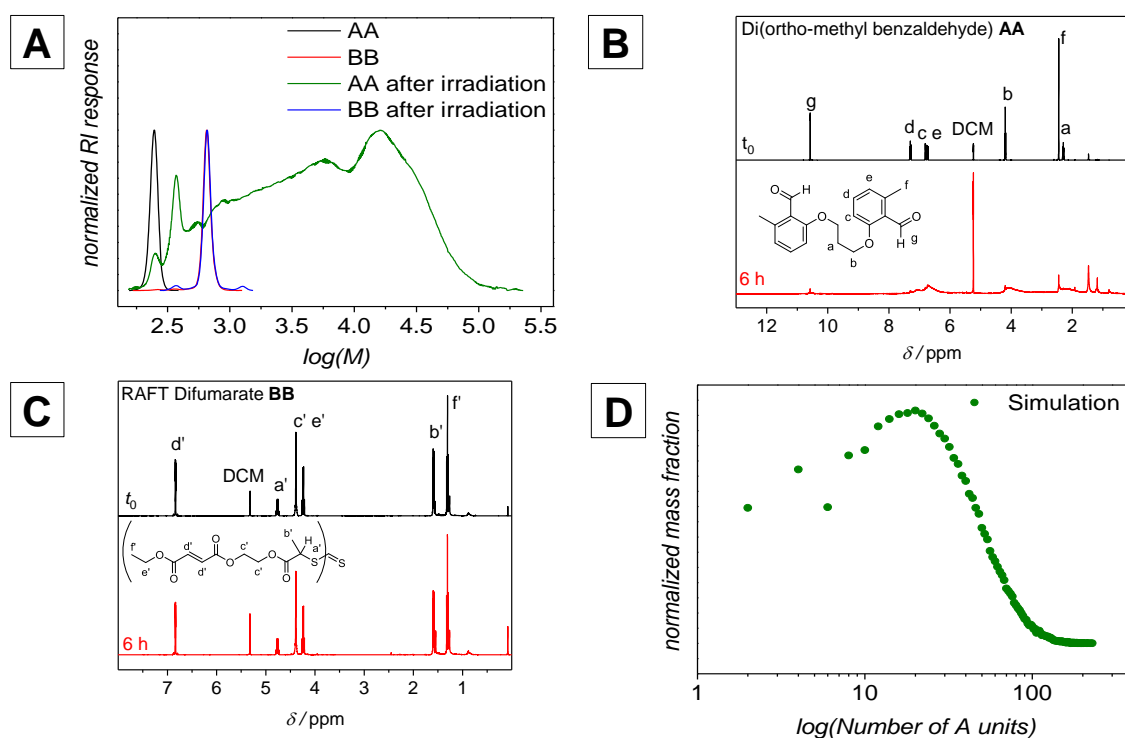


Figure 4-4. (A) Experimental THF-SEC traces obtained from the **AA** and **BB** monomer stability tests ($\lambda_{\text{max}} = 360 \text{ nm}$, $t = 6 \text{ h}$ in DCM, $T = 25 \text{ }^\circ\text{C}$, $c = 0.04 \text{ mol}\cdot\text{L}^{-1}$). (B) $^1\text{H-NMR}$ spectra of **AA** monomer before (black) and after irradiation (red). (C) $^1\text{H-NMR}$ spectra of **BB** monomer before (black) and after irradiation (red). All NMR spectra were recorded in DCM- d_2 . (D) Molar mass distribution obtained by simulation used for the determination of $k_{self,AA}$ by qualitative comparison with experimental data in (A) (normalized on peak height); $k_{self,AA} = 0.2 \text{ L}\cdot\text{mol}^{-1} \text{ s}^{-1}$; for (D) absolute molar masses are calculated from the chemical structure of **AA** while in (A) they are relative due to measurement vs. standards and broadening; for (D) by definition the monomer **AA** is located at $x = 2$, the dimer **AAAA** at $x = 4$, etc. The figure was adapted from ref.³⁸¹ with permission of the American Chemical Society.

4.2.2.2 Rate Coefficients based on Small Molecule Model System

The upcoming question addresses the dimension and ratio of both k_{main} and $k_{self,AA}$ (refer to Scheme 4-2) and thus, if the homopolymerization or self-reaction of **AA** is significantly present during the SG process in the presence of **BB**. To assess this issue, kinetic modeling is crucial to determine k_{main} and $k_{self,AA}$, since experimental analysis techniques are limited, due to overlapping signals in chromatographic or spectroscopic methods. As was illustrated in Figure 4-2, k_{main} and $k_{self,AA}$, were incrementally adjusted, based on carefully selected, yet simplified reliable model systems. By taking all relevant reaction conditions into account, an approximation of the molecular weight distribution of the SG product in qualitative manner could be obtained by simulations. Especially the generation and incorporation of the **AA** homopolymer product was simulated. The SEC trace of the experimental **AA** homopolymerization in Figure 4-4A was modeled *via* kMC simulations (refer to Figure 4-4D), focusing on the self-dimerization in the given irradiation time of 6 h (reactions of kMC model refer to Appendix 8.1.1.1). By setting $k_{self,AA}$ to $0.2 \text{ L}\cdot\text{mol}^{-1}\cdot\text{s}^{-1}$, a reasonable match between experimental and simulated data was obtained, keeping in mind that the former and latter yield relative and absolute molar masses, respectively. By comparing modeled MWD and experimental SEC traces, a match between both was achieved, including oligomers, assigning the individually resolved peaks in the simulations to specific oligomeric and polymeric species.

After determination of $k_{self,AA}$, experimental data was taken to identify k_{main} using the SG functional groups **A** and **B**. Essentially, the assessment of k_{main} necessarily includes knowledge of $k_{self,AA}$ since the main reaction cannot be accessed separately. Therefore, having determined $k_{self,AA}$, a model with monofunctional units **A** and **B** (refer to Figure 4-5A), employing the mono-fumarate molecule **F** (diethyl fumarate), was utilized to theoretically investigate both reactions occurring simultaneously. Here, dimerization leads to **A-A** ($k_{self,AA}$), whereas the main reaction yields **A-F** (k_{main}). By limiting the reactants to only monofunctional species, the investigation only involves **A**, **F**, **A-A** and **A-F** for determining the kinetics and the outcome of the reactions.

If $k_{self,AA} = k_{main}$, logical thinking implies the formation of both products **A-A** and **A-F** to the same extent. In the modeling system, an equal formation of both expected products can be observed at very low reaction times. Nevertheless, the consumption of **A** is higher due to increased demand of **A** in the simultaneous formation of **A-A** and **A-F**. Therefore, the concentration of **A** decreases faster than for **F**. At longer reaction times, the decreasing concentration profile of **A** influences the ratio of **A-A** to **A-F** formation in favor of **A-F** (refer to Figure 4-5B). In case of an equimolar feeding ratio of both functional groups, the concentration of the products increases in favor of **A-F** with advancing reaction time as a

consequence of the increased consumption of **A** (for $k_{self,AA} = k_{main}$). It becomes clear from Figure 4-5C that formation of >80% of **A-F** is achieved for $k_{self,AA} < k_{main}$ and significantly lower amounts of **A-F** are formed by increasing the amount of **A** ($r > 1$, refer to Eq. (29)).

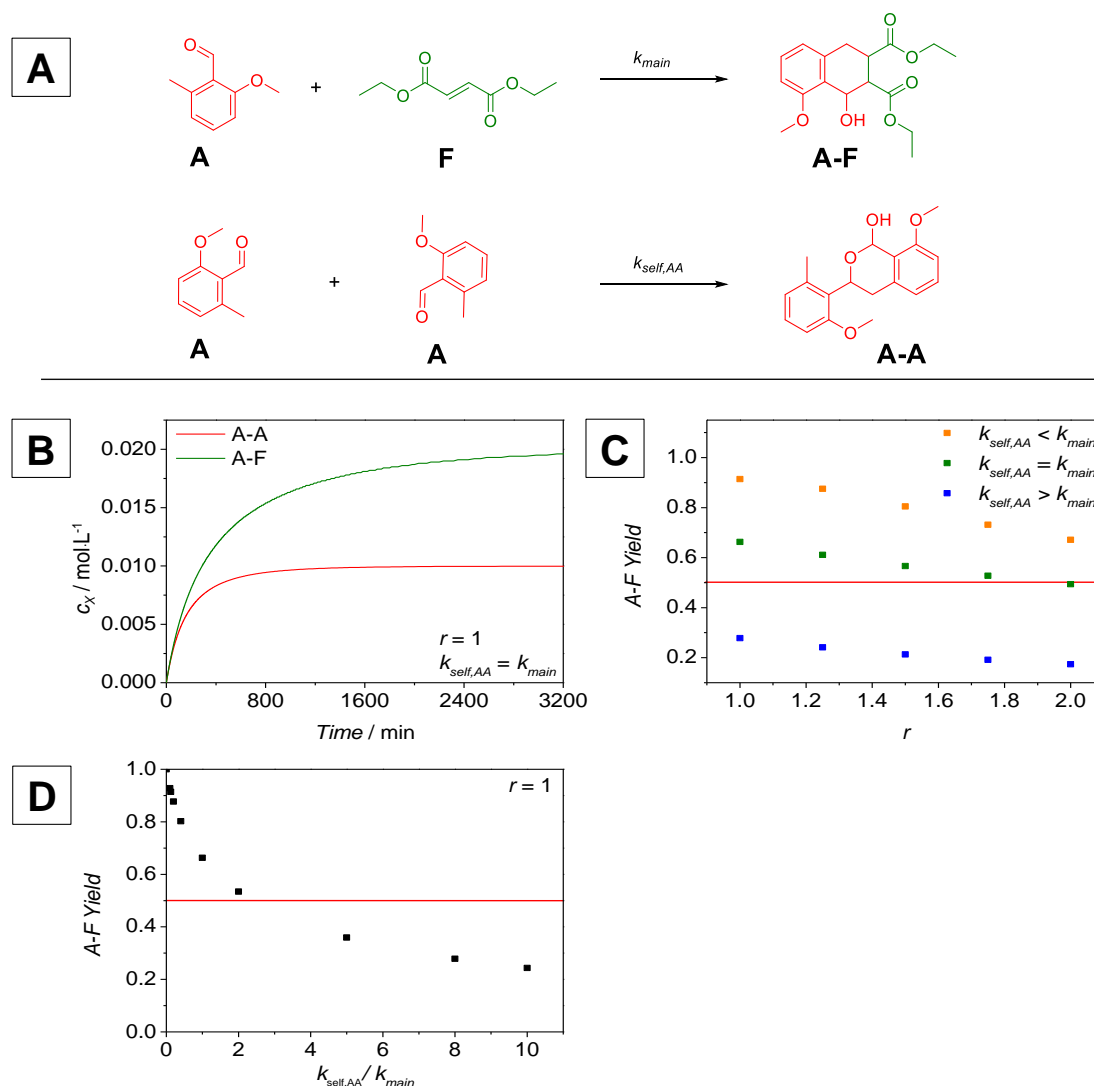


Figure 4-5. (A) Monofunctional system accounting for the reaction between diethyl fumarate **F** and **A** according to the monomer structure of the main reaction (k_{main}) and the self-reaction ($k_{self,AA}$), forming the final adducts **A-F** and **A-A**. (B) Concentration profile of both adducts **A-A** and **A-F** with time ($c_0 = 0.04 \text{ mol}\cdot\text{L}^{-1}$). (C) Calculated final yield of the product **A-F** depending on different monomer stoichiometry r . Three cases are depicted for different ratios of $k_{self,AA}$ to k_{main} (orange dots: $\frac{k_{self,AA}}{k_{main}} = 0.125$, green dots: $\frac{k_{self,AA}}{k_{main}} = 1$, blue dots: $\frac{k_{self,AA}}{k_{main}} = 8$). The red line illustrates parity between the **A-F/A-A** concentrations. (D) Calculated final yield of the **A-F** product depending on the ratio of $k_{self,AA}$ to k_{main} (red line indicates parity). The figure was reprinted from ref.³⁸¹ with permission of the American Chemical Society.

In contrast, Figure 4-5D illustrates that at equimolar conditions, $k_{self,AA}$ must exceed k_{main} by a factor of two to balance the formation of both adducts **A-F** and **A-A** or for dominating **A-A** formation. We conclude from the simulations that the ratio of $k_{self,AA}$ to k_{main} is essential to determine the ideal stoichiometric conditions (refer to Eq. (29)) for the SG polymerization when high molar masses are desired.

$$r = \frac{n_0(\text{AA})}{n_0(\text{BB or F})} \quad \text{with } n_0(\text{XX}): \text{ molarity of monomers or units XX, X} \quad (29)$$

The experimental data for the determination of k_{main} – as illustrated in Scheme 4-2 – were obtained employing a small molecule **F** in combination with monomer **AA** (refer to Figure 4-6A). Here, the formation of the small molecule adducts **F-AA-F** and **AA-F** and self-polymerization adduct **AA-AA** are competitive during the reaction. Nonetheless, the small molecule reaction is feasible to ultimately emulate the processes of the SG polymerization in a realistic manner. Two cases were explored, where (i) equimolar concentrations ($r = 1$, $c(\text{AA}) = 0.035 \text{ mol}\cdot\text{L}^{-1}$ and $c(\text{F}) = 0.070 \text{ mol}\cdot\text{L}^{-1}$) and (ii) off-stoichiometric concentrations ($r = 1.43$, $c(\text{AA}) = 0.052 \text{ mol}\cdot\text{L}^{-1}$ and $c(\text{F}) = 0.070 \text{ mol}\cdot\text{L}^{-1}$) were employed. With the input from the experimental data, the tuning of the simulation parameters obtained a qualitative match of the SEC traces, determining $k_{main} = 1.6 \text{ L}\cdot\text{mol}^{-1}\cdot\text{s}^{-1}$ (with $k_{self,AA} = 0.2 \text{ L}\cdot\text{mol}^{-1}\cdot\text{s}^{-1}$). By calculating the ratio of $k_{self,AA} / k_{main} = 0.125$, it ultimately concludes a favored incorporation of the **BB** monomer during the SG polymerization (refer to Figure 4-6B and C).

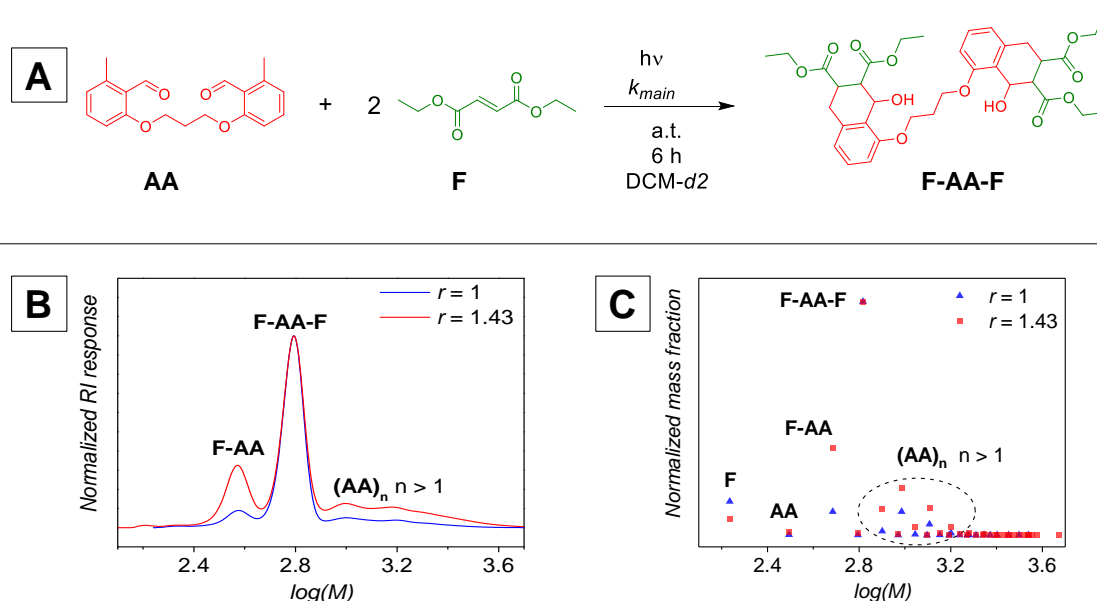


Figure 4-6. (A) Assessment of k_{main} by small molecule reaction including the monomer **AA** and its counterpart **F**, employing the prior determined $k_{self,AA}$ value ($k_{main} = 1.6 \text{ L}\cdot\text{mol}^{-1}\cdot\text{s}^{-1}$ and $k_{self,AA} = 0.2 \text{ L}\cdot\text{mol}^{-1}\cdot\text{s}^{-1}$). (B) THF-SEC trace obtained by experiments at different molar ratios r of **AA** and **F** (Eq. (29) with $B = F$) upon irradiation (reaction conditions: 6 h irradiation; $\lambda_{max} = 360 \text{ nm}$; equimolar: $r = 1$, $c(\text{AA}) = 0.035 \text{ mol}\cdot\text{L}^{-1}$ and $c(\text{F}) = 0.070 \text{ mol}\cdot\text{L}^{-1}$, off-stoichiometric: $r = 1.43$, $c(\text{AA}) = 0.052 \text{ mol}\cdot\text{L}^{-1}$ and $c(\text{F}) = 0.070 \text{ mol}\cdot\text{L}^{-1}$). (C) Simulated SEC-trace for the small molecule reaction of the reaction between **AA** and **F**. The figure was adapted from ref.³⁸¹ with permission of the American Chemical Society.

As illustrated in Figure 4-6B, the experimental SEC-trace shows the formation of two major products and additional by-products with higher molecular weights. The main signals in the SEC traces were assigned to corresponding mono- or disubstituted **AA-F** and **F-AA-F**

species, respectively. Considering the off-stoichiometry case where $r = 1.43$, the formation of high molecular weight species $(\mathbf{AA})_k$ under the specified conditions was not significant (for ESI-MS spectra and $^1\text{H-NMR}$ refer to Appendix 8.1.3.2, Figure 8-2, Figure 8-3). Therefore, it can be assumed that the homopolymerization process is not dominating, despite the presence of an excess of \mathbf{AA} . However, a careful tuning of the stoichiometric monomer ratio is essential to achieve higher molar masses in the SG polymerization, as described in the following chapter.

4.2.3 Step-Growth Polymerization and Reaction Conditions Optimization

As it was stressed, by-product formation occurs in photo-induced DA reactions with *ortho*-methyl benzaldehydes based on an undesired HDA reaction. Therefore, off-stoichiometric ratios are required to obtain high molecular weight products in order to overcome the inherently faster consumption of the \mathbf{AA} monomer. Initially, the determination of the rate coefficients of the main and the side reaction was successful. Since the combination of simulated and experimental data achieved a qualitative description of the DA process for the small molecules, the SG polymerization was evaluated and simulated in a similar fashion. It is stressed that the experimentally obtained $k_{self,AA}$ and k_{main} have been directly used in the $k\text{MC}$ model without further parameter optimization, yet.

Theory of SG polymerization states that high molecular weights are obtained at high conversions, requiring equimolar stoichiometric conditions.³² Therefore, a first SG approach was carried out under equimolar monomer feed of \mathbf{AA} and \mathbf{BB} in DCM ($c_0(\mathbf{AA}/\mathbf{BB}) = 0.02 \text{ mol}\cdot\text{L}^{-1}$ for both monomers, refer to Figure 4-7A). The mixture was irradiated for 8 h, wherein the molecular weight evolution was followed by SEC (refer to Figure 4-7B) and the conversion by $^1\text{H-NMR}$ (refer to Figure 4-7D and E). By combining SEC and NMR analysis, the functional group conversion of \mathbf{AA} with time (refer to Figure 4-7F) could be correlated with the molecular weight evolution (refer to Figure 4-7G). The conversion of \mathbf{AA} was calculated by referencing the integrals of the aryl proton resonances in *para* position with respect to the aldehyde group (refer to Figure 4-7D, green) to the integrals of the α -proton resonances of the RAFT group (refer to Figure 4-7D, blue). In terms of selecting other signals for determining the conversion, integrals of aldehyde proton resonances are unreliable (refer to Figure 4-7D, red).

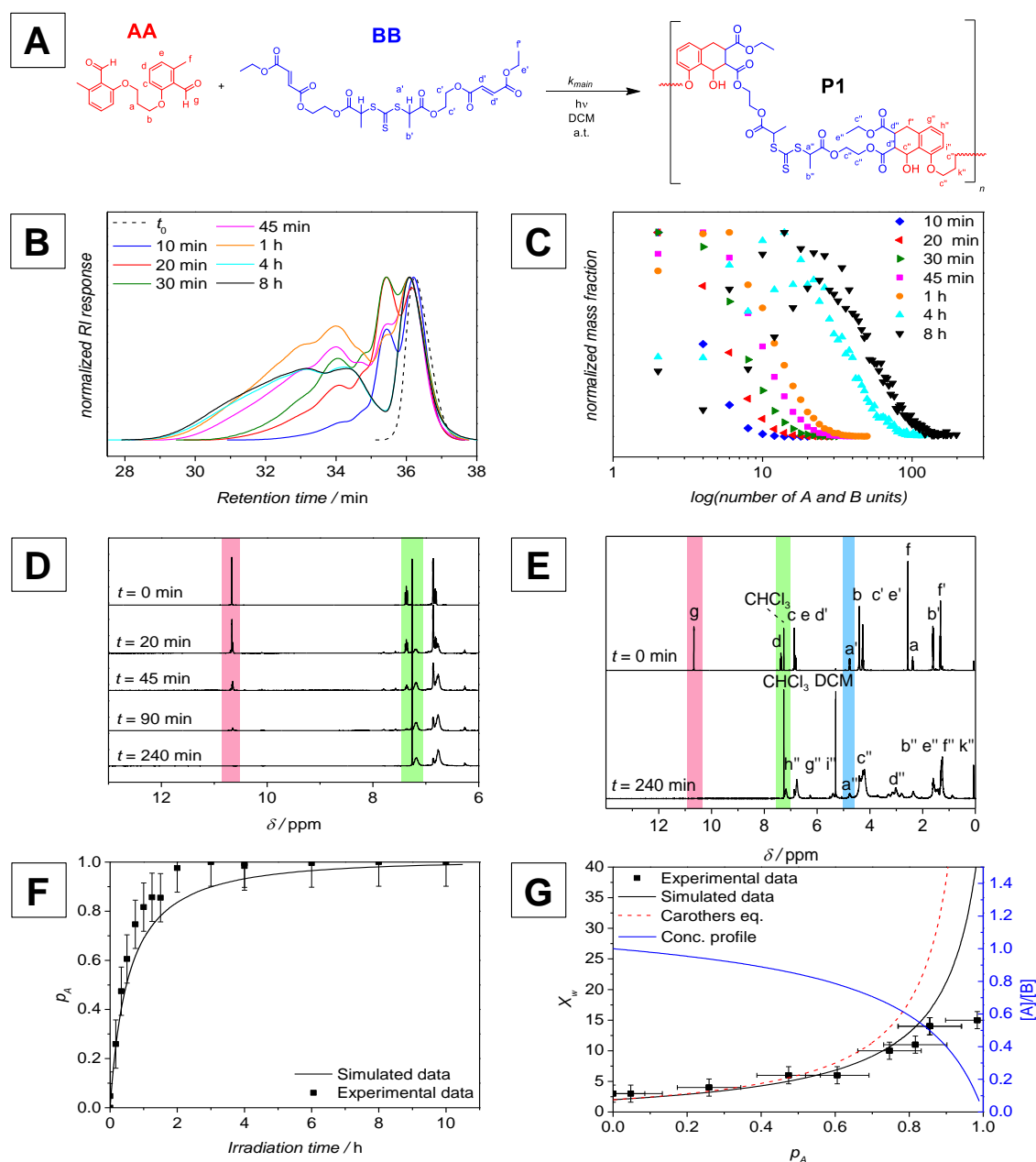


Figure 4-7. (A) Reaction scheme of the SG polymerization. (B) Experimental THF-SEC-traces of the SG polymers **P1** ($r = 1$); c_0 (**AA**, **BB**) = 0.02 mol·L⁻¹; $\lambda_{\text{max}} = 360$ nm). (C) Simulated SEC traces for SG polymerization obtained by *k*MCM ($k_{\text{main}} = 1.6$ L·mol⁻¹·s⁻¹ and $k_{\text{self,AA}} = 0.2$ L·mol⁻¹·s⁻¹ based on Figure 4-4 and Figure 4-6 (D and E) $^1\text{H-NMR}$ spectra of the SG polymerization kinetics, showing resonances of the aldehyde and the *para* proton of the phenyl ring (h'' in (E)) with respect to the benzaldehyde functionality (red, g in (E)). Full assignment in reference to (A) for **AA**, **BB**, and **P1**, additionally ESI-MS data in Appendix 8.1.4, Figure 8-6. Spectra were recorded in CDCl_3). (F) Conversion of benzaldehyde (determined both experimentally and by simulation) vs. irradiation time. (G) Carothers plot, illustrating experimental and *k*MCM simulated mass average chain length (X_w) vs. benzaldehyde conversion (evaluated by SEC and NMR, respectively). Carothers plot without parameter optimization is illustrated in red dotted line. Concentration ratio of **A** to **B** is illustrated by the blue line. The figure was adapted from ref.³⁸¹ with permission of the American Chemical Society.

In addition, an overlapping of the fumarate resonances with changing resonances of the *meta*- and *ortho*- aryl protons eliminates reliable evaluation. A broadening of all $^1\text{H-NMR}$ resonances complicated the analysis further. Nevertheless, as illustrated in Figure 4-7F,

comparable experimental and simulated data were obtained for the SG polymers with increasing irradiation time. The simulated SEC traces are in close agreement to the experimental data, showing a significant increase of the molar mass with time ($r = 1$, refer to Figure 4-7C). By considering the evolution of mass average chain length X_w , it becomes obvious that the curve obtained from Carothers' theory (refer to Figure 4-7G, red dotted line) is deviating from the experimental data as well as from the simulated evolution (black line). The deviation can be explained by the uncredited side reaction of the **AA** monomer, creating a virtual off-stoichiometry despite equimolar feeding ratio of both monomers. Nevertheless, the Carothers equation (refer to Eq. (30)) for X_w represents the basis of the simulations and in this form it is capable to include the side reactions and the virtual off-stoichiometry r :^{32,391}

$$X_w = \frac{\left(1 + \frac{1}{r}\right)(1 + p)}{\left(1 + \frac{1}{r} - \frac{2p}{r}\right)} \quad \text{with } p: \text{ conversion, } r: \text{ refer to Eq. (29)} \quad (30.)$$

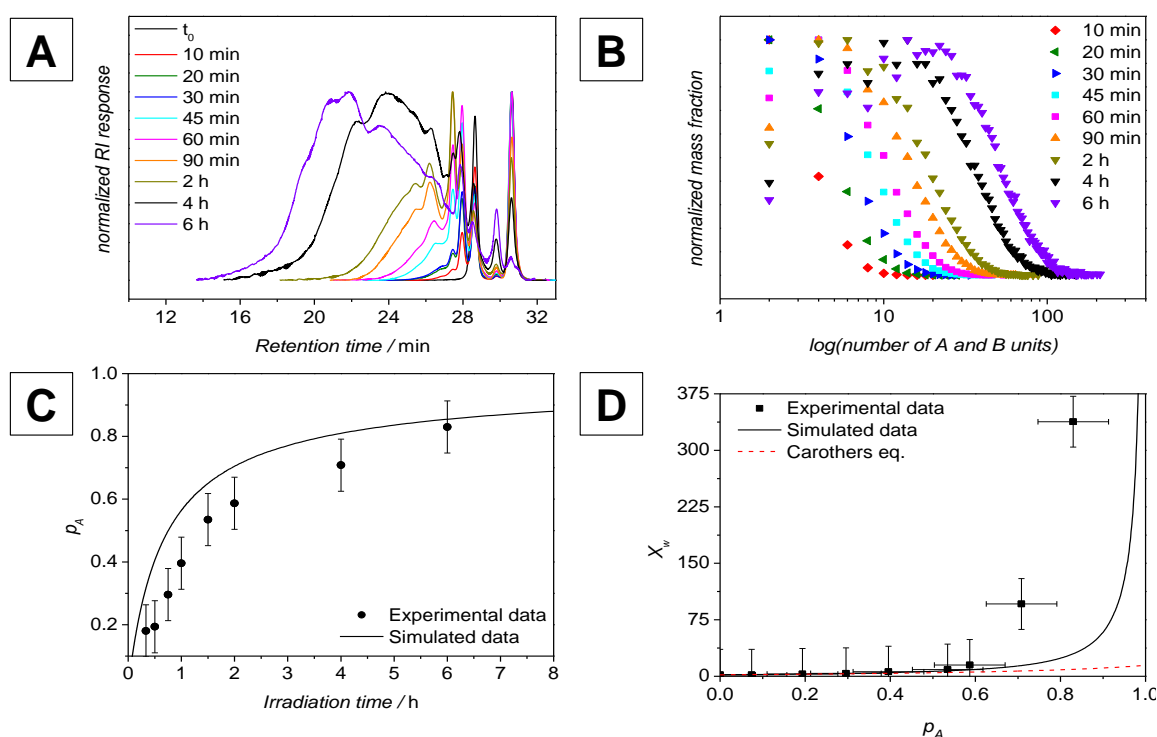


Figure 4-8. (A) SEC-traces of the SG kinetic run (relative values) with a stoichiometry of $r = 1.75$, recorded in THF ($c_0(\text{AA}) = 0.04$ to $0.07 \text{ mol}\cdot\text{L}^{-1}$ with off-stoichiometry, $c_0(\text{BB}) = 0.04 \text{ mol}\cdot\text{L}^{-1}$ in DCM ($\lambda_{\text{max}} = 360 \text{ nm}$). (B) SEC-traces of the SG polymerization (absolute values) obtained by kMC simulations (normalized by peak height). The dimers **AAAA** and **AABB** are located at $x = 4$. (C) Conversion vs. irradiation time. (D) Mass average chain length (X_w) vs. conversion, determined by SEC and NMR, respectively. Red dotted line illustrates Carothers theory, as noted in Eq. (30) for $r > 1$, and black line derived by simulations. The figure was reprinted from ref.³⁸¹ with permission of the American Chemical Society.

Carothers theory also states that high molar masses in SG polymerizations are exclusively formed at high conversions.³² Certainly, this does not hold true when the side reaction causes an intrinsic and *in situ* stoichiometric imbalance occurring at early stages of the SG (refer to Figure 4-7G, unintended $r < 1$). A few stoichiometric ratios were examined: (i) if $r = 1$, **AA** is consumed faster than **BB** leading to a majority of oligomeric and polymeric species with unreactive fumarate end-groups. Nevertheless, *k*MCC modeling can better justify the evolution of X_w , since the side reaction is taken into account. (ii) If $r = 1.75$, good agreement between simulated and experimental SEC traces was obtained (refer to Figure 4-8A-D). A significant shift to higher molar masses can be observed after irradiation for 6 h that is in close agreement with the simulated traces (refer to Figure 4-8B). When $r = 1.75$, it suggests that the overall reaction progress is slower (refer to Figure 4-8) than at $r = 1$ due to the increased occurrence of the slower **AA** homopolymerization. Thus, the overall SG polymerization is supposed to be retarded. The evolution of X_w determined by experimental and simulated data was compared to the theoretical X_w by Carothers theory in Eq. (30) (refer to Figure 4-8D). As expected, Carothers equation including the off-stoichiometry does not match the experimental data due to unaccounted side reaction. Nonetheless, *k*MCC simulations provided good approximations for the X_w evolution with conversion, since the side reaction is included in the SG processes.

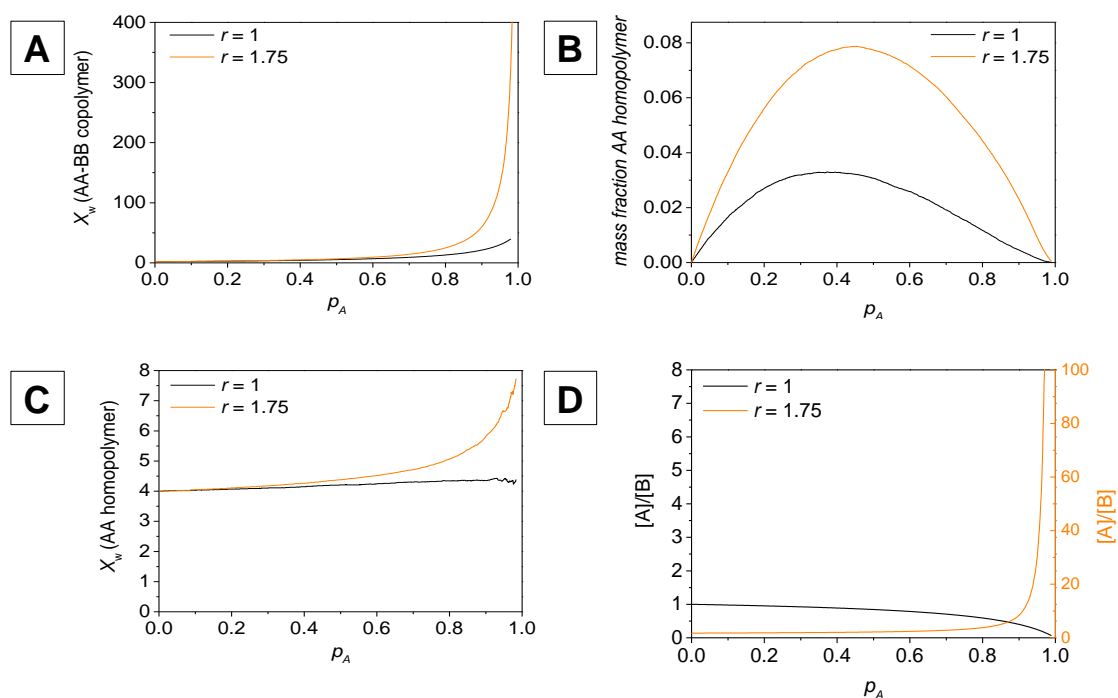


Figure 4-9. Simulated data of the cases $r = 1$ and $r = 1.75$, (A) X_w of the SG polymer **P1**, i.e. no $(\text{AA})_k$ homopolymer chains are accounted. (B) Homopolymer **AA** mass fraction vs. benzaldehyde conversion. (C) Homopolymer mass average chain length excluding the **AA** monomer. (D) Concentration ratio of both functional groups **A** and **B** vs. benzaldehyde conversion. The figure was reprinted from ref.³⁸¹ with permission of the American Chemical Society.

Further, when $r = 1.75$, high molar masses were obtained because the higher **AA** feed equalized the higher consumption of **AA** during the SG process. In simulations, the X_w profiles clearly show an increase in molar mass at conversions above 0.8 for $r = 1.75$ (refer to Figure 4-9A). Indeed, a higher fraction of homopolymerization was formed predominantly in the early stage of the polymerization, and therefore, $(\mathbf{AA})_n$ block segments were accumulated to a significant extent (increasing homopolymer fraction to approx. 50% conversion in Figure 4-9B, Figure 4-10, stage 1).

These homopolymer blocks were then subsequently incorporated into the SG copolymer due to the reaction of all available functional groups (refer to Figure 4-9B). Since coupling of homopolymer and copolymer chains occurs randomly, homopolymer blocks can react with each other to significantly increasing their block length (refer to Figure 4-9C, red), supporting the trend of X_w in Figure 4-9A (red). In this scenario, the current concentration ratio $[\mathbf{A}]:[\mathbf{B}]$ with a feeding stoichiometry of $r = 1.75$ is larger than 1 and diverges to infinity at higher conversions due to the complete consumption of the free fumarates (orange line, right y-axis, refer to Figure 4-9D). When the feeding stoichiometry is $r = 1$, the current concentration ratio $[\mathbf{A}]:[\mathbf{B}]$ is < 1 and decreases due to the increasing consumption of **A** (black line, left y-axis, refer to Figure 4-9D). At the end of the reaction, the end-groups or in general the remaining functional groups are fumarates. For illustration of the processes, the different stages of the SG polymerization are qualitatively shown in Figure 4-10.

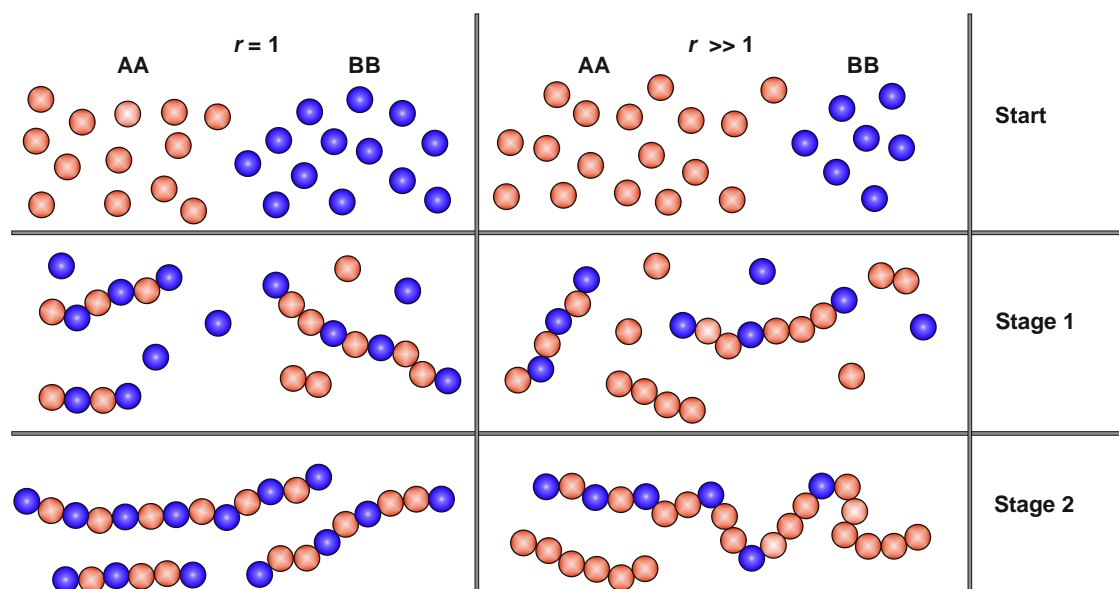


Figure 4-10. SG polymerization at different stages: At first, the monomers are present in equal molarity or off-stoichiometry. In Stage 1 high consumption of **AA** leads to the formation of homopolymer segments, in view of the discussion in Figure 4-9; left: $r = 1$ and right $r \gg 1$. For $r = 1$, **AA** consumption finally yields polymer and oligomer chains with **BB** end-groups, preventing the formation of long polymer segments. For $r \gg 1$, all fumarate groups are reacted. However, the formation of **AA** homopolymer chains is the inevitable result of the initial higher **AA** feeding ratio. The figure was reprinted from ref.³⁸¹ with permission of the American Chemical Society.

The homopolymer segments, formed during the SG, are incorporated into the copolymers with randomly distributed **AA** block lengths. For different conversions 0.1, 0.45 and 0.8, representing qualitatively the different stages in Figure 4-10, the mass chain length distributions of the SG polymers (closed symbols) were simulated for the stoichiometric cases $r = 1$ and $r = 1.75$ (refer to Figure 4-11). In addition, the independent distributions of the **AA** homopolymer (open symbols) were calculated separately. As previously shown in Figure 4-9, the contribution of the **AA** homopolymer to the overall chain length is higher at $r \gg 1$, most apparent at higher conversions. From the simulations in Figure 4-11, a more detailed evaluation of the individual distributions is allowed since conclusions from X_w do not differentiate between homo- and copolymer segments (as in Figure 4-9A and C). In case of $r = 1.75$, a rather broad distribution is obtained yielding high dispersities as precursor for the RAFT polymerization. A matter of concern would be the high dispersity that might hinder a successful RDRP. However, this approach does not focus on the control of the dispersity as in every other RDRP. Indeed, sequential SG and RAFT polymerization defines 'control' merely by the successful incorporation of corresponding monomers in the RAFT process.

In conclusion, the SG polymerization could be optimized with respect to maximize the molecular weight. Here, the simulations showed good agreement with experimental data by accounting for the side reaction into the SG process.

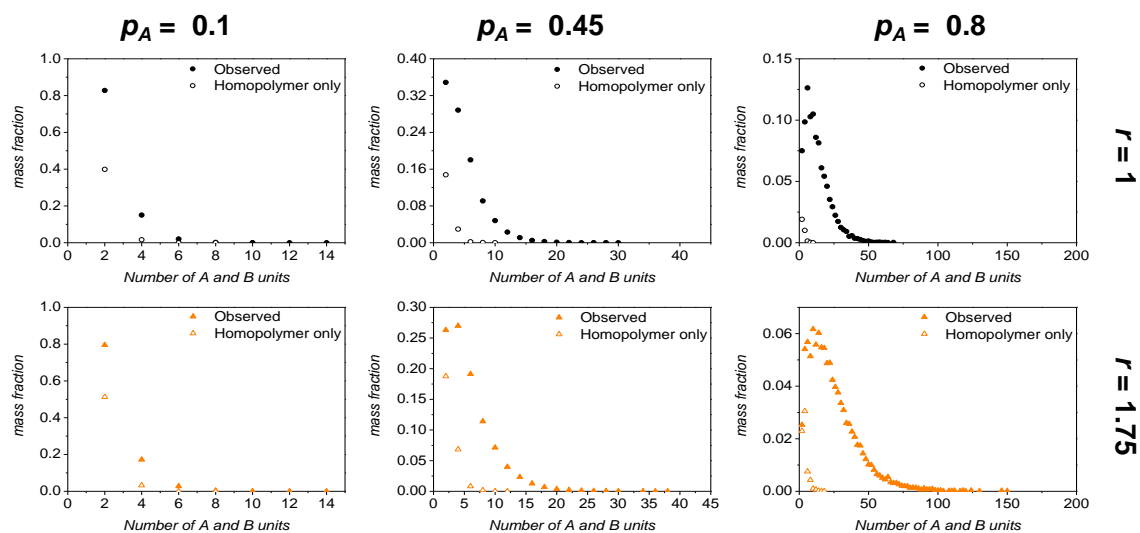


Figure 4-11. Mass chain length distributions obtained by simulations at varying benzaldehyde conversion 0.1, 0.45 and 0.8 for the case of $r = 1$ (black symbols) and $r = 1.75$ (orange) obtained by simulations. Open symbols illustrate the **AA** homopolymer conditional distribution. The figure was reprinted from ref.³⁸¹ with permission of the American Chemical Society.

4.2.4 Preparation of Suitable multi-CTA for RAFT Polymerization

As the ideal r value after SG optimization does not ideally represent the optimum for the RAFT polymerization, the SG polymer as precursor for RAFT has to fulfil some requirements. By targeting the 'best' SG polymerization, high molecular weights are of primary interest. Nonetheless, a large SG polymer could have a rather irregular incorporation of the RAFT groups due to long and impractical **AA** homopolymer blocks, being less suitable as precursor for the RDRP. Secondly, depending on the molar mass of the precursor SG polymer, the SG polymer has to be sufficiently soluble in the RAFT polymerization reaction medium. Lastly, a shorter irradiation time and higher starting feed of **AA** slows the net rate of the SG polymerization, due to a slower rate of the **AA** homopolymerization. In order to increase the molecular weight of the SG polymer successively, different stoichiometric ratios were employed. For identical SG polymerization conditions, different ranges of molar mass distributions were obtained with variable r , demonstrating highest molecular masses for $r = 1.75$ (refer to Figure 4-12A and B). Apparently, a significant increase of X_w was achieved for $r \geq 1.20$ in comparison to $r \approx 1.00$. Although the solubility of the SG polymer in DCM was acceptable for all cases, the solubility in styrene as reaction medium in the RAFT polymerization was poor for the SG polymer from $r = 1.75$. Since long block lengths and a high percentage of **AA** homopolymer are not ultimately targeted, a SG polymer with $r = 1.5$ was selected to be suitable for the multi-CTA in RAFT polymerization (refer to Chapter 4.2.5, Figure 4-14). In addition, the decrease of X_w at $r = 2$ can be explained by the slow homopolymerization of **AA**. Higher molecular weights with large excess of **AA** ($r > 1.75$) may be obtained only at longer irradiation times ($t > 6$ h).

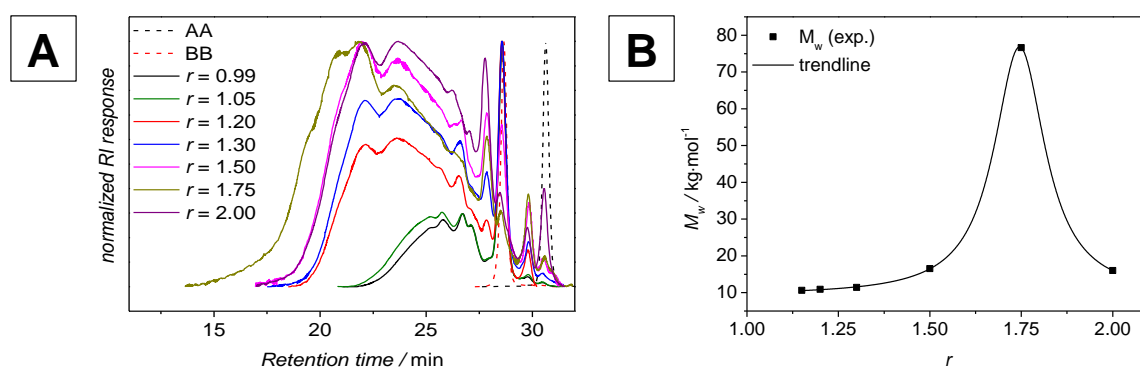
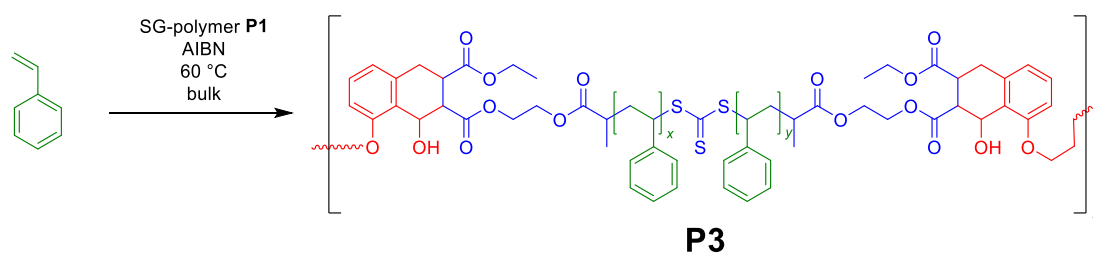


Figure 4-12. SG polymerization at different stoichiometries r (A) SEC traces and (B) mass average molar mass (M_w) vs. stoichiometry factor r as illustrated in Scheme 4-2. In (B) trend line for guiding the eye; initial **BB** concentration 0.04 mol L^{-1} in DCM, irradiation for 6 h ($\lambda_{\text{max}} = 360 \text{ nm}$). The figure was reprinted from ref.³⁸¹ with permission of the American Chemical Society.

To verify the presence of the trithiocarbonate group within the SG polymer, ^{13}C -NMR and UV-Vis spectroscopy were employed. In the ^{13}C -NMR spectra no trithiocarbonate resonances were detected, which is attributed to the plethora of macrospecies and in general weak resonances of trithiocarbonates. However, the resonances of the protons adjacent to the trithiocarbonate at 4.77 ppm in ^1H -NMR could be followed as the SG polymerization proceeds, verifying the presence of the trithiocarbonate (refer to Appendix 8.1.4, Figure 8-4, Figure 8-5). A broadening of the resonances occurs due to the polymerization, as expected. In the UV-Vis spectra, the trithiocarbonate could be successfully identified by its characteristic absorbance maximum at approx. 300 nm (refer to Appendix 8.1.4, Figure 8-7).

4.2.5 Segmented Copolymers *via* RAFT Polymerization of P1

The incorporation of RAFT moieties into the backbone of the SG polymer **P1** allows for its utilization as multi-CTA for RAFT polymerization (refer to Scheme 4-2A). As mentioned previously, an 'ideal' r -value is not necessarily universal for both SG and RAFT polymerization. A SG polymer was chosen as the appropriate multi-CTA with $r = 1.5$, implying the advantage of lower **AA** homopolymer content (refer to Figure 4-12) and suitable solubility in the polymerization medium. Here, styrene was introduced into the backbone forming polymer segments between the RAFT groups within the SG repeating unit. In a typical bulk RAFT polymerization, AIBN was employed as initiator with **P1** as the multi-CTA for 4 h at 60 °C (refer to Scheme 4-3).



Scheme 4-3. RAFT polymerization employing the SG polymer **P1** as multi-CTA to obtain the segmented copolymer **P3**.

Symmetric trithiocarbonates are capable to fragment into two directions, *i.e.* polymer chains are growing on both sides of the RAFT group. In this application, the RAFT fragmentation initiates a random reorganization and reshuffling of all polymer chains, bearing RAFT moieties. Since the number of RAFT moieties is highest for long SG chains – assuming identical homopolymer fractions in all chains – the probability of RAFT exchange is logically higher for long polymer chains, as the probability of RAFT exchange is the sum of the probabilities for each RAFT group. To describe the evolution of the

molecular weight and to understand the processes involved in the RAFT polymerization, *in silico* investigations were carried out on the basis of the SG polymer **P1** prepared at $r = 1.5$ (refer to Figure 4-13). The RAFT addition/fragmentation is described in a *kMC* calculation by one encompassing rate coefficient $k_{tr} = 5.0 \cdot 10^4 \text{ L} \cdot \text{mol}^{-1} \cdot \text{s}^{-1}$. This parameter summarizes all transfer reactions by only one rate coefficient, with respect to the later mentioned number of all identified processes during the RAFT polymerization (refer to Appendix 8.1.1.2, Table 8-2). It is important to note that at low conversions the SG polymer contributes largely to the overall molar mass of the polymer, while the opposite is true at higher conversions. Thus, higher discrepancies were observed in the molar mass distributions between the experimental and the simulated data at lower conversions, due to the polystyrene calibration in experimental SEC measurements. At higher conversions, better agreement is given since the fraction of polystyrene dominates and the SG polymer contributes less to the overall number of chain units.

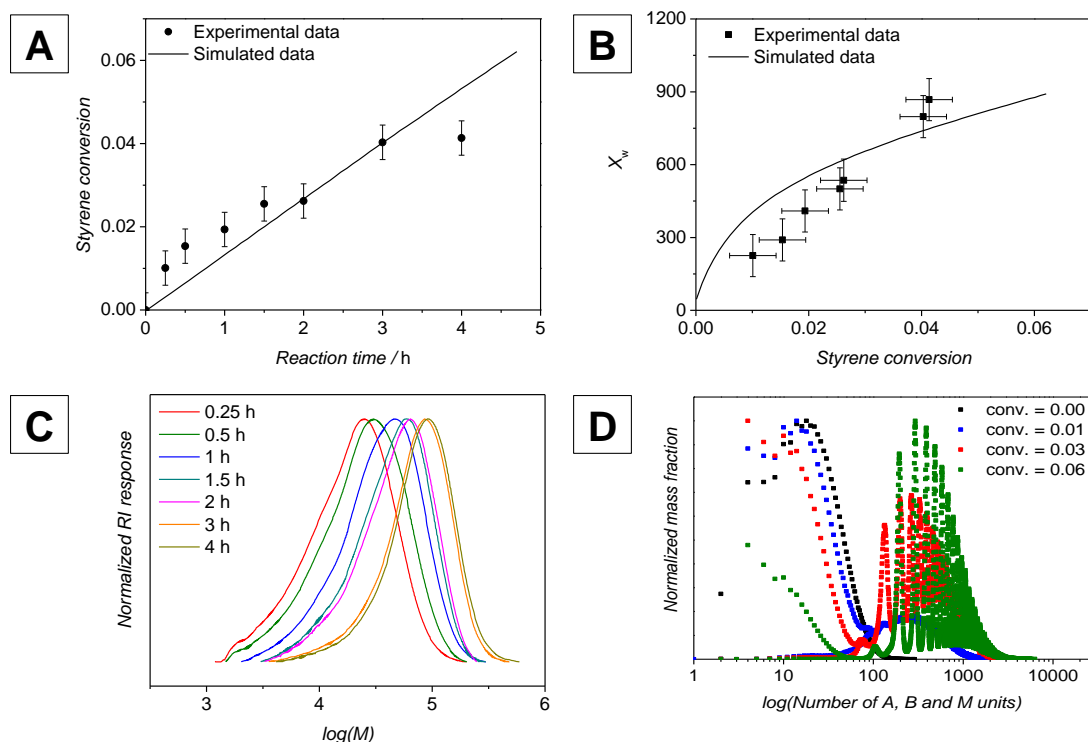


Figure 4-13. (A) Evolution of styrene conversion with reaction time. (B) Development of X_w with styrene conversion. (C) Molecular weight distributions of the segmented copolymers with time, employing a SG polymer **P1** from a stoichiometry $r = 1.5$ (normalized intensity). (D) Simulation of mass chain length distribution for varying styrene conversions (total number of units with a differentiation on the level of **A**, **B** or **M**); $[\text{Styrene}]_0 = 8.74 \text{ mol} \cdot \text{L}^{-1}$, $[\text{I}_2]_0 = 4.85 \cdot 10^{-3} \text{ mol} \cdot \text{L}^{-1}$; $[\text{mCTA}]_0 = 5 \cdot 10^{-3} \text{ mol} \cdot \text{L}^{-1}$ at $60 \text{ }^\circ\text{C}$. The figure was reprinted from ref.³⁸¹ with permission of the American Chemical Society.

Furthermore, the simulated SEC-trace for the highest styrene conversion (0.06, refer to Figure 4-13D, green) illustrates consecutive small peaks, representing styrene incorporation to macrospecies with a higher number of RAFT groups. Based on the initial

monomer feed and conversion, an average of 70 monomer units per segment is incorporated (for the case a precursor SG with $r = 1$ was used, refer to Appendix 8.1.5, Figure 8-8). After successful parameter optimization, the determination of the RAFT group distribution was examined *in silico* for a fixed chain length. In Figure 4-14, the mass chemical composition – chain length distributions (CC-CLDs) are depicted for four styrene conversions (0, 0.01, 0.03 and 0.06). The y-axis represents the number of RAFT groups whereas the chain length on the x-axis is defined as the sum of **A**, **B** and **M** (styrene) units. The information from the CC-CLD of the precursor polymer with $r = 1.5$ suggests only a small number of homopolymer segments (refer to Figure 4-14A). The white line in Figure 4-14A represents an equal number of **A** and **B** or **AA** and **BB** (RAFT) molecules, *i.e.* in practice a strictly alternating incorporation of **AA** and **BB** units. Here, the SG species are in close proximity to the white line, *i.e.* an almost perfect alternating incorporation of **BB** and thus, of RAFT moieties. Depicting a chain length of 100 units in the SG polymerization, ideally 50 **A** and 50 **B** units are incorporated into the chain, *i.e.* 25 **AA** and **BB** monomer units (also denotes RAFT moieties). Due to the homopolymerization, the species with a chain length of 100 units in Figure 4-14A illustrates only approx. 20 RAFT moieties, *i.e.* additional 10 **A** units with block lengths of 2-3. Nevertheless, the low number of additional **A** units determined by *in silico* investigations suggest that the RAFT groups are well-located in the SG polymer before the RAFT polymerization. The maximum chain length noticeably increases at a conversion of 0.01, due to incorporation of styrene. Hence, the number of units rises from 50 to 2000 (refer to Figure 4-14B) and the number of RAFT moieties from approx. 30 to 60. Clearly, the probability of a dormant chain to become active is proportional to the number of RAFT groups in a respective chain. Consequently, the release of a long multifunctional active chain is promoted at low reaction times. During the next RAFT step, a long active chain reacts with another long dormant polymer chain statistically releasing a shorter chain. As a result of this, a significant increase of the chain length of the newly formed dormant polymer chain occurs. The generation of high molar mass polymer chains bearing multiple RAFT moieties implies the broadening of high mass fractions at low styrene conversions in comparison to the SG precursor (yellow areas, refer to Figure 4-14B). By investigating the number of terminated chains, only an insignificant amount of termination events is present due to the high end-group fidelity (EGF) (refer to Figure 4-15A, refer to Appendix 8.1.5, Figure 8-10). One explanation can be attributed to diffusion, since the presence of the SG polymer at the initial stage already lowers the number of termination events at rather low styrene conversions. As expected, the growth of the maximal chain length continues at higher styrene conversions of 0.03 and 0.06 (refer to Figure 4-14C and D), concurrent with increasing incorporation of styrene units. In terms of RAFT groups, the average number is marginally decreasing to approximately 55, as

observed by the smeared yellow areas at higher styrene conversions to lower numbers of RAFT moieties (refer to Figure 4-14B-D). Apparently, the fragmentation with respect to the number of RAFT groups presumably changes. Such a phenomenon could be caused by an averaging of the polymer chain lengths with increasing styrene conversion, due to participation of also shorter polymer chains in the RAFT process. A dual shift of the RAFT group distributions with increasing styrene conversion can be observed in Figure 4-15B. Here, a shift to higher numbers of RAFT groups is observed at conversions up to 0.01, whereas a gradual shift to lower numbers of RAFT groups occurs up to styrene conversions of 0.06.

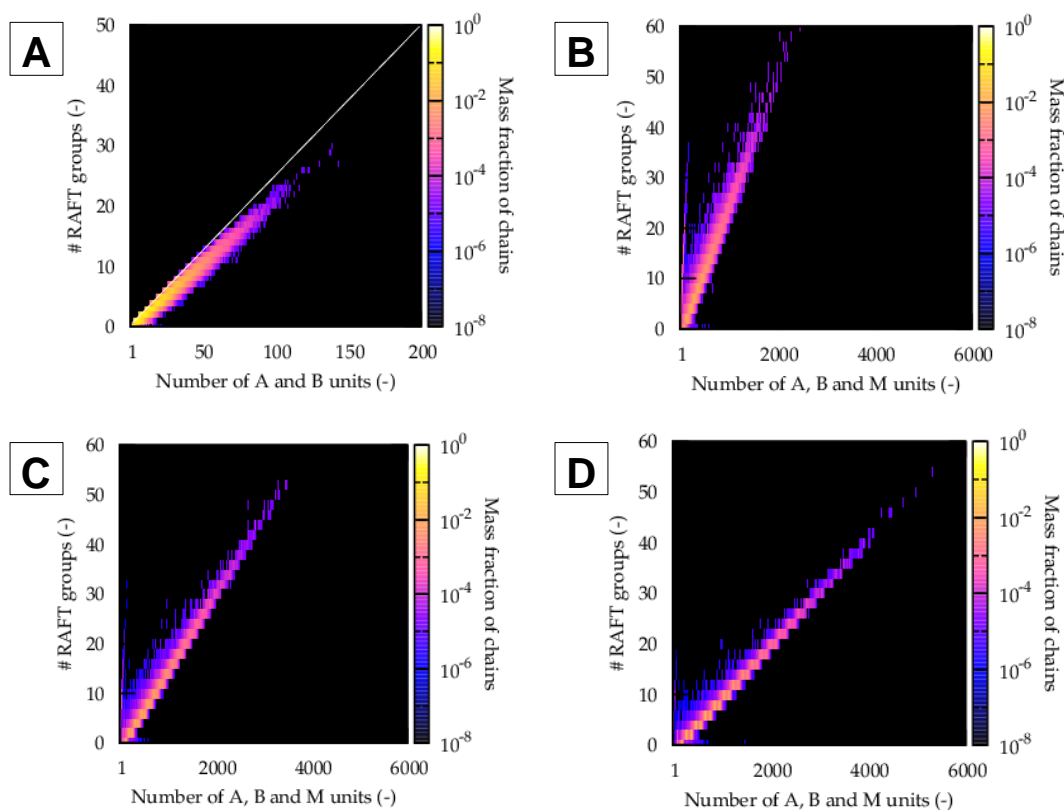


Figure 4-14. Chemical composition chain length distribution (CC-CLD) at varying styrene conversions of 0.00 (A), 0.01 (B), 0.03 (C) and 0.06 (D). On the x-axis the number of **A**, **B**, and **M** (styrene) units represents the overall chain length in the chains, on the y-axis the number of RAFT groups of a chain with length i (*i.e.* the composition) is outlined. The heat map illustrates the mass fraction of chains. To (A): White line represents ideal ratio of **A** to **B** units. In the precursor SG polymer **P1**, only slight deviation from the white line is given for the SG polymer with $r=1.5$ (only minor homopolymer segments). For the CC-CLDs for $r=1$, refer to Appendix 8.1.5, Figure 8-9. The figure was reprinted from ref.³⁸¹ with permission of the American Chemical Society.

Evidently, the RAFT group distribution of the segmented copolymer approaches the original distribution of the SG precursor polymer with an average of 13 RAFT groups. Therefore, we suppose a successful RAFT process and a well-defined synthesis of the segmented copolymers.

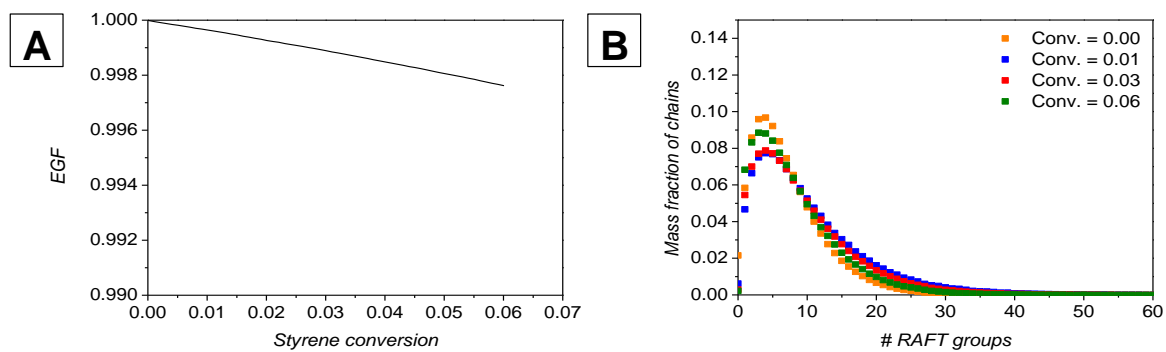
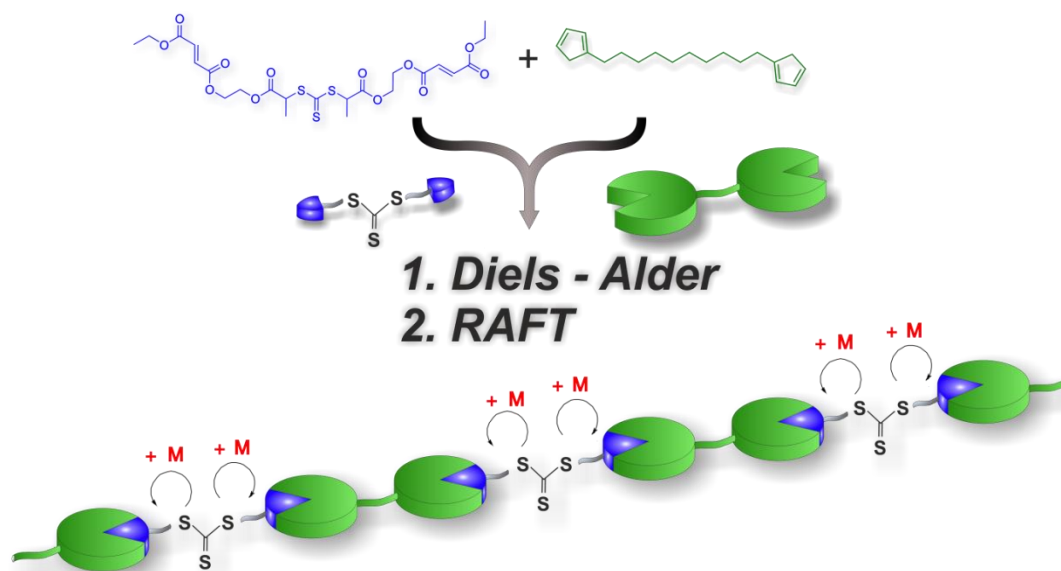


Figure 4-15. (A) End-group fidelity (EGF) vs. styrene conversion. (B) Mass chemical-composition distributions for corresponding CC-CLD in Figure 4-14. The figure was adapted from ref.³⁸¹ with permission of the American Chemical Society.

4.3 Step-Growth by Thermally Induced DA Reactions and Subsequent RAFT Polymerization: Synthesis of Segmented Copolymers

4.3.1 Reception and Concept Design

In Chapter 4.2 it was demonstrated that the utilization of photoenols from *ortho*-methyl benzaldehydes in combination with fumarates in photo-induced DA reactions led to the generation of well-defined segmented copolymers. Certainly, a side reaction was present that could be successfully described and accounted by *kMC* simulations. The disadvantages of the previously shown concept concern the SG polymerization, *i.e.* the occurring side reaction, irradiation with UV-light, and the need of an inert gas atmosphere. In this part, a concept for similar SG and subsequent RAFT polymerization is presented to overcome the aforementioned drawbacks.



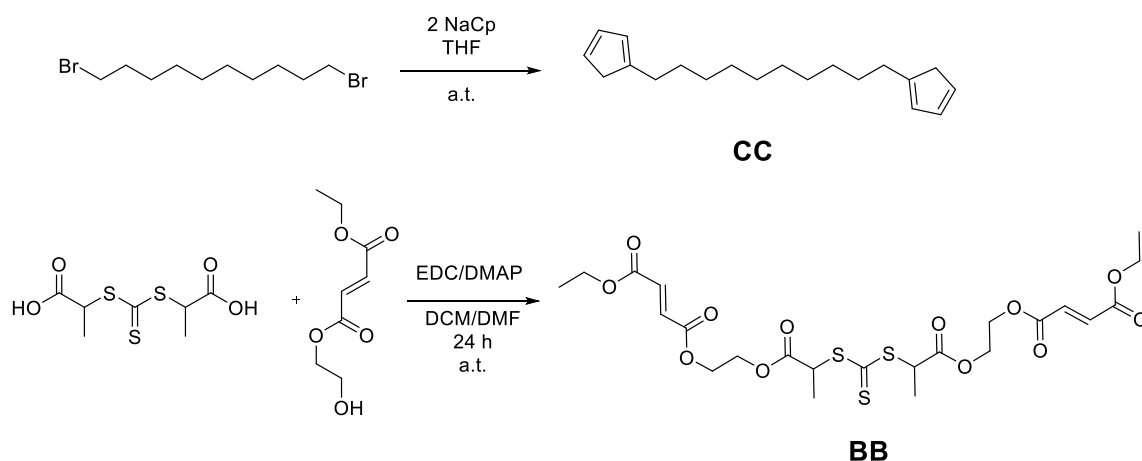
Scheme 4-4. Schematic illustration of the SG polymerization via DA reaction and subsequent RAFT polymerization. The figure was reprinted from ref.³⁹² with permission of the Royal Chemical Society.

Therefore, efficient thermally induced DA reactions are introduced. The selection of the SG system is based on highly reactive cyclic dienes, *i.e.* cyclopentadiene, in combination with a suitable dienophile, here a difumarate. Such DA systems were applied in the literature in combination with borenium salt catalysts for enantioselective product generation.³⁹³ In the current chapter, the reaction conditions for the SG polymerization are restricted to ambient temperature, no inert gas atmosphere, and the exclusion of a catalyst. In comparison to the photoenol system, the diene monomer was substituted by a di(cyclopentadienyl) (DiCp, **CC** monomer) in combination with the RAFT difumarate dienophile, referred to as monomer **BB** introduced in Chapter 4.2 (refer to Scheme 4-4).

After the SG, a subsequent RAFT polymerization employing the SG polymer as multi-CTA is carried out to obtain segmented copolymers.^B

4.3.2 Preliminary Tests, Monomer Synthesis and Stability Confirmation

The monomer design is illustrated in Scheme 4-5 including the dicyclopentadienyl (**CC**)¹⁹⁶ and the previously employed dienophile and RAFT agent with two fumarate end-groups (**BB**).³⁸¹ The synthesis of both monomers was conducted in a non-challenging procedure, yielding the monomers in good purity (for experimental details and characterization refer to Chapter 7.3).



Scheme 4-5. Design of the monomers **CC** and **BB** for the thermally induced DA SG polymerization.

Before the SG polymerization was carried out, a detailed monomer analysis and a stability test of the **CC** monomer were carried out to exclude any side reaction under the desired reaction conditions. Since monomer **BB** has already been proven to be unaffected and stable even under UV irradiation, the cyclopentadienyl **CC** monomer stability was investigated due to the common dimerization of Cp moieties under ambient conditions.³⁹⁴ During the synthesis, an inevitable amount of the **CC** monomer underwent dimerization which cannot be avoided (refer to Figure 4-16A). Therefore, directly after the synthesis, a minor part of the Cp functionalities is already unavailable for reaction. However, upon dimerization, one obtains still difunctional compounds, being available to participate in a polymerization process. To test the stability of the **CC** monomer after the synthesis, the compound was stirred without a reaction partner in DCM at the concentration of 0.2 mol·L⁻¹. In contrast to the photoenol SG system, the herein employed diene monomer

^B Parts of this chapter are reproduced or adapted from Gegenhuber, T.; Schenzel, A. M.; Goldmann, A. S.; Zetterlund, P. B.; Barner-Kowollik, C. *Chem. Commun.* **2017**, 53 (77), 10648–10651 with permission from the Royal Society of Chemistry. A. M. Schenzel was involved in the CC monomer design. P. B. Zetterlund participated in discussions and manuscript revisions. A. S. Goldmann, and C. Barner-Kowollik motivated and supervised the project.

did not show any side reactions under these conditions, illustrating only a negligible change in the SEC trace, as well as in the $^1\text{H-NMR}$ spectra (refer to Figure 4-16A and B).

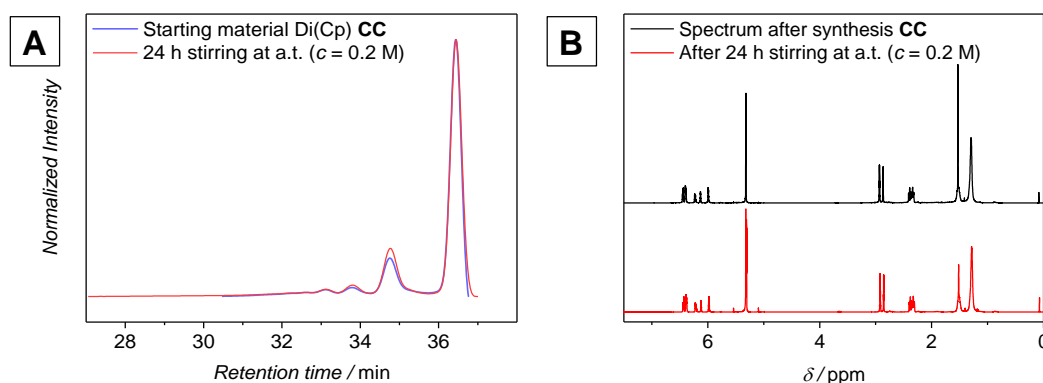
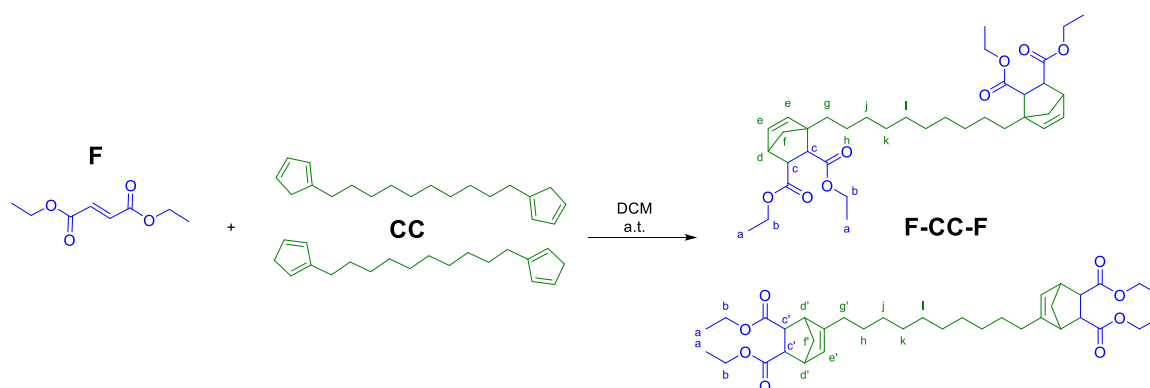


Figure 4-16. Stability test of the **CC** monomer *via* stirring at ambient temperature at the concentration of $0.2 \text{ mol}\cdot\text{L}^{-1}$ in DCM. (A) SEC-traces before and after the stability assay. (B) $^1\text{H-NMR}$ spectra of the **CC** monomer before and after the test. The figure was reprinted from ref.³⁹² with permission of the Royal Chemical Society.

4.3.3 Small Molecule Studies

Initially, to introduce the DA reaction and demonstrate its ease, a small molecule study was conducted, utilizing the **CC** monomer in combination with an excess of a monofumarate molecule (2.8 eq.), here, diethyl fumarate **F** (refer to Scheme 4-6). The reaction conditions were selected similar to the previous stability assay at ambient temperature, without catalyst or inert gas atmosphere to ultimately obtain the adduct **F-CC-F** ($c(\text{CC}) = 0.085 \text{ mol}\cdot\text{L}^{-1}$).



Scheme 4-6. Small molecule study using the **CC** monomer in combination with diethyl fumarate **F**. Due to the different constitutional isomers of **CC** in total four different isomers can be obtained, of which two are illustrated here.

In SEC analysis, a shift of the starting materials towards higher molar mass species was observed, representing the adduct **F-CC-F** (refer to Figure 4-17A). The assumed di-, tri- or n-mers of the **CC** monomer also underwent reaction with the small fumarate molecule, proving their availability in a SG polymerization. Additionally, in ESI-MS the main adduct

peak could be observed in good agreement to calculated data (refer to Figure 4-17B). In the $^1\text{H-NMR}$ spectrum of the crude product (refer to Figure 4-17C with assignment in D), residual diethyl fumarate **F** could be observed, as well as the expected corresponding signals of the adduct **F-CC-F**. The **CC** monomer is a mixture of several constitutional isomers, as the alkyl chain is attached to the Cp either at position 1 or 2 of the ene. Therefore, four different isomers can be formed in the small molecule reaction. As in DA reactions an *exo* or *endo* attack of the Cp to the double bond can occur, these species are not specifically assigned in the spectrum. *Via* the selected reaction conditions, a facile reaction procedure yielded the desired product, underpinning the ease of the method's applicability.

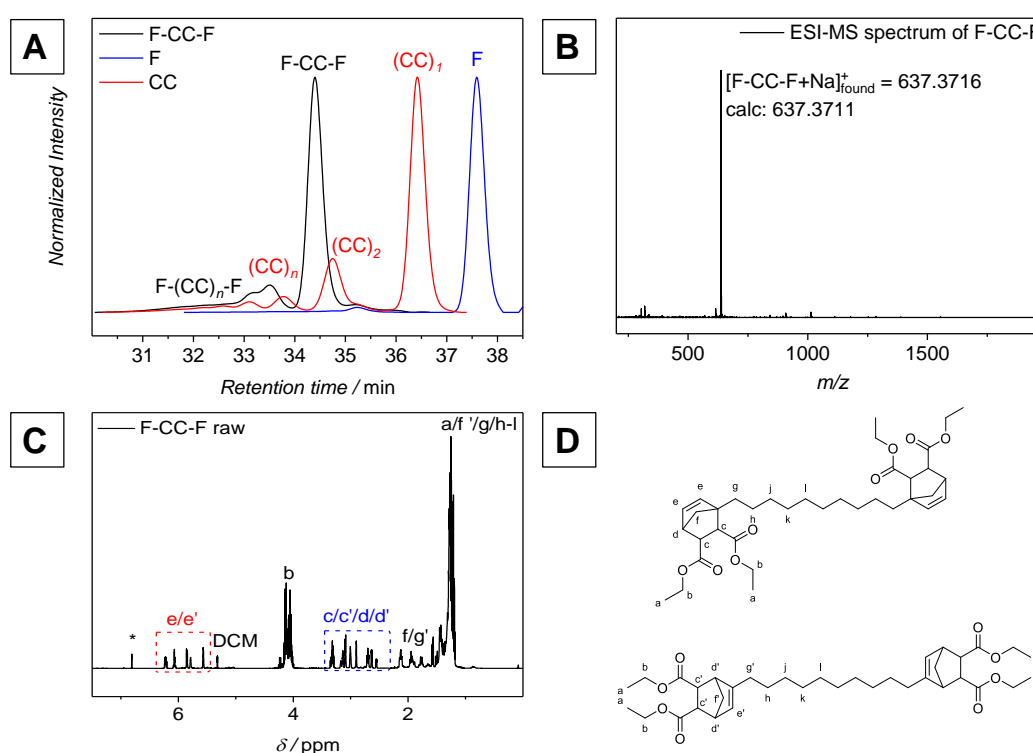
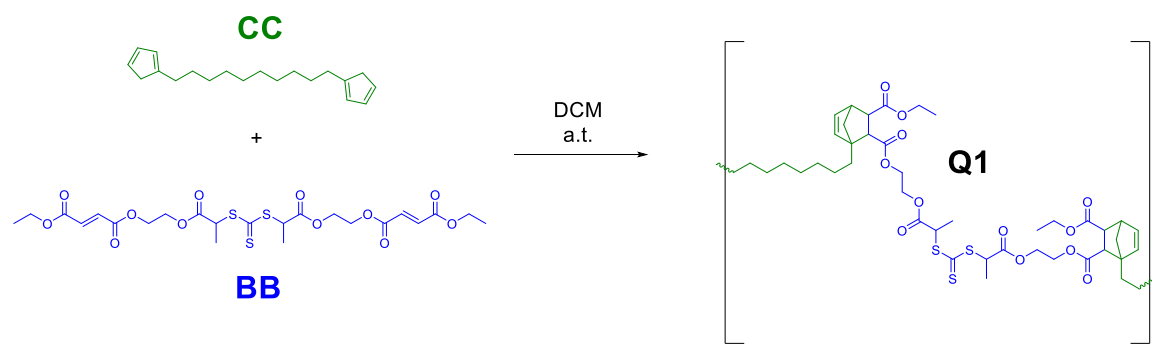


Figure 4-17. Small molecule test reaction utilizing **CC** monomer in combination with diethyl fumarate **F** (A) SEC of the adduct. (B) ESI-MS spectrum and (C) $^1\text{H-NMR}$ of the crude spectrum demonstrating residual resonances of **F** (*). Full assignment of the signals in (D). Spectrum was recorded in CD_2Cl_2 . The figure was reprinted from ref.³⁹² with permission of the Royal Chemical Society.

4.3.4 Step-Growth Polymerization and Reaction Optimization



Scheme 4-7. Thermal DA reaction for SG polymerization yielding the multi-CTA **Q1**.

At this stage, all preliminary tests showed positive results, suggesting the insensitive nature of the thermally induced DA reaction, as illustrated in Scheme 4-7. Therefore, the reaction conditions for the SG polymerization were optimized in terms of concentration and stoichiometry. In a first attempt, the concentration of the monomers in a SG polymerization in DCM were successively increased to bulk at an initial molar stoichiometry r of 1/1 (molarity of **CC/BB**), as indicated in Eq. (31).

$$r = \frac{n_0(\text{CC})}{n_0(\text{BB})} \quad (31.)$$

According to theory, the reaction rate is proportional to the concentration and thus, best results are obtained at high concentrations. In contrast to the photo-induced approach, no limitations in terms of too high monomer concentrations due to the Beer-Lambert's law are encountered. Due to the viscosity of both monomers, proper handling of the starting materials for preparation of the reaction mixture was achieved for $c(\text{BB,CC}) = 0.2 \text{ mol}\cdot\text{L}^{-1}$. Higher concentrations are in general possible, e.g. in bulk, yet poor handling of the viscous starting materials led to unreproducible results. Here, different SG polymerization attempts showed significant deviations in molecular weight in SEC analysis (refer to Figure 4-18A, black and green line). As noted, small amounts of the **CC** monomer inevitably oligomerize already during its synthesis, so the effective number of Cp units is decreased. Hence, the ideal monomer stoichiometry (refer to Eq. (31)) was addressed by successively increasing the monomer feed of **CC** to compensate the lack of Cp. Importantly, it is crucial to perform such an ideal stoichiometry analysis individually for each monomer batch. By screening different monomer ratios, a stoichiometry of $r = 1.2$ was determined to yield the highest molecular species (refer to Figure 4-18B for additional molecular characteristics refer to Appendix 8.2, Table 8-5). After successfully establishing ideal conditions for the DA reaction, a kinetic analysis of the SG polymerization was carried out at a stoichiometry of $r = 1.2$ in DCM for 20 h.

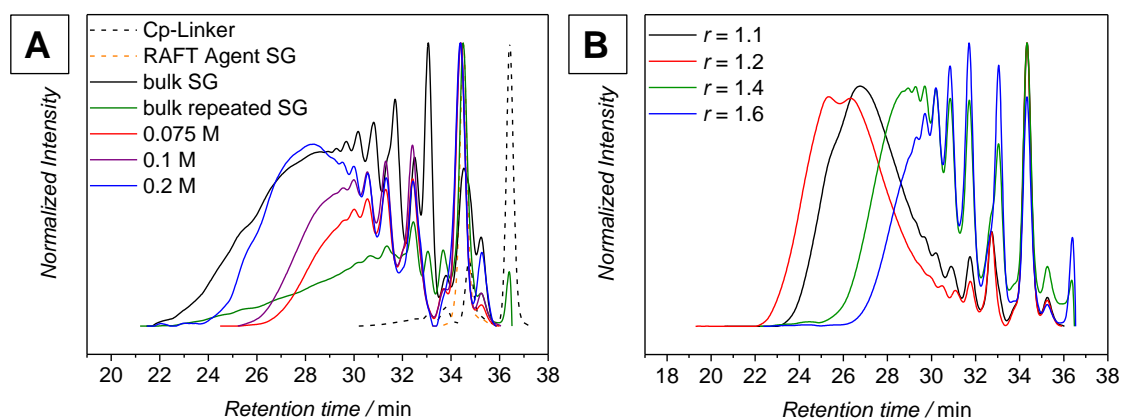


Figure 4-18. (A) SEC traces of the SG polymerization utilizing monomers **CC** and **BB**, investigating varying concentration conditions as indicated in the legend. (B) SEC-traces of SG polymers **Q1** obtained by polymerization with different stoichiometries r of **CC/BB** as indicated in the plot. Reaction conditions: $c = 0.2 \text{ mol}\cdot\text{L}^{-1}$ in DCM after 12 h. The figure was reprinted from ref.³⁹² with permission of the Royal Chemical Society.

In Figure 4-19A, the SEC-traces show the formation of high molar species, as well as vanishing fumarate resonances in the corresponding $^1\text{H-NMR}$ spectra (refer to Figure 4-19B). The conversion was calculated by the integrals of the fumarate resonances at 6.84 ppm in reference to the α -proton of the RAFT group of monomer **BB** at 4.77 ppm (all $^1\text{H-NMR}$ spectra are shown in Appendix 8.2.1, Figure 8-11). The reaction proceeded fast, showing a conversion of 66% within the first 20 min (refer to Figure 4-19C) and achieving full conversion after 20 h. By combining the SEC and NMR results, a Carothers plot based on M_w was compiled, showing excellent agreement to its calculated progression (refer to Figure 4-19D). Small deviations in the Carothers plot can be accounted for minor stoichiometric errors. By comparing the M_w evolution with SEC traces and NMR data, only traces of functional groups are present at high reaction times in the NMR spectra, *i.e.* the high molecular species were formed upon reaction of the few functional end-groups of the oligomers. A clear shift to lower retention times at long reaction times in SEC underpins this assumption. In addition to NMR and SEC analysis, the final SG polymer **Q1** was investigated by high resolution Orbitrap ESI-MS in higher-energy collisional dissociation (HCD) mode. In HCD mode, the energy input in combination with the high temperature of the ESI source triggers the *retro*-DA reaction of the adduct. The target signal of $m/z_{\text{HCD}} = 2022$ was selected and low dissociation energies were employed to observe the fragmentation of the DA species to lower m/z values (refer to Figure 4-20, full assignment of the peaks shown in Appendix 8.2.1, Table 8-7). The main signals represent species of corresponding repeating unit fragments and the neat monomer **BB**. Caused by the strong ionization of smaller species and detection limits of the instrument, species above 2500 m/z were not investigated. As could be successfully shown, the SG polymerization

does not require an elaborate synthetic setup and is simple to perform to high conversion without any catalyst, high energy input, or inert gas atmosphere.

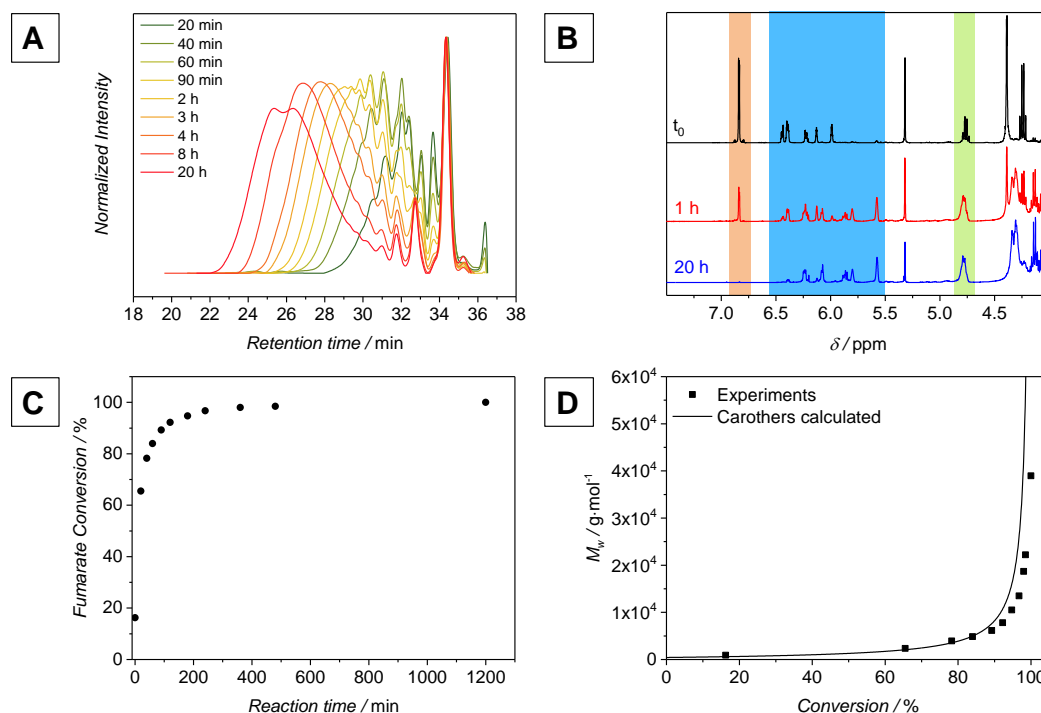


Figure 4-19. (A) THF-SEC traces of SG polymers **Q1** ($r = 1.2$) with increasing reaction times. SG polymerization conditions: $c(\mathbf{CC}) = 0.2 \text{ mol}\cdot\text{L}^{-1}$, $c(\mathbf{BB}) = 0.17 \text{ mol}\cdot\text{L}^{-1}$, solvent CD_2Cl_2 , $T = 25 \text{ }^\circ\text{C}$. M_w and M_n as well as dispersities, \mathcal{D} , are listed in Appendix 8.2.1, Table 8-6. (B) NMR spectra of **Q1** recorded at t_0 , 1 h and 20 h in CD_2Cl_2 . Areas highlighted in orange depict fumarate resonances at 6.84 ppm, areas highlighted in green show the resonances of the trithiocarbonates α -proton at 4.77 ppm (for assignment refer to Figure 4-17). Areas highlighted in blue belong to Cp double bond resonances of monomer **CC**, as well as the product double bond of **Q1**. (C) Kinetic data of the SG with a stoichiometry of $r = 1.2$. Conversion is calculated by evaluating the integrals of the fumarate to the α -protons resonances of the trithiocarbonate in the $^1\text{H-NMR}$ spectra. (D) Carothers plot illustrating the evolution of M_w with fumarate conversion of the SG polymerization (evolution of M_n in Appendix 8.2.1, Figure 8-12). The figure was adapted from ref.³⁹² with permission of the Royal Chemical Society.

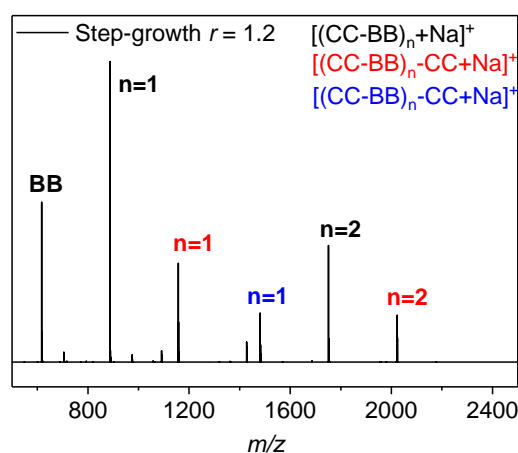
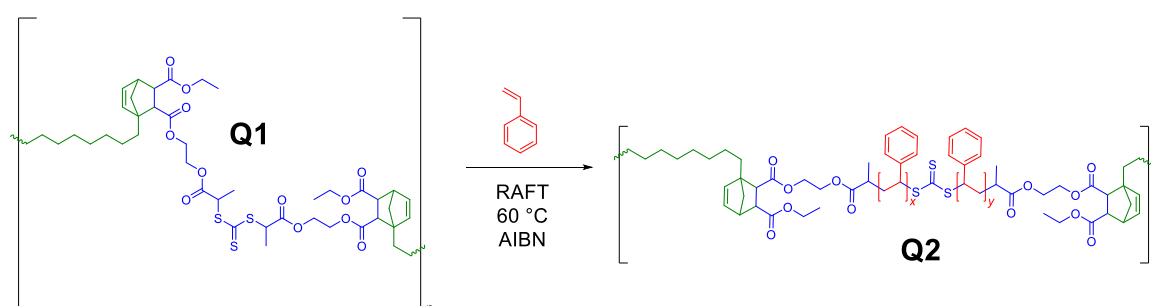


Figure 4-20. ESI-HCD-MS spectrum of the SG polymer **Q1** ($r = 1.2$). The spectrum was recorded in HCD mode, employing an energy of 10 eV to the target signal at $m/z = 2022$, triggering the *retro* DA reaction. The **CC** monomer cannot be detected due to poor ionization behavior. A solvent mixture of 3/2 THF/MeOH (V/V) and doping with sodium trifluoroacetate was applied. The figure was adapted from ref.³⁹² with permission of the Royal Chemical Society.

4.3.5 Segmented Copolymers *via* RAFT Polymerization of Q1

After the successful synthesis of a SG polymer bearing trithiocarbonate groups in the backbone of the repeating unit, **Q1** was utilized as multi-CTA in a RAFT polymerization (refer to Scheme 4-8). Prior to the polymerization, the presence of the trithiocarbonate as well as the stability of the DA adduct was addressed. The former was investigated in ^{13}C -NMR and UV-Vis spectroscopy, clearly demonstrating its resonance at approx. 219 ppm (red box, refer to Figure 4-21A) as well as its characteristic UV absorbance at 303 nm (refer to Figure 4-21B). By the naked eye, the color of the SG polymer **Q1** appeared yellowish (inset picture, refer to Figure 4-21B), typical for trithiocarbonates as well as for the **BB** monomer.



Scheme 4-8. RAFT polymerization of styrene utilizing the SG polymer **Q1** as multi-CTA yielding segmented copolymer **Q2**.

The thermal stability of the DA adduct was investigated using a small molecule (for synthesis procedure refer to Chapter 7.3.5). For this purpose a mono-CP compound was reacted with the **BB** monomer in a similar DA reaction as for the small molecule assay, yielding the adduct **Cp-BB-Cp** (refer to Figure 4-21C). Since RAFT polymerizations shall be conducted at 60 °C, the small molecule adduct was analyzed in high-temperature NMR (HT-NMR) for 110 min at 60 °C. As depicted in Figure 4-21D, differences of the NMR spectra at the beginning and the end of the annealing are negligible and no significant changes can be observed. Especially, the resonances of the fumarate protons were absent during the entire measurements. Therefore, the HT-NMR measurement successfully confirmed the thermal stability of the DA adduct at the target temperature of the RAFT polymerization at 60 °C.

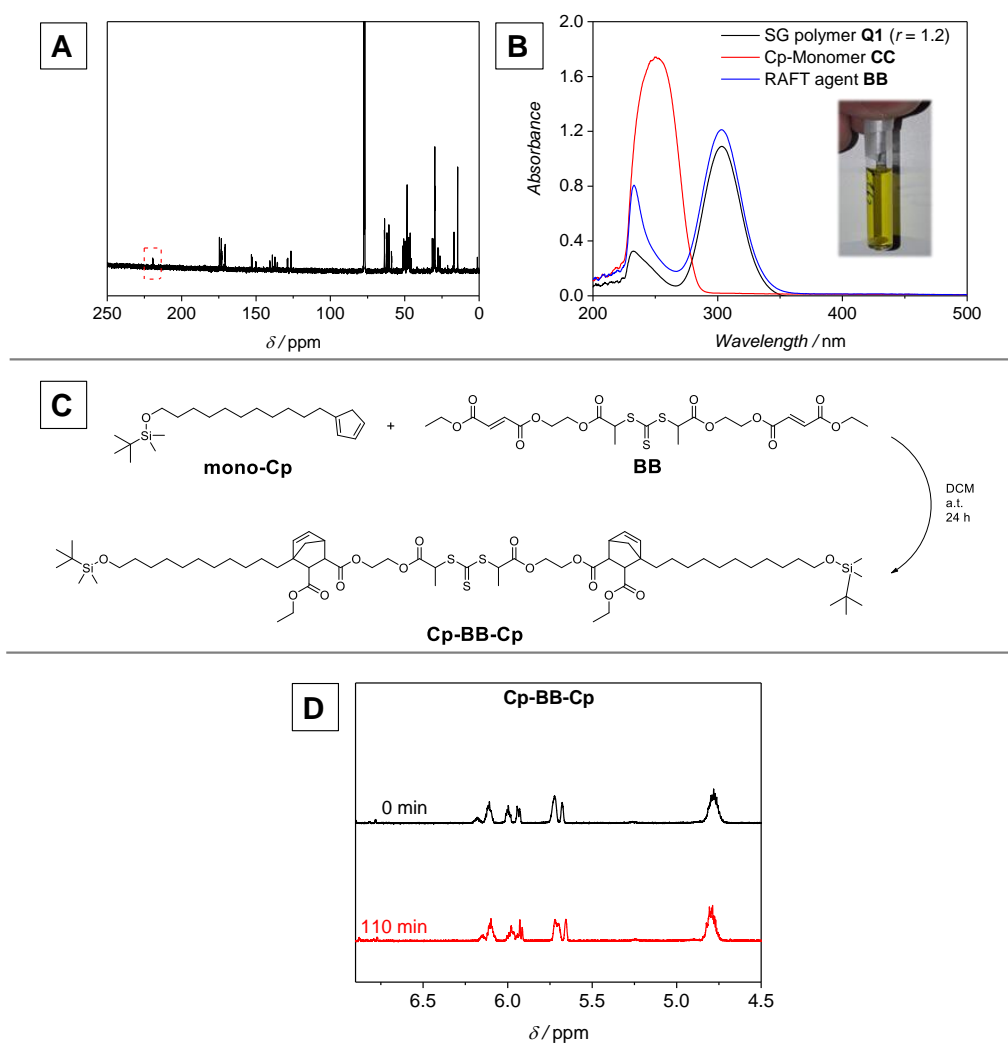


Figure 4-21. (A) ^{13}C -NMR spectrum of the SG polymer **Q1** ($r=1.2$), showing the resonance of the trithiocarbonate at 219 ppm (red box). The spectrum was recorded in CDCl_3 . (B) UV-VIS spectra of the SG polymer ($r=1.2$) and the monomers **CC** and **BB**. The spectra were recorded in DCM, at the following concentrations: $c(\mathbf{Q1}) = 24 \mu\text{mol}\cdot\text{L}^{-1}$, $c(\mathbf{CC}) = 37 \text{mmol}\cdot\text{L}^{-1}$, $c(\mathbf{BB}) = 84 \mu\text{mol}\cdot\text{L}^{-1}$. Characteristic absorbance of CS_3 at approx. 303 nm. The inset picture illustrates the SG polymer **Q1** dissolved in DCM, demonstrating the commonly yellow color of the CS_3 moiety. (C) Reaction scheme of DA reaction, generating the test molecule for the analysis of the *retro*-DA reaction in high-temperature NMR at 60°C . 2.3 eq. of the mono-Cp molecule are employed in the DA reaction. (D) ^1H -NMR spectra of the **Cp-BB-Cp** at t_0 and 110 min, observing no *retro* DA products. Spectra were recorded in toluene- d_8 at 60°C . The NMR tube was permanently kept in the instrument during the analysis. The figure was adapted from ref.³⁹² with permission of the Royal Chemical Society.

After the preliminary tests, a RAFT polymerization, as illustrated in Scheme 4-8, was carried out, employing SG polymer **Q1** as multi-CTA in combination with styrene as monomer and AIBN as initiator at 60°C (for synthesis protocol refer to Chapter 7.4.2). The M_n of **Q1** was $3,850 \text{g}\cdot\text{mol}^{-1}$, calculating the RAFT group molarity from the SEC-data ($c(\text{RAFT}) = 5 \text{mmol}\cdot\text{L}^{-1}$, calculated from $M_{n,\text{SEC}}$). Kinetic data was recorded over 24 h, demonstrating a linear evolution of $-\ln(1-p)$ with time, indicating a 1st order reaction (refer to Figure 4-22A). The development of the molecular weight is illustrated in Figure 4-22B,

showing the formation of high molecular weight species above 1,000,000 g·mol⁻¹ within several hours of polymerization. As expected, the evolution of M_n shows linear behaviour, as commonly expected for a controlled polymerizations (refer to Figure 4-22C, further data in Appendix 8.2.2, Table 8-8).

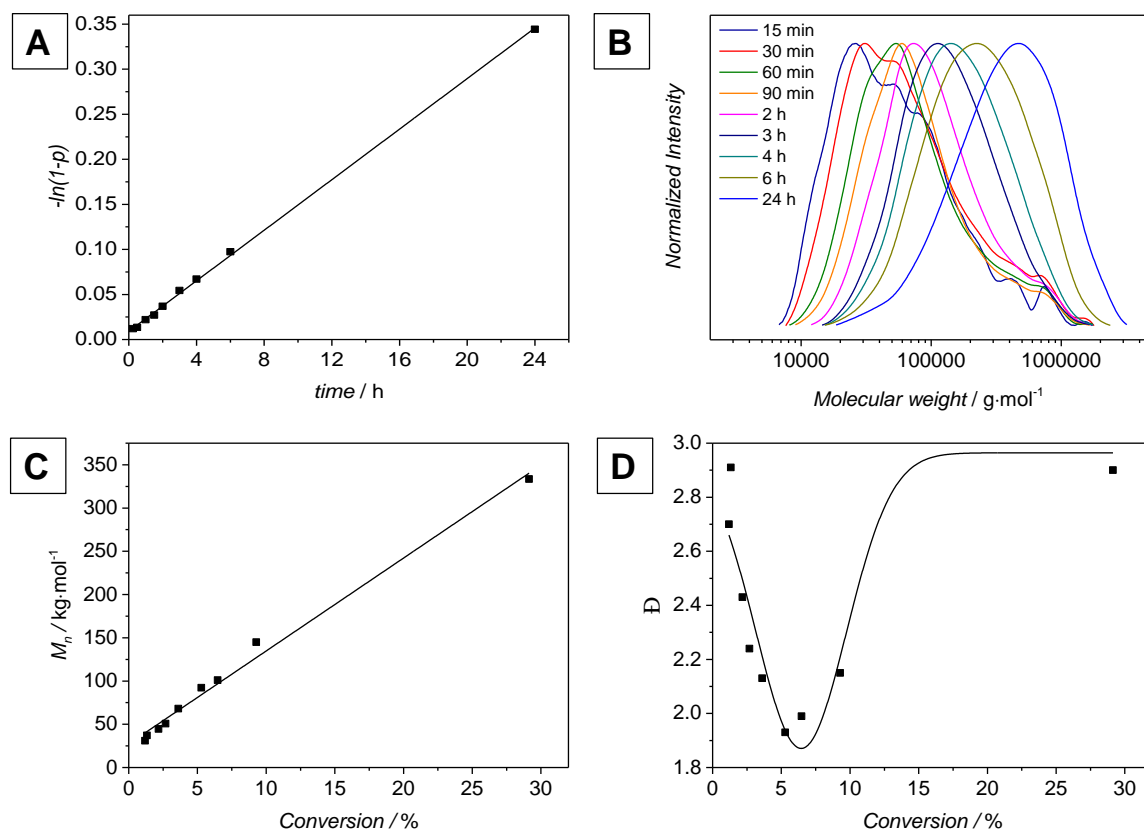


Figure 4-22. (A) $-\ln(1-p)$ vs. reaction time of the RAFT polymerization. Data was obtained by gravimetric evaluation. (B) Molecular weight distribution development of RAFT polymers **Q2** derived from the mCTA **Q1**, time as indicated in the legend. (C) Evolution of M_n with conversion of the RAFT polymerization (styrene in bulk, AIBN ($c = 1 \text{ mmol}\cdot\text{L}^{-1}$), $T = 60 \text{ }^\circ\text{C}$, $c(\text{RAFT}) = 5 \text{ mmol}\cdot\text{L}^{-1}$), the line is only for guiding the eye. Molecular weights (M_n and M_w) as well as \bar{D} can be found in Chapter 8.2.2 Table 8-8. (D) Evolution of \bar{D} with conversion. The line is only for guiding the eye. The figure was adapted from ref.³⁹² with permission of the Royal Chemical Society.

As investigated in Chapter 4.2, the presence of the RAFT groups in the repeating unit and the backbone of the SG polymer, the addition-fragmentation process becomes more complex, as in comparison to single RAFT groups. Further, the reshuffling of the trithiocarbonate moiety in all directions due to the symmetric design of the RAFT group has a drastic impact on the evolution of the RAFT polymerization. As found in case of the RAFT polymerization utilizing photoenol-based SG polymers as multi-CTAs,³⁸¹ the probability of RAFT exchange is naturally higher for long SG polymer chains, since more RAFT moieties are incorporated. Nevertheless, the probability of exchange is in general equal for all RAFT groups, *i.e.* all polystyrene blocks grow steadily. Interestingly, the

evolution of the dispersity \mathcal{D} during the RAFT process does not demonstrate a clear trend (refer to Figure 4-22D). At low styrene conversions, the dispersity decreases significantly until a turning point at 5% conversion is reached. Subsequently, the dispersity clearly increases with higher styrene conversion. As found in chapter 4.2, *kMC* simulations indicated that the tendency to participate in the RAFT exchange depends firstly on the maximal polymer chain length and secondly on the styrene conversion. However, an unambiguous statement at this stage is not possible since the differences between both the photo-induced SG and the thermally induced SG polymers as precursors for the RAFT polymerization are too significant to compare both systems. It can be assumed that several factors are influencing the RAFT process, such as polymer chain diffusion, viscosity, coiling of the high molecular weight polymer chains, and the RAFT group environment.

4.4 Conclusion

The implementation of multiple RAFT groups in the backbone of a polymer, incorporating them into the repeating unit, was achieved by utilizing photo- and thermally induced Diels-Alder (DA) reactions for step-growth (SG) polymerizations. The subsequent RAFT polymerization featuring the SG polymers as multi-CTAs affords well-defined segmented copolymers. Both approaches present fast reaction kinetics and simplicity in terms of the reaction setup.

In case of the photo-induced SG polymerization, a photoenol generated upon UV-irradiation of *ortho*-methyl benzaldehyde in combination with a difumarate bearing a RAFT group underwent a cycloaddition reaction. A side reaction of the photoenol diene species required several optimizations of the process, which was supported by *kinetic* Monte Carlo simulations. It was shown that working under off-stoichiometric conditions benefits the formation of high molar mass SG polymers since the faster consumption of the photoenol moiety can be compensated. Meanwhile, the *in silico* investigations could quantify and qualitatively describe the distribution of RAFT moieties in the SG polymer as well as the impact of the side reaction on the final SG polymer. A subsequent RAFT polymerization employing the SG polymers as multi-CTA precursor afforded well-defined copolymers incorporating styrene blocks into the SG polymer backbone. The *kinetic* Monte Carlo simulations identified up to 200 reactions being present during the RAFT exchange since at t_0 a polymeric species is already present. By using the simulations, a description of the RAFT polymer was possible, highlighting also differences in the RAFT exchange dependent on the maximum chain length of the precursor polymer.

For the thermally induced SG system, the DA reaction of di(cyclopentadienyl) and a difumarate bearing a RAFT group yielded high molar SG polymers. The absence of any

important side reaction allowed a straight-forward SG polymerization, after optimizing the reaction conditions, regarding concentration, stoichiometry, and kinetics. Due to the reaction's simplicity, *i.e.* no inert gas atmosphere, external energy input, or catalyst addition, the reaction can be regarded as one of the simplest SG approaches to yield functional polymers. Furthermore, in comparison to the photoenol system, five times higher concentrations of the monomers could be employed. High molecular weight species were obtained and subsequently employed as multi-CTA for RAFT polymerization of styrene. SEC analysis revealed high molecular weight species of the segmented copolymers beyond $1,000,000 \text{ g}\cdot\text{mol}^{-1}$.

However, both systems feature drawbacks in terms of the SG polymerization. The photo-induced system entails a not negligible side reaction, requiring adjustment of the stoichiometry. For the thermally induced system, the diene monomer synthesis already yields some dimerized species. However, the thermally induced system is superior to the photo-induced approach based on its procedural ease, the absence of any initiator or reaction trigger at ambient conditions, as well as the absence of any significant side reaction. The RAFT polymerization for either system is highly complex and both cannot be directly compared with each other since the precursor polymers are distinctly different. Furthermore, the different incorporation of RAFT moieties in each system does not allow for any comparison. However, the *in silico* investigations in case of the photo-induced system suggest diverse processes during the RAFT exchange. As the precursor already provides a molecular weight distribution at the start of the RAFT polymerization, segmented polymeric structures are consequently formed.

As both of the concepts already showed, the monomer systems are variable and the diene species or in general the highly reactive species can be readily substituted. The difumarate RAFT agent shows excellent stability and – in addition to DA reactions – can undergo further reactions *e.g.* thio Michael. Since the side reactions of the activated photoenol species and the cyclopentadienyl moieties cannot be avoided, a perfect system would feature a highly reactive functionality that features no side reaction. However, the consequence of highly reactive functionalities is often the occurrence of side reactions. In addition, any feasible reaction for the SG polymerization is restricted to demonstrate orthogonality to the RAFT group. Regarding the stoichiometry, the utilization of an AB monomer system would overcome any stoichiometric imbalances that occur by false feeding ratio in case of an AA/BB monomer system. Also, the concentration of RAFT groups would be increased, since a unimolar SG polymerization decreases the distance between the RAFT moieties. However, both systems presented in this chapter required off-stoichiometry conditions to obtain high molecular weights due to either a competing side reaction of the photoenol monomer or an inevitable loss of functional groups during

the synthesis of the Cp monomer. Therefore, the AA/BB monomer system is able to tackle any of the system's inherent issues by working under off-stoichiometry conditions. The subsequent RAFT polymerization employing the SG polymer as multi-CTA does benefit from a stable and well-defined precursor polymer. However, variations of the SG polymer's molecular weight, higher concentrations of RAFT groups, and their impact on the RAFT polymerization have not been investigated, yet. Furthermore, the RAFT mechanism appears to change during the polymerization due to the growing polystyrene blocks. Here, a comprehensive study needs to address how the RAFT mechanism is influenced by the increasing chain length and the increasing viscosity.

To conclude, a perfect SG polymer would be generated from an ideal reaction providing orthogonality to the RAFT group and does not feature any side reaction or off-stoichiometry conditions. Furthermore, if the SG reaction is perfect, the application of an AB monomer system would inherently overcome any stoichiometric imbalances. Unfortunately, synthesis and storage of an AB monomer that reacts at ambient temperature without specific reaction stimulus is not trivial. Further, such a system could be investigated regarding the SG polymer's molecular weight onto the RAFT polymerization. However, all these issues are restricted to the successful monomer synthesis and the SG reaction itself. Since the perfect reaction hardly exists, the here introduced systems show their potential and give an answer how to tackle synthetic issues in such SG polymerization systems that are encountered in the lab.

5

5 CYSTEINE-RICH DOMAIN PEPTIDES FOR STEP-GROWTH POLYMERIZATION AND SURFACE PATTERNING

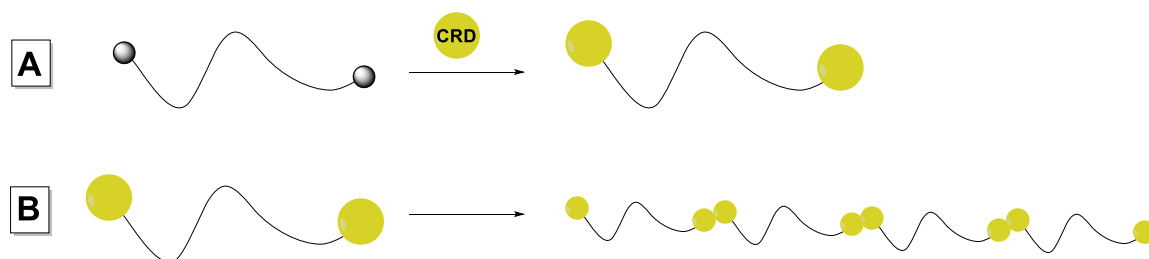
5.1 General Introduction and Outline

Cysteine-rich domains (CRDs) are peptides with a sequence length of around 20 amino acids, including six cysteine units. The thiols of the cysteine units establish a dynamic equilibrium between the thiols and the disulfides, referred to as disulfide reshuffling (refer to Chapter 3.6.2).³⁴² Due to disulfide reshuffling in CRDs, these are capable to form intra- or intermolecular disulfide bonds in a reversible manner. In this chapter, CRDs are employed in bioconjugation and SG polymerization methodologies as well as in the decoration of recodable surfaces. The present chapter is divided into two sections, the first part covers the application of CRDs as SG polymerization tool, while in the second part a strategy for recodable CRD surfaces is introduced.

5.2 CRDs as Polymerization Tool in Macromolecular Assemblies

5.2.1 Motivation

In nature, the fresh-water sea animal *Hydra* produces a capsule called nematocyst, which is loaded with a sting for prey capture or defence purposes.³⁴⁰ Specific minicollagens have been identified to play a key role in the maturation of the nematocyst capsule walls.³⁴³ A polymerization of minicollagens occurs during the maturation phase, caused by disulfide reshuffling of incorporated CRD units by an enzymatic stimulus.¹ These minicollagens consist of different protein blocks, as described in chapter 3.6.2, having their end-groups decorated with CRDs units. In order to mimic the natural process during the nematocyst's maturation, the goal of the project is to substitute the middle protein block of the minicollagen by a synthetic polymer strand, decorating the polymer's end-groups with CRDs (refer to Scheme 5-1A). The CRDs situated at the termini of the polymer chains are envisaged to enable a SG polymerization of an AA macromonomer system by generating disulfide bonds between the CRDs of multiple polymer-peptide conjugates (refer to Scheme 5-1B). Thus, suitable conditions for the CRD handling as well as bioorthogonal reactions for peptide-polymer bioconjugation need to be developed. In the last step, the SG polymerization, similar to its archetype in nature, is envisaged to occur *via* disulfide reshuffling.



Scheme 5-1. Concept overview of CRDs as polymerization tool in biomimetic material design. (A) Bioconjugation reaction, attaching the CRD to an α,ω -functional polymer, affording the macromonomer. (B) SG polymerization exploiting the disulfide reshuffling of the CRDs to form disulfide bonds between the polymer-peptide bioconjugates.

5.2.2 Folding of the CRD Peptide

The employed CRD peptide consists of a pattern of six cysteines spacing three residues, except of C₁₉ to C₂₀, and an overall amino acid sequence of 21, as illustrated in Figure 5-1A (GPC₃GSYC₇PSVC₁₁APAC₁₅APVC₁₉C₂₀A). As introduced in Chapter 3.6.2, the CRD in the current chapter is classified as an *N*-CRD, *i.e.* it forms only one intermolecular disulfide bond with another CRD unit.³⁴² In the context of the current chapter, the term CRD is equivalent to *N*-CRD.

The CRD peptide is initially in its reduced state, *i.e.* all cysteines are present as free thiols. Since the thiols can participate in different types of reactions, such as thioesterification, thio-Michael reaction³⁴⁷ or disulfide formation, all six cysteines should be oxidized in order to form intramolecular disulfide bonds. Concomitantly, the peptide is three dimensionally folded and an intrinsic protecting group of the thiols is readily installed, since the disulfide bonds can be reversible cleaved.

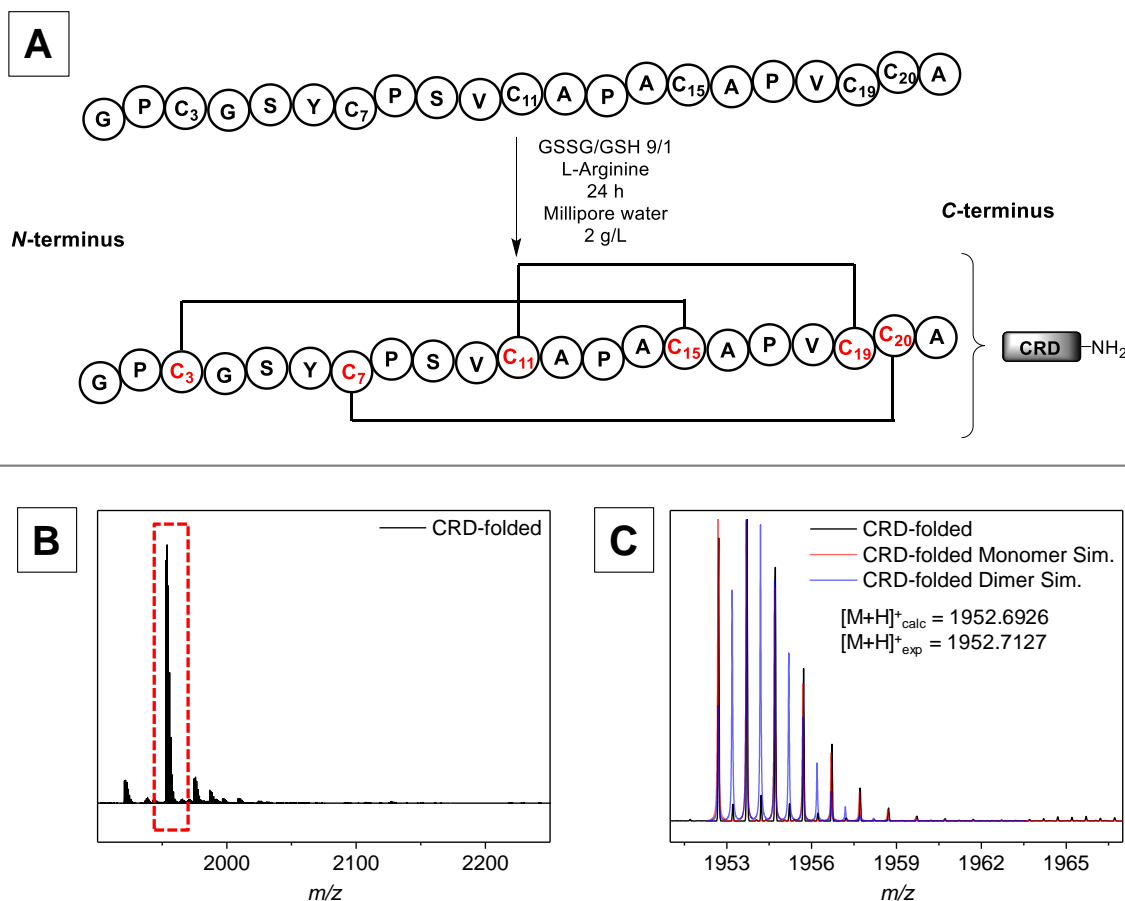


Figure 5-1. Amino acid sequence of the CRD with folding procedure to obtain three intramolecular disulfide bonds as indicated. Misfolding, *i.e.* other disulfide patterns, is neglected. ESI-MS spectra of the CRD in folded state (B) full spectrum and (C) zoom in with simulation overlay of single charged unimer and double charged dimer. The spectra were recorded in MeCN/H₂O mixture with the addition of 1% acetic acid.

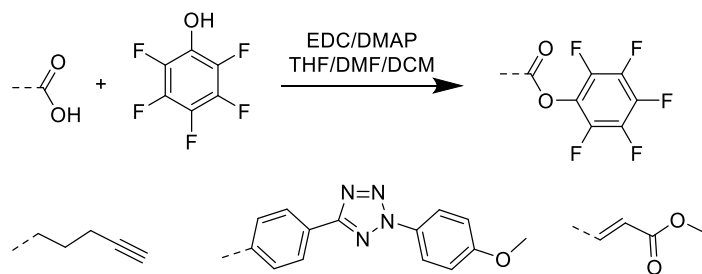
The folding occurred under mild reoxidative conditions, employing a combination of reduced glutathione (GSH) and dimerized glutathione (GSSG) in a ratio of 1/9 to induce disulfide reshuffling in Millipore water. Since the disulfide formation is pH dependent, the dynamic equilibrium can be shifted towards disulfides by increasing the pH-value (pH > 7),³³⁸ *i.e.* by the addition of L-arginine. L-arginine was shown to benefit the CRD folding in terms of stability, since an L-arginine concentration below 0.1 mol·L⁻¹ induced significant precipitation and loss of the starting material. L-arginine is referred to as an aggregation suppressor because it reduces the rate of protein association but does not

influence folding.³⁹⁵ During oxidation of the CRD, GSSG is reduced to GSH. In addition, autooxidation occurs due to the presence of oxygen in the reaction medium. The GSH enables refolding or is capable to reduce any agglomerates. The CRD concentration was limited to 2 g·L⁻¹. Thereby, intermolecular disulfide linkage becomes rather unlikely and as a consequence possible agglomeration should be avoided. The purification was conducted *via* dialysis to remove any low-molecular folding reagents, such as GSH, GSSG and L-arginine, obtaining the folded CRD ultimately after lyophilisation. A loss of material up to 50 wt.% was inevitable due to the critical molecular weight cut-off (MWCO) of the dialysis membrane (1 kDa). Nonetheless, the folded CRD was characterized in high resolution Orbitrap ESI-MS spectrometry, illustrating clearly the presence of the target species (refer to Figure 5-1B). The comparison of the measured peaks with the theoretical values shows excellent agreement, although the existence of the dimer is observed in its double charged state. However, the extent of dimerized CRD could not be determined from the ESI-MS spectra. Further, additional signals, underlying the product signals, are observed, yet could not be assigned. Attempts of CRD analysis in *N,N*-dimethylacetamide (DMAc) SEC did not achieve any useful results. The elugrams showed high noising and a strong baseline drift, detecting no reliable signal neither by refractive index (RI), nor by UV-VIS detection.

5.2.3 Functionalization of CRD-Peptides by Active Ester Chemistry for Bioconjugation

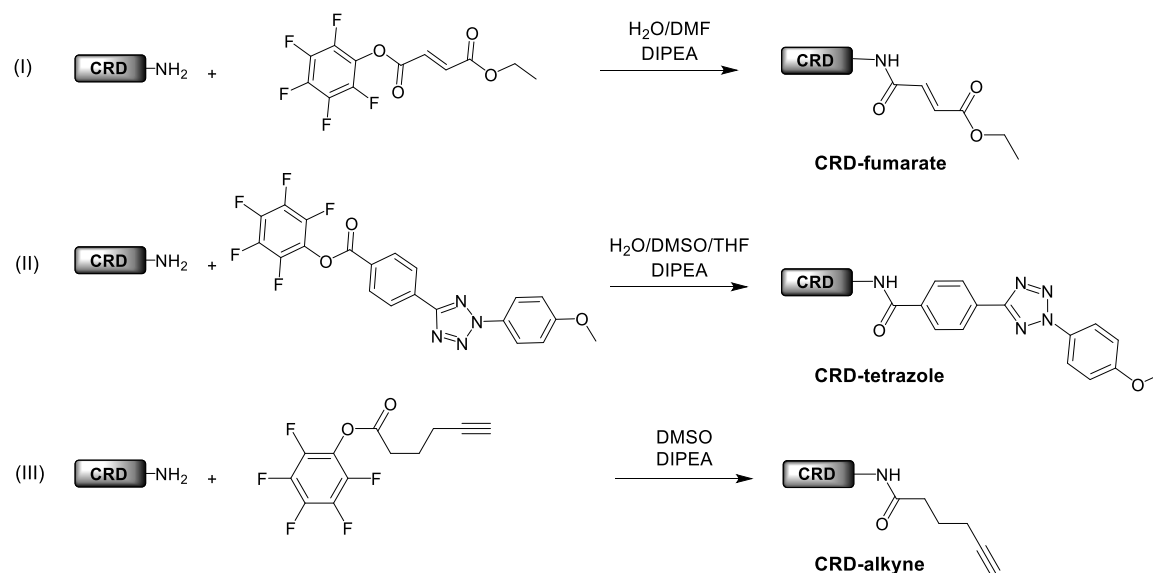
To realize the successful coupling of the CRD-peptide to a polymer, bioorthogonal anchor moieties have to be attached to the peptide. In general, the ligation reaction of the CRD to the polymer requires high conversions and high specificity, in order to circumvent complex separation of by-products and starting materials. Hence, the selected methods comprise highly efficient photo-induced reactions, specifically NITEC, thermal DA reactions and copper-catalyzed azide-alkyne cycloaddition (CuAAC). Thus, three different anchor groups were introduced to the CRD-peptide, namely an alkyne (for CuAAC), a fumarate (feasible in NITEC and thermal DA reactions), as well as a tetrazole moiety (active NITEC species). The method of choice for attaching the anchor moieties was active ester chemistry, since the synthetic preparation of active ester compounds is straight-forward and the transamidation reaction, addressing the inherent *N*-terminus, can be easily performed.¹⁶³ As illustrated in Scheme 5-2, Steglich esterifications were carried out to generate the corresponding active ester molecules for subsequent reaction with the peptide (for the synthetic protocols and characterization refer to Experimental Section 7.3.4). The syntheses of all anchor molecules were successfully conducted in a

non-challenging manner to obtain all linkers after column chromatography in good yields and sufficient purity.



Scheme 5-2. Synthesis of active ester molecules bearing ligation moieties for photo- and thermally induced reactions such as alkynes, tetrazoles, and fumarates.

For CRD functionalization, the active ester molecules were employed in reactions with the folded CRD. Here, the reaction mixture contained the peptide, the PFP-anchor molecule as well as, the sterically hindered base *N,N*-diisopropylethylamine (DIPEA), and a suitable solvent mixture (refer to Scheme 5-3).



Scheme 5-3. Introduction of anchor groups by PFP active ester chemistry, yielding functional CRDs as indicated. Equivalents: **CRD-fumarate**: CRD folded: 1 eq.; PFP-fumarate: 2 eq.; DIPEA: 2 eq. **CRD-tetrazole**: CRD folded: 1 eq.; PFP-tetrazole: 1.4 eq.; DIPEA: 1.4 eq. **CRD-alkyne**: CRD folded: 1 eq.; PFP-alkyne: 1.25 eq.; DIPEA: 1.25 eq.

Optimization of each CRD functionalization was performed in order to determine suitable reaction durations, equivalents of the PFP molecule and solvent mixture. In order to achieve full conversion, a reaction time of three days was selected for all CRD functionalizations. Furthermore, the equivalents of the PFP-molecules have been determined in several experiments for the respective linker (refer to Scheme 5-3) in the range of 1.25 to 2 equivalents. The solvent mixture for the active ester reaction has been adjusted with respect to the solubility of both, the CRD peptide as well as the respective

PFP-molecule. Here, DMSO, THF, water, DMF and combinations of these were employed as reaction media. In particular, the tetrazole-PFP ester was not soluble in solvent mixtures with high fractions of water or polar organic solvents. Hence, the addition of THF to a mixture of DMSO and water was necessary to ensure adequate solubility.

Purification of the functional CRD derivatives after functionalization was performed *via* dialysis and subsequent lyophilization. Characterization of the three functional CRD derivatives after ligation was carried out *via* ESI-MS measurements, illustrating the corresponding spectra in Figure 5-2. In case of the CRD-alkyne, the absence of the folded-CRD and the presence of the CRD-alkyne signal can be observed (refer to Figure 5-2A and B, $m/z_{\text{exp.}} = 2068.7369$, $m/z_{\text{calc.}} = 2068.7165$). In particular, excellent agreement of the experimental and calculated data is obtained. Despite doping with acetic acid, the common utilization of sodium trifluoroacetate with the instrument as doping reagent led to the appearance of the sodium adducts in the spectra. Further signals appear in the spectrum, which could not be assigned. Similar positive results were obtained for the CRD-fumarate (refer to Figure 5-2C and D $m/z_{\text{exp.}} = 2100.7249$, $m/z_{\text{calc.}} = 2100.7063$) and the CRD-tetrazole (refer to Figure 5-2C and D $m/z_{\text{exp.}} = 2252.7628$, $m/z_{\text{calc.}} = 2252.7550$). The vanished signal of the starting material (folded CRD) for all CRD functionalizations confirms full conversion or sufficient removal of the folded CRD. Since the introduction of the anchor moiety increased the unpolar character of the peptide, the missing signal of the better ionizing folded CRD in the spectra can be quantitatively interpreted as the complete absence of the folded CRD in the sample. In case of the CRD-tetrazole, solubility issues during the functionalization as well as for the product were encountered. For the CRD-fumarate, solubility problems were encountered after lyophilization of several CRD functionalization attempts.

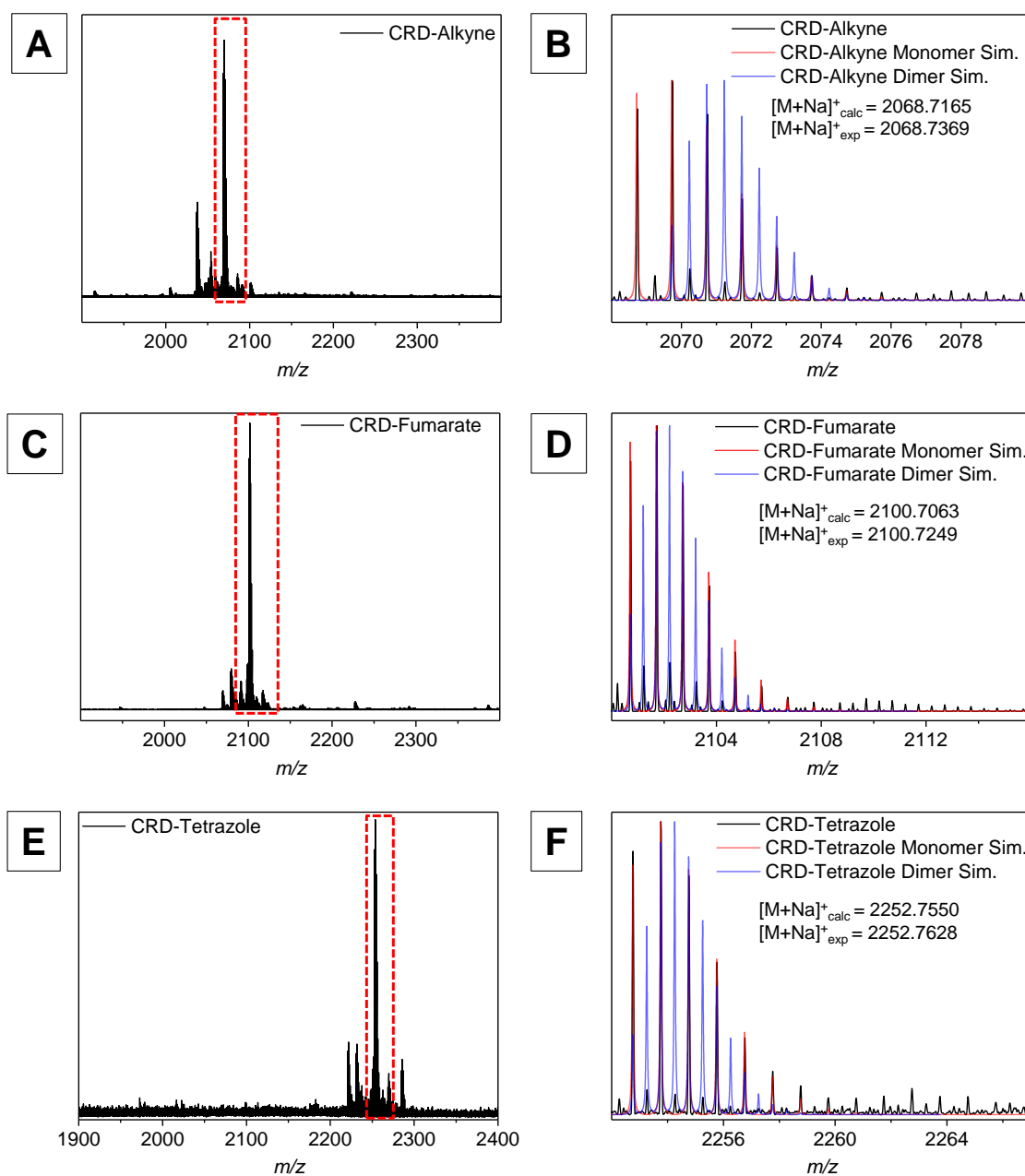


Figure 5-2. ESI-MS spectra of the CRD-alkyne (A) full and (B) zoom-in with simulated isotopic pattern overlay in (B). ESI-MS spectra of the CRD-fumarate (C) full and (D) zoom-in with simulation overlay. ESI-MS spectra of the CRD-tetrazole (E) full and (F) zoom-in with simulation overlay. All spectra were recorded via direct infusion experiments with MeCN/H₂O as solvent mixture and doping with 1% acetic acid (experimental data in Chapter 7.5.2).

5.2.4 Functionalization of CRD for In-Depth Surface Analytics

In a further CRD functionalization, a bromide moiety was introduced to the CRD with regard to its usage in surface patterning. Therefore, a corresponding PFP-bromide molecule was synthesized with a similar protocol as previously discussed for the fumarate, tetrazole and alkyne PFP molecules (refer to Figure 5-3A, experimental procedure refer to

Chapter 7.3.4). Such a bromine bearing CRD is crucial for in depth surface analysis after immobilization on a surface, since it can be ideally detected *via* time-of-flight secondary ionization mass spectrometry (ToF-SIMS) analysis (refer to Chapter 5.3). A high purity of the CRD-bromide is essential. For its task in surface patterning, the CRD-bromide should ideally not contain any non-bromine labelled CRD by-products, since such CRD derivatives will compete in immobilization reactions on the surface, as will be discussed in Chapter 5.3. In the first step, the synthesis of the bromine-PFP molecule was conducted in a routine Steglich esterification protocol, obtaining the molecule in good yields and high purity (refer to Chapter 7.3.4). For the CRD functionalization reaction, the folded CRD was employed with the bromine PFP anchor in similar reaction conditions as discussed for the aforementioned CRD functionalization (refer to Figure 5-3B).

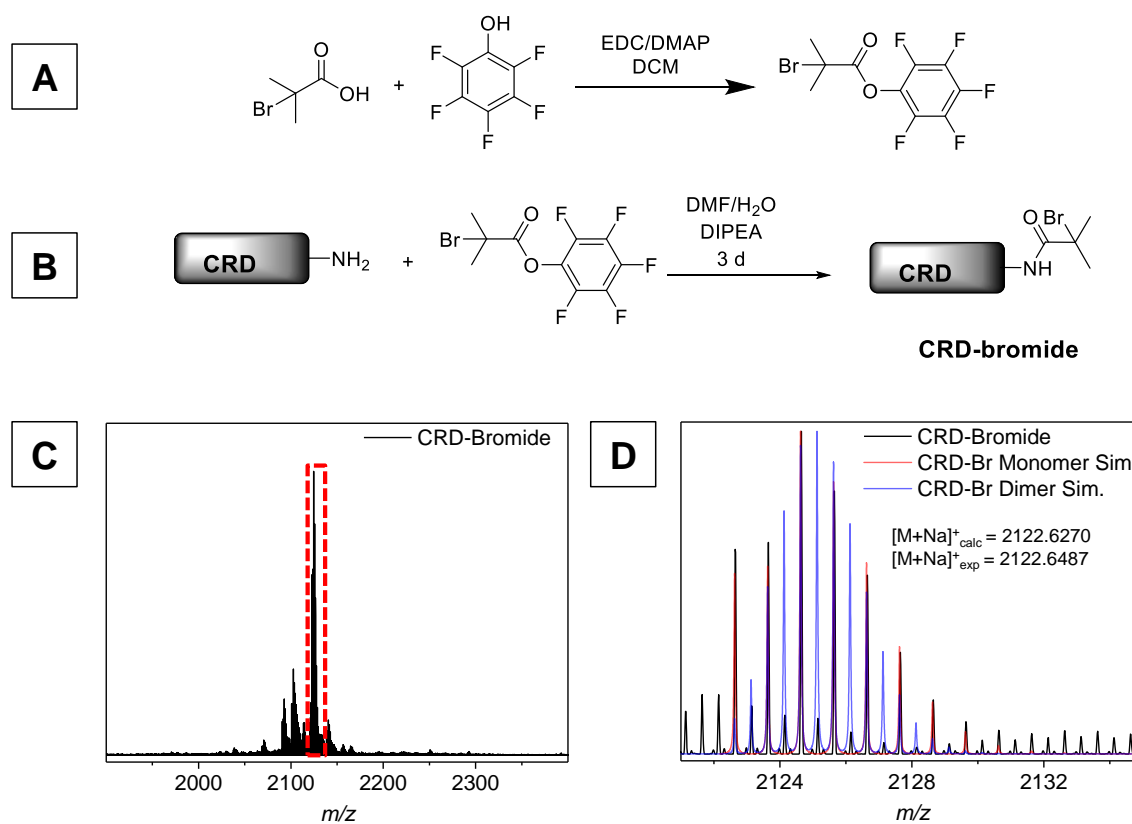


Figure 5-3. (A) Synthesis of bromide bearing PFP molecule. (B) Functionalization of folded CRD with bromide-PFP anchor molecule. Equivalents: CRD folded: 1 eq.; PFP-bromide: 2 eq.; DIPEA: 2 eq. ESI-MS spectra of the CRD-bromide (C) full spectrum and (D) zoom-in with single-charged simulated isotopic pattern and dimerized double-charged product.

In the ESI-MS spectrum of the CRD-bromide, the expected product signal can be observed (refer to Figure 5-3C, $m/z_{\text{exp.}}$ 2122.6487, $m/z_{\text{calc.}}$ 2122.6270) and no remaining starting material of the folded CRD is detected. By comparing the simulated and experimental isotopic pattern, excellent agreement is observed (refer to Figure 5-4D), although some unassignable signals are present. Since the functional CRD should show a reduced

ionization behavior in comparison with the folded CRD, an absence of signals of the folded CRD indicates full conversion of the functionalization reaction.

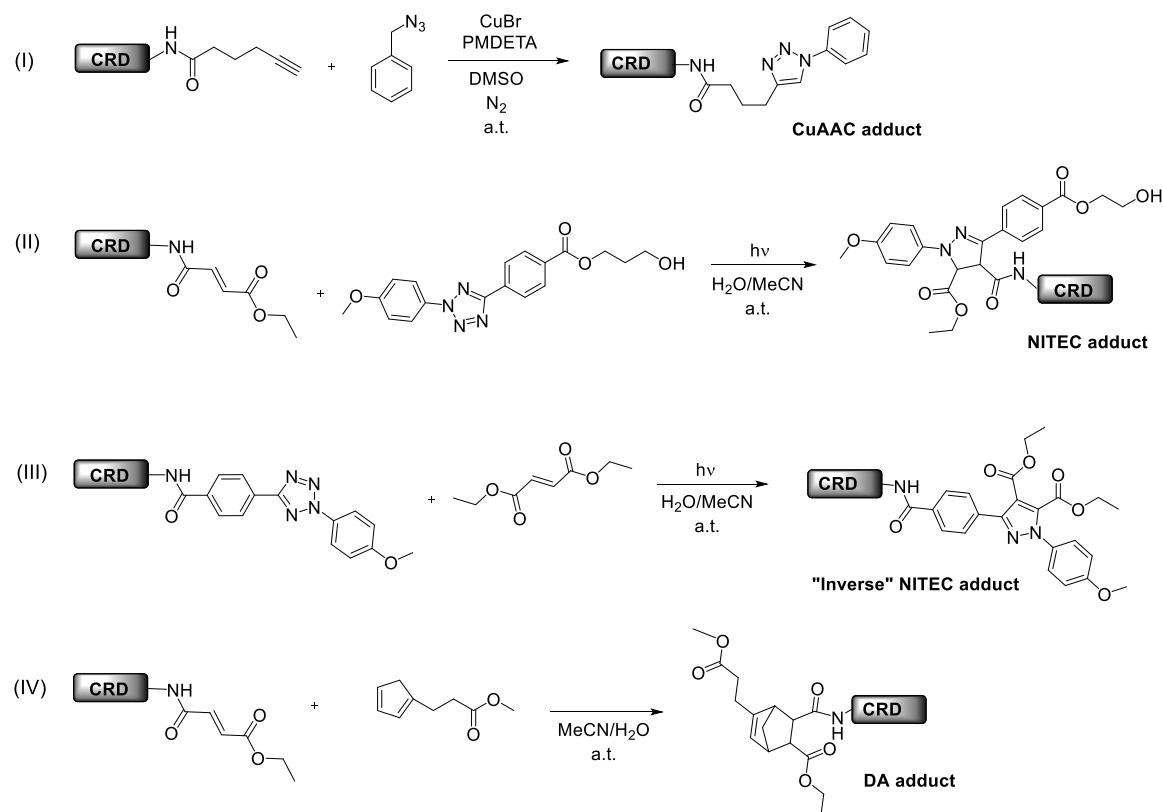
In some attempts of functionalization with the bromide moiety, the ESI-MS spectra of the purified CRD material showed remaining folded CRD. To purify the impure CRD-bromide for surface applications, purification by HPLC was carried out. First, adequate elution conditions of the CRD-bromide were determined, employing a C₁₈-reversed-phase analytic column. In the second step, these findings were envisaged to be transferred to a semi-preparative column of similar type. Test runs indicated that the addition of 1 vol.-% trifluoroacetic acid (TFA) and the utilization of an isocratic mixture of water and acetonitrile (90/10, V/V) provided low baseline noising and a narrow elution of employed CRD species. The CRD-bromide was analyzed on an analytic column at a concentration of 1 g·L⁻¹ in an isocratic mixture of H₂O/MeCN (90/10, V/V) under the addition of 0.1% TFA. The elugram of the CRD-bromide on the analytic column clearly shows elution at approx. 6.5 min and 17 min (refer to Appendix 8.3.1, Figure 8-14). By upscaling the run to a semi-preparative column at identical conditions, the elugrams changed, since only the elution of one species at approx. 15 min occurred (refer to Appendix 8.3.1, Figure 8-15). The species that eluted at approx. 15 min was collected and then analyzed in ESI-MS, showing the starting material instead of the functional CRD-bromide (refer to Appendix 8.3.2, Figure 8-16). Even extending the HPLC analysis run time beyond 30 min did not achieve the elution of a second species. Certainly, the CRD-bromide species could not further purified by HPLC. A crucial issue during the HPLC runs was the poor signal of the eluting species at the UV detector (detection at 208 nm), assuming a too low absorbance of the CRD peptides, although multiple peptide bonds are present. Reasons for the inconsistent results on the semi-preparative column may be associated with the column in general, such as hydrolyzed column material, or any strong interaction of the CRD with the column material. A further purification attempt of the CRD-bromide was carried out utilizing hydrophobic interaction chromatography (HIC), but the CRD peptide started to precipitate on the columns in multiple attempts in early stages of the run. Hence, no material could be obtained from HIC.

The CRD-bromide, employed in surface applications, was obtained from functionalization attempts, where the folded CRD was not observed in the ESI-MS spectra. Therefore, the CRD-bromide was from the high purity as indicated in the ESI-MS spectra in Figure 5-3C and D.

5.2.5 Small Molecule Bioconjugation Experiments with Functional CRDs

To test the applicability of the CRD-derivatives in bioconjugation, CRD – small molecule experiments were conducted to emulate the polymer-peptide coupling. These comprise

bioorthogonal thermal and photo-induced reactions: (i) CuAACs, employing the CRD-alkyne in combination with benzylazide, (ii) NITEC reactions, using the CRD-fumarate in combination with a small tetrazole derivative, (iii) "inverse" NITEC reactions, employing the CRD-tetrazole in combination with a small fumarate molecule, and (iv) thermally induced DA reactions with the CRD-fumarate in combination with a small cyclopentadiene derivative (refer to Scheme 5-4). In the following, the outcome and reaction designs of the orthogonal ligations are discussed.



Scheme 5-4. Bioorthogonal reactions of functional CRD-derivatives with small molecules, forming the corresponding adducts. From top to bottom: (I) CuAAC of CRD-alkyne with benzylazide. (II) NITEC of CRD-fumarate with a hydroxy functional tetrazole derivative. (III) "Inverse" NITEC of CRD-tetrazole with diethyl fumarate. (IV) Thermal DA reaction of CRD-fumarate with 3-cyclopentadienyl-methyl propionate.

5.2.5.1 CRD in CuAAC Reaction with a Small Molecule

In case of the CuAAC, the reaction between the CRD-alkyne and the benzylazide was conducted employing CuBr as catalyst and *N,N,N',N'',N''*-pentamethyldiethylenetriamine (PMDETA) as ligand. A preliminary CuBr stability test of the CRD should show whether the disulfides are affected by the auxiliary copper catalyst. Here, the folded CRD was exposed to CuBr, PMDETA and L-arginine in deionized water, showing no stability issues or any interfering reactions of the disulfides with the copper species (refer to Appendix 8.3.1, Figure 8-13).

To adequately dissolve the CRD-alkyne and the benzylazide (2 eq.), DMSO was employed as solvent and the reaction mixture containing CuBr was placed under oxygen and water free conditions by three consecutive freeze-pump-thaw cycles. The reaction was started by addition of the degassed ligand to the mixture and allowed to proceed for 24 h at ambient temperature. The purification of the crude reaction mixture was carried out by dialysis (MWCO = 1 kDa) against deionized water in order to remove any left-over benzylazide, ligand or CuBr, obtaining the product after lyophilization as a beige solid material. Since CRD derivatives caused issues in analysis with DMAc-SEC, ESI-MS spectra were recorded, showing the signal of the desired CuAAC adduct, as well as the absence of the CRD-alkyne (refer to Figure 5-4A). The assignment of the peaks demonstrates excellent agreement with theory ($m/z_{\text{exp.}} = 2201.7990$, $m/z_{\text{calc.}} = 2201.7805$). Therefore, the CuAAC is clearly recommended for polymer-peptide experiments.

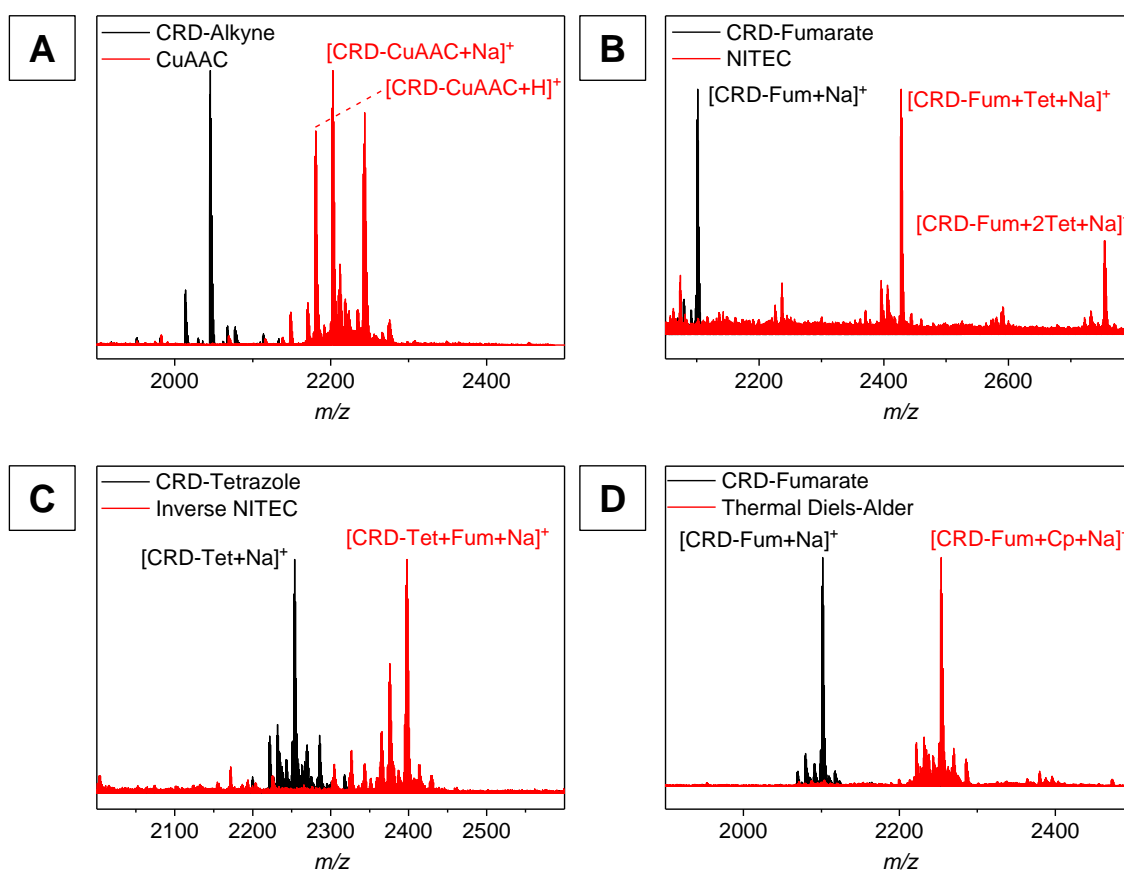


Figure 5-4. ESI-MS spectra of the bioorthogonal reaction products (red) and the functional CRD derivatives (black), as introduced in Scheme 5-4 (A) CuAAC adduct and CRD-alkyne, (B) NITEC adduct after the 2nd addition of tetrazole and CRD-fumarate, (C) “inverse” NITEC adduct and CRD-tetrazole, (D) DA adduct after second addition of the Cp-molecule and CRD-fumarate. All spectra were recorded *via* direct-infusion experiments, employing MeCN/H₂O as solvent mixture with doping of 1% acetic acid.

5.2.5.2 CRD in NITEC Reaction with a Small Molecule

In the second bioconjugation approach, the NITEC reaction was carried out by irradiating a mixture of CRD-fumarate and a tetrazole derivative, yielding the pyrazoline adduct after trapping the 1,3-nitrile-imine dipole with the fumarate moiety. The irradiation was performed for 1 h at $\lambda_{\text{max}} = 310$ nm (refer to Chapter 7.2.7), with 1.5 eq. of the tetrazole derivative (refer to Experimental Section 7.3.3). The product was subsequently analyzed in ESI-MS measurements, showing remaining peptide starting material, indicating incomplete conversion. In addition, multiple attachments of pyrazoline units on the CRD species were detected, suggesting an occurrence of the NICAL reaction (refer to Chapter 3.4.3.3). In this case, the nitrile-imine dipole has reacted with the fumarate at the *N*-terminus and the carboxyl group of the *C*-terminus, respectively. To achieve full conversion, a further 1.5 eq. of the tetrazole was added and the irradiation time was extended to a total of 5 h. In the ESI-MS spectrum of the final adduct, the absence of the CRD-fumarate was observed as well as multiple pyrazoline units attached to the CRD (refer to Figure 5-4B). The theoretical and experimental data are in good agreement (CRD with one pyrazoline unit: $m/z_{\text{exp.}} = 2427.8673$, $m/z_{\text{calc.}} = 2427.8363$), although signals appear that could not be assigned. Apparently, the 1,3-nitrile imine undergoes a NICAL reaction at the *C*-terminus of the peptide – a reaction previously reported in literature.²⁵⁰ Since the NICAL reaction does not harm the disulfides, a negative influence on the later stages of the experiments is not expected. In addition, the successful formation of the pyrazoline unit was verified by the color of the solution, being an intense fluorescent green after irradiation. Therefore, the NITEC reaction can be recommended for polymer-peptide experiments.

5.2.5.3 CRD in “Inverse” NITEC Reaction with a Small Molecule

In case of the “inverse” NITEC reaction, the functional groups were inverted utilizing the CRD-tetrazole in combination with diethyl fumarate. In this test reaction, a five-fold excess of the fumarate was employed in order to prevent the competing NICAL side reaction. In accordance to the protocol established for the NITEC approach, the irradiation time was set to 5 h at $\lambda_{\text{max}} = 310$ nm and the product was directly investigated in ESI-MS measurements without purification. In the obtained spectrum, the NITEC adduct can be unambiguously identified (refer to Figure 5-4C, $m/z_{\text{exp.}} = 2397.8388$, $m/z_{\text{calc.}} = 2397.8257$), although unassigned side signals were detected. A dimerization of the peptide (NICAL reaction of the tetrazole with the *C*-terminus of another peptide) cannot be deduced from the spectrum, *i.e.* either these species are not formed, or poor ionization of the CRD-CRD NITEC adduct impedes its detection. The color of the product solution was also intense

green and fluorescent. A clear recommendation of the “inverse” NITEC approach towards bioconjugation cannot be made, since the synthesis of the CRD-tetrazole demonstrated solubility issues, as noted in Chapter 5.2.3.

5.2.5.4 CRD in Thermally-Induced DA Reaction with Small Molecule

The last approach for the small molecule-peptide conjugations entailed a thermally driven DA reaction of the CRD-fumarate with a small Cp-molecule (1.1 eq.). Here, no catalyst was necessary, therefore, the reaction could be carried out by simply mixing both reactants at ambient temperature. After 24 h, the crude product was analyzed in ESI-MS measurements, showing the presence of the CRD-fumarate starting material and the DA-CRD adduct. Therefore, an additional 1.1 eq. of the Cp-molecule was added to stir for another 24 h at ambient temperature. Finally, the ESI-MS spectrum shows the presence of merely the DA adduct and the absence of the CRD-fumarate (refer to Figure 5-4D, $m/z_{\text{exp.}} = 2252.8174$, $m/z_{\text{calc.}} = 2252.7900$). Additional signals that are already present in the CRD-fumarate starting material could not be identified. The significant excess of the cyclopentadiene molecule was necessary, since small Cp molecules readily dimerize at ambient temperatures.³⁹⁶ Therefore, the DA reaction was crucially limited due to the Cp-dimerization and the resulting lack of the diene as reaction partner for the CRD-fumarate. Since dimerization of Cp is a serious drawback, the thermal DA approach is not recommended for the polymer-peptide bioconjugation.

5.2.6 Polymer-Peptide Ligation

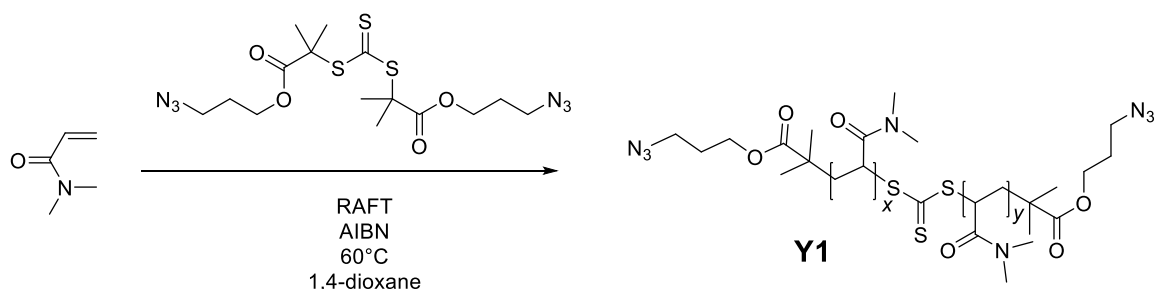
In the previous chapter, bioorthogonal reactions were assessed with respect to their effectivity, practicability and side reactions in small molecule reactions. Since the inverse NITEC and the thermal DA approaches encountered problems, the CuAAC and the regular NITEC (CRD-fumarate + tetrazole) approaches were selected for bioconjugation experiments in combination with polymers.

5.2.6.1 CuAAC Ligation for Bioconjugation^c

For the CuAAC bioconjugation reaction, a corresponding polymer is required, featuring two azide anchor sites to ultimately couple with the alkyne moiety of the CRD. Therefore, an α,ω -functional homotelechele was designed by RAFT polymerization, bearing two diazido groups at the polymer's termini. In the first step, a suitable RAFT agent was

^c Western blots were conducted by Theresa Bentele at the Ruprecht-Karls-Universität Heidelberg.

synthesized according to literature⁹⁷ to subsequently employ it in a RAFT polymerization of *N,N*-dimethylacrylamide (DMAA, refer to Scheme 5-5). The polymerization was conducted by a routine RAFT procedure with AIBN as initiator and 1,4-dioxane as solvent. The synthesized diazido-poly(dimethylacrylamide) (PDMAA) **Y1** was analyzed in DMAc-SEC, exhibiting a narrow MWD (refer to Figure 5-5A: $M_n = 13,900 \text{ g}\cdot\text{mol}^{-1}$, $D = 1.08$; for synthetic protocols refer to Chapter 7.4.3). The end-group fidelity of PDMAA was investigated in ESI-MS measurement, observing the presence of the desired repeating units with corresponding composition and excellent agreement of theoretical and experimental data (refer to Figure 5-5B, $[\text{P}_{53} + 2\text{Na}]^{2+}_{\text{exp}}$: 2873.8922, $[\text{P}_{53} + 2\text{Na}]^{2+}_{\text{calc}}$: 2873.8583).



Scheme 5-5. RAFT polymerization of *N,N*-dimethylacrylamide (DMAA) employing the diazido-RAFT agent in order to obtain poly(DMAA) **Y1**. Ratio DMAA:RAFT:AIBN of 1500:12:1. Solvent: 1,4-dioxane; $T = 60 \text{ }^\circ\text{C}$, $t = 8 \text{ h}$.

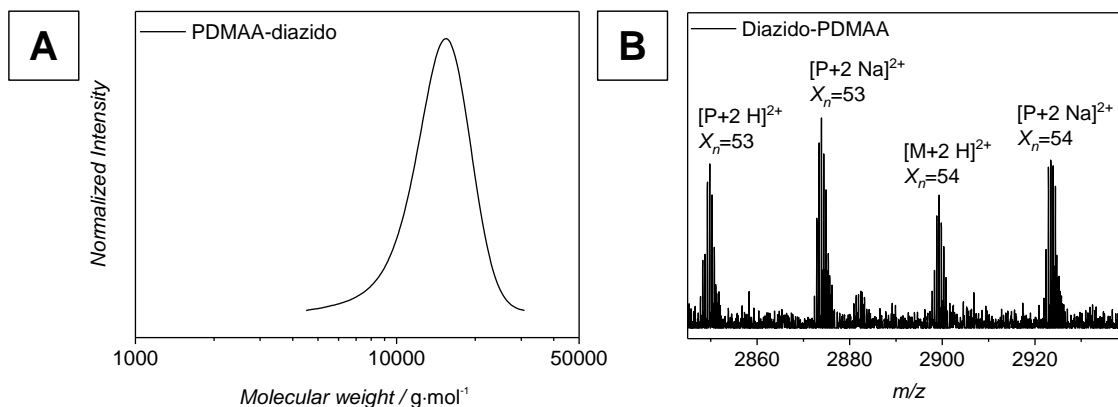


Figure 5-5. (A) Molecular weight distribution of the diazido-PDMAA **Y1** obtained by DMAc-SEC, applying a polystyrene calibration. $M_n = 13,900 \text{ g}\cdot\text{mol}^{-1}$, $D = 1.08$ (B) ESI-MS spectrum of the diazido polymer **Y1** depicting the repeating units of the corresponding polymer species as indicated. $[\text{P}_{53} + 2\text{Na}]^{2+}_{\text{exp}}$: 2873.8922; $[\text{P}_{53} + 2\text{Na}]^{2+}_{\text{calc}}$: 2873.8583. The ESI-MS direct infusion experiment was performed with THF/MeOH as solvent and sodium trifluoroacetic acid as doping agent.

In the following, the CuAAC bioconjugation experiment was carried out. Specifically, the diazido-PDMAA **Y1** was reacted with an excess of the CRD-alkyne (4.7 eq.) and CuBr/PMDETA in DMF (refer to Figure 5-6A). As solvent, DMF was employed instead of DMSO, due to better solubility of all starting materials. To provide oxygen and water free

conditions, three consecutive freeze-pump-thaw cycles conducted. The reaction was started upon addition of CuBr as a solid and allowed to proceed for 66 h at ambient temperature. Subsequently, the crude reaction mixture was purified by dialysis (MWCO = 2 kDa) against deionized water in order to remove any low molecular weight compounds. Consequently, the product was obtained by lyophilization, yielding a greenish powder, where the color is attributed to residual copper species. For analysis, DMAc-SEC was deployed, illustrating only poor shift of the product to shorter retention times, *i.e.* to higher molecular weights (refer to Figure 5-6B). In addition, the elugram unambiguously shows the presence of the starting material polymer and species that are shifted to higher retention times, *i.e.* lower molecular weights. It was not possible to assign all signals in the elugrams to specific species and a further separation of these species was not conducted. In further attempts with similar reaction conditions, identical results were obtained.

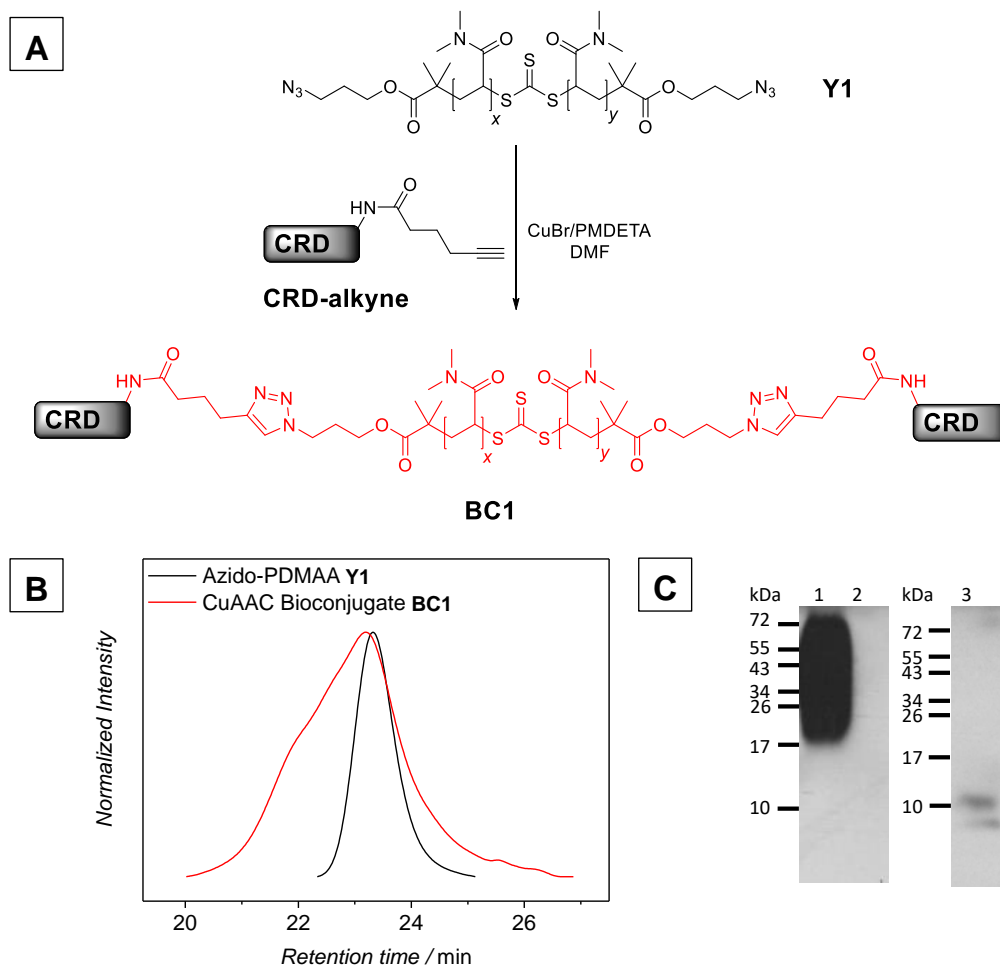


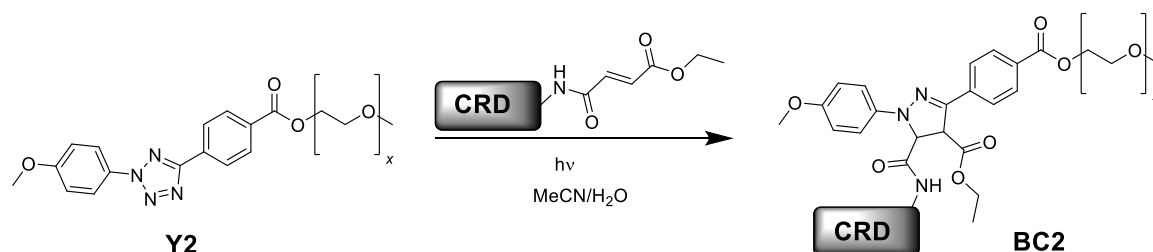
Figure 5-6. (A) Reaction scheme of the CuAAC reaction between the diazido-PDMAA **Y1** and the CRD-alkyne yielding the bioconjugate **BC1**. Reaction conditions: 4.7 eq. CRD-alkyne, 4.4 eq. CuBr, 4.4 eq. PMDETA; 1.0 eq. diazido PDMAA **Y1** in DMF under inert gas atmosphere for 66 h. (B) SEC-traces of the diazido-PDMAA (black) and the CuAAC bioconjugate product **BC1** (red). Measurement was conducted in DMAc-SEC. (C) Western blots of the CRD-bioconjugate **BC1** (1), the folded CRD (2), and a concentrated CRD-species (3) after separation *via* SDS-PAGE. Antibodies: anti-C-CRD (primary) and donkey-anti-guinea pig (secondary).

Nevertheless, to evidence the presence of CRD-species and to identify polymer-peptide bioconjugates, ESI-MS and western blot analysis were conducted. In ESI-MS, the copper residues caused very poor ionization, thus preventing a reliable measurement. To prove the presence of CRD containing species, western blot was conducted. Western blot is a standard technique in the field of biochemistry to identify and track proteins, by blotting them onto a carrier membrane and ultimately migrate them into a polymer gel, e.g. polyacrylamide gels. During the sample preparation, the protein sample is mixed with sodium dodecyl sulfate (SDS), a negatively charged surfactant, to overlay all positive charges of the protein. To denature the protein, the sample is heated to elevated temperature. Applied on the polymer gel, the denaturated and SDS loaded protein species migrate to the anode through the gel by employing a directed electric field, separating the species by their size due to differently strong interaction with the gel material, referred to as sodium dodecyl sulfate polyacrylamide gel-electrophoresis (SDS-PAGE). After the gel-electrophoresis, the proteins have to be accessible for staining. Thus, the protein species are transferred from the gel onto a membrane by employing an electric current, pulling the proteins from the gel onto the membrane. Since the protein sample does not cover the full membrane, the free areas on the membrane are blocked to prevent interactions with the staining antibodies. Subsequently, staining of the analyte is performed with specific antibodies, in order to visualize the target protein. Here, antibodies are employed to selectively stain the CRD sequence and therefore visualizing any CRD-containing species (refer to Chapter 7.2.10). In the western blot, the presence of CRDs in the bioconjugate **BC1** can be clearly confirmed after being successfully stained (refer to Figure 5-6C, trace 1). Concomitantly, the azido polymer precursor **Y1** was not stained (refer to Figure 5-6C, trace 2). However, the analysis of a polymeric distribution, already present before the CuAAC, complicates the interpretation of the western blot results. It can be concluded that CRD containing species are present but further statements according to other species bearing no CRDs cannot be made. On the other hand, successful staining of the CRD species proves coupling with the polymer, since single CRD with such short sequences are usually not or hardly detectable in western blots (refer to Figure 5-6C, trace 3).

Concluding from the SEC of the CuAAC, the reaction was not complete and a significant amount of the starting material polymer was not coupled to the CRD, although an excess of the peptide was present. Since the separation of the starting material, in particular the polymer, from the product is complex, further investigations employing the CuAAC reaction route were not conducted. Attempts using a water-SEC system for characterization of all employed species have not been able to determine ideal conditions for analysis of even the polymer precursor.

5.2.6.2 NITEC Ligation for Bioconjugation

In a second bioconjugation polymer approach, experiments *via* NITEC reaction were conducted. To simplify the reaction system, a monofunctional poly(ethylene glycol) (PEG) was employed as polymer, in order to find ideal conditions for the bioconjugation reaction with a polymeric material (refer to Scheme 5-6). Although two different CRD derivatives are available for the NITEC reaction, only the CRD-fumarate was employed, due to the aforementioned issues with the CRD-tetrazole. A commercial 2000 g·mol⁻¹ PEG-OH was functionalized with a tetrazole unit in a prior study,¹⁹⁴ showing low dispersity in SEC after functionalization (**Y2**, $M_n = 5,100$ g·mol⁻¹, $\mathcal{D} = 1.04$, refer to Figure 5-7C, black line). In the ESI-MS spectrum of the tetrazole functional PEG (Tet-PEG), the presence of the corresponding repeating unit was clearly confirmed (refer to Figure 5-7A).



Scheme 5-6. NITEC reaction between a Tet-PEG **Y2** and the CRD-fumarate upon UV irradiation, yielding the bioconjugate **BC2**.

In the first experiment, an equimolar ratio of the tetrazole-PEG and the CRD-fumarate in water/acetonitrile 9/1 (V/V) was irradiated for 2 h. The NITEC reaction was triggered upon irradiation with UV light ($\lambda_{\text{max}} = 310$ nm, refer to Chapter 7.2.7) with different additives, in order to address solubility issues by the addition of organic and inorganic bases. After the reaction, the color of the solution had changed from colorless to greenish fluorescent. However, due to visible remaining solid material, SEC analysis was not conducted. In the ESI-MS spectra yet, absence of the former tetrazole-PEG is observed, on the other hand, the presence of the desired product CRD-fumarate-PEG bioconjugate could not be proven (refer Figure 5-7B, black line).

In a second attempt, the CRD-fumarate and Tet-PEG were combined with an inorganic base, here 0.01 M NaOH in low amounts, to improve the solubility of the CRD-fumarate. The reaction was carried out in water and a slight excess of the CRD-fumarate was employed in order to reduce possible NICAL reactions. Furthermore, the addition of a base and a change in the solvent mixture ensured the complete dissolution of the starting materials. The mixture was then irradiated for 1 h with UV light ($\lambda_{\text{max}} = 310$ nm). Similar to the first experiment, the color of the solution turned from colorless to greenish fluorescent. The ESI-MS measurement revealed the absence of the Tet-PEG starting material,

however, also the desired bioconjugate product could not be observed (refer to Figure 5-7B, red line).

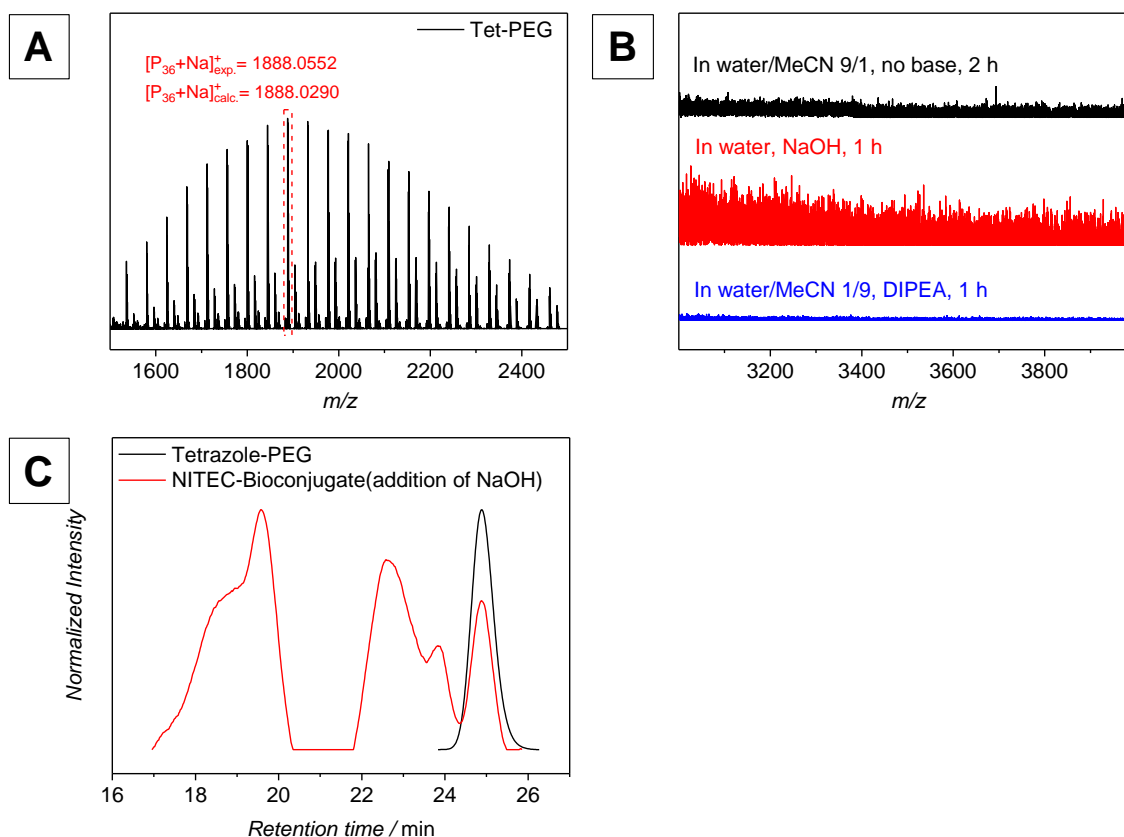


Figure 5-7. ESI-MS spectra of the (A) Tetrazole functional PEG **Y2**, (B) NITEC adducts **BC2** of the CRD-fumarate and the tetrazole-PEG after irradiation with following conditions: (black): 1 eq. CRD-fumarate, 1 eq. Tet-PEG **Y2**, in water/MeCN 9/1 V/V, irradiation for 2 h. (Red): 1 eq. CRD-fumarate, 1 eq. Tet-PEG **Y2**, in water, irradiation for 1 h, addition of 0.01 M NaOH. (Blue): 1.00 eq. CRD-fumarate, 0.75 eq. Tet-PEG **Y2**, in water/MeCN (1/9 V/V), irradiation for 1 h, addition of DIPEA. (C) SEC-traces of the tetrazole functional PEG **Y2** before irradiation (black) and the bioconjugate **BC2** after NITEC reaction upon irradiation (red, with addition of NaOH). Irradiation was carried out for 1 h.

In contrast, the SEC-trace clearly indicates the presence of species with similar size as the starting material and two further species at lower retention times (refer to Figure 5-7C, blue line), *i.e.* higher molecular weights. Since a clear shoulder can be observed at retention times of 18-20 min, possibly multiple attachments of the Tet-PEG at the CRD at either the carboxylic or thiol sites might have occurred. An influence of the base onto possible reactions of the peptide with itself could also be present, including disulfide reshuffling. The species at retention times from 22-24 min might be the target CRD-PEG adduct, yet no separation could be performed to further investigate these species. However, the shoulder here also might be an undesired by-product.

In a last attempt, the solvent mixture was changed to a high share of acetonitrile (9/1 to water, V/V). In addition, the auxiliary base was changed to the sterical hindered base DIPEA in order to exclude any negative influence of the NaOH to the reaction or the CRD.

The solubility was only slightly increased with DIPEA. The sample was then irradiated with UV light for 1 h. Similar observations as in the previous experiments were made, *i.e.* the sample showed a greenish fluorescent color after irradiation. In the ESI-MS spectrum, again the absence of both the Tet-PEG and the desired product is observed (refer to Figure 5-7B, blue line). Furthermore, SEC measurements were not performed due to poor solubility of the sample.

A major problem of the experimental procedure is the solubility of the CRD-fumarate as well as of the products. To some extent, the CRD-fumarate demonstrated issues regarding its solubility, which was encountered several times during the functionalization of the CRD. Therefore, the addition of a base was necessary to enhance solubility of the starting materials. Nevertheless, the base might interfere with the NITEC reaction and it remains unclear which reaction pathway was taken. A possible degradation of the CRD peptide upon base addition can also not be excluded. Since no clear results were obtained in HPLC of the single functional CRDs, no HPLC experiments were conducted for the bioconjugates (refer to Chapter 5.2.4). Furthermore, the DMAc-SEC analysis was critical due to poor solubility and previous mentioned detection issues of single CRDs. Therefore, a CRD containing species, which has a high mass share of the peptide, is assumed to be dominated by the CRD during SEC analysis. Thus, cross-linking or remaining of the CRD containing material in the columns might occur. The polymeric NITEC adducts have a high share of the CRD peptide and therefore, the SEC behavior could be negatively influenced by the CRD. In contrast, the bioconjugates in the CuAAC approach are unambiguously dominated by the PDMAA, due to its significantly higher mass share of the target bioconjugate. Further experiments and optimization could not be conducted, since the CRD functionalization failed for all derivatives and hence a lack of purified functional CRD-fumarate disallows to continue the studies with ESI-MS, HPLC, and SEC.

5.2.7 Conclusion

In the current chapter, the bioconjugation between CRDs and polymers has been addressed, proving to be a challenging task. The goal was the introduction of two CRD units as end-groups of a difunctional polymer. These difunctional CRD-polymer bioconjugates were envisaged to be polymerized in a SG polymerization. Problems accompanied several stages of the project, due to issues in CRD handling, solubility, characterization, and reaction stability. It was possible to establish procedures for the CRD folding and CRD functionalization, decorating successfully the *N*-terminus of the CRD with bioorthogonal anchor moieties, such as fumarates, alkynes, tetrazoles, and bromides. An emulation of polymer-peptide bioconjugation experiments was conducted in combination

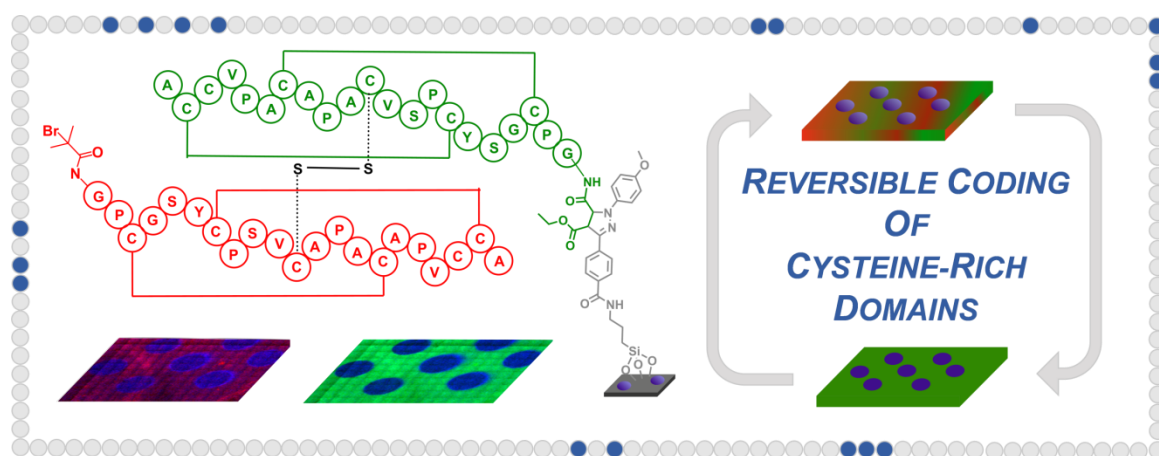
with small molecules. In these reactions, the formation of corresponding bioconjugate adducts was achieved, however, by-product formation as in case of NITEC was encountered. Nonetheless, the results of bioorthogonal reactions with small molecules could not be translated to polymeric systems, due to limitations in terms of solubility, reactivity, and conversion. Due to unsuitable and impure polymer-peptide bioconjugates, the final SG polymerization of the bioconjugate was not conducted.

A major issue within the project was the lack of suitable analysis. In SEC, general detection issues with the CRD or apparently with CRD-species occurred. In addition, the ESI-MS measurements could not provide sufficient information of the polymeric bioconjugates due to the poor ionization of polymeric adducts and instrument limitations. Nevertheless, ESI-MS was the basic characterization method of all CRD functionalization products and small molecule experiments, successfully identifying the corresponding CRD-derivatives. In HPLC runs, similar problems as for SEC were experienced, since attempts on the semi-preparative scale failed due to missing elution and non-reproducible results. The project could not be further pursued because CRD functionalization failed, *i.e.* no clean functional CRD derivatives could be obtained. Reasons can be found in apparently lower quality of different batches of the reduced CRD, although in ESI-MS spectra no significant differences of the CRD batches could be identified.

5.3 Exploiting CRDs for Recodable Surface Design

5.3.1 Motivation

CRD peptides are capable to form reversible disulfides, which is exploited during the maturation of nematocysts in nature. Therefore, functional CRD derivatives are envisaged to be immobilized onto surfaces by their dynamic disulfide bonds to utilize the reactivity of the cysteines as ligation tool in surface encoding and decoding (refer to Scheme 5-7).³⁴² In a first step, the CRD-fumarate (for preparation and characterization refer to Chapter 5.2.3) was covalently immobilized onto a plain surface by a photo-induced reaction in a spatially resolved fashion using NITEC chemistry. In a second step, a CRD-bromide species (for preparation and characterization refer to Chapter 5.2.4) is employed to form a disulfide bond with the previously immobilized CRD on the surface. By emulating the cysteine reshuffling in nature, the surface encoding is envisaged to be achieved by switching the disulfide bonds from an intra- to an intermolecular linkage. To erase or decode the motif, the disulfide reshuffling has to switch the linkage from an inter- to an intramolecular pattern. The characterization is conducted by ToF-SIMS analysis, selectively imaging characteristic groups of the corresponding materials at specific locations on the surface.^D



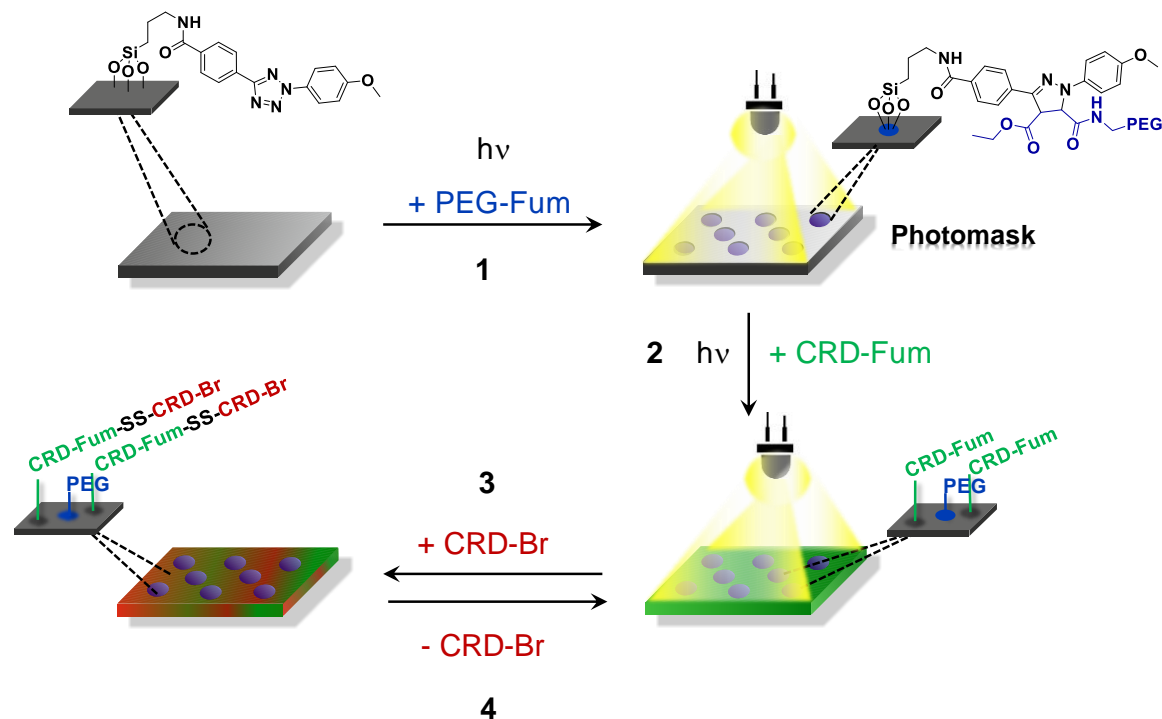
Scheme 5-7. Overview of the CRD functional surfaces and respective ToF-SIMS ion maps. The scheme was reprinted from ref.²⁵⁸ with permission from the Royal Chemical Society.

5.3.2 Surface Preparation and Design

To generate spatially resolved surface patterns, photo-induced reactions in combination with photomasks were employed. In the first step, a silicon wafer was functionalized with

^D Parts of this chapter are reproduced or adapted from T. Gegenhuber, D. Abt, A. Welle, S. Özbek, A. S. Goldmann and C. Barner-Kowollik, *J. Mater. Chem. B*, 2017, **5**, 4993–5000 with permission from the Royal Society of Chemistry (Ref.²⁵⁸). D. Abt and A. Welle conducted the ToF-SIMS measurements, S. Özbek was involved in the development of the CRDs folding procedure. A. S. Goldmann, and C. Barner-Kowollik supervised and motivated the project.

tetrazole moieties by silanization, which could be conducted in a facile and straight-forward procedure.²⁵⁷ Subsequently a patterning on the surface was obtained *via* the NITEC reaction by immobilizing a functional PEG-fumarate and a CRD-fumarate in consecutive reactions. The photo reaction of the former generates a peptide repellent/passivating area, whereas the photo reaction of the latter forms a peptide rich area on the surface (refer to Scheme 5-8).



Scheme 5-8. Illustration of the (1) immobilization of PEG-fumarate onto a tetrazole functionalized plain surface upon NITEC reaction. (2) Attachment of CRD-fumarate by NITEC reaction upon irradiation. (3) Immobilization of CRD-bromide by reoxidation and reshuffling of the disulfide bonds. (4) Removal of the CRD-bromide by reoxidation and reshuffling of the disulfide bonds. The scheme was adapted from ref.²⁵⁸ with permission from the Royal Chemical Society.

To attach the PEG onto the surface, the tetrazole functional surface was mounted in a special sample holder and covered with a photomask with a dot layout (for setup refer to Chapter 7.2.8). Next, the surface was immersed into a solution, containing the fumarate functional PEG, and irradiated for 8 h with UV light to trigger the NITEC reaction in the light exposed areas ($\lambda_{\text{max}} = 310$ nm, refer to Chapter 7.2.7). Subsequently, the wafer was unmounted from the sample holder setup and rinsed with organic solvents, here toluene and DCM, in order to remove any adsorbed and non-reacted material. For each modification stage, the surfaces were analyzed by ToF-SIMS. In the current step the characteristic ethylene glycol fragment ($\text{C}_2\text{H}_5\text{O}^-$) stemming from the immobilized PEG chains is clearly detected in the dotted sections and a sharp contrast to the non-irradiated areas can be observed in the ToF-SIMS mappings (refer to Figure 5-8A).

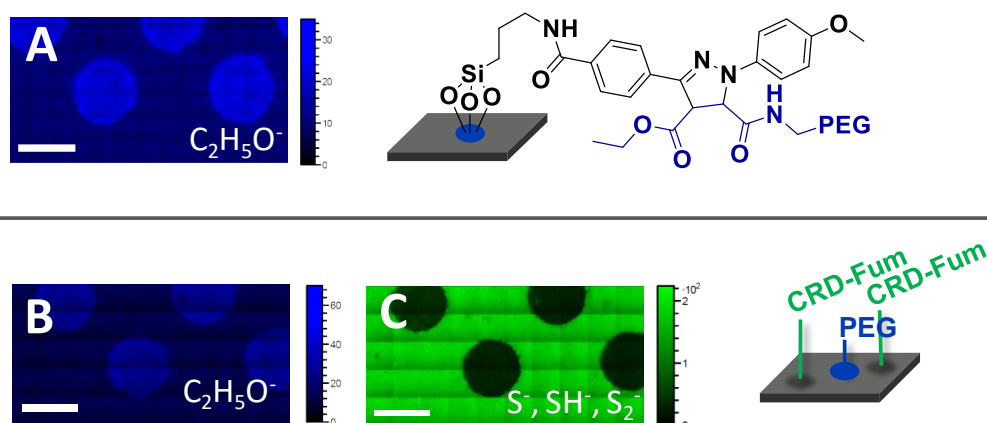


Figure 5-8. ToF-SIMS ion maps of the consecutively conducted photo-induced surface immobilization as illustrated in Scheme 5-8. (A) Surface after PEG attachment *via* the NITEC reaction, representing the fragment $C_2H_5O^-$. (B) Surface after CRD-fumarate immobilization *via* the NITEC reaction, representing the fragment $C_2H_5O^-$. (C) Surface after CRD-fumarate immobilization *via* the NITEC reaction, representing the sum of S^- , HS^- , S_2^- fragments. The figure was adapted from ref.²⁵⁸ with permission from the Royal Chemical Society.

In the second stage of the patterning procedure, the wafer was immersed into a solution of CRD-fumarate in water/MeCN (1/1, V/V) without any photomask. The wafer was irradiated for 24 h with UV light and subsequently rinsed with Millipore water, a 0.1 M sodium hydroxide solution and ethanol. Note that the rinsing procedure was carried out to the same extent and in case of the NaOH in same concentrations for all surfaces. In the ToF-SIMS ion maps in Figure 5-8B and C, the ethylene glycol fragment ($C_2H_5O^-$) within the dotted areas as well as the sulfur related fragments (S^- , S_2^- and HS^-) are detected outside the dots. Hence, a successful co-immobilization of both components was shown and the absence of the corresponding sulfur signals within the dots evidences the repellent character of the PEG, preventing CRD accumulation (ToF-SIMS overlay refer to Chapter 8.4 Figure 8-17). With regard to the protein related signals, the sulfur secondary ions certainly prove the presence of the CRD peptide, since the CN^- secondary ion, a common benchmark for peptides,³⁹⁷ is affected by the underlying tetrazole layer and pyrazoline residuals. However, the intensity of the sulfur fragments is moderate due to an overall low sulfur content within the peptide (9.9 wt.%).

As previously discussed in Chapter 3.4.3.3, the CRD-fumarate might undergo the NICAL reaction, competing with NITEC, since the carboxylic acid at the C-terminus of the peptide is readily available.²⁵⁰ Nevertheless, attachment *via* the C-terminus has no impact on the further strategy, because the disulfide bonds are not affected, merely immobilizing the CRD upside down. In addition, a reaction of tetrazoles with thiols at this stage is rather unlikely, since the CRD units are folded and the thiols are oxidized.

5.3.3 Surface Encoding and Erasing of CRD Peptides

After the photo-induced patterning with the PEG and the CRD, the surface is ready to be employed in an encoding and erasing procedure. To selectively monitor the attachment and detachment of a further CRD unit, a CRD-bromide was synthesized (refer to Chapter 5.2.4). In ToF-SIMS analysis the bromine fragment associated with the CRD-species can be excellently traced. As illustrated in Scheme 5-7, the encoding was achieved by immobilization of the CRD-bromide outside the dot pattern by disulfide formation. A disulfide reshuffling can be induced at neutral pH values in phosphate buffer solution (PBS) without the addition of any organic solvent. To trigger the disulfide reshuffling, the wafer was incubated in PBS at pH = 7 for 2 h. Concomitantly, a solution of the CRD-bromide in PBS at pH = 7 was prepared with a CRD concentration of 0.25 g·L⁻¹. The buffer at pH = 7 should induce the dynamic disulfide-thiol equilibrium of the CRD peptide, which has been found in a previous study.³⁴³ The low CRD-bromide concentration should prevent any dimerization potential of the CRD in solution. For both vessels, nitrogen was percolated in order to reduce the oxygen in the reaction environment. After 2 h of incubation, the silicon wafer bearing the pattern consisting of PEG and CRD was transferred into the solution of the CRD-bromide for 6 h of incubation. Next, the surface was withdrawn from the solution and rinsed with Millipore water, 0.1 M NaOH, and ethanol.

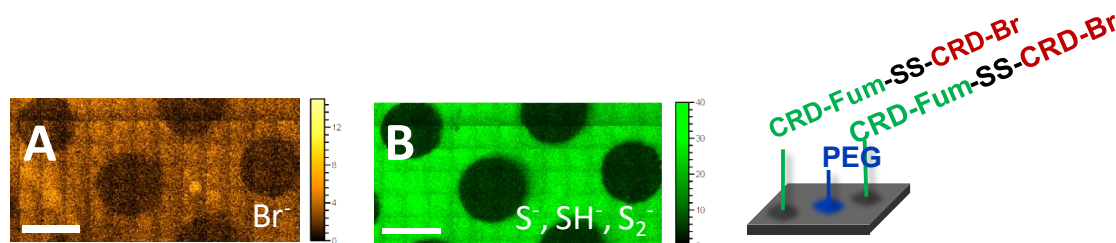
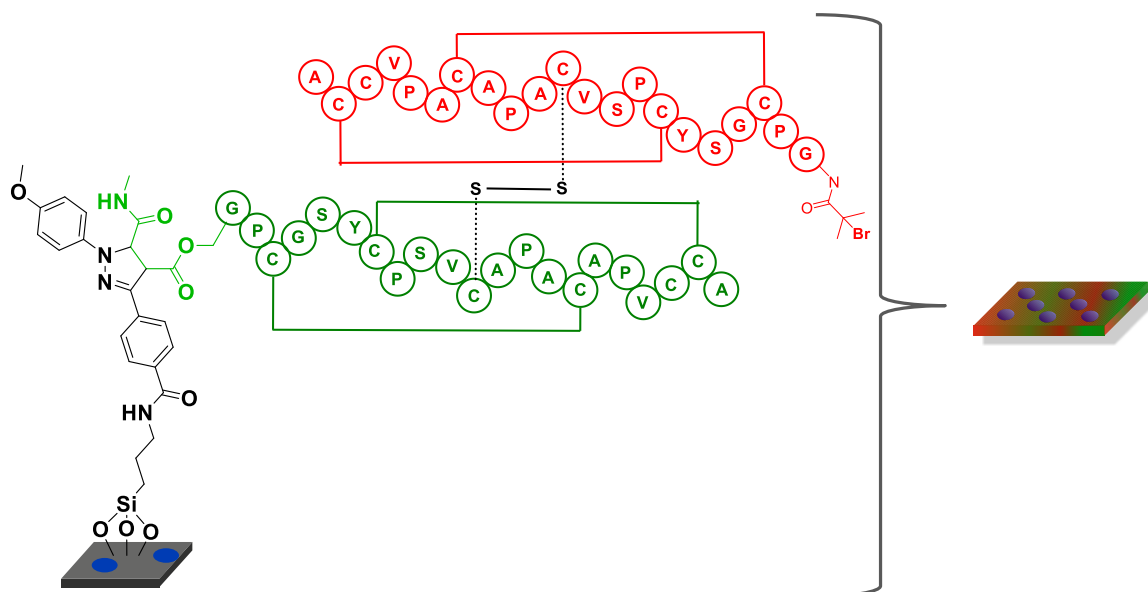


Figure 5-9. ToF-SIMS ion maps of the encoded surfaces as illustrated in Scheme 5-8. (A) Surface after CRD-bromide immobilization, representing the sum of ⁸¹Br⁻, ⁷⁹Br⁻ fragments. (B) Surface after CRD-bromide immobilization, representing the sum of S⁻, HS⁻, S₂⁻ secondary ions. ToF-SIMS spectra of A-B are depicted Figure 5-11A (bromine) and B (sulfur). The figure was adapted from ref.²⁵⁸ with permission from the Royal Chemical Society.

The surface was analyzed in ToF-SIMS, clearly illustrating the coexistence of the bromine fragments (⁷⁹Br⁻, ⁸¹Br⁻) in Figure 5-9A as well as the sulfur related fragments (S⁻, S₂⁻ and HS) in Figure 5-9B adjacent to the dot pattern of the PEG (overlay refer to Appendix 8.4, Figure 8-18). In the ToF-SIMS ion maps, the ion count of the bromine fragment signals is as expected low, caused by the low share of the bromine within the peptide (3.8 wt.%). The CRD-bromide in the immobilized state is illustrated in Scheme 5-9.



Scheme 5-9. Illustration of the encoded surface showing the CRD-fumarate (green) attached covalently to the surface by the pyrazoline units. The CRD-bromide (red) linked by disulfide bond to the CRD-fumarate after a reoxidative reaction. The illustration portrays the state, which is shown in the ToF-SIMS ion map in Figure 5-9A and B. The figure was adapted from ref.²⁵⁸ with permission from the Royal Chemical Society.

To erase the written pattern of the CRD-bromide, a PBS at pH = 7 with additional GSH with a concentration of 2.5 M was employed to reduce the disulfides of the CRDs and hence, releasing the CRD-bromide from the surface. The erasing was carried out by incubating the surface with the immobilized CRD-bromide into the PBS/GSH mixture for 10 min while shaking. Subsequently, the silicon wafer was rinsed with Millipore water and a 0.1 M NaOH solution. Directly thereafter, the wafer was transferred into a fresh PBS/GSH solution. This procedure was repeated five times to ensure the complete release of the CRD-bromide from the surface. Finally, the surface was rinsed with Millipore water, 0.1 M NaOH solution, and ethanol. The analysis was conducted by ToF-SIMS measurements, showing the absence of the bromine fragments on the entire surface (refer to Figure 5-10A), while the sulfur related fragments are preserved outside of the dot pattern (refer to Figure 5-10B).

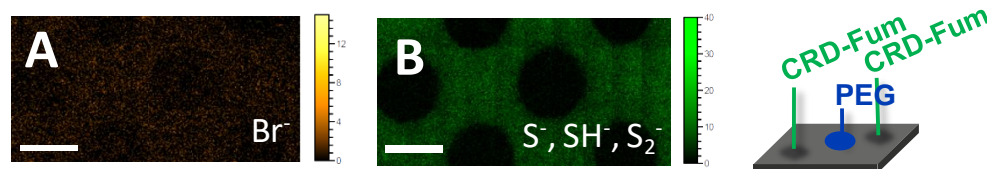


Figure 5-10. ToF-SIMS ion maps of the erased surfaces as illustrated in Scheme 5-8. (A) Surface after CRD-bromide removal, representing the sum of ^{81}Br , ^{79}Br fragments. (B) Surface after CRD-bromide removal, representing the sum of S^- , HS^- , S_2^- fragments. ToF-SIMS spectra of A-B are depicted Figure 5-11A (bromine) and B (sulfur). The figure was adapted from ref.²⁵⁸ with permission from the Royal Chemical Society.

After the erasing, the near absence of the bromine fragments verifies the following assumptions: (i) Since the rinsing procedure was carried out after each step, a physical adsorption of the CRD derivatives on the surface was avoided and an adequate concentration of the CRD-bromide for the encoding was selected. (ii) Since the bromine fragments could be detected after the encoding, a covalent attachment of the CRD-bromide on the surface is evidenced, since the rinsing procedure should have otherwise removed it.

Clearly, the intensity of the sulfur and the bromine species changed after erasing, therefore, the ToF-SIMS spectra of the encoded and erased surface were examined. To ensure comparable results, a normalization of the corresponding areas in the mapping by the primary ion dose was conducted. By comparing the spectra of both the encoded and erased stages, the bromine intensity decreases about 84% (refer to Figure 5-11A), whereas the sulfur intensity (S^-) is lowered about approx. 70% (refer to Figure 5-11B). Therefore, the sulfur signals remains at a higher extent in comparison to the CRD-bromide, assuming the layer of the CRD-fumarate remains at the surface.

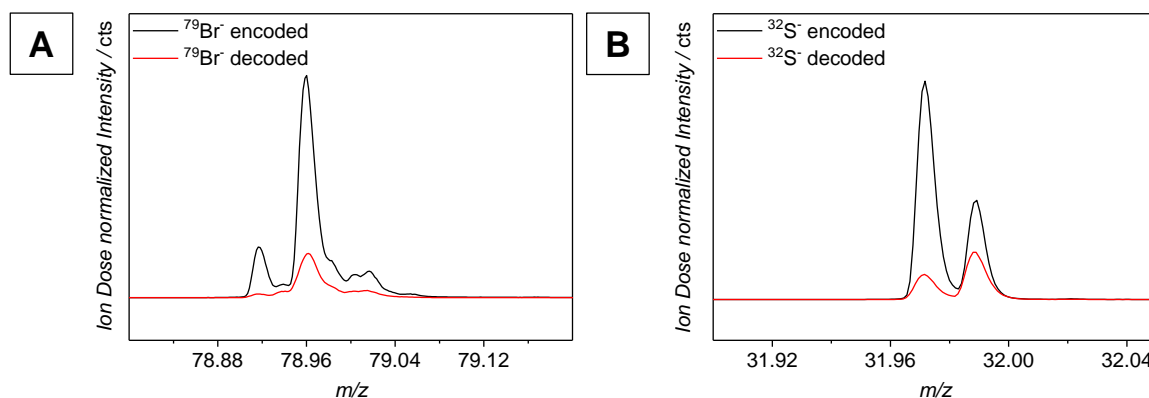


Figure 5-11. ToF-SIMS spectra of (A) $^{79}\text{Br}^-$ fragment, $m/z = 78.92$ (peak indicated with red arrow) with primary ion dose normalization (related to the mappings in Figure 5-9A (black) and Figure 5-10A (red)). (B) ToF-SIMS spectra of the main sulfur signal, $m/z = 31.97$, with primary ion dose normalization (related to the mappings in Figure 5-9B (black) and Figure 5-10B (red)). The figure was adapted from ref.²⁵⁸ with permission from the Royal Chemical Society.

An explanation for the large decrease in the sulfur intensity can be given by the analytic method, since ToF-SIMS is a destructive surface characterization method. In addition, the multiple rinsing steps with the diluted NaOH solution might also cause degradation of the CRD to a certain extent. Nevertheless, the evaluation demonstrates the successful release of the CRD-bromide from the surface. As demonstrated, the utilization of the CRD's disulfide bonds for the reversible coding of surfaces is a powerful tool, due to mild writing and erasing steps in buffer solution at neutral pH. In an earlier step, a photopatterning by the NITEC reaction of a PEG-fumarate and a CRD-fumarate generated a peptide repellent and a peptide rich area on the surface. Such an approach might also be expanded by

synthesizing other CRD derivatives, bearing e.g. markers for conventional analytical methods, such as fluorescence microscopes. Furthermore, CRDs could be employed in reversible hydrogels, triggering the gel formation and degradation by disulfide reshuffling with pH and addition of oxidation/reduction reagents.³⁹⁸

5.3.4 Conclusions

Spatially-resolved surface coding in a reversible fashion was demonstrated by utilization of CRD peptides in a reoxidative procedure. Here, the goal was to develop a reversible encoding and decoding method of CRD functional surfaces with traceable CRD-derivatives for in-depth surface analysis techniques. An inverse dot pattern of CRDs was generated onto tetrazole functional silicon wafers by the NITEC reaction, immobilizing a peptide repellent consisting of PEG in a dotted pattern as well as the CRD outside of the dots. The analysis of all surfaces was conducted *via* ToF-SIMS, revealing the presence of the CRD peptide and the PEG in the corresponding areas of the surface. After the immobilization of the CRD, a CRD-bromide was attached on the surface by the formation of intermolecular disulfides between the CRD and the CRD in solution. Here, the disulfide formation was triggered under reoxidative conditions at pH = 7, enabling a dynamic reshuffling of the disulfides from an intramolecular to an intermolecular linkage. Due to a rigorous rinsing procedure, physical adsorption of the CRD onto the surface could be avoided, emphasizing the covalent attachment of the CRD *via* intermolecular disulfide bonds. In the last stage, the CRD-bromide pattern was erased from the surface under similar reoxidative conditions, adding GSH to trigger reduction of the disulfide bonds.

In summary, CRD-peptides could be successfully employed in a spatially resolved encoding and decoding procedure on functional surfaces *via* reversible disulfide formation. The dynamic nature of the CRD's disulfide reshuffling is of interest for several applications, such as reversible hydrogels as well as on further disulfide or thiol functional surfaces.³⁹⁹

6

6 CONCLUDING REMARKS

The demand for reactions with low sensitivity and high specificity for the synthesis of tailor-made materials led to the development of a plethora of chemistries with mild reaction triggers and conditions.^{183,192,301,400–402} In general, a key feature of reactions with broad applicability is orthogonality, *i.e.* the ability to address a specific functionality in the presence of other functional groups. For polymeric systems, stoichiometric feed ratio of the starting materials, high yields, and simple purification procedures are essential features of such reactions.¹⁸⁴ Chemical reactions that fulfill many of these criteria, are Diels – Alder (DA) reactions.¹⁹² Essentially, DA reactions demonstrate high atom economy and, with respect to the diene and dienophile, can be conducted under mild reaction conditions, *e.g.* at ambient temperature. An excellent example for photo-induced DA reactions are photo-caged dienes, which are obtained from *e.g.* *ortho*-methyl benzaldehydes or *ortho*-methyl benzophenones.^{266,274} Here, upon irradiation with UV light, *ortho*-quinodimethane species are generated, readily available to undergo [4+2] cycloadditions with electron deficient enes. An highly reactive species for thermally induced DA and hetero DA (HDA) reactions are cyclic dienes, such as cyclopentadiene, demonstrating fast yet reversible reactions with electron deficient enes.^{144,392} Here, the reversible nature of the HDA reaction allows for an application in self-healing, or bonding and debonding on demand materials.^{153,196} Furthermore, with respect to suitable dienes and dienophiles, the progress of the HDA or *retro* HDA reaction can be monitored by a color change, referred to as a self-reporting system.¹⁹⁶ An application of such reactions in step-growth (SG) polymerization is uncommon, since the generation of feasible starting materials is rather complex and reaction conditions might become highly elaborate.¹²⁶

In Chapter 4, reactions with the aforementioned characteristics have been employed in SG polymerizations and bioorthogonal functionalizations. Highly specific DA reactions

were exploited in SG polymerization to obtain multi-chain transfer agent (mCTA) polymers. Here, difunctional *ortho*-benzaldehydes and cyclopentadienes monomers were separately employed in a DA reaction with a difunctional fumarate, bearing a trithiocarbonate moiety. However, a critical side-reaction of the photo-induced DA reaction of the *ortho*-methyl benzaldehyde with itself could be identified and overcome by adjusting the stoichiometric feeding ratio of the monomers. The implementation of multiple trithiocarbonate moieties in the backbone of a polymer allowed the application of these polymers as multi chain transfer agents (multi-CTAs) in reversible addition fragmentation chain transfer (RAFT) polymerization for chain extension with styrene. After RAFT polymerization, segmented copolymers were obtained with high molecular weight species. In addition, *in silico* calculations provided in-depth insights into the mechanistic processes underpinning the SG and, respectively, the RAFT polymerization. The calculations provided data, which is inaccessible by experimental characterization methods. In a second approach, a di(cyclopentadiene) monomer was employed in a thermally-induced DA reaction with a difunctional fumarate bearing a trithiocarbonate, yielding well-defined SG polymers. Here, the DA reaction demonstrates high reaction rates, absence of by-product formation, and a simple reaction procedure. Therefore, the outcome of the thermally induced DA reaction underpins the convenient and straight-forward nature of the process. In a similar fashion to the photo-induced system, the SG polymers were successfully utilized as multi-CTA in RAFT polymerization, obtaining segmented copolymers with high molecular weights. In the thermally-induced DA approach, the SG polymerization showed fast reaction rates and the insensitivity of the reaction represents an almost perfect SG system. However, the RAFT polymerization of styrene with the SG polymer as multi-CTA is highly complex, due to the polymeric structure of the precursor. A comprehensive study needs to address the influence of the precursor's molecular weight on the RAFT polymerization and how the RAFT mechanism unfolds during the polymerization with increasing chain length and viscosity.

In Chapter 5, cysteine-rich domains (CRDs) were employed as synthetic tool for SG polymerization and surface functionalization. CRDs are short peptide motifs that bear six cysteine units, readily available for disulfide formation in an intra- or intermolecular fashion.¹ Upon triggering disulfide formation, intramolecular disulfides generate a three dimensional structure of the CRD, whereas intermolecular disulfide bonds lead to the formation of CRD-CRD species, either in linear or crosslinked fashion.³⁴² Due to the reversible character of the disulfides, an equilibrium between the disulfides and the thiols can be induced at neutral pH, referred to as disulfide reshuffling.³⁴⁰ In Chapter 5.2, CRDs were functionalized with anchor moieties for bioorthogonal reactions, such as photo- and thermally induced DA reactions, nitrile-imine mediated tetrazole-ene cycloaddition

(NITEC), as well as for the copper-catalyzed azide-alkyne cycloaddition (CuAAC). Subsequently, functional CRDs were employed in the aforementioned highly specific reactions with small molecules, in order to ultimately transfer them to an α,ω - functional polymer. The functionalization of the CRDs and the subsequent bioorthogonal reactions with small molecules were successfully performed. However, a coupling of the functional CRDs to the polymer could not be achieved although diverse chemical approaches were followed. Therefore, the bioconjugate, *i.e.* a difunctional macromonomer with CRD as termini, could not be obtained and a SG polymerization was carried out. In order to obtain well-defined bioconjugate macromonomers, the peptide starting materials have to be separated from any impurities and contamination, harming the successful bioconjugation. Furthermore, HPLC methods have to be fully established in order to purify the outcome of the bioconjugation.

In Chapter 5.3, functional CRDs were immobilized onto surfaces in a spatially resolved fashion by NITEC. In the next step, a second functional CRD was attached to the CRD-surface by disulfide reshuffling and subsequently released from the surface under mild reoxidative conditions. Due to the special functionalization of the second CRD, its presence on the surface could be explicitly monitored by time-of-flight secondary ionization mass spectrometry (ToF-SIMS). It was shown by ToF-SIMS that the second CRD was successfully attached and released from the surface, evidencing a covalent attachment of the CRD. Functional CRDs as reversible units for surface functionalization could be immobilized onto different thiol functional surfaces, in order to simplify the process of the spatially resolved surface patterning. Here, the immobilization of thiols in a simplified manner could enhance the method for surface encoding.

7

7 EXPERIMENTAL SECTION

7.1 Materials

Pentafluorophenol (PFP, Aldrich, $\geq 99\%$), sodium azide (Acros, 99%+), benzyl bromide (Aldrich, 98%), hexynoic acid (Acros, 97%), 4-(*N,N*-dimethylamino)pyridine (DMAP, Aldrich, $>99\%$), 1-ethyl-3-(3-dimethylaminopropyl) carbodiimide hydrochloride (EDC, Carl Roth, $>99\%$), diisopropyl ethyl amine (DIPEA, Carl Roth, $\geq 99\%$), thionyl chloride (Aldrich, $\geq 99\%$), glutathione (GSH, AppliChem, $\geq 97\%$), glutathione oxidized (GSSG, TCI, $>98\%$), L-arginine (Carl Roth, $>98.5\%$), sodium hydroxide (NaOH, Carl Roth, $\geq 98\%$), dipotassium hydrogen phosphate (Carl Roth, $\geq 99\%$), chloroform (Fischer, p.a.), acetone (Fischer, p.a.), sodium sulfide (Aldrich, $\geq 98\%$), carbon disulfide (VWR, 99.9%), 1,3-propanediol (Aldrich, 98%), 3-azido-1-propanol (Aldrich, $\geq 96\%$), triethylamine (Merck, $\geq 99\%$), diethyl fumarate (Alfa, 98%; monofunctional **F**) 2-bromo-propionic acid (Aldrich, $\geq 99\%$), 1,3-dibromopropane (Aldrich, 99%), ethylene glycol (Alfa, 99%), potassium carbonate (Acros, 99%+, anhydrous), 2,3-dimethylanisole (Aldrich, 97%), potassium peroxodisulfate (Acros, 99%), copper sulfate pentahydrate (Acros, 99%), aluminum chloride (AlCl_3 , Merck, $\geq 98\%$), 11-bromo-1-undecanol (Alfa, 97%), *N,N,N',N'',N''*-pentamethyldiethylenetriamine (PMDETA, Merck, $\geq 98\%$), tetrabutylammonium bromide (Merck, $\geq 99\%$), *tert*-butyldimethylsilyl chloride (TBDMSCl, TCI, $>98\%$), 1-methylimidazole (Aldrich, 99%), sodium cyclopentadienyl (NaCp, Aldrich, 2 M in THF), 1,10-dibromodecane (Acros, 97%), monoethyl fumarate (Aldrich, 95%), 4-formylbenzoic acid (Aldrich, 97%), NaNO_2 (VWR, $\geq 99\%$), 4-anisidine (Aldrich, $\geq 99\%$), *p*-toluenesulfonyl hydrazide (Aldrich, 97%), and pyridine (Aldrich, $\geq 99\%$) were used as received. Copper-I-bromide (CuBr, Fluka) was purified by sequential washing with acetic acid, ethanol and diethyl ether with subsequently drying under reduced pressure. The CuBr was stored under inert gas atmosphere.

Azobisisobutyronitrile (AIBN, Aldrich, 98%) was recrystallized from methanol. Styrene (TCI, >99%) and *N,N*-dimethylacrylamide (DMAA, 99%) were destabilized before the polymerization by filtering the monomer through an Alox B column. The solvents dichloromethane (DCM, Fischer, p.a.), *n*-hexane (Fischer, p.a.) *N,N*-dimethylformamide (DMF, Fischer, p.a.), toluene (Fischer, p.a.), ethanol (Fischer, p.a.), methanol (Fischer, p.a.) acetonitrile (MeCN, Fischer, p.a.), tetrahydrofuran (THF, Fischer, HPLC grade), ethyl acetate (Merck, p.a.), and cyclohexane (Merck, p.a.) were used as received. The solvent 1,4-dioxane (Carl Roth, HPLC grade, non-stab.) for RAFT polymerization was filtered through an Alox B column prior to polymerization in order to remove any peroxides. The anhydrous solvents DCM (Acros, $\geq 99.9\%$) and DMF (Acros, $\geq 99.9\%$) were used as received. Deuterated solvents CD_2Cl_2 (DCM-*d*2), CDCl_3 , toluene-*d*8, and dimethylsulfoxide-*d*6 (DMSO-*d*6) for NMR spectroscopy were purchased from Eurisotop and Aldrich, respectively. The CRD with the sequence GPC₃GSYC₇PSVC₁₁APAC₁₅APVC₁₉C₂₀A was purchased from Biomatik (<http://www.biomatik.com>) in a purity of >95% (HPLC). Dialysis tubes used were from SpectrumLabs, employing Spectra/Por 6 with a MWCO of 1 kDa and 2kDa made of regenerated cellulose. Benzylazide⁴⁰³, the tetrazole-silane,⁴⁰⁴ and the PEG-fumarate¹⁹⁴ were synthesized according to literature procedures.

7.2 Instrumentation

7.2.1 Nuclear Magnetic Resonance (NMR) Spectroscopy

NMR measurements were carried out on a Bruker Avance III 400 spectrometer (¹H: 400 MHz, ¹³C{¹H}: 101 MHz, ¹⁹F: 377 MHz). The δ scale was referenced to deuterated solvents, indicated in the respective measurement. Evaluation was performed by TopSpin 7.1 PL7.

7.2.2 Size Exclusion Chromatography in THF

SEC measurements of all thermal DA SG reactions, photo-induced small molecule experiments and the monomer stability for the photoenol SG were carried out on an Agilent 1200 system, comprising an auto-sampler, a PLgel 5 μm bed-size guard column (50 \times 7.5 mm), one PLgel 5 μm Mixed E column (300 \times 7.5 mm), three PLgel 5 μm Mixed C columns (300 \times 7.5 mm) and a differential refractive index detector as well as an UV detector using THF as eluent at 35 °C with a flow rate of 1 mL·min⁻¹. The SEC system was calibrated using linear polystyrene standards ranging from 160 g·mol⁻¹ to 6·10⁶ g·mol⁻¹.

The THF-SEC measurements of the photo-induced SG polymerization using $r = 1$ were carried out on a Polymer Laboratories PL-GPC 50 Plus integrated system, operating with an autosampler. The column array were a PLgel 5 μm bead-size guard column (50 \times 7.5 mm), one PLgel 5 μm Mixed E column (300 \times 7.5 mm), three PLgel 5 μm Mixed C columns (300 \times 7.5 mm). For detection, a refractive index detector using THF as eluent was installed. The system was operated at 35 $^{\circ}\text{C}$ at a flow rate of 1 $\text{mL}\cdot\text{min}^{-1}$. The calibration was performed with linear polystyrene standards ranging from 476 $\text{g}\cdot\text{mol}^{-1}$ to $2.5\cdot 10^6$ $\text{g}\cdot\text{mol}^{-1}$.

SEC measurements of the photo-induced SG experiments, *i.e.* products such as off-stoichiometry SG polymer ($r > 1$) and RAFT polymers, were determined using a TOSOH Eco-SEC HLC-8320 GPC System, comprising an autosampler, a SDV 5 μm bead-size guard column (50 \times 8 mm, PSS) followed by three SDV 5 μm columns (300 \times 8 mm, subsequently 100 \AA , 1000 \AA and 10^5 \AA pore size, PSS), a differential refractive index (DRI) detector, and an UV detector (set up at 300 nm). THF was used as eluent at 30 $^{\circ}\text{C}$ with a flow rate of 1 $\text{mL}\cdot\text{min}^{-1}$. The SEC system was calibrated using linear polystyrene (PS) standards ranging from 266 $\text{g}\cdot\text{mol}^{-1}$ to $2.5\cdot 10^6$ $\text{g}\cdot\text{mol}^{-1}$.

7.2.3 Size Exclusion Chromatography in DMAc

The SEC measurements of the diazido polymer was performed on a PL-SEC 50 Plus Integrated System, comprising an autosampler, a PLgel 5 μm bead-size guard column (50 \times 7.5 mm) followed by three PLgel 5 μm Mixed C column (300 \times 7.5 mm), and a differential refractive index (RI) detector using *N,N*-dimethylacetamide (DMAc) containing 0.03 wt.% LiBr as the eluent at 50 $^{\circ}\text{C}$ with a flow rate of 1 $\text{mL}\cdot\text{min}^{-1}$. The SEC system is calibrated using linear polystyrene (PS) standards ranging from 474 $\text{g}\cdot\text{mol}^{-1}$ to $2.5\cdot 10^6$ $\text{g}\cdot\text{mol}^{-1}$.

7.2.4 Electrospray Ionization Mass Spectrometry (ESI-MS)

High-resolution mass spectra (HRMS) were obtained using a Q Exactive (Orbitrap) mass spectrometer (Thermo Fisher Scientific, San Jose, CA, USA) equipped with a HESI II probe. The instrument calibration was carried out in the m/z range 74 – 1822, using calibration solutions from Thermo Scientific. A constant spray voltage of 4.7 kV and a dimensionless sheath gas of 5 were applied. The capillary temperature and the S-lens RF level were set to 320 $^{\circ}\text{C}$ and 62, respectively. The samples were dissolved in a THF/MeOH mixture (3/2, V/V) containing 100 μmol of sodium trifluoroacetate and injected with a flow of 5 to 10 $\mu\text{L}\cdot\text{min}^{-1}$, respectively. The higher-energy collisional dissociation (HCD)

measurements were performed with a collision energy of 10 eV. The concentration of the injected samples was in the range of 0.1 and 0.3 mg·mL⁻¹.

Data of the RAFT agent TRITT was recorded on a LXQ mass spectrometer (ThermoFisher Scientific, San Jose, CA, USA) equipped with an atmospheric pressure ionization source operating in the nebulizer assisted electrospray mode. The instrument was calibrated in the *m/z* range 195 – 1822 using a standard containing caffeine, Met-Arg-Phe-Ala acetate (MRFA) and a mixture of fluorinated phosphazenes (Ultramark 1621) (all from Aldrich). A constant spray voltage of 4.5 kV was used and nitrogen at a dimensionless sweep gas flow-rate of 2 (approx. 3 L·min⁻¹) and a dimensionless sheath gas flow-rate of 12 (approx. 1 L·min⁻¹) were applied. The capillary voltage, the tube lens offset voltage and the capillary temperature were set to 60 V, 110 V and 275 °C respectively.

7.2.5 UV VIS Spectroscopy

The UV-VIS spectra of the data for thermal DA SG polymerization were recorded on OceanOptics USB4000 spectrometer coupled to an USB-ISS-UV-Vis detecting unit. The measurements were conducted in DCM at ambient temperature, using quartz glass cuvettes (Starna GmbH, 10 mm). The concentrations were varying, in order to keep the absorbance below the value of 2.

All other UV-VIS spectra were recorded on a Varian Cary 300 Bio spectrometer equipped with a temperature controlled cell holder. Absorption spectra in the range of 200 to 800 nm were recorded with a resolution of 1 nm and a split width of 2 nm. All measurements were carried out in DCM at ambient temperature, employing quartz glass cuvettes (Starna GmbH, *l* = 10 mm).

7.2.6 ToF-SIMS

Time-of-flight secondary ion mass spectrometry (ToF-SIMS) was conducted with a TOF.SIMS⁵ instrument (ION-TOF GmbH, Münster, Germany), equipped with a Bi cluster liquid metal primary ion source and a non-linear time-of-flight analyzer. The Bi source was operated in the bunched mode providing 1 ns Bi₃⁺ ion pulses at 25 keV energy and a lateral resolution of approx. 4 μm for all surfaces. Images larger than the maximum deflection range of the primary ion gun of 500 × 500 μm² were obtained using the manipulator stage scan mode. Primary ion doses were kept below 10¹¹ ions·cm⁻² (static SIMS limit).

7.2.7 Photo Reactor Setup

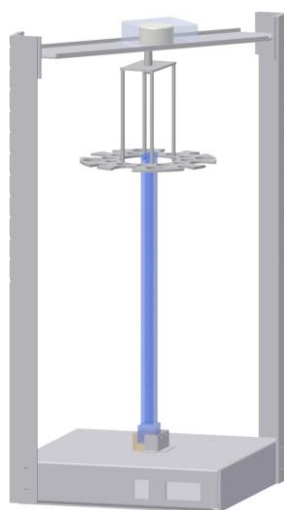


Figure 7-1. Schematic setup of the photoreactor used in this study. The samples are placed in the holder and rotated during the irradiation.²⁶⁶

The photo-induced reactions were performed in a custom-built photoreactor (refer to Figure 7-1), employing an ARIMED B6 UV lamp from Cosmedico for the NITEC reactions with a spectral emission in the range of 290-400 nm ($\lambda_{\text{max}} = 310$ nm, refer to Figure 7-2), and iSOLde Cleo Compact PL-L 36 W ($\lambda_{\text{max}} = 360$ nm, refer to Figure 7-3) for the photoenol experiments.

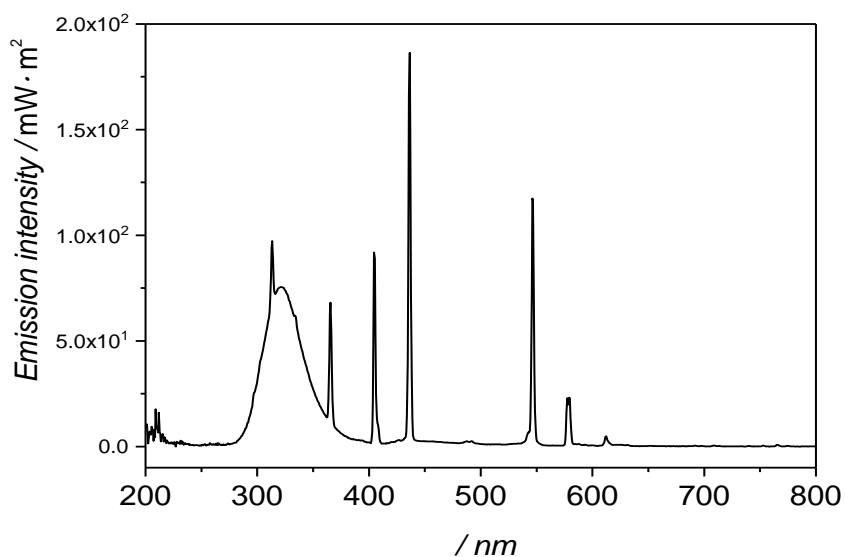


Figure 7-2. Emission spectrum of the lamp Cosmedico ARIMED B6.

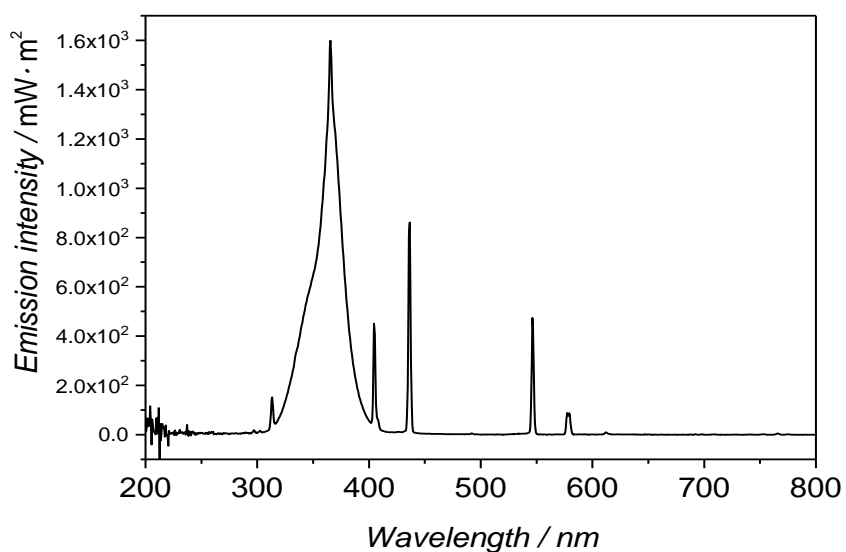


Figure 7-3. Emission spectrum of the lamp iSOLde Cleo Compact PL-L 36 W.

7.2.8 Sample Holder for Surface Patterning

The parts of the sample holder and the photomask consist of stainless steel. The setup is assembled with two screws (refer to Figure 7-4). The photomask is placed between the silicon wafer and the lid of the sample holder.

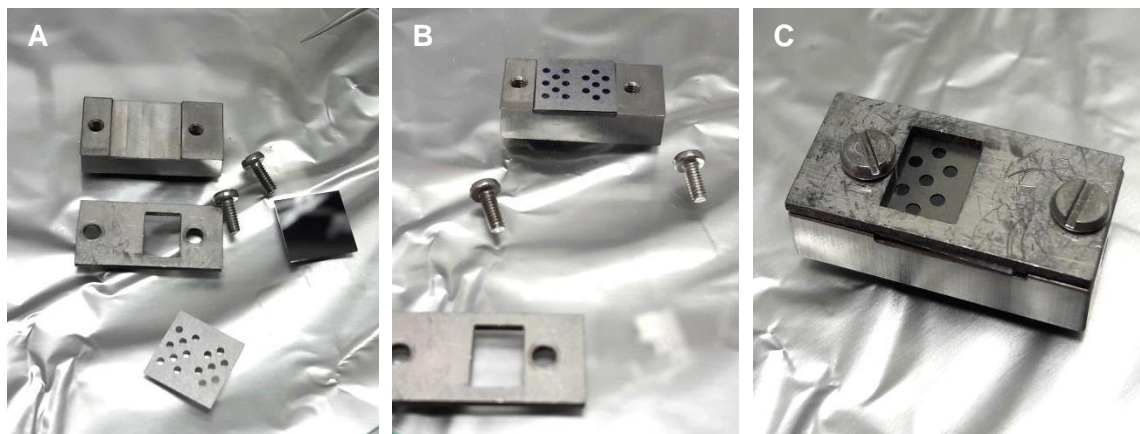


Figure 7-4. Assembly of the sample holder for the photo-induced spatially resolved surface immobilization. **A:** Individual parts disassembled, **B:** Surface and photomask placed onto the sample holder. **C:** Sample holder fully assembled with the photomask mounted onto the silicon wafer.

7.2.9 High Performance Liquid Chromatography (HPLC)

Analytic and semi-preparative HPLC measurements were conducted with a Jasco LC-2000 Plus Series system equipped with two PU 2,087 Plus pumps (flow up to 50 mL·min⁻¹) and a diode array detector (MD-2010 Plus 195–650 nm). The purification of the compounds was performed in reverse phase mode with a 218TP Vydac C18 column

(analytic: 4.6 mm × 250 mm, semi-preparative: 10 mm × 250 mm, Grace Davison Discovery Science).

7.2.10 SDS Page and Western Blotting

For the SDS Page, a 12% polyacrylamide gel (refer to Table 7-1) was prepared in water. The samples were incubated by adding sample buffer (0.5 M Tris at pH = 6.8, glycerol, SDS, β -mercaptoethanol, bromophenol blue) and heating to 95 °C for 10 min. Afterwards, the supernatant water was removed. For electrophoresis, the gel was mounted into a holder. Subsequently, the gel was run at a constant current of 20 mA until the blue dye front migrated out of the gel. After running the samples, they were blotted onto a nitrocellulose membrane at ambient temperature at a current of 360 mA. Unspecified bonds were blocked *via* a blocking buffer (5% milk, tween, PBS). In the next step, the membrane was incubated in a primary anti-body (anti-C-CRD) medium over night at 4 °C. Subsequently, the membrane was washed with washing solution three times. The membrane was then incubated with a secondary anti-body (donkey-anti-guinea pig) medium for 1 h at ambient temperature in the blocking buffer and washed with a PBS/tween solution. Finally, the membrane was incubated with a 1:2 mixture of extracellular loop media (ECL) 1 (coumaric acid, luminol, Tris pH = 8) and ECL2 (hydrogen peroxide, Tris pH = 8) for 30 s. The detection of the blot was performed on an ECL Chemocam Imager from INTAS.

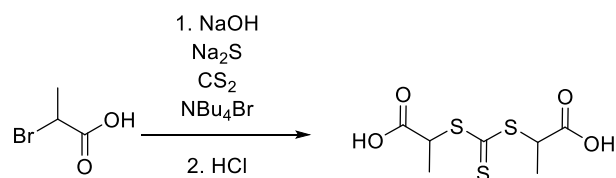
Table 7-1. Composition of the gels, employed for the SDS-PAGE from acrylamide (AA) and bisacrylamide (BA).

12 % SDS /PAA Gel		
	Running Gel	Stacking Gel
H₂O	4,5 ml	3,25 ml
40 % AA / BA	3,0 ml	0,5 ml
Upper Tris, pH 6.8	/	1,25 ml
Lower Tris, pH 8.8	2,5 ml	/
10 % APS	40 μ l	25 μ l
TEMED	20 μ l	10 μ l

7.3 Synthesis Procedures of Small Molecules

7.3.1 RAFT Agent Syntheses

Synthesis of *S,S*-(2-dipropionic acid)trithiocarbonate (DTC)



Scheme 7-1. Synthesis of *S,S*-(dipropyl)trithiocarbonate (DTC).

In an adapted approach from literature,⁴⁰⁵ in a round bottom flask, 12.00 g sodium sulfide (50.0 mmol, 1.0 eq.) and 1.61 g tetrabutylammonium bromide (5.0 mmol, 0.1 eq.) were dissolved in 35 mL deionized water and 100 mL acetone. While cooling, 10.1 mL carbon disulfide (12.68 g, 166.5 mmol, 3.3 eq.) were added dropwise. The reaction solution turned deep red and was allowed for stirring for 19 h at ambient temperature. The next day, in a another flask, 12 mL of a 25% sodium hydroxide solution (4.00 g NaOH, 100.0 mmol) was cooled to 0 °C and 9 mL 2-bromo propionic acid (15.30 g, 100.0 mmol, 2.0 eq.) was added dropwise. Now, the solution of the 2-bromo propionic acid was added dropwise to the cooled CS₂ containing reaction mixture, turning yellowish and eventually brownish with progressive reaction time. After stirring for 3 h, the reaction mixture was extracted with DCM and brine solution. The DCM phase was separated and extracted several times with 5% NaOH solution. The combined aqueous phase was cooled and concentrated hydrochloric acid was added slowly until no further precipitation of a yellow solid was observed. Next, the acidified and turbid aqueous phase was extracted multiple times with DCM until the aqueous layer remained pale yellowish. The organic layer was dried over Na₂SO₄ and the solvent was removed under reduced pressure. For purification, the crude high viscous oil was recrystallized from toluene / ethyl acetate (4.9/1, V/V) at a concentration of 0.25 g/mL at 70 °C. The recrystallization solution was firstly stored at ambient temperature, then at 4 °C and ultimately at -20 °C for 10 days to obtain flake like yellow crystals (3.55 g, 28%).

¹H-NMR (400 MHz, DMSO, 25 °C): δ (ppm): 13.20 (s, 2H, COOH), 4.66 (q, 2H, ³J = 7.4 Hz), 1.52 (d, 6H, ³J = 7.4 Hz).

¹³C-NMR (101 MHz, DMSO, 25 °C): δ (ppm): 220.3 (CS₃), 171.4 (COOH), 48.5 (S-CH-CH₃), 16.7 (CH₃).

ESI-MS: *m/z* [M+Na]⁺_{exp.}: 276.9632, [M+Na]⁺_{calc.}: 276.9633.

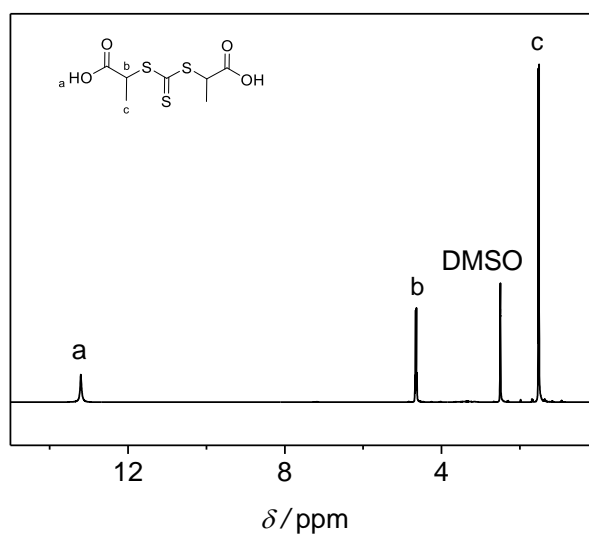


Figure 7-5. ^1H -NMR spectrum of *S,S*-(dipropyl)trithiocarbonate (DTC). The spectrum was recorded in $\text{DMSO-}d_6$.

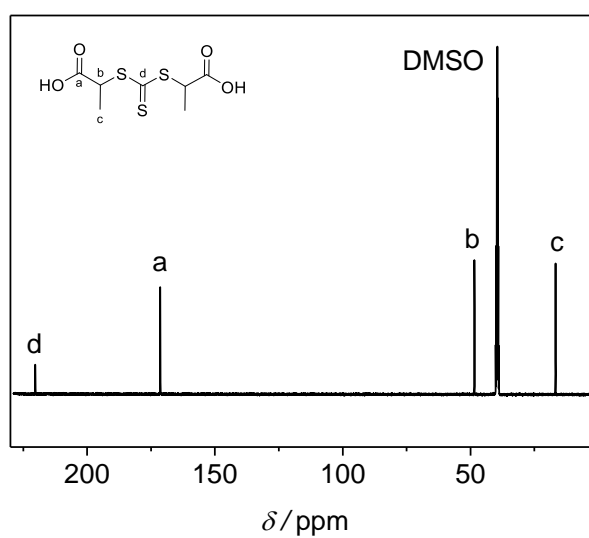
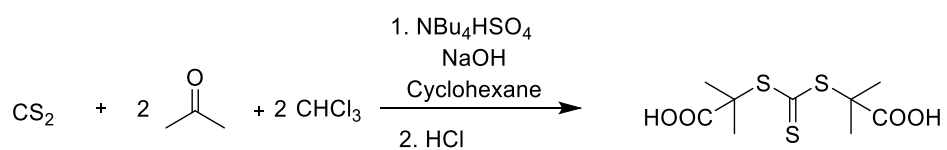


Figure 7-6. ^{13}C -NMR spectrum of *S,S*-(dipropyl)trithiocarbonate (DTC). The spectrum was recorded in $\text{DMSO-}d_6$.

Synthesis of *S,S*-di((2-methyl)propionic acid) trithiocarbonate (TRITT)



Scheme 7-2. Synthesis of *S,S*-di((2-methyl)propionic acid) trithiocarbonate (TRITT).

According to literature procedure,¹⁰⁹ in a round bottom flask 5.4 mL carbon disulfide (6.85 g, 90.0 mmol, 1.00 eq.), 16.5 mL acetone (13.1 g, 225.0 mmol, 2.50 eq.), 18.2 mL chloroform (26.90 g, 225.0 mmol, 2.50 eq.) and 0.60 g tetrabutylammonium hydrogen sulfate (1.8 mmol, 0.02 eq.) were mixed with 30 mL cyclohexane. The reaction mixture was cooled and slightly percolated with nitrogen for 10 min. A solution of 50% NaOH was prepared (50.40 g, 1260.0 mmol, 14 eq.) in 50 mL deionized water. Subsequently, the NaOH solution was added dropwise to the mixture in cyclohexane while keeping the solution below 25 °C. After addition of the NaOH solution, the mixture was stirred for 4 h. Afterwards, 225 mL deionized water was added and the crude product was precipitated by acidifying the solution with concentrated hydrochloric acid (HCl) until no precipitation of a yellow solid was observed. The turbid suspension was filtered of and the yellow solid was recrystallized from an isopropanol / water mixture (38/62, V/V) at 70 °C at a concentration of 0.19 g·mL⁻¹. For recrystallization, the solution was kept at 4 °C for at least 10 days. After filtration and drying, the product was obtained as yellow crystals (2.75 g, 24%).

¹H-NMR (400 MHz, DMSO, 25 °C): δ (ppm): 12.91 (s, 2H, COOH), 1.59 (s, 6H). ¹³C-NMR (101 MHz, DMSO, 25 °C): δ (ppm): 219.0 (CS₃), 173.1 (COOH), 56.2 (S-C-(CH₃)₂), 25.0 (CH₃).

ESI-MS: m/z [M+Na]⁺_{exp}: 305.08, [M+Na]⁺_{calc}: 304.99.

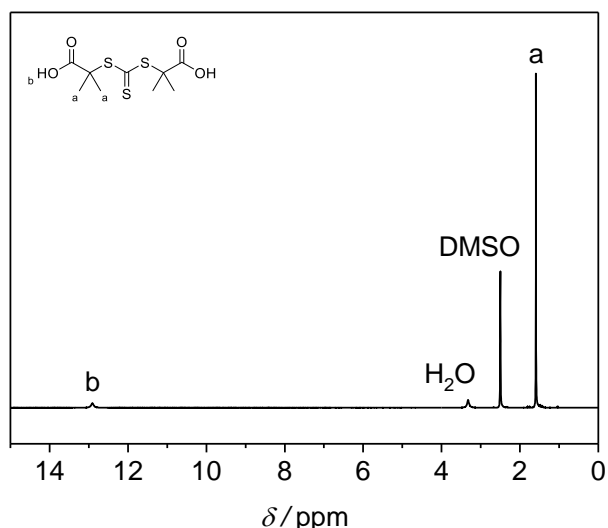


Figure 7-7. ¹H-NMR spectrum of S,S-di((2-methyl)propionic acid) trithiocarbonate (TRITT). The spectrum was recorded in DMSO-*d*₆.

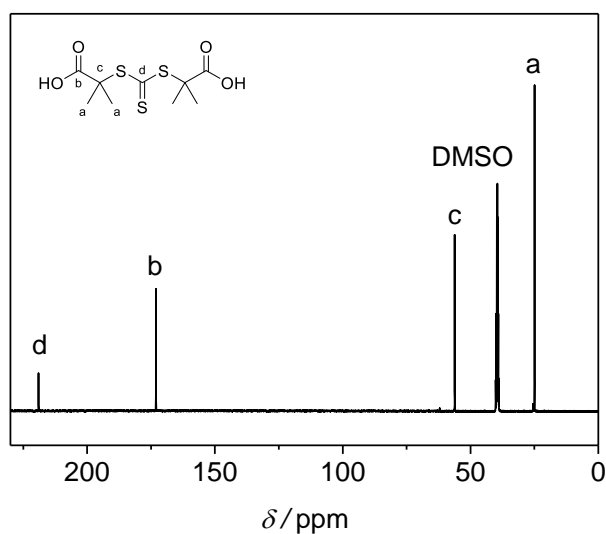
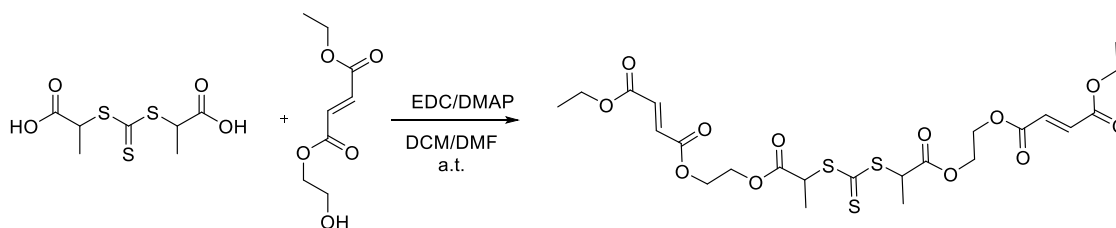


Figure 7-8. ^{13}C -NMR spectrum of *S,S*-di((2-methyl)propionic acid) trithiocarbonate (TRITT). The spectrum was recorded in $\text{DMSO-}d_6$.

Synthesis of di(isopropionic acid ethyl-ester ethyl fumarate) trithiocarbonate (**BB** monomer)



Scheme 7-3. Synthesis of di(isopropionic acid ethyl-ester ethyl fumarate) trithiocarbonate (**BB** monomer).

In a round bottom flask 420 mg DTC (1.65 mmol, 1.00 eq.), 668 mg 2-hydroxyethyl-ethyl fumarate (refer to synthesis route in Chapter 7.3.5) (3.55 mmol, 2.15 eq.) and 61 mg DMAP (0.50 mmol, 0.30 eq.) were dissolved in a mixture of 10 mL dry DCM and 1 mL dry DMF. The solution was cooled to 0 °C and 665 mg EDC (3.47 mmol, 2.10 eq.) was added. The solution shortly turned intensively red and was allowed to reach ambient temperature, before being stirred for 24 h. Next, the solution mixture was washed with 5% hydrochloric acid, saturated NaHCO_3 solution and brine. The combined organic phase was dried over Na_2SO_4 and the solvent was removed under reduced pressure. The crude product was purified by flash chromatography (silica gel, cyclohexane/ethyl acetate, 2/1, V/V) to obtain the product as a yellowish oil (687 mg, 70%).

^1H -NMR (400 MHz, CDCl_3 , 25 °C): δ (ppm): 6.86 (s, 4H, $\text{HC}=\text{CH}$), 4.77-4.75 (m, 2H, CHS), 4.40 (m, 8H, $-\text{CH}_2\text{O}$), 4.27-4.25 (m, 4H, CH_2O), 1.61-1.59 (m, 6H, $\text{CH}_2\text{-CHS}$), 1.32 (t, $^3J = 7.03$ Hz, 6H, $-\text{CH}_3$).

^{13}C -NMR (101 MHz, CDCl_3 , 25 °C): δ (ppm): 219.5 (**C=S**), 170.7 (**S-CH(CH₃)-C=O**) 164.8 (**HC=CH**), 134.7 (**C=O**), 132.9, (**C=O**), 63.3 (**CH₂-CH₂-C=O**), 62.8 (**CH₂-CH₂-C=O**), 61.6 (**CH₃-CH₂-C=O**), 48.3 (**CH(CH₃)-S**) 16.7 (**(CH₃)CH-S**), 14.2 (**CH₃-CH₂-C=O**).

ESI-MS: m/z $[\text{M}+\text{Na}]^+_{\text{exp}}$: 617.0786, $[\text{M}+\text{Na}]^+_{\text{calc}}$: 617.0792.

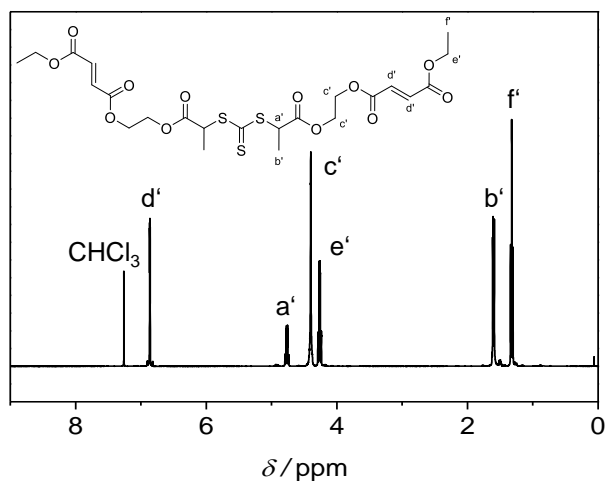


Figure 7-9. ^1H -NMR spectrum of di(isopropionic acid ethyl-ester ethyl fumarate) trithiocarbonate (**BB** monomer). The spectrum was recorded in CDCl_3 .

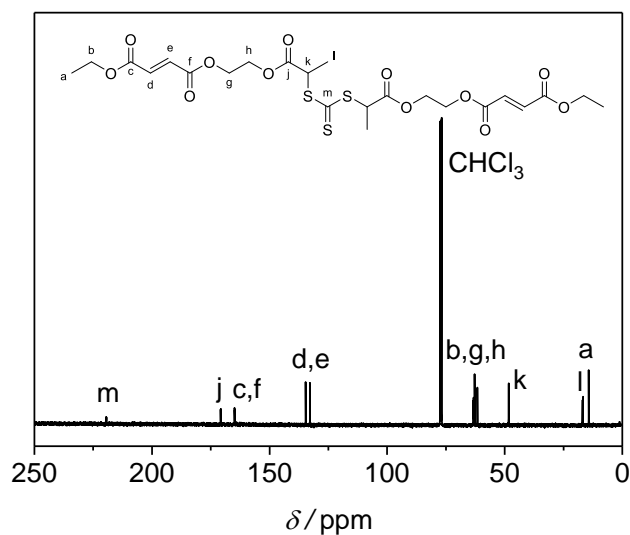


Figure 7-10. ^{13}C -NMR spectrum of di(isopropionic acid ethyl-ester ethyl fumarate) trithiocarbonate (**BB** monomer). The spectrum was recorded in CDCl_3 .

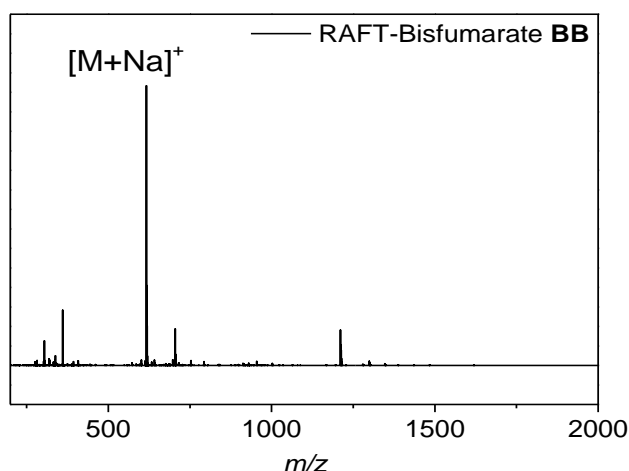
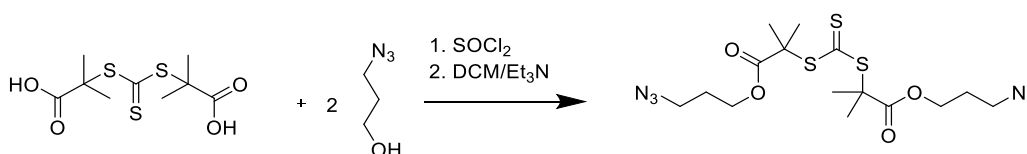


Figure 7-11. ESI-MS spectrum of the RAFT difumarate **BB** monomer. The spectrum was recorded *via* a direct-infusion experiment in THF/MeOH (3/2, V/V) by doping with sodium trifluoroacetate.

Synthesis of Diazido-RAFT Agent



Scheme 7-4. Synthesis of the diazido-trithiocarbonate *via* acid chlorides.

According to literature procedure,⁹⁷ in a flame-dried Schlenk flask 0.8 g TRITT (2.83 mmol, 1 eq.) was set under nitrogen atmosphere and subsequently 29 mL thionyl chloride (339.96 mmol, 120 eq.) were added. The flask was connected to a wash bottle and the reaction mixture was stirred and heated to reflux for 4 h until the thionyl chloride was removed under reduced pressure. In a second flame-dried flask, 0.86 g 3-azido-propanol (8.50 mmol, 3 eq.) and 0.9 mL triethylamine (6.23 mmol, 2 eq.) were dissolved in 20 mL dry DCM and cooled to 0 °C. The *in situ* generated acid chloride was dissolved in 20 mL dry DCM and added dropwise to the solution of the 3-azido-propanol while cooling. Afterwards, the reaction solution was stirred overnight. To remove any acidic residuals, the crude mixture was washed with NaHCO₃ and brine multiple times. The combined organic layer was dried over Na₂SO₄ and the solvent was removed under reduced pressure. The final product was obtained after flash chromatography (silica gel, cyclohexane/ethyl acetate, 5/1, V/V) to obtain a yellowish high viscous oil (268 mg, 21%).
¹H-NMR (400 MHz, DMSO, 25 °C): δ (ppm): 4.08 (t, ³J = 6.1 Hz, 4H, OCH₂-CH₂), 3.38 (t, ³J = 6.9 Hz, 4H, CH₂-N₃), 1.82 (m, 4H, CH₂-CH₂-CH₂), 1.62 (s, 12H, CH₃).

^{13}C -NMR (101 MHz, DMSO, 25 °C): δ (ppm): 219.0 (C=S), 171.5 (C=O) 62.8 (O-CH₂), 56.2 (CH(CH₃)-S), 47.6 (CH₂-N₃), 27.4 (CH₂-CH₂-CH₂), 24.7 ((CH₃)CH-S).

ESI-MS: m/z [M+Na]⁺_{exp}: 471.0913, [M+Na]⁺_{calc}: 471.0913.

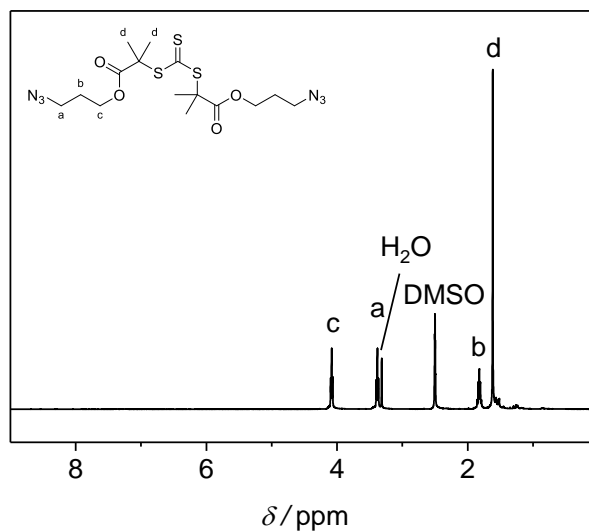


Figure 7-12. ^1H -NMR spectrum of the diazido-RAFT agent. The spectrum was recorded in DMSO- d_6 .

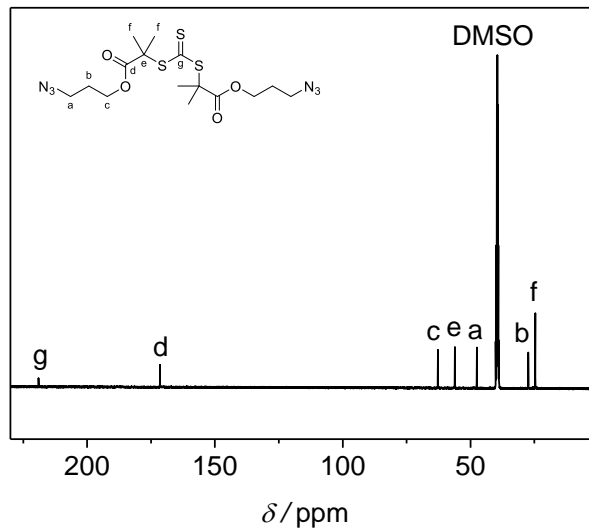


Figure 7-13. ^{13}C -NMR spectrum of the diazido-RAFT agent. The spectrum was recorded in DMSO- d_6 .

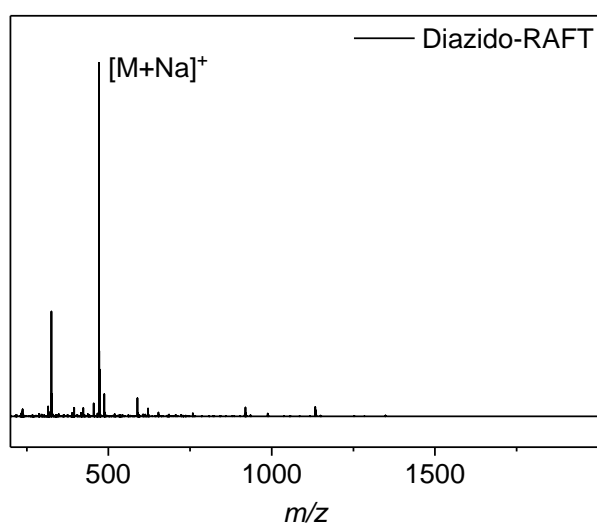
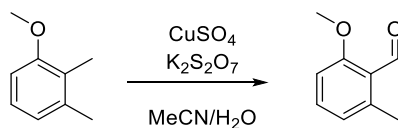


Figure 7-14. ESI-MS spectrum of the diazido-RAFT agent. The spectrum was recorded *via* direct-infusion experiment in THF/MeOH (3/2, V/V) by doping with sodium trifluoroacetate.

7.3.2 Photoenol Compounds

Synthesis of 2-methoxy-5-methyl benzaldehyde



Scheme 7-5. Synthesis of 2-methoxy-5-methyl benzaldehyde by oxidation of 2,3-dimethylanisole.

According to literature procedure,¹²⁸ in a 500 mL round bottom flask, 3.50 g 2,3-dimethyl anisole (26.7 mmol, 1.00 eq.), 6.52 copper sulfate pentahydrate (26.2 mmol, 1.02 eq.) and 20.84 g potassium peroxodisulfate (77.1 mmol, 3.00 eq.) were added to a mixture of 250 mL acetonitrile/ water (1/1, V/V). The vigorously stirred suspension was placed in an oil bath kept at 90°C until TLC showed no starting material remaining. After 45 min the mixture was cooled to ambient temperature and the undissolved copper salt was removed by filtration. In order to separate the phase, 75 mL DCM were added and subsequent extraction of the aqueous phase with approx. 50 mL DCM. The combined organic layer was dried over MgSO₄. After removal of the solvent under reduced pressure, the crude product was purified by flash chromatography (silica gel, cyclohexane/ethyl acetate, 5/1, V/V), yielding a yellow solid (2.6 g, 68%).

¹H-NMR (CDCl₃, 400 MHz): δ (ppm): 10.64 (s, 1H, CHO), 7.38 (t, ³J = 7.97 Hz, 1H, ArH), 6.81 (t, ³J = 7.97 Hz, 2H, ArH), 3.89 (s, 3H, OCH₃), 2.57 (s, 3H, CH₃).

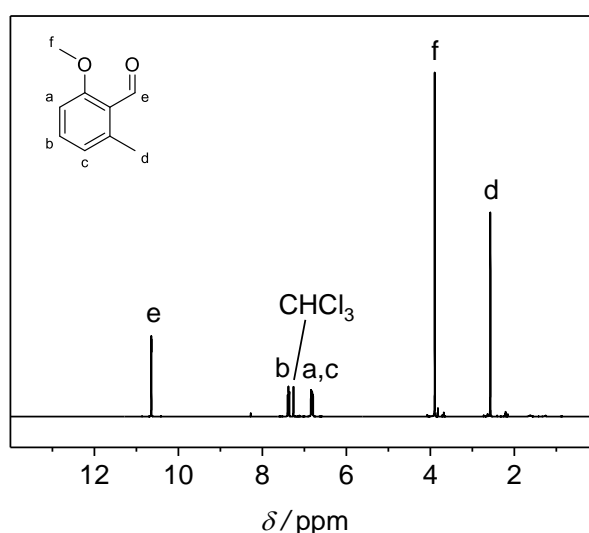
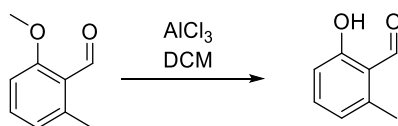


Figure 7-15. ¹H-NMR spectrum 2-methoxy-5-methyl benzaldehyde. The spectrum was recorded in CDCl₃.

Synthesis of 2-hydroxy-5-methyl benzaldehyde

Scheme 7-6. Ether cleavage of 2-methoxy-5-methyl benzaldehyde yielding 2-hydroxy-5-methyl benzaldehyde.

According to literature procedure,¹²⁸ 2.62 g 2-methoxy-6-methylbenzaldehyde (17.5 mmol, 1.00 eq.) was dissolved in 38 mL dry DCM and cooled to 0 °C. Subsequently, 6.99 g AlCl₃ (52.4 mmol, 3.00 eq.) were added and the mixture was stirred at ambient temperature overnight. The mixture was cooled to 0 °C and the reaction was quenched dropwise with 50 mL H₂O and the phases were separated. The aqueous layer was extracted three times with approx. 50 mL DCM. The combined organic layers were dried over MgSO₄ and the solvent was evaporated. The brown crude product was purified by flash chromatography (silica gel, cyclohexane/ethyl acetate, 2/1, V/V), yielding a yellowish solid (1.95 g, 82%).
¹H-NMR (CDCl₃, 400 MHz): δ (ppm): 11.91 (s, 1H, OH), 10.32 (s, 1H, CHO), 7.38 (t, ³J = 7.9 Hz, 1H, ArH), 6.76 (dd, ³J = 25.3, 7.9 Hz, 2H, ArH), 2.61 (s, 3H, CH₃).

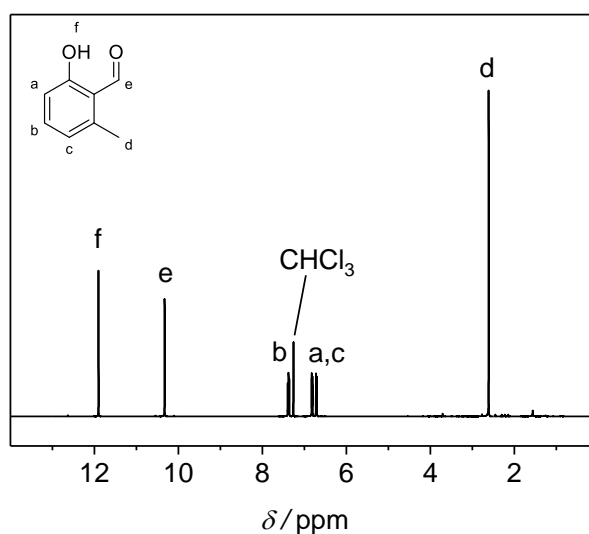
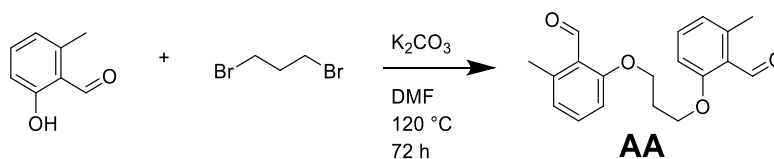


Figure 7-16. ¹H-NMR spectrum of 2-hydroxy-5-methyl benzaldehyde. The spectrum was recorded in CDCl₃.

Synthesis of 6,6'-(propane-1,3-diylbis(oxy))bis(2-methyl benzaldehyde) (AA monomer)



Scheme 7-7. Williamson ether synthesis of 2-hydroxy-6-methyl-benzaldehyde (**AA** monomer).

Adapted from literature procedure,²¹⁹ in a round bottom flask 0.5 g 2-hydroxy-6-methyl-benzaldehyde (3.67 mmol, 2.4 eq.), 0.309 g 1,3-dibromopropane (1.53 mmol, 1.0 eq.), and 1.06 g potassium carbonate (7.65 mmol, 5.0 eq.) were dispersed in 17 mL DMF. The solution was heated to 120 °C and stirred for 72 h. After cooling, the solvent was removed under reduced pressure and the crude product was dispersed in DCM. The organic phase was washed with 5% of hydrochloric acid, saturated NaHCO₃ solution and brine. The combined organic phase was dried over Na₂SO₄ and the solvent was removed under reduced pressure. The crude product was purified by flash chromatography (silica gel, cyclohexane/ethyl acetate 5/1, V/V). Finally, the product was recrystallized from *n*-hexane/ethyl acetate (10/6, V/V) at 70 °C to obtain colorless crystals (120 mg, 25%).

¹H-NMR (400 MHz, CDCl₃, 25 °C): δ (ppm): 10.67 (s, 2H, CHO), 7.39-7.37 (m, 2H, ArH), 6.84-6.80 (m, 4H, ArH), 4.27 (t, ³J = 6.0 Hz, 4H, -CH₂O), 2.56 (s, 6H, Ar-CH₃), 2.38 (dt, ³J = 5.9 Hz, 2H, -CH₂).

¹³C-NMR (101 MHz, CDCl₃, 25 °C): δ (ppm): 192.1 (C=O), 162.4 (C_{Ar}-O), 142.3 (C_{Ar}-CH₃), 134.7 (C_{Ar}), 124.5 (C_{Ar}), 123.5 (C_{Ar}-CHO), 110.0 (C_{Ar}), 64.92 (CH₂-CH₂-O), 29.3 (CH₂-CH₂-O), 21.6 (C_{Ar}-CH₃).

ESI-MS: *m/z* [M+Na]⁺_{exp.}: 335.1255, [M+Na]⁺_{calc.}: 335.1254.

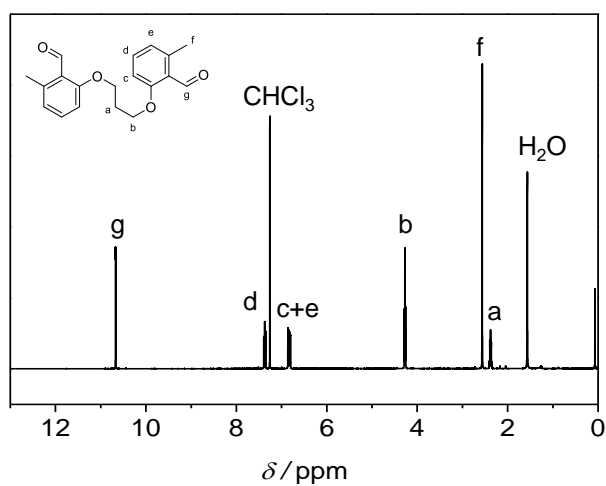


Figure 7-17. ¹H NMR spectrum of 6'-(propane-1,3-diylbis(oxy))bis(2-methyl benzaldehyde) (AA monomer). The spectrum was recorded in CDCl₃.

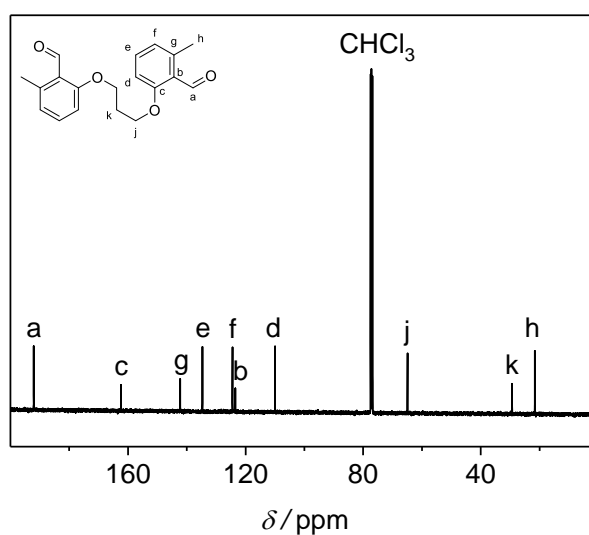


Figure 7-18. ¹³C-NMR spectrum of 6'-(propane-1,3-diylbis(oxy))bis(2-methyl benzaldehyde) (AA monomer). The spectrum was recorded in CDCl₃.

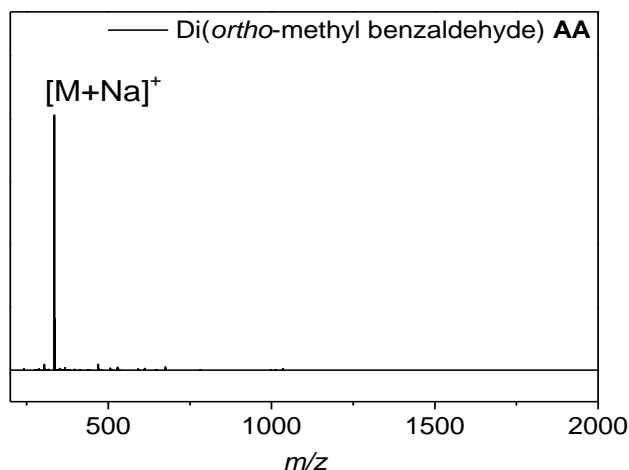
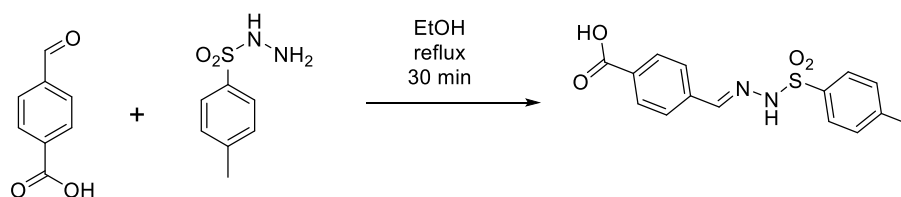


Figure 7-19. ESI-MS spectrum of the 6'-(propane-1,3-diylbis(oxy))bis(2-methyl benzaldehyde) (**AA** monomer). The spectrum was recorded *via* direct-infusion experiment in THF/MeOH (3/2, V/V) by doping with sodium trifluoroacetate.

7.3.3 Tetrazole Syntheses

Synthesis of 4-((2-tosylhydrazono)methyl)benzoic acid



Scheme 7-8. Synthesis of 4-((2-tosylhydrazono)methyl)benzoic acid.

According to literature procedure,²⁵⁶ a mixture of 8.00 g 4-formyl-benzoic acid (53.3 mmol, 1 eq.) and 9.92 g *p*-toluenesulfonyl hydrazide (53.3 mmol, 1 eq.) in 120 mL ethanol was heated to reflux for 30 min. The solution was diluted with 120 mL deionized water and the precipitate was filtered off. The solid was washed with 120 mL aqueous ethanol to obtain a colorless solid (16.6 g, 98%).

¹H-NMR (DMSO, 400 MHz): δ (ppm): 13.07 (s, 1H, COOH), 11.68 (s, 1H, HC=N), 7.96 (s, 1H, -NH-SO₂), 7.94 (d, ³J = 8.3 Hz, 2H, ArH), 7.77 (d, ³J = 8.2 Hz, 2H, ArH), 7.66 (d, ³J = 8.2 Hz, 2H, ArH), 7.41 (d, ³J = 8.3 Hz, 2H, ArH), 2.35 (s, 3H, CH₃).

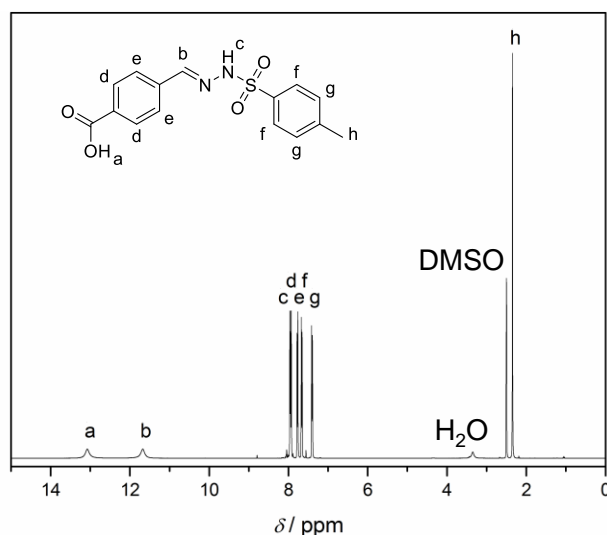
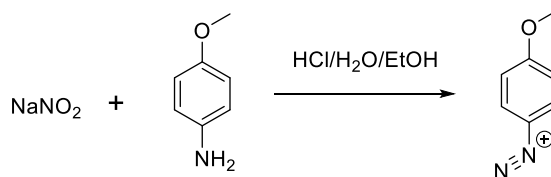


Figure 7-20. $^1\text{H-NMR}$ spectrum of 4-((2-tosylhydrazono)methyl)benzoic acid. The spectrum was recorded in $\text{DMSO-}d_6$.

Synthesis of Methoxy-Tetrazole Acid²⁵⁶

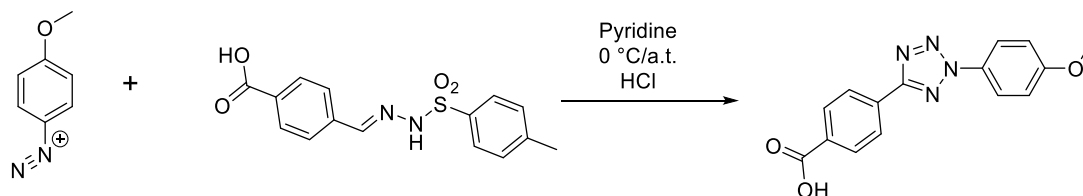
Preparation of the Diazonium Salt:



Scheme 7-9. Generation of the diazonium salt towards the tetrazole synthesis.

In a round bottom flask, 9.725 g 4-anisidine (52.2 mmol, 1 eq.) was dissolved in a mixture of conc. HCl (14 mL), H_2O (43 mL) and EtOH (43 mL) and cooled to 0°C . A cooled solution of 3.603 g NaNO_2 (52.2 mmol, 1 eq.) in 22 mL H_2O was added dropwise and stirred for 10 min at 0°C .

Preparation of the Tetrazole:



Scheme 7-10. Tetrazole formation from diazonium salt and sulfonyl hydrazide.

The *in situ* generated diazonium salt solution was added dropwise to a solution of 16.6 g hydrazone (52.2 mmol, 1 eq.) in 320 mL pyridine at -10°C to -5°C over a period of 45 min. After complete addition the solution was stirred at 0°C for 30 min and at ambient

temperature overnight. The turbid solution was poured into 800 mL HCl solution (10%), the precipitate was filtered off and washed with 400 mL EtOH to yield a pale purple to reddish solid (9.96 g, 65%).

$^1\text{H-NMR}$ (DMSO, 400 MHz): δ (ppm): 13.23 (s, 1H, COOH), 8.24 (d, $^3J = 8.1$ Hz, 2H, ArH), 8.13 (d, $^3J = 8.1$ Hz, 2H, ArH), 8.05 (d, $^3J = 8.8$ Hz, 2H, ArH), 7.20 (d, $^3J = 8.8$ Hz, 2H, ArH), 3.86 (s, 3H, CH₃).

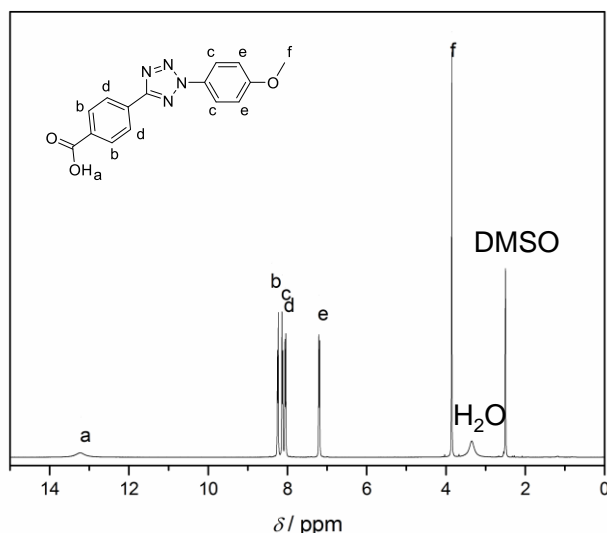
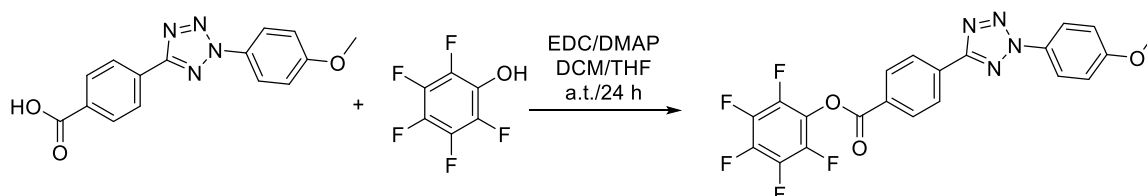


Figure 7-21. $^1\text{H-NMR}$ spectrum of methoxy-tetrazole acid. The spectrum was recorded in DMSO- d_6 .

Tetrazole Pentafluorophenol-Ester



Scheme 7-11. Esterification of tetrazole acid with pentafluorophenol.

In a round bottom flask, 100 mg tetrazole acid (0.34 mmol, 1.0 eq.), 93 mg PFP (0.51 mmol, 1.5 eq.) and 8 mg DMAP (0.07 mmol, 0.2 eq.) were dissolved in 20 mL THF. Then, the solution was cooled to 0 °C. The reaction was started by adding 78 mg EDC (0.41 mmol, 1.2 eq.) and 10 mL DCM. The mixture was allowed to reach ambient temperature and stirred overnight. The crude mixture was washed with 5% hydrochloric acid, NaHCO₃ and brine solution. Subsequently, the combined organic phase was dried over Na₂SO₄ and the solvent was removed under reduced pressure. The final product was obtained after flash chromatography (silica gel, cyclohexane/ethyl acetate, 3/1, V/V), obtaining a yellow solid (90 mg, 58%).

$^1\text{H-NMR}$ (400 MHz, CDCl_3 , 25 °C): δ (ppm): 8.45-8.34 (m, 4H, C_{Ar}), 8.13 (d, 2H, $^3J = 10$ Hz, C_{Ar}) 7.09 (d, 2H, $^3J = 10$ Hz, C_{Ar}), 3.91 (s, 3H, CH_3).

$^{19}\text{F-NMR}$ (377 MHz, CDCl_3 , 25 °C): δ (ppm): -162.1 (m, 2F, *meta*), -157.6 (m, 1F, *para*), -152.3 (m, 2F, *ortho*).

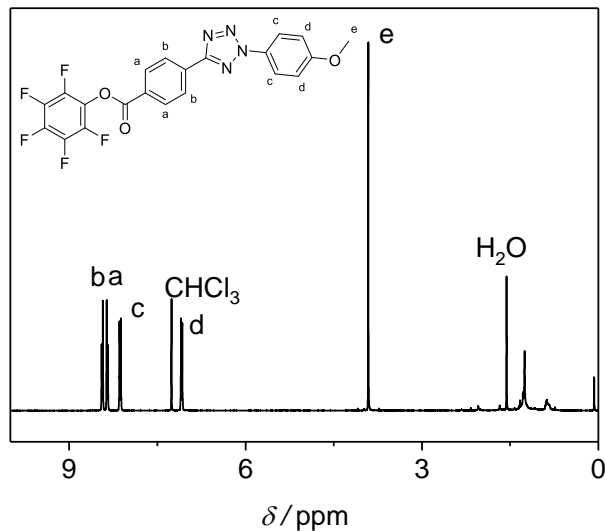


Figure 7-22. $^1\text{H-NMR}$ spectrum of tetrazole-acid pentafluorophenol ester. The spectrum was recorded in CDCl_3 .

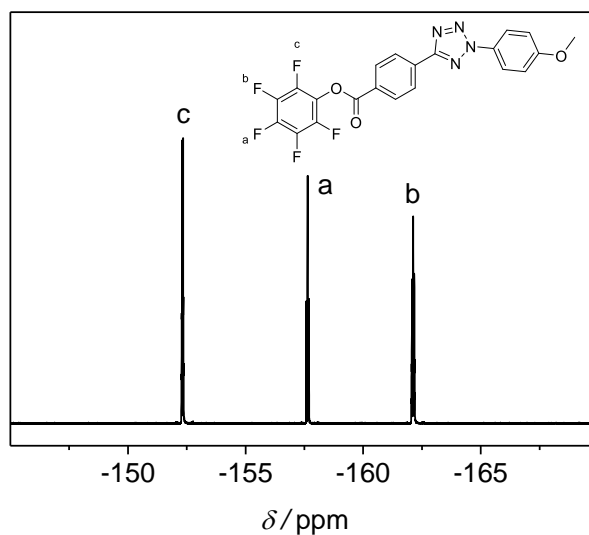
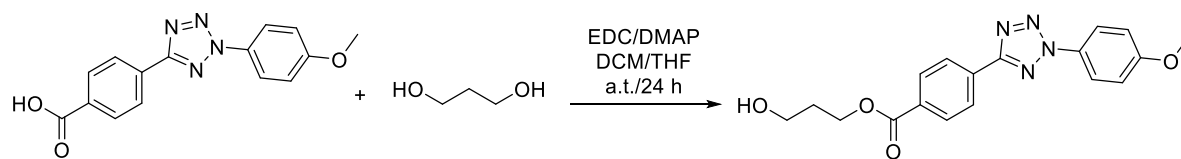


Figure 7-23. $^{19}\text{F-NMR}$ spectrum of tetrazole-acid pentafluorophenol ester. The spectrum was recorded in CDCl_3 .

Tetrazole Propanediol Ester Synthesis



Scheme 7-12. Esterification of tetrazole acid with 1,3-propanediol.

In a round bottom flask, 300 mg tetrazole acid (1.0 mmol, 1.0 eq.), 770 mg 1,3-propanediol (10.1 mmol, 10 eq.) and 25 mg DMAP (0.2 mmol, 0.2 eq.) were dissolved in 10 mL THF and 2.5 mL DCM. Then, the solution was cooled to 0 °C. The reaction was started by adding 233 mg EDC (1.2 mmol, 1.2 eq.). The mixture was allowed to reach ambient temperature and stirred overnight. The crude mixture was washed with 5% hydrochloric acid, NaHCO₃ and brine solution. Subsequently, the combined organic phase was dried over Na₂SO₄ and the solvent was removed under reduced pressure. The final product was obtained after flash chromatography (silica gel, cyclohexane/ethyl acetate, 4/1, V/V), obtaining a pale-yellow solid (171 mg, 52%).

¹H-NMR (400 MHz, CDCl₃, 25 °C): δ (ppm): 8.34-8.32 (m, 2H, C_{Ar}), 8.20-8.18 (m, 4H, C_{Ar}) 7.09-7.06 (m, 2H, C_{Ar}), 4.54 (t, ³J = 6.1 Hz, 2H, -COO-CH₂-), 3.91 (s, 3H, O-CH₃) 3.81 (t, 2H, ³J = 6.0 Hz, CH₂-OH), 2.05 (dt, 2H, ³J = 6.0 Hz, CH₂-CH₂-CH₂).

¹³C-NMR (101 MHz, CDCl₃, 25 °C): δ (ppm): 166.6 (C=O), 164.2 (C_{Tet}), 160.9 (C_{Ar}-OCH₃), 131.8 (C_{Ar}-COO), 131.7 (C_{Ar}), 130.5 (C_{Ar}), 130.4 (C_{Ar}-NR₂), 127.1 (C_{Ar}), 121.6 (C_{Ar}), 114.9 (C_{Ar}), 62.2 (COO-CH₂-), 59.3 (CH₂-CH₂-OH), 55.9 (H₃C-O), 32.1 (CH₂-CH₂-CH₂).

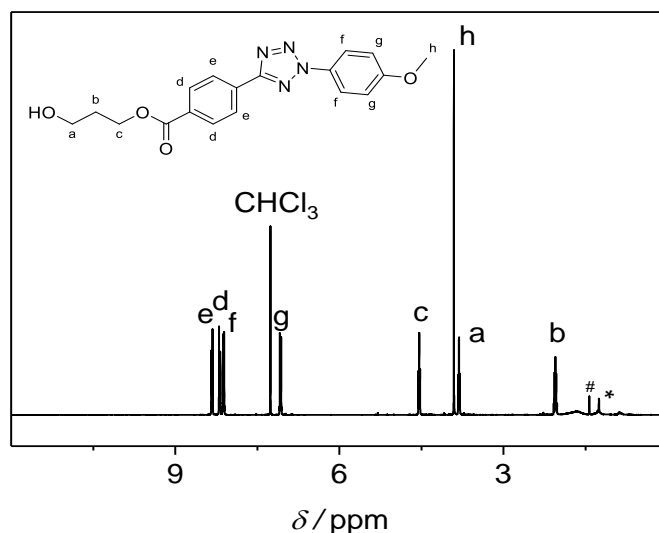


Figure 7-24. ¹H-NMR spectrum of tetrazole-acid 1,3-propanediol ester. The spectrum was recorded in CDCl₃.

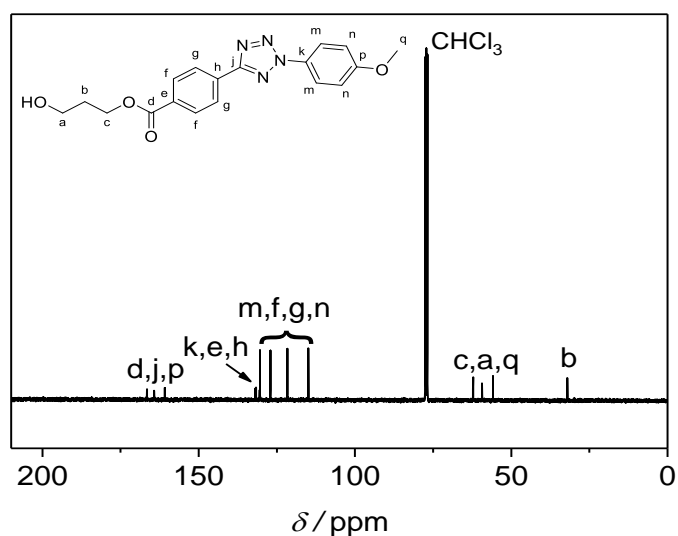
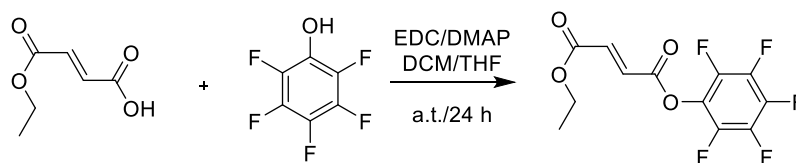


Figure 7-25. ^{13}C -NMR spectrum of tetrazole-acid 1,3-propanediol ester. The spectrum was recorded in CDCl_3 .

7.3.4 Pentafluorophenol Active Ester Molecules

Fumarate Pentafluorophenol-Ester



Scheme 7-13. Esterification of monoethyl fumarate with pentafluorophenol.

In a round bottom flask, 2.00 g monoethyl fumarate (13.8 mmol, 1.00 eq.), 3.19 g PFP (17.4 mmol, 1.25 eq.) and 0.34 g DMAP (2.8 mmol, 0.20 eq.) were dissolved in 25 mL of a mixture of DCM/THF, using only as much THF as necessary to dissolve the monoethyl fumarate. Next, the solution was cooled to 0 °C. The reaction was started by adding 3.32 g EDC (17.4 mmol, 1.25 eq.). The mixture was allowed to reach ambient temperature and stirred overnight. The next day, the solvent was removed under reduced pressure and the crude product was dissolved in DCM. The organic phase was washed with 5% hydrochloric acid, NaHCO_3 and brine solution. Subsequently, the combined organic phase was dried over Na_2SO_4 and the solvent was removed under reduced pressure. The final product was obtained after gel flash chromatography (silica gel, cyclohexane/ethyl acetate, 3/1, V/V), obtaining a pale yellowish oil (2.8 g, 65%).

^1H -NMR (400 MHz, CDCl_3 , 25 °C): δ (ppm): 7.14-7.04 (m, 2H, $\text{HC}=\text{CH}$), 4.32 (q, 2H, $^3J = 7.4$ Hz, O- CH_2), 1.34 (t, 3H, $^3J = 7.4$ Hz, CH_3 - CH_2).

^{19}F -NMR (377 MHz, CDCl_3 , 25 °C): δ (ppm): -161.9 (m, 2F, *meta*), -157.2 (m, 1F, *para*), -152.4 (m, 2F, *ortho*).

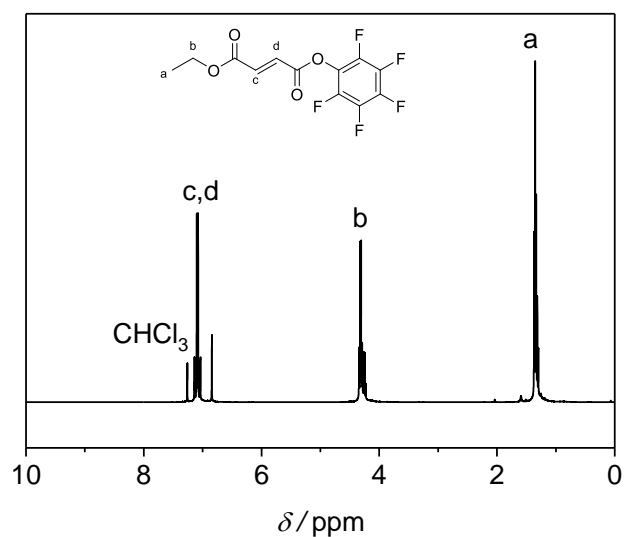


Figure 7-26. ^1H -NMR spectrum of ethyl-fumarate pentafluorophenol ester. The spectrum was recorded in CDCl_3 .

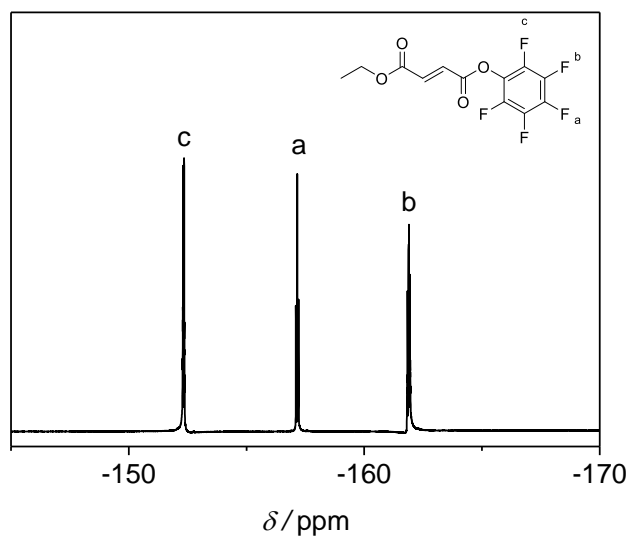
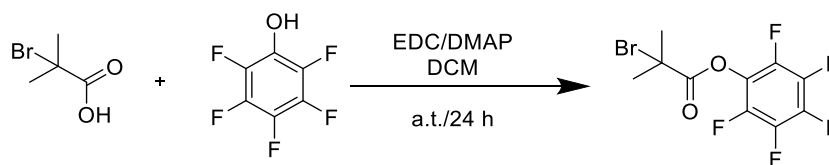


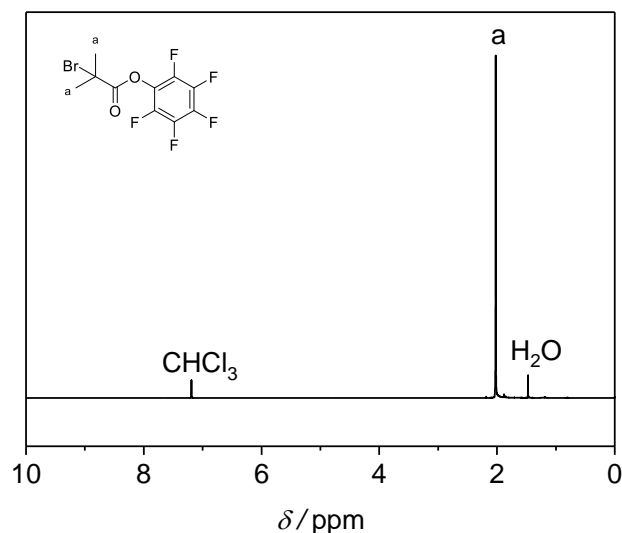
Figure 7-27. ^{19}F -NMR spectrum of ethyl-fumarate pentafluorophenol ester. The spectrum was recorded in CDCl_3 .

Bromide-Pentafluorophenol-Ester**Scheme 7-14.** Esterification of 2-bromo-2-methyl propionic acid with pentafluorophenol.

In a round bottom flask, 835 mg 2-bromo-2-methyl propionic acid (5.00 mmol, 2.0 eq.), 460 mg PFP (2.50 mmol, 1.0 eq.) and 152 mg DMAP (1.25 mmol, 0.5 eq.) were dissolved in 40 mL DCM. Then, the solution was cooled to 0 °C. The reaction was started by adding the 959 mg EDC (5.00 mmol, 2.0 eq.). The mixture was allowed to reach ambient temperature and stirred overnight. The crude mixture was washed with 5% hydrochloric acid, NaHCO₃ and brine solution. Subsequently, the combined organic phase was dried over Na₂SO₄ and the solvent was removed under reduced pressure. The final product was obtained after gel flash chromatography (silica gel, cyclohexane/ethyl acetate, 10/1, V/V), obtaining a colorless oil (1.06 g, 63%).

¹H-NMR (400 MHz, CDCl₃, 25 °C): δ (ppm): 2.09 (s, 6H, CH₃).

¹⁹F-NMR (377 MHz, CDCl₃, 25 °C): δ (ppm): -161.9 (m, 2F, *meta*), -157.2 (m, 1F, *para*), -152.8 (m, 2F, *ortho*).

**Figure 7-28.** ¹H-NMR spectrum of 2-bromo-2-methyl propionic acid pentafluorophenol ester. The spectrum was recorded in CDCl₃.

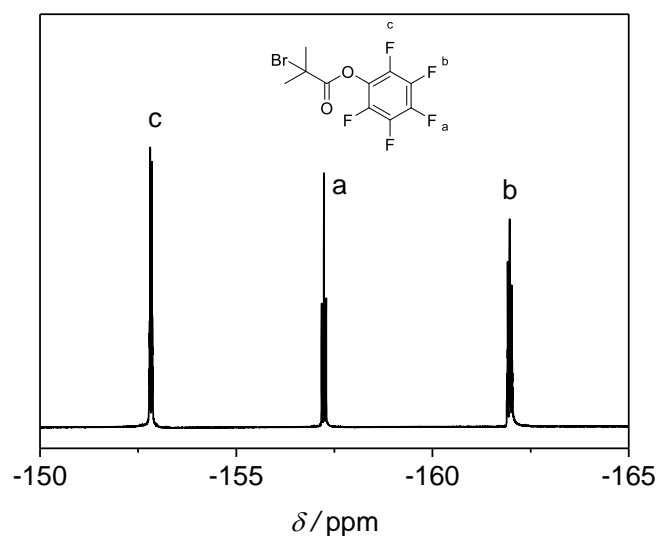
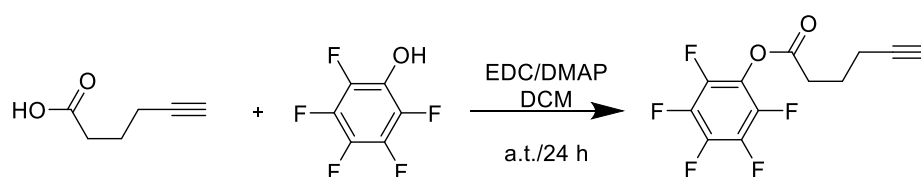


Figure 7-29. ^{19}F -NMR spectrum of 2-bromo-2-methyl propionic acid pentafluorophenol ester. The spectrum was recorded in CDCl_3 .

Alkyne-Pentafluorophenol-Ester



Scheme 7-15. Esterification of hexynoic acid with pentafluorophenol.

In a round bottom flask, 500 mg hexynoic acid (4.46 mmol, 1.0 eq.), 1.23 g PFP (6.69 mmol, 1.5 eq.) and 109 mg DMAP (0.89 mmol, 0.2 eq.) were dissolved in 25 mL DCM. Then, the solution was cooled to 0 °C. The reaction was started by adding the 1.11 g EDC (5.80 mmol, 1.3 eq.). The mixture was allowed to reach ambient temperature and stirred overnight. The crude mixture was washed with 5% hydrochloric acid, NaHCO_3 and brine solution. Subsequently, the combined organic phase was dried over Na_2SO_4 and the solvent was removed under reduced pressure. The final product was obtained after gel flash chromatography (silica gel, cyclohexane/ethyl acetate, 4/1, V/V), obtaining a light colorless oil (1.08 g, 87%).

^1H -NMR (400 MHz, DMSO, 25 °C): δ (ppm): 2.90-2.86 (m, 3H, OC- CH_2 , $\text{C}\equiv\text{CH}$), 2.31-2.27 (m, 2H, CH_2 - CH_2 - $\text{C}\equiv\text{CH}$), 1.84-1.81 (m, 2H, CH_2 - CH_2 - $\text{C}\equiv\text{CH}$).

^{19}F -NMR (377 MHz, DMSO, 25 °C): δ (ppm): -162.3 (m, 2F, *meta*), -157.3 (m, 1F, *para*), -153.8 (m, 2F, *ortho*).

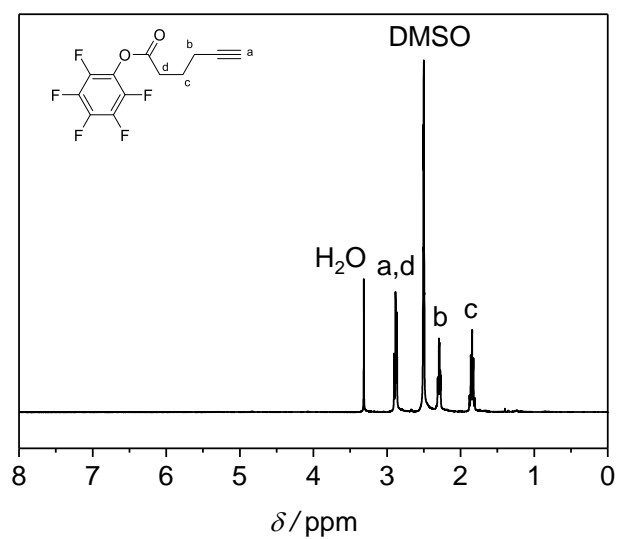


Figure 7-30. $^1\text{H-NMR}$ spectrum of 5-hexynoic acid pentafluorophenol ester. The spectrum was recorded in $\text{DMSO-}d_6$.

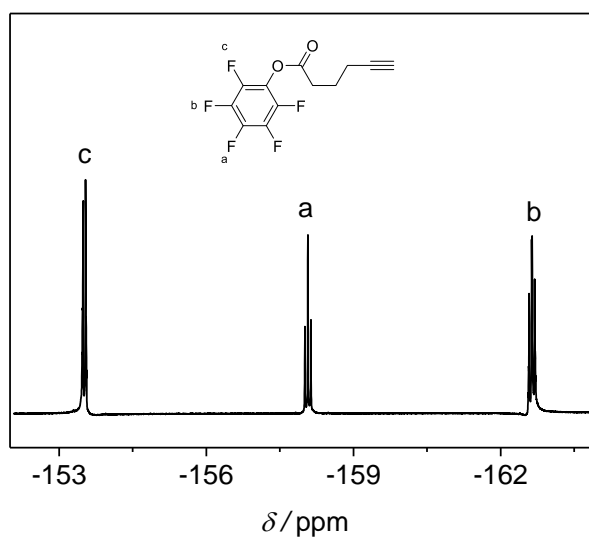
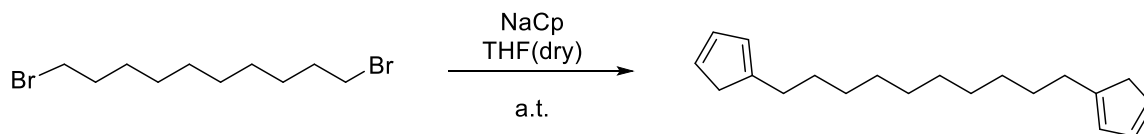


Figure 7-31. $^{19}\text{F-NMR}$ spectrum of 5-hexynoic acid pentafluorophenol ester. The spectrum was recorded in $\text{DMSO-}d_6$.

7.3.5 Further Small Molecule Synthesis Protocols

Synthesis of 1,10-di(cyclopentadienyl)-decane (CC monomer)

Scheme 7-16. Synthesis of 1,10-di(cyclopentadienyl)-decane monomer **CC**.

According to literature,¹⁹⁶ in a dry round bottom flask 30.01 g 1,10-dibromo-decane (0.10 mol, 1 eq.) was dissolved in dry THF in an inert gas atmosphere. The solution was cooled to 0 °C and 100 mL of a 2 M solution of sodium cyclopentadienyl in THF (0.20 mol, 2 eq.) were added dropwise. After addition, the brown solution was stirred for 1 h and the reaction mixture was allowed to reach ambient temperature and stirred for 16 h. The suspension was filtered over silica employing ethyl acetate. After removal of the solvent, the brown oil was dissolved in *n*-hexane and filtered over silica employing *n*-hexane. After the evaporation of the solvent the product was obtained as a colorless oil (23.66 g, 87%) that was stored at -20 °C.

¹H-NMR (400 MHz, CD₂Cl₂, 25 °C): δ (ppm): 6.43-5.98 (m, 6H, Cp **HC=CH**), 2.88 (d, 4H, **CH₂**,Cp), 2.40-2.31 (m, 4H, (CH₂)₃-**CH₂**-Cp), 1.55-1.46 (m, 4H, (CH₂)₃-**CH₂**-Cp), 1.36-1.21 (m, 12H, (CH₂)₃-**CH₂**-Cp).

¹³C-NMR (101 MHz, CDCl₃, 25 °C): δ(ppm): 150.2 (CH₂CH₂**C**_{Cp}), 147.5 (CH₂CH₂**C**_{Cp}), 135.0 (**C**_{Cp}), 133.6 (**C**_{Cp}), 132.6 (**C**_{Cp}), 130.4 (**C**_{Cp}), 126.3 (**C**_{Cp}), 125.7 (**C**_{Cp}), 43.4 (**C**_{Cp}), 41.3 (**C**_{Cp}), 30.9 (CH₂CH₂Cp), 30.0 (CH₂), 29.9 (CH₂), 29.8 (CH₂), 29.7 (CH₂), 29.6 (CH₂), 29.0 (CH₂).

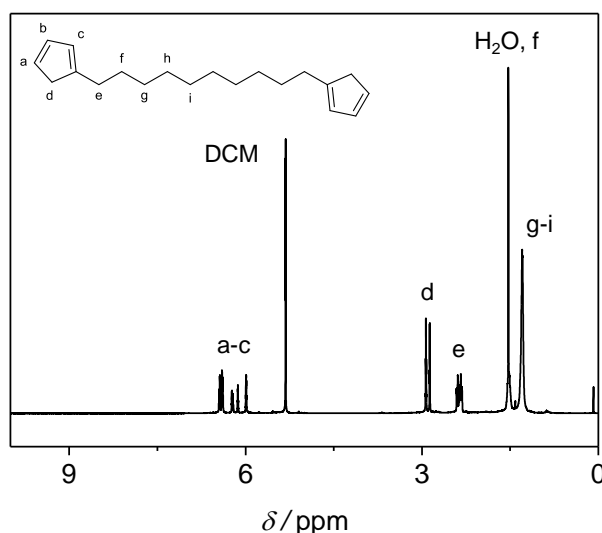


Figure 7-32. ¹H-NMR spectrum of 1,10-di(cyclopentadienyl)-decane (**CC** monomer). The spectrum was recorded in CD₂Cl₂.

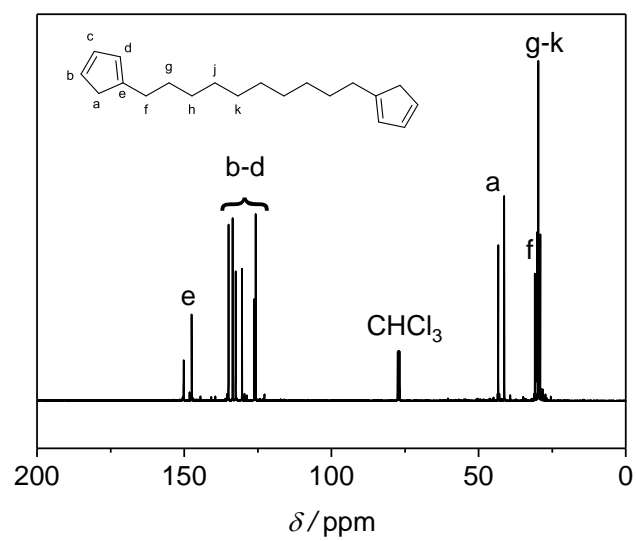
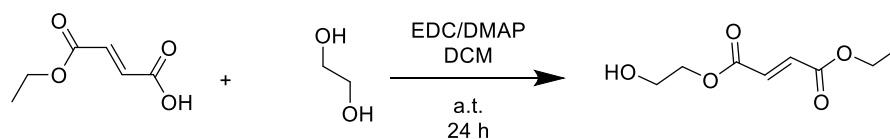


Figure 7-33. ^{13}C -NMR spectrum of 1,10-di(cyclopentadienyl)-decane (**CC** monomer). The spectrum was recorded in CDCl_3 .

Synthesis of 2-hydroxyethyl-ethyl fumarate



Scheme 7-17. Synthesis of 2-hydroxyethyl-ethyl fumarate for **BB** synthesis.

In a round bottom flask 2.00 g monoethyl fumarate (13.88 mmol, 1.0 eq.), 8.61 g ethylene glycol (138.77 mmol, 10.0 eq.), and 339 mg DMAP (2.78 mmol, 0.2 eq.) were dissolved in a mixture of 24 mL dry DCM and 9 mL dry THF. The solution was cooled to 0 °C and 3.19 g EDC (16.65 mmol, 1.2 eq.) was added. The solution was allowed to reach ambient temperature and stirred overnight. Afterwards, the solvent was evaporated under reduced pressure. Subsequently, the crude product was dissolved in DCM and washed with 5% hydrochloric acid, saturated NaHCO₃ solution and brine. The combined organic phase was dried over Na₂O₄ and the solvent was removed under reduced pressure. The crude product was purified by flash chromatography (silica gel, cyclohexane/ethyl acetate, 1/1, V/V) to obtain a colorless oil (2.01 g, 77%).

¹H-NMR (400 MHz, DMSO-d₆, 25 °C): δ (ppm): 6.89 (m, 2H, HC=CH), 4.88 (t, ³J = 6.04 Hz, 1H, OH), 4.22-4.15 (m, 4H, CH₂O), 3.64-3.60 (m, 2H, CH₂O), 1.25 (t, ³J = 7.19 Hz, 3H, -CH₃).

¹³C-NMR (101 MHz, CDCl₃, 25 °C): δ (ppm): 165.3 (HC=CH), 165.0 (HC=CH), 134.5 (C=O), 133.1, (C=O), 67.0 (HOCH₂-CH₂-C=O), 61.6 (CH₃-CH₂-C=O), 61.1 (HOCH₂-CH₂-C=O), 14.2 (CH₃-CH₂-C=O).

ESI-MS: *m/z* [M+Na]⁺_{exp}: 211.0578, [M+Na]⁺_{calc}: 211.0577.

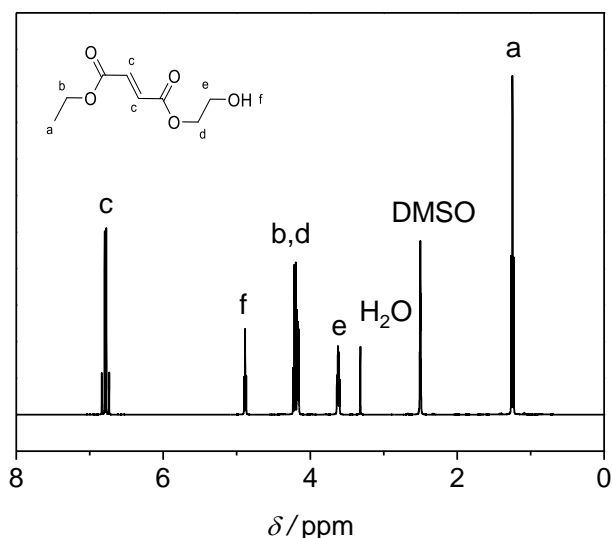


Figure 7-34. ¹H-NMR spectrum of 2-hydroxyethyl-ethyl fumarate. The spectrum was recorded in DMSO-*d*₆.

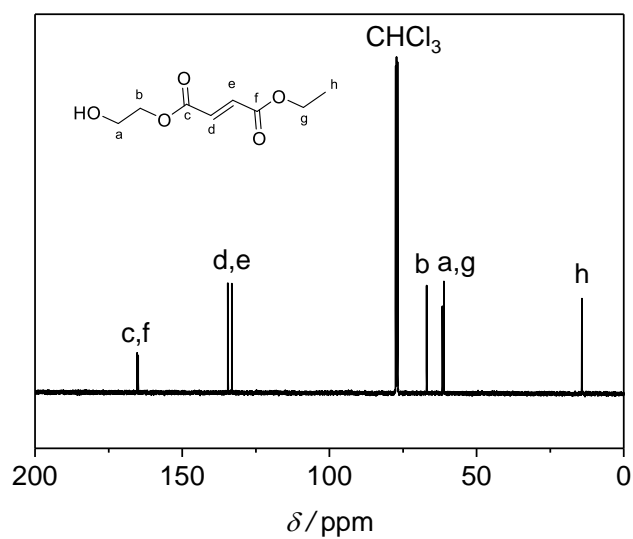


Figure 7-35. ^{13}C -NMR spectrum of 2-hydroxyethyl-ethyl fumarate. The spectrum was recorded in CDCl_3 .

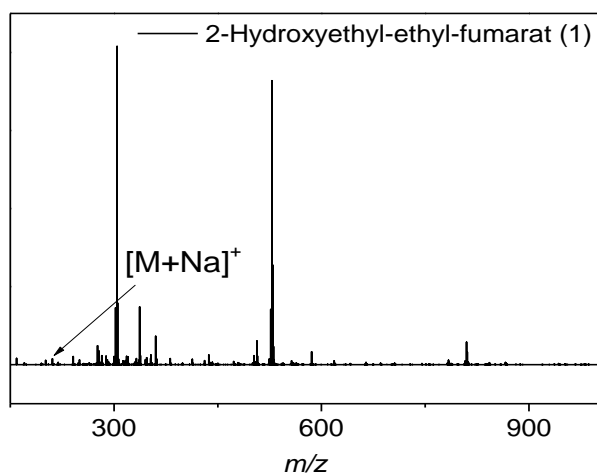
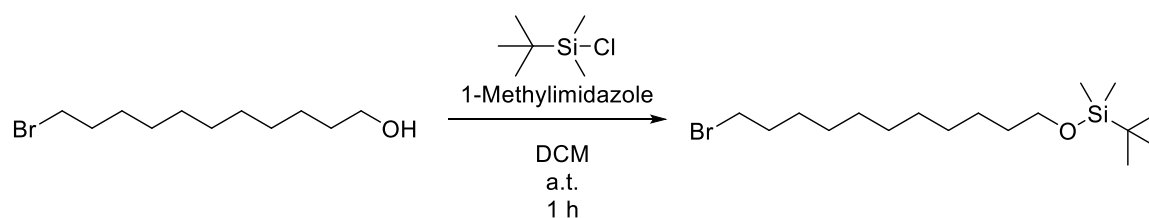


Figure 7-36. ESI-MS spectrum of 2-hydroxyethyl-ethyl fumarate. The spectrum was recorded via a direct-infusion experiments using a solvent mixture of THF/MeOH (3/2, V/V) by doping with sodium trifluoroacetate.

Synthesis of ((11-bromoundecyl)oxy)(tert-butyl)dimethylsilane



Scheme 7-18. Protection of 11-bromoundecan-1-ol with silyl-ether.

In a 100 mL Schlenk flask 4.00 g 11-bromoundecan-1-ol (15.9 mmol, 1.00 eq.) and 2.80 g TBDMSCl (18.5 mmol, 1.20 eq.) were dissolved in 15 mL dry DCM under inert gas atmosphere. Subsequently 3.9 mL 1-methylimidazole (49.0 mmol, 3.00 eq.) was added to the dissolved material. The mixture was stirred for 1 h at ambient temperature under inert gas atmosphere. The reaction was quenched with 20 mL of water, followed by the addition of 90 mL ethyl acetate. The organic layer was washed with saturated aqueous solution of Na_2CO_3 and deionized water, and dried over Na_2SO_4 . After evaporation of the solvent, the residue was purified by flash chromatography (silica gel, cyclohexane/ethyl acetate, 93/7, V/V) to obtain a yellowish oil (5.15 g, 88%).

$^1\text{H-NMR}$ (400 MHz, CDCl_3 , 25 °C): δ (ppm): 3.59 (t, $^3J = 6.6$ Hz, 2 H, SiO-CH₂-CH₂), 3.40 (t, $^3J = 6.9$ Hz, 2 H, Br-CH₂-CH₂), 1.89-1.80 (m, 2 H, Br-CH₂-CH₂-CH₂), 1.49 (q, $^3J = 6.7$ Hz, 2 H, SiO-CH₂-CH₂), 1.46-1.37 (m, 2 H, SiO-CH₂-CH₂-CH₂), 1.27 (s, 12 H, CH₂-CH₂-CH₂), 0.89 (s, 9 H, C-CH₃), 0.4 (s, 6 H, Si-(CH₃)₂).

$^{13}\text{C-NMR}$ (101 MHz, CDCl_3 , 25 °C): δ (ppm): 63.5 (CH₂-CH₂-O), 34.2 (Br-CH₂-CH₂), 33.0 (CH₂-CH₂-CH₂-O), 33.0 (Br-CH₂-CH₂-CH₂), 29.7 (Si-C-(CH₃)₃), 29.6 (CH₂-CH₂-CH₂), 29.6 (CH₂-CH₂-CH₂), 28.9 (CH₂-CH₂-CH₂), 28.3 (CH₂-CH₂-CH₂), 26.1 (CH₃), -5.1 (Si-(CH₃)₂).

ESI-MS: m/z [M+Na]⁺_{exp}: 387.1688, [M+Na]⁺_{calc}: 387.1695.

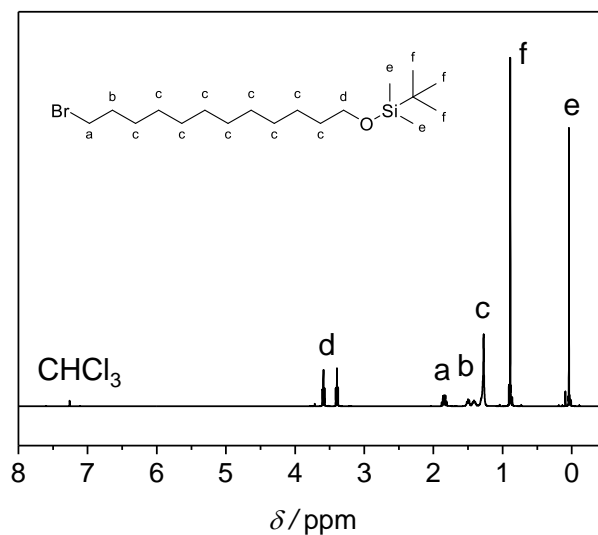


Figure 7-37. ¹H-NMR spectrum of ((11-bromoundecyl)oxy)(tert-butyl)dimethylsilane (precursor of Mono-Cp). The spectrum was recorded in CDCl₃.

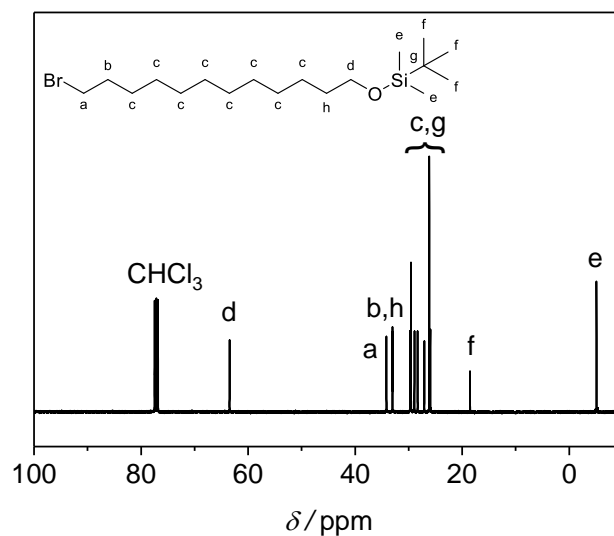
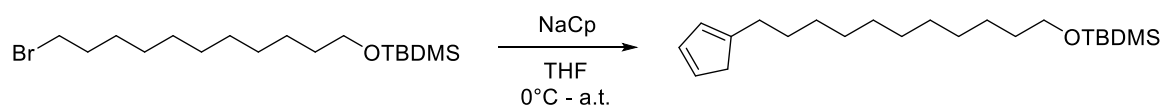


Figure 7-38. ¹³C-NMR spectrum of ((11-bromoundecyl)oxy)(tert-butyl)dimethylsilane (precursor of Mono-Cp). The spectrum was recorded in CDCl₃.

Synthesis of *tert*-butyl((11-(cyclopenta-1,3-dien-1-yl)undecyl)oxy)dimethylsilane (Mono-Cp)



Scheme 7-19. Synthesis of the *tert*-butyl((11-(cyclopenta-1,3-dien-1-yl)undecyl)oxy)dimethylsilane (Mono-Cp).

To a cooled solution of ((11-bromoundecyl)oxy)(*tert*-butyl)dimethylsilane (3.60 g, 9.0 mmol, 1.00 eq.) in dry THF (25 mL), sodium cyclopentadienyl (5.5 mL of a 2.0 M solution in THF, 11.0 mmol, 1.20 eq.) was added. After stirring for 1 h at 0 °C, the reaction mixture was allowed to warm to ambient temperature and stirred overnight. The suspension was filtered off and the residual solution was filtered by flash chromatography (silica gel, cyclohexane/ethyl acetate, 93/7, V/V). The crude product was concentrated and isolated by flash chromatography (silica gel, cyclohexane/toluene 4/1, V/V) to obtain a colorless oil (1.7 g, 54%).

$^1\text{H-NMR}$ (400 MHz, CDCl_3 , 25 °C): δ (ppm): 6.49-5.96 (m, 3 H, $\text{CH-CH}_{\text{ar}}\text{-CH}$), 3.60 (t, $^3J = 6.6$ Hz, 2 H, $\text{Si-O-CH}_2\text{-CH}_2$), 2.92-2.87 (m, 2 H, $\text{CH}_{\text{ar}}\text{-CH}_2\text{-CH}_{\text{ar}}$), 2.44-2.30 (m, 2 H, $\text{CH}_2\text{-CH}_2\text{-CH}_2$), 1.59-1.39 (m, 4 H, $\text{CH-(CH}_2\text{)}_2\text{-CH}_{\text{ar}}$), 1.27 (s, 14 H, $\text{CH-(CH}_2\text{)}_7\text{-CH}_{\text{ar}}$), 0.93-0.86 (m, 9 H, $\text{Si-C-(CH}_3\text{)}_3$), 0.08-0.02 (m, 6 H, $\text{Si-(CH}_3\text{)}_2$).

$^{13}\text{C-NMR}$ (101 MHz, CDCl_3 , 25 °C): δ (ppm): 150.5 ($\text{CH}_2\text{CH}_2\text{C}_{\text{Cp}}$), 148.6 ($\text{CH}_2\text{CH}_2\text{C}_{\text{Cp}}$), 135.0, (C_{Cp}), 133.7 (C_{Cp}), 132.6 (C_{Cp}), 130.5 (C_{Cp}), 126.2 (C_{Cp}), 125.8 (C_{Cp}), 63.5 ($\text{CH}_2\text{-CH}_2\text{-O}$), 43.4 (Cp-CH_2), 41.3 (Cp-CH_2), 33.1 ($\text{CH}_2\text{-CH}_2\text{-O}$), 30.9 ($\text{Si-C-(CH}_3\text{)}_3$), 30.0 ($\text{CH}_2\text{-CH}_2\text{-CH}_2$), 29.8 ($\text{CH}_2\text{-CH}_2\text{-CH}_2$), 29.8 ($\text{CH}_2\text{-CH}_2\text{-CH}_2$), 29.7 ($\text{CH}_2\text{-CH}_2\text{-CH}_2$), 29.6 ($\text{CH}_2\text{-CH}_2\text{-CH}_2$), 29.0 ($\text{CH}_2\text{-CH}_2\text{-CH}_2$), 26.2 ($\text{C}_q\text{-CH}_3$), -5.1 ($\text{Si-(CH}_3\text{)}_2$).

ESI-MS: m/z $[\text{M}+\text{Na}]^+_{\text{exp.}}$: 373.2911, $[\text{M}+\text{Na}]^+_{\text{calc.}}$: 373.2897.

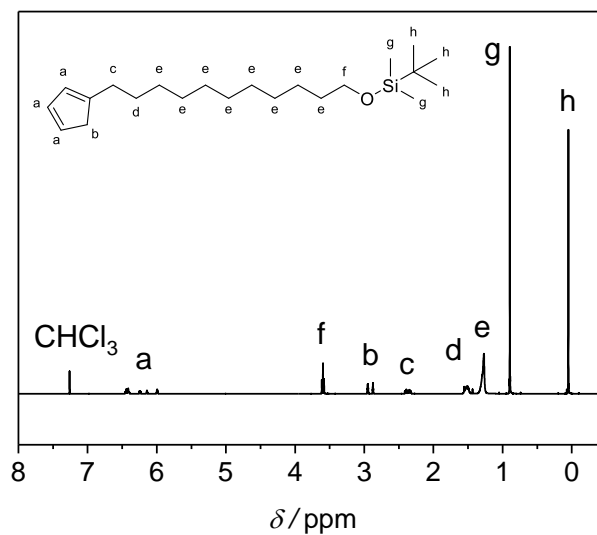


Figure 7-39. $^1\text{H-NMR}$ spectrum of *tert*-butyl((11-(cyclopenta-1,3-dien-1-yl)undecyl)oxy)dimethylsilane (Mono-Cp). The spectrum was recorded in CDCl_3 .

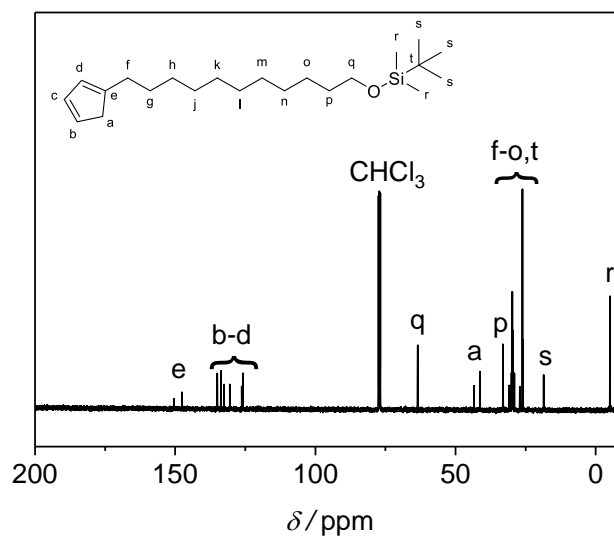
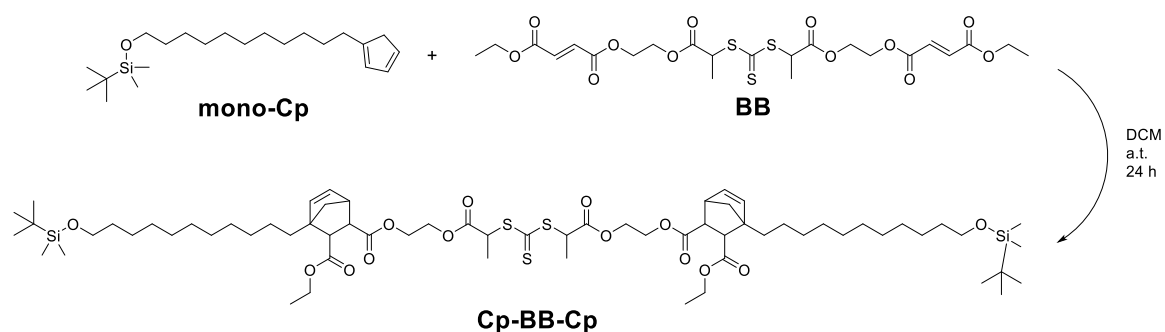


Figure 7-40. $^{13}\text{C-NMR}$ spectrum of *tert*-butyl((11-(cyclopenta-1,3-dien-1-yl)undecyl)oxy)dimethylsilane (Mono-Cp). The spectrum was recorded in CDCl_3 .

DA Reaction of monomer **BB** and Mono-**Cp**

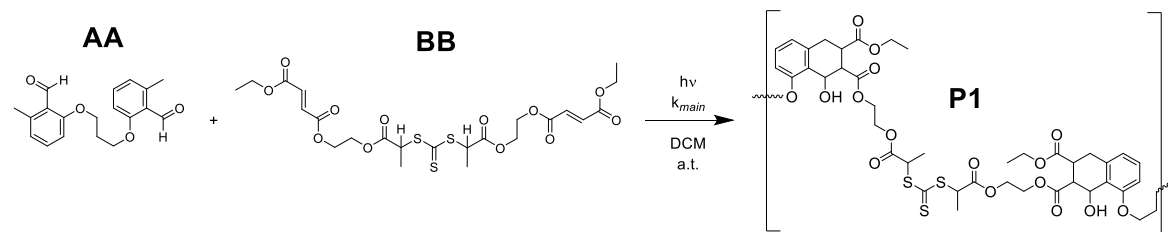
Scheme 7-20. DA reaction of the monomer **BB** and the **mono-Cp** compound.

The **Cp-BB-Cp** molecule was synthesized by mixing 10.0 mg of the **mono-Cp** (0.029 mmol, 2.3 eq.) and 7.4 mg **BB** monomer (0.012 mmol, 1.0 eq.) in 1 mL DCM for 24 h at ambient temperature. The stability assay was carried out with the unpurified **Cp-BB-Cp** in toluene-*d*₈ at 60 °C in a sealed NMR tube inside the NMR instrument (spectra shown in Chapter 4.3.5).

7.4 Polymerization Procedures

7.4.1 Step-Growth Procedures

7.4.1.1 Photo-induced Step-Growth Polymerization with Photoenols



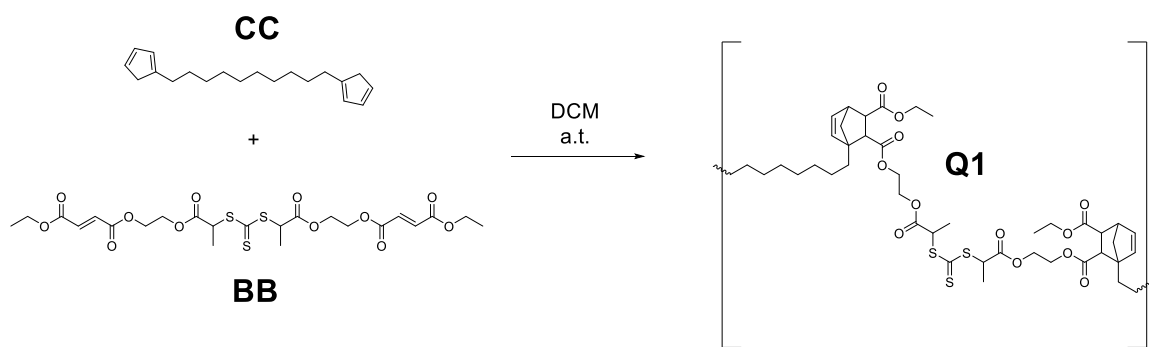
Scheme 7-21. Reaction scheme for the step-growth polymerization of **AA** and **BB**, forming the SG polymer.

In a typical experiment, monomer **AA** (initial concentration 0.02, 0.04 mol L⁻¹) and **BB** (initial concentration 0.02 mol L⁻¹, 0.04 mol L⁻¹ up to 0.081 mol L⁻¹) were transferred into a headspace vial and dissolved in DCM (0.5 mL). To express a deliberate stoichiometric imbalance, the quantity r is defined, representing the excess based on the initial number of **A** vs. **B** functional groups.

We note that in case monofunctional species are employed, Eq. (29) is kept in line with the convention to maintain the initial number of benzaldehyde functional groups in the nominator and the initial number of ene groups in the denominator.

The vial was sealed and nitrogen was percolated through the solution for at least 2 min. Afterwards the sample was placed in a custom-made photo reactor (refer to Chapter 7.2.7) for the irradiation duration at ambient temperature ($\lambda_{\max} = 360$ nm). After the reaction, the solvent was removed under reduced pressure to obtain a yellowish/orange solid.

7.4.1.2 Thermal Step-Growth Polymerization with Cyclopentadienes

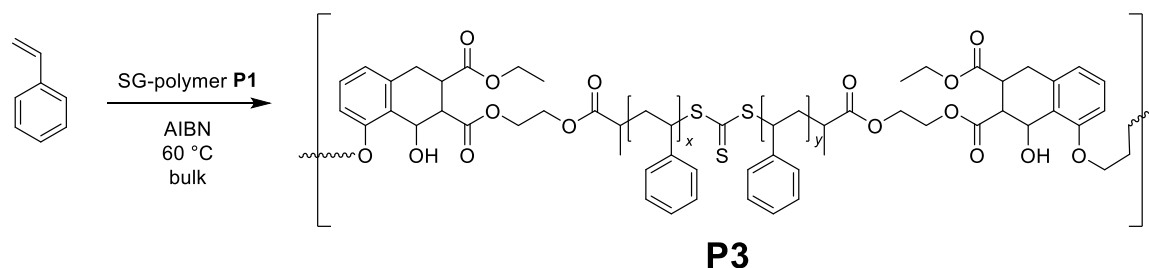


Scheme 7-22. SG polymerization by DA reaction using monomer **CC** and **BB** in DCM at ambient temperature.

In a typical step-growth polymerization procedure, monomer **CC** ($0.2 \text{ mol}\cdot\text{L}^{-1}$, 1.2 eq.) and monomer **BB** ($0.17 \text{ mol}\cdot\text{L}^{-1}$, 1.0 eq.) were separately dissolved in DCM and subsequently mixed. The SG polymerization was allowed to stir under ambient conditions ($T = 25 \text{ }^\circ\text{C}$) for the desired time. After the polymerization, the solvent was removed under reduced pressure at ambient temperature to obtain the step-growth polymer as a yellowish rubber-like solid.

7.4.2 RAFT Polymerization with multi-Chain-Transfer Agents

RAFT Polymerization of Styrene with SG Polymers from Photo-induced DA Reaction

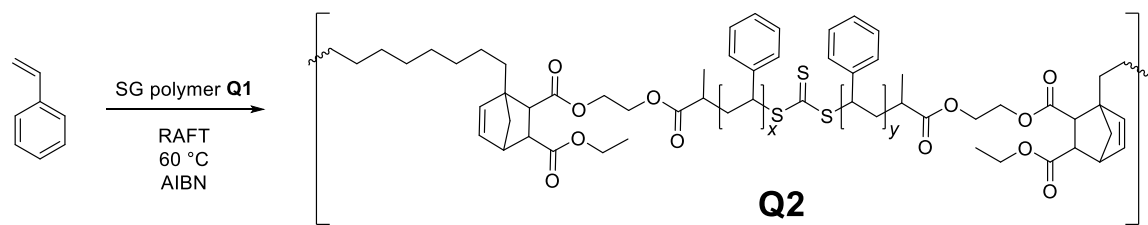


Scheme 7-23. RAFT polymerization of styrene using the SG polymer **P1** as multifunctional CTA, obtained in a photo-induced SG polymerization ((**AA**)_k homopolymer segments not shown for simplicity).

In a typical procedure 0.7 mg (0.004 mmol, 1 eq.) AIBN and 20 mg of the step-growth precursor polymer **P1** were dissolved in 4.01 g (38.5 mmol, 8740 eq.) of styrene. The headspace vial was sealed and nitrogen was percolated through the solution for at least 15 min. Subsequently, the vial was placed in an oil bath at $60 \text{ }^\circ\text{C}$ and stirred for the predefined polymerization duration. To terminate the polymerization, the solution was quenched in liquid nitrogen and exposed to air for at least 10 min. The crude polymerization solution was diluted with THF and precipitated into ice-cold methanol. The

polymer was filtered off, washed several times with ice-cold methanol, and dried under reduced pressure at ambient temperature.

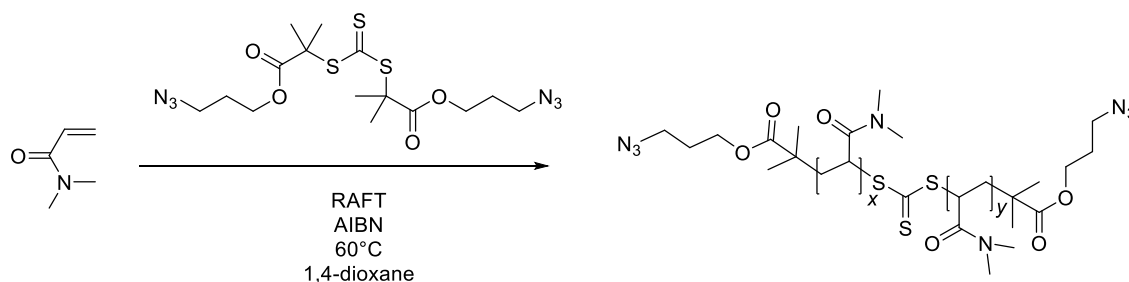
RAFT Polymerization of Styrene with SG Polymers from Thermal DA Reaction



Scheme 7-24. RAFT polymerization of styrene using the SG polymer **Q1** as multifunctional CTA, obtained in a thermally induced SG polymerization.

In a typical RAFT procedure 1.8 mg (0.012 mmol, 3 eq.) AIBN and 50 mg of the step-growth precursor polymer **Q1** ($n(\text{RAFT}) = 5 \text{ mmol}$, 15 Eq.) were dissolved in 10.50 g (100.9 mmol, 8727 eq.) of styrene. The stock solution was split into different headspace vials ($V = 1.2 \text{ mL}$ per vial), sealed and nitrogen was percolated through the solutions for 10 min. Subsequently, the vials were placed in a pre-heated sample holder at 60 °C and stirred for the predefined polymerization time. To terminate the polymerization, the solution was quenched in liquid nitrogen and exposed to air. The crude polymerization solution was exposed to reduced pressure in order to remove any volatile components to obtain the polymer without precipitation.

7.4.3 RAFT Polymerization with conventional RAFT Agents



Scheme 7-25. RAFT polymerization of DMAA with diazido-RAFT agent.

In a 15 mL head space vial, 1.78 g dimethylacrylamide (DMAA, 18 mmol, 1500 eq.), 65 mg azido-RAFT agent (0.14 mmol, 12 eq.) and 2 mg AIBN (0.012 mmol, 1 eq.) were dissolved 8 mL 1,4-dioxane. The head space vial was sealed and the solution was percolated with nitrogen for 30 min. To start the polymerization, the sealed vial was placed in a preheated oil bath at 60 °C for 8 h. To terminate the polymerization, the sealed vial was quenched in liquid nitrogen and exposed to air for 10 min. The final polymer was obtained by two

precipitation cycles, diluting the reaction mixture with THF and adding dropwise into ice-cold diethyl ether. The final precipitate was filtered off and the polymer was dried at 40 °C under reduced pressure (656 mg). The polymer was stored at -20 °C.

ESI-MS: m/z $[P_{53} + 2Na]^{2+}_{exp}$: 2873.8922, $[P_{53} + 2Na]^{2+}_{calc}$: 2873.8583.

Table 7-2. Molecular characteristics of the PDMAA-diaziido Polymer. Molecular weight distribution is illustrated in Chapter 5.2.6.1 in Figure 5-5.

$M_n / \text{g}\cdot\text{mol}^{-1}$	$M_w / \text{g}\cdot\text{mol}^{-1}$	\bar{D}
13,900	14,950	1.08

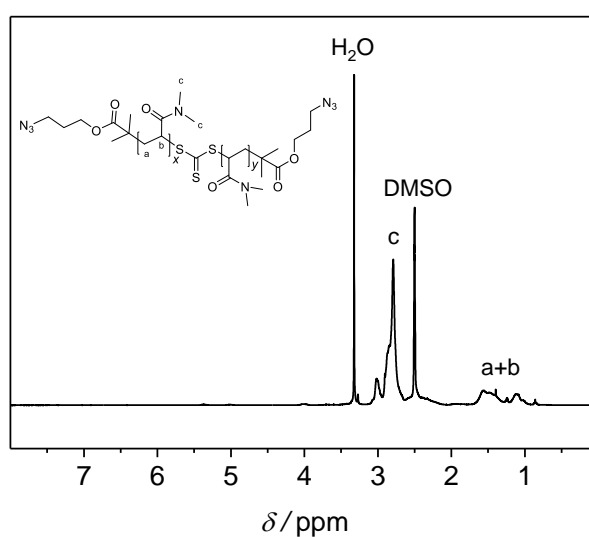


Figure 7-41. ¹H-NMR spectrum of poly(dimethyl acrylamide) with α,ω-functional azido groups. The spectrum was recorded in DMSO-*d*₆.

7.5 Reactions with CRD Peptides

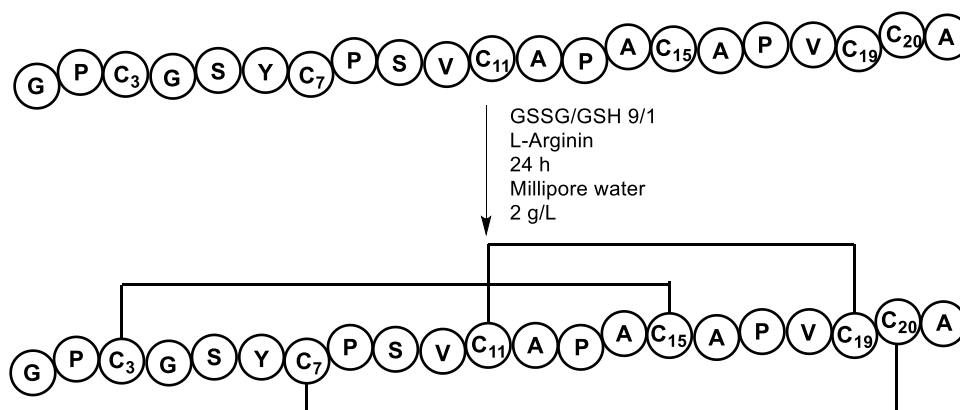
7.5.1 Folding of the CRD

Characteristic of the CRD peptide:

Sequence (one letter code):

GPCGSYCPSVCAPACAPVCCA

Molecular weight: 1959.34 g/mol (reduced state)



Scheme 7-26. Folding of the CRD by intramolecular thiol oxidation.

In a round bottom flask, 100 mg of the CRD in reduced state (0.051 mmol, 1.0 eq.), 1.5 mg of GSH (0.005 mmol, 0.1 eq.), 27.5 mg of GSSG (0.045 mmol, 0.9 eq.) and 871 mg of L-arginine (5 mmol, 100.0 eq.) were dissolved in 100 mL Millipore water. The solution was stirred at ambient temperature overnight. Afterwards, the reaction solution was transferred into a dialysis tube (MWCO: 1 kDa) and dialyzed against deionized water for three days by exchanging the dialysis bath three times. Finally, the solution was lyophilized to obtain a colorless white powder (50 mg, 50%).

ESI-MS: m/z $[M+H]^+$ _{exp}: 1952.7127, $[M+H]^+$ _{calc}: 1952.6926.

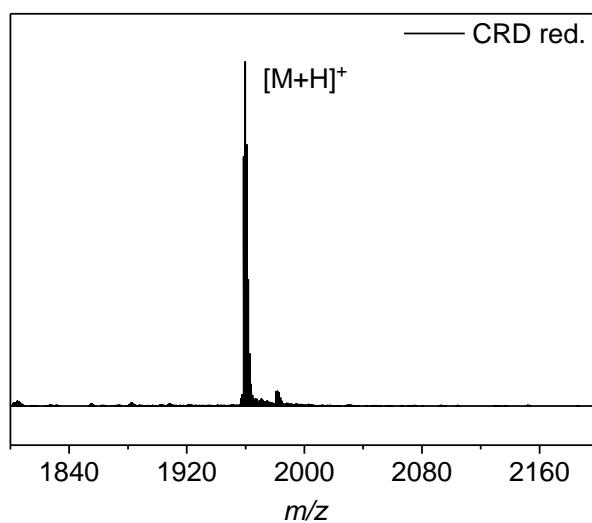
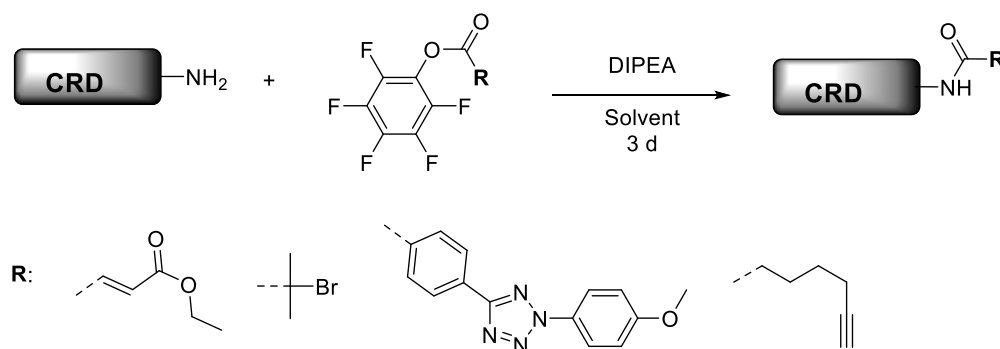


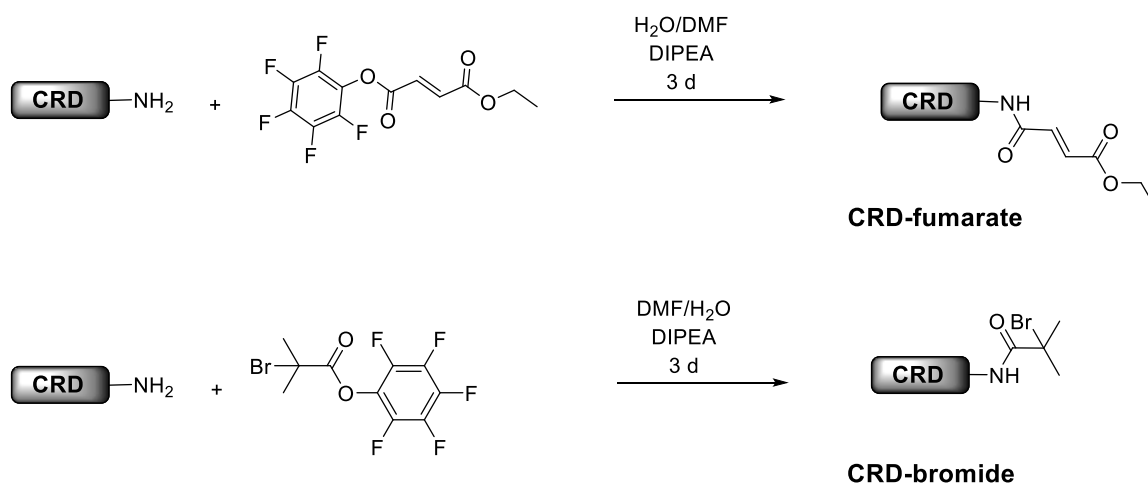
Figure 7-42. ESI-MS spectrum of the CRD in reduced state as starting material for the folding. The spectrum was recorded in MeCN/H₂O mixture with the addition of 1% acetic acid.

7.5.2 Functionalization of the CRD-Peptide



Scheme 7-27. Introduction of functional groups to the CRD by active ester chemistry using PFP ester molecules bearing a fumarate, bromide, tetrazole and alkyne group.

7.5.2.1 Fumarate and Bromide CRD-Functionalization



Scheme 7-28. Functionalization of the folded CRD with the fumarate and the bromide bearing active esters.

The functionalizations of the CRD-peptide were conducted with the same procedure for both linker molecules: The folded CRD (30 mg, 0.015 mmol, 1.00 eq.) and the respective linker (linker 1 and linker 2, see below) were dissolved in 10 mL DMF/water (1/1, V/V). After the CRD was dissolved, 5.5 μ L DIPEA (4 mg, 0.031 mmol, 2.00 eq.) was added to the solution. The reaction mixture was stirred at ambient temperature for three days. Afterwards, the solution was transferred into a dialysis tube (MWCO: 1 kDa) and incubated for three days, changing the dialysis bath three times. Finally, the solution was lyophilized to obtain a white colorless powder.

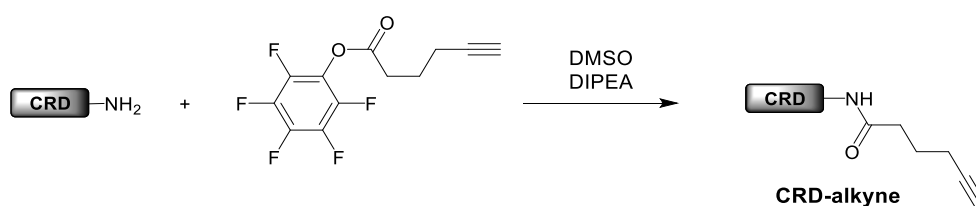
Linker 1 (PFP-fumarate): 6.0 μ L, 9.5 mg, 0.031 mmol, 2.00 eq. Yield: 7.5 mg (25%)

Linker 2 (PFP-bromide): 5.5 μ L, 10.2 mg, 0.031 mmol, 2.00 eq. Yield: 5 mg (16%)

CRD-fumarate: ESI-MS: m/z [M+Na]⁺_{exp.}: 2101.7249, [M+Na]⁺_{calc.}: 2101.7063.

CRD-bromide: ESI-MS: m/z [M+Na]⁺_{exp.}: 2124.6506, [M+Na]⁺_{calc.}: 2124.6249.

7.5.2.2 Alkyne CRD-Functionalization

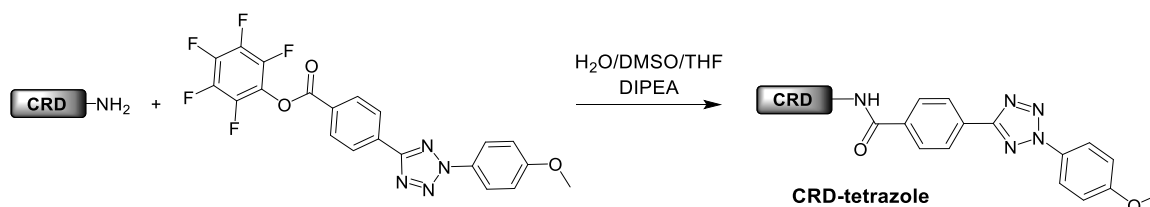


Scheme 7-29. Functionalization of the folded CRD with the alkyne bearing active ester.

In a round bottom flask, 50 mg folded CRD (0.026 mmol, 1.00 eq.) and 8.9 mg alkyne-PFP linker (0.032 mmol, 1.25 eq.) were dissolved in 15 mL DMSO. After the CRD was dissolved, 5.7 μ L DIPEA (4.1 mg, 0.032 mmol, 1.25 eq.) was added to the solution. The reaction mixture was stirred at ambient temperature for three days. Afterwards, the solution was transferred into a dialysis tube (MWCO: 1 kDa) and incubated for three days, changing the dialysis bath three times. Finally, the solution was lyophilized to obtain a white colorless powder (21 mg, 40 %).

ESI-MS: m/z $[M+Na]^+$ _{exp.}: 2068.7369 $[M+Na]^+$ _{calc.}: 2068.7165.

7.5.2.3 Tetrazole CRD-Functionalization

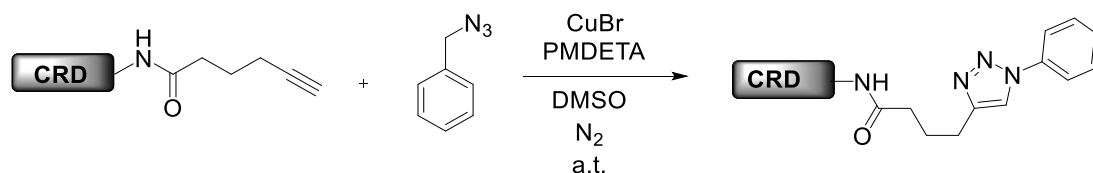


Scheme 7-30. Functionalization of the folded CRD with the tetrazole bearing active ester.

In a round bottom flask, 30 mg folded CRD (0.015 mmol, 1.0 eq.) and 10 mg tetrazole-PFP linker (0.022 mmol, 1.4 eq.) were dissolved in 2.5 mL water, 5 mL DMSO and 5 mL THF. After the CRD and the linker were dissolved, 3.8 μ L DIPEA (2.8 mg, 0.022 mmol, 1.4 eq.) was added to the solution. The reaction mixture was stirred at ambient temperature for three days. Afterwards, the solution was transferred into a dialysis tube (MWCO: 1 kDa) and incubated for three days, changing the dialysis bath three times. Finally, the solution was lyophilized to obtain a white colorless powder (20 mg, 58 %). ESI-MS: m/z $[M+Na]^+$ _{exp.}: 2252.7628 $[M+Na]^+$ _{calc.}: 2252.7550.

7.5.3 Small Molecule Ligations of functional CRD

7.5.3.1 Copper-catalyzed Azide-Alkyne Cycloaddition of CRD-alkyne

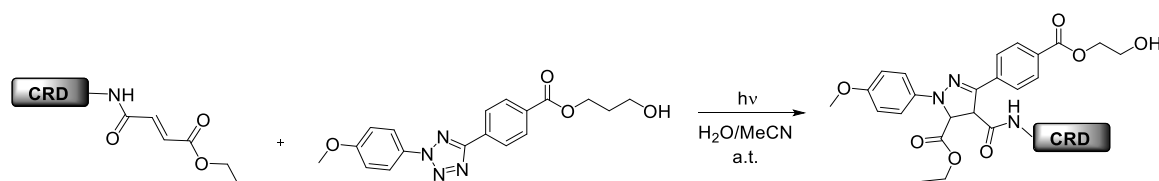


Scheme 7-31. CuAAC of the CRD-alkyne and benzylazide using CuBr and PMDETA.

In a 25 mL Schlenk tube, 40.0 mg CRD-alkyne (0.02 mmol, 1.00 eq.), 5.2 mg benzylazide (0.04 mmol, 2.00 eq.) and 2 mg CuBr (0.15 mmol, 0.71 eq.) were dissolved in 20 mL DMSO. The solution was degassed by three consecutive freeze-pump-thaw cycles to finally start the reaction by adding 3 μ L *N,N,N',N'',N''*-pentamethyldiethylenetriamine (PMDETA, 0.015 mmol, 0.75 eq.). The tube was sealed air tight and allowed to stir at ambient temperature for 24 h. Afterwards, the solution was transferred into a dialysis tube (MWCO: 1 kDa) and incubated for three days, changing the dialysis bath three times. Finally, the product was obtained by lyophilization of the aqueous solution as a beige powder (20 mg, 47 %).

ESI-MS: m/z $[M+Na]^+_{exp}$: 2201.7990, $[M+Na]^+_{calc}$: 2201.7805.

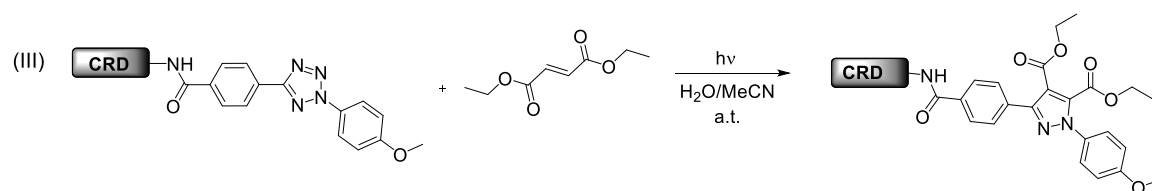
7.5.3.2 Photo-induced Ligation of CRD-Fumarate *via* NITEC



Scheme 7-32. NITEC reaction of the CRD-fumarate and a tetrazole-OH derivative.

In a preparation vial, 4.2 mg CRD-fumarate (0.0020 mmol, 1.0 eq.) were dissolved in a mixture of deionized water and MeCN (1/1, V/V). Subsequently, 1 mg of the tetrazole-OH (0.0057 mmol, 2.8 eq.) was added and the reaction mixture was irradiated for 1 h (λ_{max} = 310 nm, refer to Chapter 7.2.7). Since no full conversion was achieved, according to the ESI-MS spectra, another 1 mg (0.0057 mmol, 2.8 eq.) of the tetrazole-OH was added and the irradiation was extended for 4 h. The crude mixture was subsequently analyzed *via* direct-infusion experiments at ESI-MS to prove the existence of the product. ESI-MS: m/z $[M+Na]^+_{exp}$: 2427.8673, $[M+Na]^+_{calc}$: 2427.8363.

7.5.3.3 Photo-induced Ligation of CRD-Tetrazole via “Inverse” NITEC

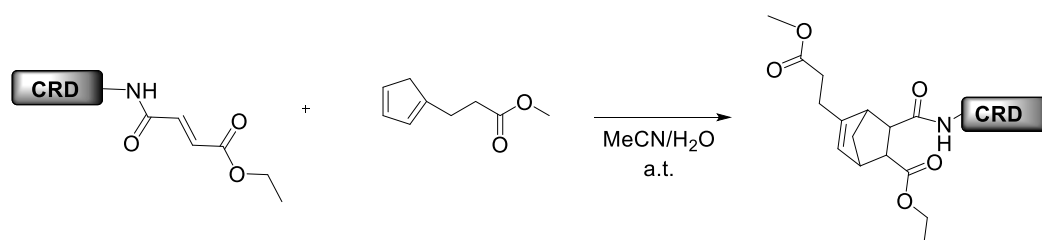


Scheme 7-33. “Inverse” NITEC reaction of the CRD-tetrazole and diethyl fumarate.

In a preparation vial, 2 mg CRD-tetrazole (0.0009 mmol, 1 eq.) were dissolved in a mixture of deionized water and MeCN (1/1, V/V). Subsequently, 0.8 mg diethyl fumarate (0.0045 mmol, 5 eq.) were added and the reaction was irradiated for 5 h ($\lambda_{\text{max}} = 310$ nm, refer to Chapter 7.2.7). The crude mixture was subsequently analyzed *via* direct-infusion experiments at ESI-MS to prove the existence of the product.

ESI-MS: m/z $[M+Na]^+$ _{exp.}: 2397.8388, $[M+Na]^+$ _{calc.}: 2397.8257.

7.5.3.4 Thermally Induced DA Ligation of the CRD-Fumarate and Cyclopentadienyl



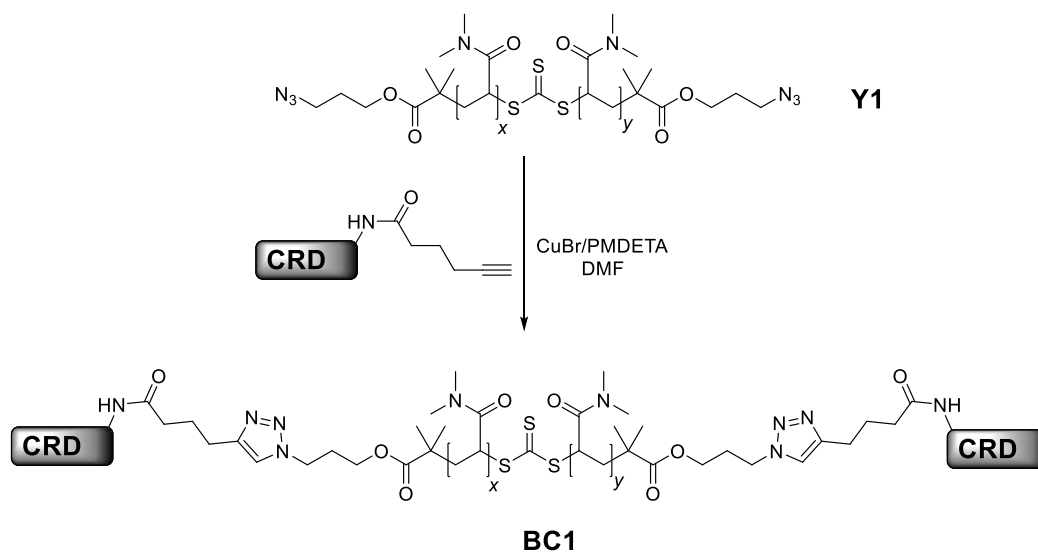
Scheme 7-34. DA reaction of the CRD-fumarate and the 3-cyclopentadienyl-methyl propionate.

In a preparation vial, 3 mg CRD-fumarate (0.0014 mmol, 1.0 eq.) was dissolved in a mixture of deionized water and MeCN (1/1, V/V). Then, a stock solution of the 3-cyclopentadienyl-methyl propionate in MeCN/H₂O (1/1, V/V) was prepared. An amount of 1.1 eq. 3-cyclopentadienyl-methyl propionate was added to the solution of the CRD-fumarate. The reaction was stirred for 24 h at ambient temperature. The crude mixture was analyzed *via* direct-infusion experiments at ESI-MS, showing incomplete conversion. Therefore, additional 1.1 eq. of the 3-cyclopentadienyl-methyl propionate was added to stir for another 24 h at ambient temperature. The crude mixture was subsequently analyzed in ESI-MS, proving the existence of the DA adduct.

ESI-MS: m/z $[M+Na]^+$ _{exp.}: 2252.8174, $[M+Na]^+$ _{calc.}: 2252.7900.

7.5.4 Polymer-Peptide Ligation Reactions

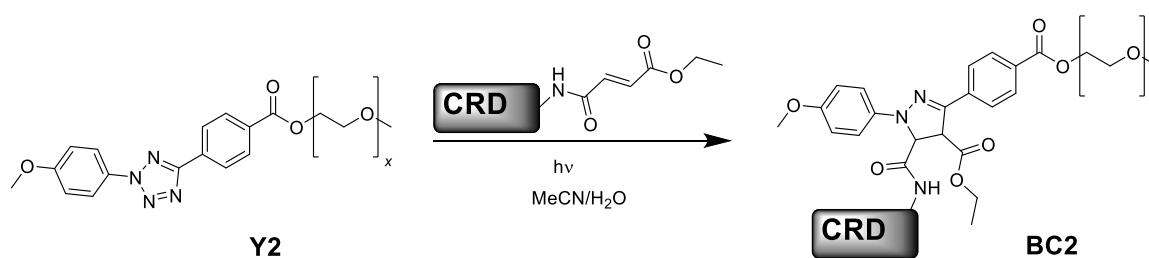
7.5.4.1 CuAAC of CRD-Alkyne and Diazido-PDMAA



Scheme 7-35. Reaction scheme of the CuAAC reaction between the diazido-PDMAA **Y1** and the CRD-alkyne, yielding the bioconjugate **BC1**.

In a 50 mL Schlenk flask, 35 mg CRD-alkyne (0.017 mmol, 4.7 eq.), 15.7 μ L PMDETA (13 mg, 0.075 mmol, 4.4 eq.) and 51 mg diazido-PDMAA (0.004 mmol, 1 eq.) were dissolved in 12 mL DMF and subsequently degassed by three consecutive freeze-pump-thaw cycles. To start the reaction, 11 mg CuBr (0.075 mmol, 4.4 eq.) was added and the reaction mixture was allowed to stir for 66 h. Afterwards, the solution was transferred into a dialysis tube (MWCO: 2 kDa) and incubated for three days, changing the dialysis bath three times. The final product was obtained by lyophilization, obtaining a greenish powder.

7.5.4.2 NITEC Bioconjugation of CRD-Fumarate and PEG-Tetrazole



Scheme 7-36. NITEC reaction between a tetrazole-PEG **Y2** and the CRD-fumarate upon UV irradiation, yielding the bioconjugate **BC2**.

Approach without base

In a head space vial, 2 mg CRD-fumarate (0.90 μmol , 1 eq.) and 0.51 mg tetrazole endcapped polyethylene glycol (Tet-PEG, 0.90 μmol , 1 eq.) were dissolved in 250 μL acetonitrile and 2.25 mL water. The reaction mixture was irradiated with UV light for 2 h ($\lambda_{\text{max}} = 310 \text{ nm}$, refer to Chapter 7.2.7). After the reaction, the crude mixture was directly analyzed *via* ESI-MS with further dilution (refer to Figure 5-7B, Chapter 5.2.6.2).

Approach with additional inorganic base to increase solubility

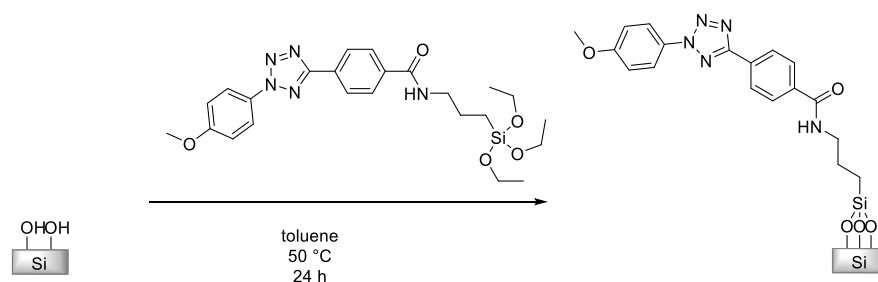
In a head space vial, 0.5 mg CRD-fumarate (0.22 μmol , 1 eq.), 0.49 mg Tet-PEG (0.22 μmol , 1 eq.) and 200 μL of 0.01 M NaOH in water were dissolved in 400 μL deionized water. The reaction mixture was irradiated with UV light for 2 h ($\lambda_{\text{max}} = 310 \text{ nm}$, refer to Chapter 7.2.7). After the reaction, the crude mixture was subsequently analyzed *via* ESI-MS with further dilution (refer to Figure 5-7B, Chapter 5.2.6.2).

Approach with additional base to increase solubility

In a head space vial, 0.66 mg CRD-fumarate (0.29 μmol , 1.00 eq.), 0.51 mg tetrazole endcapped polyethylene glycol (Tet-PEG, 0.21 μmol , 0.75 eq.) and 5 μL DIPEA (29.00 μmol , 65.00 eq.) were dissolved in 450 μL acetonitrile and 50 μL water. The reaction mixture was irradiated with UV light for 1 h ($\lambda_{\text{max}} = 310 \text{ nm}$, refer to Chapter 7.2.7). After the reaction, the crude mixture was subsequently analyzed *via* ESI-MS with further dilution (refer to Figure 5-7B, Chapter 5.2.6.2).

7.6 Preparation and Functionalization of Surfaces

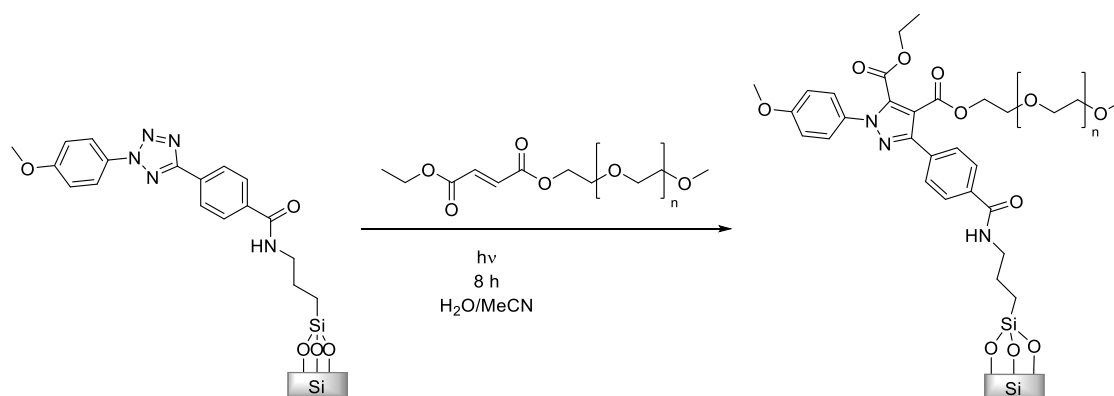
7.6.1.1 Silanization of Silicon wafers with Tetrazole-Silane



Scheme 7-37. Functionalization with tetrazole groups of the silicon wafer by silanization.

Adapted from literature procedure,²⁵⁷ a silicon wafer was cut into pieces of 1×1 cm² and cleaned by rinsing with organic solvents and water. In order to activate the silicon surface, the wafer was transferred into a plasma oven (air) and kept there at the maximum power level for at least 30 min. Meanwhile, a solution of the tetrazole-silane in toluene at a concentration of 2 g·L⁻¹ was prepared in a headspace vial. After the wafer has been exposed to the plasma, it was transferred immediately into the headspace vial. The headspace vial was sealed and put into an incubator, shaking the vial for 24 h at 50 °C under light exclusion. The next day, the surface was rinsed with toluene, DCM and ethanol and finally dried under a nitrogen stream.

7.6.1.2 Immobilization of Polyethylene Glycol onto the Surface

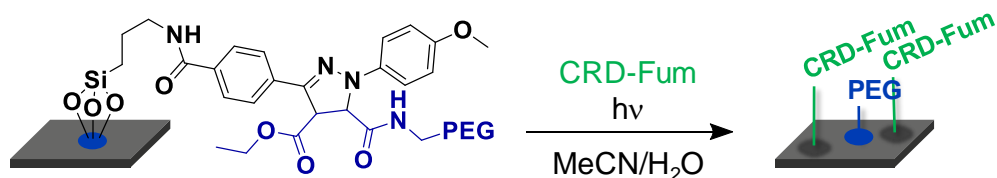


Scheme 7-38. Immobilization of PEG-fumarate onto the tetrazole functionalized surface.

The immobilization of the PEG was performed using a dotted photomask. First, the silicon wafer was mounted to a special sample holder, employing on top of the wafer the photomask (refer to Chapter 7.2.8). A solution of PEG-fumarate was prepared with a concentration of 1 g·L⁻¹. The surface, mounted in the sample holder, was immersed in the

solution and irradiated with UV light for 8 h ($\lambda_{\max} = 310$ nm). Subsequently, the surface was withdrawn from the sample holder, rinsed with DCM, ethanol, and Millipore water and dried under a nitrogen stream.

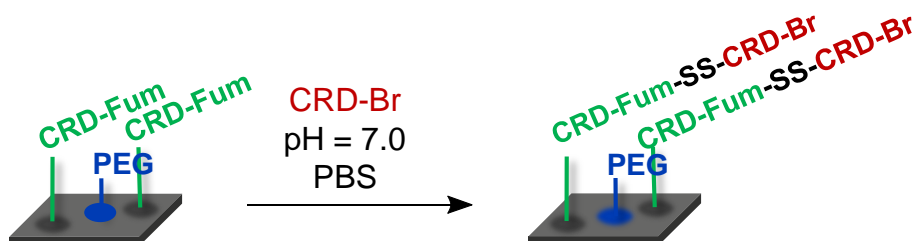
7.6.1.3 Immobilization of CRD-Fumarate onto the Surface



Scheme 7-39. Attachment of CRD-fumarate onto the surface *via* NITEC upon irradiation.

In order to covalently link the CRD-fumarate to the surface, a solution of CRD-fumarate with a concentration of $1 \text{ g}\cdot\text{L}^{-1}$ in Millipore water/acetonitrile (1/1, V/V) was prepared. The surface was then immersed into the solution and irradiated with UV light for 24 h. After the irradiation, the surface was cleaned with Millipore water, 0.1 M NaOH solution, and ethanol. Finally, the surface was dried under a nitrogen stream.

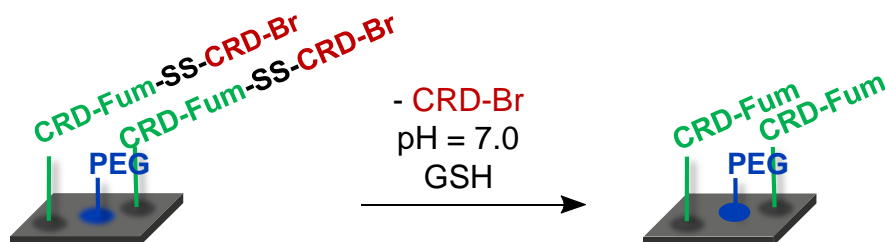
7.6.1.4 Encoding the Surface *via* CRD-CRD Dimerization



Scheme 7-40. Attachment of CRD-bromide onto the CRD-covered area *via* reoxidative conditions.

The immobilization of the CRD-bromide onto the surface was carried out in two subsequent steps. First, a solution of the CRD-bromide was prepared at a concentration of $0.25 \text{ g}\cdot\text{L}^{-1}$ in 10 mM PBS at pH = 7. Additionally, the surface was transferred into 1 mL of a 10 mM PBS solution at pH = 7. Both solutions were percolated with nitrogen and incubated for 2 h. After 2 h, the silicon wafer with the CRD-fumarate was transferred into the CRD-bromide solution and incubated for 6 h at ambient temperature. Afterwards, the surface was rinsed off with Millipore water, 0.1 M NaOH, and ethanol. Finally, the surface was dried under a nitrogen stream.

7.6.1.5 Erasing of the CRD-Bromide from the Surface



Scheme 7-41. Erasing of the CRD-bromide from the surface.

In order to remove the immobilized CRD-bromide from the surface, the surface was transferred into a 10 mM PBS solution at pH = 7 containing 2.5 M GSH. The surface was shaken in an incubator for 10 min, rinsed with Millipore water and 0.1 M NaOH and transferred to a fresh 10 mM PBS solution, containing 2.5 M GSH. This step was repeated five times to finally rinse the surface with Millipore water, 0.1 M NaOH, and ethanol. Finally, the surface was stored in 10 mM PBS solution overnight in order to reoxidize the disulfide bonds of the CRD immobilized to the surface. Afterwards, the surface was rinsed with Millipore water and ethanol to finally dry the surface under a nitrogen stream.

8

8 APPENDIX

8.1 Step-Growth by Photo-Induced DA Reactions and Subsequent RAFT Polymerization: Synthesis of Segmented Copolymers^E

8.1.1 Tables of Reactions identified for SG and RAFT Polymerization

8.1.1.1 Reaction Scheme of the Step-Growth Polymerization

Table 8-1. Reactions considered for simulations of the SG polymerization.

#	Reaction	$k / \text{L}\cdot\text{mol}^{-1}\cdot\text{s}^{-1}$
1	$AA \xrightarrow{2k_{act}} AA^*$	$2.08 \cdot 10^{-2}$
2	$AA^* \xrightarrow{k_{deact}} AA$	3.0
3	$AA^* \xrightarrow{k_{act}} A^*A^*$	
4	$A^*A^* \xrightarrow{2k_{deact}} AA^*$	
5	$AA^* + BB \xrightarrow{2k_{main}} D_{AA, BB;4}$	1.6
6	$A^*A^* + BB \xrightarrow{4k_{main}} D_{AA^*, BB;4}$	

^E Parts of this chapter were reproduced from with permission from American Chemical Society. L. De Keer conducted the *in silico* calculations and contributed equally in the project. P. H. M. Van Steenberge, M.-F. Reyniers and D. R. D'hooge supervised the *in silico* investigations and participated in the scientific discussions. J. O. Mueller participated in the scientific discussions and J.P. Menzel contributed with the concentration profile in photo-induced reactions. A. S. Goldmann, and C. Barner-Kowollik supervised the experimental part as well as the entire project.

Table continued from previous page

7	$D_{AA,AA;i} \xrightarrow{2k_{act}} D_{AA,AA^*;i}$	
8	$D_{AA,AA^*;i} \xrightarrow{k_{deact}} D_{AA,AA;i}$	
9	$D_{AA,AA^*;i} \xrightarrow{k_{act}} D_{AA^*,AA^*;i}$	
10	$D_{AA^*,AA^*;i} \xrightarrow{2k_{deact}} D_{AA,AA^*;i}$	
11	$D_{AA,BB;i} \xrightarrow{k_{act}} D_{AA^*,BB;i}$	
12	$D_{AA^*,BB;i} \xrightarrow{k_{deact}} D_{AA,BB;i}$	
13	$AA^* + D_{AA,BB;i} \xrightarrow{k_{main}} D_{AA,AA;i+2}$	
14	$AA^* + D_{AA^*,BB;i} \xrightarrow{k_{main}} D_{AA,AA^*;i+2}$	
15	$AA^* + D_{BB,BB;i} \xrightarrow{2k_{main}} D_{AA,BB;i+2}$	
16	$A^*A^* + D_{AA,BB;i} \xrightarrow{2k_{main}} D_{AA,AA^*;i+2}$	
17	$A^*A^* + D_{AA^*,BB;i} \xrightarrow{2k_{main}} D_{AA^*,AA^*;i+2}$	
18	$A^*A^* + D_{BB,BB;i} \xrightarrow{4k_{main}} D_{AA^*,BB;i+2}$	
19	$BB + D_{AA,AA^*;i} \xrightarrow{2k_{main}} D_{AA,BB;i+2}$	
20	$BB + D_{AA^*,AA^*;i} \xrightarrow{4k_{main}} D_{AA^*,BB;i+2}$	
21	$BB + D_{AA^*,BB;i} \xrightarrow{2k_{main}} D_{BB,BB;i+2}$	
22	$D_{AA,AA^*;i} + D_{AA,BB;j} \xrightarrow{k_{main}} D_{AA,AA;i+j}$	
23	$D_{AA,AA^*;i} + D_{AA^*,BB;j} \xrightarrow{k_{main}} D_{AA,AA^*;i+j}$	
24	$D_{AA,AA^*;i} + D_{BB,BB;j} \xrightarrow{2k_{main}} D_{AA,BB;i+j}$	
25	$D_{AA^*,AA^*;i} + D_{AA,BB;j} \xrightarrow{2k_{main}} D_{AA,AA^*;i+j}$	
26	$D_{AA^*,AA^*;i} + D_{AA^*,BB;j} \xrightarrow{2k_{main}} D_{AA^*,AA^*;i+j}$	
27	$D_{AA^*,AA^*;i} + D_{BB,BB;j} \xrightarrow{4k_{main}} D_{AA^*,BB;i+j}$	
28	$D_{BB,BB;i} + D_{AA^*,BB;j} \xrightarrow{2k_{main}} D_{BB,BB;i+j}$	
29	$D_{AA^*,BB;i} + D_{AA^*,BB;j} \xrightarrow{2k_{main}} D_{AA^*,BB;i+j}$	
30	$D_{AA,BB;i} + D_{AA^*,BB;j} \xrightarrow{k_{main}} D_{AA,BB;i+j}$	
31	$AA^* + AA \xrightarrow{2k_{selfAA}} D_{AA,AA;4}^H$	0.2
32	$D_{AA,AA;i}^H \xrightarrow{2k_{act}} D_{AA,AA^*;i}^H$	

Table continued from previous page

33	$D_{AA,AA^*;i}^H \xrightarrow{k_{deact}} D_{AA,AA;i}^H$
34	$D_{AA,AA;i}^H + AA^* \xrightarrow{2k_{selfAA}} D_{AA,AA;i+2}^H$
35	$D_{AA,AA^*;i}^H + AA \xrightarrow{2k_{selfAA}} D_{AA,AA;i+2}^H$
36	$D_{AA,AA;i}^H + D_{AA,AA^*;j}^H \xrightarrow{2k_{selfAA}} D_{AA,AA;i+j}^H$
37	$D_{AA,AA^*;i}^H + D_{AA,AA^*;j}^H \xrightarrow{2k_{selfAA}} D_{AA,AA^*;i+j}^H$
38	$D_{AA,AA^*;i}^H + BB \xrightarrow{2k_{main}} D_{AA,BB;i+2}$
39	$AA^* + D_{AA,BB;i} \xrightarrow{k_{selfAA}} D_{AA,BB;i+1}$
40	$AA^* + D_{AA,AA;i} \xrightarrow{2k_{selfAA}} D_{AA,AA;i+2}$
41	$AA + D_{AA^*,BB;i} \xrightarrow{2k_{selfAA}} D_{AA,BB;i+2}$
42	$AA + D_{AA,AA^*;i} \xrightarrow{2k_{selfAA}} D_{AA,AA;i+2}$
43	$D_{AA,BB;i} + D_{AA^*,BB;j} \xrightarrow{k_{selfAA}} D_{BB,BB;i+j}$
44	$D_{AA,BB;i} + D_{AA,AA^*;j} \xrightarrow{k_{selfAA}} D_{AA,BB;i+j}$
45	$D_{AA,BB;i} + D_{AA,AA^*;j}^H \xrightarrow{k_{selfAA}} D_{AA,BB;i+j}$
46	$D_{AA^*,BB;i} + D_{AA,AA;j} \xrightarrow{2k_{selfAA}} D_{AA,BB;i+j}$
47	$D_{AA^*,BB;i} + D_{AA,AA^*;j} \xrightarrow{k_{selfAA}} D_{AA^*,BB;i+j}$
48	$D_{AA^*,BB;i} + D_{AA,AA;j}^H \xrightarrow{2k_{selfAA}} D_{AA,BB;i+j}$
49	$D_{AA^*,BB;i} + D_{AA,AA^*;j}^H \xrightarrow{k_{selfAA}} D_{AA^*,BB;i+j}$
50	$D_{AA,AA;i} + D_{AA,AA^*;j} \xrightarrow{2k_{selfAA}} D_{AA,AA;i+j}$
51	$D_{AA,AA;i} + D_{AA,AA^*;j}^H \xrightarrow{2k_{selfAA}} D_{AA,AA;i+j}$
52	$D_{AA,AA^*;i} + D_{AA,AA;j}^H \xrightarrow{2k_{selfAA}} D_{AA,AA;i+j}$
53	$D_{AA,AA^*;i} + D_{AA,AA^*;j}^H \xrightarrow{2k_{selfAA}} D_{AA,AA^*;i+j}$
54	$D_{BB,BB;i} + D_{AA,AA^*;j} \xrightarrow{2k_{main}} D_{AA,BB;i+j}$

8.1.1.2 Reaction Scheme of the RAFT Polymerization

Table 8-2. Reactions considered for simulations of the RAFT polymerization (kinetic parameters are given in Table 8-4).

#	Reaction
1	$I_2 \xrightarrow{f, k_{dis}} 2R_0$
2	$R_0 + M \xrightarrow{k_{p1}} R_{R_0;1}$
3	$R_{R_0;i} + M \xrightarrow{k_p} R_{R_0;i+1}$
4	$R_{R_0;i} + R_{R_0;j} \xrightarrow{k_t} P_{R_0;i+j}$
5	$R_{M,AA;i,X} + C \xrightarrow{k_{p,RM,AA}} R_{M,AA;i+1,X}$
6	$R_{M,BB;i,X} + C \xrightarrow{k_{p,RM,BB}} R_{M,BB;i+1,X}$
7	$R_{M,R_0;i,X} + C \xrightarrow{k_{p,RM,R_0}} R_{M,R_0;i+1,X}$
8	$R_{mM,AA;i,X} + C \xrightarrow{k_{p,RmM,AA}} R_{mM,AA;i+1,X}$
9	$R_{mM,BB;i,X} + C \xrightarrow{k_{p,RmM,AA}} R_{mM,BB;i+1,X}$
10	$R_{mM,R_0;i,X} + C \xrightarrow{k_{p,RmM,R_0}} R_{mM,R_0;i+1,X}$
11	$R_{M,AA;i,X_1} + R_{M,AA;j,X_2} \xrightarrow{k_{t,RM,AA,RM,AA}} D_{mAA,AA;i+j,X_1+X_2}$
12	$R_{M,AA;i,X_1} + R_{M,BB;j,X_2} \xrightarrow{k_{t,RM,AA,RM,BB}} D_{mAA,BB;i+j,X_1+X_2}$
13	$R_{M,AA;i,X_1} + R_{M,R_0;j,X_2} \xrightarrow{k_{t,RM,AA,RM,R_0}} D_{mAA,R_0;i+j,X_1+X_2}$
14	$R_{M,AA;i,X_1} + R_{mM,AA;j,X_2} \xrightarrow{k_{t,RM,AA,RmM,AA}} D_{mAA,AA;i+j,X_1+X_2}$
15	$R_{M,AA;i,X_1} + R_{mM,BB;j,X_2} \xrightarrow{k_{t,RM,AA,RmM,BB}} D_{mAA,BB;i+j,X_1+X_2}$
16	$R_{M,AA;i,X_1} + R_{mM,R_0;j,X_2} \xrightarrow{k_{t,RM,AA,RmM,R_0}} D_{mAA,R_0;i+j,X_1+X_2}$
17	$R_{M,AA;i,X} + R_{R_0;j} \xrightarrow{k_{t,RM,AA,R_0}} D_{mAA,R_0;i+j,X}$
18	$R_{M,BB;i,X_1} + R_{M,BB;j,X_2} \xrightarrow{k_{t,RM,BB,RM,BB}} D_{mBB,BB;i+j,X_1+X_2}$
19	$R_{M,BB;i,X_1} + R_{M,R_0;j,X_2} \xrightarrow{k_{t,RM,BB,RM,R_0}} D_{mBB,R_0;i+j,X_1+X_2}$
20	$R_{M,BB;i,X_1} + R_{mM,AA;j,X_2} \xrightarrow{k_{t,RM,BB,RmM,AA}} D_{mAA,BB;i+j,X_1+X_2}$
21	$R_{M,BB;i,X_1} + R_{mM,BB;j,X_2} \xrightarrow{k_{t,RM,BB,RmM,BB}} D_{mBB,BB;i+j,X_1+X_2}$

Table continued from previous page

22	$R_{M,BB;i,X_1} + R_{mM,R_0;j,X_2} \xrightarrow{k_{t,RM,BB,RmM,R_0}} D_{mBB,R_0;i+j,X_1+X_2}$
23	$R_{M,BB;i,X} + R_{R_0;j} \xrightarrow{k_{t,RM,BB,R_0}} D_{mBB,R_0;i+j,X}$
24	$R_{M,R_0;i,X_1} + R_{M,R_0;j,X_2} \xrightarrow{k_{t,RM,R_0,RM,R_0}} D_{mR_0,R_0;i+j,X_1+X_2}$
25	$R_{M,R_0;i,X_1} + R_{mM,AA;j,X_2} \xrightarrow{k_{t,RM,R_0,RmM,AA}} D_{mAA,R_0;i+j,X_1+X_2}$
26	$R_{M,R_0;i,X_1} + R_{mM,BB;j,X_2} \xrightarrow{k_{t,RM,R_0,RmM,BB}} D_{mBB,R_0;i+j,X_1+X_2}$
27	$R_{M,R_0;i,X_1} + R_{mM,R_0;j,X_2} \xrightarrow{k_{t,RM,R_0,RmM,R_0}} D_{mR_0,R_0;i+j,X_1+X_2}$
28	$R_{M,R_0;i,X} + R_{R_0;j} \xrightarrow{k_{t,RM,R_0,R_0}} D_{mR_0,R_0;i+j,X}$
29	$R_{mM,AA;i,X_1} + R_{mM,AA;j,X_2} \xrightarrow{k_{t,RmM,AA,RmM,AA}} D_{mAA,AA;i+j,X_1+X_2}$
30	$R_{mM,AA;i,X_1} + R_{mM,BB;j,X_2} \xrightarrow{k_{t,RmM,AA,RmM,BB}} D_{mAA,BB;i+j,X_1+X_2}$
31	$R_{mM,AA;i,X_1} + R_{mM,R_0;j,X_2} \xrightarrow{k_{t,RmM,AA,RmM,R_0}} D_{mAA,R_0;i+j,X_1+X_2}$
32	$R_{mM,AA;i,X} + R_{R_0;j} \xrightarrow{k_{t,RmM,AA,R_0}} D_{mAA,R_0;i+j,X}$
33	$R_{mM,BB;i,X_1} + R_{mM,BB;j,X_2} \xrightarrow{k_{t,RmM,BB,RmM,BB}} D_{mBB,BB;i+j,X_1+X_2}$
34	$R_{mM,BB;i,X_1} + R_{mM,R_0;j,X_2} \xrightarrow{k_{t,RmM,BB,RmM,R_0}} D_{mBB,R_0;i+j,X_1+X_2}$
35	$R_{mM,BB;i,X} + R_{R_0;j} \xrightarrow{k_{t,RmM,BB,R_0}} D_{mBB,R_0;i+j,X}$
36	$R_{mM,R_0;i,X_1} + R_{mM,R_0;j,X_2} \xrightarrow{k_{t,RmM,R_0,RmM,R_0}} D_{mR_0,R_0;i+j,X_1+X_2}$
37	$R_{mM,R_0;i,X} + R_{R_0;j} \xrightarrow{k_{t,RmM,R_0,R_0}} D_{mR_0,R_0;i+j,X}$
38	$D_{AA,AA;i,X_1} + R_{R_0;j} \xrightarrow{k_{trDAA,AA,R_0}} D_{AA,R_0;i+j-l,X_1-X_2} + R_{M,AA;l,X_2}$
39	$D_{AA,AA;i,X_1} + R_{R_0;j} \xrightarrow{k_{trDAA,AA,R_0}} D_{AA,R_0;i+j-l,X_1-X_2} + R_{M,AA;l,X_2}$
40	$D_{AA,AA;i,X_1} + R_{M,AA;j,X_2} \xrightarrow{k_{trDAA,AA,RM,AA}} D_{mAA,AA;i+j-l,X_1+X_2-X_3} + R_{M,AA;l,X_3}$
41	$D_{AA,AA;i,X_1} + R_{M,AA;j,X_2} \xrightarrow{k_{trDAA,AA,RM,AA}} D_{mAA,AA;i+j-l,X_1+X_2-X_3} + R_{M,AA;l,X_3}$
42	$D_{AA,AA;i,X_1} + R_{M,BB;j,X_2} \xrightarrow{k_{trDAA,AA,RM,BB}} D_{mAA,BB;i+j-l,X_1+X_2-X_3} + R_{M,AA;l,X_3}$
43	$D_{AA,AA;i,X_1} + R_{M,BB;j,X_2} \xrightarrow{k_{trDAA,AA,RM,BB}} D_{mAA,BB;i+j-l,X_1+X_2-X_3} + R_{M,AA;l,X_3}$
44	$D_{AA,AA;i,X_1} + R_{M,R_0;j,X_2} \xrightarrow{k_{trDAA,AA,RM,R_0}} D_{mAA,R_0;i+j-l,X_1+X_2-X_3} + R_{M,AA;l,X_3}$

Table continued from previous page

45	$D_{AA,AA;i,X_1} + R_{M,R_0;j,X_2} \xrightarrow{k_{trD_{AA,AA}R_{M,R_0}}} D_{mAA,R_0;i+j-l,X_1+X_2-X_3} + R_{M,AA;l,X_3}$
46	$D_{AA,AA;i,X_1} + R_{mM,AA;j,X_2} \xrightarrow{k_{trD_{AA,AA}R_{mM,AA}}} D_{mAA,AA;i+j-l,X_1+X_2-X_3} + R_{M,AA;l,X_3}$
47	$D_{AA,AA;i,X_1} + R_{mM,AA;j,X_2} \xrightarrow{k_{trD_{AA,AA}R_{mM,AA}}} D_{mAA,AA;i+j-l,X_1+X_2-X_3} + R_{M,AA;l,X_3}$
48	$D_{AA,AA;i,X_1} + R_{mM,BB;j,X_2} \xrightarrow{k_{trD_{AA,AA}R_{mM,BB}}} D_{mAA,BB;i+j-l,X_1+X_2-X_3} + R_{M,AA;l,X_3}$
49	$D_{AA,AA;i,X_1} + R_{mM,BB;j,X_2} \xrightarrow{k_{trD_{AA,AA}R_{mM,BB}}} D_{mAA,BB;i+j-l,X_1+X_2-X_3} + R_{M,AA;l,X_3}$
50	$D_{AA,AA;i,X_1} + R_{mM,R_0;j,X_2} \xrightarrow{k_{trD_{AA,AA}R_{mM,R_0}}} D_{mAA,R_0;i+j-l,X_1+X_2-X_3} + R_{M,AA;l,X_3}$
51	$D_{AA,AA;i,X_1} + R_{mM,R_0;j,X_2} \xrightarrow{k_{trD_{AA,AA}R_{mM,R_0}}} D_{mAA,R_0;i+j-l,X_1+X_2-X_3} + R_{M,AA;l,X_3}$
52	$D_{AA,BB;i,X_1} + R_{R_0;j} \xrightarrow{k_{trD_{AA,BB}R_{R_0}}} D_{BB,R_0;i+j-l,X_1-X_2} + R_{M,AA;l,X_2}$
53	$D_{AA,BB;i,X_1} + R_{R_0;j} \xrightarrow{k_{trD_{AA,BB}R_{R_0}}} D_{AA,R_0;i+j-l,X_1-X_2} + R_{M,BB;l,X_2}$
54	$D_{AA,BB;i,X_1} + R_{M,AA;j,X_2} \xrightarrow{k_{trD_{AA,BB}R_{M,AA}}} D_{mAA,BB;i+j-l,X_1+X_2-X_3} + R_{M,AA;l,X_3}$
55	$D_{AA,BB;i,X_1} + R_{M,AA;j,X_2} \xrightarrow{k_{trD_{AA,BB}R_{M,AA}}} D_{mAA,AA;i+j-l,X_1+X_2-X_3} + R_{M,BB;l,X_3}$
56	$D_{AA,BB;i,X_1} + R_{M,BB;j,X_2} \xrightarrow{k_{trD_{AA,BB}R_{M,BB}}} D_{mBB,BB;i+j-l,X_1+X_2-X_3} + R_{M,AA;l,X_3}$
57	$D_{AA,BB;i,X_1} + R_{M,BB;j,X_2} \xrightarrow{k_{trD_{AA,BB}R_{M,BB}}} D_{mAA,BB;i+j-l,X_1+X_2-X_3} + R_{M,BB;l,X_3}$
58	$D_{AA,BB;i,X_1} + R_{M,R_0;j,X_2} \xrightarrow{k_{trD_{AA,BB}R_{M,R_0}}} D_{mBB,R_0;i+j-l,X_1+X_2-X_3} + R_{M,AA;l,X_3}$
59	$D_{AA,BB;i,X_1} + R_{M,R_0;j,X_2} \xrightarrow{k_{trD_{AA,BB}R_{M,R_0}}} D_{mAA,R_0;i+j-l,X_1+X_2-X_3} + R_{M,BB;l,X_3}$
60	$D_{AA,BB;i,X_1} + R_{mM,AA;j,X_2} \xrightarrow{k_{trD_{AA,BB}R_{mM,AA}}} D_{mAA,BB;i+j-l,X_1+X_2-X_3} + R_{M,AA;l,X_3}$
61	$D_{AA,BB;i,X_1} + R_{mM,AA;j,X_2} \xrightarrow{k_{trD_{AA,BB}R_{mM,AA}}} D_{mAA,AA;i+j-l,X_1+X_2-X_3} + R_{M,BB;l,X_3}$
62	$D_{AA,BB;i,X_1} + R_{mM,BB;j,X_2} \xrightarrow{k_{trD_{AA,BB}R_{mM,BB}}} D_{mBB,BB;i+j-l,X_1+X_2-X_3} + R_{M,AA;l,X_3}$
63	$D_{AA,BB;i,X_1} + R_{mM,BB;j,X_2} \xrightarrow{k_{trD_{AA,BB}R_{mM,BB}}} D_{mAA,BB;i+j-l,X_1+X_2-X_3} + R_{M,BB;l,X_3}$
64	$D_{AA,BB;i,X_1} + R_{mM,R_0;j,X_2} \xrightarrow{k_{trD_{AA,BB}R_{mM,R_0}}} D_{mBB,R_0;i+j-l,X_1+X_2-X_3} + R_{M,AA;l,X_3}$
65	$D_{AA,BB;i,X_1} + R_{mM,R_0;j,X_2} \xrightarrow{k_{trD_{AA,BB}R_{mM,R_0}}} D_{mAA,R_0;i+j-l,X_1+X_2-X_3} + R_{M,BB;l,X_3}$
66	$D_{BB,BB;i,X_1} + R_{R_0;j} \xrightarrow{k_{trD_{BB,BB}R_{R_0}}} D_{BB,R_0;i+j-l,X_1-X_2} + R_{M,BB;l,X_2}$
67	$D_{BB,BB;i,X_1} + R_{R_0;j} \xrightarrow{k_{trD_{BB,BB}R_{R_0}}} D_{BB,R_0;i+j-l,X_1-X_2} + R_{M,BB;l,X_2}$
68	$D_{BB,BB;i,X_1} + R_{M,AA;j,X_2} \xrightarrow{k_{trD_{BB,BB}R_{M,AA}}} D_{mAA,BB;i+j-l,X_1+X_2-X_3} + R_{M,BB;l,X_3}$

Table continued from previous page

69	$D_{BB, BB; i, X_1} + R_{M, AA; j, X_2} \xrightarrow{k_{tr} D_{BB, BB} R_{M, AA}} D_{mAA, BB; i+j-l, X_1+X_2-X_3} + R_{M, BB; l, X_3}$
70	$D_{BB, BB; i, X_1} + R_{M, BB; j, X_2} \xrightarrow{k_{tr} D_{BB, BB} R_{M, BB}} D_{mBB, BB; i+j-l, X_1+X_2-X_3} + R_{M, BB; l, X_3}$
71	$D_{BB, BB; i, X_1} + R_{M, BB; j, X_2} \xrightarrow{k_{tr} D_{BB, BB} R_{M, BB}} D_{mBB, BB; i+j-l, X_1+X_2-X_3} + R_{M, BB; l, X_3}$
72	$D_{BB, BB; i, X_1} + R_{M, R_0; j, X_2} \xrightarrow{k_{tr} D_{BB, BB} R_{M, R_0}} D_{mBB, R_0; i+j-l, X_1+X_2-X_3} + R_{M, BB; l, X_3}$
73	$D_{BB, BB; i, X_1} + R_{M, R_0; j, X_2} \xrightarrow{k_{tr} D_{BB, BB} R_{M, R_0}} D_{mBB, R_0; i+j-l, X_1+X_2-X_3} + R_{M, BB; l, X_3}$
74	$D_{BB, BB; i, X_1} + R_{mM, AA; j, X_2} \xrightarrow{k_{tr} D_{BB, BB} R_{mM, AA}} D_{mAA, BB; i+j-l, X_1+X_2-X_3} + R_{M, BB; l, X_3}$
75	$D_{BB, BB; i, X_1} + R_{mM, AA; j, X_2} \xrightarrow{k_{tr} D_{BB, BB} R_{mM, AA}} D_{mAA, BB; i+j-l, X_1+X_2-X_3} + R_{M, BB; l, X_3}$
76	$D_{BB, BB; i, X_1} + R_{mM, BB; j, X_2} \xrightarrow{k_{tr} D_{BB, BB} R_{mM, BB}} D_{mBB, BB; i+j-l, X_1+X_2-X_3} + R_{M, BB; l, X_3}$
77	$D_{BB, BB; i, X_1} + R_{mM, BB; j, X_2} \xrightarrow{k_{tr} D_{BB, BB} R_{mM, BB}} D_{mBB, BB; i+j-l, X_1+X_2-X_3} + R_{M, BB; l, X_3}$
78	$D_{BB, BB; i, X_1} + R_{mM, R_0; j, X_2} \xrightarrow{k_{tr} D_{BB, BB} R_{mM, R_0}} D_{mBB, R_0; i+j-l, X_1+X_2-X_3} + R_{M, BB; l, X_3}$
79	$D_{BB, BB; i, X_1} + R_{mM, R_0; j, X_2} \xrightarrow{k_{tr} D_{BB, BB} R_{mM, R_0}} D_{mBB, R_0; i+j-l, X_1+X_2-X_3} + R_{M, BB; l, X_3}$
80	$D_{AA, R_0; i, X} + R_{R_0; j} \xrightarrow{k_{tr} D_{AA, R_0} R_{R_0}} D_{R_0, R_0; i+j-l, X-X_1} + R_{M, AA; l, X_1}$
81(*)	$D_{AA, R_0; i, X} + R_{R_0; j} \xrightarrow{k_{tr} D_{AA, R_0} R_{R_0}} D_{AA, R_0; i+j-l, X(-X_1)} + R_{R_0; l} / R_{M, R_0; l, X_1}$
82	$D_{AA, R_0; i, X_1} + R_{M, AA; j, X_2} \xrightarrow{k_{tr} D_{AA, R_0} R_{M, AA}} D_{mAA, R_0; i+j-l, X_1+X_2-X_3} + R_{M, AA; l, X_3}$
83	$D_{AA, R_0; i, X_1} + R_{M, AA; j, X_2} \xrightarrow{k_{tr} D_{AA, R_0} R_{M, AA}} D_{mAA, AA; i+j-l, X_1+X_2-(X_3)} + R_{R_0; l} / R_{M, R_0; l, X_3}$
84	$D_{AA, R_0; i, X_1} + R_{M, BB; j, X_2} \xrightarrow{k_{tr} D_{AA, R_0} R_{M, BB}} D_{mBB, R_0; i+j-l, X_1+X_2-X_3} + R_{M, AA; l, X_3}$
85	$D_{AA, R_0; i, X_1} + R_{M, BB; j, X_2} \xrightarrow{k_{tr} D_{AA, R_0} R_{M, BB}} D_{mAA, BB; i+j-l, X_1+X_2-(X_3)} + R_{R_0; l} / R_{M, R_0; l, X_3}$
86	$D_{AA, R_0; i, X_1} + R_{M, R_0; j, X_2} \xrightarrow{k_{tr} D_{AA, R_0} R_{M, R_0}} D_{mR_0, R_0; i+j-l, X_1+X_2-X_3} + R_{M, AA; l, X_3}$
87	$D_{AA, R_0; i, X_1} + R_{M, R_0; j, X_2} \xrightarrow{k_{tr} D_{AA, R_0} R_{M, R_0}} D_{mAA, R_0; i+j-l, X_1+X_2(-X_3)} + R_{R_0; l} / R_{M, R_0; l, X_3}$
88	$D_{AA, R_0; i, X_1} + R_{mM, AA; j, X_2} \xrightarrow{k_{tr} D_{AA, R_0} R_{mM, AA}} D_{mAA, R_0; i+j-l, X_1+X_2-X_3} + R_{M, AA; l, X_3}$
89	$D_{AA, R_0; i, X_1} + R_{mM, AA; j, X_2} \xrightarrow{k_{tr} D_{AA, R_0} R_{mM, AA}} D_{mAA, AA; i+j-l, X_1+X_2-(X_3)} + R_{R_0; l} / R_{M, R_0; l, X_3}$
90	$D_{AA, R_0; i, X_1} + R_{mM, BB; j, X_2} \xrightarrow{k_{tr} D_{AA, R_0} R_{mM, BB}} D_{mBB, R_0; i+j-l, X_1+X_2-X_3} + R_{M, AA; l, X_3}$
91	$D_{AA, R_0; i, X_1} + R_{mM, BB; j, X_2} \xrightarrow{k_{tr} D_{AA, R_0} R_{mM, BB}} D_{mAA, BB; i+j-l, X_1+X_2-(X_3)} + R_{R_0; l} / R_{M, R_0; l, X_3}$

Table continued from previous page

92	$D_{AA,R_0;i,X_1} + R_{mM,R_0;j,X_2} \xrightarrow{k_{trD_{AA,R_0}R_{mM,R_0}}} D_{mR_0,R_0;i+j-l,X_1+X_2-X_3} + R_{M,AA;l,X_3}$
93	$D_{AA,R_0;i,X_1} + R_{mM,R_0;j,X_2} \xrightarrow{k_{trD_{AA,R_0}R_{mM,R_0}}} D_{mAA,R_0;i+j-l,X_1+X_2(-X_3)} + R_{R_0;l}/R_{M,R_0;l,X_3}$
94	$D_{BB,R_0;i,X} + R_{R_0;j} \xrightarrow{k_{trD_{BB,R_0}R_{R_0}}} D_{R_0,R_0;i+j-l,X-X_1} + R_{M,BB;l,X_1}$
95	$D_{BB,R_0;i,X} + R_{R_0;j} \xrightarrow{k_{trD_{BB,R_0}R_{R_0}}} D_{BB,R_0;i+j-l,X(-X_1)} + R_{R_0;l}/R_{M,R_0;l,X_1}$
96	$D_{BB,R_0;i,X_1} + R_{M,AA;j,X_2} \xrightarrow{k_{trD_{BB,R_0}R_{M,AA}}} D_{mAA,R_0;i+j-l,X_1+X_2-X_3} + R_{M,BB;l,X_3}$
97	$D_{BB,R_0;i,X_1} + R_{M,AA;j,X_2} \xrightarrow{k_{trD_{BB,R_0}R_{M,AA}}} D_{mAA,BB;i+j-l,X_1+X_2} + R_{R_0;l}$
98	$D_{BB,R_0;i,X_1} + R_{M,BB;j,X_2} \xrightarrow{k_{trD_{BB,R_0}R_{M,BB}}} D_{mBB,R_0;i+j-l,X_1+X_2-X_3} + R_{M,BB;l,X_3}$
99	$D_{BB,R_0;i,X_1} + R_{M,BB;j,X_2} \xrightarrow{k_{trD_{BB,R_0}R_{M,BB}}} D_{mBB,BB;i+j-l,X_1+X_2} + R_{R_0;l}$
100	$D_{BB,R_0;i,X_1} + R_{M,R_0;j,X_2} \xrightarrow{k_{trD_{BB,R_0}R_{M,R_0}}} D_{mR_0,R_0;i+j-l,X_1+X_2-X_3} + R_{M,BB;l,X_3}$
101	$D_{BB,R_0;i,X_1} + R_{M,R_0;j,X_2} \xrightarrow{k_{trD_{BB,R_0}R_{M,R_0}}} D_{mBB,R_0;i+j-l,X_1+X_2(-X_3)} + R_{M,R_0;l,X_3}/R_{R_0;l}$
102	$D_{BB,R_0;i,X_1} + R_{mM,AA;j,X_2} \xrightarrow{k_{trD_{BB,R_0}R_{mM,AA}}} D_{mAA,R_0;i+j-l,X_1+X_2-X_3} + R_{M,BB;l,X_3}$
103	$D_{BB,R_0;i,X_1} + R_{mM,AA;j,X_2} \xrightarrow{k_{trD_{BB,R_0}R_{mM,AA}}} D_{mAA,BB;i+j-l,X_1+X_2(-X_3)} + R_{M,R_0;l,X_3}/R_{R_0;l}$
104	$D_{BB,R_0;i,X_1} + R_{mM,BB;j,X_2} \xrightarrow{k_{trD_{BB,R_0}R_{mM,BB}}} D_{mBB,R_0;i+j-l,X_1+X_2-X_3} + R_{M,BB;l,X_3}$
105	$D_{BB,R_0;i,X_1} + R_{mM,BB;j,X_2} \xrightarrow{k_{trD_{BB,R_0}R_{mM,BB}}} D_{mBB,BB;i+j-l,X_1+X_2(-X_3)} + R_{M,R_0;l,X_3}/R_{R_0;l}$
106	$D_{BB,R_0;i,X_1} + R_{mM,R_0;j,X_2} \xrightarrow{k_{trD_{BB,R_0}R_{mM,R_0}}} D_{mR_0,R_0;i+j-l,X_1+X_2-X_3} + R_{M,BB;l,X_3}$
107	$D_{BB,R_0;i,X_1} + R_{mM,R_0;j,X_2} \xrightarrow{k_{trD_{BB,R_0}R_{mM,R_0}}} D_{mBB,R_0;i+j-l,X_1+X_2(-X_3)} + R_{M,R_0;l,X_3}/R_{R_0;l}$
108	$D_{mAA,AA;i,X_1} + R_{R_0;j} \xrightarrow{k_{trD_{mAA,AA}R_{R_0}}} D_{mAA,R_0;i+j-l,X_1-X_2} + R_{mM,AA;l,X_2}$
109	$D_{mAA,AA;i,X_1} + R_{R_0;j} \xrightarrow{k_{trD_{mAA,AA}R_{R_0}}} D_{mAA,R_0;i+j-l,X_1-X_2} + R_{mM,AA;l,X_2}$
110	$D_{mAA,AA;i,X_1} + R_{M,AA;j,X_2} \xrightarrow{k_{trD_{mAA,AA}R_{M,AA}}} D_{mAA,AA;i+j-l,X_1+X_2-X_3} + R_{mM,AA;l,X_3}$
111	$D_{mAA,AA;i,X_1} + R_{M,AA;j,X_2} \xrightarrow{k_{trD_{mAA,AA}R_{M,AA}}} D_{mAA,AA;i+j-l,X_1+X_2-X_3} + R_{mM,AA;l,X_3}$
112	$D_{mAA,AA;i,X_1} + R_{M,BB;j,X_2} \xrightarrow{k_{trD_{mAA,AA}R_{M,BB}}} D_{mAA,BB;i+j-l,X_1+X_2-X_3} + R_{mM,AA;l,X_3}$
113	$D_{mAA,AA;i,X_1} + R_{M,AA;j,X_2} \xrightarrow{k_{trD_{mAA,AA}R_{M,BB}}} D_{mAA,BB;i+j-l,X_1+X_2-X_3} + R_{mM,AA;l,X_3}$
114	$D_{mAA,AA;i,X_1} + R_{M,R_0;j,X_2} \xrightarrow{k_{trD_{mAA,AA}R_{M,R_0}}} D_{mAA,R_0;i+j-l,X_1+X_2-X_3} + R_{mM,AA;l,X_3}$

Table continued from previous page

115	$D_{mAA,AA;i,X_1} + R_{m,R_0;j,X_2} \xrightarrow{k_{trD_{mAA,AA}R_{m,R_0}}} D_{mAA,R_0;i+j-l,X_1+X_2-X_3} + R_{mM,AA;l,X_3}$
116	$D_{mAA,AA;i,X_1} + R_{mM,AA;j,X_2} \xrightarrow{k_{trD_{mAA,AA}R_{mM,AA}}} D_{mAA,AA;i+j-l,X_1+X_2-X_3} + R_{mM,AA;l,X_3}$
117	$D_{mAA,AA;i,X_1} + R_{mM,AA;j,X_2} \xrightarrow{k_{trD_{mAA,AA}R_{mM,AA}}} D_{mAA,AA;i+j-l,X_1+X_2-X_3} + R_{mM,AA;l,X_3}$
118	$D_{mAA,AA;i,X_1} + R_{mM,BB;j,X_2} \xrightarrow{k_{trD_{mAA,AA}R_{mM,BB}}} D_{mAA,BB;i+j-l,X_1+X_2-X_3} + R_{mM,AA;l,X_3}$
119	$D_{mAA,AA;i,X_1} + R_{mM,BB;j,X_2} \xrightarrow{k_{trD_{mAA,AA}R_{mM,BB}}} D_{mAA,BB;i+j-l,X_1+X_2-X_3} + R_{mM,AA;l,X_3}$
120	$D_{mAA,AA;i,X_1} + R_{mM,R_0;j,X_2} \xrightarrow{k_{trD_{mAA,AA}R_{mM,R_0}}} D_{mAA,R_0;i+j-l,X_1+X_2-X_3} + R_{mM,AA;l,X_3}$
121	$D_{mAA,AA;i,X_1} + R_{mM,R_0;j,X_2} \xrightarrow{k_{trD_{mAA,AA}R_{mM,R_0}}} D_{mAA,R_0;i+j-l,X_1+X_2-X_3} + R_{mM,AA;l,X_3}$
122	$D_{mAA,BB;i,X_1} + R_{R_0;j} \xrightarrow{k_{trD_{mAA,BB}R_{R_0}}} D_{mBB,R_0;i+j-l,X_1-X_2} + R_{mM,AA;l,X_2}$
123	$D_{mAA,BB;i,X_1} + R_{R_0;j} \xrightarrow{k_{trD_{mAA,BB}R_{R_0}}} D_{mAA,R_0;i+j-l,X_1-X_2} + R_{mM,BB;l,X_2}$
124	$D_{mAA,BB;i,X_1} + R_{M,AA;j,X_2} \xrightarrow{k_{trD_{mAA,BB}R_{M,AA}}} D_{mAA,BB;i+j-l,X_1+X_2-X_3} + R_{mM,AA;l,X_3}$
125	$D_{mAA,BB;i,X_1} + R_{M,AA;j,X_2} \xrightarrow{k_{trD_{mAA,BB}R_{M,AA}}} D_{mAA,AA;i+j-l,X_1+X_2-X_3} + R_{mM,BB;l,X_3}$
126	$D_{mAA,BB;i,X_1} + R_{M,BB;j,X_2} \xrightarrow{k_{trD_{mAA,BB}R_{M,BB}}} D_{mBB,BB;i+j-l,X_1+X_2-X_3} + R_{mM,AA;l,X_3}$
127	$D_{mAA,BB;i,X_1} + R_{M,BB;j,X_2} \xrightarrow{k_{trD_{mAA,BB}R_{M,BB}}} D_{mAA,BB;i+j-l,X_1+X_2-X_3} + R_{mM,BB;l,X_3}$
128	$D_{mAA,BB;i,X_1} + R_{m,R_0;j,X_2} \xrightarrow{k_{trD_{mAA,BB}R_{m,R_0}}} D_{mBB,R_0;i+j-l,X_1+X_2-X_3} + R_{mM,AA;l,X_3}$
129	$D_{mAA,BB;i,X_1} + R_{m,R_0;j,X_2} \xrightarrow{k_{trD_{mAA,BB}R_{m,R_0}}} D_{mAA,R_0;i+j-l,X_1+X_2-X_3} + R_{mM,BB;l,X_3}$
130	$D_{mAA,BB;i,X_1} + R_{mM,AA;j,X_2} \xrightarrow{k_{trD_{mAA,BB}R_{mM,AA}}} D_{mAA,BB;i+j-l,X_1+X_2-X_3} + R_{mM,AA;l,X_3}$
131	$D_{mAA,BB;i,X_1} + R_{mM,AA;j,X_2} \xrightarrow{k_{trD_{mAA,BB}R_{mM,AA}}} D_{mAA,AA;i+j-l,X_1+X_2-X_3} + R_{mM,BB;l,X_3}$
132	$D_{mAA,BB;i,X_1} + R_{mM,BB;j,X_2} \xrightarrow{k_{trD_{mAA,BB}R_{mM,BB}}} D_{mBB,BB;i+j-l,X_1+X_2-X_3} + R_{mM,AA;l,X_3}$
133	$D_{mAA,BB;i,X_1} + R_{mM,BB;j,X_2} \xrightarrow{k_{trD_{mAA,BB}R_{mM,BB}}} D_{mAA,BB;i+j-l,X_1+X_2-X_3} + R_{mM,BB;l,X_3}$
134	$D_{mAA,BB;i,X_1} + R_{mM,R_0;j,X_2} \xrightarrow{k_{trD_{mAA,BB}R_{mM,R_0}}} D_{mBB,R_0;i+j-l,X_1+X_2-X_3} + R_{mM,AA;l,X_3}$
135	$D_{mAA,BB;i,X_1} + R_{mM,R_0;j,X_2} \xrightarrow{k_{trD_{mAA,BB}R_{mM,R_0}}} D_{mAA,R_0;i+j-l,X_1+X_2-X_3} + R_{mM,BB;l,X_3}$
136	$D_{mBB,BB;i,X_1} + R_{R_0;j} \xrightarrow{k_{trD_{mBB,BB}R_{R_0}}} D_{mBB,R_0;i+j-l,X_1-X_2} + R_{mM,BB;l,X_2}$
137	$D_{mBB,BB;i,X_1} + R_{R_0;j} \xrightarrow{k_{trD_{mBB,BB}R_{R_0}}} D_{mBB,R_0;i+j-l,X_1-X_2} + R_{mM,BB;l,X_2}$
138	$D_{mBB,BB;i,X_1} + R_{M,AA;j,X_2} \xrightarrow{k_{trD_{mBB,BB}R_{M,AA}}} D_{mAA,BB;i+j-l,X_1+X_2-X_3} + R_{mM,BB;l,X_3}$

Table continued from previous page

139	$D_{mBB, BB; i, X_1} + R_{M, AA; j, X_2} \xrightarrow{k_{tr} D_{mBB, BB} R_{M, AA}} D_{mAA, BB; i+j-l, X_1+X_2-X_3} + R_{mM, BB; l, X_3}$
140	$D_{mBB, BB; i, X_1} + R_{M, BB; j, X_2} \xrightarrow{k_{tr} D_{mBB, BB} R_{M, BB}} D_{mBB, BB; i+j-l, X_1+X_2-X_3} + R_{mM, BB; l, X_3}$
141	$D_{mBB, BB; i, X_1} + R_{M, BB; j, X_2} \xrightarrow{k_{tr} D_{mBB, BB} R_{M, BB}} D_{mBB, BB; i+j-l, X_1+X_2-X_3} + R_{mM, BB; l, X_3}$
142	$D_{mBB, BB; i, X_1} + R_{M, R_0; j, X_2} \xrightarrow{k_{tr} D_{mBB, BB} R_{M, R_0}} D_{mBB, R_0; i+j-l, X_1+X_2-X_3} + R_{mM, BB; l, X_3}$
143	$D_{mBB, BB; i, X_1} + R_{M, R_0; j, X_2} \xrightarrow{k_{tr} D_{mBB, BB} R_{M, R_0}} D_{mBB, R_0; i+j-l, X_1+X_2-X_3} + R_{mM, BB; l, X_3}$
144	$D_{mBB, BB; i, X_1} + R_{mM, AA; j, X_2} \xrightarrow{k_{tr} D_{mBB, BB} R_{mM, AA}} D_{mAA, BB; i+j-l, X_1+X_2-X_3} + R_{mM, BB; l, X_3}$
145	$D_{mBB, BB; i, X_1} + R_{mM, AA; j, X_2} \xrightarrow{k_{tr} D_{mBB, BB} R_{mM, AA}} D_{mAA, BB; i+j-l, X_1+X_2-X_3} + R_{mM, BB; l, X_3}$
146	$D_{mBB, BB; i, X_1} + R_{mM, BB; j, X_2} \xrightarrow{k_{tr} D_{mBB, BB} R_{mM, BB}} D_{mBB, BB; i+j-l, X_1+X_2-X_3} + R_{mM, BB; l, X_3}$
147	$D_{mBB, BB; i, X_1} + R_{mM, BB; j, X_2} \xrightarrow{k_{tr} D_{mBB, BB} R_{mM, BB}} D_{mBB, BB; i+j-l, X_1+X_2-X_3} + R_{mM, BB; l, X_3}$
148	$D_{mBB, BB; i, X_1} + R_{mM, R_0; j, X_2} \xrightarrow{k_{tr} D_{mBB, BB} R_{mM, R_0}} D_{mBB, R_0; i+j-l, X_1+X_2-X_3} + R_{mM, BB; l, X_3}$
149	$D_{mBB, BB; i, X_1} + R_{mM, R_0; j, X_2} \xrightarrow{k_{tr} D_{mBB, BB} R_{mM, R_0}} D_{mBB, R_0; i+j-l, X_1+X_2-X_3} + R_{mM, BB; l, X_3}$
150	$D_{mAA, R_0; i, X} + R_{R_0; j} \xrightarrow{k_{tr} D_{mAA, R_0} R_{R_0}} D_{mR_0, R_0; i+j-l, X-X_1} + R_{mM, AA; l, X_1}$
151	$D_{mAA, R_0; i, X} + R_{R_0; j} \xrightarrow{k_{tr} D_{mAA, R_0} R_{R_0}} D_{mAA, R_0; i+j-l, X(-X_1)} + R_{R_0; l} / R_{mM, R_0; l, X_1}$
152	$D_{mAA, R_0; i, X_1} + R_{M, AA; j, X_2} \xrightarrow{k_{tr} D_{mAA, R_0} R_{M, AA}} D_{mAA, R_0; i+j-l, X_1+X_2-X_3} + R_{mM, AA; l, X_3}$
153	$D_{mAA, R_0; i, X_1} + R_{M, AA; j, X_2} \xrightarrow{k_{tr} D_{mAA, R_0} R_{M, AA}} D_{mAA, AA; i+j-l, X_1+X_2(-X_3)} + R_{R_0; l} / R_{mM, R_0; l, X_3}$
154	$D_{mAA, R_0; i, X_1} + R_{M, BB; j, X_2} \xrightarrow{k_{tr} D_{mAA, R_0} R_{M, BB}} D_{mBB, R_0; i+j-l, X_1+X_2-X_3} + R_{mM, AA; l, X_3}$
155	$D_{mAA, R_0; i, X_1} + R_{M, BB; j, X_2} \xrightarrow{k_{tr} D_{mAA, R_0} R_{M, BB}} D_{mAA, BB; i+j-l, X_1+X_2(-X_3)} + R_{R_0; l} / R_{mM, R_0; l, X_3}$
156	$D_{mAA, R_0; i, X_1} + R_{M, R_0; j, X_2} \xrightarrow{k_{tr} D_{mAA, R_0} R_{M, R_0}} D_{mR_0, R_0; i+j-l, X_1+X_2-X_3} + R_{mM, AA; l, X_3}$
157	$D_{mAA, R_0; i, X_1} + R_{M, R_0; j, X_2} \xrightarrow{k_{tr} D_{mAA, R_0} R_{M, R_0}} D_{mAA, R_0; i+j-l, X_1+X_2(-X_3)} + R_{R_0; l} / R_{mM, R_0; l, X_3}$
158	$D_{mAA, R_0; i, X_1} + R_{mM, AA; j, X_2} \xrightarrow{k_{tr} D_{mAA, R_0} R_{mM, AA}} D_{mAA, R_0; i+j-l, X_1+X_2-X_3} + R_{mM, AA; l, X_3}$
159	$D_{mAA, R_0; i, X_1} + R_{mM, AA; j, X_2} \xrightarrow{k_{tr} D_{mAA, R_0} R_{mM, AA}} D_{mAA, AA; i+j-l, X_1+X_2(-X_3)} + R_{R_0; l} / R_{mM, R_0; l, X_3}$
160	$D_{mAA, R_0; i, X_1} + R_{mM, BB; j, X_2} \xrightarrow{k_{tr} D_{mAA, R_0} R_{mM, BB}} D_{mBB, R_0; i+j-l, X_1+X_2-X_3} + R_{mM, AA; l, X_3}$
161	$D_{mAA, R_0; i, X_1} + R_{mM, BB; j, X_2} \xrightarrow{k_{tr} D_{mAA, R_0} R_{mM, BB}} D_{mAA, BB; i+j-l, X_1+X_2(-X_3)} + R_{R_0; l} / R_{mM, R_0; l, X_3}$

Table continued from previous page

162	$D_{mAA,R_0;i,X_1} + R_{mM,R_0;j,X_2} \xrightarrow{k_{trD_{mAA,R_0}R_{mM,R_0}}} D_{mR_0,R_0;i+j-l,X_1+X_2-X_3} + R_{mM,AA;l,X_3}$
163	$D_{mAA,R_0;i,X_1} + R_{mM,R_0;j,X_2} \xrightarrow{k_{trD_{mAA,R_0}R_{mM,R_0}}} D_{mAA,R_0;i+j-l,X_1+X_2(-X_3)} + R_{R_0;l/R_{mM,R_0;l,X_3}}$
164	$D_{mBB,R_0;i,X} + R_{R_0;j} \xrightarrow{k_{trD_{mBB,R_0}R_{R_0}}} D_{mR_0,R_0;i+j-l} + R_{mM,BB;l,X}$
165	$D_{mBB,R_0;i,X} + R_{R_0;j} \xrightarrow{k_{trD_{mBB,R_0}R_{R_0}}} D_{mBB,R_0;i+j-l,X(-X_1)} + R_{R_0;l/R_{mM,R_0;l,X_1}}$
166	$D_{mBB,R_0;i,X_1} + R_{M,AA;j,X_2} \xrightarrow{k_{trD_{mBB,R_0}R_{M,AA}}} D_{mAA,R_0;i+j-l,X_1+X_2-X_3} + R_{mM,BB;l,X_3}$
167	$D_{mBB,R_0;i,X_1} + R_{M,AA;j,X_2} \xrightarrow{k_{trD_{mBB,R_0}R_{M,AA}}} D_{mAA,BB;i+j-l,X_1+X_2(-X_3)} + R_{R_0;l/R_{mM,R_0;l,X_3}}$
168	$D_{mBB,R_0;i,X_1} + R_{M,BB;j,X_2} \xrightarrow{k_{trD_{mBB,R_0}R_{M,BB}}} D_{mBB,R_0;i+j-l,X_1+X_2-X_3} + R_{mM,BB;l,X_3}$
169	$D_{mBB,R_0;i,X_1} + R_{M,BB;j,X_2} \xrightarrow{k_{trD_{mBB,R_0}R_{M,BB}}} D_{mBB,BB;i+j-l,X_1+X_2(-X_3)} + R_{R_0;l/R_{mM,R_0;l,X_3}}$
170	$D_{mBB,R_0;i,X_1} + R_{M,R_0;j,X_2} \xrightarrow{k_{trD_{mBB,R_0}R_{M,R_0}}} D_{mR_0,R_0;i+j-l,X_1+X_2-X_3} + R_{mM,BB;l,X_3}$
171	$D_{mBB,R_0;i,X_1} + R_{M,R_0;j,X_2} \xrightarrow{k_{trD_{mBB,R_0}R_{M,R_0}}} D_{mBB,R_0;i+j-l,X_1+X_2(-X_3)} + R_{R_0;l/R_{mM,R_0;l,X_3}}$
172	$D_{mBB,R_0;l,X_1} + R_{mM,AA;j,X_2} \xrightarrow{k_{trD_{mBB,R_0}R_{mM,AA}}} D_{mAA,R_0;i+j-l,X_1+X_2-X_3} + R_{mM,BB;l,X_3}$
173	$D_{mBB,R_0;i,X_1} + R_{mM,AA;j,X_2} \xrightarrow{k_{trD_{mBB,R_0}R_{mM,AA}}} D_{mAA,BB;i+j-l,X_1+X_2(-X_3)} + R_{R_0;l/R_{mM,R_0;l,X_3}}$
174	$D_{mBB,R_0;l,X_1} + R_{mM,BB;j,X_2} \xrightarrow{k_{trD_{mBB,R_0}R_{mM,BB}}} D_{mBB,R_0;i+j-l,X_1+X_2-X_3} + R_{mM,BB;l,X_3}$
175	$D_{mBB,R_0;i,X_1} + R_{mM,BB;j,X_2} \xrightarrow{k_{trD_{mBB,R_0}R_{mM,BB}}} D_{mBB,BB;i+j-l,X_1+X_2(-X_3)} + R_{R_0;l/R_{mM,R_0;l,X_3}}$
176	$D_{mBB,R_0;i,X_1} + R_{mM,R_0;j,X_2} \xrightarrow{k_{trD_{mBB,R_0}R_{mM,R_0}}} D_{mR_0,R_0;i+j-l,X_1+X_2-X_3} + R_{mM,BB;l,X_3}$
177	$D_{mBB,R_0;i,X_1} + R_{mM,R_0;j,X_2} \xrightarrow{k_{trD_{mBB,R_0}R_{mM,R_0}}} D_{mBB,R_0;i+j-l,X_1+X_2(-X_3)} + R_{R_0;l/R_{mM,R_0;l,X_3}}$
178	$D_{R_0,R_0;i,X_1} + R_{R_0;j} \xrightarrow{k_{trD_{R_0,R_0}R_{R_0}}} D_{R_0,R_0;i+j-l,X_1(-X_2)} + R_{R_0;l/R_{M,R_0;l,X_2}}$
179	$D_{R_0,R_0;i,X_1} + R_{R_0;j} \xrightarrow{k_{trD_{R_0,R_0}R_{R_0}}} D_{R_0,R_0;i+j-l,X_1(-X_2)} + R_{R_0;l/R_{M,R_0;l,X_2}}$
180	$D_{R_0,R_0;i,X_1} + R_{M,AA;j,X_2} \xrightarrow{k_{trD_{R_0,R_0}R_{M,AA}}} D_{mAA,R_0;i+j-l,X_1+X_2(-X_3)} + R_{R_0;l/R_{M,R_0;l,X_3}}$
181	$D_{R_0,R_0;i,X_1} + R_{M,AA;j,X_2} \xrightarrow{k_{trD_{R_0,R_0}R_{M,AA}}} D_{mAA,R_0;i+j-l,X_1+X_2(-X_3)} + R_{R_0;l/R_{M,R_0;l,X_3}}$
182	$D_{R_0,R_0;i,X_1} + R_{M,BB;j,X_2} \xrightarrow{k_{trD_{R_0,R_0}R_{M,BB}}} D_{mBB,R_0;i+j-l,X_1+X_2(-X_3)} + R_{R_0;l/R_{M,R_0;l,X_3}}$
183	$D_{R_0,R_0;i,X_1} + R_{M,BB;j,X_2} \xrightarrow{k_{trD_{R_0,R_0}R_{M,BB}}} D_{mBB,R_0;i+j-l,X_1+X_2(-X_3)} + R_{R_0;l/R_{M,R_0;l,X_3}}$
184	$D_{R_0,R_0;i,X_1} + R_{M,R_0;j,X_2} \xrightarrow{k_{trD_{R_0,R_0}R_{M,R_0}}} D_{mR_0,R_0;i+j-l,X_1+X_2(-X_3)} + R_{R_0;l/R_{M,R_0;l,X_3}}$

Table continued from previous page

185	$D_{R_0,R_0;i,X_1} + R_{M,R_0;j,X_2} \xrightarrow{k_{tr}D_{R_0,R_0}R_{M,R_0}} D_{mR_0,R_0;i+j-l,X_1+X_2(-X_3)} + R_{R_0;l}/R_{M,R_0;l,X_3}$
186	$D_{R_0,R_0;i,X_1} + R_{mM,AA;j,X_2} \xrightarrow{k_{tr}D_{R_0,R_0}R_{mM,AA}} D_{mAA,R_0;i+j-l,X_1+X_2(-X_3)} + R_{R_0;l}/R_{M,R_0;l,X_3}$
187	$D_{R_0,R_0;i,X_1} + R_{mM,AA;j,X_2} \xrightarrow{k_{tr}D_{R_0,R_0}R_{mM,AA}} D_{mAA,R_0;i+j-l,X_1+X_2(-X_3)} + R_{R_0;l}/R_{M,R_0;l,X_3}$
188	$D_{R_0,R_0;i,X_1} + R_{mM,BB;j,X_2} \xrightarrow{k_{tr}D_{R_0,R_0}R_{mM,BB}} D_{mBB,R_0;i+j-l,X_1+X_2(-X_3)} + R_{R_0;l}/R_{M,R_0;l,X_3}$
189	$D_{R_0,R_0;i,X_1} + R_{mM,BB;j,X_2} \xrightarrow{k_{tr}D_{R_0,R_0}R_{mM,BB}} D_{mBB,R_0;i+j-l,X_1+X_2(-X_3)} + R_{R_0;l}/R_{M,R_0;l,X_3}$
190	$D_{R_0,R_0;i,X_1} + R_{mM,R_0;j,X_2} \xrightarrow{k_{tr}D_{R_0,R_0}R_{mM,R_0}} D_{mR_0,R_0;i+j-l,X_1+X_2(-X_3)} + R_{R_0;l}/R_{M,R_0;l,X_3}$
191	$D_{R_0,R_0;i,X_1} + R_{mM,R_0;j,X_2} \xrightarrow{k_{tr}D_{R_0,R_0}R_{mM,R_0}} D_{mR_0,R_0;i+j-l,X_1+X_2(-X_3)} + R_{R_0;l}/R_{M,R_0;l,X_3}$
192	$D_{mR_0,R_0;i,X_1} + R_{R_0;j} \xrightarrow{k_{tr}D_{cm,R_0}R_{R_0}} D_{mR_0,R_0;i+j-l,X_1(-X_2)} + R_{R_0;l}/R_{mM,R_0;l,X_2}$
193	$D_{mR_0,R_0;i,X_1} + R_{R_0;j} \xrightarrow{k_{tr}D_{mR_0,R_0}R_{R_0}} D_{mR_0,R_0;i+j-l,X_1(-X_2)} + R_{R_0;l}/R_{mM,R_0;l,X_2}$
194	$D_{mR_0,R_0;i,X_1} + R_{M,AA;j,X_2} \xrightarrow{k_{tr}D_{mR_0,R_0}R_{M,AA}} D_{mAA,R_0;i+j-l,X_1+X_2(-X_3)} + R_{R_0;l}/R_{mM,R_0;l,X_3}$
195	$D_{mR_0,R_0;i,X_1} + R_{M,AA;j,X_2} \xrightarrow{k_{tr}D_{mR_0,R_0}R_{M,AA}} D_{mAA,R_0;i+j-l,X_1+X_2(-X_3)} + R_{R_0;l}/R_{mM,R_0;l,X_3}$
196	$D_{mR_0,R_0;i,X_1} + R_{M,BB;j,X_2} \xrightarrow{k_{tr}D_{mR_0,R_0}R_{M,BB}} D_{mBB,R_0;i+j-l,X_1+X_2(-X_3)} + R_{R_0;l}/R_{mM,R_0;l,X_3}$
197	$D_{mR_0,R_0;i,X_1} + R_{M,BB;j,X_2} \xrightarrow{k_{tr}D_{mR_0,R_0}R_{M,BB}} D_{mBB,R_0;i+j-l,X_1+X_2(-X_3)} + R_{R_0;l}/R_{mM,R_0;l,X_3}$
198	$D_{mR_0,R_0;i,X_1} + R_{M,R_0;j,X_2} \xrightarrow{k_{tr}D_{mR_0,R_0}R_{M,R_0}} D_{mR_0,R_0;i+j-l,X_1+X_2(-X_3)} + R_{R_0;l}/R_{mM,R_0;l,X_3}$
199	$D_{mR_0,R_0;i,X_1} + R_{M,R_0;j,X_2} \xrightarrow{k_{tr}D_{mR_0,R_0}R_{M,R_0}} D_{mR_0,R_0;i+j-l,X_1+X_2(-X_3)} + R_{R_0;l}/R_{mM,R_0;l,X_3}$
200	$D_{mR_0,R_0;i,X_1} + R_{mM,AA;j,X_2} \xrightarrow{k_{tr}D_{mR_0,R_0}R_{mM,AA}} D_{mAA,R_0;i+j-l,X_1+X_2(-X_3)} + R_{R_0;l}/R_{mM,R_0;l,X_3}$
201	$D_{mR_0,R_0;i,X_1} + R_{mM,AA;j,X_2} \xrightarrow{k_{tr}D_{mR_0,R_0}R_{mM,AA}} D_{mAA,R_0;i+j-l,X_1+X_2(-X_3)} + R_{R_0;l}/R_{mM,R_0;l,X_3}$
202	$D_{mR_0,R_0;i,X_1} + R_{mM,BB;j,X_2} \xrightarrow{k_{tr}D_{mR_0,R_0}R_{mM,BB}} D_{mBB,R_0;i+j-l,X_1+X_2(-X_3)} + R_{R_0;l}/R_{mM,R_0;l,X_3}$
203	$D_{mR_0,R_0;i,X_1} + R_{mM,BB;j,X_2} \xrightarrow{k_{tr}D_{mR_0,R_0}R_{mM,BB}} D_{mBB,R_0;i+j-l,X_1+X_2(-X_3)} + R_{R_0;l}/R_{mM,R_0;l,X_3}$
204	$D_{mR_0,R_0;i,X_1} + R_{mM,R_0;j,X_2} \xrightarrow{k_{tr}D_{mR_0,R_0}R_{mM,R_0}} D_{mR_0,R_0;i+j-l,X_1+X_2(-X_3)} + R_{R_0;l}/R_{mM,R_0;l,X_3}$
205	$D_{mR_0,R_0;i,X_1} + R_{mM,R_0;j,X_2} \xrightarrow{k_{tr}D_{mR_0,R_0}R_{mM,R_0}} D_{mR_0,R_0;i+j-l,X_1+X_2(-X_3)} + R_{R_0;l}/R_{mM,R_0;l,X_3}$

8.1.2 Simulation of photochemical *ortho*-methyl benzaldehyde conversion at different substrate concentrations

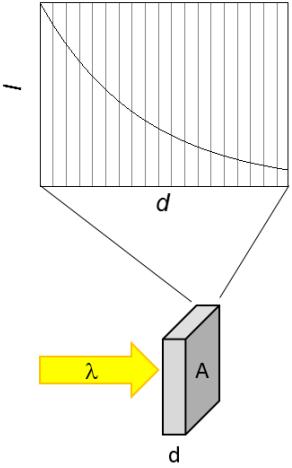
In Chapter 4.2 a concentration dependence of the photo-induced activation step (photoenolization) has been discussed. In this context, the activation rate coefficient is adjusted for the simulations. Here, the relation of substrate concentration and conversion is described.

An algorithm was developed to simulate the conversion of photoreactions. The time and space dependent attenuation of light in sample solutions undergoing photoreactions has to be taken into consideration. Photo-induced transformation of photoactive functionalities can cause said functional groups to undergo drastic changes in their capability to attenuate incident light. Simulations were performed with a photochemistry algorithm to qualitatively explain the observed conversion of the *ortho*-methyl benzaldehyde (MBA) species in solutions of varying concentrations. Beer-Lambert's law quantifies the influence of sample concentration on the attenuation of light in a uniform solution. Quantification by this is suitable for static systems, where components never change in absorptivity. As the extinction coefficient contained in Beer-Lambert's law is lacking a temporal component which would account for changes over time, an adapted approach for dynamic systems need to be developed. The efficiency of photo-induced reactions, relying solely on the absorption of incident light, is subject to the attenuation of light in a solution. Extrapolating from two or more experiments, identical apart from compound concentrations, one can obtain qualitative insights into conversion trends. Here, one assumes an arbitrary quantum yield for the reaction and simulate iteratively changes in local compound concentrations. Thus, it changes the light attenuation profiles. Table 8-3 summarizes experimental parameters and observed conversion values, parameters used to simulate the photoreactions and simulation results.

Before irradiation, the distribution of reactants and products in solution is uniform and the concentration of the reactants at each point in the solution is known and static. The photonic field that is present in the solution at the time the irradiation starts, can be described by the classical Beer-Lambert law. If both the intensity of the incident light, or number of photons, as well as the molar attenuation coefficient of all light absorbing species in the solution is known, the number of photons penetrating each part of the solution can be calculated precisely. Furthermore, the number of photons, which are absorbed by the photoactivatable compound and thus the number of excited states can be predicted. The local conversion can be subsequently calculated based on the quantum yield of the photoreaction. Subsequent irradiation will not yield the same results, as a part of the incident light will be absorbed by non-reactive components, if those are still capable

of attenuating light. Description of the solution for each infinitesimal point in time would still be possible by classical methods, yet would also require an infinite number of calculations. To overcome this dilemma, both the solution volume and the reaction time are divided into increments in an iterative approach. Sufficiently thin subdivisions of the solution in combination with satisfyingly short time increments should thereby yield usable results. For these calculations, the solution is treated as a batch of thin segments, stacked perpendicular to the direction of the beam. Furthermore, the irradiation time is treated iteratively as individual irradiation events, each lasting one second, during which a defined number of photons hits the solution. Light is attenuated per current compound distribution and inflicts changes to this distribution to a degree dependent on the absorbed light by the reactant and the predefined quantum yield. It is assumed that the molecule distribution can be assumed to be almost uniform within a sufficiently small segment of the solution. This assumption was tested by performing a set of simulations with increasing numbers of segments, yielding nearly constant conversion values for $n_{dx} > 1000$. Transient species in this reaction have only short lifetimes in solution.⁴⁰⁶ Therefore, the absorptivity of the transient species can be neglected. Diffusion of the molecules and convection in the solution will inevitably change the spatial distribution of the species over longer times. Literature and independent calculations indicate however that diffusion does not significantly change the outcome of the simulation.⁴⁰⁷ Based on these approximations, a new spatial distribution of reactants and products is calculated iteratively in every cycle. Overall conversion is calculated from the final compound concentrations.

Table 8-3. Top: Relevant experimental parameters are listed as well as measured conversion values p_{MBA} at two different substrate concentrations. Bottom: Experimental parameters were used to derive a hypothetical cuboid irradiation geometry and absorption parameters that were used for the iterative simulation of conversion. As noted previously, the quantum yield was set to an arbitrary value. Simulated conversion values are shown for the two substrate concentrations for both at $\lambda_{\text{max}} = 320$ nm and 360 nm with monochromatic light. The table was adapted from ref.³⁸¹ with the permission of the American Chemical Society.

Experimental:			
<u>Sample solution:</u> $V = 0.5$ mL CH_2Cl_2			
<u>Reaction tube:</u> crimped 0.7 mL photovial			
<u>Irradiation geometry of solution:</u> cylindrical, $R = 3$ mm			
<u>Light source:</u> one PL-L lamp ($320 \text{ nm} < \lambda < 420 \text{ nm}$; $\lambda_{\text{max}} = 360 \text{ nm}$) in a custom-built photoreactor (refer to Chapter 7.2.7)			
<u>Irradiation time:</u> $t = 6$ h			
$c_{\text{MBA}} = 0.02 \text{ mol L}^{-1}$		$c_{\text{MBA}} = 0.07 \text{ mol L}^{-1}$	
$p_{\text{MBA}} > 99\%$		$p_{\text{MBA}} = 70\%$	
Simulation			
<u>Sample solution:</u> $V = 0.5$ mL			
<u>Irradiation geometry of solution:</u> cuboid, $d = 3$ mm, $A = 1.66 \text{ cm}^2$			
<u>Light source:</u> monochromatic light, parallel beam path			
<u>Assumed quantum yield:</u> $\Phi = 0.5$			
<u>Irradiation time:</u> $t = 6$ h ($t = 21600$ s, $k = 21600$)			
<u>Photons impinging onto sample solution per second:</u> $n_p = 4$ nmol			
<u>Number of simulated segments:</u> $n_{\text{dx}} = 2000$			
$\lambda = 320 \text{ nm}$		$\lambda = 360 \text{ nm}$	
$\epsilon_{\text{MBA}} = 3440 \text{ L mol}^{-1} \text{ cm}^{-1}$; $\epsilon_{\text{product}} = 80 \text{ L mol}^{-1} \text{ cm}^{-1}$		$\epsilon_{\text{MBA}} = 100 \text{ L mol}^{-1} \text{ cm}^{-1}$; $\epsilon_{\text{product}} = 0 \text{ L mol}^{-1} \text{ cm}^{-1}$	
$c_{\text{MBA}} = 0.02 \text{ mol L}^{-1}$	$c_{\text{MBA}} = 0.07 \text{ mol L}^{-1}$	$c_{\text{MBA}} = 0.02 \text{ mol L}^{-1}$	$c_{\text{MBA}} = 0.07 \text{ mol L}^{-1}$
$p_{\text{MBA}} = 42\%$	$p_{\text{MBA}} = 12\%$	$p_{\text{MBA}} = 15\%$	$p_{\text{MBA}} = 6\%$

8.1.3 Experimental Data and Characterization

8.1.3.1 Stability Test Monomer AA and BB

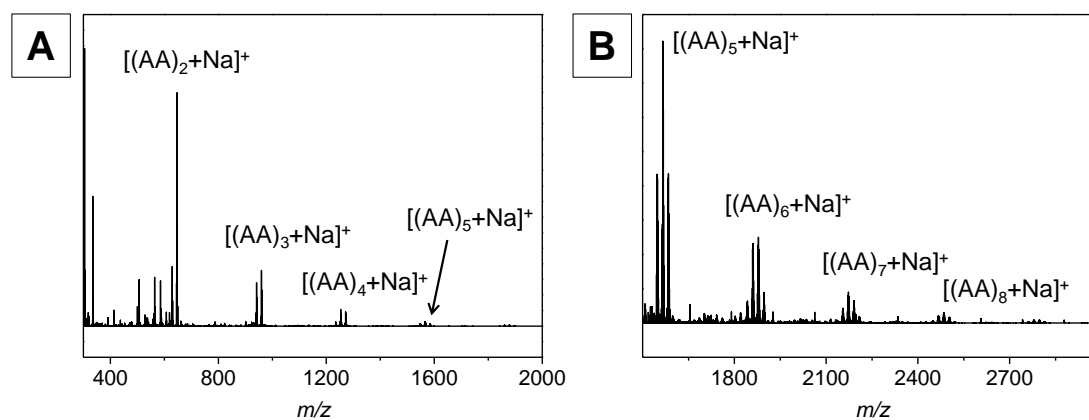


Figure 8-1. ESI-MS spectra of the di(*ortho*-methyl benzaldehyde) **AA** monomer stability assay. The spectra were recorded in direct-infusion experiments in THF/MeOH (3/2, V/V) by doping with sodium trifluoroacetate. A shift of -2 and -18 m/z , respectively, from the main product of each repeating unit can be observed.

8.1.3.2 Rate Coefficients based on Small Molecule Model System

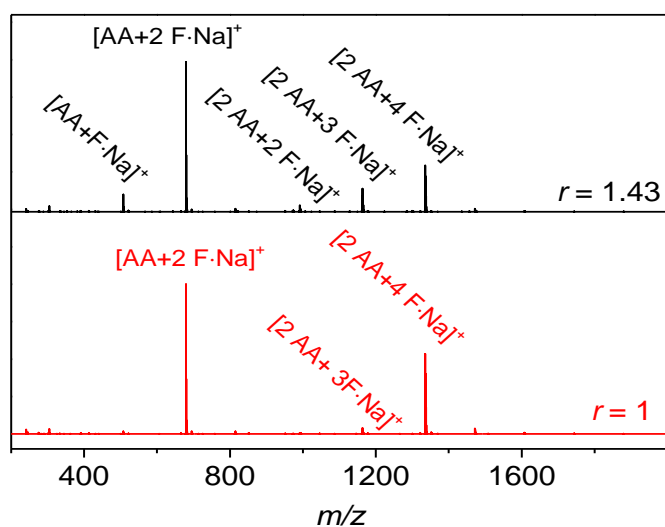


Figure 8-2. ESI-spectra of small molecule model reactions, employing **BB** monomer with diethyl fumarate (**F**) in different stoichiometries as indicated in the spectra. The samples were injected without any purification of the crude product after 6 h of irradiation. The spectra were recorded *via* direct-infusion experiments in THF/MeOH (3/2, V/V) by doping with sodium trifluoroacetate.

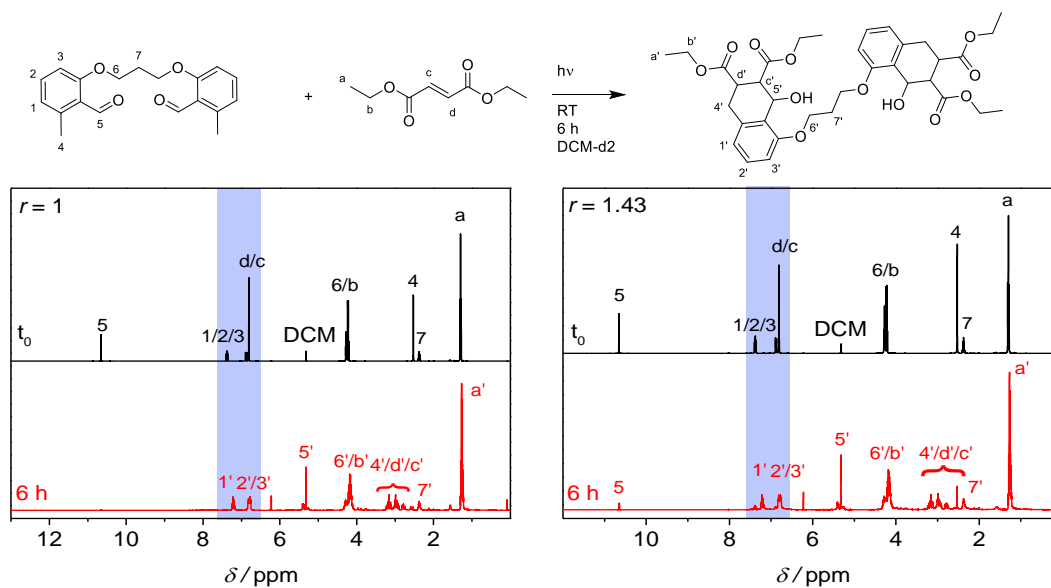


Figure 8-3. $^1\text{H-NMR}$ spectra of the small molecule experiment of diethyl fumarate (**F**) and di(*ortho*-methyl benzaldehyde) **AA** in DCM-d_2 before and after irradiation at different stoichiometries r of the functional groups. The blue area indicates the area of the aromatic (1, 2, 3 and 1', 2', 3') and the fumarate protons (d/c), respectively.

8.1.4 Step-Growth Polymerization and Reaction Conditions Optimization

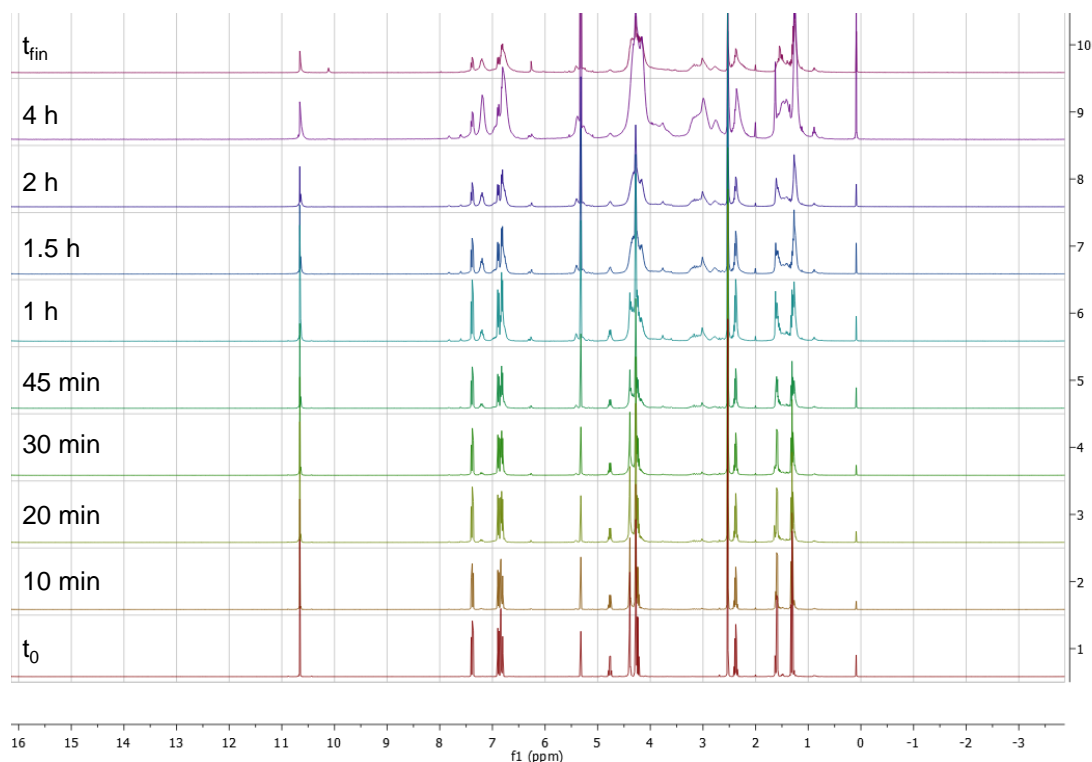


Figure 8-4. $^1\text{H-NMR}$ spectra of kinetic run of step-growth polymerization of **AA** and **BB** with $r = 1.75$. The spectra were recorded in DCM-d_2 after irradiation without any further purification or dilution.

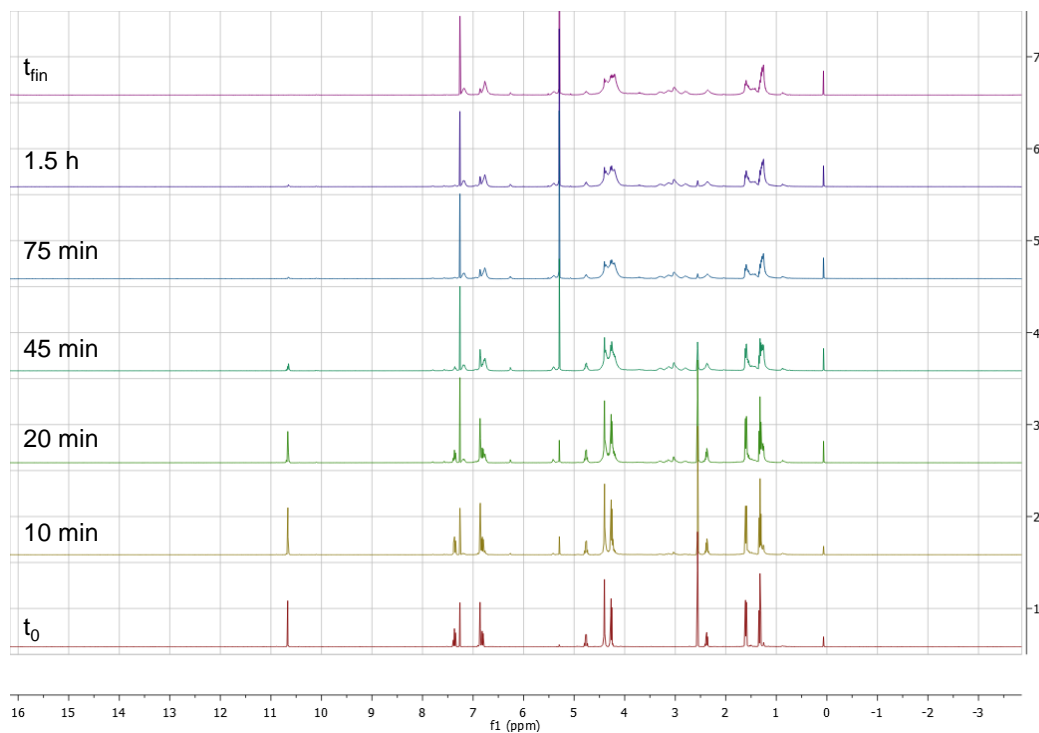


Figure 8-5. $^1\text{H-NMR}$ spectra of kinetic run of step-growth polymerization of **AA** and **BB** with $r = 1$. The spectra were recorded in CDCl_3 after irradiation without any further purification or dilution.

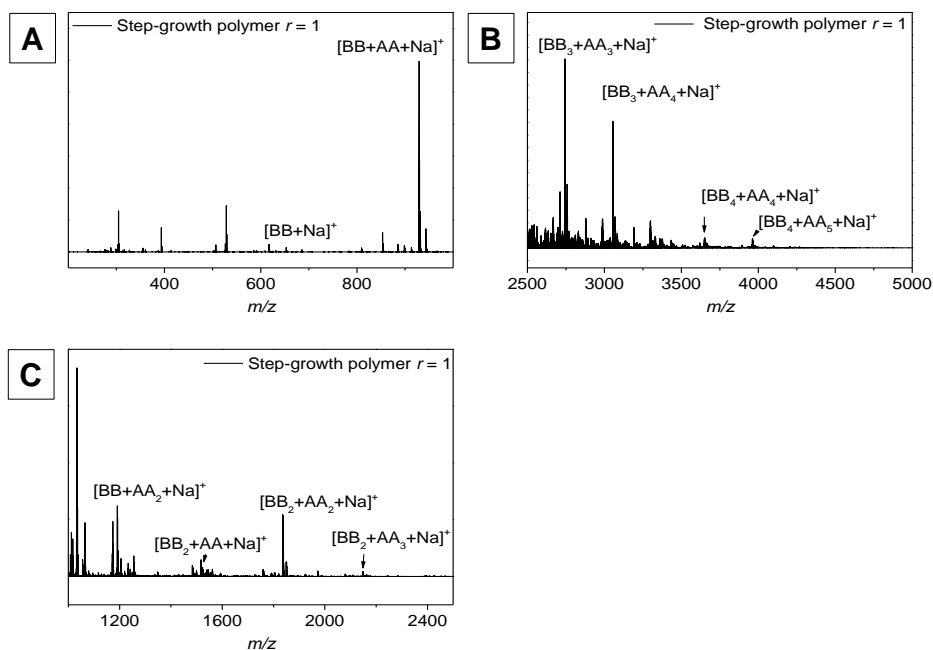


Figure 8-6. ESI-MS spectra of a typical SG polymer with an **AA/BB** monomer stoichiometry of $r = 1$ at different m/z ranges, including the assignment of the observed polymer species. The spectra were recorded *via* direct-infusion experiments in THF/MeOH (3/2, V/V) by doping with sodium trifluoroacetate.

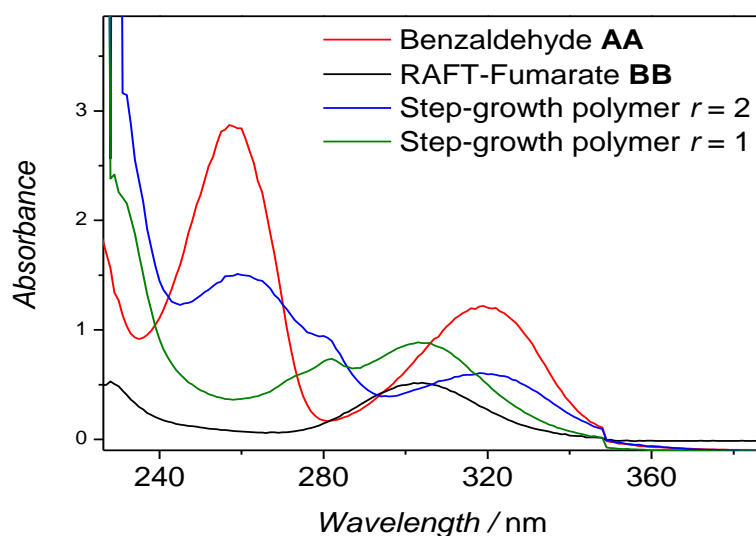


Figure 8-7. UV-VIS spectra of the monomers **AA** and **BB** and corresponding step-growth polymers SGP with different monomer stoichiometries $r = 1$ and $r = 2$ (refer to legend), recorded in DCM. Concentrations: $c(\mathbf{AA}) = 101 \mu\text{mol}\cdot\text{L}^{-1}$, $c(\mathbf{BB}) = 26 \mu\text{mol}\cdot\text{L}^{-1}$, $c(\text{SGP } r = 1) = 96 \mu\text{mol}\cdot\text{L}^{-1}$, $c(\text{SGP } r = 2) = 59 \mu\text{mol}\cdot\text{L}^{-1}$.

8.1.5 Segmented Copolymers by RAFT Polymerization

Table 8-4. Overview of the reactions for the simulation of the RAFT polymerization, together with the corresponding Arrhenius parameters. Also specified are the intrinsic rate coefficients at 333 K.

Reaction	Reaction equation	A^a	E_a^c	$k(333 \text{ K})^a$
Initiator decomposition ^d	$I_2 \xrightarrow{f, k_d} 2R_1$	$2.67 \cdot 10^{15b}$	1.30 10^5	$1.10 \cdot 10^{-5b}$
Propagation	$R_{i,X} + M \xrightarrow{k_p} R_{i+1,X}$	$4.27 \cdot 10^7$	3.25 10^4	$3.41 \cdot 10^2$
Termination	$R_{i,X_1} + R_{j,X_2} \xrightarrow{k_p} D_{i+j,X_1+X_2}$	$1.00 \cdot 10^9$		$1.00 \cdot 10^9$
Exchange	$D_{i,X_1} + R_{j,X_2} \xrightleftharpoons{k_{ex}} D_{i+j-l,X_1+X_2-X_3} + R_{l,X_3}$	$5.00 \cdot 10^4$		$5.00 \cdot 10^4$

^a $\text{L}\cdot\text{mol}^{-1}\cdot\text{s}^{-1}$ except ^b s^{-1} , ^c $\text{J}\cdot\text{mol}^{-1}$, ^d $f_{\text{chem}}=0.7$

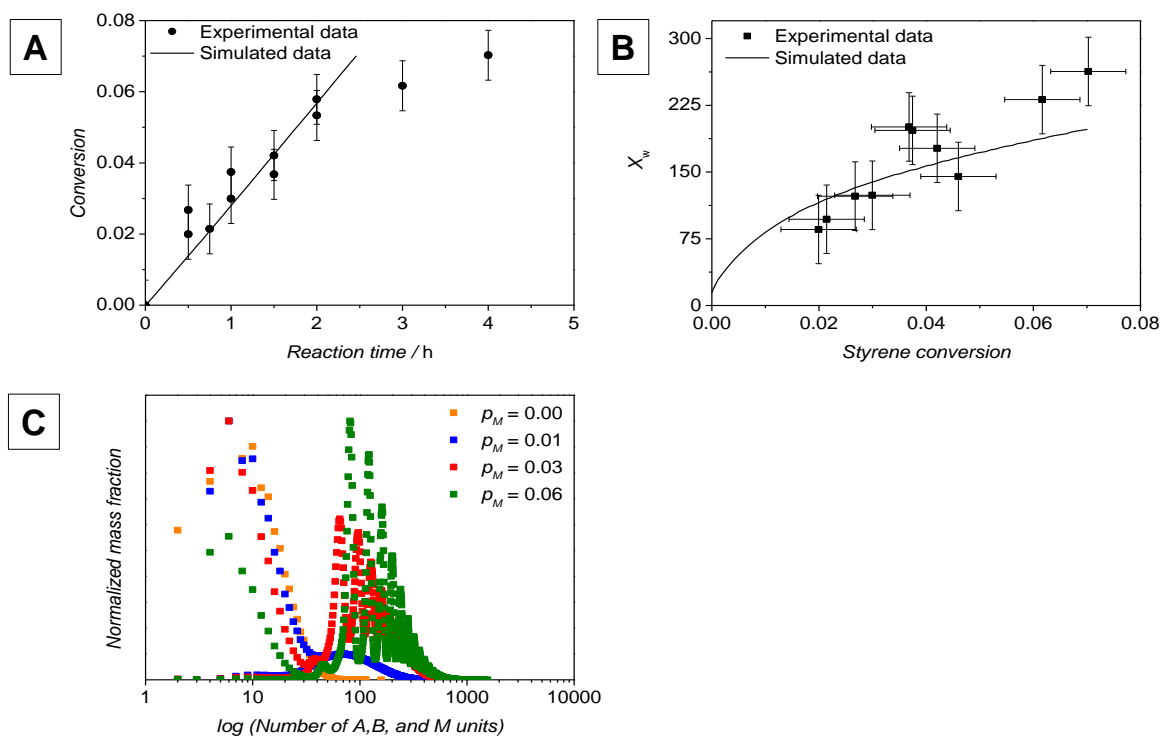
Data for RAFT polymerization $r = 1$ 

Figure 8-8. (A) Comparison of the experimental and simulation data for the RAFT polymerization for (a) styrene conversion vs. time and (B) mass-average chain length vs. styrene conversion. (C) mass chain length distribution for different styrene conversions; $[\text{Styrene}]_0 = 8.74 \text{ mol}\cdot\text{L}^{-1}$, $[\text{I}_2]_0 = 4.85 \cdot 10^{-3} \text{ mol}\cdot\text{L}^{-1}$.

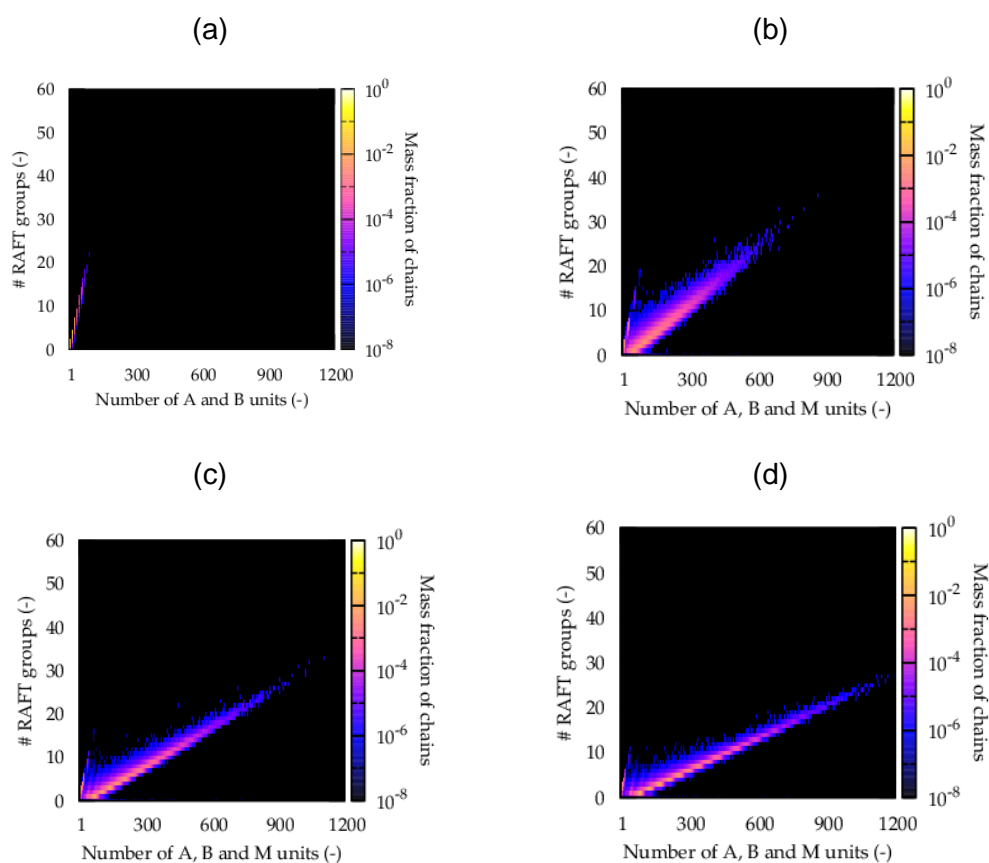


Figure 8-9. Mass chemical composition chain length distribution for different styrene conversions: (a) 0.00, (b) 0.01, (c) 0.04, (d) 0.07; the x-axis represents the chain length (represented by the number of A, B and C units), the y-axis represents the composition (represented by the number of RAFT groups) and the colors represent the mass fraction of chains; $[\text{Styrene}]_0 = 8.74 \text{ mol}\cdot\text{L}^{-1}$, $[\text{I}_2]_0 = 4.85 \cdot 10^{-3} \text{ mol}\cdot\text{L}^{-1}$. Precursor polymer with stoichiometry of $r = 1$.

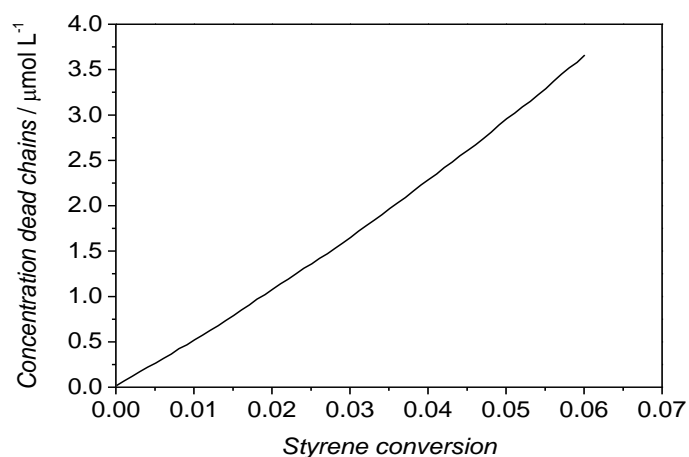


Figure 8-10. Concentration of dead chains in $\text{mol}\cdot\text{L}^{-1}$ vs. styrene conversion.

8.2 Step-Growth by Thermally Induced DA Reactions and Subsequent RAFT Polymerization: Synthesis of Segmented Copolymers

8.2.1 Step-Growth Polymerization

Table 8-5. Results of the SG polymerization for stoichiometry determination, obtained by THF-SEC applying a polystyrene calibration, using different stoichiometries r of the monomers **CC/BB**, indicating the highest molecular weight for $r = 1.2$.

Stoichiometry r	$M_n / \text{g}\cdot\text{mol}^{-1}$	$M_w / \text{g}\cdot\text{mol}^{-1}$	\mathcal{D}
1.1	3,650	23,750	6.49
1.2	4,150	40,000	9.67
1.4	2,100	8,250	3.97
1.6	1,850	5,600	3.00

Table 8-6. Molecular results of the SG polymers obtained by thermal DA cycloaddition. Conversion was obtained by evaluation of $^1\text{H-NMR}$ spectra of the corresponding samples, M_n , M_w and \mathcal{D} values were obtained by THF-SEC applying a polystyrene calibration.

Reaction time/min	Conversion	$M_n / \text{g}\cdot\text{mol}^{-1}$	$M_w / \text{g}\cdot\text{mol}^{-1}$	\mathcal{D}
20	0.66	1,200	2,350	1.97
40	0.78	1,650	3,950	2.4
60	0.84	2,050	4,850	2.36
90	0.89	2,500	6,150	2.44
120	0.92	2,800	7,800	2.81
180	0.95	3,150	10,500	3.35
240	0.97	3,250	13,500	4.1
360	0.98	3,650	18,700	5.15
480	0.99	3,900	22,200	5.65
1200	1	3,850	38,960	10.2

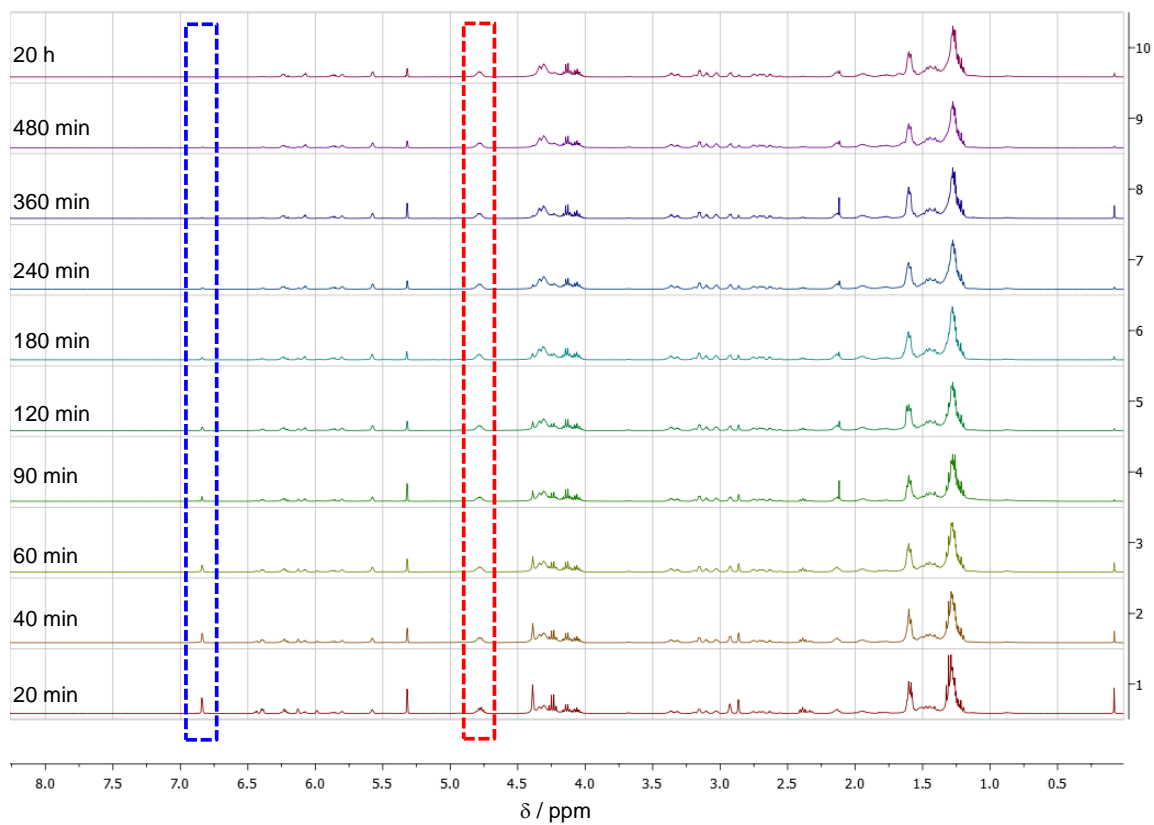


Figure 8-11. $^1\text{H-NMR}$ spectra of the SG polymerization kinetics. All measurements were recorded in CD_2Cl_2 . The blue box highlights the fumarate resonances, the red box highlights the resonances of the α -proton to the trithiocarbonate.

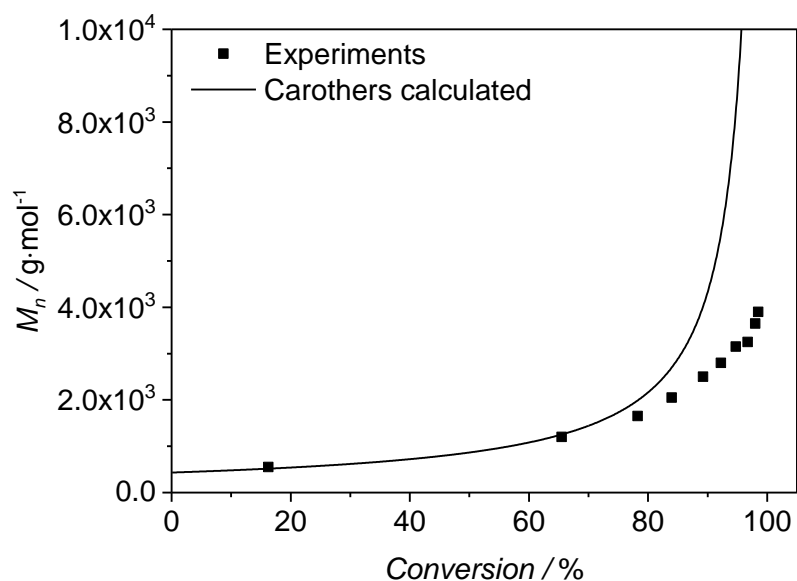


Figure 8-12. Carothers plots of the SG polymerization with a monomer stoichiometry of $r = 1.2$, M_n vs. conversion. Conversion was obtained by evaluation of $^1\text{H-NMR}$ spectra of corresponding samples, referencing the integrals of the fumarate resonances to the unchanged α -protons of the trithiocarbonate. M_n and M_w values were determined by THF-SEC applying a polystyrene calibration.

Table 8-7. Assignment from ESI-HCD-MS spectrum signals of the SG polymer ($r = 1.2$) from Figure 4-20.

#	m/z_{found}	$m/z_{\text{calc.}}$	$\Delta m/z_{\text{exp}}$	$\Delta m/z_{\text{theo}}$	R
n = 2	2022.8833	2022.8767	0.0066	0.0417	48,500
n = 2	1751.6455	1751.6386	0.0069	0.0353	49,500
n = 1	1481.406	1481.4039	0.0021	0.0265	55,800
n = 1	1157.5491	1157.5487	0.0004	0.0179	64,600
n = 2	887.3136	887.3139	0.0003	0.0123	71,900
BB	617.0788	617.0792	0.0004	0.0072	85,950

8.2.2 Segmented Copolymers *via* RAFT Polymerization of Q1

Table 8-8. Molecular results of the polystyrene obtained by RAFT polymerization. Conversion was obtained by gravimetric evaluation, M_n , M_w , and \bar{D} values were obtained by THF-SEC applying a polystyrene calibration.

Reaction time/min	Conversion	$M_n / \text{g}\cdot\text{mol}^{-1}$	$M_w / \text{g}\cdot\text{mol}^{-1}$	\bar{D}
15	0.012	30,900	83,400	2.7
30	0.013	37,000	107,800	2.91
60	0.022	44,500	107,800	2.43
90	0.027	50,700	113,200	2.24
120	0.036	68,000	145,000	2.13
180	0.053	92,300	178,300	1.93
240	0.065	101,100	218,700	1.99
360	0.093	145,000	311,200	2.15
1440	0.291	333,500	965,800	2.9

8.3 Cysteine-Rich Domain Peptides for Step-Growth Polymerization and Surface Patterning

8.3.1 ESI-MS Spectra

Stability test of the folded CRD with CuBr

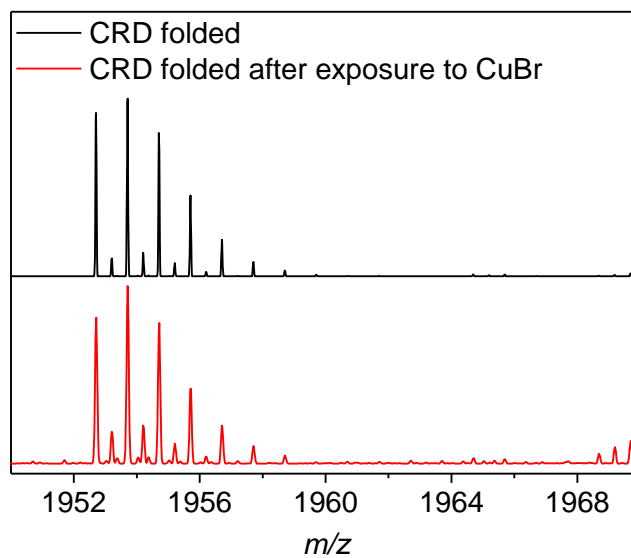


Figure 8-13. ESI-MS spectra of the folded CRD before (black) and after (red) exposure to CuBr with PMDETA and L-arginine. The spectra were recorded in H₂O/MeCN with 1% acetic acid as doping agent.

8.3.2 High Performance Liquid Chromatography

Analysis of the CRD-bromide in HPLC measurement:

Conditions for analytic measurement:

Concentration of the CRD-bromide: 1 g·L⁻¹

Solvent: isocratic with MeCN/H₂O 10/90 (V/V) and 0.1% trifluoro acetic acid (TFA)

Column: Vydac 218 C₁₈ reversed- phase (250 mm × 4.6 mm)

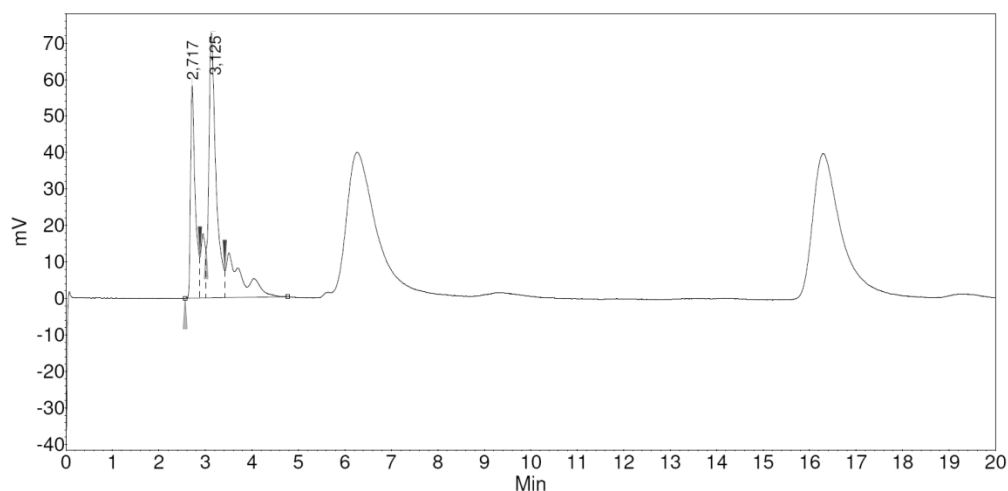


Figure 8-14. HPLC elugram of the CRD-bromide in an analytic measurement. Isocratic solvent mixture was MeCN/H₂O (10/90, V/V) with addition of 0.1% trifluoro acetic acid (TFA).

Conditions for semi-preparative measurement:

Concentration of the CRD-bromide: 1 g·L⁻¹

Solvent: isocratic with MeCN/H₂O 10/90 (V/V) and 0.1% trifluoro acetic acid (TFA)

Column: Vydac 218 C₁₈ reversed- phase (250 mm × 10 mm)

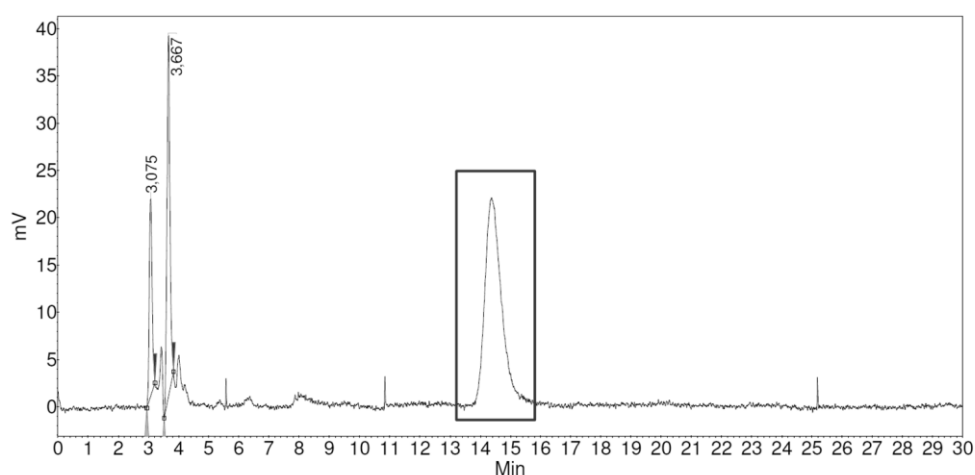


Figure 8-15. HPLC elugram of the CRD-bromide in a semi-preparative measurement. Solvent mixture was MeCN/H₂O 10/90 (V/V) with and 0.1% trifluoro acetic acid (TFA). The box represents the elution of the sample taken for ESI-MS in Figure 8-16.

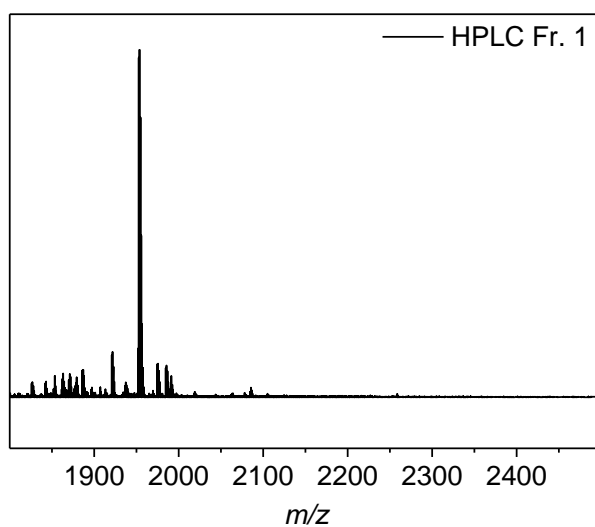


Figure 8-16. ESI-MS spectrum of the collected sample, as indicated in Figure 8-15. The main signal can be assigned to the folded CRD but not to the CRD-bromide. Spectrum was recorded in MeCN/H₂O mixture with 1% acetic acid as doping agent.

8.4 CRDs in Recodable Surfaces

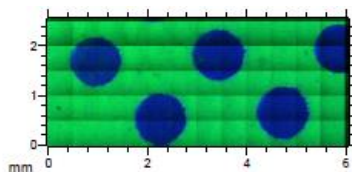


Figure 8-17. Surface after immobilization of the CRD-fumarate and the PEG-fumarate. ToF-SIMS overlay of the signals from S⁻, HS⁻, S₂⁻ (green), C₂H₅O⁻ (blue).

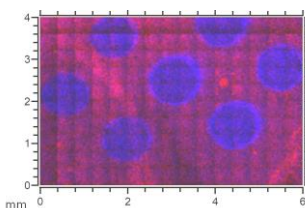


Figure 8-18. Surface after attaching the CRD-bromide to the surface. ToF-SIMS overlay of Sum of ⁸¹Br, Br (red), C₂H₅O⁻ (blue).

8.5 List of Abbreviations

AA	Acrylamide
ABS	Copolymer consisting of polyacrylonitrile-co-polybutadiene-co-polystyrene
APS	Ammonium persulfate
ARGET	Activator regenerated by electron transfer
ATRP	Atomic transfer radical polymerization
BA	Bisacrylamide
BCP	Block copolymer
C/Cys	Cysteine
CDCl ₃	<i>deutero</i> -Chloroform
CD ₂ Cl ₂	<i>dideutero</i> -methylene chloride
CH	Cyclohexane
Cp	Cyclopentadiene/cyclopentadienyl
CRD	Cysteine-rich domain
CSIRO	Commonwealth Scientific and Industrial Research Organization
CTA	Chain transfer agent
CuAAC	Copper-catalyzed azide-alkyne cycloaddition
DA	Diels – Alder
DCM	Dichloromethane/methylene chloride
DiBent	<i>S,S</i> -Dibenzyltrithiocarbonate
DLW	Direct-laser writing
DMAP	4-Dimethylaminopyridin
DNA	Deoxyribonucleic acid
DMAc	<i>N,N</i> -Dimethylacetamide
DMF	<i>N,N</i> -Dimethylformamide
DMSO	Dimethyl sulfoxide
DoPAT	2-(dodecylthiocarbonylthio)-propionic acid
DPE	1,1-Diphenylethylene
DTC	<i>S,S</i> -(dipropyl)trithiocarbonate
Đ	Dispersity
<i>e.g.</i>	<i>exempli grata</i> (for instance)
ECL	Extracellular loop
EDC	1-Ethyl-3-(3-dimethylaminopropyl)carbodiimide
EA	Ethyl acetate
EGF	End-group fidelity
ESI-MS	Electrospray ionization mass spectrometry

EtOH	Ethanol
FMO	Frontier molecular orbital
FRP	Free-radical polymerization
G or Gly	Glycine
GPC	Gel-permeation chromatography
GSH	Glutathione
GSSG	Glutathione in dimerized state (<i>via</i> disulfide bond)
H ₂ O	Water
HCl	Hydrochloric acid
HDA	Hetero Diels – Alder
HIC	Hydrophobic interaction chromatography
HOMO	Highest occupied molecular orbital
HPLC	High performance liquid chromatography
ISC	Intersystem crossing
<i>i.e.</i>	<i>id est</i> (that is to say)
<i>k</i> MC	kinetic Monte Carlo
<i>k</i> _p	Propagation rate coefficient
LCST	Lower critical solution temperature
LUMO	Lowest unoccupied molecular orbital
MADIX	Macromolecular design <i>via</i> interchange of xanthates
MBA	<i>ortho</i> -methyl benzaldehyde
MC	Monte Carlo
MeCN	Acetonitrile
MeOH	Methanol
MMA	Methyl methacrylate
MWCO	Molecular weight cut-off
MWD	Molecular weight distribution
<i>m/z</i>	Mass to charge ratio
NEt ₃	Triethylamine
NICAL	Nitrile-imine carboxylic acid ligation
NIPAAm	<i>N</i> -isopropylacrylamide
NITEC	Nitrile-imine mediated tetrazole-ene cycloaddition
NMP	Nitroxide mediated radical polymerization
NMR	Nuclear magnetic resonance
PA	Polyamide
PAA	Polyacrylamide
PBS	Phosphate buffer solution

PE	Photoenol
PEG	Poly(ethylene glycol)
PET	Poly(ethylene terephthalate)
PMDETA	<i>N,N,N',N'',N'''</i> -pentamethyldiethylenetriamine
PMMA	Poly(methyl methacrylate)
PP	Polypropylene
PS	Polystyrene
PVC	Polyvinylchloride
RAFT	Reversible addition-fragmentation chain transfer
RDRP	Reversible-deactivation radical polymerization
R_f	Retardation factor
RI	Refractive index
RNA	Ribonucleic acid
ROP	Ring-opening polymerization
R_p	Propagation rate
SAN	Copolymer polystyrene-co-polyacrylonitrile
SCNP	Single-chain nanoparticle
SDS	Sodium dodecyl sulfate
SDS-PAGE	Sodium dodecyl sulfate polyacrylamide gel electrophoresis
SEC	Size exclusion chromatography
SG	Step-growth
SGP	Step-growth polymer
SPPS	Solid phase peptide synthesis
STED	Stimulated emission depletion
TBDMSCI	<i>tert</i> -Butyldimethylsilyl chloride
TEMED	<i>N,N,N',N'</i> -Tetramethylethylenediamine
Tet-PEG	Tetrazole functional poly(ethylene glycol)
TFA	Trifluoroacetate
THF	Tetrahydrofuran
TLC	Thin-layer chromatography
ToF-SIMS	Time-of-flight secondary ionization mass spectrometry
Tris	Tris(hydroxymethyl)aminomethane
UCST	Upper critical solution temperature
UV	Ultraviolet
Vis	Visible
vs.	versus

8.6 List of Figures

- Figure 3-1. RAFT polymerization as starting point for postmodification, self-assembly, gelation and stimuli responsive materials. The figure is reproduced from A. P. Vogt and B. S. Sumerlin, *Soft Matter*, 2009, 5, 2347–2351 with permission of The Royal Society of Chemistry.⁹³ 31
- Figure 3-2. Schematic evolution of degree of polymerization with conversion for different polymerization techniques: step-growth (solid line), controlled and living methodologies (dashed line), and free-radical polymerization (dash-dotted line).³³ 33
- Figure 3-3. Left: MO of the diene 1,3-butadiene and of the dienophile ethylene. Right: LUMO and HOMO of the dienophile and diene undergoing a common electron demand DA reaction.¹⁸⁵ In this illustration, the size of the MOs does not represent the orbital coefficients. 42
- Figure 3-4. Symmetry of HOMO and LUMO of substituted and unsubstituted dienes and dienophiles, determining the regioselectivity in terms of unsymmetric DA reactants. The size of the lobe is proportional to their electron density coefficient. 44
- Figure 3-5. Jablonski diagram, showing the transition of electronic and vibrational states during photochemical processes upon irradiation of molecules..... 47
- Figure 3-6. a) Functionalization of Si wafer with tetrazoles and subsequent attachment of maleimide-functional azobenzenes on the entire surface upon irradiation via NITEC. b) Spatial resolved attachment of azobenzenes via NITEC applying a meander shaped photomask. c) Cis-trans isomerization of azobenzenes on the surface upon irradiation in a spatial resolved fashion employing a half-covering photomask. The figure was reprinted from E. Blasco, M. Piñol, L. Oriol, B. V. K. J. Schmidt, A. Welle, V. Trouillet, M. Bruns and C. Barner-Kowollik, *Adv. Funct. Mater.*, 2013, 23, 4011–4019. with permission of John Wiley and Sons.²⁵⁷ 57
- Figure 3-7. Schematic view of primary, secondary, tertiary and quaternary structures of proteins..... 59
- Figure 3-8. Simplified illustration of translation of mRNA to obtain the peptide chain. A: Process in the ribosome showing tRNA participating in the decoding of the mRNA. P-site: tRNA attached to the growing peptide. A-site: next loaded tRNA arrives. E-site: unloaded tRNA leaves the ribosome. B: mRNA code is translated to a peptide chain. 64
- Figure 4-1. General concept of photo- (AA) or thermally induced (CC) Diels-Alder SG polymerization of corresponding monomers and subsequent RAFT polymerization. 74

- Figure 4-2. Research concept of both experimental and in silico investigations for designing the reaction conditions of the SG as well as the RAFT polymerization. The figure is adapted from ref.³⁸¹ with permission of the American Chemical Society. 75
- Figure 4-3. (A) Oligomerization of AA and BB in photo-induced SG polymerization into multifunctional RAFT CTA ($D_{X,Y}$; X,Y are end-groups); Full list of all 54 reactions in Table 8-1 in the Appendix 8.1.1; (B) Exchange reactions in the RAFT process (monomer M: styrene) and chronologically ordered divisions of the macrospecies formed. Definition of macrospecies: Table 4-1 (definition based on end-groups; R_0 : AIBN fragment); full list of all 205 reactions in Table 8-2. The figure was reprinted from ref.³⁸¹ with permission of the American Chemical Society. 77
- Figure 4-4. (A) Experimental THF-SEC traces obtained from the AA and BB monomer stability tests ($\lambda_{max} = 360$ nm, $t = 6$ h in DCM, $T = 25$ °C, $c = 0.04$ mol·L⁻¹). (B) ¹H-NMR spectra of AA monomer before (black) and after irradiation (red). (C) ¹H-NMR spectra of BB monomer before (black) and after irradiation (red). All NMR spectra were recorded in DCM-d₂. (D) Molar mass distribution obtained by simulation used for the determination of $k_{self,AA}$ by qualitative comparison with experimental data in (A) (normalized on peak height); $k_{self,AA} = 0.2$ L·mol⁻¹ s⁻¹; for (D) absolute molar masses are calculated from the chemical structure of AA while in (A) they are relative due to measurement vs. standards and broadening; for (D) by definition the monomer AA is located at $x = 2$, the dimer AAAA at $x = 4$, etc. The figure was adapted from ref.³⁸¹ with permission of the American Chemical Society. 82
- Figure 4-5. (A) Monofunctional system accounting for the reaction between diethyl fumarate F and A according to the monomer structure of the main reaction (k_{main}) and the self-reaction ($k_{self,AA}$), forming the final adducts A-F and A-A. (B) Concentration profile of both adducts A-A and A-F with time ($c_0 = 0.04$ mol·L⁻¹). (C) Calculated final yield of the product A-F depending on different monomer stoichiometry r . Three cases are depicted for different ratios of $k_{self,AA}$ to k_{main} (orange dots: $k_{self,AA}/k_{main} = 0.125$, green dots: $k_{self,AA}/k_{main} = 1$, blue dots: $k_{self,AA}/k_{main} = 8$) The red line illustrates parity between the A-F/A-A concentrations. (D) Calculated final yield of the A-F product depending on the ratio of $k_{self,AA}$ to k_{main} (red line indicates parity). The figure was reprinted from ref.³⁸¹ with permission of the American Chemical Society. 84
- Figure 4-6. (A) Assessment of k_{main} by small molecule reaction including the monomer AA and its counterpart F, employing the prior determined $k_{self,AA}$ value ($k_{main} = 1.6$ L·mol⁻¹·s⁻¹ and $k_{self,AA} = 0.2$ L·mol⁻¹·s⁻¹). (B) THF-SEC trace obtained by experiments at

different molar ratios r of AA and F (Eq. (29) with $B = F$) upon irradiation (reaction conditions: 6 h irradiation; $\lambda_{\max} = 360$ nm; equimolar: $r = 1$, $c(\text{AA}) = 0.035$ mol·L⁻¹ and $c(\text{F}) = 0.070$ mol·L⁻¹, off-stoichiometric: $r = 1.43$, $c(\text{AA}) = 0.052$ mol·L⁻¹ and $c(\text{F}) = 0.070$ mol·L⁻¹). (C) Simulated SEC-trace for the small molecule reaction of the reaction between AA and F. The figure was adapted from ref.³⁸¹ with permission of the American Chemical Society..... 85

Figure 4-7. (A) Reaction scheme of the SG polymerization. (B) Experimental THF-SEC-traces of the SG polymers P1 ($r = 1$); $c_0(\text{AA}, \text{BB}) = 0.02$ mol·L⁻¹; $\lambda_{\max} = 360$ nm). (C) Simulated SEC traces for SG polymerization obtained by kMC ($k_{\text{main}} = 1.6$ L·mol⁻¹·s⁻¹ and $k_{\text{self,AA}} = 0.2$ L·mol⁻¹·s⁻¹ based on Figure 4-4 and Figure 4-6 (D and E) ¹H-NMR spectra of the SG polymerization kinetics, showing resonances of the aldehyde and the para proton of the phenyl ring (h'' in (E)) with respect to the benzaldehyde functionality (red, g in (E)). Full assignment in reference to (A) for AA, BB, and P1, additionally ESI-MS data in Appendix 8.1.4, Figure 8-6. Spectra were recorded in CDCl₃). (F) Conversion of benzaldehyde (determined both experimentally and by simulation) vs. irradiation time. (G) Carothers plot, illustrating experimental and kMC simulated mass average chain length (X_w) vs. benzaldehyde conversion (evaluated by SEC and NMR, respectively). Carothers plot without parameter optimization is illustrated in red dotted line. Concentration ratio of A to B is illustrated by the blue line. The figure was adapted from ref.³⁸¹ with permission of the American Chemical Society..... 87

Figure 4-8. (A) SEC-traces of the SG kinetic run (relative values) with a stoichiometry of $r = 1.75$, recorded in THF ($c_0(\text{AA}) = 0.04$ to 0.07 mol·L⁻¹ with off-stoichiometry, $c_0(\text{BB}) = 0.04$ mol·L⁻¹ in DCM ($\lambda_{\max} = 360$ nm). (B) SEC-traces of the SG polymerization (absolute values) obtained by kMC simulations (normalized by peak height). The dimers AAAA and AABB are located at $x = 4$. (C) Conversion vs. irradiation time. (D) Mass average chain length (X_w) vs. conversion, determined by SEC and NMR, respectively. Red dotted line illustrates Carothers theory, as noted in Eq. (30) for $r > 1$, and black line derived by simulations. The figure was reprinted from ref.³⁸¹ with permission of the American Chemical Society..... 88

Figure 4-9. Simulated data of the cases $r = 1$ and $r = 1.75$, (A) X_w of the SG polymer P1, i.e. no (AA)_k homopolymer chains are accounted. (B) Homopolymer AA mass fraction vs. benzaldehyde conversion. (C) Homopolymer mass average chain length excluding the AA monomer. (D) Concentration ratio of both functional groups A and B vs. benzaldehyde conversion. The figure was reprinted from ref.³⁸¹ with permission of the American Chemical Society..... 89

- Figure 4-10. SG polymerization at different stages: At first, the monomers are present in equal molarity or off-stoichiometry. In Stage 1 high consumption of AA leads to the formation of homopolymer segments, in view of the discussion in Figure 4-9; left: $r = 1$ and right $r \gg 1$. For $r = 1$, AA consumption finally yields polymer and oligomer chains with BB end-groups, preventing the formation of long polymer segments. For $r \gg 1$, all fumarate groups are reacted. However, the formation of AA homopolymer chains is the inevitable result of the initial higher AA feeding ratio. The figure was reprinted from ref.³⁸¹ with permission of the American Chemical Society. 90
- Figure 4-11. Mass chain length distributions obtained by simulations at varying benzaldehyde conversion 0.1, 0.45 and 0.8 for the case of $r = 1$ (black symbols) and $r = 1.75$ (orange) obtained by simulations. Open symbols illustrate the AA homopolymer conditional distribution. The figure was reprinted from ref.³⁸¹ with permission of the American Chemical Society. 91
- Figure 4-12. SG polymerization at different stoichiometries r (A) SEC traces and (B) mass average molar mass (M_w) vs. stoichiometry factor r as illustrated in Scheme 4-2. In (B) trend line for guiding the eye; initial BB concentration 0.04 mol L^{-1} in DCM, irradiation for 6 h ($\lambda_{\text{max}} = 360 \text{ nm}$). The figure was reprinted from ref.³⁸¹ with permission of the American Chemical Society. 92
- Figure 4-13. (A) Evolution of styrene conversion with reaction time. (B) Development of X_w with styrene conversion. (C) Molecular weight distributions of the segmented copolymers with time, employing a SG polymer P1 from a stoichiometry $r = 1.5$ (normalized intensity). (D) Simulation of mass chain length distribution for varying styrene conversions (total number of units with a differentiation on the level of A, B or M); $[\text{Styrene}]_0 = 8.74 \text{ mol}\cdot\text{L}^{-1}$, $[\text{I}_2]_0 = 4.85\cdot 10^{-3} \text{ mol}\cdot\text{L}^{-1}$; $[\text{mCCTA}]_0 = 5\cdot 10^{-3} \text{ mol}\cdot\text{L}^{-1}$ at $60 \text{ }^\circ\text{C}$. The figure was reprinted from ref.³⁸¹ with permission of the American Chemical Society. 94
- Figure 4-14. Chemical composition chain length distribution (CC-CLD) at varying styrene conversions of 0.00 (A), 0.01 (B), 0.03 (C) and 0.06 (D). On the x-axis the number of A, B, and M (styrene) units represents the overall chain length in the chains, on the y-axis the number of RAFT groups of a chain with length i (i.e. the composition) is outlined. The heat map illustrates the mass fraction of chains. To (A): White line represents ideal ratio of A to B units. In the precursor SG polymer P1, only slight deviation from the white line is given for the SG polymer with $r = 1.5$ (only minor homopolymer segments). For the CC-CLDs for $r = 1$, refer to Appendix 8.1.5,

- Figure 8-9. The figure was reprinted from ref.³⁸¹ with permission of the American Chemical Society. 96
- Figure 4-15. (A) End-group fidelity (EGF) vs. styrene conversion. (B) Mass chemical-composition distributions for corresponding CC-CLD in Figure 4-14. The figure was adapted from ref.³⁸¹ with permission of the American Chemical Society. 97
- Figure 4-16. Stability test of the CC monomer via stirring at ambient temperature at the concentration of 0.2 mol·L⁻¹ in DCM. (A) SEC-traces before and after the stability assay. (B) ¹H-NMR spectra of the CC monomer before and after the test. The figure was reprinted from ref.³⁹² with permission of the Royal Chemical Society. 100
- Figure 4-17. Small molecule test reaction utilizing CC monomer in combination with diethyl fumarate F (A) SEC of the adduct. (B) ESI-MS spectrum and (C) ¹H-NMR of the crude spectrum demonstrating residual resonances of F (*). Full assignment of the signals in (D). Spectrum was recorded in CD₂Cl₂. The figure was reprinted from ref.³⁹² with permission of the Royal Chemical Society. 101
- Figure 4-18. (A) SEC traces of the SG polymerization utilizing monomers CC and BB, investigating varying concentration conditions as indicated in the legend. (B) SEC-traces of SG polymers Q1 obtained by polymerization with different stoichiometries *r* of CC/BB as indicated in the plot. Reaction conditions: *c* = 0.2 mol·L⁻¹ in DCM after 12 h. The figure was reprinted from ref.³⁹² with permission of the Royal Chemical Society. 103
- Figure 4-19. (A) THF-SEC traces of SG polymers Q1 (*r* = 1.2) with increasing reaction times. SG polymerization conditions: *c* (CC) = 0.2 mol·L⁻¹, *c* (BB) = 0.17 mol·L⁻¹, solvent CD₂Cl₂, *T* = 25 °C. *M_w* and *M_n* as well as dispersities, *Đ*, are listed in Appendix 8.2.1, Table 8-6. (B) NMR spectra of Q1 recorded at *t*₀, 1 h and 20 h in CD₂Cl₂. Areas highlighted in orange depict fumarate resonances at 6.84 ppm, areas highlighted in green show the resonances of the trithiocarbonates α-proton at 4.77 ppm (for assignment refer to Figure 4-17). Areas highlighted in blue belong to Cp double bond resonances of monomer CC, as well as the product double bond of Q1. (C) Kinetic data of the SG with a stoichiometry of *r* = 1.2. Conversion is calculated by evaluating the integrals of the fumarate to the α-protons resonances of the trithiocarbonate in the ¹H-NMR spectra. (D) Carothers plot illustrating the evolution of *M_w* with fumarate conversion of the SG polymerization (evolution of *M_n* in Appendix 8.2.1, Figure 8-12). The figure was adapted from ref.³⁹² with permission of the Royal Chemical Society. 104
- Figure 4-20. ESI-HCD-MS spectrum of the SG polymer Q1 (*r* = 1.2). The spectrum was recorded in HCD mode, employing an energy of 10 eV to the target signal at *m/z* =

- 2022, triggering the retro DA reaction. The CC monomer cannot be detected due to poor ionization behavior. A solvent mixture of 3/2 THF/MeOH (V/V) and doping with sodium trifluoroacetate was applied. The figure was adapted from ref.³⁹² with permission of the Royal Chemical Society..... 104
- Figure 4-21. (A) ¹³C-NMR spectrum of the SG polymer Q1 ($r = 1.2$), showing the resonance of the trithiocarbonate at 219 ppm (red box). The spectrum was recorded in CDCl₃. (B) UV-VIS spectra of the SG polymer ($r = 1.2$) and the monomers CC and BB. The spectra were recorded in DCM, at the following concentrations: $c(Q1) = 24 \mu\text{mol}\cdot\text{L}^{-1}$, $c(CC) = 37 \text{mmol}\cdot\text{L}^{-1}$, $c(BB) = 84 \mu\text{mol}\cdot\text{L}^{-1}$. Characteristic absorbance of CS₃ at approx. 303 nm. The inset picture illustrates the SG polymer Q1 dissolved in DCM, demonstrating the commonly yellow color of the CS₃ moiety. (C) Reaction scheme of DA reaction, generating the test molecule for the analysis of the retro-DA reaction in high-temperature NMR at 60 °C. 2.3 eq. of the mono-Cp molecule are employed in the DA reaction. (D) ¹H-NMR spectra of the Cp-BB-Cp at t_0 and 110 min, observing no retro DA products. Spectra were recorded in toluene-d₈ at 60 °C. The NMR tube was permanently kept in the instrument during the analysis. The figure was adapted from ref.³⁹² with permission of the Royal Chemical Society..... 106
- Figure 4-22. (A) $-\ln(1-p)$ vs. reaction time of the RAFT polymerization. Data was obtained by gravimetric evaluation. (B) Molecular weight distribution development of RAFT polymers Q2 derived from the mCTA Q1, time as indicated in the legend. (C) Evolution of M_n with conversion of the RAFT polymerization (styrene in bulk, AIBN ($c = 1 \text{mmol}\cdot\text{L}^{-1}$), $T = 60 \text{ }^\circ\text{C}$, $c(\text{RAFT}) = 5 \text{mmol}\cdot\text{L}^{-1}$), the line is only for guiding the eye. Molecular weights (M_n and M_w) as well as \bar{D} can be found in Chapter 8.2.2 Table 8-8. (D) Evolution of \bar{D} with conversion. The line is only for guiding the eye. The figure was adapted from ref.³⁹² with permission of the Royal Chemical Society. 107
- Figure 5-1. Amino acid sequence of the CRD with folding procedure to obtain three intramolecular disulfide bonds as indicated. Misfolding, i.e. other disulfide patterns, is neglected. ESI-MS spectra of the CRD in folded state (B) full spectrum and (C) zoom in with simulation overlay of single charged unimer and double charged dimer. The spectra were recorded in MeCN/H₂O mixture with the addition of 1% acetic acid. 113
- Figure 5-2. ESI-MS spectra of the CRD-alkyne (A) full and (B) zoom-in with simulated isotopic pattern overlay in (B). ESI-MS spectra of the CRD-fumarate (C) full and (D) zoom-in with simulation overlay. ESI-MS spectra of the CRD-tetrazole (E) full and

- (F) zoom-in with simulation overlay. All spectra were recorded via direct infusion experiments with MeCN/H₂O as solvent mixture and doping with 1% acetic acid (experimental data in Chapter 7.5.2). 117
- Figure 5-3. (A) Synthesis of bromide bearing PFP molecule. (B) Functionalization of folded CRD with bromide-PFP anchor molecule. Equivalents: CRD folded: 1 eq.; PFP-bromide: 2 eq.; DIPEA: 2 eq. ESI-MS spectra of the CRD-bromide (C) full spectrum and (D) zoom-in with single-charged simulated isotopic pattern and dimerized double-charged product. 118
- Figure 5-4. ESI-MS spectra of the bioorthogonal reaction products (red) and the functional CRD derivatives (black), as introduced in Scheme 5-4 (A) CuAAC adduct and CRD-alkyne, (B) NITEC adduct after the 2nd addition of tetrazole and CRD-fumarate, (C) “inverse” NITEC adduct and CRD-tetrazole, (D) DA adduct after second addition of the Cp-molecule and CRD-fumarate. All spectra were recorded via direct-infusion experiments, employing MeCN/H₂O as solvent mixture with doping of 1% acetic acid. 121
- Figure 5-5. (A) Molecular weight distribution of the diazido-PDMAA Y1 obtained by DMAc-SEC, applying a polystyrene calibration. $M_n = 13,900 \text{ g}\cdot\text{mol}^{-1}$, $\mathcal{D} = 1.08$ (B) ESI-MS spectrum of the diazido polymer Y1 depicting the repeating units of the corresponding polymer species as indicated. $[\text{P}_{53} + 2\text{Na}]^{2+}_{\text{exp}}$: 2873.8922; $[\text{P}_{53} + 2\text{Na}]^{2+}_{\text{calc}}$: 2873.8583. The ESI-MS direct infusion experiment was performed with THF/MeOH as solvent and sodium trifluoroacetic acid as doping agent.... 124
- Figure 5-6. (A) Reaction scheme of the CuAAC reaction between the diazido-PDMAA Y1 and the CRD-alkyne yielding the bioconjugate BC1. Reaction conditions: 4.7 eq. CRD-alkyne, 4.4 eq. CuBr, 4.4. eq. PMDETA; 1.0 eq. diazido PDMAA Y1 in DMF under inert gas atmosphere for 66 h. (B) SEC-traces of the diazido-PDMAA (black) and the CuAAC bioconjugate product BC1 (red). Measurement was conducted in DMAc-SEC. (C) Western blots of the CRD-bioconjugate BC1 (1), the folded CRD (2), and a concentrated CRD-species (3) after separation via SDS-PAGE. Antibodies: anti-C-CRD (primary) and donkey-anti-guinea pig (secondary)..... 125
- Figure 5-7. ESI-MS spectra of the (A) Tetrazole functional PEG Y2, (B) NITEC adducts BC2 of the CRD-fumarate and the tetrazole-PEG after irradiation with following conditions: (black): 1 eq. CRD-fumarate, 1 eq. Tet-PEG Y2, in water/MeCN 9/1 V/V, irradiation for 2 h. (Red): 1 eq. CRD-fumarate, 1 eq. Tet-PEG Y2, in water, irradiation for 1 h, addition of 0.01 M NaOH. (Blue): 1.00 eq. CRD-fumarate, 0.75 eq. Tet-PEG Y2, in water/MeCN (1/9 V/V), irradiation for 1 h, addition of DIPEA. (C) SEC-traces of the tetrazole functional PEG Y2 before irradiation (black) and the

bioconjugate BC2 after NITEC reaction upon irradiation (red, with addition of NaOH). Irradiation was carried out for 1 h.	128
Figure 5-8. ToF-SIMS ion maps of the consecutively conducted photo-induced surface immobilization as illustrated in Scheme 5-8. (A) Surface after PEG attachment via the NITEC reaction, representing the fragment $C_2H_5O^-$. (B) Surface after CRD-fumarate immobilization via the NITEC reaction, representing the fragment $C_2H_5O^-$. (C) Surface after CRD-fumarate immobilization via the NITEC reaction, representing the sum of S^- , HS^- , S_2^- fragments. The figure was adapted from ref. ²⁵⁸ with permission from the Royal Chemical Society.	133
Figure 5-9. ToF-SIMS ion maps of the encoded surfaces as illustrated in Scheme 5-8. (A) Surface after CRD-bromide immobilization, representing the sum of $^{81}Br^-$, $^{79}Br^-$ fragments. (B) Surface after CRD-bromide immobilization, representing the sum of S^- , HS^- , S_2^- secondary ions. ToF-SIMS spectra of A-B are depicted Figure 5-11A (bromine) and B (sulfur). The figure was adapted from ref. ²⁵⁸ with permission from the Royal Chemical Society.....	134
Figure 5-10. ToF-SIMS ion maps of the erased surfaces as illustrated in Scheme 5-8. (A) Surface after CRD-bromide removal, representing the sum of $^{81}Br^-$, $^{79}Br^-$ fragments. (B) Surface after CRD-bromide removal, representing the sum of S^- , HS^- , S_2^- fragments. ToF-SIMS spectra of A-B are depicted Figure 5-11A (bromine) and B (sulfur). The figure was adapted from ref. ²⁵⁸ with permission from the Royal Chemical Society.....	135
Figure 5-11. ToF-SIMS spectra of (A) $^{79}Br^-$ fragment, $m/z = 78.92$ (peak indicated with red arrow) with primary ion dose normalization (related to the mappings in Figure 5-9A (black) and Figure 5-10A (red)). (B) ToF-SIMS spectra of the main sulfur signal, $m/z = 31.97$, with primary ion dose normalization (related to the mappings in Figure 5-9B (black) and Figure 5-10B (red)). The figure was adapted from ref. ²⁵⁸ with permission from the Royal Chemical Society.....	136
Figure 7-1. Schematic setup of the photoreactor used in this study. The samples are placed in the holder and rotated during the irradiation. ²⁶⁶	147
Figure 7-2. Emission spectrum of the lamp Cosmedico ARIMED B6.	147
Figure 7-3. Emission spectrum of the lamp iSOLde Cleo Compact PL-L 36 W.....	148
Figure 7-4. Assembly of the sample holder for the photo-induced spatially resolved surface immobilization. A: Individual parts disassembled, B: Surface and photomask placed onto the sample holder. C: Sample holder fully assembled with the photomask mounted onto the silicon wafer.	148
Figure 7-5. 1H -NMR spectrum of S,S-(dipropyl)trithiocarbonate (DTC). The spectrum was recorded in $DMSO-d_6$	151

Figure 7-6. ^{13}C -NMR spectrum of S,S-(dipropyl)trithiocarbonate (DTC). The spectrum was recorded in DMSO- d_6 .	151
Figure 7-7. ^1H -NMR spectrum of S,S-di((2-methyl)propionic acid) trithiocarbonate (TRITT). The spectrum was recorded in DMSO- d_6 .	152
Figure 7-8. ^{13}C -NMR spectrum of S,S-di((2-methyl)propionic acid) trithiocarbonate (TRITT). The spectrum was recorded in DMSO- d_6 .	153
Figure 7-9. ^1H -NMR spectrum of di(isopropionic acid ethyl-ester ethyl fumarate) trithiocarbonate (BB monomer). The spectrum was recorded in CDCl_3 .	154
Figure 7-10. ^{13}C -NMR spectrum of di(isopropionic acid ethyl-ester ethyl fumarate) trithiocarbonate (BB monomer). The spectrum was recorded in CDCl_3 .	154
Figure 7-11. ESI-MS spectrum of the RAFT difumarate BB monomer. The spectrum was recorded via a direct-infusion experiment in THF/MeOH (3/2, V/V) by doping with sodium trifluoroacetate.	155
Figure 7-12. ^1H -NMR spectrum of the diazido-RAFT agent. The spectrum was recorded in DMSO- d_6 .	156
Figure 7-13. ^{13}C -NMR spectrum of the diazido-RAFT agent. The spectrum was recorded in DMSO- d_6 .	156
Figure 7-14. ESI-MS spectrum of the diazido-RAFT agent. The spectrum was recorded via direct-infusion experiment in THF/MeOH (3/2, V/V) by doping with sodium trifluoroacetate.	157
Figure 7-15. ^1H -NMR spectrum 2-methoxy-5-methyl benzaldehyde. The spectrum was recorded in CDCl_3 .	158
Figure 7-16. ^1H -NMR spectrum of 2-hydroxy-5-methyl benzaldehyde. The spectrum was recorded in CDCl_3 .	159
Figure 7-17. ^1H NMR spectrum of 6'-(propane-1,3-diylbis(oxy))bis(2-methyl benzaldehyde) (AA monomer). The spectrum was recorded in CDCl_3 .	161
Figure 7-18. ^{13}C -NMR spectrum of 6'-(propane-1,3-diylbis(oxy))bis(2-methyl benzaldehyde) (AA monomer). The spectrum was recorded in CDCl_3 .	161
Figure 7-19. ESI-MS spectrum of the 6'-(propane-1,3-diylbis(oxy))bis(2-methyl benzaldehyde) (AA monomer). The spectrum was recorded via direct-infusion experiment in THF/MeOH (3/2, V/V) by doping with sodium trifluoroacetate.	162
Figure 7-20. ^1H -NMR spectrum of 4-((2-tosylhydrazono)methyl)benzoic acid. The spectrum was recorded in DMSO- d_6 .	163
Figure 7-21. ^1H -NMR spectrum of methoxy-tetrazole acid. The spectrum was recorded in DMSO- d_6 .	164
Figure 7-22. ^1H -NMR spectrum of tetrazole-acid pentafluorophenol ester. The spectrum was recorded in CDCl_3 .	165

Figure 7-23. ^{19}F -NMR spectrum of tetrazole-acid pentafluorophenol ester. The spectrum was recorded in CDCl_3 .	165
Figure 7-24. ^1H -NMR spectrum of tetrazole-acid 1,3-propanediol ester. The spectrum was recorded in CDCl_3 .	166
Figure 7-25. ^{13}C -NMR spectrum of tetrazole-acid 1,3-propanediol ester. The spectrum was recorded in CDCl_3 .	167
Figure 7-26. ^1H -NMR spectrum of ethyl-fumarate pentafluorophenol ester. The spectrum was recorded in CDCl_3 .	168
Figure 7-27. ^{19}F -NMR spectrum of ethyl-fumarate pentafluorophenol ester. The spectrum was recorded in CDCl_3 .	168
Figure 7-28. ^1H -NMR spectrum of 2-bromo-2-methyl propionic acid pentafluorophenol ester. The spectrum was recorded in CDCl_3 .	169
Figure 7-29. ^{19}F -NMR spectrum of 2-bromo-2-methyl propionic acid pentafluorophenol ester. The spectrum was recorded in CDCl_3 .	170
Figure 7-30. ^1H -NMR spectrum of 5-hexynoic acid pentafluorophenol ester. The spectrum was recorded in DMSO-d_6 .	171
Figure 7-31. ^{19}F -NMR spectrum of 5-hexynoic acid pentafluorophenol ester. The spectrum was recorded in DMSO-d_6 .	171
Figure 7-32. ^1H -NMR spectrum of 1,10-di(cyclopentadienyl)-decane (CC monomer). The spectrum was recorded in CD_2Cl_2 .	172
Figure 7-33. ^{13}C -NMR spectrum of 1,10-di(cyclopentadienyl)-decane (CC monomer). The spectrum was recorded in CDCl_3 .	173
Figure 7-34. ^1H -NMR spectrum of 2-hydroxyethyl-ethyl fumarate. The spectrum was recorded in DMSO-d_6 .	174
Figure 7-35. ^{13}C -NMR spectrum of 2-hydroxyethyl-ethyl fumarate. The spectrum was recorded in CDCl_3 .	175
Figure 7-36. ESI-MS spectrum of 2-hydroxyethyl-ethyl fumarate. The spectrum was recorded via a direct-infusion experiments using a solvent mixture of THF/MeOH (3/2, V/V) by doping with sodium trifluoroacetate.	175
Figure 7-37. ^1H -NMR spectrum of ((11-bromoundecyl)oxy)(tert-butyl)dimethylsilane (precursor of Mono-Cp). The spectrum was recorded in CDCl_3 .	177
Figure 7-38. ^{13}C -NMR spectrum of ((11-bromoundecyl)oxy)(tert-butyl)dimethylsilane (precursor of Mono-Cp). The spectrum was recorded in CDCl_3 .	177
Figure 7-39. ^1H -NMR spectrum of tert-butyl((11-(cyclopenta-1,3-dien-1-yl)undecyl)oxy)dimethylsilane (Mono-Cp). The spectrum was recorded in CDCl_3 .	179

- Figure 7-40. ^{13}C -NMR spectrum of tert-butyl((11-(cyclopenta-1,3-dien-1-yl)undecyl)oxy)dimethylsilane (Mono-Cp). The spectrum was recorded in CDCl_3 179
- Figure 7-41. ^1H -NMR spectrum of poly(dimethyl acrylamide) with α,ω -functional azido groups. The spectrum was recorded in DMSO-d_6 184
- Figure 7-42. ESI-MS spectrum of the CRD in reduced state as starting material for the folding. The spectrum was recorded in $\text{MeCN}/\text{H}_2\text{O}$ mixture with the addition of 1% acetic acid..... 186
- Figure 8-1. ESI-MS spectra of the di(ortho-methyl benzaldehyde) AA monomer stability assay. The spectra were recorded in direct-infusion experiments in THF/MeOH (3/2, V/V) by doping with sodium trifluoroacetate. A shift of - 2 and -18 m/z, respectively, from the main product of each repeating unit can be observed.... 212
- Figure 8-2. ESI-spectra of small molecule model reactions, employing BB monomer with diethyl fumarate (F) in different stoichiometries as indicated in the spectra. The samples were injected without any purification of the crude product after 6 h of irradiation. The spectra were recorded via direct-infusion experiments in THF/MeOH (3/2, V/V) by doping with sodium trifluoroacetate..... 212
- Figure 8-3. ^1H -NMR spectra of the small molecule experiment of diethyl fumarate (F) and di(ortho-methyl benzaldehyde) AA in DCM-d_2 before and after irradiation at different stoichiometries r of the functional groups. The blue area indicates the area of the aromatic (1, 2, 3 and 1', 2', 3') and the fumarate protons (d/c), respectively..... 213
- Figure 8-4. ^1H -NMR spectra of kinetic run of step-growth polymerization of AA and BB with $r = 1.75$. The spectra were recorded in DCM-d_2 after irradiation without any further purification or dilution. 213
- Figure 8-5. ^1H -NMR spectra of kinetic run of step-growth polymerization of AA and BB with $r = 1$. The spectra were recorded in CDCl_3 after irradiation without any further purification or dilution. 214
- Figure 8-6. ESI-MS spectra of a typical SG polymer with an AA/BB monomer stoichiometry of $r = 1$ at different m/z ranges, including the assignment of the observed polymer species. The spectra were recorded via direct-infusion experiments in THF/MeOH (3/2, V/V) by doping with sodium trifluoroacetate..... 214
- Figure 8-7. UV-VIS spectra of the monomers AA and BB and corresponding step-growth polymers SGP with different monomer stoichiometries $r = 1$ and $r = 2$ (refer to legend), recorded in DCM . Concentrations: $c(\text{AA}) = 101 \mu\text{mol}\cdot\text{L}^{-1}$, $c(\text{BB}) = 26 \mu\text{mol}\cdot\text{L}^{-1}$, $c(\text{SGP } r = 1) = 96 \mu\text{mol}\cdot\text{L}^{-1}$, $c(\text{SGP } r = 2) = 59 \mu\text{mol}\cdot\text{L}^{-1}$ 215

- Figure 8-8. (A) Comparison of the experimental and simulation data for the RAFT polymerization for (a) styrene conversion vs. time and (B) mass-average chain length vs. styrene conversion. (C) mass chain length distribution for different styrene conversions; $[\text{Styrene}]_0=8.74 \text{ mol}\cdot\text{L}^{-1}$, $[\text{I}_2]_0=4.85\cdot 10^{-3} \text{ mol}\cdot\text{L}^{-1}$ 216
- Figure 8-9. Mass chemical composition chain length distribution for different styrene conversions: (a) 0.00, (b) 0.01, (c) 0.04, (d) 0.07; the x-axis represents the chain length (represented by the number of A, B and C units), the y-axis represents the composition (represented by the number of RAFT groups) and the colors represent the mass fraction of chains; $[\text{Styrene}]_0=8.74 \text{ mol}\cdot\text{L}^{-1}$, $[\text{I}_2]_0=4.85\cdot 10^{-3} \text{ mol}\cdot\text{L}^{-1}$. Precursor polymer with stoichiometry of $r = 1$ 217
- Figure 8-10. Concentration of dead chains in $\text{mol}\cdot\text{L}^{-1}$ vs. styrene conversion..... 217
- Figure 8-11. $^1\text{H-NMR}$ spectra of the SG polymerization kinetics. All measurements were recorded in CD_2Cl_2 . The blue box highlights the fumarate resonances, the red box highlights the resonances of the α -proton to the trithiocarbonate..... 219
- Figure 8-12. Carothers plots of the SG polymerization with a monomer stoichiometry of $r = 1.2$, M_n vs. conversion. Conversion was obtained by evaluation of $^1\text{H-NMR}$ spectra of corresponding samples, referencing the integrals of the fumarate resonances to the unchanged α -protons of the trithiocarbonate. M_n and M_w values were determined by THF-SEC applying a polystyrene calibration. 220
- Figure 8-13. ESI-MS spectra of the folded CRD before (black) and after (red) exposure to CuBr with PMDETA and L-arginine. The spectra were recorded in $\text{H}_2\text{O}/\text{MeCN}$ with 1% acetic acid as doping agent. 222
- Figure 8-14. HPLC elugram of the CRD-bromide in an analytic measurement. Isocratic solvent mixture was $\text{MeCN}/\text{H}_2\text{O}$ (10/90, V/V) with addition of 0.1% trifluoro acetic acid (TFA). 223
- Figure 8-15. HPLC elugram of the CRD-bromide in a semi-preparative measurement. Solvent mixture was $\text{MeCN}/\text{H}_2\text{O}$ 10/90 (V/V) with and 0.1% trifluoro acetic acid (TFA). The box represents the elution of the sample taken for ESI-MS in Figure 8-16..... 223
- Figure 8-16. ESI-MS spectrum of the collected sample, as indicated in Figure 8-15. The main signal can be assigned to the folded CRD but not to the CRD-bromide. Spectrum was recorded in $\text{MeCN}/\text{H}_2\text{O}$ mixture with 1% acetic acid as doping agent. 224
- Figure 8-17. Surface after immobilization of the CRD-fumarate and the PEG-fumarate. ToF-SIMS overlay of the signals from S^- , HS^- , S_2^- (green), $\text{C}_2\text{H}_5\text{O}^-$ (blue). 224

Figure 8-18. Surface after attaching the CRD-bromide to the surface. ToF-SIMS overlay of Sum of $^{81}\text{Br}^-$, Br^- (red), $\text{C}_2\text{H}_5\text{O}^-$ (blue)..... 224

8.7 List of Schemes

Scheme 3-1. Cationic polymerization upon initiation with IX of the monomer M.	7
Scheme 3-2. Conventional initiators in cationic polymerization (clockwise): Photo acid generators (PAG), Lewis acids, and oxonium ions.	7
Scheme 3-3. Monomers applicable for cationic polymerization. Monomers in the top row are employed in industrial scale, whereas the monomers in the bottom row are employed in other polymerization techniques on industrial scale.	8
Scheme 3-4. Termination reactions in cationic polymerization. Counterion recombination, counterion cleavage, and formation of unreactive chain ends.	9
Scheme 3-5. Transfer reactions in cationic polymerization. Proton transfer to the monomer, hydride transfer to the polymer, and proton elimination at the active chain end.	9
Scheme 3-6. Controlled cationic polymerization of vinyl ether (top) and isobutylene (bottom). ^{35,37}	10
Scheme 3-7. Anionic polymerization of styrene with sec-butyl lithium as initiator.	11
Scheme 3-8. Typical monomers in anionic polymerization, featuring styrene derivatives, dienes, vinylpyridines, (meth)acrylates, acrylamides, acrylonitrile, or cyclic monomers such as siloxanes, lactones, lactames, and epoxides.	12
Scheme 3-9. Sequential anionic polymerization of styrene and MMA. After consumption of styrene, the chain ends are decorated with DPE in order to reduce the chain end reactivity. ⁴⁵	12
Scheme 3-10. Different states of ions at active chain-end in anionic polymerization of styrene. With: $k_{\pm,c}$: propagation coefficient for contact ion-pairs; $k_{\pm,s}$: propagation coefficient for solvent separated ion-pairs; k : propagation coefficient for free ion-pairs. With: $k_{\pm,c} \ll k_{\pm,s} < k$. ³⁶	13
Scheme 3-11. Influence of the solvents polarity on the microstructure of polybutadiene. Anionic polymerization of 1,3-butadiene with lithium cation: Top: Polymerization in polar medium yields 1,2-polybutadiene. Bottom: Polymerization in unpolar medium yields 1,4-polybutadiene (only cis shown). ⁴⁶	14
Scheme 3-12. Aggregation of chain ends and dissolving aggregates by THF addition forming monoetherate complexes.	15
Scheme 3-13. General radical polymerization mechanism: (I) Initiator decay (here homolytic cleavage) and (II) initiation of the polymerization by addition of the radical initiator I to the double bond of the monomer M. (III) Propagation of the polymerization with further vinyl monomer units M. (IV) Transfer of the radical by transfer agent, solvent, or dead chain X. (Va) Termination via recombination, (Vb)	

termination via disproportionation of two active chains reacting, yielding a saturated and an unsaturated polymer chain.	16
Scheme 3-14. Selection of important polymers generated from radical polymerization processes.....	19
Scheme 3-15. Fundamental mechanism of atomic transfer radical polymerization (ATRP). ⁶⁴	21
Scheme 3-16. Fundamental mechanism of nitroxide-mediated polymerization (NMP). ⁶⁰	22
Scheme 3-17. Mechanism of RAFT polymerization described in five steps. (I) Decomposition of the initiator I, reacting with a monomer unit M to start the propagating chain P _n [•] . (II) In the pre-equilibrium (a) all initiated polymer chains are added to a RAFT group. (b) R-group is eliminated in order to start further chains. (III) During propagation, polymer chains in active state add monomer units. (IV) In the core-equilibrium the propagating chain P _n is added to the RAFT group and the polymer radical P _m is eliminated. (V) Termination by e.g. recombination. ⁸⁶	24
Scheme 3-18. Fundamental structural elements of RAFT agents. Different variations of R- and Z-groups are shown on the right side with respect to the according RAFT group type, indicated by the color. ⁸¹	26
Scheme 3-19. Trithiocarbonates as symmetric RAFT groups, showing symmetric fragmentation (red) depending on the CTAs structure, e.g. for symmetric S,S-dibenzyl trithiocarbonate (DiBent). Regular RAFT fragmentation for asymmetric trithiocarbonate 2-(dodecylthiocarbonylthio)-propionic acid (DoPAT) in black. ...	27
Scheme 3-20. Cross table of RAFT agents and suitable monomers for RAFT polymerization. ♦: suitable, •: not suitable.....	28
Scheme 3-21. Selection of RAFT agents with unprotected orthogonal functional groups at the R- and Z-group, as indicated. ^{97,98,100,101,105,107,108}	28
Scheme 3-22. Examples of the postmodification of RAFT groups: Ligation (left) by thermal and photo-induced DA reaction, and RAFT group removal (right) via aminolysis, oxidation or thermal treatment. ^{128,134,153-156}	30
Scheme 3-23. RAFT polymers in postmodification aminolysis and thiol-ene reaction. ¹³¹	31
Scheme 3-24. SG polymerization of an AA/BB (top) and SG or ROP of an AB (bottom) monomer system. The AB monomer system yields PA 6, whereas the AA/BB monomer system yields PA 6.6.	33
Scheme 3-25. Reversible nature of a polyesterification reaction with the equilibrium constant K.....	34
Scheme 3-26. Polymerization of monomers, dimers, and n, m-mers to form oligomeric species. ³²	34

Scheme 3-27. Tetra- and trimers during SG polymerization of adipic acid and 1,6-hexamethylenediamine, undergoing cyclization in case of tetramers. The trimer cannot form a cycle, due to missing functional site.	37
Scheme 3-28. Cyclization and depolymerization of polysiloxanes by backbiting yielding small cyclic siloxanes.	38
Scheme 3-29. Polymers prepared via SG polymerization by polycondensation or polyaddition reactions. ¹⁷³	39
Scheme 3-30. Most elemental case of the DA cycloaddition of a 1,3-dibutadiene as the diene and ethylene as dienophile, forming cyclohexene as the unsaturated six-membered ring.	41
Scheme 3-31. DA reactions unraveled by O. Diels and K. Alder. ^{186,188}	41
Scheme 3-32. Attack of double bonds in DA reaction leading to a pseudo transition state and the final formation of the product (top part). Formation of endo/exo adduct upon DA reaction of cyclopentadiene and methyl acrylate (bottom part). ¹⁸⁵	43
Scheme 3-33. HDA and rHDA of a di(sorbyl)derivative and a phosphoryl dithioesters forming the SG polymer upon addition of ZnCl ₂ as catalyst at elevated temperatures and depolymerizing the polymer at high temperatures. ¹²⁶	45
Scheme 3-34. Cyclopentadienyl and dithioester as components in self-healing materials based on a HDA and retro-HDA reaction. ¹⁵³	45
Scheme 3-35. Bonding/debonding on demand by employing a retro HDA reaction. Debonding is evidenced by the occurrence of a reddish color from the free phosphoryl-dithioester. ¹⁹⁶	46
Scheme 3-36. Cleavage of benzoin upon irradiation in a Norrish type I reaction forming the highly reactive benzoyl (A) and the less reactive benzyl alcohol (B) radical. .	48
Scheme 3-37. Aryl substituted tetrazole dissociation upon irradiation. Substituents at C- and N-termini influence the dissociation wavelength.	49
Scheme 3-38. Reactions of tetrazoles after dissociation upon irradiation to the 1,3-nitrile-imine dipole intermediate reacting with water, thiols, double bonds - usually substituted with electron withdrawing groups R ₄ (NITEC) - carboxylic acids (NICAL) and imidazoles (clockwise order).	50
Scheme 3-39. Photo-induced diene formation of different photoreactive compounds. A subsequent trapping of the formed species usually comprises electron deficient dienophiles, such as maleimides, fumarates or acrylates.	52
Scheme 3-40. Mechanism suggested by Porter of photoenol activation and relaxation upon irradiation and corresponding lifetimes τ valid given for reactions in cyclohexane. ²⁷⁶	53

- Scheme 3-41. Possible side reactions known for ortho-methyl benzaldehydes, benzo/acetophenons and derivatives. 54
- Scheme 3-42. Deactivation of the photoreactivity of photoenols based on ortho-methyl benzaldehyde derivatives with amines.²⁸⁰ 54
- Scheme 3-43. Photo-induced ligation techniques: Phenacyl and pyreneacyl sulfides yield thioaldehydes and subsequent reaction with cyclopentadiene. Azirines yield nitrile ylides upon irradiation and are trapped with electron deficient enes. Coumarin and anthracene dimerization upon irradiation with corresponding wavelength regime and retro reaction at shorter wavelengths (from top to bottom).^{271,272,301,302,304} 55
- Scheme 3-44. General constitution of α -amino acids (left behalf). Glycine as simplest example of an α -amino acid, L- and D-alanine as example for enantiomers of α -amino acids (center, top row). L-proline, a cyclic amino acid with a secondary amine, L-cysteine with a thiol- and L-arginine with a guanidine group (center, bottom row). General protein backbone with the peptide bond and residual R (right behalf)..... 58
- Scheme 3-45. Fundamental reaction scheme of the solid phase peptide synthesis (SPPS) referred to as Merrifield peptide synthesis.³²³ An N-protected amino acid (A) is attached to a solid support via the C-terminus, (B), and deprotected from Z to obtain the free amine, (C). Z represents a protecting group that can be cleaved under gentle conditions, e.g. urethanes, in contrast to P_x that entails a permanent specific protection of the side residual and has to be stable under the amidation coupling conditions. Then, a second activated N-protected amino acid (D) is added in high concentrations and coupled via amide formation to yield the dimer or n-mer (E) attached to solid support. Capping as part of the procedure is not included in the scheme, as the capping concerns faulty sequences only. After washing, the cycle starts again to finally yield the protected peptide (F) with the corresponding sequence with a length $n+1$. After deprotection of Z, the peptide is released from the solid support and all permanent protecting groups are cleaved to obtain the final protein/peptide (G). Here, the deprotection of Z can also cause deprotection of labile P_x groups.³²⁶ 61
- Scheme 3-46. List of nucleobases (left behalf), nucleoside of deoxyribose and cytosine (middle, center) and nucleotide of deoxyribose and cytosine monophosphate (bottom, center). Right-hand side: Base pairs of nucleobases of adenine (A) and thymine (T) in DNA and guanine (G) and cytosine (C) by hydrogen bonds (dotted lines). 62

Scheme 3-47. Exemplary structural motifs of CRDs: Left: N-CRD in reduced state (GPCGSYCPSVCAPACAPVCCA). Right: C-CRD in reduced state (GPCPPVCVAQCVPPTCPQYCCPA).....	65
Scheme 3-48. Active ester chemistry in trans(thio)esterification and transamidation reactions by condensation of NHS-derivatives and PFP active esters (left behalf). Ring-opening reactions for azlactones forming diamides and amido-(thio)esters (right behalf). ^{102,358–360}	67
Scheme 3-49. Alkylation (top) and further acylation compounds (bottom), besides active esters addressing amine moieties of peptides. ³⁴⁷	68
Scheme 3-50. Exemplary reactions for bioconjugation, such as traceless Staudinger ligation (top), Paternò-Büchi [2+2] cycloaddition of modified cellulose (center), and tetrazine/cyclopropene based inverse electron demand DA reaction (bottom). ^{366,371,370}	69
Scheme 3-51. 1,3-dipolar cycloadditions, either Cu ^I catalyzed (top) or strain-promoted (bottom). ^{347,367}	69
Scheme 4-1. Synthesis and introduction of AA and BB monomers.....	80
Scheme 4-2. (A) Main reaction pathway for photo-induced SG polymerization employing di(ortho-methyl benzaldehyde) monomer AA in combination with the difumarate-RAFT monomer BB yielding P1. Isomers are omitted for simplicity. (B) Photo-induced dimerization of monomer AA, undergoing AA homopolymerization yielding P2; the DA self-reaction occurs after activation to the intermediate state A(*)A*; P2 or AA oligomer species can also follow the main reaction (k_{main}) pathway, leading to random copolymer with undefined sequences of (AA) _k AABB. (C) RAFT polymerization employing SG polymer P1 as multi-CTA for segmented copolymer synthesis. For simplicity, only one example of the constitutional isomers of the different polymers is illustrated.	81
Scheme 4-3. RAFT polymerization employing the SG polymer P1 as multi-CTA to obtain the segmented copolymer P3.	93
Scheme 4-4. Schematic illustration of the SG polymerization via DA reaction and subsequent RAFT polymerization. The figure was reprinted from ref. ³⁹² with permission of the Royal Chemical Society	98
Scheme 4-5. Design of the monomers CC and BB for the thermally induced DA SG polymerization.	99
Scheme 4-6. Small molecule study using the CC monomer in combination with diethyl fumarate F. Due to the different constitutional isomers of CC in total four different isomers can be obtained, of which two are illustrated here.....	100
Scheme 4-7. Thermal DA reaction for SG polymerization yielding the multi-CTA Q1. .	102

Scheme 4-8. RAFT polymerization of styrene utilizing the SG polymer Q1 as multi-CTA yielding segmented copolymer Q2.	105
Scheme 5-1. Concept overview of CRDs as polymerization tool in biomimetic material design. (A) Bioconjugation reaction, attaching the CRD to an α,ω -functional polymer, affording the macromonomer. (B) SG polymerization exploiting the disulfide reshuffling of the CRDs to form disulfide bonds between the polymer-peptide bioconjugates.	112
Scheme 5-2. Synthesis of active ester molecules bearing ligation moieties for photo- and thermally induced reactions such as alkynes, tetrazoles, and fumarates.	115
Scheme 5-3. Introduction of anchor groups by PFP active ester chemistry, yielding functional CRDs as indicated. Equivalents: CRD-fumarate: CRD folded: 1 eq.; PFP-fumarate: 2 eq; DIPEA: 2 eq. CRD-tetrazole: CRD folded: 1 eq.; PFP-tetrazole: 1.4 eq.; DIPEA: 1.4 eq. CRD-alkyne: CRD folded: 1 eq.; PFP-alkyne: 1.25 eq.; DIPEA: 1.25 eq.	115
Scheme 5-4. Bioorthogonal reactions of functional CRD-derivatives with small molecules, forming the corresponding adducts. From top to bottom: (I) CuAAC of CRD-alkyne with benzylazide. (II) NITEC of CRD-fumarate with a hydroxy functional tetrazole derivative. (III) "Inverse" NITEC of CRD-tetrazole with diethyl fumarate. (IV) Thermal DA reaction of CRD-fumarate with 3-cyclopentadienyl-methyl propionate.	120
Scheme 5-5. RAFT polymerization of N,N-dimethylacrylamide (DMAA) employing the diazido-RAFT agent in order to obtain poly(DMAA) Y1. Ratio DMAA:RAFT:AIBN of 1500:12:1. Solvent: 1,4-dioxane; T = 60 °C, t = 8 h.	124
Scheme 5-6. NITEC reaction between a Tet-PEG Y2 and the CRD-fumarate upon UV irradiation, yielding the bioconjugate BC2.	127
Scheme 5-7. Overview of the CRD functional surfaces and respective ToF-SIMS ion maps. The scheme was reprinted from ref. ²⁵⁸ with permission from the Royal Chemical Society.	131
Scheme 5-8. Illustration of the (1) immobilization of PEG-fumarate onto a tetrazole functionalized plain surface upon NITEC reaction. (2) Attachment of CRD-fumarate by NITEC reaction upon irradiation. (3) Immobilization of CRD-bromide by reoxidation and reshuffling of the disulfide bonds. (4) Removal of the CRD-bromide by reoxidation and reshuffling of the disulfide bonds. The scheme was adapted from ref. ²⁵⁸ with permission from the Royal Chemical Society.	132
Scheme 5-9. Illustration of the encoded surface showing the CRD-fumarate (green) attached covalently to the surface by the pyrazoline units. The CRD-bromide (red) linked by disulfide bond to the CRD-fumarate after a reoxidative reaction. The	

illustration portrays the state, which is shown in the ToF-SIMS ion map in Figure 5-9A and B. The figure was adapted from ref. ²⁵⁸ with permission from the Royal Chemical Society.....	135
Scheme 7-1. Synthesis of S,S-(dipropyl)trithiocarbonate (DTC).....	150
Scheme 7-2. Synthesis of S,S-di((2-methyl)propionic acid) trithiocarbonate (TRITT). .	151
Scheme 7-3. Synthesis of di(isopropionic acid ethyl-ester ethyl fumarate) trithiocarbonate (BB monomer).....	153
Scheme 7-4. Synthesis of the diazido-trithiocarbonate via acid chlorides.....	155
Scheme 7-5. Synthesis of 2-methoxy-5-methyl benzaldehyde by oxidation of 2,3-dimethylanisole.....	158
Scheme 7-6. Ether cleavage of 2-methoxy-5-methyl benzaldehyde yielding 2-hydroxy-5-methyl benzaldehyde.	159
Scheme 7-7. Williamson ether synthesis of 2-hydroxy-6-methyl-benzaldehyde (AA monomer).....	160
Scheme 7-8. Synthesis of 4-((2-tosylhydrazono)methyl)benzoic acid.....	162
Scheme 7-9. Generation of the diazonium salt towards the tetrazole synthesis.....	163
Scheme 7-10. Tetrazole formation from diazonium salt and sulfonyl hydrazide.....	163
Scheme 7-11. Esterification of tetrazole acid with pentafluorophenol.	164
Scheme 7-12. Esterification of tetrazole acid with 1,3-propanediol.....	166
Scheme 7-13. Esterification of monoethyl fumarate with pentafluorophenol.	167
Scheme 7-14. Esterification of 2-bromo-2-methyl propionic acid with pentafluorophenol.	169
Scheme 7-15. Esterification of hexynoic acid with pentafluorophenol.....	170
Scheme 7-16. Synthesis of 1,10-di(cyclopentadienyl)-decane monomer CC.....	172
Scheme 7-17. Synthesis of 2-hydroxyethyl-ethyl fumarate for BB synthesis.....	174
Scheme 7-18. Protection of 11-bromoundecan-1-ol with silyl-ether.....	176
Scheme 7-19. Synthesis of the tert-butyl((11-(cyclopenta-1,3-dien-1-yl)undecyl)oxy)dimethylsilane (Mono-Cp).....	178
Scheme 7-20. DA reaction of the monomer BB and the mono-Cp compound.	180
Scheme 7-21. Reaction scheme for the step-growth polymerization of AA and BB, forming the SG polymer.	181
Scheme 7-22. SG polymerization by DA reaction using monomer CC and BB in DCM at ambient temperature.	182
Scheme 7-23. RAFT polymerization of styrene using the SG polymer P1 as multifunctional CTA, obtained in a photo-induced SG polymerization ((AA) _k homopolymer segments not shown for simplicity).	182

Scheme 7-24. RAFT polymerization of styrene using the SG polymer Q1 as multifunctional CTA, obtained in a thermally induced SG polymerization.	183
Scheme 7-25. RAFT polymerization of DMAA with diazido-RAFT agent.	183
Scheme 7-26. Folding of the CRD by intramolecular thiol oxidation.	185
Scheme 7-27. Introduction of functional groups to the CRD by active ester chemistry using PFP ester molecules bearing a fumarate, bromide, tetrazole and alkyne group.	186
Scheme 7-28. Functionalization of the folded CRD with the fumarate and the bromide bearing active esters.	187
Scheme 7-29. Functionalization of the folded CRD with the alkyne bearing active ester.	188
Scheme 7-30. Functionalization of the folded CRD with the tetrazole bearing active ester.	188
Scheme 7-31. CuAAC of the CRD-alkyne and benzylazide using CuBr and PMDETA.	189
Scheme 7-32. NITEC reaction of the CRD-fumarate and a tetrazole-OH derivative. ...	189
Scheme 7-33. "Inverse" NITEC reaction of the CRD-tetrazole and diethyl fumarate... ..	190
Scheme 7-34. DA reaction of the CRD-fumarate and the 3-cyclopentadienyl-methyl propionate.	190
Scheme 7-35. Reaction scheme of the CuAAC reaction between the diazido-PDMAA Y1 and the CRD-alkyne, yielding the bioconjugate BC1.	191
Scheme 7-36. NITEC reaction between a tetrazole-PEG Y2 and the CRD-fumarate upon UV irradiation, yielding the bioconjugate BC2.....	192
Scheme 7-37. Functionalization with tetrazole groups of the silicon wafer by silanization.	193
Scheme 7-38. Immobilization of PEG-fumarate onto the tetrazole functionalized surface.	193
Scheme 7-39. Attachment of CRD-fumarate onto the surface via NITEC upon irradiation.	194
Scheme 7-40. Attachment of CRD-bromide onto the CRD-covered area via reoxidative conditions.....	194
Scheme 7-41. Erasing of the CRD-bromide from the surface.....	195

8.8 List of Tables

Table 4-1. Overview of the macrospecies for the kinetic modeling of the RAFT polymerization after the SG polymerization (AA homopolymer segments are omitted). Species exchange as shown in Figure 4-3. Full list of reactions refer to Table 8-2 in the Appendix 8.1.1. The table was reprinted from ref. ³⁸⁰ with permission of the American Chemical Society.....	79
Table 7-1. Composition of the gels, employed for the SDS-PAGE from acrylamide (AA) and bisacrylamide (BA).	149
Table 7-2. Molecular characteristics of the PDMAA-diazido Polymer. Molecular weight distribution is illustrated in Chapter 5.2.6.1 in Figure 5-5.	184
Table 8-1. Reactions considered for simulations of the SG polymerization.....	197
Table 8-2. Reactions considered for simulations of the RAFT polymerization (kinetic parameters are given in Table 8-4).....	200
Table 8-3. Top: Relevant experimental parameters are listed as well as measured conversion values p_{MBA} at two different substrate concentrations. Bottom: Experimental parameters were used to derive a hypothetical cuboid irradiation geometry and absorption parameters that were used for the iterative simulation of conversion. As noted previously, the quantum yield was set to an arbitrary value. Simulated conversion values are shown for the two substrate concentrations for both at $\lambda_{\text{max}} = 320$ nm and 360 nm with monochromatic light. The table was adapted from ref. ³⁸⁰ with the permission of the American Chemical Society.....	211
Table 8-4. Overview of the reactions for the simulation of the RAFT polymerization, together with the corresponding Arrhenius parameters. Also specified are the intrinsic rate coefficients at 333 K.	215
Table 8-5. Results of the SG polymerization for stoichiometry determination, obtained by THF-SEC applying a polystyrene calibration, using different stoichiometries r of the monomers CC/BB, indicating the highest molecular weight for $r = 1.2$	218
Table 8-6. Molecular results of the SG polymers obtained by thermal DA cycloaddition. Conversion was obtained by evaluation of ¹ H-NMR spectra of the corresponding samples, M_n , M_w and \bar{D} values were obtained by THF-SEC applying a polystyrene calibration.....	218
Table 8-7. Assignment from ESI-HCD-MS spectrum signals of the SG polymer ($r = 1.2$) from Figure 4-20.....	220
Table 8-8. Molecular results of the polystyrene obtained by RAFT polymerization. Conversion was obtained by gravimetric evaluation, M_n , M_w , and \bar{D} values were obtained by THF-SEC applying a polystyrene calibration.	221

9

9 REFERENCES

- (1) Özbek, S.; Pertz, O.; Schwager, M.; Lustig, A.; Holstein, T.; Engel, J. *J. Biol. Chem.* **2002**, 277 (51), 49200–49204.
- (2) Zhou, Y.; Huang, W.; Liu, J.; Zhu, X.; Yan, D. *Adv. Mater.* **2010**, 22 (41), 4567–4590.
- (3) Elias, H.-G. *Makromoleküle Band 3 Industrielle Polymere und Synthesen*, 6th ed.; WILEY-VCH Verlag GmbH & Co. KGaA: Weinheim, Germany, 2001.
- (4) Sheldon, R. A. *Chem. Soc. Rev.* **2012**, 41 (4), 1437–1451.
- (5) Bonan, G. B. *Science* **2008**, 320 (5882), 1444–1449.
- (6) Chován, T.; Guttman, A. *Trends Biotechnol.* **2002**, 20 (3), 116–122.
- (7) Blower, P. *Dalt. Trans.* **2006**, No. 14, 1705–1711.
- (8) Staudinger, H. *Berichte der Dtsch. Chem. Gesellschaft (A B Ser.)* **1920**, 53 (6), 1073–1085.
- (9) Carothers, W. H. *J. Am. Chem. Soc.* **1929**, 51 (8), 2548–2559.
- (10) Carothers, W. H. *Chem. Rev.* **1931**, 8 (3), 353–426.
- (11) Flory, P. J. *J. Chem. Phys.* **1942**, 10 (1), 51–61.
- (12) Flory, P. J.; Rehner, J. *J. Chem. Phys.* **1943**, 11 (11), 521–526.
- (13) Zalasiewicz, J.; Waters, C. N.; Ivar do Sul, J. A.; Corcoran, P. L.; Barnosky, A. D.; Cearreta, A.; Edgeworth, M.; Gałuszka, A.; Jeandel, C.; Leinfelder, R.; McNeill, J. R.; Steffen, W.; Summerhayes, C.; Wagnreich, M.; Williams, M.; Wolfe, A. P.; Yonan, Y. *Anthropocene* **2016**, 13, 4–17.
- (14) He, P.; He, L. *Biomacromolecules* **2009**, 10 (7), 1804–1809.
- (15) Ren, J. M.; McKenzie, T. G.; Fu, Q.; Wong, E. H. H.; Xu, J.; An, Z.; Shanmugam, S.; Davis, T. P.; Boyer, C.; Qiao, G. G. *Chem. Rev.* **2016**, 116 (12), 6743–6836.
- (16) Hadjichristidis, N.; Pitsikalis, M.; Pispas, S.; Iatrou, H. *Chem. Rev.* **2001**, 101 (12),

- 3747–3792.
- (17) Von Freymann, G.; Ledermann, A.; Thiel, M.; Staude, I.; Essig, S.; Busch, K.; Wegener, M. *Adv. Funct. Mater.* **2010**, *20* (7), 1038–1052.
- (18) Haedler, A. T.; Kreger, K.; Issac, A.; Wittmann, B.; Kivala, M.; Hammer, N.; Köhler, J.; Schmidt, H.-W.; Hildner, R. *Nature* **2015**, *523* (7559), 196–199.
- (19) Voit, B. I.; Lederer, A. *Chem. Rev.* **2009**, *109* (11), 5924–5973.
- (20) Dong, R.; Zhou, Y.; Zhu, X. *Acc. Chem. Res.* **2014**, *47* (7), 2006–2016.
- (21) Lee, C. C.; MacKay, J. A.; Fréchet, J. M. J.; Szoka, F. C. *Nat. Biotechnol.* **2005**, *23* (12), 1517–1526.
- (22) Claussen, K. U.; Scheibel, T.; Schmidt, H. W.; Giesa, R. *Macromol. Mater. Eng.* **2012**, *297* (10), 938–957.
- (23) Bates, F. S.; Fredrickson, G. H. *Phys. Today* **1999**, *52* (2), 32–38.
- (24) Bates, F. S.; Hillmyer, M. a.; Lodge, T. P.; Bates, C. M.; Delaney, K. T.; Fredrickson, G. H. *Science* **2012**, *336* (6080), 434–440.
- (25) Du, J.; O'Reilly, R. K. *Chem. Soc. Rev.* **2011**, *40* (5), 2402–2416.
- (26) Tasdelen, M. A.; Yagci, Y. *Angew. Chemie - Int. Ed.* **2013**, *52* (23), 5930–5938.
- (27) Gao, Y.; Newland, B.; Zhou, D.; Matyjaszewski, K.; Wang, W. *Angew. Chemie - Int. Ed.* **2017**, *56* (2), 450–460.
- (28) Wang, J.-S.; Matyjaszewski, K. *Macromolecules* **1995**, *28* (1), 7901–7910.
- (29) Georges, M. K.; Veregin, R. P. N.; Kazmaier, P. M.; Hamer, G. K.; Saban, M. *Macromolecules* **1994**, *27* (24), 7228–7229.
- (30) Mayadunne, R. T. A.; Rizzardo, E.; Chiefari, J.; Chong, Y. K.; Moad, G.; Thang, S. H. *Macromolecules* **1999**, *32* (21), 6977–6980.
- (31) *Makromoleküle Band 1 Chemische Strukturen und Synthesen*; Elias, H.-G., Ed.; WILEY-VCH Verlag GmbH & Co. KGaA: Weinheim, Germany, 1999.
- (32) Odian, G. *Principles of Polymerization*, 4th ed.; John Wiley & Sons, Inc.: Hoboken, NJ, USA, 2004.
- (33) Lechner, M. D.; Nordmeier, E. H.; Gehrke, K. *Makromolekulare Chemie*, 4th ed.; Birkhäuser: Basel, 2010.
- (34) Sutthasupa, S.; Shiotsuki, M.; Sanda, F. *Polym. J.* **2010**, *42* (12), 905–915.
- (35) Aoshima, S.; Kanaoka, S. *Chem. Rev.* **2009**, *109* (11), 5245–5287.
- (36) Baskaran, D.; Müller, A. H. E. *Prog. Polym. Sci.* **2007**, *32* (2), 173–219.
- (37) Li, Y.; Liu, Z.; Li, Y.; Yang, Y.; Huang, X. *J. Polym. Sci. Part A Polym. Chem.* **2013**, *51* (21), 4505–4514.
- (38) *Makromoleküle Band 4 Anwendungen*; Elias, H.-G., Ed.; WILEY-VCH Verlag GmbH & Co. KGaA: Weinheim, Germany, 2002.
- (39) Perova, M. S.; Antipov, K. A.; Galimzyanova, R. Y.; Khakimullin, Y. N. *Polym. Sci.*

- Ser. D* **2012**, 5 (1), 26–29.
- (40) Webster, O. W. *J. Polym. Sci. Part A Polym. Chem.* **2000**, 38 (16), 2855–2860.
- (41) Hashimoto, K. *Prog. Polym. Sci.* **2000**, 25 (10), 1411–1462.
- (42) Clayden, J.; Greeves, N.; Warren, S. G. *Organic chemistry*, 2nd ed.; Oxford University Press: New York, 2012.
- (43) Hirao, A.; Goseki, R.; Ishizone, T. *Macromolecules* **2014**, 47 (6), 1883–1905.
- (44) Lynd, N. A.; Meuler, A. J.; Hillmyer, M. A. *Prog. Polym. Sci.* **2008**, 33 (9), 875–893.
- (45) Freyss, D.; Rempp, P.; Benoît, H. *J. Polym. Sci. Lett.* **1964**, 2, 217–222.
- (46) Hsieh, H. L.; Quirk, R. P. *Anionic polymerization: principles and practical applications*; Marcel Dekker: New York, 1996.
- (47) Halasa, A. F.; Lohr, D. F.; Hall, J. E. *J. Polym. Sci. Polym. Chem. Ed.* **1981**, 19 (6), 1357–1360.
- (48) Carlotti, S.; Desbois, P.; Warzelhan, V.; Deffieux, A. *Polymer* **2009**, 50 (14), 3057–3067.
- (49) Barner-Kowollik, C.; Russell, G. T. *Prog. Polym. Sci.* **2009**, 34 (11), 1211–1259.
- (50) de Gennes, P. G.; Leger, L. *Annu. Rev. Phys. Chem.* **1982**, 33 (1), 49–61.
- (51) Trommsdorff, V. E.; Köhle, H.; Lagally, P. *Die Makromol. Chemie* **1948**, 1 (3), 169–198.
- (52) Schulz, G. V.; Blaschke, F. *Zeitschrift für Phys. Chemie* **1942**, B51, 75–102.
- (53) *Die Kunststoffe und ihre Eigenschaften*; Eyerer, P., Elsner, P., Hirth, T., Eds.; VDI-Buch; Springer Berlin Heidelberg: Berlin, Heidelberg, 2005.
- (54) Salejova, G.; Kosek, J. *Macromol. Symp.* **2006**, 243 (1), 233–246.
- (55) Jenkins, A. D.; Jones, R. G.; Moad, G. *Pure Appl. Chem.* **2009**, 82 (2), 483–491.
- (56) Matyjaszewski, K. *Macromolecules* **2012**, 45 (10), 4015–4039.
- (57) Matyjaszewski, K.; Tsarevsky, N. V. *J. Am. Chem. Soc.* **2014**, 136 (18), 6513–6533.
- (58) Moad, G.; Rizzardo, E.; Thang, S. H. *Aust. J. Chem.* **2012**, 65 (8), 985–1076.
- (59) Perrier, S. *Macromolecules* **2017**, 50 (19), 7433–7447.
- (60) Nicolas, J.; Guillaneuf, Y.; Lefay, C.; Bertin, D.; Gigmès, D.; Charleux, B. *Prog. Polym. Sci.* **2013**, 38 (1), 63–235.
- (61) Tebben, L.; Studer, A. *Angew. Chemie - Int. Ed.* **2011**, 50 (22), 5034–5068.
- (62) Stenzel, M. H.; Barner-Kowollik, C. *Mater. Horiz.* **2016**, 3, 471–477.
- (63) Kato, M.; Kamigaito, M.; Sawamoto, M.; Higashimura, T. *Macromolecules* **1995**, 28 (5), 1721–1723.
- (64) Matyjaszewski, K.; Xia, J. *Chem. Rev.* **2001**, 101 (9), 2921–2990.
- (65) Krys, P.; Matyjaszewski, K. *Eur. Polym. J.* **2017**, 89, 482–523.
- (66) Opsteen, J. A.; van Hest, J. C. M. *Chem. Commun.* **2005**, 109 (1), 57–59.
- (67) Inglis, A. J.; Paulöhr, T.; Barner-Kowollik, C. *Macromolecules* **2010**, 43 (1), 33–36.

- (68) Chmielarz, P.; Fantin, M.; Park, S.; Isse, A. A.; Gennaro, A.; Magenau, A. J. D.; Sobkowiak, A.; Matyjaszewski, K. *Prog. Polym. Sci.* **2017**, *69*, 47–78.
- (69) Bortolamei, N.; Isse, A. A.; Magenau, A. J. D.; Gennaro, A.; Matyjaszewski, K. *Angew. Chemie - Int. Ed.* **2011**, *50* (48), 11391–11394.
- (70) Pan, X.; Malhotra, N.; Simakova, A.; Wang, Z.; Konkolewicz, D.; Matyjaszewski, K. *J. Am. Chem. Soc.* **2015**, *137* (49), 15430–15433.
- (71) Frick, E.; Anastasaki, A.; Haddleton, D. M.; Barner-Kowollik, C. *J. Am. Chem. Soc.* **2015**, *137* (21), 6889–6896.
- (72) Anastasaki, A.; Nikolaou, V.; Zhang, Q.; Burns, J.; Samanta, S.; Waldron, C.; Haddleton, A. J.; Mchale, R.; Fox, D. J.; Percec, V.; Wilson, P.; Haddleton, D. M. *J. Am. Chem. Soc.* **2014**, *136* (3), 1141–1149.
- (73) Pietrasik, J.; Dong, H.; Matyjaszewski, K. *Macromolecules* **2006**, *39* (19), 6384–6390.
- (74) Broyer, R. M.; Grover, G. N.; Maynard, H. D. *Chem. Commun.* **2011**, *47* (8), 2212–2226.
- (75) Beckwith, A. L. J.; Bowry, V. W.; O'Leary, M.; Moad, G.; Rizzardo, E.; Solomon, D. H. *J. Chem. Soc. Chem. Commun.* **1986**, No. 13, 1003–1004.
- (76) Braunecker, W. A.; Matyjaszewski, K. *Prog. Polym. Sci.* **2007**, *32*, 93–146.
- (77) Abreu, C. M. R.; Mendonça, P. V.; Serra, A. C.; Noble, B. B.; Guliashvili, T.; Nicolas, J.; Coote, M. L.; Coelho, J. F. J. *Macromolecules* **2016**, *49* (2), 490–498.
- (78) Qiao, X. G.; Dugas, P.-Y.; Charleux, B.; Lansalot, M.; Bourgeat-Lami, E. *Polym. Chem.* **2017**, *8* (27), 4014–4029.
- (79) Ballard, N.; Simula, A.; Aguirre, M.; Leiza, J. R.; van Es, S.; Asua, J. M. *Polym. Chem.* **2016**, *7* (45), 6964–6972.
- (80) Harrisson, S.; Couvreur, P.; Nicolas, J. *Polym. Chem.* **2011**, *2* (8), 1859–1865.
- (81) Moad, G.; Rizzardo, E.; Thang, S. H. *Polymer* **2008**, *49* (5), 1079–1131.
- (82) Moad, G.; Rizzardo, E.; Thang, S. H. *Aust. J. Chem.* **2006**, *59* (10), 669–692.
- (83) Moad, G.; Rizzardo, E.; Thang, S. H. *Aust. J. Chem.* **2009**, *62* (11), 1402–1472.
- (84) Chiefari, J.; Chong, Y. K. B.; Ercole, F.; Krstina, J.; Jeffery, J.; Le, T. P. T.; Mayadunne, R. T. A.; Meijs, G. F.; Moad, C. L.; Moad, G.; Rizzardo, E.; Thang, S. H. *Macromolecules* **1998**, *31* (16), 5559–5562.
- (85) Charmot, D.; Corpart, P.; Adam, H.; Zard, S. Z.; Biadatti, T.; Bouhadir, G. *Macromol. Symp.* **2000**, *150* (1), 23–32.
- (86) Barner-Kowollik, C. *Handbook of RAFT Polymerization*; Wiley-VCH Verlag GmbH & Co. KGaA: Weinheim, Germany, 2008.
- (87) Feldermann, A.; Coote, M. L.; Stenzel, M. H.; Davis, T. P.; Barner-Kowollik, C. *J. Am. Chem. Soc.* **2004**, *126* (48), 15915–15923.

-
- (88) Fijten, M. W. M.; Paulus, R. M.; Schubert, U. S. *J. Polym. Sci. Part A Polym. Chem.* **2005**, *43* (17), 3831–3839.
- (89) Theis, A.; Feldermann, A.; Charton, N.; Stenzel, M. H.; Davis, T. P.; Barner-Kowollik, C. *Macromolecules* **2005**, *38* (7), 2595–2605.
- (90) Johnston-Hall, G.; Theis, A.; Monteiro, M. J.; Davis, T. P.; Stenzel, M. H.; Barner-Kowollik, C. *Macromol. Chem. Phys.* **2005**, *206* (20), 2047–2053.
- (91) Szablan, Z.; Toy, A. A.; Terrenoire, A.; Davis, T. P.; Stenzel, M. H.; Müller, A. H. E.; Barner-Kowollik, C. *J. Polym. Sci. Part A Polym. Chem.* **2006**, *44* (11), 3692–3710.
- (92) Feldermann, A.; Stenzel, M. H.; Davis, T. P.; Vana, P.; Barner-Kowollik, C. *Macromolecules* **2004**, *37* (7), 2404–2410.
- (93) Vogt, A. P.; Sumerlin, B. S. *Soft Matter* **2009**, *5* (12), 2347–2351.
- (94) Keddie, D. J.; Moad, G.; Rizzardo, E.; Thang, S. H. *Macromolecules* **2012**, *45* (13), 5321–5342.
- (95) Zhang, L.; Chen, Y. *Polymer* **2006**, *47* (15), 5259–5266.
- (96) Chong, B. Y. K.; Le, T. P. T.; Moad, G.; Rizzardo, E.; Thang, S. H. *Macromolecules* **1999**, *32* (6), 2071–2074.
- (97) Ooi, H. W.; Jack, K. S.; Peng, H.; Whittaker, A. K. *Polym. Chem.* **2013**, *4* (17), 4788–4800.
- (98) Kaupp, M.; Quick, A. S.; Rodriguez-Emmenegger, C.; Welle, A.; Trouillet, V.; Pop-Georgievski, O.; Wegener, M.; Barner-Kowollik, C. *Adv. Funct. Mater.* **2014**, *24* (36), 5649–5661.
- (99) Estupiñán, D.; Gegenhuber, T.; Blinco, J. P.; Barner-Kowollik, C.; Barner, L. *ACS Macro Lett.* **2017**, *6* (3), 229–234.
- (100) Kaupp, M.; Tischer, T.; Hirschbiel, A. F.; Vogt, A. P.; Geckle, U.; Trouillet, V.; Hofe, T.; Stenzel, M. H.; Barner-Kowollik, C. *Macromolecules* **2013**, *46* (17), 6858–6872.
- (101) Pöttsch, R.; Fleischmann, S.; Tock, C.; Komber, H.; Voit, B. I. *Macromolecules* **2011**, *44* (9), 3260–3269.
- (102) Börner, H. G.; Sütterlin, R. I.; Theato, P.; Wiss, K. T. *Macromol. Rapid Commun.* **2014**, *35* (2), 180–185.
- (103) Grover, G. N.; Lee, J.; Matsumoto, N. M.; Maynard, H. D. *Macromolecules* **2012**, *45* (12), 4958–4965.
- (104) Robin, M. P.; Jones, M. W.; Haddleton, D. M.; O'Reilly, R. K. *ACS Macro Lett.* **2012**, *1* (1), 222–226.
- (105) Claus, T. K.; Telitel, S.; Welle, A.; Bastmeyer, M.; Vogt, A. P.; Delaittre, G.; Barner-Kowollik, C. *Chem. Commun.* **2017**, *53* (10), 1599–1602.
- (106) Hufendiek, A.; Trouillet, V.; Meier, M. A. R.; Barner-Kowollik, C. *Biomacromolecules* **2014**, *15* (7), 2563–2572.

- (107) Dürr, C. J.; Emmerling, S. G. J.; Lederhose, P.; Kaiser, A.; Brandau, S.; Klimpel, M.; Barner-Kowollik, C. *Polym. Chem.* **2012**, *3* (4), 1048–1060.
- (108) Wuest, K. N. R.; Trouillet, V.; Goldmann, A. S.; Stenzel, M. H.; Barner-Kowollik, C. *Macromolecules* **2016**, *49* (5), 1712–1721.
- (109) Lai, J. T.; Filla, D.; Shea, R. *Macromolecules* **2002**, *35* (18), 6754–6756.
- (110) Zhang, H.; Deng, J.; Lu, L.; Cai, Y. *Macromolecules* **2007**, *40* (26), 9252–9261.
- (111) Smith, A. E.; Xu, X.; McCormick, C. L. *Prog. Polym. Sci.* **2010**, *35* (1–2), 45–93.
- (112) Millard, P.-E.; Barner, L.; Reinhardt, J.; Buchmeiser, M. R.; Barner-Kowollik, C.; Müller, A. H. E. *Polymer* **2010**, *51* (19), 4319–4328.
- (113) Xu, J.; Jung, K.; Atme, A.; Shanmugam, S.; Boyer, C. *J. Am. Chem. Soc.* **2014**, *136* (14), 5508–5519.
- (114) York, A. W.; Kirkland, S. E.; McCormick, C. L. *Adv. Drug Deliv. Rev.* **2008**, *60* (9), 1018–1036.
- (115) Dan, K.; Ghosh, S. *Polym. Chem.* **2014**, *5* (12), 3901–3909.
- (116) Utama, R. H.; Stenzel, M. H.; Zetterlund, P. B. *Macromolecules* **2013**, *46* (6), 2118–2127.
- (117) Chong, B. Y. K.; Krstina, J.; Le, T. P. T.; Moad, G.; Postma, A.; Rizzardo, E.; Thang, S. H. *Macromolecules* **2003**, *36* (7), 2256–2272.
- (118) Schilli, C. M.; Zhang, M.; Rizzardo, E.; Thang, S. H.; Chong, Y. K.; Edwards, K.; Karlsson, G.; Müller, A. H. E. *Macromolecules* **2004**, *37* (21), 7861–7866.
- (119) Barner, L.; Davis, T. P.; Stenzel, M. H.; Barner-Kowollik, C. *Macromol. Rapid Commun.* **2007**, *28* (5), 539–559.
- (120) Martin, L.; Gody, G.; Perrier, S. *Polym. Chem.* **2015**, *6* (27), 4875–4886.
- (121) Kerr, A.; Hartlieb, M.; Sanchis, J.; Smith, T.; Perrier, S. *Chem. Commun.* **2017**, *53* (87), 11901–11904.
- (122) Lutz, J.-F.; Börner, H. G. *Prog. Polym. Sci.* **2008**, *33* (1), 1–39.
- (123) Boyer, C.; Bulmus, V.; Davis, T. P.; Admiral, V.; Liu, J.; Perrier, S. *Chem. Rev.* **2009**, *109* (11), 5402–5436.
- (124) Langer, M.; Mueller, J. O.; Goldmann, A. S.; Schacher, F. H.; Barner-Kowollik, C. *ACS Macro Lett.* **2016**, *5* (5), 597–601.
- (125) Goldmann, A. S.; Glassner, M.; Inglis, A. J.; Barner-Kowollik, C. *Macromol. Rapid Commun.* **2013**, *34* (10), 810–849.
- (126) Zhou, J.; Guimard, N. K.; Inglis, A. J.; Namazian, M.; Lin, C. Y.; Coote, M. L.; Spyrou, E.; Hilf, S.; Schmidt, F. G.; Barner-Kowollik, C. *Polym. Chem.* **2012**, *3* (3), 628–639.
- (127) Glassner, M.; Delaittre, G.; Kaupp, M.; Blinco, J. P.; Barner-Kowollik, C. *J. Am. Chem. Soc.* **2012**, *134* (17), 7274–7277.

- (128) Oehlenschlaeger, K. K.; Mueller, J. O.; Heine, N. B.; Glassner, M.; Guimard, N. K.; Delaittre, G.; Schmidt, F. G.; Barner-Kowollik, C. *Angew. Chemie Int. Ed.* **2013**, *52* (2), 762–766.
- (129) Moad, G.; Rizzardo, E.; Thang, S. H. *Polym. Int.* **2011**, *60* (1), 9–25.
- (130) Zhang, X.; Dou, H.; Zhang, Z.; Zhang, W.; Zhu, X.; Zhu, J. *J. Polym. Sci. Part A Polym. Chem.* **2013**, *51* (18), 3907–3916.
- (131) Qiu, X.-P.; Winnik, F. M. *Macromol. Rapid Commun.* **2006**, *27* (19), 1648–1653.
- (132) Zhang, S.-S.; Cui, K.; Huang, J.; Zhao, Q.-L.; Cao, S.-K.; Ma, Z. *RSC Adv.* **2015**, *5* (55), 44571–44577.
- (133) Blidi, I.; Coutelier, O.; Destarac, M. *J. Polym. Sci. Part A Polym. Chem.* **2014**, *52* (18), 2616–2624.
- (134) Willcock, H.; O'Reilly, R. K. *Polym. Chem.* **2010**, *1* (2), 149–157.
- (135) Barner-Kowollik, C.; Davis, T. P.; Heuts, J. P. A.; Stenzel, M. H.; Vana, P.; Whittaker, M. *J. Polym. Sci. Part A Polym. Chem.* **2003**, *41* (3), 365–375.
- (136) Sandeau, A.; Mazières, S.; Vergelati, C.; Corriol, C.; Destarac, M. *Polym. Chem.* **2011**, *2* (11), 2490–2499.
- (137) Skey, J.; O'Reilly, R. K. *Chem. Commun.* **2008**, No. 35, 4183.
- (138) Schmidt, B. V. K. J.; Barner-Kowollik, C. *Polym. Chem.* **2014**, *5* (7), 2461–2472.
- (139) Albertin, L.; Wolnik, A.; Ghadban, A.; Dubreuil, F. *Macromol. Chem. Phys.* **2012**, *213* (17), 1768–1782.
- (140) Albertin, L.; Stenzel, M. H.; Barner-Kowollik, C.; Davis, T. P. *Polymer* **2006**, *47* (4), 1011–1019.
- (141) Lowe, A. B.; McCormick, C. L. *Prog. Polym. Sci.* **2007**, *32* (3), 283–351.
- (142) Chan, J. W.; Yu, B.; Hoyle, C. E.; Lowe, A. B. *Chem. Commun.* **2008**, No. 40, 4959–4961.
- (143) Boyer, C.; Stenzel, M. H.; Davis, T. P. *J. Polym. Sci. Part A Polym. Chem.* **2011**, *49* (3), 551–595.
- (144) Inglis, A. J.; Sinnwell, S.; Davis, T. P.; Barner-Kowollik, C.; Stenzel, M. H. *Macromolecules* **2008**, *41* (12), 4120–4126.
- (145) Wang, C. E.; Stayton, P. S.; Pun, S. H.; Convertine, A. J. *J. Control. Release* **2015**, *219*, 345–354.
- (146) Hao, X.; Nilsson, C.; Jesberger, M.; Stenzel, M. H.; Malmström, E.; Davis, T. P.; Östmark, E.; Barner-Kowollik, C. *J. Polym. Sci. Part A Polym. Chem.* **2004**, *42* (23), 5877–5890.
- (147) Gupta, M. K.; Meyer, T. A.; Nelson, C. E.; Duvall, C. L. *J. Control. Release* **2012**, *162* (3), 591–598.
- (148) Rui, L.; Liu, L.; Wang, Y.; Gao, Y.; Zhang, W. *ACS Macro Lett.* **2016**, *5* (1), 112–

- 117.
- (149) Xie, Y.; Moreno, N.; Calo, V.; Cheng, H.; Hong, P.-Y.; Sougrat, R.; Behzad, A. R.; Tayouo, R.; Nunes, S. *Polym. Chem.* **2016**, *7* (18), 3076–3089.
- (150) Jones, E. R.; Mykhaylyk, O. O.; Semsarilar, M.; Boerakker, M.; Wyman, P.; Armes, S. P. *Macromolecules* **2016**, *49* (1), 172–181.
- (151) Mäkinen, L.; Varadharajan, D.; Tenhu, H.; Hietala, S. *Macromolecules* **2016**, *49* (3), 986–993.
- (152) Charleux, B.; Delaittre, G.; Rieger, J.; D'Agosto, F. *Macromolecules* **2012**, *45* (17), 6753–6765.
- (153) Oehlenschlaeger, K. K.; Mueller, J. O.; Brandt, J.; Hilf, S.; Lederer, A.; Wilhelm, M.; Graf, R.; Coote, M. L.; Schmidt, F. G.; Barner-Kowollik, C. *Adv. Mater.* **2014**, *26* (21), 3561–3566.
- (154) Harrisson, S. *Macromolecules* **2009**, *42* (4), 897–898.
- (155) Jesson, C. P.; Pearce, C. M.; Simon, H.; Werner, A.; Cunningham, V. J.; Lovett, J. R.; Smallridge, M. J.; Warren, N. J.; Armes, S. P. *Macromolecules* **2017**, *50* (1), 182–191.
- (156) Postma, A.; Davis, T. P.; Moad, G.; O'Shea, M. S. *Macromolecules* **2005**, *38* (13), 5371–5374.
- (157) Xu, J.; He, J.; Fan, D.; Wang, X.; Yang, Y. *Macromolecules* **2006**, *39* (25), 8616–8624.
- (158) Wu, Y.; Zhou, Y.; Zhu, J.; Zhang, W.; Pan, X.; Zhang, Z.; Zhu, X. *Polym. Chem.* **2014**, *5* (19), 5546–5550.
- (159) Pearson, S.; Lu, H.; Stenzel, M. H. *Macromolecules* **2015**, *48* (4), 1065–1076.
- (160) De Brouwer, H.; Schellekens, M. A. J.; Klumperman, B.; Monteiro, M. J.; German, A. L. *J. Polym. Sci. Part A Polym. Chem.* **2000**, *38* (19), 3596–3603.
- (161) Quinn, J. F.; Barner, L.; Barner-Kowollik, C.; Rizzardo, E.; Davis, T. P. *Macromolecules* **2002**, *35* (20), 7620–7627.
- (162) Carmean, R. N.; Figg, C. A.; Scheutz, G. M.; Kubo, T.; Sumerlin, B. S. *ACS Macro Lett.* **2017**, *6* (2), 185–189.
- (163) Roth, P. J.; Jochum, F. D.; Zentel, R.; Theato, P. *Biomacromolecules* **2010**, *11* (1), 238–244.
- (164) Petton, L.; Ciolino, A. E.; Stamenović, M. M.; Espeel, P.; Du Prez, F. E. *Macromol. Rapid Commun.* **2012**, *33* (15), 1310–1315.
- (165) Barbey, R.; Perrier, S. *ACS Macro Lett.* **2013**, *2* (5), 366–370.
- (166) Guimard, N. K.; Ho, J.; Brandt, J.; Lin, C. Y.; Namazian, M.; Mueller, J. O.; Oehlenschlaeger, K. K.; Hilf, S.; Lederer, A.; Schmidt, F. G.; Coote, M. L.; Barner-Kowollik, C. *Chem. Sci.* **2013**, *4*, 2752–2759.

- (167) Jenkins, A. D.; Kratochvíl, P.; Stepto, R. F. T.; Suter, U. W. *Pure Appl. Chem.* **1996**, *68* (12), 2287–2311.
- (168) Carothers, W. H. *Trans. Faraday Soc.* **1936**, *32*, 39–49.
- (169) Yokozawa, T.; Ohta, Y. *Chem. Rev.* **2016**, *116* (4), 1950–1968.
- (170) Ritchie, C. D. *Can. J. Chem.* **1986**, *64* (12), 2239–2250.
- (171) Kricheldorf, H. R. *Macromol. Rapid Commun.* **2009**, *30* (16), 1371–1381.
- (172) Bischoff, R.; Cray, S. E. *Prog. Polym. Sci.* **1999**, *24* (2), 185–219.
- (173) Kaiser, W. *Kunststoffchemie für Ingenieure*; Carl Hanser Verlag GmbH & Co. KG: München, 2011.
- (174) de Ilarduya, A. M.; Muñoz-Guerra, S. *Macromol. Chem. Phys.* **2014**, *215* (22), 2138–2160.
- (175) Kim, N. *J. Coatings Technol. Res.* **2017**, *14* (1), 21–34.
- (176) Suriano, F.; Coulembier, O.; Hedrick, J. L.; Dubois, P. *Polym. Chem.* **2011**, *2* (3), 528–533.
- (177) Nelson, A. M.; Long, T. E. *Macromol. Chem. Phys.* **2014**, *215* (22), 2161–2174.
- (178) Liaw, D. J.; Wang, K. L.; Huang, Y. C.; Lee, K. R.; Lai, J. Y.; Ha, C. S. *Prog. Polym. Sci.* **2012**, *37* (7), 907–974.
- (179) Dove, A. P.; Meier, M. A. R. *Macromol. Chem. Phys.* **2014**, *215* (22), 2135–2137.
- (180) Matos, M.; Sousa, A. F.; Fonseca, A. C.; Freire, C. S. R.; Coelho, J. F. J.; Silvestre, A. J. D. *Macromol. Chem. Phys.* **2014**, *215* (22), 2175–2184.
- (181) Jiang, Y.; Van Ekenstein, G. O. R. A.; Woortman, A. J. J.; Loos, K. *Macromol. Chem. Phys.* **2014**, *215* (22), 2185–2197.
- (182) Yu, S.; Liu, F.; Yu, J.; Zhang, S.; Cabanetos, C.; Gao, Y.; Huang, W. *J. Mater. Chem. C* **2017**, *5* (1), 29–40.
- (183) Kolb, H. C.; Finn, M. G.; Sharpless, K. B. *Angew. Chemie - Int. Ed.* **2001**, *40* (11), 2004–2021.
- (184) Barner-Kowollik, C.; Du Prez, F. E.; Espeel, P.; Hawker, C. J.; Junkers, T.; Schlaad, H.; Van Camp, W. *Angew. Chemie Int. Ed.* **2011**, *50* (1), 60–62.
- (185) Bruice, P. Y. *Organic chemistry*, 5th ed.; Pearson Prentice Hall: Upper Saddle River, NJ, 2007.
- (186) Diels, O.; Alder, K. *Justus Liebig's Ann. der Chemie* **1928**, *460* (1), 98–122.
- (187) Diels, O.; Alder, K. *Berichte der Dtsch. Chem. Gesellschaft (A B Ser.)* **1929**, *62* (3), 554–562.
- (188) Diels, O.; Alder, K. *Justus Liebig's Ann. der Chemie* **1931**, *486* (1), 191–202.
- (189) Diels, O.; Alder, K. *Justus Liebig's Ann. der Chemie* **1933**, *505* (1), 103–150.
- (190) Diels, O.; Alder, K. *Justus Liebig's Ann. Chem.* **1934**, *510* (1), 87–128.
- (191) Nicolaou, K. C.; Snyder, S. A.; Montagnon, T.; Vassilikogiannakis, G. *Angew.*

- Chemie - Int. Ed.* **2002**, *41* (10), 1668–1698.
- (192) Iha, R. K.; Wooley, K. L.; Nyström, A. M.; Burke, D. J.; Kade, M. J.; Hawker, C. J. *Chem. Rev.* **2009**, *109* (11), 5620–5686.
- (193) Gheneim, R.; Perez-Berumen, C.; Gandini, A. *Macromolecules* **2002**, *35* (19), 7246–7253.
- (194) Nebhani, L.; Sinnwell, S.; Lin, C. Y.; Coote, M. L.; Stenzel, M. H.; Barner-Kowollik, C. *J. Polym. Sci. Part A Polym. Chem.* **2009**, *47* (22), 6053–6071.
- (195) Zhang, Y.; Broekhuis, A. A.; Picchioni, F. *Macromolecules* **2009**, *42* (6), 1906–1912.
- (196) Schenzel, A. M.; Klein, C.; Rist, K.; Moszner, N.; Barner-Kowollik, C. *Adv. Sci.* **2016**, *3* (3), 1500361.
- (197) Nandivada, H.; Jiang, X.; Lahann, J. *Adv. Mater.* **2007**, *19* (17), 2197–2208.
- (198) Preuss, C. M.; Goldmann, A. S.; Trouillet, V.; Walther, A.; Barner-Kowollik, C. *Macromol. Rapid Commun.* **2013**, *34* (8), 640–644.
- (199) Yuksekdag, Y. N.; Gevrek, T. N.; Sanyal, A. *ACS Macro Lett.* **2017**, *6* (4), 415–420.
- (200) Shimizu, T.; Kanamori, K.; Maeno, A.; Kaji, H.; Doherty, C. M.; Nakanishi, K. *Langmuir* **2017**, *33* (18), 4543–4550.
- (201) Pahnke, K.; Brandt, J.; Gryn'ova, G.; Lin, C. Y.; Altintas, O.; Schmidt, F. G.; Lederer, A.; Coote, M. L.; Barner-Kowollik, C. *Angew. Chemie - Int. Ed.* **2016**, *55* (4), 1514–1518.
- (202) Xu, X.; He, L.; Zhu, B.; Li, J.; Li, J. *Polym. Chem.* **2017**, *8* (5), 807–823.
- (203) Breschi, L.; Mazzoni, A.; Ruggeri, A.; Cadenaro, M.; Di Lenarda, R.; De Stefano Dorigo, E. *Dent. Mater.* **2008**, *24* (1), 90–101.
- (204) Chen, M.; Zhong, M.; Johnson, J. A. *Chem. Rev.* **2016**, *116* (17), 10167–10211.
- (205) Webb, A. R.; Holick, M. F. *Annu. Rev. Nutr.* **1988**, *8* (1), 375–399.
- (206) Atkinson, R. *Atmos. Environ.* **2000**, *34* (12–14), 2063–2101.
- (207) Roth, H. D. *Angew. Chemie Int. Ed. English* **1989**, *28* (9), 1193–1207.
- (208) Dessauer, R.; Paris, J. P. In *Advances in Photochemistry Volume 1*; Jr., W. A. N., Hammond, G. S., Jr., J. N. P., Eds.; John Wiley & Sons, Inc.: Hoboken, NJ, USA, 1963; pp 275–321.
- (209) Trommsdorff, H. *Ann. der Pharm.* **1834**, *11* (2), 190–207.
- (210) Arons, A. B.; Peppard, M. B. *Am. J. Phys.* **1965**, *33* (5), 367–374.
- (211) Bodenstern, M.; Weigert, F.; Luther, R.; Franck, J.; Ornstein, L. S.; Lindemann, F. A.; Rice, J.; Christiansen, J. A.; Baly, E. C. C.; Rice; Rideal, E. K.; Allmand, A. J.; von Halban, H.; Lasareff, P.; Bowen, E. J.; Taylor, H. S.; Chapman, D. L.; Roy, S. C.; Langedyk, S. L.; Padoa, M.; Rawlins, F. I. G. *Trans. Faraday Soc.* **1926**, *21*, 515–524.
- (212) Ciamician, G.; Silber, P. *Berichte der Dtsch. Chem. Gesellschaft* **1901**, *34* (2),

- 1530–1543.
- (213) Ciamician, G.; Silber, P. *Berichte der Dtsch. Chem. Gesellschaft* **1901**, *34* (2), 2040–2046.
- (214) Ciamician, G.; Silber, P. *Berichte der Dtsch. Chem. Gesellschaft* **1902**, *35* (4), 4128–4131.
- (215) Ciamician, G.; Silber, P. *Berichte der Dtsch. Chem. Gesellschaft* **1908**, *41* (2), 1928–1935.
- (216) Buback, M.; Junkers, T.; Vana, P. *Macromol. Rapid Commun.* **2005**, *26* (10), 796–802.
- (217) Frick, E.; Ernst, H. A.; Voll, D.; Wolf, T. J. A.; Unterreiner, A.-N.; Barner-Kowollik, C. *Polym. Chem.* **2014**, *5* (17), 5053–5068.
- (218) Quick, A. S.; Fischer, J.; Richter, B.; Pauloehrl, T.; Trouillet, V.; Wegener, M.; Barner-Kowollik, C. *Macromol. Rapid Commun.* **2013**, *34* (4), 335–340.
- (219) Quick, A. S.; Rothfuss, H.; Welle, A.; Richter, B.; Fischer, J.; Wegener, M.; Barner-Kowollik, C. *Adv. Funct. Mater.* **2014**, *24* (23), 3571–3580.
- (220) Lang, X.; Chen, X.; Zhao, J. *Chem. Soc. Rev.* **2014**, *43* (1), 473–486.
- (221) Kale, M. J.; Avanesian, T.; Christopher, P. *ACS Catal.* **2014**, *4* (1), 116–128.
- (222) Jablonski, A. *Nature* **1933**, *131* (3319), 839–840.
- (223) Mustroph, H.; Ernst, S. *Chemie unserer Zeit* **2011**, *45* (4), 256–269.
- (224) Atkins, P. W. *Physical Chemistry*, 8th ed.; Oxford University Press: New York, 2006.
- (225) Norrish, R. G. W.; Kirkbride, F. W. *J. Chem. Soc.* **1932**, 1518–1530.
- (226) Bamford, C. H.; Norrish, R. G. W. *J. Chem. Soc.* **1935**, 1504–1511.
- (227) Fast, D. E.; Lauer, A.; Menzel, J. P.; Kelterer, A. M.; Gescheidt, G.; Barner-Kowollik, C. *Macromolecules* **2017**, *50* (5), 1815–1823.
- (228) Wolf, T. J. A.; Voll, D.; Barner-Kowollik, C.; Unterreiner, A. N. *Macromolecules* **2012**, *45* (5), 2257–2266.
- (229) Frick, E.; Schweigert, C.; Noble, B. B.; Ernst, H. A.; Lauer, A.; Liang, Y.; Voll, D.; Coote, M. L.; Unterreiner, A.-N.; Barner-Kowollik, C. *Macromolecules* **2016**, *49* (1), 80–89.
- (230) Moriarty, K. M.; Kliegman, J. M.; Shovlin, C. *J. Am. Chem. Soc.* **1967**, *89* (23), 5958–5959.
- (231) Clovis, J. S.; Eckell, A.; Huisgen, R.; Sustmann, R.; Wallbillich, G.; Weberndörfer, V. *Chem. Ber.* **1967**, *100* (5), 1593–1601.
- (232) Bach, F. L.; Karliner, J.; Van Lear, G. E. *J. Chem. Soc. D Chem. Commun.* **1969**, 276 (19), 1110–1111.
- (233) Scheiner, P. *J.C.S Chem. Comm.* **1972**, No. 11, 781–782.
- (234) Sato, E.; Kanaoka, Y.; Padwa, A. *J. Org. Chem.* **1982**, *47* (22), 4256–4260.

- (235) Darkow, R.; Yoshikawa, M.; Kitao, T.; Tomaschewski, G.; Schellenberg, J. *J. Polym. Sci. Part A Polym. Chem.* **1994**, *32* (9), 1657–1664.
- (236) Song, W.; Wang, Y.; Qu, J.; Madden, M. M.; Lin, Q. *Angew. Chemie - Int. Ed.* **2008**, *47* (15), 2832–2835.
- (237) Wang, Y.; Lin, Q. *Org. Lett.* **2009**, *11* (16), 3570–3573.
- (238) Yu, Z.; Ho, L. Y.; Lin, Q. *J. Am. Chem. Soc.* **2011**, *133* (31), 11912–11915.
- (239) Dürr, C. J.; Lederhose, P.; Hlalele, L.; Abt, D.; Kaiser, A.; Brandau, S.; Barner-Kowollik, C. *Macromolecules* **2013**, *46* (15), 5915–5923.
- (240) Mueller, J. O.; Voll, D.; Schmidt, F. G.; Delaittre, G.; Barner-Kowollik, C. *Chem. Commun.* **2014**, *50* (99), 15681–15684.
- (241) Lederhose, P.; Chen, Z.; Müller, R.; Blinco, J. P.; Wu, S.; Barner-Kowollik, C. *Angew. Chemie Int. Ed.* **2016**, *55* (40), 12195–12199.
- (242) Weinberg, P.; Grummt, U. W.; Csongar, C. *J. für Prakt. Chemie* **1988**, *330* (6), 887–892.
- (243) Wang, Y.; Hu, W. J.; Song, W.; Lim, R. K. V.; Lin, Q. *Org. Lett.* **2008**, *10* (17), 3725–3728.
- (244) Arndt, S.; Wagenknecht, H.-A. *Angew. Chemie Int. Ed.* **2014**, *53* (52), 14580–14582.
- (245) Lederhose, P.; Wüst, K. N. R.; Barner-Kowollik, C.; Blinco, J. P. *Chem. Commun.* **2016**, *52* (35), 5928–5931.
- (246) Blasco, E.; Sugawara, Y.; Lederhose, P.; Blinco, J. P.; Kelterer, A.-M.; Barner-Kowollik, C. *ChemPhotoChem* **2017**, *1* (5), 159–163.
- (247) Dietrich, M.; Delaittre, G.; Blinco, J. P.; Inglis, A. J.; Bruns, M.; Barner-Kowollik, C. *Adv. Funct. Mater.* **2012**, *22* (2), 304–312.
- (248) Zheng, S. L.; Wang, Y.; Yu, Z.; Lin, Q.; Coppens, P. *J. Am. Chem. Soc.* **2009**, *131* (50), 18036–18037.
- (249) Feng, W.; Li, L.; Yang, C.; Welle, A.; Trapp, O.; Levkin, P. A. *Angew. Chemie - Int. Ed.* **2015**, *54* (30), 8732–8735.
- (250) Li, Z.; Qian, L.; Li, L.; Bernhammer, J. C.; Huynh, H. V.; Lee, J. S.; Yao, S. Q. *Angew. Chemie - Int. Ed.* **2016**, *55* (6), 2002–2006.
- (251) Heiler, C.; Offenloch, J. T.; Blasco, E.; Barner-Kowollik, C. *ACS Macro Lett.* **2017**, *6* (1), 56–61.
- (252) Zhang, Y.; Liu, W.; Zhao, Z. *Molecules* **2014**, *19* (1), 306–315.
- (253) Kaupp, M.; Hildebrandt, K.; Trouillet, V.; Mueller, P.; Quick, A. S.; Wegener, M.; Barner-Kowollik, C. *Chem. Commun.* **2016**, *52* (9), 1975–1978.
- (254) Hildebrandt, K.; Kaupp, M.; Molle, E.; Menzel, J. P.; Blinco, J. P.; Barner-Kowollik, C. *Chem. Commun.* **2016**, *52* (60), 9426–9429.

- (255) Abt, D.; Schmidt, B. V. K. J.; Pop-Georgievski, O.; Quick, A. S.; Danilov, D.; Kostina, N. Y.; Bruns, M.; Wenzel, W.; Wegener, M.; Rodriguez-Emmenegger, C.; Barner-Kowollik, C. *Chem. - A Eur. J.* **2015**, *21* (38), 13186–13190.
- (256) Rodriguez-Emmenegger, C.; Preuss, C. M.; Yameen, B.; Pop-Georgievski, O.; Bachmann, M.; Mueller, J. O.; Bruns, M.; Goldmann, A. S.; Bastmeyer, M.; Barner-Kowollik, C. *Adv. Mater.* **2013**, *25* (42), 6123–6127.
- (257) Blasco, E.; Piñol, M.; Oriol, L.; Schmidt, B. V. K. J.; Welle, A.; Trouillet, V.; Bruns, M.; Barner-Kowollik, C. *Adv. Funct. Mater.* **2013**, *23* (32), 4011–4019.
- (258) Gegenhuber, T.; Abt, D.; Welle, A.; Özbek, S.; Goldmann, A. S.; Barner-Kowollik, C. *J. Mater. Chem. B* **2017**, *5* (25), 4993–5000.
- (259) Willenbacher, J.; Wuest, K. N. R.; Mueller, J. O.; Kaupp, M.; Wagenknecht, H.-A.; Barner-Kowollik, C. *ACS Macro Lett.* **2014**, *3* (6), 574–579.
- (260) Offenloch, J. T.; Willenbacher, J.; Tzvetkova, P.; Heiler, C.; Mutlu, H.; Barner-Kowollik, C. *Chem. Commun.* **2017**, *53* (4), 775–778.
- (261) Wang, C.; Zieger, M. M.; Schenzel, A.; Wegener, M.; Willenbacher, J.; Barner-Kowollik, C.; Bowman, C. N. *Adv. Funct. Mater.* **2017**, *27* (7), 1605317.
- (262) Hildebrandt, K.; Pauloehrl, T.; Blinco, J. P.; Linkert, K.; Börner, H. G.; Barner-Kowollik, C. *Angew. Chemie Int. Ed.* **2015**, *54* (9), 2838–2843.
- (263) Tischer, T.; Rodriguez-Emmenegger, C.; Trouillet, V.; Welle, A.; Schueler, V.; Mueller, J. O.; Goldmann, A. S.; Brynda, E.; Barner-Kowollik, C. *Adv. Mater.* **2014**, *26* (24), 4087–4092.
- (264) Stolzer, L.; Vigovskaya, A.; Barner-Kowollik, C.; Fruk, L. *Chem. - A Eur. J.* **2015**, *21* (41), 14309–14313.
- (265) Yang, N. C.; Rivas, C. *J. Am. Chem. Soc.* **1961**, *83* (9), 2213–2213.
- (266) Pauloehrl, T.; Delaittre, G.; Winkler, V.; Welle, A.; Bruns, M.; Börner, H. G.; Greiner, A. M.; Bastmeyer, M.; Barner-Kowollik, C. *Angew. Chemie Int. Ed.* **2012**, *51* (4), 1071–1074.
- (267) Kessar, S. V.; Singh, T.; Mankotia, A. K. S. *J. Chem. Soc., Chem. Commun.* **1989**, No. 21, 1692–1693.
- (268) Lin, C.; Zhen, L.; Cheng, Y.; Du, H.-J.; Zhao, H.; Wen, X.; Kong, L.-Y.; Xu, Q.-L.; Sun, H. *Org. Lett.* **2015**, *17* (11), 2684–2687.
- (269) Arai, N.; Ohkuma, T. *J. Org. Chem.* **2017**, *82* (14), 7628–7636.
- (270) Arumugam, S.; Popik, V. V. *J. Am. Chem. Soc.* **2011**, *133* (39), 15730–15736.
- (271) Glassner, M.; Oehlenschlaeger, K. K.; Welle, A.; Bruns, M.; Barner-Kowollik, C. *Chem. Commun.* **2013**, *49* (6), 633–635.
- (272) Tuten, B. T.; Menzel, J. P.; Pahnke, K.; Blinco, J. P.; Barner-Kowollik, C. *Chem. Commun.* **2017**, *53* (32), 4501–4504.

- (273) Maurer, D. P.; Fan, R.; Thamattoor, D. M. *Angew. Chemie Int. Ed.* **2017**, *56* (16), 4499–4501.
- (274) Gruending, T.; Oehlenschlaeger, K. K.; Frick, E.; Glassner, M.; Schmid, C.; Barner-Kowollik, C. *Macromol. Rapid Commun.* **2011**, *32* (11), 807–812.
- (275) Sammes, P. G. *Tetrahedron* **1976**, *32* (4), 405–422.
- (276) Porter, G.; Tchir, M. F. *J. Chem. Soc. D Chem. Commun.* **1970**, *6* (20), 1372–1373.
- (277) Ishida, N.; Yano, T.; Yuhki, T.; Murakami, M. *Chem. - An Asian J.* **2017**, *12* (15), 1905–1908.
- (278) Yates, P.; Mackay, A. C.; Garneau, F. X. *Tetrahedron Lett.* **1968**, *9* (52), 5389–5392.
- (279) Findlay, D. M.; Tchir, M. F. *J. Chem. Soc. Chem. Commun.* **1974**, No. 13, 514–515.
- (280) Hildebrandt, K.; Elies, K.; D'hooge, D. R.; Blinco, J. P.; Barner-Kowollik, C. *J. Am. Chem. Soc.* **2016**, *138* (22), 7048–7054.
- (281) Tischer, T.; Claus, T. K.; Bruns, M.; Trouillet, V.; Linkert, K.; Rodriguez-Emmenegger, C.; Goldmann, A. S.; Perrier, S.; Börner, H. G.; Barner-Kowollik, C. *Biomacromolecules* **2013**, *14* (12), 4340–4350.
- (282) Richter, B.; Pauloehrl, T.; Kaschke, J.; Fichtner, D.; Fischer, J.; Greiner, A. M.; Wedlich, D.; Wegener, M.; Delaittre, G.; Barner-Kowollik, C.; Bastmeyer, M. *Adv. Mater.* **2013**, *25* (42), 6117–6122.
- (283) Preuss, C. M.; Tischer, T.; Rodriguez-Emmenegger, C.; Zieger, M. M.; Bruns, M.; Goldmann, A. S.; Barner-Kowollik, C. *J. Mater. Chem. B* **2014**, *2* (1), 36–40.
- (284) Delaittre, G.; Goldmann, A. S.; Mueller, J. O.; Barner-Kowollik, C. *Angew. Chemie - Int. Ed.* **2015**, *54* (39), 11388–11403.
- (285) Glassner, M.; Oehlenschlaeger, K. K.; Gruending, T.; Barner-Kowollik, C. *Macromolecules* **2011**, *44* (12), 4681–4689.
- (286) Winkler, M.; Mueller, J. O.; Oehlenschlaeger, K. K.; Montero De Espinosa, L.; Meier, M. A. R.; Barner-Kowollik, C. *Macromolecules* **2012**, *45* (12), 5012–5019.
- (287) Hirschbiel, A. F.; Konrad, W.; Schulze-Sünninghausen, D.; Wiedmann, S.; Luy, B.; Schmidt, B. V. K. J.; Barner-Kowollik, C. *ACS Macro Lett.* **2015**, *4* (10), 1062–1066.
- (288) Steinkoenig, J.; Bloesser, F. R.; Huber, B.; Welle, A.; Trouillet, V.; Weidner, S. M.; Barner, L.; Roesky, P. W.; Yuan, J.; Goldmann, A. S.; Barner-Kowollik, C. *Polym. Chem.* **2016**, *7*, 451–461.
- (289) Altintas, O.; Willenbacher, J.; Wuest, K. N. R.; Oehlenschlaeger, K. K.; Krolla-Sidenstein, P.; Gliemann, H.; Barner-Kowollik, C. *Macromolecules* **2013**, *46* (20), 8092–8101.
- (290) Stolzer, L.; Ahmed, I.; Rodriguez-Emmenegger, C.; Trouillet, V.; Bockstaller, P.; Barner-Kowollik, C.; Fruk, L. *Chem. Commun.* **2014**, *50* (34), 4430–4433.

- (291) Kerbs, A.; Mueller, P.; Kaupp, M.; Ahmed, I.; Quick, A. S.; Abt, D.; Wegener, M.; Niemeyer, C. M.; Barner-Kowollik, C.; Fruk, L. *Chem. - A Eur. J.* **2017**, *23* (21), 4990–4994.
- (292) Vigovskaya, A.; Abt, D.; Ahmed, I.; Niemeyer, C. M.; Barner-Kowollik, C.; Fruk, L. *J. Mater. Chem. B* **2016**, *4* (3), 442–449.
- (293) Stolzer, L.; Quick, A. S.; Abt, D.; Welle, A.; Naumenko, D.; Lazzarino, M.; Wegener, M.; Barner-Kowollik, C.; Fruk, L. *Chem. Commun.* **2015**, *51* (16), 3363–3366.
- (294) Richter, B.; Hahn, V.; Bertels, S.; Claus, T. K.; Wegener, M.; Delaittre, G.; Barner-Kowollik, C.; Bastmeyer, M. *Adv. Mater.* **2017**, *29* (5), 1604342.
- (295) Mueller, P.; Zieger, M. M.; Richter, B.; Quick, A. S.; Fischer, J.; Mueller, J. B.; Zhou, L.; Nienhaus, G. U.; Bastmeyer, M.; Barner-Kowollik, C.; Wegener, M. *ACS Nano* **2017**, *11* (6), 6396–6403.
- (296) Zydziak, N.; Feist, F.; Huber, B.; Mueller, J. O.; Barner-Kowollik, C. *Chem. Commun.* **2015**, *51* (10), 1799–1802.
- (297) Zydziak, N.; Konrad, W.; Feist, F.; Afonin, S.; Weidner, S.; Barner-Kowollik, C. *Nat. Commun.* **2016**, *7*, 13672.
- (298) Wuest, K. N. R.; Trouillet, V.; Köppe, R.; Roesky, P. W.; Goldmann, A. S.; Stenzel, M. H.; Barner-Kowollik, C. *Polym. Chem.* **2017**, *8* (5), 838–842.
- (299) Kühni, J.; Belser, P. *Org. Lett.* **2007**, *9* (10), 1915–1918.
- (300) Pauloehrl, T.; Delaittre, G.; Bruns, M.; Meißler, M.; Börner, H. G.; Bastmeyer, M.; Barner-Kowollik, C. *Angew. Chemie Int. Ed.* **2012**, *51* (36), 9181–9184.
- (301) Mueller, J. O.; Schmidt, F. G.; Blinco, J. P.; Barner-Kowollik, C. *Angew. Chemie Int. Ed.* **2015**, *54* (35), 10284–10288.
- (302) Chen, Y.; Wu, J.-D. *J. Polym. Sci. Part A Polym. Chem.* **1994**, *32* (10), 1867–1875.
- (303) Pauloehrl, T.; Welle, A.; Bruns, M.; Linkert, K.; Börner, H. G.; Bastmeyer, M.; Delaittre, G.; Barner-Kowollik, C. *Angew. Chemie Int. Ed.* **2013**, *52* (37), 9714–9718.
- (304) Fages, F.; Desvergne, J.; Frisch, I.; Bouas-Laurent, H. *J. Chem. Soc., Chem. Commun.* **1988**, No. 21, 1413–1415.
- (305) Schreier, W. J.; Schrader, T. E.; Koller, F. O.; Gilch, P.; Crespo-Hernández, C. E.; Swaminathan, V. N.; Carell, T.; Zinth, W.; Kohler, B. *Science* **2007**, *315* (5812), 625–629.
- (306) Wagner, P. J.; Lindstrom, M. J. *J. Am. Chem. Soc.* **1987**, *109* (10), 3062–3067.
- (307) Frisch, H.; Marschner, D.; Goldmann, A.; Barner-Kowollik, C. *Angew. Chemie Int. Ed.* **2017**, in press.
- (308) Lejars, M.; Margailan, A.; Bressy, C. *Chem. Rev.* **2012**, *112* (8), 4347–4390.
- (309) Blaszykowski, C.; Sheikh, S.; Thompson, M. *Chem. Soc. Rev.* **2012**, *41* (17), 5599–

- 5612.
- (310) Stetsovych, O.; Švec, M.; Vacek, J.; Chocholoušová, J. V.; Jančařík, A.; Rybáček, J.; Kosmider, K.; Stará, I. G.; Jelínek, P.; Starý, I. *Nat. Chem.* **2016**, *9* (3), 213–218.
- (311) Wedler-Jasinski, N.; Delbosc, N.; Virolleaud, M.-A.; Montarnal, D.; Welle, A.; Barner, L.; Walther, A.; Bernard, J.; Barner-Kowollik, C. *Chem. Commun.* **2016**, *52* (56), 8753–8756.
- (312) Prins, L. J.; Reinhoudt, D. N.; Timmerman, P. *Angew. Chemie Int. Ed.* **2001**, *40* (13), 2382–2426.
- (313) Preuss, C. M.; Goldmann, A. S.; Trouillet, V.; Walther, A.; Barner-Kowollik, C. *Macromol. Rapid Commun.* **2013**, *34* (8), 640–644.
- (314) Arumugam, S.; Orski, S. V.; Locklin, J.; Popik, V. V. *J. Am. Chem. Soc.* **2012**, *134* (1), 179–182.
- (315) Arumugam, S.; Popik, V. V. *J. Am. Chem. Soc.* **2012**, *134* (20), 8408–8411.
- (316) Berg, J. M.; Tymoczko, J. L.; Stryer, L. *Stryer Biochemie*; Springer Berlin Heidelberg: Berlin, Heidelberg, 2013.
- (317) Winter, G.; Todd, C. D.; Trovato, M.; Forlani, G.; Funck, D. *Front. Plant Sci.* **2015**, *6* (534), 1–14.
- (318) Zhang, W. H.; Otting, G.; Jackson, C. J. *Curr. Opin. Struct. Biol.* **2013**, *23* (4), 581–587.
- (319) Connor, R. E.; Tirrell, D. A. *Polym. Rev.* **2007**, *47* (1), 9–28.
- (320) Foster, A. W.; Osman, D.; Robinson, N. J. *J. Biol. Chem.* **2014**, *289* (41), 28095–28103.
- (321) Dobson, C. M. *Nature* **2003**, *426* (6968), 884–890.
- (322) Merrifield, R. *J. Am. Chem. Soc.* **1963**, *85* (14), 2149–2154.
- (323) Amblard, M.; Fehrentz, J.-A.; Martinez, J.; Subra, G. In *Peptide Synthesis and Applications*; Humana Press: Totowa, NJ, 2005; Vol. 298, pp 3–24.
- (324) Hackenberger, C. P. R.; Schwarzer, D. *Angew. Chemie - Int. Ed.* **2008**, *47* (52), 10030–10074.
- (325) Isidro-Llobet, A.; Álvarez, M.; Albericio, F. *Chem. Rev.* **2009**, *109* (6), 2455–2504.
- (326) Coin, I.; Beyermann, M.; Bienert, M. *Nat. Protoc.* **2007**, *2* (12), 3247–3256.
- (327) Fodor, S.; Read, J.; Pirrung, M.; Stryer, L.; Lu, A.; Solas, D. *Science* **1991**, *251* (4995), 767–773.
- (328) Regnier, F. E. *Anal. Chem.* **1983**, *55* (13), 1298A–1306A.
- (329) Hansen, P. R.; Oddo, A. In *Methods in Molecular Biology*; 2015; Vol. 1348, pp 33–50.
- (330) Thakkar, A.; Trinh, T. B.; Pei, D. *ACS Comb. Sci.* **2013**, *15* (2), 120–129.
- (331) Abdel-Aal, A. B. M.; Papageorgiou, G.; Raz, R.; Quibell, M.; Burlina, F.; Offer, J. J.

- Pept. Sci.* **2016**, 22 (5), 360–367.
- (332) Tomiuk, J.; Loeschcke, V. *Grundlagen der Evolutionsbiologie und Formalen Genetik*; Springer Berlin Heidelberg: Berlin, Heidelberg, 2017.
- (333) Fujishima, K.; Kanai, A. *Front. Genet.* **2014**, 5 (142), 1–11.
- (334) Balbás, P.; Lorence, A. *Recombinant Gene Expression*, 3rd ed.; Lorence, A., Ed.; Methods in Molecular Biology; Humana Press: Totowa, NJ, 2012; Vol. 824.
- (335) Rosano, G. L.; Ceccarelli, E. A. *Recombinant protein expression in microbial systems*; Rosano, G. L., Ceccarelli, E. A., Eds.; Frontiers Research Topics; Frontiers Media SA, 2014.
- (336) Bucciantini, M.; Giannoni, E.; Chiti, F.; Baroni, F.; Formigli, L.; Zurdo, J.; Taddei, N.; Ramponi, G.; Dobson, C. M.; Stefani, M. *Nature* **2002**, 416 (6880), 507–511.
- (337) Zaretsky, J. Z.; Wreschner, D. H. *Transl. Oncogenomics* **2008**, 2008 (3), 99–136.
- (338) Meier, S.; Jensen, P. R.; Adamczyk, P.; Bächinger, H. P.; Holstein, T. W.; Engel, J.; Ozbek, S.; Grzesiek, S. *J. Mol. Biol.* **2007**, 368 (3), 718–728.
- (339) Pokidysheva, E.; Milbradt, A. G.; Meier, S.; Renner, C.; Haussinger, D.; Bachinger, H. P.; Moroder, L.; Grzesiek, S.; Holstein, T. W.; Ozbek, S.; Engel, J. *J. Biol. Chem.* **2004**, 279 (29), 30395–30401.
- (340) Beckmann, A.; Özbek, S. *Int. J. Dev. Biol.* **2012**, 56 (6–8), 577–582.
- (341) David, C. N.; Özbek, S.; Adamczyk, P.; Meier, S.; Pauly, B.; Chapman, J.; Hwang, J. S.; Gojobori, T.; Holstein, T. W. *Trends Genet.* **2008**, 24 (9), 431–438.
- (342) Tursch, A.; Mercadante, D.; Tennigkeit, J.; Gräter, F.; Özbek, S. *Sci. Rep.* **2016**, 6 (1), 25709.
- (343) Meier, S.; Jensen, P. R.; David, C. N.; Chapman, J.; Holstein, T. W.; Grzesiek, S.; Ozbek, S. *Curr. Biol.* **2007**, 17 (2), 173–178.
- (344) Anfinsen, C. B. *Science* **1973**, 181 (4096), 223–230.
- (345) Ruiz-Hitzky, E.; Darder, M.; Aranda, P.; Ariga, K. *Adv. Mater.* **2010**, 22 (3), 323–336.
- (346) González-Valdez, J.; Rito-Palomares, M.; Benavides, J. *Anal. Bioanal. Chem.* **2012**, 403 (8), 2225–2235.
- (347) Canalle, L. A.; Löwik, D. W. P. M.; van Hest, J. C. M. *Chem. Soc. Rev.* **2010**, 39 (1), 329–353.
- (348) Crivat, G.; Taraska, J. W. *Trends Biotechnol.* **2012**, 30 (1), 8–16.
- (349) Altman, G. H.; Diaz, F.; Jakuba, C.; Calabro, T.; Horan, R. L.; Chen, J.; Lu, H.; Richmond, J.; Kaplan, D. L. *Biomaterials* **2003**, 24 (3), 401–416.
- (350) Ihara, T.; Fujii, T.; Mukae, M.; Kitamura, Y.; Jyo, A. *J. Am. Chem. Soc.* **2004**, 126 (29), 8880–8881.
- (351) Gauthier, M. A.; Klok, H.-A. *Chem. Commun.* **2008**, 32 (23), 2591–2611.

- (352) Das, A.; Theato, P. *Chem. Rev.* **2016**, *116* (3), 1434–1495.
- (353) Adamczyk, M.; Fishpaugh, J. R.; Heuser, K. J. *Bioconjug. Chem.* **1997**, *8* (2), 253–255.
- (354) Mädler, S.; Bich, C.; Touboul, D.; Zenobi, R. *J. Mass Spectrom.* **2009**, *44* (5), 694–706.
- (355) Figueiras, A.; Hombach, J.; Veiga, F.; Bernkop-Schnürch, A. *Eur. J. Pharm. Biopharm.* **2009**, *71* (2), 339–345.
- (356) Li, Y.; Duong, H. T. T.; Jones, M. W.; Basuki, J. S.; Hu, J.; Boyer, C.; Davis, T. P. *ACS Macro Lett.* **2013**, *2* (10), 912–917.
- (357) Tsumoto, H.; Takahashi, K.; Suzuki, T.; Nakagawa, H.; Kohda, K.; Miyata, N. *Bioorganic Med. Chem. Lett.* **2008**, *18* (2), 657–660.
- (358) Carter, M. C. D.; Lynn, D. M. *Chem. Mater.* **2016**, *28* (14), 5063–5072.
- (359) Nicolas, J.; Mantovani, G.; Haddleton, D. M. *Macromol. Rapid Commun.* **2007**, *28* (10), 1083–1111.
- (360) Boere, K. W. M.; Van Den Dikkenberg, J.; Gao, Y.; Visser, J.; Hennink, W. E.; Vermonden, T. *Biomacromolecules* **2015**, *16* (9), 2840–2851.
- (361) Caliceti, P.; Schiavon, O.; Sartore, L.; Monfardini, C.; Veronese, F. M. *J. Bioact. Compat. Polym.* **1993**, *8* (1), 41–50.
- (362) Salmaso, S.; Semenzato, A.; Bersania, S.; Chinol, M.; Paganelli, G.; Caliceti, P. *Biochim. Biophys. Acta - Gen. Subj.* **2005**, *1726* (1), 57–66.
- (363) Gong, Y.; Leroux, J.-C. C.; Gauthier, M. a. *Bioconjug. Chem.* **2015**, *26* (7), 1179–1181.
- (364) Brosnan, S. M.; Schlaad, H. *Polymer* **2014**, *55* (22), 5511–5516.
- (365) Schilling, C. I.; Jung, N.; Biskup, M.; Schepers, U.; Bräse, S. *Chem. Soc. Rev.* **2011**, *40*, 4840–4871.
- (366) Conradi, M.; Ramakers, G.; Junkers, T. *Macromol. Rapid Commun.* **2016**, *37* (2), 174–180.
- (367) Huisgen, R. *Angew. Chemie* **1963**, *75* (13), 604–637.
- (368) Iha, R. K.; Wooley, K. L.; Nyström, A. M.; Burke, D. J.; Kade, M. J.; Hawker, C. J. *Chem. Rev.* **2009**, *109* (11), 5620–5686.
- (369) Jawalekar, A. M.; Malik, S.; Verkade, J. M. M.; Gibson, B.; Barta, N. S.; Hodges, J. C.; Rowan, A.; Van Delft, F. L. *Molecules* **2013**, *18* (7), 7346–7363.
- (370) Merkel, M.; Arndt, S.; Ploschik, D.; Cserép, G. B.; Wenge, U.; Kele, P.; Wagenknecht, H. A. *J. Org. Chem.* **2016**, *81* (17), 7527–7538.
- (371) Saxon, E.; Armstrong, J. I.; Bertozzi, C. R. *Org. Lett.* **2000**, *2* (14), 2141–2143.
- (372) Chaffey-Millar, H.; Stewart, D.; Chakravarty, M. M. T.; Keller, G.; Barner-Kowollik, C. *Macromol. Theory Simulations* **2007**, *16* (6), 575–592.

- (373) Ren, X.; Rinke, P.; Joas, C.; Scheffler, M. *J. Mater. Sci.* **2012**, *47* (21), 7447–7471.
- (374) Doherty, D. C.; Holmes, B. N.; Leung, P.; Ross, R. B. *Comput. Theor. Polym. Sci.* **1998**, *8* (1–2), 169–178.
- (375) Van Steenberge, P. H. M.; D'hooge, D. R.; Wang, Y.; Zhong, M.; Reyniers, M.-F.; Konkolewicz, D.; Matyjaszewski, K.; Marin, G. B. *Macromolecules* **2012**, *45* (21), 8519–8531.
- (376) Platkowski, K.; Reichert, K.-H. *Chemie Ing. Tech.* **1997**, *69* (4), 513–516.
- (377) Martinez-Urreaga, J.; Mira, J.; Gonzalez-Fernandez, C. *Chem. Eng. Educ.* **2003**, *37* (1), 14–19.
- (378) Brandão, A. L. T.; Soares, J. B. P.; Pinto, J. C.; Alberton, A. L. *Macromol. React. Eng.* **2015**, *9* (3), 141–185.
- (379) Elowitz, M. B. *Science* **2002**, *297* (5584), 1183–1186.
- (380) Drache, M.; Drache, G. *Polymers* **2012**, *4* (4), 1416–1442.
- (381) Gegenhuber, T.; De Keer, L.; Goldmann, A. S.; Van Steenberge, P. H. M.; Mueller, J. O.; Reyniers, M.-F.; Menzel, J. P.; D'hooge, D. R.; Barner-Kowollik, C. *Macromolecules* **2017**, *50* (17), 6451–6467.
- (382) Van Steenberge, P. H. M.; D'hooge, D. R.; Reyniers, M.-F.; Marin, G. B. *Chem. Eng. Sci.* **2014**, *110*, 185–199.
- (383) Van Steenberge, P. H. M.; Vandenberghe, J.; D'hooge, D. R.; Reyniers, M.-F.; Adriaensens, P. J.; Lutsen, L.; Vanderzande, D. J. M.; Marin, G. B. *Macromolecules* **2011**, *44* (22), 8716–8726.
- (384) D'hooge, D. R.; Van Steenberge, P. H. M.; Reyniers, M. F.; Marin, G. B. *Prog. Polym. Sci.* **2015**, *58*, 59–89.
- (385) Derboven, P.; Van Steenberge, P. H. M.; Reyniers, M. F.; Barner-Kowollik, C.; D'hooge, D. R.; Marin, G. B. *Macromol. Theory Simulations* **2016**, *25* (2), 104–115.
- (386) Destarac, M. *Polym. Rev.* **2011**, *51* (2), 163–187.
- (387) Moad, G.; Chiefari, J.; Chong, (Bill) Y. K.; Krstina, J.; Mayadunne, R. T. A.; Postma, A.; Rizzardo, E.; Thang, S. H. *Polym. Int.* **2000**, *49* (9), 993–1001.
- (388) Hernández-Ortiz, J. C.; Van Steenberge, P. H. M.; Reyniers, M.-F.; Marin, G. B.; D'hooge, D. R.; Duchateau, J. N. E.; Remerie, K.; Toloza, C.; Vaz, A. L.; Schreurs, F. *AIChE J.* **2017**, *61* (3), 1–15.
- (389) D'hooge, D. R.; Reyniers, M.-F.; Marin, G. B. *Macromol. React. Eng.* **2013**, *7* (8), 362–379.
- (390) Johnston-Hall, G.; Monteiro, M. J. *J. Polym. Sci. Part A Polym. Chem.* **2008**, *46* (10), 3155–3173.
- (391) Choi, K. Y.; McAuley, K. B. In *Polymer Reaction Engineering*; Blackwell Publishing Ltd: Oxford, UK; pp 273–314.

-
- (392) Gegenhuber, T.; Schenzel, A. M.; Goldmann, A. S.; Zetterlund, P. B.; Barner-Kowollik, C. *Chem. Commun.* **2017**, 53 (77), 10648–10651.
- (393) Kumar, S. N.; Yu, I. F.; Chein, R.-J. *Org. Lett.* **2017**, 19 (1), 22–25.
- (394) am Ende, D. J.; Whritenour, D. C.; Coe, J. W. *Org. Process Res. Dev.* **2007**, 11 (6), 1141–1146.
- (395) Baynes, B. M.; Wang, D. I. C.; Trout, B. L. *Biochemistry* **2005**, 44 (12), 4919–4925.
- (396) Gendron, R. AL; Berg, D. J.; Barclay, T. *Can. J. Chem.* **2002**, 80 (10), 1285–1292.
- (397) Michel, R.; Castner, D. G. *Surf. Interface Anal.* **2006**, 38 (11), 1386–1392.
- (398) Culver, H. R.; Clegg, J. R.; Peppas, N. A. *Acc. Chem. Res.* **2017**, 50 (2), 170–178.
- (399) Li, L.; Feng, W.; Welle, A.; Levkin, P. A. *Angew. Chemie - Int. Ed.* **2016**, 55 (44), 13765–13769.
- (400) Yoshizawa, M. *Science* **2006**, 312 (5771), 251–254.
- (401) McKay, C. S.; Finn, M. G. *Chem. Biol.* **2014**, 21 (9), 1075–1101.
- (402) Jewett, J. C.; Bertozzi, C. R. *Chem. Soc. Rev.* **2010**, 39 (4), 1272–1279.
- (403) Tona, V.; de la Torre, A.; Padmanaban, M.; Ruider, S.; González, L.; Maulide, N. *J. Am. Chem. Soc.* **2016**, 138 (27), 8348–8351.
- (404) Peled, A.; Naddaka, M.; Lellouche, J.-P. *J. Mater. Chem.* **2011**, 21 (31), 11511–11517.
- (405) Nguyen, D.; Zondanos, H. S.; Farrugia, J. M.; Serelis, A. K.; Such, C. H.; Hawkett, B. S. *Langmuir* **2008**, 24 (5), 2140–2150.
- (406) Haag, R.; Wirz, J.; Wagner, P. J. *Helv. Chim. Acta* **1977**, 60 (8), 2595–2607.
- (407) Parnis, J. M.; Oldham, K. B. *J. Photochem. Photobiol. A Chem.* **2013**, 267, 6–10.

LIST OF ALL PUBLICATIONS AND CONFERENCE CONTRIBUTIONS

Publications

- (1) Gegenhuber, T.; Gröschel, A. H.; Löbling, T. I.; Drechsler, M.; Ehlert, S.; Förster, S.; Schmalz, H. Noncovalent Grafting of Carbon Nanotubes with Triblock Terpolymers: Toward Patchy 1D Hybrids. *Macromolecules* **2015**, *48*, 1767–1776.
- (2) Gegenhuber, T.; Krekhova, M.; Schöbel, J.; Gröschel, A. H.; Schmalz, H. “Patchy” Carbon Nanotubes as Efficient Compatibilizers for Polymer Blends. *ACS Macro Lett.* **2016**, *5*, 306–310.
- (3) Estupiñán, D.; Gegenhuber, T.; Blinco, J. P.; Barner-Kowollik, C.; Barner, L. Self-Reporting Fluorescent Step-Growth RAFT Polymers Based on Nitrile Imine-Mediated Tetrazole-Ene Cycloaddition Chemistry. *ACS Macro Lett.* **2017**, *6*, 229–234.
- (4) Gegenhuber, T.; Abt, D.; Welle, A.; Özbek, S.; Goldmann, A. S.; Barner-Kowollik, C. Spatially Resolved Photochemical Coding of Reversibly Anchored Cysteine-Rich Domains. *J. Mater. Chem. B* **2017**, *5*, 4993–5000.
- (5) Gegenhuber, T.[§]; De Keer, L.[§]; Goldmann, A. S.; Van Steenberge, P. H. M.; Mueller, J. O.; Reyniers, M.-F.; Menzel, J. P.; D’hooge, D. R.; Barner-Kowollik, C. Fusing Light-Induced Step-Growth Processes with RAFT Chemistry for Segmented Copolymer Synthesis: A Synergetic Experimental and Kinetic Modeling Study. *Macromolecules* **2017**, *50*, 6451–6467.
- (6) Gegenhuber, T.; Schenzel, A. M.; Goldmann, A. S.; Zetterlund, P. B.; Barner-Kowollik, C. A Facile Route to Segmented Copolymers by Fusing Ambient Temperature Step-Growth and RAFT Polymerization. *Chem. Commun.* **2017**, *53*, 10648–10651.

Contributions to Conferences

- (1) T. Gegenhuber, L. De Keer, A. S. Goldmann, P.H.M. Van Steenberge, M.F. Reyniers, D. R. D’hooge, C. Barner-Kowollik *Step-Growth polymers as MACRO chain transfer agents – an experimental and theoretical study*, 14th Annual UNESCO/IUPAC Workshop and Conference on Macromolecules & Materials, Stellenbosch South Africa, **April 2017**, oral presentation.

[§]: T.G. and L.d.K. contributed equally.

CURRICULUM VITAE

Not available in the electronic version.

ACKNOWLEDGEMENTS DANKSAGUNG

Zum Schluss möchte ich noch ein paar Menschen danken, die mich während meiner Doktorarbeit unterstützt haben bzw. mit denen ich zusammengearbeitet habe. Als erstes danke ich meinem Betreuer Christopher Barner-Kowollik für seine aufopferungsvolle Art, mit der wir auch bei größten Problemen Lösungen gefunden haben. Gleichzeitig danke ich Anja Goldmann für die Ko-Betreuung. Zusammen haben wir v.a. im Jahr 2017 noch (fast) alle unsere Ziele erreicht. Vielen Dank für Eure Geduld und Eure Zeit!

Ich danke der Baden-Württemberg-Stiftung für die Finanzierung meiner Doktorarbeit, sowie Hr. Awenius für die Betreuung als Vertreter der Stiftung. Gleichzeitig danke ich unseren Kooperationspartnern an der Ruprecht-Karls-Universität Heidelberg Hr. Dr. Suat Özbek, sowie Theresa Bentele für die Kooperation im CRD Projekt. Dem Studiengang *Macromolecular Science* an der Universität Bayreuth danke ich für die langjährige Mitgliedschaft im Elitenetzwerk Bayern, den damit verbundenen spannenden Seminaren bzw. für die Reisemittel für meinen Auslandsaufenthalt in Australien.

Keine Doktorarbeit wäre möglich ohne gute Kolleginnen und Kollegen. Ich danke allen aktuellen und ehemaligen Macroarcians, seien es Labor-, Büro- und/oder Kooperationspartnern, für die vielen wissenschaftlichen Diskussionen, sowie der ein oder anderen ruhigen Stunde bei gemeinsamen Grillabenden und natürlich Doktorfeiern! Meinen Laborkollegen danke ich für die komplett durchorganisierte und super Stimmung in 3.22, wodurch das Arbeiten dort immer Spaß gemacht hat. To the proof readers of my thesis, thank you for inspiring comments, troubleshooting and for finding many typos/errors in my my supervision.

To my friends at the KIT, I really appreciated the time we spent together, for all the support in hard times but also the fun we had in the good times together. Because of you, there was another reason to come to work. Somehow everybody spread or left within the last years, but I hope we can keep in contact, as we already did beyond different continents and time zones!

Von der administrativen Seite danke ich Evelyn, Fr. Schneider, Vincent und Katharina für ihre Arbeit rund um die Arbeitsgruppe, ohne die die Organisation nicht laufen würde.

To my colleagues and cooperation partners Lies, Dagmar and Paul in Ghent, thank you for your complex contribution to our polymerization reactions! I guess our project really hit it off.

I highly appreciate my colleagues and cooperation partners at the UNSW in Sydney, especially Per Zetterlund for hosting my terrific stay in Australia and Florent for our joint venture. I also highly appreciate my friends in Sydney, thank you for the nice time we spent

together, either at the lab, office, lunch tables, field trips or some occasional beers! I will never forget this awesome and special experience.

Viele Grüße an die Großen 10, die Wilde 13, meine (wechselhafte) aber tolle Klettergruppe, die Fußball-Gruppe für Ablenkung und ein paar außerberufliche Aktivitäten. Zum Ende hin danke ich meinem Freundeskreis aus der pfälzischen Heimat, danke für Euren Support über Jahre hinweg. Gerade wenn es in Karlsruhe einmal nicht so lief, konnte ich bei Euch immer Kraft tanken und den Stress für gewisse Zeit vergessen, auf Euch war und ist immer Verlass!

Wenn man eines nicht vergessen sollte, dann woher man kommt. Daher gilt nun ganz am Ende mein allergrößter Dank meinen Eltern für finanzielle sowie psychologische Unterstützung. Ihr habt mir nicht nur das Studium zuvor schon ermöglicht, sondern auch die Möglichkeit gegeben, jetzt noch den Dokortitel in Angriff zu nehmen. Zurückzahlen kann ich das niemals, ich bin einfach nur froh, weiß aber dass ich das zu einem Gros Euch zu verdanken habe. Meinen anderen Familienmitgliedern in Römerberg, danke für die Unterstützung, meinem kleinen Baby-Neffen/Patenkind hoffe ich einmal ähnlich zur Seite stehen zu können. Nach fast 10 Jahren von Zuhause weg, mal sehen wohin die Reise weitergeht.

*„Es ist Sommer und es ist heiß,
da ess´ ich ein Zitroneneis“*

From "Zitroneneis" – Die Ärzte